MAX-PLANCK-INSTITUT FÜR RADIOASTRONOMIE
BONN

GLOSTAR

Investigating Tracers of Early High-Mass Star Formation

HANS VIETVIET NGUYEN

2022

MAX-PLANCK-INSTITUT FÜR RADIOASTRONOMIE
BONN

GLOSTAR: Investigating Tracers of Early High-Mass Star Formation

Dissertation

zur

Erlangung des Doktorgrades (*Dr. rer. nat.*)

der

Mathematisch-Naturwissenschaftlichen Fakultät

der

Rheinischen Friedrich–Wilhelms–Universität, Bonn

vorgelegt von
Hans Vietviet NGUYEN
aus
Pembroke, Canada

Bonn 2022

Angefertigt mit Genehmigung der Mathematisch-Naturwissenschaftlichen Fakultät der Rheinischen Friedrich–Wilhelms–Universität Bonn
Prepared with the permission from the Faculty of Mathematics and Natural Sciences of the University of Bonn

1. Referent / *First Referee*: Prof. Dr. Karl M. Menten
2. Referent / *Second Referee*: Prof. Dr. Pavel Kroupa

Tag der Promotion / *Conferral Date*: 2023.04.18
Erscheinungsjahr / *Year of Publication*: 2023

To my family

Luận án này con xin kính tặng Ông Ngoại, Bà Ngoại, và Bà Nội cua con

"It is important to draw wisdom from many different places. If we take it from only one place, it becomes rigid and stale."

&

"Sometimes life is like this dark tunnel, you can't always see the light at the end of the tunnel, but if you just keep moving, you will come to a better place."

Iroh
Avatar: The Last Airbender

RHEINISCHE FRIEDRICH–WILHELMS–UNIVERSITÄT BONN

Abstract

by Hans Nguyen

for the degree of

Doctor rerum naturalium

High-mass stars ($>8\,M_\odot$) are not as numerous as their less massive counterparts but have a much more profound impact on their environment within their native galaxies. They inject a large amount of energy into the interstellar medium (ISM) and enrich their surroundings with heavy elements that in turn play a role in the star formation process. Despite their importance, our understanding of their formation process is not as developed as that of low-mass stars. This thesis focuses on studying tracers of high-mass star formation, as by developing an understanding of the environments and conditions of the birthplaces of these massive objects, we can better understand high-mass stars and their impact on their surroundings. In particular, we use data obtained as part of the GLObal view on STAR formation (GLOSTAR) survey using the *Karl G. Jansky* Very Large Array (VLA) to complete these studies.

The term massive young stellar object (MYSO) has been used to describe a wide range of evolutionary stages. They start as objects that are still deeply embedded in their parental dense molecular cloud core and can be detected through the use of near-infrared (NIR) photometry. As they develop, they start to ionise their surroundings and eventually form into compact HII regions (for which we use radio data to detect in this thesis). The HII region phase, gives a clear indication that, in particular, 'high-mass' star formation has recently occurred.The first topic on this thesis investigates the presence of YSOs with HII regions detected with centimetre radio wavelength data as it is unknown how many of the NIR identified YSOs trace HII regions. We provide a census of this inside the region known as the central molecular zone (CMZ) as the unique conditions in the CMZ make for an interesting laboratory to study high-mass star formation in an extreme environment. Our results show that the majority of these NIR-identified YSOs lack VLA radio counterparts. This suggests that these sources may not be sufficiently evolved to feature signs of HII regions. However, we find that since most of these sources also lack dust emission, it is more likely that they are older and have dispersed their natal clouds.

The 6.7 GHz methanol (CH_3OH) maser has been shown to be an exclusive tracer of the earliest stages of high-mass star formation. A census of 6.7 GHz CH_3OH masers can be used to compile a complete sample of the birthplaces of high-mass stars within our Galaxy. Many surveys have been conducted to obtain such a sample. With the upgrades to the VLA, GLOSTAR can provide the most sensitive unbiased survey of 6.7 GHz CH_3OH masers to date. As part of this thesis, we produce a catalogue within the region covered by -2° to 60° in Galactic longitude and $\pm1^\circ$ in Galactic latitudes using the

VLA D-configuration data. Due to the improved sensitivity of the GLOSTAR survey, we are able to detect many new masers which we use to study the environments of early high-mass star formation by using ancillary dust continuum and radio continuum data. In comparing with ATLASGAL 870 μm compact source catalogue, we find that the newly detected masers are more likely to be associated with less massive stars. From the radio continuum data, by comparing the radio source and maser flux distributions, we find no correlation with respect to angular offset, suggesting that the maser and radio source are powered by unrelated mechanisms.

The data taken for GLOSTAR using the VLA is obtained in two configurations of the array, both D-configuration and B-configuration which were observed in two separate epochs. The higher resolution of the B-configuration allows for the distinction of multiple masers from a given maser in the D-configuration and provides better positional accuracy of the maser. Additionally, the access to two epochs of observations allows us to study the time variability of the maser emission. We produce a catalogue for the pilot region of GLOSTAR with improved positions for the 6.7 GHz methanol masers. We also compared the brightness variation for the main velocity peaks between the D-configuration and B-configuration observations and produce a catalogue of potential variable masers.

List of publications

Relevant First-Author Publications

The following list indicates the relevant first-author publications that are discussed and presented in this thesis. These thesis research project culminates in two peer-reviewed and published research publications. In addition, one more manuscript is in preparation for submission to the Astrophysics & Astronomy journal.

1. **Nguyen H.**, Rugel, M. R., Menten, K. M., Brunthaler, A., Dzib, S. A., Yang, A. Y., Kauffmann, J., Pillai, T. G. S., Nandakumar, G., Schultheis, M., Urquhart, J. S., Dokara, R., Gong, Y., Medina, S.-N. X., Ortiz-León, G. N., Reich, W., Wyrowski, F., Beuther, H., Cotton, W. D., Csengeri, T., Pandian, J. D., Roy, N. (2021), *A global view on star formation: The GLOSTAR Galactic plane survey. IV. Radio continuum detections of young stellar objects in the Galactic Centre region*, Astronomy & Astrophysics, 651, A88. DOI:10.1051/0004-6361/202140802

   Author's Contribution: H. N. performed the scientific analysis and wrote the manuscript with the supervision and comments from the co-authors. G. S. N. provided the catalogue of sources that was used as the starting point of this paper. The radio continuum data used was processed by S. A. D. and A. B. and was provided to H. N. as part of the GLOSTAR collaboration.

2. **Nguyen, H.**, Rugel, M. R., Murugeshan, C., Menten, K. M., Brunthaler, A., Urquhart, J. S., Dokara, R., Dzib, S. A., Gong, Y., Khan, S., Medina, S.-N, X., Ortiz-León, G. N., Reich, W., Wyrowski, F., Yang, A. Y., Beuther, H., Cotton, W. D., Pandian, J. D. (2022), *A global view on star formation: The GLOSTAR Galactic plane survey. V. 6.7 GHz methanol maser catalogue*, Astronomy & Astrophysics, 666, A59. DOI:10.1051/0004-6361/202244115

   Author's Contribution: H. N. performed the scientific analysis and wrote the manuscript with the supervision and comments from the co-authors. H. N. performed the calibration and imaging of the spectral line data used in this work as part of the GLOSTAR collaboration. The search code was developed by C. M. and H. N. and was updated by H. N. and is presented in this paper.

3. **Nguyen, H.**, et al., (2022), *A global view on star formation: The GLOSTAR Galactic plane survey. IX. Resolving regions of 6.7 GHz methanol maser emission and the search for variability in Galactic longitude range of* $28^\circ < l < 36^\circ$, in prep.

   Author's Contribution: H. N. performed the scientific analysis and wrote the manuscript with comments from the co-authors. H. N. performed the calibration and imaging of the spectral line data as part of the GLOSTAR collaboration.

Relevant Co-Authored Publications

The author of this dissertation has contributed as co-author to these papers throughout the duration of this thesis project.

1. Medina, S.-N. X., Urquhart, J. S., Dzib, S. A., Brunthaler, A., Cotton, B., Menten, K. M., Wyrowski, F., Beuther, H., Billington, S. J., Carrasco-Gonzalez, C., Csengeri, T., Gong, Y., Hofner, P., **Nguyen, H.**, Ortiz-León, G. N., Ott, J., Pandian, J. D., Roy, N., Sarkar, E., Wang, Y., Winkel, B., (2019) *GLOSTAR: Radio Source Catalog I. 28° < l < 36° and |b| < 1°*, Astronomy & Astrophysics, 627, A175. DOI:10.1051/0004-6361/201935249

   Author's Contribution: H. N. provided comments that helped improve the manuscript.

2. Brunthaler, A., Menten, K. M., Dzib, S. A., Cotton, W. D., Wyrowski, F., Dokara, R., Gong, Y., Medina, S.-N. X., Müller, P., **Nguyen, H.**, Ortiz-León, G. N., Reich, W., Rugel, M. R., Urquhart, J. S., Winkel, B., Yang, A. Y., Beuther, H., Billington, S., Carrasco-Gonzalez, C., Csengeri, T., Murugeshan, C., Pandian, J. D., Roy, N., (2021) *A global view on star formation: The GLOSTAR Galactic plane survey. I. Overview and first results for the Galactic longitude range* 28° < l < 36°, Astronomy & Astrophysics, 651, A85. DOI:10.1051/0004-6361/202039856

   Author's Contribution: H. N. wrote sections for the manuscript pertaining to the spectral line data of the GLOSTAR project.

3. Ortiz-León, G. N., Menten, K. M., Brunthaler, A., Csengeri, T., Urquhart, J. S., Wyrowski, F., Gong, Y., Rugel, M. R., Dzib, S. A., Yang, A. Y., **Nguyen, H.**, Cotton, W. D., Medina, S.-N. X., Dokara, R., König, C., Beuther, H., Pandian, J. D., Reich, W., Roy, N., (2021) *A global view on star formation: the GLOSTAR Galactic plane survey. III. 6.7 GHz methanol maser survey in Cygnus X*, Astronomy & Astrophysics, 651, A87. DOI:10.1051/0004-6361/202140817

   Author's Contribution: H. N. provided comments that helped improve the manuscript. Additionally, H. N. helped with the usage of the search code used in the analysis and discussed the results with the lead-author.

4. Khan, S., Pandian, J. D., Lal, D. V., Rugel, M. R., Brunthaler, A., Menten, K. M., Wyrowski, F., Medina, S.-N. X., Dzib, S. A., **Nguyen, H.**, (2002) *A multiwavelength study of the W33 Main ultracompact* HII *region*, Astronomy & Astrophysics, 664, A140. DOI:10.1051/0004-6361/202140914

   Author's Contribution: H. N. provided comments that helped improve the manuscript.

5. Dzib, S. A., Yang, A. Y., Urquhart, J. S., Medina, S. -N. X., Brunthaler, A., Menten, K. M., Wyrowski, F., Cotton, W. D., Dokara, R., Ortiz-León, G. N., Rugel, M. R., **Nguyen, H.**, Gong, Y., Chakraborty, A., Beuther, H., Billington, S. J., Carrasco-Gonzalez, C., Csengeri, T., Hofner, P., Ott, J., Pandian, J. D., Roy, N., Yanza, V., (2022) *A global view on star formation: The GLOSTAR Galactic plane survey. VI. Radio Source Catalog II:* $28^\circ < l < 36^\circ$ *and* $|b| < 1^\circ$*, VLA B-configuration*, Astronomy & Astrophysics, accepted (2022), eprint arXiv:2210.00560.

   Author's Contribution: H. N. provided comments that helped improve the manuscript.

6. Yan, Y. T., Henkel, C., Menten, K. M., Gong, Y., **Nguyen, H.**, Ott, J., Ginsburg, A., Wilson, T. L., Brunthaler, A., Belloche, A., Zhang, J. S., Budaiev, N., Jeff, D., (2022) *Discovery of non-metastable ammonia masers in Sagittarius B2*, Astronomy & Astrophysics, 666, L15. DOI:10.1051/0004-6361/202245024

   Author's Contribution: H. N. provided comments that helped improve the manuscript. Additionally, H. N. helped with the usage of the search code used in the analysis.

7. Dokara, R., Gong, Y., Reich, W., Rugel, M., Brunthaler, A., Menten, K. M., Dzib, S. A., **Nguyen, H.**, Ortiz-León, G. N., Urquhart, J., Wyrowski, F., Yang, A., Anderson, L. D., Beuther, H., Csengeri, T., Müller, P., Ott, J., Pandian, J. D., Roy, N., (2022) *A global view on star formation: The GLOSTAR Galactic plane survey. VII. Supernova remnants in the Galacitc longitude range* $28^\circ < l < 36^\circ$, Astronomy & Astrophysics, accepted (2022), eprint arXiv:2211.13811.

   Author's Contribution: H. N. provided comments that helped improve the manuscript.

Contents

Chapter 1

Introduction

Overview

When we grow up and first learn about the world and what it is made of, we are often taught that everything is made up of molecules and atoms. As we delve deeper into the subject, we learn that even they are made up of constituents such as electrons and protons. Analogously, stars can be thought of as the building blocks of galaxies and that their properties and evolution have a direct influence on their host galaxies. As such, it is imperative that we understand how stars form as this will help address long-standing questions regarding our own origin and that of the Universe.

High-mass stars in particular, despite being far less numerous than their lower-mass counterparts, are extremely important to these studies as they impact their host galaxies physically, chemically, and morphologically. They provide both the energies and environments capable of creating the heavy elements seen in the Universe that are part of the molecules capable of creating life. However, in contrast to low-mass stars, the process of their formation is not as well understood. There are some difficulties that contribute to this, one of them being the very fact that they are more massive. Massive stars evolve on shorter timescales and can stay deeply embedded in their natal environment, where the high dust content makes them invisible at visual, near-infrared (NIR), and even shorter wavelengths. Regions undergoing massive star formation are often more distant, requiring instruments with sufficient sensitivity and angular resolution. Furthermore, they tend to form in clusters which can make the interpretation of the observational data more difficult.

To study them, we observe snapshots of many star forming regions using different tracers/wavelengths in order to obtain a census of the different evolutionary stages in a star's life. Due to the embedded nature of these early high-mass star forming regions, we need to go to wavelengths like the infrared, submillimetre, and radio, that can penetrate the obscuring dust. This thesis aims to contribute to this study by finding and investigating certain tracers of high-mass star formation (HMSF). In this way, information on the physical conditions of the birthplaces of high-mass stars can be obtained. The following sections give the background needed on high-mass stars to appreciate the scientific content of this thesis. In particular, description of 6.7 GHz methanol masers, massive young stellar objects, and HII regions are given in this chapter as they are the main objects of interest used in this work.

1.1 Star formation

The birthplaces of stars are situated in the dense regions of the interstellar medium (ISM) known as giant molecular clouds (GMCs) with typical sizes and masses of $\sim 2 - 100$ parsecs and $\sim 10^4 - 10^6\,\mathrm{M}_\odot$ respectively (Larson 2003). These clouds have typical molecular hydrogen densities of $\mathrm{n}_{H_2} \sim 20\,\mathrm{cm}^{-3}$ and within these clouds, clumps with higher densities are found ($\mathrm{n}_{H_2} \sim 10^3\,\mathrm{cm}^{-3}$, Larson 2003) to collapse, and under certain conditions give rise to stars. These stars burn their nuclear fuel, thus synthesising heavier elements, and eventually re-inject this matter and energy back into their surroundings and potentially repeating the cycle. However, depending on how much mass the star had at its birth, the physical processes and consequences of this cycle can greatly differ. In particular, high-mass stars (e.g., $M \geq 8\,\mathrm{M}_\odot$) directly influence the evolution of their host galaxies via many astrophysical processes. Their UV radiation ionises the surrounding molecular clouds and they inject a large amount of energy and momentum into the ISM, driving strong shocks, thereby providing an important source of mixing and turbulence into the ISM (Zinnecker & Yorke 2007). This can directly affect future generations of stars by either promoting the collapse of molecular clouds or disrupting them (e.g., Urquhart et al. 2007; Deharveng et al. 2010; Thompson et al. 2012). High-mass stars also enrich their surroundings with heavy elements that in turn play a role in the star formation process as well as the chemical evolution of galaxies (Motte et al. 2018).

Understanding the processes involved in the formation of high-mass stars remains a challenge in modern astronomy. High-mass stars evolve quickly and thus their early evolutionary stages are short-lived. They are also less numerous than their lower-mass counterparts, making them harder to find and observe. They form in clusters and begin their nuclear fusion processes while still deeply embedded in their natal environments, that is even before they have finished accreting their final mass and reach the main sequence. The high dust content of this environment at this stage makes them invisible at near-infrared and shorter wavelengths. One of the central questions is whether high-mass star formation is a scaled-up version of the low-mass star formation process, or if it follows a different path altogether.

1.1.1 Low-mass star formation

Stars that have masses $\leq 8\,\mathrm{M}_\odot$ are considered to be 'low-mass' and in comparison to their 'high-mass' siblings, are expected to live for billions of years. While they only have a fraction of the mass and luminosity of their counterparts, they are by far, more numerous, dominating the mass allocation for a given galaxy as can be seen when looking at the distribution of the masses of stars, which is described by the initial mass function (IMF; Salpeter 1955; Kroupa 2001). They end their lives by ejecting their outer shells as planetary nebulae leaving behind a remnant white dwarf.

We can quantify their long lifespan by looking at the Kelvin–Helmholtz ($t_{\rm KH}$) and free-fall (t_{ff}) timescales. The free-fall timescale is the time required for a dense part of a molecular cloud, a "core", to collapse under the influence of only its own gravity. It is given by,

$$t_{ff} = \left(\frac{3\pi}{32G\rho}\right)^{1/2} \tag{1.1}$$

(Spitzer 1978), where G is the gravitational constant and ρ is the density of the gas. This defines the formation timescale of a star where the mass of its starting gas core surpasses its Jeans mass or the equivalent mass at which gravity will overcome gas pressure and the core begins to collapse. This mass is given by

$$M_{\rm Jeans} \simeq 1.1\,{\rm M}_\odot \left[\frac{T_{\rm gas}}{10\,{\rm K}}\right]^{3/2} \left[\frac{\rho}{10^{-19}\,{\rm g\,cm^{-3}}}\right]^{-1/2}. \tag{1.2}$$

For a typical core with a volume density of $10^5\,{\rm cm^{-3}}$ (Lada 1999), this corresponds to a free-fall time $\sim 10^5$ years. On the other hand, the Kelvin–Helmholtz timescale is the time required for a star to radiate its current gravitational binding energy away with its current luminosity,

$$t_{\rm KH} = \frac{GM^2}{RL}, \tag{1.3}$$

where M is the mass of the star, R is its radius, and L its luminosity. If taking our own Sun as an example, with a mass of $1\,{\rm M}_\odot$ and luminosity of $1\,{\rm L}_\odot$, this corresponds to a timescale of $\sim 10^7$ years. With $t_{\rm KH} > t_{ff}$, this means that the star will accumulate all of its mass before it begins generating energy from nuclear fusion in its core (Kahn 1974; McKee & Ostriker 2007). Once the molecular cloud core begins to collapse, the core does not immediately heat up as it is efficiently cooled by thermal emission from dust. Naturally, the central density of the cloud begins to increase while the temperature remains $\sim 10\,{\rm K}$ due to efficient radiation from the dust. While we first presented equation 1.1 with a constant density, cores are better described with an inherent density profile ($\rho \propto r^{-2}$, Larson 2003) which means that the inner regions of the core collapse at a faster rate than the exterior regions which leads to a central protostar forming. The infall of the dust and gas of the gravitationally bound core leads to the formation of an accretion disk around the young protostar. Through this accretion disk, matter is transported onto the protostar, gaining more mass. The protostar develops powerful outflows, which are powered by jets that effectively reduce the angular momentum of the spinning protostar (McKee & Ostriker 2007). The star continues to accrete matter until the density of the inner region is high enough such that it becomes optically thick (meaning that the material is opaque at certain wavelengths), which inhibits radiative cooling, thus increasing the temperature of the core (Shu et al. 1987). When it has enough mass and attained a high enough temperature, the stellar core will fuse hydrogen into helium and start its life as a true star.

1.1.2 High-mass star formation

In contrast, stars with higher masses also have high luminosities, making their $t_{\rm KH}$ timescales much shorter. Given that both low- and high-mass stars originate in regions with similar densities ($\sim 10^5\,{\rm cm}^{-3}$, Lada 1999), in comparison to low-mass stars, high-mass stars will already begin radiating before the natal core has collapsed. Unlike for low-mass stars, in high-mass stars hydrogen burning will begin before the core has reached its final mass. However, this presents a problem for the accretion of the mass for the high-mass star as the radiative pressure should prevent any more matter from accreting onto the protostar (Beuther et al. 2007), and thus should limit the mass of the star to be that of when it developed its hydrogen burning core. This would suggest a universal mass limit for developing stars of about $10\,{\rm M}_\odot$ (Shu et al. 1987; Wolfire & Cassinelli 1987); however, stars with masses in excess of $150\,{\rm M}_\odot$ have been observed (e.g. Crowther et al. 2010). How then do we reconcile the formation of such massive stars?

Contrary to initial theories that suggested that high-mass star formation is simply a scaled up version of the low-mass star formation process, other mechanisms and processes must be involved to overcome this radiation pressure barrier such as higher accretion rates (e.g., Wolfire & Cassinelli 1987) and/or non-spherical accretion geometries, e.g., disk accretion, where the accretion is focused onto an equatorial plane (e.g., Yorke & Sonnhalter 2002). Two prevalent theoretical scenarios currently discussed are the competitive accretion model (e.g., André 2002; Bonnell & Bate 2006; Krumholz & Bonnell 2007; Murray & Chang 2012) and the turbulent core model (e.g., McKee & Tan 2003; Krumholz et al. 2009). The competitive accretion model is defined on the basis that depending on where young stars are found in a collapsing cloud, the amount of mass available for them to accrete more material differs. This model posits that stars form in stellar clusters from the gravitational fragmentation of the cloud and will need to compete for all of the available mass in the surrounding volume. Assuming then that the gas is free to move under the same gravitational force as the forming stars, the gravitational potentials of the individual stars combine into a larger scale *cluster* potential that funnels the gas toward the cluster core. Therefore, stars that form in the centre of the stellar cluster have access to more mass than those at the outer edges of the cloud, which allows them to grow more massive as well as at a higher rate. Conversely, the turbulent core model, which is indeed a scaled up version of the low-mass analogue, uses higher accretion rates that are the result of the effect of turbulence in a collapsing system in order to surpass the radiative pressure barrier involved at the higher luminosities of high-mass stars.

It is possible that both models are involved to some degree, however, astronomical observations are needed to obtain the properties of the earliest phases of high-mass star formation in order to better refine the initial conditions of the physical parameters for these theoretical models. This, however, is challenging, as briefly mentioned in Chapter 1.1 due to their rarity, large distances, as well as high levels of extinction inherent to the early phases of their formation. Since they are short-lived, the likelihood of observing a high-mass star in comparison to their low-mass counterparts is

reduced. Because of this rarity, it means also that there are not very many nearby candidates for observations, providing another technical barrier in achieving sufficient angular resolution and sensitivity to resolve individual sources in a given stellar cluster. Furthermore, the young high-mass stars are generally invisible in the optical and NIR wavelengths due to their embedded nature. In this regard, radio and sub-millimetre observations provide a much needed window to peer into dust to observe these natal regions.

1.1.2.1 Evolutionary sequence

As mentioned previously, studying the earliest stages of high-mass star formation is perhaps the most straightforward approach in learning about their formation mechanisms. These stages are described in general in Fig. 1.1 on which we elaborate in this section.

Young stellar objects (YSOs) are defined as protostars or pre-main-sequence stars that form by the accumulation of material onto a protostar from a circumstellar disk or envelope. The phase of their evolution is often classified into different evolutionary stages based on the slope of their spectral energy distribution (SED; flux density vs wavelength) in the MIR. Observationally, *massive* young stellar objects (MYSOs) are defined as infrared-bright objects that have a SED that peaks at $\sim$100 μm and a total luminosity, $L > 10^4\,\mathrm{L}_\odot$. As of now, there is no solid observational evolutionary sequence for the formation of massive young stellar objects (MYSOs). Motte et al. (2018) propose an evolutionary scheme based on observational constraints that depend on hierarchical collapse and clump-fed accretion models (e.g., Vázquez-Semadeni et al. 2009; Smith et al. 2009). A caveat for this scheme is that it does not yet consider that most high-mass stars we see are formed in binaries.

The proposed evolutionary sequence starts in molecular complexes ($\sim$100 pc) that host massive clouds where clusters of OB stars (stars with spectral types O or early-type B that are hot and massive, known for their immense UV radiation) form. Massive clumps/clouds ($\sim$1 pc) form structures called ridges or hubs under a global but controlled collapse. Inside these clouds, massive cloud fragments are IR-quiet (invisible at IR wavelengths) and are called massive dense cores (MDC; $\sim$0.1 pc) that host low-mass prestellar cores. This starless phase lasts for about one free-fall time ($\sim 10^4$ years). Over time, material is fed into the MDC and the low-mass prestellar cores due to the global collapse of the host molecular cloud complex. The collapse of the ridges/hubs generate a stream through which the gas flows allowing the low-mass prestellar cores to become protostars. These protostars are $\sim$0.02 pc in size and contain low-mass ($< 8\,\mathrm{M}_\odot$) stellar embryos. This is the start of the formation of YSOs. Through the inflows, they become high-mass protostars where the low-mass stellar embryo has strong accretion rates and outflows. When the stellar embryo reaches the $8\,\mathrm{M}_\odot$ threshold, it is considered a high-mass stellar embryo. At this point, the temperatures of the high-mass protostars rise, leading to a sharp increase of their luminosity and they become IR-bright (visible at IR wavelengths). These hot molecular cores (HMC) grow in size, and they develop HII regions (namely hyper-compact HII regions at first, which we describe in Chap-

ter 1.1.3) as the stellar embryos produce UV fields that increase in strength and ionise the surrounding molecular gas. Alongside stellar outflows and winds, the gas accretion towards the newborn star is slowed and eventually halted, ending the main accretion phase for a high-mass star.

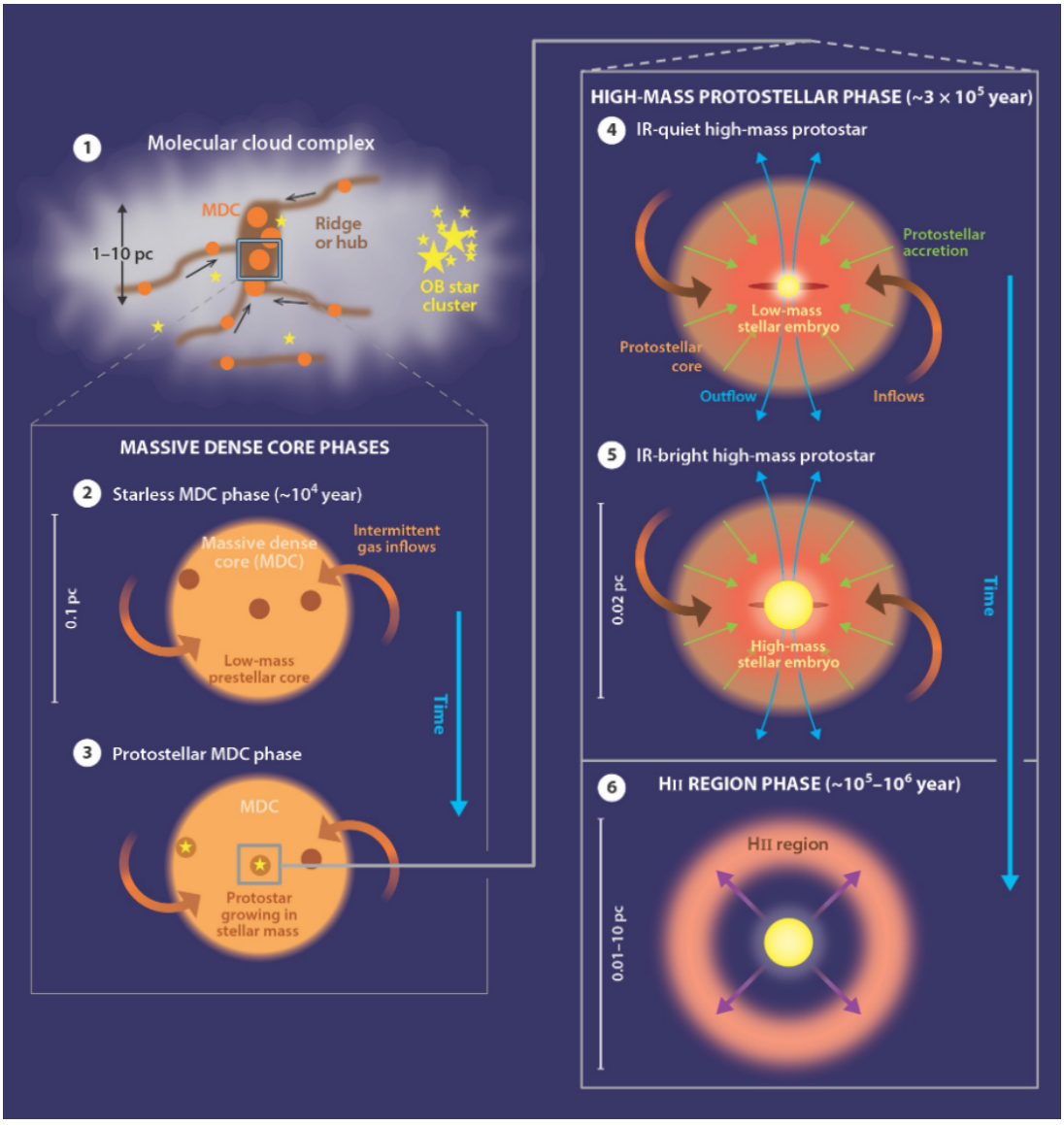

Figure 1.1: The proposed evolutionary sequence based on global hierarchical collapse and clump-fed accretion models using observational constraints (Tigé et al. 2017; Motte et al. 2018).

1.1.3 HII regions

As discussed above, as the MYSO is evolving, its UV radiation increases. Given that MYSOs evolve surrounded by neutral gas, their strong UV fields will completely ionise the surrounding gas into HII, forming a sphere with a radius R_s, the Strömgren radius (Strömgren 1939). At this radius, there is a boundary shell that has an approximate thickness of 10^{14} cm in which there is an equilibrium between the ionisation and recombination. The regions within the Strömgren radius are called HII regions. These start in a more compact stage as hyper-compact (HC) HII region ($<$0.01 pc), further evolving with time to become an ultra-compact (UC; $<$0.1 pc), and compact HII region ($<$0.5 pc) (Wood & Churchwell 1989; Garay et al. 1993; Kurtz et al. 1994; Becker et al. 1994; Mezger & Henderson 1967; Habing & Israel 1979). They can be observed in the infrared and at radio wavelengths. The radiation from the central source heats the dust in a shell around the ionised gas. This is re-emitted as thermal radiation with a pseudo-blackbody spectrum that peaks in the infrared at roughly $\sim$100 μm. At wavelengths longer than 3 mm the dust emission decreases rapidly, and the dominant emission is thermal 'free-free' radio radiation from the ionised gas. As these high-mass stars form in clusters, the most massive stars dominate the observed luminosity and disrupt their environment due to their strong stellar winds and UV emission. They blow away their natal dust envelope forming classical HII regions ($\sim$ 10 pc) and OB associations. These HII regions are the only phenomenon that have been firmly established to have a physical connection to the birth of massive stars, making them unquestionable sites of high-mass star-formation. Studies of these small and dense regions therefore allow for the characterisation of the recently formed high-mass stars but can also probe the dynamics and morphologies of their environment.

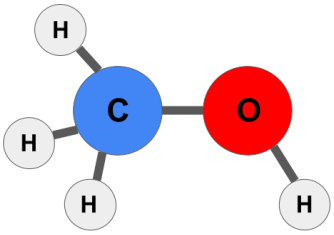

Figure 1.2: Chemical structure of a methanol molecule, consisting of carbon, oxygen, and hydrogen atoms.

1.2 Methanol masers

Methanol masers are amongst the best signposts of high-mass star formation. They appear ubiquitously, generally have high intensities, which make them easy to detect, and are not affected by the high dust extinction inherent to their environment. They are also compact, making them very useful for astrometric and kinematic studies. Furthermore, each maser species requires specific conditions in order for maser action to occur, thus making them specific tracers of the environment that they inhabit. In particular, this thesis explores the diagnostic properties of one such maser transition, namely, the $5_1 - 6_0\mathrm{A}^+$transition of methanol at 6.7 GHz.

1.2.1 A brief history of interstellar masers

The commonly known *laser* has a microwave predecessor known as a *maser* which stands for **m**icrowave **a**mplification by **s**timulated **e**mission of **r**adiation and is used to encompass coherent emission at a specific frequency in both the microwave and radio frequency regimes. Weaver et al. (1965) was originally searching for hydroxyl (OH) absorption but serendipitously discovered OH emission toward HII regions. It quickly became apparent that this strong emission had non-thermal origins. As it was a newly discovered kind of emission, it was not clear at first if maser emission could occur in space. The environment in molecular gas clouds, in fact, are ideal for the natural occurrence of population inversion needed to produce a maser. Following this, Cheung et al. (1969) discovered water (H_2O) maser emission which appeared even stronger than the previously discovered OH masers. However, it wasn't until Barrett et al. (1971a, 1975) discovered the first methanol (CH_3OH, see Fig. 1.2) maser lines at 25 GHz in Orion-KL that one of the most prolific species of interstellar masers was found. In the following two decades, strong CH_3OH maser emission was detected in the 12.2 GHz $2_0 - 3_1\mathrm{E}$ transition (Batrla et al. 1987) and the 6.7 GHz $5_1 - 6_0\mathrm{A}^+$ transitions (Menten 1991b). In particular, the 6.7 GHz CH_3OH maser was found to be the second strongest and second most abundant interstellar maser line after the 22.2 GHz H_2O maser (Caswell et al. 1995) and often more than an order of magnitude stronger than associated OH masers. Unlike the water maser, which can be seen in low and high-mass star forming regions, it is unique in that it exclusively traces high-mass star forming regions (Minier et al. 2003; Ellingsen 2006; Xu et al. 2008). As mentioned above, specific maser species re-

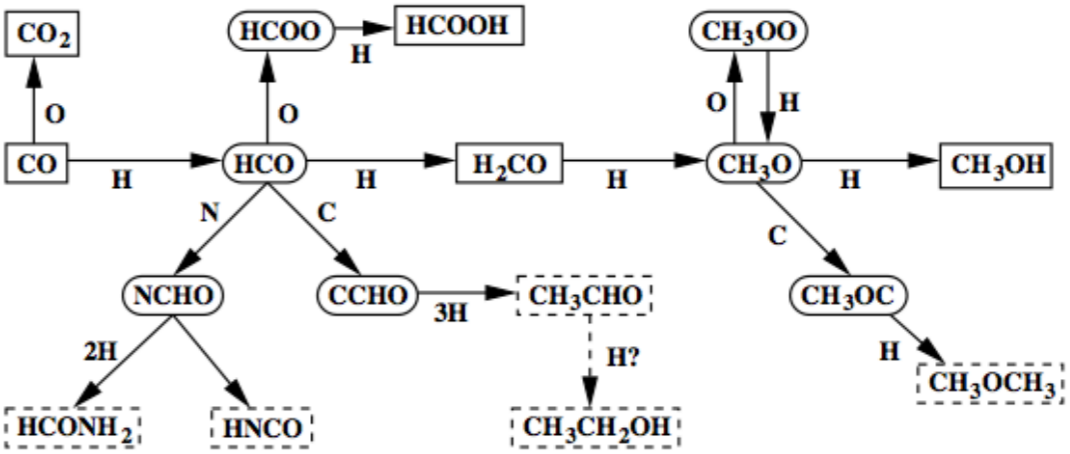

Figure 1.3: Grain-surface reactions responsible for the formation of methanol, from van Dishoeck & Hogerheijde (1999) based on the work of Tielens & Hagen (1982). Solid boxes show molecules observed in interstellar ices, whereas dashed boxes show those observed in the gas phase.

quire specific conditions in order to begin masing. For the 6.7 GHz maser, its formation environment of dust and gas with densities greater than $10^6\,\mathrm{cm}^{-3}$ and temperatures greater than 150 K supports that this maser is found surrounding MYSOs due to the intense radiation of these early forming high-mass stars. Furthermore, it has been observed that very few of these CH_3OH masers have radio continuum counterparts suggesting that they trace a very specific stage of early high-mass star formation and are closely related to MYSOs or very compact and early hyper-compact HII regions (Urquhart et al. 2013a, 2015; Billington et al. 2019). In this way, the observed complex line shapes, high intensities, and presence of other CH_3OH maser species make it a unique signpost and probe of the high-mass star formation process.

1.2.2 Formation of the methanol molecule in molecular clouds

The formation of CH_3OH occurs on the surface of interstellar dust grains located in dense molecular cores (van Dishoeck & Blake 1998), where carbon monoxide (CO) repeatedly undergoes hydrogenation (van Dishoeck & Hogerheijde 1999). This is illustrated in Fig. 1.3. Four phases define grain surface reactions: accretion, diffusion, reaction, and ejection. Atomic or molecular species accrete on the grains at a temperature dependent rate related to both the accreting gas species and the dust grain, the cross-section of the grain and the overall density of the environment (Tielens 2005). As the atoms and molecules move along the surface of the dust grain, they overcome binding energy barriers to meet and react with other molecules, to form, amongst others, methanol. Once the central protostellar object starts to produce energy, the dust grains in its host core get heated and their ice mantles sublimate, greatly increasing the gas phase abundances of the molecules that had formed on the mantles.

1.2.3 Radiative Transfer and Maser Excitation

We provide here an overview of the theory behind maser emission presented in detail, e.g., by Elitzur (1982). To first put into context one of the defining features of maser emission, its intensity, we introduce the concept of *brightness temperature*, that will be used to compare radiation intensities. At the late 19$^{\text{th}}$ century, Planck's law was formulated by German physicist Max Planck to describe the spectral density of electromagnetic radiation emitted by a black body (an idealised opaque and non-reflective body) in thermal equilibrium. The source's *brightness*, $B_\nu(T)$, could then be given as a function of the source's temperature, T, for a given frequency, ν:

$$B_\nu(T) = \frac{2h\nu^3}{c^2}\left(\frac{1}{e^{h\nu/kT}-1}\right), \tag{1.4}$$

where c is the speed of light, h is the Planck constant, and k is the Stefan-Boltzmann constant, and $B_\nu(T)$ and is measured in units of $\mathrm{W\,m^{-2}\,Hz^{-1}\,sr^{-1}}$. For a given intensity I_ν, we define the brightness temperature, T_b, as the temperature of a blackbody that will that result in the same amount of radiation emitted at a given frequency:

$$I_\nu = B_\nu(T_b). \tag{1.5}$$

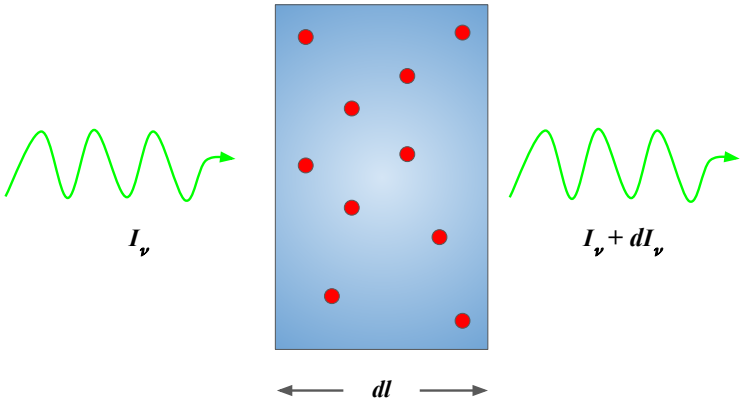

Figure 1.4: Shown is the setup for the radiative transfer equation where some intensity I_ν is travelling through a medium of path length dl where the change in intensity dI_ν can be caused by emission from the medium itself or absorption from interacting with the medium.

Now let us consider the environment from which radiation travels in the interstellar medium. Consider radiation with intensity I_ν travelling through empty space. It then encounters some material. This material either increases or decreases the intensity along the path of the material (Figure 1.4). The material itself can be emitting or absorbing some of the intensity. This change to I_ν is characterised by dI_ν, where[1]

[1] A more complete derivation can be found in Draine (2011), Chapter 7.

$$dI_\nu = -I_\nu \kappa_\nu dl + \varepsilon_\nu dl \tag{1.6}$$

where κ_ν is the attenuation or absorption coefficient and ε_ν is the emissivity or emission coefficient over a path length dl.

We can now introduce the source function

$$S_\nu = \varepsilon_\nu / \kappa_\nu, \tag{1.7}$$

and the description of the optical depth as,

$$d\tau_\nu = \kappa_\nu dl, \tag{1.8}$$

to represent the radiative transfer equation in the form of

$$\frac{dI_\nu}{d\tau_\nu} = -I_\nu + S_\nu. \tag{1.9}$$

Let us now characterise this source function by considering radiative transfer in one dimension. Here, we need descriptions of both the absorption coefficient and the emission coefficient. For a spectral line that results from a transition between two energy levels, the line absorption coefficient, κ_ν, is then given by

$$\kappa_\nu = (B_{12}N_1 - B_{21}N_2)\frac{h\nu_0}{4\pi}\phi(\nu), \tag{1.10}$$

where B_{ij} represents the coefficients for stimulated transitions between the two energy levels, N_i is the volume density population for the lower (N_1) and upper (N_2) energy levels, $h\nu_0$ is the energy separation between the levels, and $\phi(\nu)$ is a normalised profile centred on ν_0. Similarly, the emission coefficient is given by

$$\varepsilon_\nu = N_2 A_{21}\frac{h\nu_0}{4\pi}\phi(\nu), \tag{1.11}$$

where A_{21} is the Einstein coefficient for spontaneous emission. We substitute these relations into Eq. 1.7 to obtain the line-source function:

$$S_\nu = \frac{A_{21}N_2}{B_{12}N_1 - B_{21}N_2}. \tag{1.12}$$

We now introduce a few useful definitions. The statistical weights, g_i, to describe the populations per magnetic sublevel, n_i, in terms of the volume density population as:

$$n_i = N_i/g_i, \quad i = 1, 2. \tag{1.13}$$

Furthermore, the above coefficients for the transitions obey the following Einstein relations:

$$g_1 B_{12} = g_2 B_{21}; \quad A_{21} = B_{21}\frac{2h\nu^3}{c^2}. \tag{1.14}$$

Lastly, we define the excitation temperature, T_x, for the transition between the two levels as:

$$\frac{n_2}{n_1} = \exp(-h\nu/kT_x). \tag{1.15}$$

Using Einstein's relations and Eq. 1.13, we can write Eq. 1.12 in terms of the ratio of the magnetic sublevels

$$S_\nu = \frac{2h\nu^3}{c^2}\frac{1}{\frac{n_1}{n_2}-1} = B_\nu(T_x), \tag{1.16}$$

where we see that with Eq. 1.15, the source function is the same as the Planck function at a temperature, T_x. This allows us to write the radiative transfer equation in familiar terms

$$\frac{dI_\nu}{d\tau_\nu} = B_\nu(T_x) - B_\nu(T_b). \tag{1.17}$$

This equation is commonly presented in terms of temperature under the assumption of the Rayleigh-Jeans limit as

$$\frac{dT_b}{d\tau} = -T_b + T_x, \tag{1.18}$$

whose solution is

$$T_b = T_x[1 - \exp(-\tau)] + T_c \exp(-\tau), \tag{1.19}$$

where T_c is the brightness temperature of the background radiation coming from a continuum source or the cosmic microwave background. A constant excitation temperature is also assumed.

The optical depth of the traversed matter, τ_ν (dimensionless), characterises the attenuation of the incident radiation. The medium is optically thick to the incoming radiation if $\tau_\nu \gg 1$, and optically thin if $\tau_\nu \ll 1$. The optical depth is frequency dependent.

Since, according to the Planck function, brightness increases monotonically with increasing temperature (for a given ν), Eq. 1.17 implies that $T_b \leq T_x$, or explicitly, that the brightness temperature cannot be higher than the line excitation temperature. However, high angular resolution observations of some radio wavelength spectral lines have measured brightness temperatures in excess of 10^{12} K which is far above any plausible excitation temperature. Clearly, these brightness temperatures cannot correspond to the typical kinetic temperatures of the molecules as they generally break into their components at temperatures above a few thousand Kelvin. It turns out that in the case where the populations are inverted, namely where $n_2 > n_1$, this can bring about a negative excitation temperature for T_x and in this way, the medium acts as an amplifier which can result in the large brightness temperatures that we see. This "population inversion" is one of the core concepts for maser emission.

1.2.3.1 Rate equations

In order for maser emission to occur in space, multiple energy levels of a certain molecule should be involved. Much like a laser, in order to have a maser, there must be an energy state that is overpopulated in a multi-level system and a mechanism to generate a "population inversion".

Figure 1.5 illustrates the masing scheme by considering three energy levels labelled 1, 2, and 3 where A_{21}, B_{12}, B_{21} are the Einstein coefficients, C_{21}, C_{12}, are the collisional rates, P_1, P_2 represent radiative pumping rates and Γ_1 and Γ_2 the loss rates out of

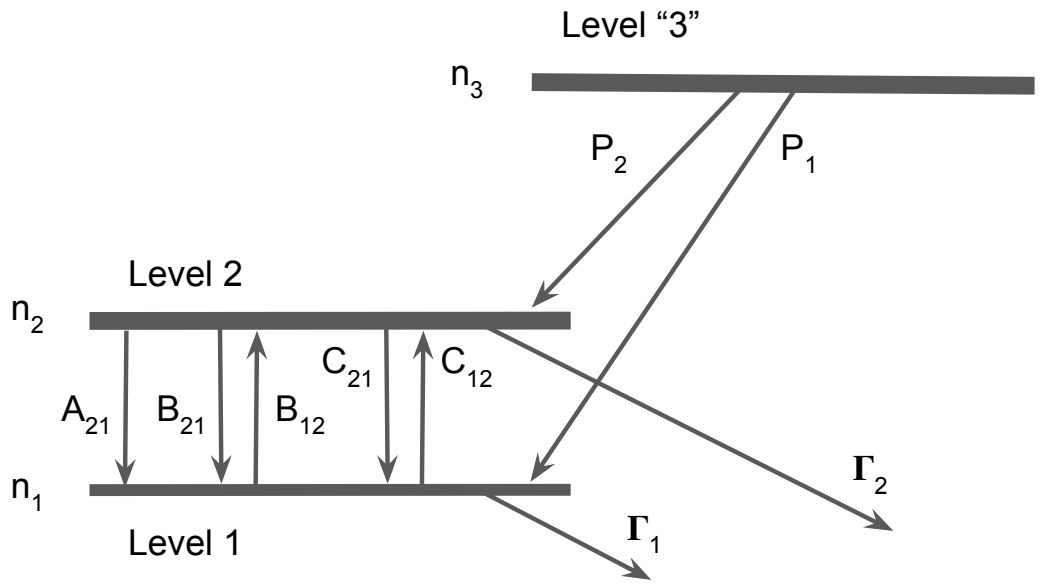

Figure 1.5: Schematic of the energy levels and the ‘three’ level model supporting the over population of level 2 leading to maser emission.

the maser levels into any other energy. To obtain a maser emission from a transition between energy levels 1 and 2, there must be more molecules in the upper energy state 2 than in the lower energy state 1. This requires a pumping channel in which molecules are temporarily pumped to a higher energy state, level 3 (which includes any level with greater energy than level 2), either collisionally or radiatively, following which the molecules decay to level 2, thereby enhancing the population of level 2 relative to level 1 and causing a population inversion.

We use the rate equations to describe the transitions between levels shown in Fig. 1.5 with the following

$$\frac{dN_2}{dt} = \tilde{P}_2 - \Gamma_2 N_2 - A_{21} N_2 - J(N_2 B_{21} - N_1 B_{12}) - (N_2 C_{21} - N_1 C_{12}), \tag{1.20}$$

$$\frac{dN_1}{dt} = \tilde{P}_1 - \Gamma_1 N_1 + A_{21} N_2 - J(N_1 B_{12} - N_2 B_{21}) - (N_1 C_{12} - N_2 C_{21}), \tag{1.21}$$

with the radiation field, J, being

$$J = \int J_\nu \phi(\nu) d\nu. \tag{1.22}$$

In combination with Eq. 1.14 and

$$g_1 C_{12} = g_2 C_{21} \exp(-h\nu/kT), \tag{1.23}$$

we can rewrite the rate equations in terms of the populations per sublevel (e.g., n_2). This is because as the observed masers found in astronomy are generally stable over

time periods greater than that of the rate equations, and thus it can be assumed to be in a steady state. And so, we define the pump rate per sublevel

$$P_i = \tilde{P}_i/g_i, \tag{1.24}$$

to obtain the steady state level populations for the maser as

$$0 = P_2 - \Gamma n_2 - A_{21}n_2 - B_{21}J(n_2 - n_1) - C_{21}(n_2 - n_1\exp(-h\nu/kT)), \tag{1.25}$$

$$0 = P_1 - \Gamma n_1 + A_{21}n_2 + B_{21}J(n_2 - n_1) + C_{21}(n_2 - n_1\exp(-h\nu/kT)), \tag{1.26}$$

where we have assumed equal statistical weights, $g_1 = g_2 \equiv g$, and equal loss rates, $\Gamma_1 = \Gamma_2 \equiv \Gamma$ in order to simplify the equations. The addition of these two equations then give the overall population of the maser system

$$n_{12} \equiv n_1 + n_2 = (P_1 + P_2)/\Gamma = 2P/\Gamma, \tag{1.27}$$

where P is the average pump rate into the maser levels.

1.2.3.2 Population inversion

To quantify population inversion, we solve for the population difference $\Delta n \equiv n_2 - n_1$. For simplicity, spontaneous decays and collisional exchange terms will be omitted. This is acceptable in the case where A_{21} and C_{21} are much less than Γ. In defining $\Delta P \equiv P_2 - P_1$, we have

$$\Delta n = \frac{\Delta n_0}{1 + J/J_s}, \tag{1.28}$$

where $\Delta n_0 = \Delta P/\Gamma$, and $J_s = \Gamma/2B_{21}$. The parameter J_s is used to describe the radiation intensity value where the level populations begin to be affected by the induced transitions. In the case where $J \ll J_2$, Eq. 1.28 reduces to $\Delta n = \Delta n_0$ meaning that the difference in the populations of the levels does not depend on J, the radiation field.

As such, in order to have a population inversion, one would need that $\Delta n_0 > 0 \Rightarrow \Delta P > 0 \Rightarrow P_2 > P_1$. This means that the pump rate per sublevel of the lower level must be less than that of the upper level. The efficiency of this pumping process is given by

$$\eta = \Delta P/2P = \Delta n_0/n \tag{1.29}$$

which shows that each pumping event produces a maser photon with an efficiency described by η which depends on the mechanics of the pumping scheme used.

In the context of the radiative transfer equation, it can be shown that Eq. 1.19 can be solved in the linear case to be

$$T_b = (T_x + T_c)\exp(\kappa_0 l) - T_x, \tag{1.30}$$

where we have used

$$\kappa = \frac{\kappa_0}{1 + J/J_s}, \tag{1.31}$$

as derived from Eq. 1.10 and Eq. 1.28. From Eq. 1.30, we see that the brightness temperature can increase exponentially in the case where the absorption coefficient describes amplification as detailed in the sections above. In this case where $J \ll J_s$, this range of intensities correspond to an "unsaturated" maser. However, the exponential growth cannot continue indefinitely as J approaches J_s, the radiation will start to affect the level populations. The induced emission will outweigh the absorption, thus leading to a decrease in the population inversion. This leads to the maser becoming "saturated". In this case, the maser scheme is reaching its maximal efficiency and the saturated maser produces radiation as opposed to amplifying the radiation. The increase in radiation therefore comes from additional emitting volume along the line of sight. It can be shown that the solution for the brightness temperature in the "saturated" case is

$$T_b = T_s[1 + \kappa_0(l - l_s)], \tag{1.32}$$

where T_s is the temperature where saturation occurs, and l_s denotes the regions where the maser becomes saturated. We refer the reader to Elitzur (1982) for a complete discussion on this subject.

1.2.3.3 Pumping mechanisms: the difference between Class I and Class II

As discussed in the above section, the emission from a seed photon is amplified as it goes through the masing medium, i.e., the interstellar molecular medium or cloud within which this maser resides. The medium requires large scale coherence in velocity within the maser line's width in order for the amplification of the maser emission to occur. As mentioned above, maser pumping may be due to collisional (as in Class I CH_3OH masers) or radiative processes (as in Class II CH_3OH masers). We describe these two mechanisms here.

Originally classified by their associations to outflows from protostars, Class I and Class II methanol masers, are now known to be distinguished rather by their pumping mechanisms. Class I methanol masers are excited through collisions and as such, were found to be associated with outflows at the interfaces of its shock front with ambient interstellar material, frequently significantly offset from a protostar in position and velocity (Menten 1991b; Cragg et al. 1992). Therefore, it can provide information on these shocks. Class II masers on the other hand are exclusively found in the close vicinity of MYSOs in high-mass star forming regions and are radiatively pumped by the intense mid-infrared radiation from the protostar (Sobolev et al. 2006). In particular, they trace the *earliest* stages of HMSF (as described in Sect 1.1.2.1) as, for instance, the 6.7 GHz methanol masers begin to appear during the hot molecular core stage (Fig. 1.6).

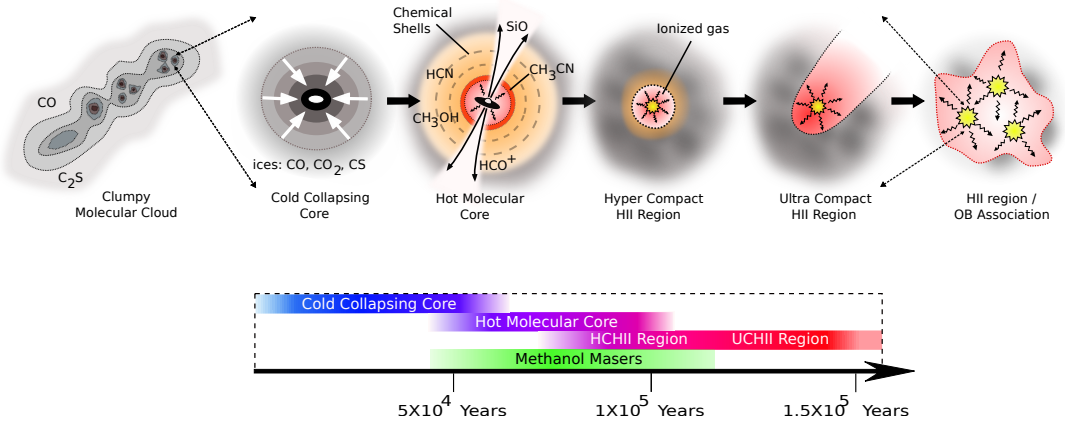

Figure 1.6: Schematic showing the proposed evolutionary sequence of high mass stars as well as their associated timeline with methanol masers. Starting from the left, the stages are as follows: : Clumpy molecular clouds found in massive filaments, host massive dense cores, which collapse due to gravity. This increases the density and temperature where it accretes material from its natal cloud and forms a 'hot' molecular core. These cores have temperatures >100-150 K (van Dishoeck & Blake 1998), where the heat and outflows from the central protostar evaporate ices from the dust grains of the surrounding environment, which drives a rich chemistry that leads to the production of complex hydrocarbons. For stellar embryos of sufficient mass (>8 $M_\odot$), they become IR-bright and are considered high-mass stellar embryos. They grow in size and the UV-radiation from the high-mass protostars creates a bubble of ionised gas, known as an ultra-compact HII region. The region expands and develops into an HII region with the OB association inside (Tigé et al. 2017; Motte et al. 2018). Image credit: Cormac Purcell.

In order for **collisional pumping** to support a population inversion, collisional interactions by the far dominant hydrogen molecule H_2 must occur in such a way that an over population of the upper energy level of the maser transition is achieved. This could be either due to transitions from level 3 into level 2 that are preferred over those to level 1, or the population of level 1 becomes depleted (Cohen 1989; Reid & Moran 1988). This form of pumping can be limited under high density conditions as too many collisions can result in the thermalisation of the gas and stop the maser action (Elitzur 1982).

Radiative pumping, on the other hand, in general should not be able to induce a population inversion if the pumping radiation is strictly that of a blackbody. However, if the radiation is not that of a blackbody it is then possible for it to cause pumping, that is, if the dominant source of radiation is from an external source (Elitzur 1982). This can be brought about by dust emission and thus the optical depths for certain transition can be different, resulting in preferential transitions to certain levels, i.e., from level 1 to level 3.

1.3 6.7 GHz Methanol maser surveys

Dedicated maser searches have been performed using two different strategies: targeted and blind surveys (listed in Table 1.1). Targeted surveys observe colour-selected infrared (IR) sources or known regions of active star formation. Blind surveys, on the other hand, generally cover large regions of the sky. Targeted surveys focus only on well-known sites and may miss masers in little-studied regions, but are more likely to detect weaker maser sources – since more observing time can be spent on a simple position compared to blind surveys. Furthermore, targeted surveys will miss masers in unexpected locations. Unbiased surveys, however, can detect all sources in the covered area of sky but are limited by the sensitivity of the observations (mainly due to observation time constraints).

In 2004, Pestalozzi et al. (2005) compiled a catalogue of 6.7 GHz methanol masers which we summarise here as well as explaining more recent surveys in detail. Menten (1991a) observed a sample of 123 star-forming regions and detected 80 Class II masers which served as a motivation for targeted searches for 6.7 GHz methanol masers. Previous targeted surveys selected point sources that were detected using the Infrared Astronomical Satellite (IRAS; Neugebauer et al. 1984). They selected sources whose IR colours are normally associated with UC HII regions as well as sources that already had detections of other maser species (e.g., OH, H_2O, 12.2 GHz CH_3OH masers). MacLeod et al. (1992) targeted known 12.2 GHz methanol masers and reported 6.7 GHz methanol masers towards all of them. They then targeted OH maser sites and similarly detected methanol masers (MacLeod & Gaylard 1992; Gaylard & MacLeod 1993). Schutte et al. (1993) targeted UC HII regions which were selected based on their IR colours (as in Wood & Churchwell 1989) and laid the foundation for using methanol masers as direct tracers of regions of HMSF. Caswell et al. (1995) detected 245 6.7 GHz methanol masers found towards known star forming regions and OH masers and constructed a

Table 1.1: Summary of 6.7 GHz methanol maser surveys since the maser compilation of Pestalozzi et al. (2005).

Targeted	Observations	Sensitivity	Total Detections	New Detections
Pestalozzi et al. (2005)	-	0.06-4 Jy	898	-
Ellingsen (2007)	200	0.5 Jy	38	9
Yang et al. (2017)	1473	1.5 Jy K^{-1}	12	3
Yang et al. (2019b)	1873	1.5 Jy K^{-1}	224	32
Unbiased	Range	Sensitivity	Total Detections	New Detections
Pestalozzi et al. (2005)	-	0.16-1 Jy	308	-
Pandian et al. (2007)	$35^\circ < l < 55^\circ$; $\lvert b\rvert \leq 0.4^\circ$	0.09 Jy	86	48
MMB[a]	$186^\circ < l < 360^\circ$; $\lvert b\rvert < 2^\circ$	0.2 Jy	972	322
	$0^\circ < l < 60^\circ$; $\lvert b\rvert < 2^\circ$			
Rickert et al. (2019)	$\lvert l\rvert < 1.5^\circ$; $\lvert b\rvert \leq 0.3^\circ$	0.08 Jy/beam	43	16
Ortiz-León et al. (2021)	$76^\circ < l < 83^\circ$; $-1^\circ < b < 2^\circ$	0.028 Jy/beam	13	2
Nguyen et al. (2022)[b]	$-2^\circ < l < 60^\circ$; $\lvert b\rvert \leq 1^\circ$	0.018 Jy/beam	554	84

[a] Compilation of the collaborations work from Caswell et al. (2010); Green et al. (2010); Caswell et al. (2011); Green et al. (2012), and Breen et al. (2015).
[b] The results of which are presented as part of this thesis in Sect. 4.

luminosity function. They concluded that within the Milky Way Galaxy there should be ∼500 sites hosting 6.7 GHz methanol masers. van der Walt et al. (1995) found in their studies of methanol masers towards IRAS sources that methanol masers were more likely to be found in the inner regions of the Milky Way and along the Galactic plane. Walsh et al. (1997) detected 201 6.7 GHz methanol masers towards 535 IRAS sources and found that these sources were predominately in the inter-arm regions of the Milky Way. Slysh et al. (1999) and Szymczak et al. (2000) targeted IRAS sources in the Northern Hemisphere but found only ∼10% to have methanol masers. Furthermore, there were even IRAS sources that did not have typical UC HII region colours that had methanol maser associations (Szymczak et al. 2000; Szymczak & Kus 2000).

Further targeted searches were done by Ellingsen (2007) and Yang et al. (2017, 2019b). Ellingsen (2007) targeted 200 mid-infrared (MIR) sources from the Galactic Legacy Infrared Mid-Plane Survey Extraordinaire (GLIMPSE) survey, which were selected based on the MIR colours characterising young high-mass star forming regions. They had a detection rate of ∼20% which they suggest might mean that these targets were at an earlier stage of star formation, before 6.7 GHz methanol maser emission could be seen. Yang et al. (2017) studied 1473 sources from the all-sky Wide-Field Infrared Survey Explorer (WISE) point catalogue (Wright et al. 2010) with a detection rate of ∼2% which confirms previous results that most methanol masers are situated along the Galactic plane. They did a primary search at high galactic latitudes ($|b| > 2^\circ$) in order to find more isolated and simpler star forming environments than those generally found in the Galactic plane. These targets would make for cleaner environments upon which to study the origins of methanol masers. The authors follow up this investigation with 1875 WISE infrared point sources that are situated in the Galactic plane. They detect 224 methanol maser sites, 32 of which are new. They produce a catalogue of

1085 6.7 GHz methanol maser sources after combining their findings with all previous surveys, including blind surveys.

The first blind survey targeted on 6.7 GHz methanol maser emission was performed by Ellingsen et al. (1996) where they covered a 10.6 $\deg^2$ area of the sky. They were able to detect 50 masers, 26 of which were new. This was sufficient evidence for the advantage of blind surveys with many of the new detections not being associated with IRAS sources. They were, however, limited to a sensitivity of 2.6 Jy. Caswell (1996a) surveyed a region along the Galactic plane covering 330.°8 to 339.°8 and detected 57 masers, 21 of which were new. They continued their survey in the Galactic Centre and detected 23 masers, most of which were known (Caswell 1996b). Rickert et al. (2019) focused on the central molecular zone in this area with the improved Karl G. Jansky Very Large Array (VLA) and found 43 6.7 GHz methanol masers sites, of which 16 were new. Szymczak et al. (2002) surveyed a $\sim$21 $\deg^2$ region of the Galactic plane and detected 100 masers, 26 of which were new. The Arecibo Methanol Maser Galactic Plane Survey by Pandian et al. (2007) improved the detection rate for blind surveys as they were able to be complete at the level of 0.27 Jy making it the most sensitive blind survey at the time. They detected 86 sources, 48 of which were new, with most of the new detections having flux densities lower than 2 Jy. They covered a region of 18.2 $\deg^2$.

New technological advancements in telescope receivers allowed the ambitious Methanol Multibeam (MMB) survey to be realised (Green et al. 2008, 2009). The MMB survey detected $\sim$970 6.7 GHz methanol masers, 322 of which for the first time (Caswell et al. 2010; Green et al. 2010; Caswell et al. 2011; Green et al. 2012; Breen et al. 2015). The survey provided the first Galaxy-wide catalogue from one project with an improved and uniform sensitivity of $\sim$0.17 Jy, facilitating Galaxy-wide statistics for methanol masers. Since the angular resolutions of the single dish observations were not sufficient to associate masers with the young stellar objects, they conducted interferometric follow-up observations to obtain better positions.

Using the VLA and the Effelsberg 100-m telescope, the **Glo**bal view on **Star** formation in the Milky Way (GLOSTAR) survey, is one of the latest efforts to conduct an unbiased survey in the radio regime to characterise star-forming regions in the Milky Way (discussed in full in Chapter 2.2). The 6.7 GHz methanol spectral line data is one of the key components of this survey. As part of this thesis, the data was reduced and analysed, thereby providing the most sensitive catalogue of Class II 6.7 GHz methanol masers to date. This work constitutes a significant part of this thesis and is presented in Chapters 4 and 5. Our GLOSTAR observations have an order of magnitude higher angular resolution than the MMB survey. This increases the position accuracy to about 1 arcsec. The survey also provides sensitive radio continuum observations of the Galactic centre, thereby providing an opportunity to peer into the processes involved in HMSF in one of the most interesting places in the Galaxy, the Central Molecular Zone.

1.4 An interesting laboratory: The Central Molecular Zone

An area of particular interest for studies of high-mass star formation in extreme environments is the Central Molecular Zone (CMZ). It contains giant molecular clouds (GMCs) with different properties from the GMCs in the Galactic disk (e.g., Henshaw et al. 2022, and the references therein). It is situated around the Galactic Centre (GC), covering approximately a 200 pc sized region at a distance of 8.2 kpc from Earth (Gravity Collaboration et al. 2019). It has an estimated mass of $\sim 5 \times 10^7\,\mathrm{M}_\odot$ which is $3 - 10\%$ of all the molecular material in the Milky Way. Furthermore, it is dense ($\sim 10^4\,\mathrm{cm}^{-3}$, Morris & Serabyn 1996; Ferrière et al. 2007), being at least 100 times more so than other GMCs in the Galaxy. The physical conditions within the CMZ are also more extreme in comparison to other regions hosting GMCs as it has stronger radiation fields (Lis et al. 2001; Clark et al. 2013), hotter gas and dust kinetic temperatures (Ginsburg et al. 2016; Longmore et al. 2012), higher pressure and magnetic field strengths (for a full review of the conditions of the CMZ, see e.g., Morris & Serabyn 1996; Henshaw et al. 2022). Given its high density, one might expect a high concentration of high-mass star formation to occur in the region. As such, the particularly extreme environment of the CMZ makes it a unique laboratory to understand the star formation process, as it will help to answer the question of how these physical conditions affect the star formation activity in other regions of our Galaxy and also other galaxies. It is clear then that the question of present-day high-mass star formation in this region is an important one as despite the amount of dense gas available, the star formation rate (SFR) is lower than expected in comparison to other regions. There is ongoing star formation, (e.g., in Sgr B2: Figer et al. 2002; Schneider et al. 2014; Lis & Goldsmith 1990; Schmiedeke et al. 2016) but not at the rate predicted by Lada et al. (2010). They derived a linear relationship between the SFR and the amount of *dense* molecular gas, of which the CMZ has in excess. The star formation rate in the CMZ has been found to be at least one order of magnitude smaller than expected (e.g., Longmore et al. 2013; Barnes et al. 2017; Kauffmann et al. 2017b; Lu et al. 2019; Nguyen et al. 2021). We see from the study by Kauffmann et al. (2017b) that already on the scale of individual clouds, the SFR in these clouds is suppressed when compared to clouds in our solar neighbourhood (see Fig. 1.7).

There are many theoretical attempts to explain this low SFR in the CMZ, ranging from arguments that its molecular clouds are still too young, that the inherent extinction in such a high column density region obscures the total number of young massive stars or that the extreme conditions resulting in a high degree of turbulence prevent the onset of star formation (Kruijssen et al. 2014; Krumholz & Kruijssen 2015; Krumholz et al. 2017). Therefore, understanding star formation in the CMZ will help us understand not only star formation in the CMZ, but star formation in the central regions of other galaxies and allow us to compare with conditions in the bulk of the Milky Way Galaxy.

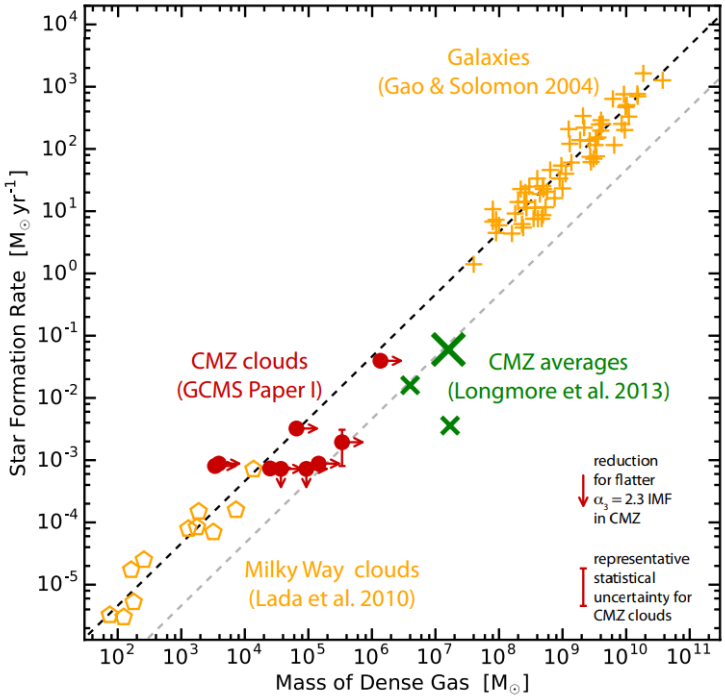

Figure 1.7: The observed star formation rates as a function of dense gas masses for different groups of molecular clouds as done by Gao & Solomon (2004), Lada et al. (2010), Longmore et al. (2013), and Kauffmann et al. (2017a). Image credit Kauffmann et al. (2017a).

1.5 Scientific goals and outline of this thesis

As described in the previous sections of this chapter, the current understanding of the earliest stages of high-mass stars still needs improvement. Observational studies are key in building an empirically supported evolution scheme. However, there are inherent difficulties to observing these deeply embedded and rare sources. As such, this thesis attempts to address questions related to the evolution of high-mass stars using radio wavelength data procured as a part of the GLOSTAR survey (detailed in Chapter 2) to peer into the birthplace of these massive stellar objects.

Indirect tracers that relate to different stages of HMSF are used to characterise MYSOs and their environments. One of the aims of this thesis is therefore to further our understanding of the overlap between certain tracers of HMSF using photometrically identified YSO candidates and HII regions detected in the radio regime, which is discussed in Chapter 3 and Appendix A. This is investigated in the unique and extreme environments of the Central Molecular Zone of our Galaxy as it provides an interesting laboratory to study the star formation rate in molecular clouds. Our goal is to investigate the presence of centimetre wavelength radio continuum counterparts to a sample of YSO candidates which we use to constrain the current SFR in the CMZ. To do this, we use 5.8 GHz radio continuum data from GLOSTAR using the VLA in the D-configuration and present a catalogue of radio continuum counterparts. We investigate their nature by calculating their spectral indices and use this property to classify sources as bona fide HII regions or otherwise. We also cross-match the YSO candidates with the APEX Telescope Large Area Survey of the Galaxy (ATLASGAL; Schuller et al. 2009a) 870 μm dust emission data, which trace the early natal environments of high-mass stars. If the YSO is still very young, we would expect to see it embedded in a compact cold dust envelope traced by sub-millimetre wavelengths. As such, we investigate if there is any clear association of these YSOs with either the earliest or the latest stages of massive star formation in order to shed light on the complete spread of evolutionary stages of this census of YSOs. Lastly, given the unexpected SFR of the CMZ, we infer the SFR from the free-free emission of the HII regions detected using GLOSTAR radio continuum data.

Another avenue to develop studies about HMSF is to obtain statistically robust catalogues of the locations of recent HMSF. Since the 6.7 GHz Class II methanol maser is a ubiquitous and specific tracer of the earliest stages of HMSF, a catalogue thereof can outline the distribution of star formation in the Milky Way galaxy. To that end, we present the current most sensitive catalogue of sources emitting this line obtained from GLOSTAR VLA D-configuration observations in Chapter 4 and Appendix B. The data reduction techniques used to calibrate and process the data are detailed therein. In particular, the details of a source extraction code that was developed specifically for the detection of point sources in “dirty" radio images is described in detail. We also present the methodology for dealing with difficulties of handling the large size of the GLOSTAR data, detailing the benefits and drawbacks in producing our maser catalogue in this way. The positions, velocity components and integrated fluxes are determined for the masers. We additionally search for dust continuum and radio continuum associations

to determine the physical properties of the population of sources with detected maser emission and the difference in these properties for newly detected sources with respect to the total population.

Lastly, GLOSTAR also procured higher angular resolution VLA B-configuration data for a subset of the full coverage of the project field. Chapter 5 presents this higher resolution data towards the methanol masers detected in the pilot region of GLOSTAR ($28^\circ < l < 36^\circ$ in galactic longitude and $|b| < 1^\circ$ in galactic latitude). Associated masers in both catalogues are then compared, where we have searched for occurrences where maser spots have split into multiple sources when resolved with higher-resolution data in order to investigate the velocity structure of these maser distributions. Additionally, as we have access to two epochs of observations, we are able to investigate maser variability. Maser variability is a topic of high interest for high-mass star formation as with the determination of the processes that drive maser variability, we can better understand the processes involved in the development of the MYSO hosting the maser. We briefly discuss this for a few select sources.

Chapter 2

Observations and Data Analysis

Overview

We describe the background and usual terminology for the physical quantities and experimental observables used in this thesis, particularly those pertaining to radio astronomy. An in-depth discussion and derivation of the topics presented below can be found in Thompson (1999), Wilson et al. (2013), and Klein (2014). The instruments and techniques used to obtain data are also described herein.

2.1 Observations at radio wavelengths

2.1.1 The radio window

The first radio emission from the Milky Way were detected by the physicist and radio engineer Karl Guthe Jansky in 1931. He was initially tasked with investigating potential interference problems with transatlantic voice transmissions for the Bell telephone laboratories company. He detected a periodic signal at a wavelength (λ) of 14.6 m (equivalent to a frequency, ν, of 20.5 MHz) that he at first hypothesised was coming from the Sun. However, upon closer examination, the period was exactly that of a sidereal day, 23 hours and 56 minutes. What Jansky instead detected was not the Sun, but emission coming from the centre of the Milky Way.

In 1938, Grote Reber followed up on these findings at the shorter wavelength of 1.87 m (160 MHz), using a parabolic dish reflector that he built himself (Reber 1944). The serendipitous discovery by Jansky and the engineering efforts by Reber and others laid the foundation for what is now known as the field of radio astronomy. From an initial repeating signal in the 1930s, and homemade engineering efforts, radio astronomy is now a science with large collaborations and complex instruments that are designed for specific tasks such as imaging the shadow of the black hole at the centre of a galaxy (Event Horizon Telescope Collaboration et al. 2019, 2022)

However, ground-based observations are not without their inherent problems. The "radio window" corresponds to the lowest frequencies of the electromagnetic spectrum used in astronomy, usually defined as the range from a few MHz to the THz regime (i.e., λ=10 m to 0.3 mm or ν = 30 MHz to 1 THz, see Fig. 2.1). The lower limit of the radio window is determined by the Earth's ionosphere where the charged particles therein reflect radio waves (with λ>30 m) back into space. On the other end, the upper limit is governed by the existence of certain molecules in the troposphere such as O_2 and, predominantly, H_2O that absorb the incoming emission from outer space. While

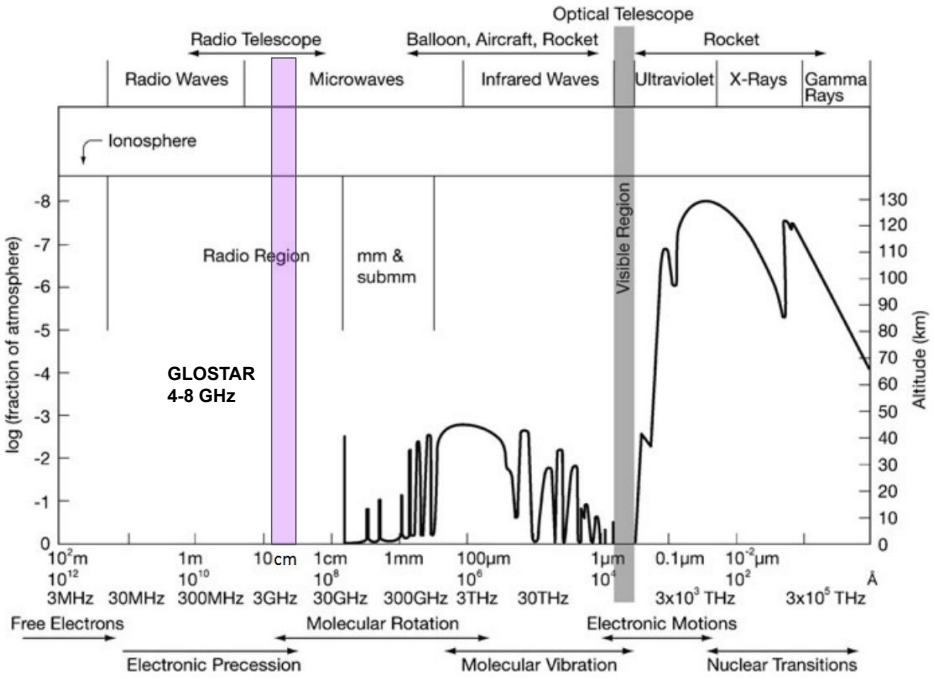

Figure 2.1: Shown is the general transmission of the electromagnetic spectrum through the Earth's atmosphere. The black curve shows a transmission of 50% corresponding to the required altitude (right-axis) or fraction of the atmosphere (left-axis). The wavelength/frequency for the radiation is shown on the bottom axis. The purple shading shows the approximate coverage of frequencies used in this work. Image adapted from Wilson et al. (2012).

the "radio window" is bounded, it is a very large one that allows for ground-based observatories whereas some wavelengths might necessitate space-based telescopes and airborne observatories.

The atmosphere is not the only obstacle to astronomy, but the development of civilisation itself is bringing disturbances to radio astronomy in particular. Radio signals are used in various aspects of human life such as cell phones and can produce so-called Radio Frequency Interference (RFI) that is often stronger than astronomical radio signals and impedes observations at certain frequencies or makes them impossible altogether. While there are international agreements to reserve small portions of the radio frequency range for radio astronomy studies exclusively, it has begun to be a struggle for radio astronomers to observe many parts of the radio window.

2.1.2 Radio measurements

Recall the Planck distribution introduced in Sect. 1.2.3 in Eq. 1.4:

$$B_\nu(T) = \frac{2h\nu^3}{c^2}\left(\frac{1}{e^{h\nu/kT}-1}\right). \tag{2.1}$$

This can be used to describe the sources we observe in the sky with our radio telescopes provided they are black bodies as we can eventually compute the amount of energy that is radiated within a particular range of frequencies. If they are not, we can still use this relation but with additional corrections. Integrating over all frequencies would give the total brightness:

$$B(T) = \int B(\nu, T)\,\mathrm{d}\nu \quad (\text{units} : \mathrm{W\,m^{-2}\,sr^{-1}}), \tag{2.2}$$

and integrating this again over angular area would give us the flux, S:

$$S = \int B(T)\,\mathrm{d}\Omega \quad (\text{units} : \mathrm{W\,m^{-2}}), \tag{2.3}$$

which is just the power received per unit area. A related quantity, the flux density S_ν, is what is used in radio astronomy, which is the Planck function integrated over solid angle:

$$S_\nu = \int B_\nu(T)\,\mathrm{d}\Omega, \tag{2.4}$$

and is a quantity defined per unit frequency or per unit bandwidth and has a specific unit, the Jansky (Jy), commemorating Karl G. Jansky. This unit is used to account for the order of magnitude of flux densities typically encountered in radio astronomy and so $1\,\mathrm{Jy} = 10^{-26}\,\mathrm{W\,m^{-2}\,Hz^{-1}}$.

At radio frequencies, where the photon energy is considered to be small enough such that $h\nu \ll kT$, the brightness can be approximated using the *Rayleigh-Jeans* approximation, giving:

$$B_\nu(T) = \frac{2kT\nu^2}{c^2}, \tag{2.5}$$

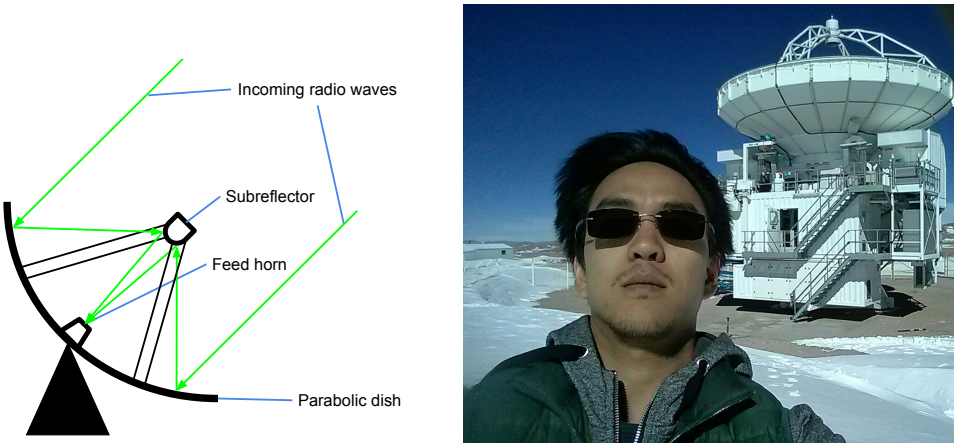

Figure 2.2: *Left*: A simple schematic of a single-dish radio antenna. The green arrows depict the path of the incoming radiation as it is collected into a focal point and fed to the feed horn and eventually the receiver for further processing of the signal. *Right*: A young PhD student is shown at the high-altitude of the Chajnantor summit in Chile in front of an example of a radio telescope, the 12-m Atacama Pathfinder EXperiment telescope (APEX).

where T is the temperature of a blackbody with the same surface brightness at a given frequency. In the case of radio astronomy, it is often customary to measure the brightness of an extended source by this temperature, which is designated as the brightness temperature, T_b, given that these two properties are directly proportional. Using this notation, the flux density from Eq. 2.4 can be described as:

$$S_\nu = \int B_\nu(T)\,\mathrm{d}\Omega = \frac{2k\nu^2}{c^2}\int T_b\,\mathrm{d}\Omega. \tag{2.6}$$

Radio telescopes, however, measure a quantity called the *antenna temperature*, T_A. To relate this to the physical quantity, brightness temperature, we must first develop an understanding of how a single dish radio telescope works.

2.1.3 Single dish radio telescopes

The most simple and common setup for a telescope to make observations at radio wavelengths would be a single parabolic dish (antenna) that focuses the incoming radiation to a subreflector (or "feed") from where it can be further processed. A simple schematic is given in Fig. 2.2. The angular resolution (Θ), which is defined as the telescope's ability to differentiate a given source's features, or its ability to distinguish a source from a nearby neighbour, is dependent on the telescope diameter, D, and the observed wavelength λ as given by:

$$\Theta \propto \frac{\lambda}{D}. \tag{2.7}$$

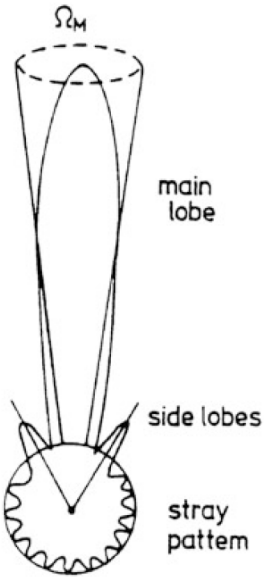

Figure 2.3: Sketch of the polar power pattern showing the main beam, and near and far side lobes. The weaker far sidelobes have been combined to form the "stray pattern". Image credit: Wilson et al. (2012).

When a radio antenna points to a position on the sky, it measures the power of the incoming signal. The power pattern of an antenna describes the response of the antenna to a source as a function of the angular distance from the antenna axis. This can be seen in Fig. 2.3. The pattern of the beam solid angle, $\Omega_{\rm A}$, is given in polar coordinates given by:

$$\Omega_{\rm A} = \iint P_{\rm n}(\theta, \phi)\, {\rm d}\Omega, \tag{2.8}$$

where $P_n(\theta, \phi)$ is the antenna power pattern normalised with respect to its peak as a function of the angular sizes.

In the case of an ideal antenna, the normalised power pattern would be such that $P_{\rm n} = 1$ for the full beam solid angle, $\Omega_{\rm A}$ when integrated over the full sphere and $P_{\rm n} = 0$ otherwise. However, as can be seen in Fig. 2.3, the power pattern is not so isotropic in reality as no ideal antenna exists, but has instead a much higher response in a specific angular area, known as the main lobe. The other areas are known as the side lobes. The better the quality of an antenna, the more the power is concentrated in the *main beam solid angle* as defined by:

$$\Omega_{\rm MB} = \iint\limits_{\rm main\,lobe} P_{\rm n}(\theta, \phi)\, {\rm d}\Omega. \tag{2.9}$$

This effectiveness is given by the quantity, $\eta_{\rm MB}$, the main beam efficiency:

$$\eta_{\rm MB} = \frac{\Omega_{\rm MB}}{\Omega_{\rm A}}. \tag{2.10}$$

Using Eq. 2.8, if we were to integrate over the beam solid angle, we would obtain an expression for the flux density as the convolution of the position dependent brightness with the antenna power pattern:

$$S_\nu = \iint B_\nu(\theta,\phi) P_{\rm n}(\theta,\phi)\,{\rm d}\Omega. \tag{2.11}$$

As radio telescopes receive electromagnetic waves, the power received by an antenna from an element of the solid angle of the sky, per unit frequency is given by[1],

$$P_\nu = \frac{1}{2} A_{\rm eff} \int B P_{\rm n}\,{\rm d}\Omega = \frac{1}{2} A_{\rm eff} \iint B(\theta,\phi) P_{\rm n}(\theta,\phi)\,{\rm d}\Omega, \tag{2.12}$$

where the factor of $1/2$ accounts for polarisation (the incoming radiation is generally assumed to be unpolarised). The actual area over which the dish effectively collects and reflects radiation is what we define as the effective collecting area, $A_{\rm eff}$, which can be expressed in terms of the total beam solid angle ($\Omega_{\rm A}$), as,

$$A_{\rm eff} = \frac{\lambda^2}{\Omega_{\rm A}}. \tag{2.13}$$

Thus, we see from Eq. 2.11 that the right side of Eq. 2.12 can be put in terms of the flux density:

$$P_\nu = \frac{1}{2} A_{\rm eff} S_\nu. \tag{2.14}$$

Additionally, we see that if we substitute Eq. 2.5, 2.8, and 2.13 into Eq. 2.14, we obtain

$$P_\nu = kT. \tag{2.15}$$

What we get is the well known *Johnson-Nyquist theorem* (1928)[2] which can be used to relate the power per unit frequency received by the antenna and its temperature, T. This is valid under the Rayleigh-Jeans approximation, where the temperature here is designated as the antenna temperature, $T_{\rm A}$. As such, in equating Eq. 2.15 with Eq. 2.14, we have:

$$S_\nu = \frac{2k}{A_{\rm eff}} T_{\rm A}. \tag{2.16}$$

Recall Eq. 2.6 which when we equate to the above equation we get

$$T_{\rm A} = A_{\rm eff} \frac{\nu^2}{c^2} \int T_b d\Omega. \tag{2.17}$$

The antenna temperature is then the convolution of the sky brightness with the beam pattern and can be considered the *beam-averaged* measurement of the brightness temperature.

[1] It is also for each polarisation, which we do not discuss here.

[2] Strictly speaking, it states that the available noise power of a resistor is proportional to its temperature.

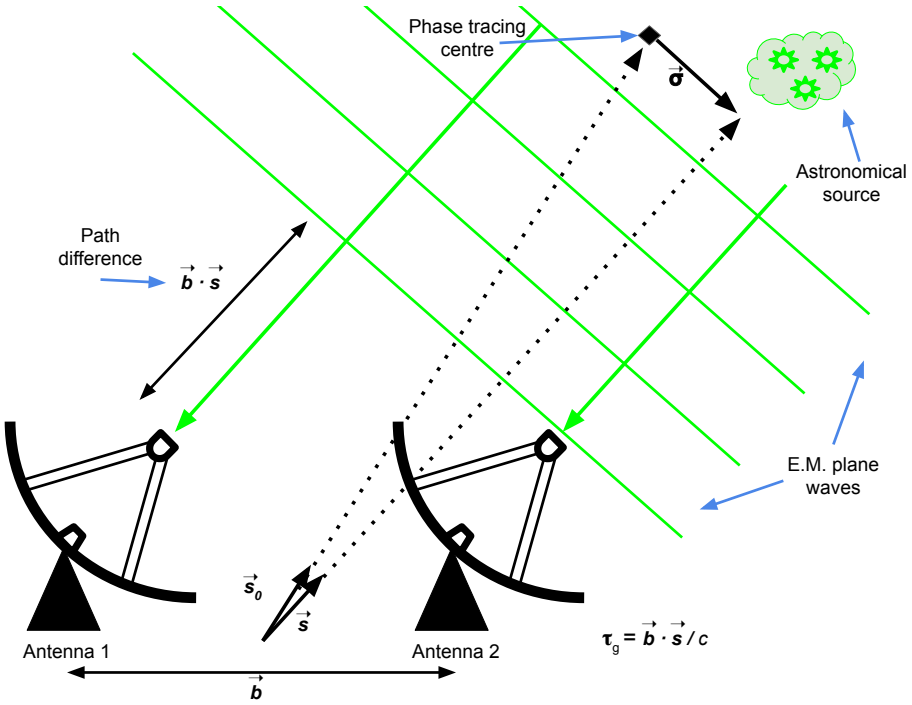

Figure 2.4: Schematic of a two-element interferometer observing a source in the far-field such that the incoming radiation (green) arrives as plane waves. They are separated by the baseline vector, $\vec{b}$. The unit vector, $\vec{s}$, points to an arbitrary point in the field of view (FOV) whereas the unit vector $\vec{s}_0$ points towards the phase tracing centre of the interferometer array. The arrival time difference of a given plane of radiation between Antenna 1 and 2 is the geometric time delay, τ_g, where c is the speed of light. Image adapted from Wilson et al. (2012).

2.1.4 Interferometry

As discussed in the above section, the angular resolution from a single dish radio telescope is approximated by $\Theta \propto \lambda/D$, where λ is the wavelength of the incoming radio radiation and D is the diameter of the dish. In order to obtain higher angular resolution data to better resolve sources on the sky, this means we would need to increase D for a given wavelength of observation. However, current engineering and materials put a limit on the size of the telescope, with the largest being the Five hundred meter Aperture Spherical Telescope (FAST) with a diameter $\sim$500 m. Fortunately, Albert Abraham Michelson (Jenkins & White 2001) showed that one can obtain a similar resolving power $\Theta \approx \lambda/D$ of a single dish, by using two individual dishes of diameter d separated by a distance equivalent to that of the larger single dish, where $d \ll D$. It is from this principle that the field of radio interferometry has developed.

To elucidate this concept in practice, we begin with the simplest setup, that of two radio antennae as shown in Fig. 2.4. The individual dish size is smaller than their separation, which we define now as the baseline vector, $\vec{b}$. We define the unit vector

$\vec{s}_0$, which points to the centre of the region to be mapped, and $\vec{s} = \vec{s}_0 + \vec{\sigma}$ to be an arbitrary position in the field. For a sufficiently far source, we can consider the incoming radiation as electromagnetic plane waves. As such, one can see in the illustration in Fig. 2.4 that a given plane wave will arrive at Antenna 1 after Antenna 2 separated in time by a geometric time delay, τ_g due to the difference in path length. We express this in terms of the dot-product of the vectors as

$$\tau_g = \frac{\vec{b} \cdot \vec{s}}{c}. \tag{2.18}$$

We make some simplifying assumptions for this basic case, where the emission is monochromatic and noise from the celestial background and instrumentation of the telescope are neglected. Then, the signal received by Antenna 1 at time $t - \tau_g$ and by Antenna 2 at time t induces voltages given by:

$$U_1(t) = U_{1,0} \cos(2\pi\nu(t - \tau_g)) \tag{2.19}$$
$$U_2(t) = U_{2,0} \cos(2\pi\nu t), \tag{2.20}$$

where $U_{1,0}$ and $U_{2,0}$ is the strength of the voltages. These voltages are fed into a *correlator* where the combination of the two signals is performed via cross-correlation, i.e., the time average of the product of the two signals where:

$$\begin{aligned} U_2(t)U_1(t) &= U_{2,0} \cos(2\pi\nu t) \times U_{1,0} \cos(2\pi\nu(t - \tau_g)) \\ &= U_{1,0}U_{2,0} \cos(2\pi\nu t) \cos(2\pi\nu(t - \tau_g)) \\ &= U_{1,0}U_{2,0} \cdot \frac{1}{2}\big(\cos(2\pi\nu t + 2\pi\nu(t - \tau_g)) + \cos(2\pi\nu t - 2\pi\nu(t - \tau_g))\big) \\ &= \frac{U_{1,0}U_{2,0}}{2}\big(\cos(2\pi\nu(2t - \tau_g)) + \cos(2\pi\nu\tau_g)\big). \end{aligned}$$

This is done in order to approximate the coherence between the signals arriving at the two antennae in order to eventually produce images (discussed in Section 2.2.3). In the case where the time over which we perform the averaging is sufficiently large, i.e., much greater than over one oscillation of cosine ($t' \gg (2\pi\nu)^{-1}$), then the average over time t' will be similar to the average over one oscillation period. Thus, the high frequency term, $\cos(2\pi\nu(2t - \tau_g))$, can be neglected. As such, the output power from the correlator is:

$$P(\tau_g) = \langle U_1(t)U_2(t) \rangle = U_{1,0}U_{2,0} \cos(2\pi\nu\tau_g). \tag{2.21}$$

Recall from Eq. 2.12 that the power received from a radio telescope is proportional to the effective collecting area, the brightness distribution and the telescope's power pattern integrated over the source solid angle. It becomes clear then that the product of the amplitudes $U_{1,0}$ and $U_{2,0}$ is a representation of the total power received from the source and depends on both the specifications of the interferometer and the properties of the source. The interferometer's sensitivity is determined by its effective collective area, $A(\vec{s}) = \sqrt{A_1(\vec{s}) \cdot A_2(\vec{s})}$, and the bandwidth of the receiver system, $\Delta\nu$, while the source properties are given by the brightness distribution $B(\vec{s})$ and the two-dimensional

angular extent of the source. We therefore can express the output power as the integral over the solid angle of the source:

$$P(\tau_{\rm g}) = \Delta\nu \int\limits_{\rm source} A(\vec{s})B(\vec{s})\cos(2\pi\nu\tau_{\rm g})\,{\rm d}\Omega. \tag{2.22}$$

With our definition of $\tau_{\rm g}$ (Eq. 2.18) and $\vec{s}$, we can rewrite Eq. 2.22 in terms of $\vec{s}_0$, as it is in this direction that the so-called phase tracking centre is situated. This position is the pointing centre of all the telescopes of the interferometer array. When integrating over the solid angle, Ω, the varying quantity is therefore described by $\vec{\sigma}$. Doing so gives us:

$$\begin{aligned} P &= \Delta\nu \int A(\vec{\sigma})B(\vec{\sigma})\cos(2\pi\nu\frac{\vec{b}\cdot(\vec{s}_0+\vec{\sigma})}{c})\,{\rm d}\Omega \\ &= \Delta\nu \int A(\vec{\sigma})B(\vec{\sigma})\Big(\cos(2\pi\frac{\nu}{c}\vec{b}\cdot\vec{s}_0)\cos(2\pi\frac{\nu}{c}\vec{b}\cdot\vec{\sigma}) \\ &\quad - \sin(2\pi\frac{\nu}{c}\vec{b}\cdot\vec{s}_0)\sin(2\pi\frac{\nu}{c}\vec{b}\cdot\vec{\sigma})\Big)\,{\rm d}\Omega \\ &= \Delta\nu\cos(2\pi\frac{\nu}{c}\vec{b}\cdot\vec{s}_0)\int A(\vec{\sigma})B(\vec{\sigma})\cos(2\pi\frac{\nu}{c}\vec{b}\cdot\vec{\sigma})\,{\rm d}\Omega \\ &\quad - \Delta\nu\sin(2\pi\frac{\nu}{c}\vec{b}\cdot\vec{s}_0)\int A(\vec{\sigma})B(\vec{\sigma})\sin(2\pi\frac{\nu}{c}\vec{b}\cdot\vec{\sigma})\,{\rm d}\Omega, \end{aligned} \tag{2.23}$$

where we have used the trigonometric property $\cos(\alpha \pm \beta) = \cos(\alpha)\cos(\beta) \mp \sin(\alpha)\sin(\beta)$. We now define the complex visibility function

$$V \equiv |V|\cdot e^{i\phi_v} = \iint\limits_{\rm source} A_n(\vec{\sigma})B(\vec{\sigma})e^{-2\pi i\frac{\nu}{c}\vec{b}\cdot\vec{\sigma}}\,{\rm d}\Omega, \tag{2.24}$$

where $A_n(\vec{\sigma}) = A(\vec{\sigma})/A_0$ is the antenna response relative to its maximal value of A_0 which occurs when the source position is in the centre of the antenna beam. The amplitude, |V|, and the phase, ϕ_v, of the correlator output are a measure for the visibility amplitude and phase, respectively. We can separate this complex function into its real and imaginary components:

$$|V|\cos(\phi_v) = \int\limits_{\rm source} A_n(\vec{\sigma})B(\vec{\sigma})\cos(2\pi\frac{\nu}{c}\vec{b}\cdot\vec{\sigma})\,{\rm d}\Omega, \tag{2.25}$$

$$|V|\sin(\phi_v) = \int\limits_{\rm source} A_n(\vec{\sigma})B(\vec{\sigma})\sin(2\pi\frac{\nu}{c}\vec{b}\cdot\vec{\sigma})\,{\rm d}\Omega, \tag{2.26}$$

and one can immediately see its similarity to Eq. 2.23. We can therefore express the power response in terms of the visibility components. In substituting them into Eq. 2.23, we can expand and use the same trigonometric property used above to simplify the expression into:

$$P = A_0|V|\Delta\nu\cos\Big(2\pi\frac{\nu}{c}\vec{b}\cdot\vec{s}_0 - \phi_v\Big). \tag{2.27}$$

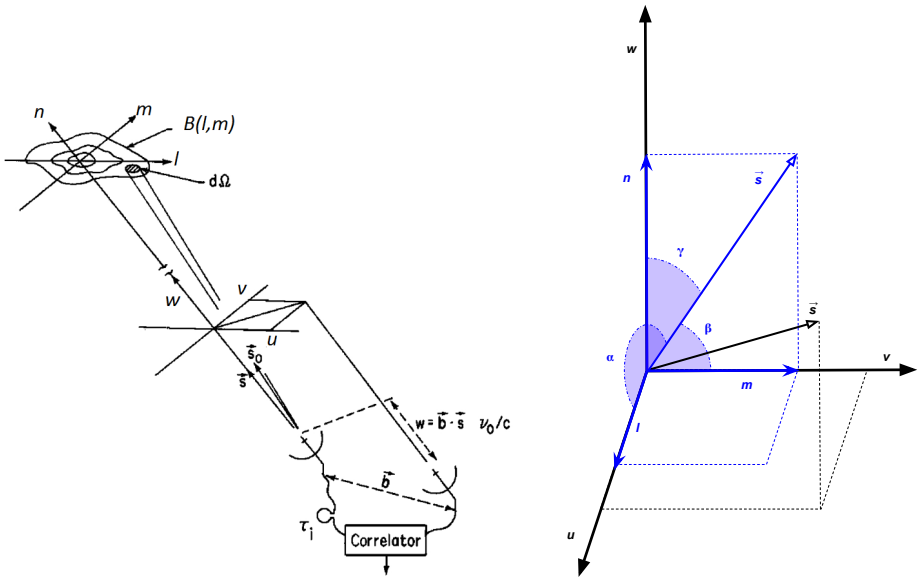

Figure 2.5: *Left*: Coordinate system used to relate the location of radio telescopes on the Earth (baseline $\vec{\boldsymbol{b}}$) with those of celestial objects (in direction of $\vec{\boldsymbol{s}}$). The u- and v-axes point towards East and North, respectively, while w points towards the phase tracking centre $\vec{\boldsymbol{s}}_0$. Image credits: Thompson (1999). *Right*: Illustration of the same coordinate systems showing the direction cosines of $\vec{\boldsymbol{s}}$.

It is clear that when $\phi_v = 0$, this implies that $\vec{\sigma} = 0$ and thus the source is located directly in line of $\vec{\boldsymbol{s}}_0$. As such, the visibility phase carries with it the information about the position of the source relative to the phase tracking centre.

The main intention of measuring the visibilities from the |V| and ϕ_v is to recover the brightness distribution of the source being observed on the plane of the sky as it enters the visibility function in Eq. 2.24. In practical terms, this means producing an image that represents the celestial sky observed by the radio interferometer. To do this, we need to relate the coordinate system of the telescope with that of the observed sky. We introduce the u, v, w- and l, m, n-coordinate systems to relate the coordinate system of the antennas to that of the celestial sky. A basic sketch is shown in Fig. 2.5. In this coordinate system, the source vector $\vec{\boldsymbol{s}}$ is given by the direction cosines

$$\vec{\boldsymbol{s}} = (\cos\alpha, \cos\beta, \cos\gamma) = (l, m, \sqrt{1 - l^2 - m^2}), \tag{2.28}$$

where we have described the source unit vector in terms of an east-west component on the sky, l, a north-south component, m, and $n = \sqrt{1 - l^2 - m^2}$, the orthogonal component of the unit vector. The baseline vector $\vec{\boldsymbol{b}}$ has components (u, v, w) such that

$$\frac{\vec{\boldsymbol{b}}}{\lambda} = (u, v, w), \tag{2.29}$$

and is the baseline length in units of wavelength. Here, u is the east-west direction, v is the north-south direction, and w is the vertical component in the up-down direction.

The visibility function (Eq. 2.24) can be rewritten as

$$V(u,v,w) = \int_{-\infty}^{\infty}\int_{-\infty}^{\infty} A_n(l,m)B_n(l,m) \times \exp\{-2\pi i[ul+vm+w(\sqrt{1-l^2-m^2}-1)]\}\frac{\mathrm{d}l\mathrm{d}m}{\sqrt{1-l^2-m^2}}. \tag{2.30}$$

Now if we assume that the correlation is performed near to or at the pointing centre, this means that $A_n(0,0) \approx 1$ and Eq. 2.30 can be approximated as

$$V(u,v) \approx \iint B(l,m) \times \exp\{-2\pi i(ul+vm)\}\,\mathrm{d}l\mathrm{d}m, \tag{2.31}$$

where we see that the visibility function is nothing but the Fourier spectrum of the brightness distribution as measured with an interferometer. As such, we can invert this equation to obtain the brightness distribution by measuring the visibility for many different baselines. We note that a single baseline of the interferometer will only be able to provide a very limited coverage of the uv-plane. Furthermore, the interferometer is sensitive to different size-scales which is dependent on the length of the baseline itself. To receive information on multiple scales for the source, we need multiple baselines. To obtain smaller-scale structure, one would need baselines of greater length. The situation where having a limited number of data points in uv-space is illustrated in Fig. 2.6. Furthermore, the largest angular scale of the emission which the array is sensitive to is governed by the length of the shortest baseline. In essence, extended emission of sources, where extended means larger than the full-width at half-maximum

$$\mathrm{FWHM} : \theta = 1.22\frac{\lambda}{|\vec{\boldsymbol{b}}_{\mathrm{min}}|},$$

where $|\vec{\boldsymbol{b}}_{\mathrm{min}}|$ is the length of the shortest baseline, is resolved out and not recovered well.

In effect, it is actually not necessary to measure all the visibilities simultaneously to produce the final image. Using again the simplest interferometer consisting of only two antennas, if we are able to change the position of one of these antennas, we would be able to have multiple baselines and thus greater uv-coverage. Taking multiple sets of observations this way and combining them to produce a final image of the sky is the basis of what is called aperture synthesis, a technique developed by Sir Martin Ryle for which he was awarded the Nobel Prize for physics in 1974. In practice, we can better reconstruct the brightness distribution $B(l,m)$ by using a few other techniques to obtain a greater coverage of the uv-plane. While we used as our simplest case, having only two antennas in our interferometer, the natural next step would be to make use of many more antennas at varying distances from each other to increase the number of individual baselines. Since, we can consider each antenna pair as a baseline, the total number of baselines formed by an array of N antennas is given by N(N-1)/2. Furthermore, one can observe for an extended period of time and make use of what is known as Earth rotation synthesis. Earth rotation synthesis takes advantage of the

fact that for a pair of stationary antennas, the baseline $\vec{\boldsymbol{b}}$ position vector changes its position relative to the source vector continuously as the Earth naturally rotates. As such, an observation integrated over a finite time, $\Delta t_{\rm i}$, provides a different sample of the visibility function and thus, another component of the brightness distribution.

Since the visibility function is in practice sampled discretely, we use a sampling function, $\mathfrak{S}(u,v)$, such that it gives the values for u and v where the $V(u,v)$ is sampled and zero everywhere else (i.e., where no data has been taken). It has the form

$$\mathfrak{S}(u,v) = \sum_k w_k \delta(u-u_k, v-v_k), \tag{2.32}$$

and is a sum of a two-dimensional Dirac-delta function where w_k are the weighting factors and (u_k, v_k) are the coordinates where the visibilities are recorded. The resultant sampled visibility is then given by the product of the sampling function with the visibility function:

$$V^{\mathfrak{s}}(u,v) = \mathfrak{S}(u,v) \cdot V(u,v). \tag{2.33}$$

To reconstruct the real brightness distribution, one needs to (as mentioned above) perform an inverse Fourier transform of the visibilities:

$$\begin{aligned} B^{\rm D} &= \mathcal{F}^{-1}(V^{\mathfrak{s}}(u,v)) = \mathcal{F}^{-1}\mathfrak{S}(u,v) * \mathcal{F}^{-1}V(u,v) \\ B^{\rm D} &= \mathfrak{B}^{\rm D} * B, \end{aligned} \tag{2.34}$$

where we have used the convolution theorem. $B^{\rm D}$ represents the *dirty* image and is the image that is reconstructed from the sampled visibilities. Then, in order to obtain the real image described by the brightness distribution $B = \mathcal{F}^{-1}V(u,v)$, one needs to deconvolve $\mathfrak{B}^{\rm D} = \mathcal{F}^{-1}\mathfrak{S}(u,v)$ from the dirty image. To perform the deconvolution, we use the `CLEAN` algorithm (Högbom 1974). This will be discussed in greater detail in Section 2.2.3.

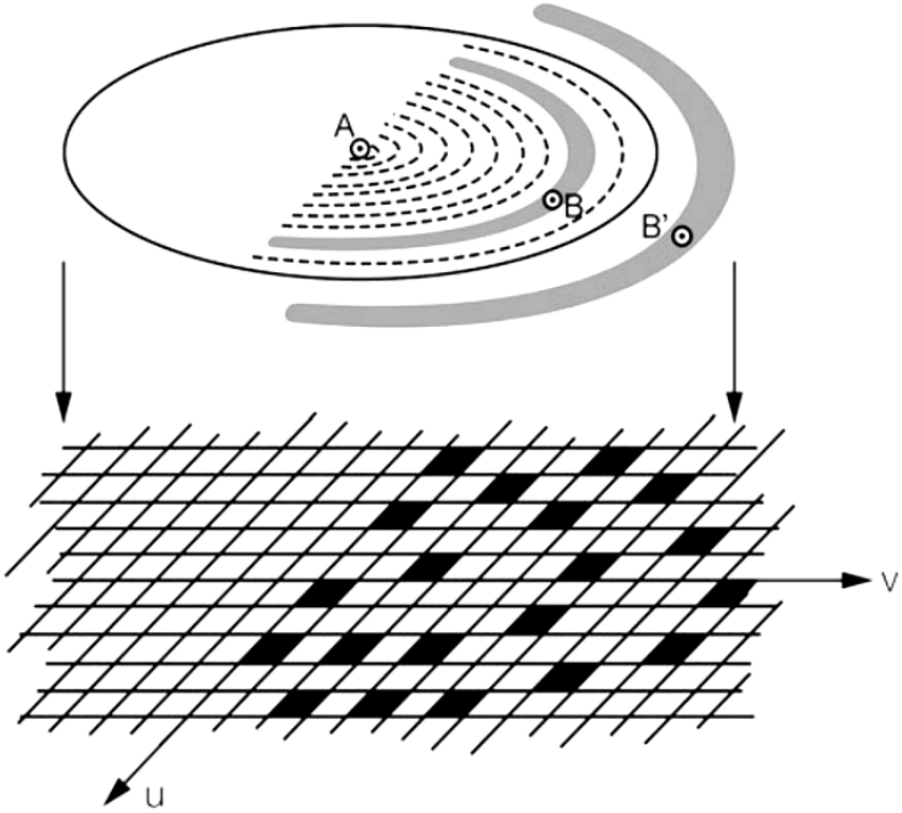

Figure 2.6: This sketch illustrates the fact that not all positions in the *uv*-plane have data. The locations in the *uv*-plane which are filled with correlated data from the outputs of three antennas (A, B, and B′) located along an east-west baseline. The data are taken at discrete time intervals while tracking a source. The regions filled in *black* represent those where data was taken; there is no data for those not filled. The data are the correlation of antenna A with B and A with B′. The filled squares form parts of elliptical rings. The correlation of antenna B with B′ produces the region close to the origin since the spacing between B and B′ is small. The gaps between regions are exaggerated. This missing data gives rise to an imperfect estimate of Eq. 2.30. Image credits: Wilson et al. (2013).

2.2 A Global view on Star formation: The GLOSTAR survey

We provide a summary of the motivation for the GLOSTAR survey and the details of observations used as part of this thesis. While the full details are found in Brunthaler et al. (2021), we explore some of the intricacies here as some of the data products (the spectral line data) were produced as a part of this thesis.

As mentioned above, the electromagnetic spectrum is wide, and its radiation emerges from a wide diversity of sources. In studying celestial objects, different wavelengths allow us different perspectives of what is happening in our very own Galaxy and in the Universe as a whole. Over the past decade, many efforts were made to survey the Galactic plane comprehensively over many different wavelengths. Fig. 2.7 shows how the Milky Way can look vastly different depending on the wavelength regime. As such, multi-wavelength surveys enable investigations of not only individual local phenomena such as stars, stellar clusters, ionised gas and molecular or atomic clouds, but studies of our Galaxy as a whole which we can then compare to other galaxies. Some of the most widely used surveys in the infrared, (sub-)millimetre, and radio regimes include:

- **Infrared** – e.g., GLIMPSE (Churchwell et al. 2009), MIPS Galactic Plane Survey (MIPSGAL, Carey et al. 2009), Herschel infrared Galactic Plane Survey (Hi-GAL, Molinari et al. 2010),

- **(Sub-)millimetre** – e.g., ATLASGAL (Schuller et al. 2009b; Csengeri et al. 2014), Bolocam Galactic Plane Survey (BGPS, Aguirre et al. 2011), WISE (Wright et al. 2010), JCMT Plane Survey (JPS, Moore et al. 2015; Eden et al. 2017),

- **Radio** – e.g., Multi-Array Galactic Plane Imaging Survey (MAGPIS, Becker 1990; Becker et al. 1994), Sino-German 6 cm survey (Han et al. 2015), Coordinated Radio and Infrared Survey for High-Mass Star Formation (CORNISH, Hoare et al. 2012; Purcell et al. 2013), The HI, OH, Recombination line survey of the Milky Way (THOR, Bihr et al. 2015; Beuther et al. 2016; Wang et al. 2020), Southern Galactic Plane Survey (SGPS, McClure-Griffiths et al. 2005), VLA Galactic Plane Survey (VGPS, Stil et al. 2006), Canadian Galactic Plane Survey (CGPS, Taylor et al. 2003), H2O southern Galactic Plane Survey (HOPS, Walsh et al. 2011).

The combination of these surveys allows us to study all the evolutionary stages involved in high-mass star formation in an unbiased way (e.g., König et al. 2017; Elia et al. 2017; Urquhart et al. 2018c) for the first time.

With an emphasis on studying star formation, the infrared surveys (e.g., GLIMPSE) catalogue millions of sources which preferentially select young and evolved stars from their hot circumstellar dust emission (e.g., Robitaille et al. 2008). Complementary to this are surveys in the sub-millimetre regime (e.g., ATLASGAL) which study the cool dust inside molecular clouds where these young and evolved stars form. They

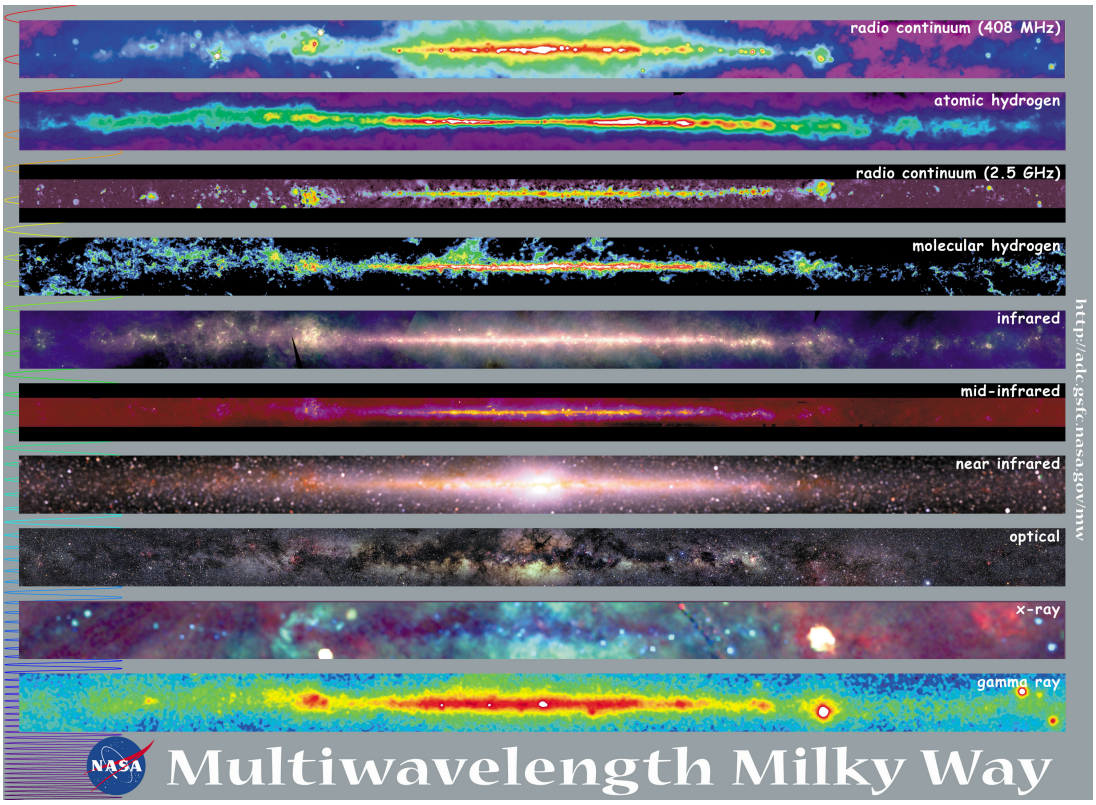

Figure 2.7: View of the Milky Way at different wavelengths. ©NASA

have already catalogued the properties (e.g, temperature, density) of thousands of dust clumps (e.g, Urquhart et al. 2018a). On the other hand, radio studies can observe atomic hydrogen, which is widely distributed and traces where the majority of the mass of the ISM is located whilst also providing information on the velocity structure of the neutral gas (e.g., VGPS). Studying the ionised gas, however, is crucial to understand both the early and late phases of high-mass star formation as it can arise from nebulae surrounding the newly formed massive hot stars. These studies centre on obtaining the radio continuum spectral index in order to classify the nature of the ionised gas and thus benefit from studies over a range of radio frequencies. To this end, CORNISH, while not the first survey, was at the time, the most uniformly sensitive, homogeneous and complete survey of compact radio-emission sources at 5 GHz towards the northern Galactic plane. It is a very successful survey, which has detected many thousands of radio sources to be identified and studied (e.g., Urquhart et al. 2013b; Cesaroni et al. 2015; Kalcheva et al. 2018; Irabor et al. 2018). However, CORNISH was designed to focus on the ultra-compact HII region stage of high mass star formation. The technology of the correlator at the time limited the bandwidth available to ∼50 MHz and the focus on UC HII regions makes it less sensitive to emission from larger angular scales (i.e., $>20''$) which does not provide the whole picture. In addition, they did not observe spectral line data.

To address these shortcomings, the Global view on Star formation in the Milky Way (GLOSTAR; Brunthaler et al. 2021) survey has been designed to take advantage of the vastly improved capabilities of modern digital instrumentation of current radio telescopes. Whereas CORNISH used the Very Large Array (VLA) (see Fig. 2.8, at right), GLOSTAR benefits from the upgrade of the VLA into the Karl G. Jansky Very Large Array, (also known as JVLA[3]). As part of this upgrade, new receivers with much wider bandwidths and lower system noise allow for better observations along with a continuous frequency coverage from 1–50 GHz. Furthermore, with the Wideband Interferometric Digital ARchitecture (WIDAR) correlator, the VLA's spectroscopic performance is improved by orders of magnitude, in terms of instantaneous frequency coverage and spectral resolution. Finally, as large surveys inevitably have higher time costs, any reduction of the overhead time (the time used for a telescope to set up before an observation scan) would allow for more time spent on target. To this end, the "dead time" due to the slew and settling time of the antennas between observations was much reduced from the 20 s typical of the old VLA. All of these improvements enable the VLA to make extremely sensitive and efficient surveys (for a more in-depth description, see Perley et al. 2011).

To add to the current study of HMSF, GLOSTAR is designed to be an unbiased survey that detects and characterises star-forming regions in the Milky Way Galaxy. It detects tell-tale tracers of star formation: compact, ultra- and hyper-compact HII regions and molecular masers that trace different stages of early stellar evolution and pinpoints the very centres of the early phase of star-forming activity. Combined with the submm surveys such as ATLASGAL and the continually updated Bar and Spiral

[3]Initially known as the EVLA (Expanded VLA).

Figure 2.8: Images of the telescopes used as part of the GLOSTAR survey. © Norbert Tacken/MPIfR (Effelsberg telescope); NRAO/AUI/NSF (Very Large Array).

Structure Legacy (BeSSeL) Survey[4], GLOSTAR offers a nearly complete census of the number, luminosities, and masses of massive star forming clusters. These clusters cover a large range of evolutionary stages and thus allow for a unique dataset to obtain a *global view* on star formation in our Galaxy. Apart from information on high-mass star formation, the GLOSTAR survey allows efficient identification and imaging of supernova remnants (Dokara et al. 2021), planetary nebulae, and extragalactic background sources (Medina et al. 2019; Dzib et al. 2022; Yang et al. in prep).

It uses the extremely wideband (4–8 GHz) C-band receivers of the VLA and observes target fields in both the D-configuration ($\sim 18''$) and B-configuration ($\sim 1''$) in order to have good surface brightness sensitivity for extended structures as well as higher resolution for more compact objects respectively. To obtain the zero spacings for the D-configuration data, the Effelsberg 100-m single dish telescope (see Fig. 2.8, at left), is also used. In combining both D-configuration and B-configuration data, we can make images that benefit from the surface brightness sensitivity of the D-configuration and the high resolution of the B-configuration, resulting in the best possible images for intermediate size sources. While the GLOSTAR survey uses both the VLA and the Effeslberg telescope, only the VLA was used as part of this thesis. We refer the reader to the overview paper by Brunthaler et al. (2021) for the full details that involve Effelsberg. An example of the current work to combine the two datasets is shown in Fig. 2.9 that illustrates the importance of obtaining complimentary single-dish observations.

2.2.1 Observations

The GLOSTAR survey covers the range from $-2^\circ < l < 60^\circ$ in Galactic longitude and $|b| < 1^\circ$ in latitude and, in addition, the Cygnus X star-forming complex. This corresponds to 145 square degrees in total. While the entirety of the survey has been covered with the VLA D-configuration and almost completely with the Effelsberg radio telescope, the region between $40^\circ < l < 56^\circ$ has not been observed yet in the B-

[4]See http://bessel.vlbi-astrometry.org for more details.

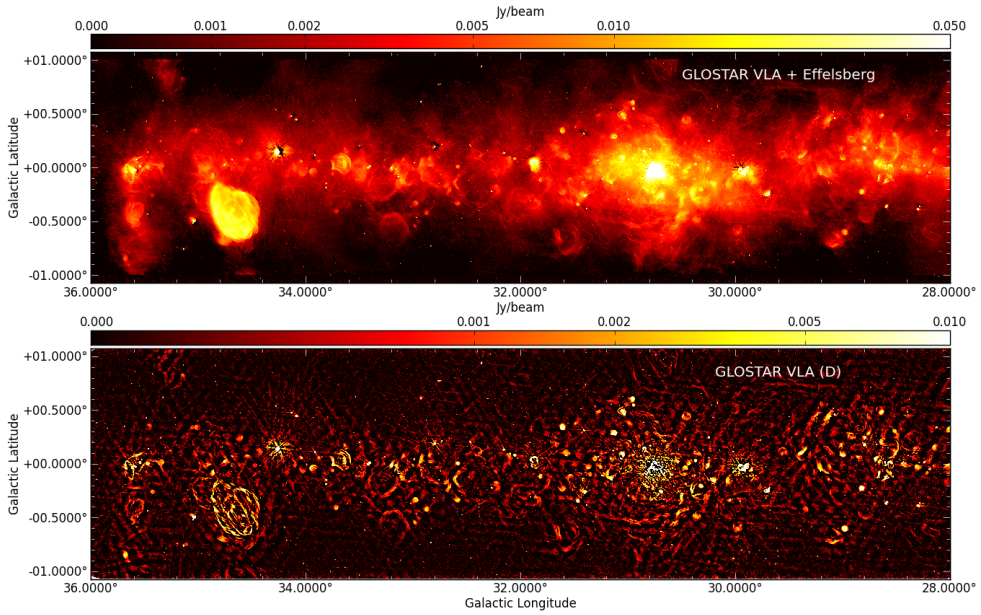

Figure 2.9: Figure is taken from Brunthaler et al. (2021) and shows the benefit of adding Effelsberg data. *Top:* Radio continuum image of the pilot region in the range $28° < l < 36°$ from the combination of the VLA D-configuration and the Effelsberg single dish images. *Bottom:* D-configuration VLA image of the full continuum of the same longitude range which was already presented in Medina et al. (2019).

Table 2.1: Table of observation properties adapted from Brunthaler et al. (2021) which lists observed lines, bandwidth, number of channels and polarization products, channel spacings, velocity coverage, and theoretical sensitivity for two visits of one pointing (for the full 1 GHz for the continuum and 1 channel for spectral lines) of the VLA observations. For l=58°–60°, the RRLs H115α (4268.142 MHz), H102α (6106.855 MHz) and H103α (5931.544 MHz) were observed instead of H110α and H96α. The central LSR velocity changed for different parts of the survey based on longitude-velocity plots of CO in the Milky Way.

Line	Frequency [MHz]	Bandwidth [MHz]	Chan. & pol. prod.	Resolution [km s^{-1}]	Coverage [km s^{-1}]	1σ rms in 15 sec [mJy beam^{-1}]
Continuum	4200–5200	8×128	8×64×4	-	-	0.09
H114α	4380.954	8	128×2	4.3	547	11
H113α	4497.776	8	128×2	4.2	533	11
H112α	4618.789	8	128×2	4.1	529	11
H_2CO	4829.660	4	1024×2	0.24	248	45
H110α	4874.157	8	128×2	3.8	492	11
Continuum	6400–7400	8×128	8×64×4	-	-	0.08
CH_3OH	6668.518	8	2048×2	0.18	360	38
H99α	6676.076	8	128×2	2.8	359	11
H98α	6881.486	8	128×2	2.7	348	11
H96α	7318.296	8	128×2	2.5	328	11

configuration. For some regions, between $-2° < l < 12°$, the hybrid DnC and BnA configurations were used when possible, as the Northern arm of the array is in the more extended configuration which ensures a more circular synthesized beam. When these hybrid configurations were no longer available (after 2016), combinations of D-, C-, B-, and A- configurations were used where applicable. Observing methanol, formaldehyde, and radio recombination lines as well as the radio continuum, the survey aims to detect various tracers of different stages of early star formation in order to gain information on the start of the stellar evolution process of massive stars.

The C-band radio continuum emission was observed with two 1-GHz wide basebands in full polarization mode. The observed spectral lines are the following: the 6.7 GHz (5_1–6_0 A^+) methanol maser emission line to pinpoint unambiguously the locations of early high-mass protostars, seven radio recombination lines (RRLs) to study the kinematics and properties of the ionized gas, and the 4.829 GHz ($1_{1,0}$–$1_{1,1}$) transition of formaldehyde (H_2CO), where absorption measurements can solve distance ambiguities. The observational setups are shown in Table 2.1 which is adapted from Brunthaler et al. (2021). The table also shows the expected sensitivities for two scans (total integration time of 15 s) where the final sensitivity is expected to be at least a factor of two better due to the observing strategy which is discussed below. Of particular note is that for the Galactic Centre region ($-2° < l < 2°$), the bandwidth of the spectral line observations were doubled at the loss of the velocity resolution due to the very broad velocity range seen in the central region of the Milky Way.

As discussed above, proper planning of the observation scans is vital for the ef-

ficiency of large surveys. For a given observation, a $2^\circ \times 1^\circ$ region of the Galactic plane was mapped, taking roughly five hours. The region is covered by ∼676 pointings where each pointing is observed for 11 seconds twice. Taking into account the overhead from moving the antennas, the total on-source integration time is 15 seconds (as stated above). An example of the layout of the pointings is shown in Fig. 2.10, where the pointings spread out according to a hexagonal grid with a spacing of $\theta_{\rm hex}$ =3.25′ (chosen such that $\theta_{\rm hex} = \theta_{\rm B}/2$, where $\theta_{\rm B} = 6.5'$ is the primary beam at the central frequency of the higher continuum band). The final sensitivities are better than the reported values in Table 2.1 because of this overlapping strategy as each pointing is also covered by six neighbouring fields. Furthermore, since fields are observed at different times, a better *uv*-coverage is obtained compared to a single pointing.

2.2.2 Calibration

All data needs to be calibrated to correct for instrumental or environmental effects.In terms of interferometric data, some of the main aspects of calibration include calibration of the absolute (flux density) scale, calibration of the signals at different frequencies relative to each other over the observing bandwidth (bandpass and delay), and calibration of the time dependent effects (complex gain; i.e., phase and amplitude) of changing conditions due to the atmosphere and instrument. This section is adapted from the NRAO CASA documentation[5].

The flux density scale calibration is needed as when the visibilities are measured, it is given in terms of relative signal strength and relative phase. As such, it needs to be rescaled in order to represent the flux density as measured from the sky visibilities. This is typically done through observations of a calibrator source with (an assumed) known and constant flux density and source structure. The measured visibilities are then compared with a model and rescaled accordingly.

The *delay* is the result of small errors in the correlator model (e.g., inaccurate antenna and source positions as well as atmospheric delays and cable length variations due to changing temperatures). These small impurities cause small deviations from the correlator model that is seen as a time-constant linear phase slope as a function of frequency within an intermediate frequency (IF) baseband. If the delay is not corrected, when averaging frequencies for a continuum image, the continuum signal is decorrelated and is not a correct representation of the sky. Furthermore, deviations of the amplitude and phase response at different frequencies (e.g. at the edge of the band) occur independently of the delay and also need to be corrected in order to obtain better signal-to-noise and dynamic range for the data. The delay and the bandpass can be also calibrated by an observation of a very strong continuum source, typically the primary flux density calibrator.

The antenna gain calibration (complex gain) is meant to account for not only the changing conditions of the instrument, but also of the environment over time. Examples of time variable instrument properties includes receiver power level settings,

[5]https://science.nrao.edu/facilities/vla/docs/manuals/obsguide/calibration

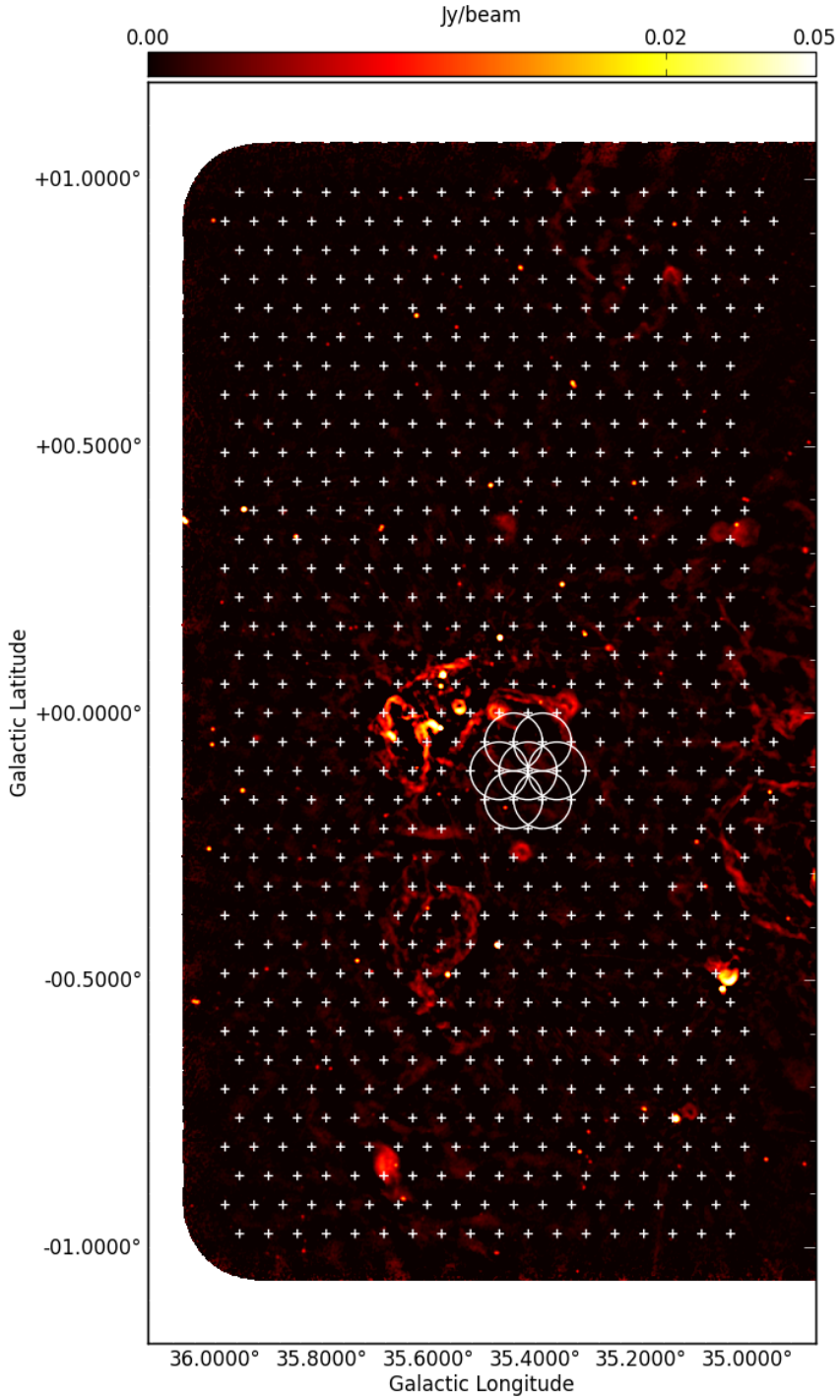

Figure 2.10: Pointing configuration of a single observation spanning the range of $35° < l < 36°$ and $|b| < 1°$. The background image shows our D-configuration continuum data. Also shown are the primary beam sizes at the centre frequency of the higher frequency continuum band (6.9 GHz) of one central pointing and its six neighbouring pointings. Taken from Brunthaler et al. (2021).

and corruption of baseband samplers. Examples of time variable environmental properties include the atmosphere (ionosphere for low frequencies; troposphere for high frequencies), water content in the sky, and RFI. As it is a time variable correction, gain calibration must be performed regularly and is done as repeated scans on the complex gain calibrator to measure the changes in visibility amplitude and phase on the gain calibrator. These changes are then interpolated to the target field scan and large fluctuations are removed. While this corrects most of the above-mentioned effects, RFI is not accounted for in this way and data affected by RFI needs to be removed (flagged).

2.2.2.1 Continuum Data

This thesis made use of the continuum data obtained by GLOSTAR but was not reduced by the author (whereas the spectral line data, was). It is described here nonetheless for posterity (Brunthaler et al. 2021).

The data was calibrated, edited and imaged using the Obit package (Cotton 2008), which interoperates with the classic Astronomical Image Processing Software package (AIPS) (Greisen 2003) to use instrumental calibration signals and observations of celestial sources[6]. Calibration scripts were written to specifically handle the GLOSTAR continuum data calibration and is described in detail in the works by Medina et al. (2019) and Brunthaler et al. (2021). Listed are the steps taken in the scripts to calibrate and edit the data to prepare it for imaging:

1. **Convert from Archive format.** The data were converted from archive format (ASDM/BDF) to AIPS format.

2. **Initial flagging.** The flag table was initialized to the flags determined by the online system. Data were compared to running medians in time (each scan is at least 3 or 4 times the correlator dump time of 2 seconds) and frequency flagging the outliers. Antennas were flagged when shadowed by other antennas.

3. **Switched power calibration.** An amplitude correction based on the switched power signal corrected for variations in system temperature.

4. **Parallactic angle correction.** A time dependent correction was applied to the calibration table for the parallactic angle of the antennas.

5. **Delay calibration.** Group delay corrections were determined from calibrator data and applied to all sources.

6. **Bandpass calibration.** Bandpass corrections were determined from the primary flux density calibrator 3C 286 using a model of the calibrator.

7. **Amplitude & Phase calibration.** Gain solutions were determined for the amplitude and phase calibrators and were used to determine the spectrum of the

[6]CASA was not used in this case as it was not optimised for the specific nature of GLOSTAR continuum data.

phase calibrator that was then used to calibrate the target data. Solutions for 3C 286 used a structural and spectral model and were forced to the spectrum of Perley & Butler (2013a).

8. **Post calibration flagging.** Another editing pass was done comparing the data with a running mean in frequency.

9. **Rinse and repeat.** The solutions from the various calibration steps were compared with median values and outliers flagged, both in the solutions and the accumulated flag table. After the first calibration pass, the calibration tables were deleted, the flag table kept and the calibration repeated. This ensures that the calibration used well-edited data.

10. **Cross hand delay calibration.** The polarized calibrator, 3C 286, was used to determine cross–hand delay residuals.

11. **Instrumental polarization calibration.** The polarization state of the secondary calibrator and the instrumental polarization were determined using observations over a range of parallactic angle.

12. **Cross hand phase calibration.** A cross–hand residual phase spectrum was determined from data on the polarized calibrator 3C 286 and the polarization model of Perley & Butler (2013b). This corrects the polarization angle on the sky.

2.2.2.2 Spectral Line Data

For the spectral line data, the Common Astronomy Software Applications (CASA) package was used for the calibration steps. We used a modified version of the VLA scripted pipeline[7] (version 1.3.8) for CASA (version 4.6.0) that has been adapted to work with spectral line data where changes have been boldfaced:

1. Loads the data into a CASA measurement set (MS) and obtains information about the observing set-up from the MS. **No Hanning smoothing was performed in order to preserve the spectral resolution.**

2. Applies online flags and other deterministic flags (shadowed data, end channels of sub-bands, etc.).

3. Prepares models for primary flux density calibrators.

4. Derives pre-determined calibrations (antenna position corrections, gain curves, atmospheric opacity corrections, requantizer gains, etc.).

5. Iteratively determines initial delay and bandpass calibrations, including flagging of RFI and some automated identification of system problems.

[7] https://science.nrao.edu/facilities/vla/data-processing/pipeline/scripted-pipeline

6. Derives initial gain calibration, and derives the spectral index of the bandpass calibrator.

7. Derives final delay, bandpass, and gain calibrations, and applies them to the data.

8. Runs the RFI flagging algorithm on **only the calibration scans as it can often flag the spectral lines we want to observe**.

9. **Statistical weights were not calculated as this sometimes affects bright sources, which is a concern for very strong masers**.

After an initial run of the calibration pipeline, we perform quality checks and manually flag further erroneous data and rerun the pipeline until satisfied. For the work done in this thesis, we personally calibrated the D-configuration data in the galactic longitude ranges of $-2°$ to $28°$ and $36°$ to $60°$, while the range from $28°$ to $36°$ was calibrated by a collaborator. For the B-configuration, we calibrated the range from $28°$ to $36°$ in galactic longitude. This is approximately 31 TB of data.

2.2.3 Imaging: the `CLEAN` algorithm

As mentioned previously in Sect. 2.1.4, we can produce a so-called *dirty* image from the direct Fourier transform of the uv data. However, this is often not the best representation of an observed field since the sampling of the uv-plane is not continuous and there are, inevitably, missing (u, v) data points that come from unsampled regions in the uv-plane. Furthermore, the dirty image often contains features such as negative intensity artefacts which cannot be real.

Above, we made the assumption in our formulation that the visibility function $V = 0$ for all unmeasured visibilities. In order to mitigate the listed shortcomings of producing a dirty image, we instead give values for V for these positions of (u, v) that are based off a model of the assumed intensity distribution. The `CLEAN` algorithm developed by Högbom (1974) aims to do exactly this by representing the radio sky as a collection of point sources. The main algorithm is as follows:

1. Find the strength and position of the peak (i.e., of the greatest absolute intensity) in the dirty image.

2. Subtract from the dirty image, at the position of the peak, the dirty beam multiplied by the peak strength and a damping factor γ (≤ 1 , usually termed the loop gain).

3. The peak position and its strength are recorded as a model component, called the `CLEAN` component.

4. Go to (1) and repeat these steps for a fixed number of iterations or until no flux density peak higher than a threshold is found. The search for peaks may be constrained to specified areas of the image, called `CLEAN` *windows*.

5. Convolve the accumulated point source model with an idealized `CLEAN` beam (usually an elliptical Gaussian fitted to the central lobe of the dirty beam). The image produced is the `CLEAN`ed image.

6. Add the residuals of the dirty image to the `CLEAN`ed image.

The Clark-Högbom algorithm (Clark 1980) improves on this method by shifting part of the computation from the image plane to the uv-plane. It is composed of two iteration cycles, named the minor and major cycles. In the minor cycle, `CLEAN` components are selected from the dirty image where their intensity is both above a threshold fraction of the dirty image peak and is greater than the intensity of the greatest sidelobe. A regular Högbom `CLEAN` is then performed until there are no more valid `CLEAN` components. In the major cycle, the `CLEAN` components are then Fourier transformed back to the visibility (uv) plane. They are then convolved with the weighted sampling function (inverse transform of the beam), transformed back to the image plane, and finally subtracted from the dirty image. The specific details for the imaging process used for the GLOSTAR data in this thesis are presented in Chapters 3, 4, and 5 where they are used.

Spectral line data products of radio astronomy often come in what is known as a *data cube* and is used extensively in this thesis. Data cubes consist of voxels, which represent intensities in three dimensions. In our work, the dimensions are typical two positional dimensions, representing the position on the sky, while the third dimension is the spectral dimension. This spectral axis, is discretely represented as individual channels and corresponds to the frequency information of the observations (often converted to velocity for analysis). A basic illustration of a data cube is shown in Fig. 2.11. Examples of how one can interpret data cubes in a practical sense are shown in Fig. 2.12, which shows a data cube collapsed along the spectral axis, and in Fig. 2.13 which shows the information represented by one pixel along the spectral axis.

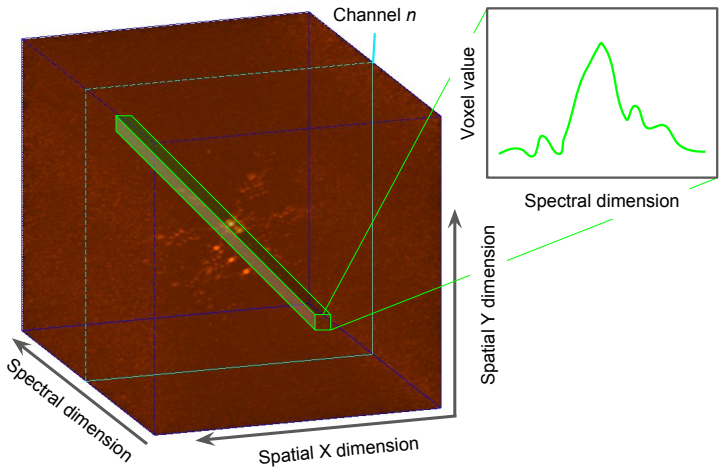

Figure 2.11: Example data cube.

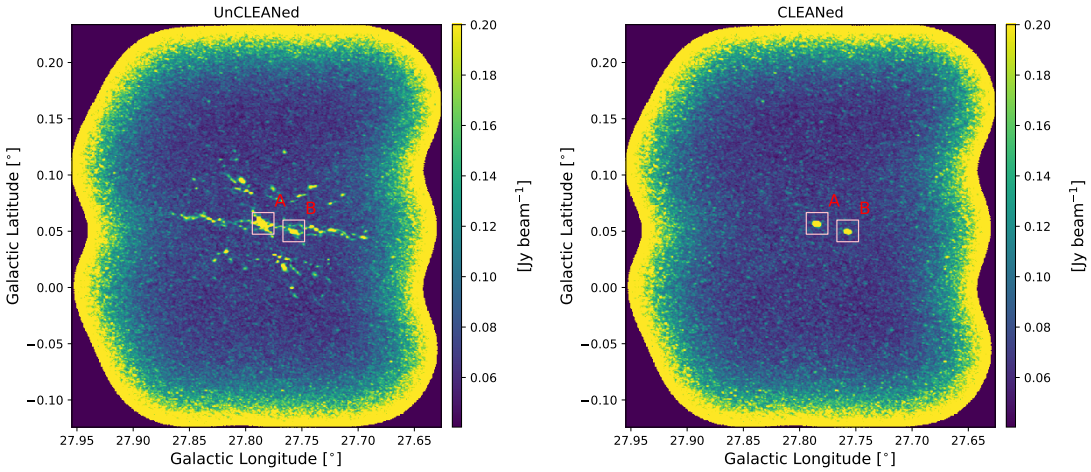

Figure 2.12: Example data products of an unCLEANed (*left*) and CLEANed (*right*) data cube. We show peak intensity maps, which shows at each pixel, the value of the channel (velocity) with maximum intensity. It is clear the effect the CLEAN algorithm gives by providing a clear picture of astronomical sources, allowing for the identification of weaker sources in the presence of stronger sources. Two sources, in this case, 6.7 GHz methanol masers are labelled as A and B.

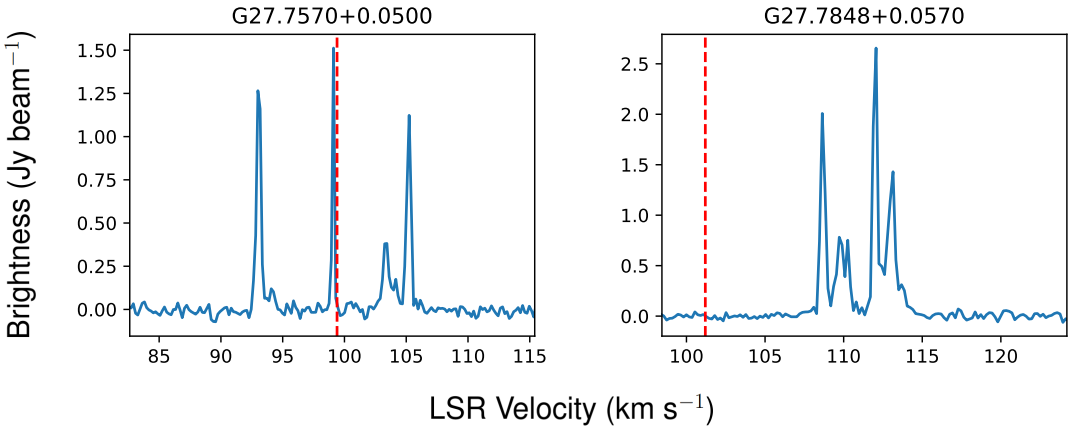

Figure 2.13: We show as an example the spectra of the two 6.7 GHz methanol masers shown in Fig. 2.12. From the data cube, we take all the intensity along the spectral axis at a given pixel and plot them against their corresponding velocity. The *left* source corresponds to source A, and the *right*, source B. The red-dashed line represents the known velocity of dust clumps that these maser sources are associated with. Taken from Nguyen et al. (2022).

Chapter 3

GLOSTAR: Radio Continuum Detections of YSOs in the CMZ

This chapter is a summary of the article published in Astronomy and Astrophysics (see Appendix A) titled **"A global view on star formation: The GLOSTAR Galactic plane survey. IV. Radio continuum detections of young stellar objects in the Galactic Centre region"** by:

H. Nguyen, M. R. Rugel, K. M. Menten, A. Brunthaler, S. A. Dzib,A. Y. Yang, J. Kauffmann, T. G. S. Pillai, G. Nandakumar, M. Schultheis, J. S. Urquhart, R. Dokara, Y. Gong, S-N. X. Medina, G. N. Ortiz-León, W. Reich, F. Wyrowski, H. Beuther, W. D. Cotton, T. Csengeri, J. D. Pandian, and N. Roy
2021, A&A, 651, A88[1].

3.1 Context

As discussed in Chapter 1.1.2, high-mass stars play a key role in many astrophysical processes as they affect not only their local environment, but also the star and planetary formation processes at galactic scales. It is therefore crucial to understand their formation and the relevant processes involved in their formation. An interesting laboratory to conduct such an investigation is the giant molecular cloud complex at the centre of the Milky Way, the Central Molecular Zone (CMZ). The CMZ's physical conditions are extreme in comparison to those in other GMCs in the Milky Way as the temperature, the pressure, and the magnetic field strengths are much higher. This makes the CMZ an interesting laboratory for studying HMSF (Morris & Serabyn 1996). Furthermore, despite the amount of dense gas available, the SFR is lower than expected in comparison to other regions.

One way to calculate the SFR and thus study HMSF, is to count the number of YSOs to directly estimate the current ongoing star formation that is occurring. However, studying YSOs in the CMZ can be difficult, as the distance and environment give rise to a large and spatially variable extinction problem. It can make late-type evolved stars like asymptotic giant branch (AGB) stars look similar to YSOs in the infrared. One of the most recent studies to disentangle the contamination of late-type evolved stars from YSOs within photometric catalogues was performed by Nandakumar

[1]H. Nguyen et al. 2021, A&A, 651, A88, reproduced with permission from ©ESO.

et al. (2018). Using a sample of 2.2 μm near infrared sources, they devised a new colour-colour- diagram criterion which they propose separates YSOs from late-evolved stars and searched in the area of the CMZ to produce a sample of 334 YSO candidates. It is this set of 334 YSOs that we examine to study HMSF.

3.2 Aims

The first goal is to understand the nature of 2.2 μm sources in the CMZ. However, at the distance of the Galactic Centre, they are both far away and suffer from high extinction levels. As a primary diagnostic, we make a comparison to the nearby Orion Nebular Cluster (ONC) which is considered the template region for high-mass star formation. Is it possible to see Orion-like sources in the CMZ? If so, are the YSO candidates classified by Nandakumar et al. (2018) Orion-like? Are they even YSOs? How well do 2.2 μm sources trace other signposts of HMSF like HII regions? To address these questions, we use GLOSTAR radio observations to probe these sources and investigate their nature in order to constrain their evolutionary stages, provide a census on their relation with HII regions, and ultimately estimate the SFR in the CMZ.

3.3 Methods

To address the first question we use 2.2 μm data from the Cosmic Background Explorer (COBE) space-based mission to estimate the flux of the ONC. We then scale the flux to the distance of the CMZ to determine if it would be possible to observe ONC-like sources given the limiting sensitivity of the instruments used to produce the 2.2 μm sources from the study of Nandakumar et al. (2018). We use the YSO candidate sample as targets to search for radio continuum counterparts. The radio data used were obtained as a part of the GLOSTAR survey, where observations of the Galactic Centre were performed using the D-configuration of the VLA. It covers a region of from $l = -2^\circ$ to 2° and $b = -1^\circ$ to 1° with a frequency coverage of two 1 GHz bands in the range from 4 to 8 GHz. We classified radio continuum sources as potential HII regions and calculated their physical properties such as their fluxes, their sizes, and their morphology. Using ancillary data from the ATLASGAL survey at 870 μm to trace the surrounding dust, we further characterised these sources.

3.4 Results

Using the 2.2 μm COBE data (Boggess et al. 1992), we find that the integrated flux density of the ONC is 630 mJy. Once scaled to the distance of the CMZ, this results in a value of 1.49 mJy. This corresponds to Ks filter magnitude of $\sim$14. This is just above the limiting magnitude for the Ks filter and therefore suggests that we should be able to see ONC-like sources in the CMZ in the study by Nandakumar et al. (2018).

From the sample of 334 YSO candidates, we initially find 100 cases of coincident GLOSTAR radio continuum emission. However, the extended radio continuum emis-

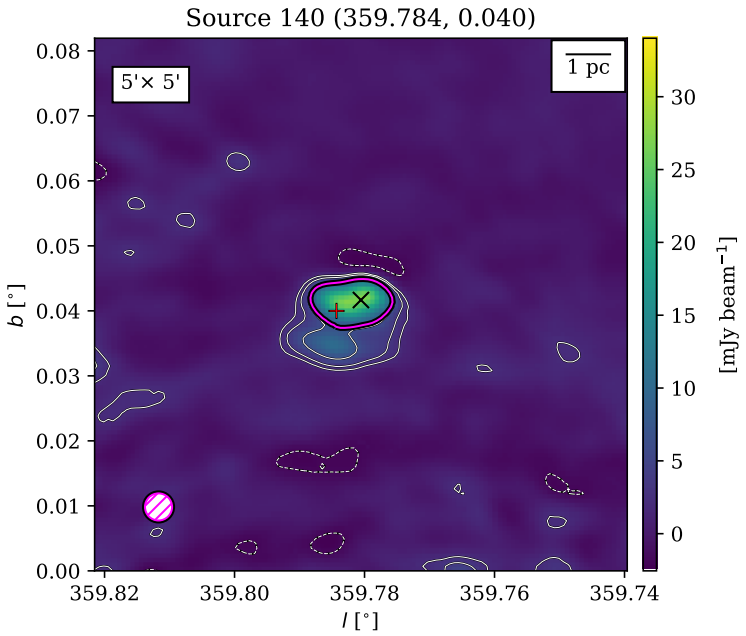

Figure 3.1: Detection of a GLOSTAR 5.8 GHz counterpart for source 140 (G359.784+0.040) from Nandakumar et al. (2018). The GLOSTAR 5.8 GHz continuum map is shown in colour with positions of the peak radio emission and the YSO marked with a black X and red cross, respectively. White contours correspond to 3, 5, and 10 σ ($\sigma = 0.634\,\mathrm{mJy\,beam^{-1}}$). The magenta contour outlines the area from which the flux density was calculated. The colour bar maximum was chosen to be 1.5× the peak intensity of the coinciding 5.8 GHz source. The beamsize is shown in magenta in the bottom left corner. Adapted from Fig. 3 in Nguyen et al. (2021).

sion features can be very complicated, especially in a region like the Galactic Centre. We therefore focus mainly on compact sources where possible. Additionally, we use the multiple frequency bands of the GLOSTAR data to check for artefacts. This reduces our list to 35 potential counterparts. An example is shown in Fig. 3.1 of source 140 from Nandakumar et al. (2018), where we have plotted the YSO candidate as a red cross on top of the GLOSTAR D-configuration continuum.

The fluxes of these radio counterparts range from 0.9 mJy to 3.3 Jy where the calculated thermal indices and literature support their HII region classification. The comparison with the dust continuum data finds that 94 YSO candidates have ATLASGAL 870 μm emission counterparts when compared to an emission map (provided by collaborator Dr. James Urquhart). Of these, 14 sources also have the aforementioned GLOSTAR radio continuum counterpart. In assuming spherical geometry for most of these sources, we can calculate physical properties which can give us the number of Lyman continuum photons. These are the photons emitted by the developing star that ionises the surrounding medium, thus producing an HII region. This value is associated to a given spectral type of star which has an associated mass based on models (Davies

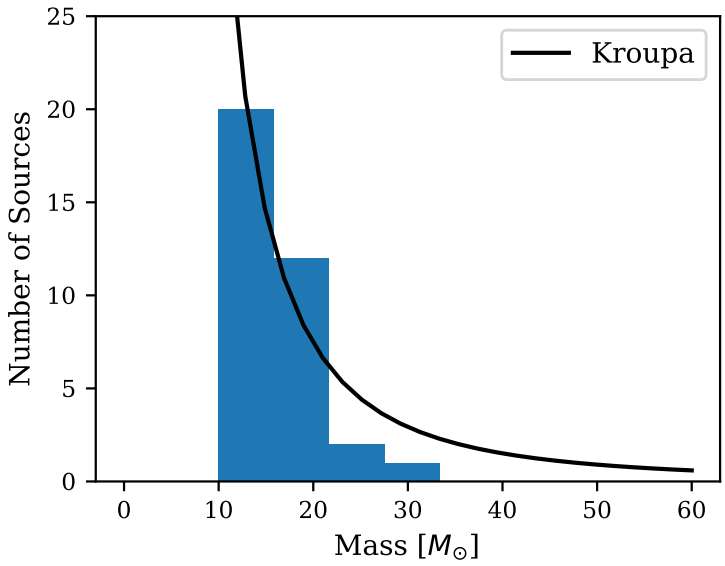

Figure 3.2: Mass distribution of calculated zero-age-main-sequence (ZAMS) masses for the HII regions with associated YSOs. The black line represents the fitted Kroupa IMF (Kroupa 2001). Adapted from Fig. 12 in Nguyen et al. (2021).

et al. 2011). Using these masses, we plot their distribution in Fig. 3.2 which we use to estimate an initial mass function (IMF). With the IMF, we can estimate the total mass of stars in the CMZ. In assuming the same formation timescale from Nandakumar et al. (2018) of 0.75 ± 0.25 Myr, we can then calculate the SFR to be $0.04 \pm 0.02\,\mathrm{M}_\odot\ \mathrm{yr}^{-1}$ which is consistent with the results of Nandakumar et al. (2018) and other independent investigations. We note, however, that our sample size of 35 is small and that we only sampled stars that are currently associated with radio emission. There are likely star forming regions that have yet to exhibit radio emission. We follow the method of from Kauffmann et al. (2017a) to calculate the SFR by using the total ionising flux of HII regions we detected, as well as known sources from literature to estimate the SFR in the CMZ to be $0.068\,\mathrm{M}_\odot\ \mathrm{yr}^{-1}$.

3.5 Conclusions

Given that YSOs should be embedded in their natal dust clouds, we expect to see an association with the ATLASGAL dust emission. The 94 sources that have dust associations are consistent with this general picture. The YSO candidates without dust emission are perhaps not YSOs, or at least not *massive* YSOs and are instead, associated with lower-mass dust clumps. Furthermore, we detected 35 compact radio continuum counterparts and calculated their physical properties and classified them as potential HII regions based on their spectral indices and the associated literature. We do not find a strong correlation between the 2.2 μm sources and 5.8 GHz radio continuum, this suggests that sources without a radio continuum counterpart have not yet evolved to the stage of exhibiting an HII region or, conversely, are older and have dispersed their natal clouds. Since many lack dust emission, the latter is more likely. Our estimates of the SFR in the CMZ are consistent with other studies in the literature, which use different methods.

Chapter 4

GLOSTAR: 6.7 GHz Methanol Maser Catalogue

This chapter is a summary of the article published in Astronomy and Astrophysics (see Appendix B) titled **"A global view on star formation: The GLOSTAR Galactic plane survey. V. 6.7 GHz methanol maser catalogue"** by:

H. Nguyen, M. R. Rugel, C. Murugeshan, K. M. Menten, A. Brunthaler, J. S. Urquhart, R. Dokara, S. A. Dzib, Y. Gong, S. Khan, S-N. X. Medina, G. N. Ortiz-León, W. Reich, F. Wyrowski, A. Y. Yang, H. Beuther, W. D. Cotton, and J. D. Pandian
2022, A&A, 666, A59[1].

4.1 Context

One of the clearest signposts of recent high-mass star formation (HMSF) is the Class II methanol (CH3OH) maser and it has proven to be an indispensable tool in the study of HMSF. While maser emission was previously known, it was discovered in space for the first time by Barrett et al. (1971b) at 25 GHz towards Orion-KL. Many other methanol maser lines have been discovered since then, notably those at 6.7 and 12.2 GHz (Batrla et al. 1987; Menten 1991b). They are classified by the pumping mechanism that facilitates maser emission as either collisional pumping (Class I: Batrla et al. 1987; Cragg et al. 1992; Voronkov et al. 2010, 2014; Leurini et al. 2016) or radiative pumping (Class II: Menten 1991a,b; Caswell et al. 2010). In particular, Class II CH_3OH masers have already proven to be one of the clearest signposts of HMSF, with the 6.7 GHz line from the $5_1 - 6_0A^+$ transition being the brightest and most widespread in the Galaxy (Menten 1991b, 1993; Walsh et al. 1997, 1998). It is unique in that it exclusively traces high-mass star forming regions (Minier et al. 2003; Ellingsen 2006; Xu et al. 2008). They are found in the surrounding dust and gas of MYSOs. Their usefulness in the study of HMSF has therefore motivated many surveys to date, both targeted (e.g. Menten 1991b; MacLeod et al. 1992; Caswell et al. 1995; Caswell 1996a; Ellingsen et al. 1996; van der Walt et al. 1996; Walsh et al. 1997; Ellingsen 2007; Yang et al. 2019b) and unbiased surveys (Rickert et al. 2019; Pestalozzi et al. 2005; Pandian et al. 2007; Caswell et al. 2010; Green et al. 2010; Caswell et al. 2011; Green et al. 2012; Breen et al. 2015; Ortiz-León et al. 2021).

[1]H. Nguyen et al. 2022, A&A, 666, A59, reproduced with permission from ©ESO.

4.2 Aims

With over 1000 Class II 6.7 GHz methanol masers discovered in our Milky Way Galaxy to date, we endeavour to increase this sample using modern observatories. Due to the technological upgrades of the VLA (Perley et al. 2011), the methanol data from the GLOSTAR survey provides the most sensitive and unbiased catalogue to date with which to study high-mass star forming regions.

4.3 Methods

The GLOSTAR survey is a blind survey in the radio regime. With a frequency range from 4–8 GHz, radio continuum data as well as the 6.7 GHz methanol line (and other spectral lines) are obtained. The full details are found in Brunthaler et al. (2021). For this work, the VLA D-configuration data is used for the regions covered from the Galactic Centre to $l = 60°$. We calibrate the methanol data using `CASA` while the continuum data is calibrated using `Obit` (performed by Dr. S. A. Dzib). To handle the difficulties of large datasets and the long computation time needed to image large regions, we chose to search for maser sources using *dirty* images. We developed a source extraction code (SEC) to specifically handle these images to efficiently detect potential masers while minimising false positives. Once a final list of masers is compiled, we use the `CLEAN` algorithm to reduce the data allowing for the determination of the physical properties of these masers such as their flux. We then compare the GLOSTAR VLA D-configuration 5.8 GHz continuum source catalogue and ancillary 870 μm ATLASGAL survey emission maps to further characterise the maser sources.

4.4 Results

We detect a total of 554 methanol masers, out of which 84 are new, and catalogue their positions, velocity components, and integrated fluxes. It is because of our sensitivity ($\sim$ 18 mJy beam^{-1}) that we are able to detect many new masers in comparison to previous blind surveys. We plot the positions of the detected maser relative to the spiral arms of the Milky Way in Fig. 4.1. The brightest detected maser is G9.6213+0.1961 with a peak flux density of $\sim$5700 Jy while the weakest has $\sim$0.09 Jy. The newly detected masers have a flux range of 0.16–5.4 Jy. We have compared our detections with other contemporary 6.7 GHz maser surveys such as the AMGPS (Pandian et al. 2007), the MMB survey (Green et al. 2009), and the catalogue of Yang et al. (2019b) in order to compare the physical properties as well as verify new detections. Using the MMB as a reference, we find that their are no systemic differences in the maser positions as well as the maser fluxes.

In using ATLASGAL emission maps, we find dust association of $\sim$97% which is consistent with previous studies (e.g., Billington et al. 2019). We use the ATLASGAL compact source catalogue (CSC) to obtain the physical properties of the dust clumps associated with methanol maser emission. We perform a statistical analysis towards

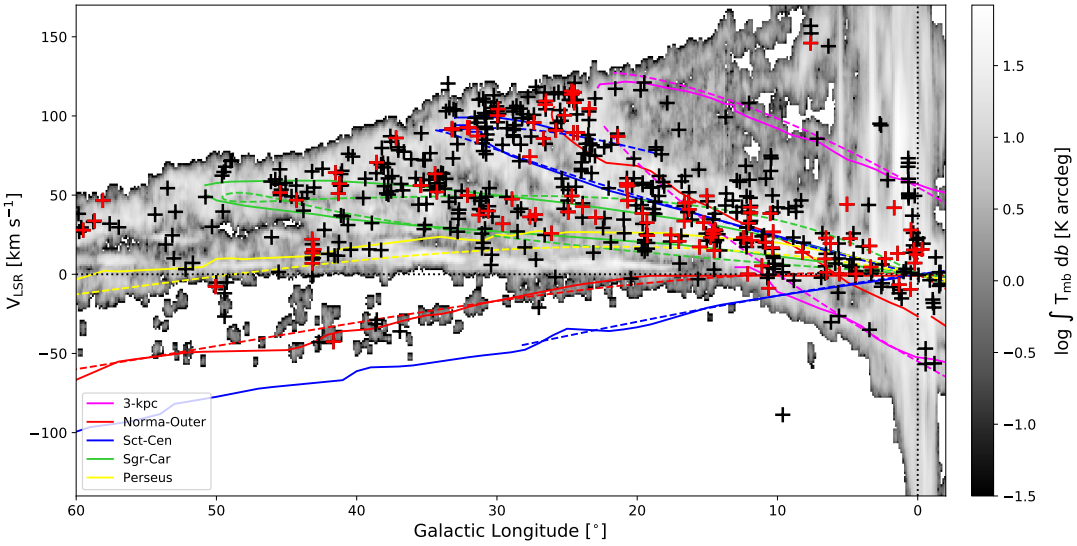

Figure 4.1: Distribution of detected 6.7 GHz methanol maser velocity with respect to Galactic longitude. Black crosses represent detections of known sources in the GLOSTAR survey and red crosses represent new detections. The dashed lines represent the updated spiral arm models of Taylor & Cordes (1993) as used in, e.g. Schuller et al. (2021) while the solid lines are the spiral arm descriptions from Reid et al. (2019). The background shows the CO emission from Dame et al. (2001). Adapted from Fig. 6 in Nguyen et al. (2022).

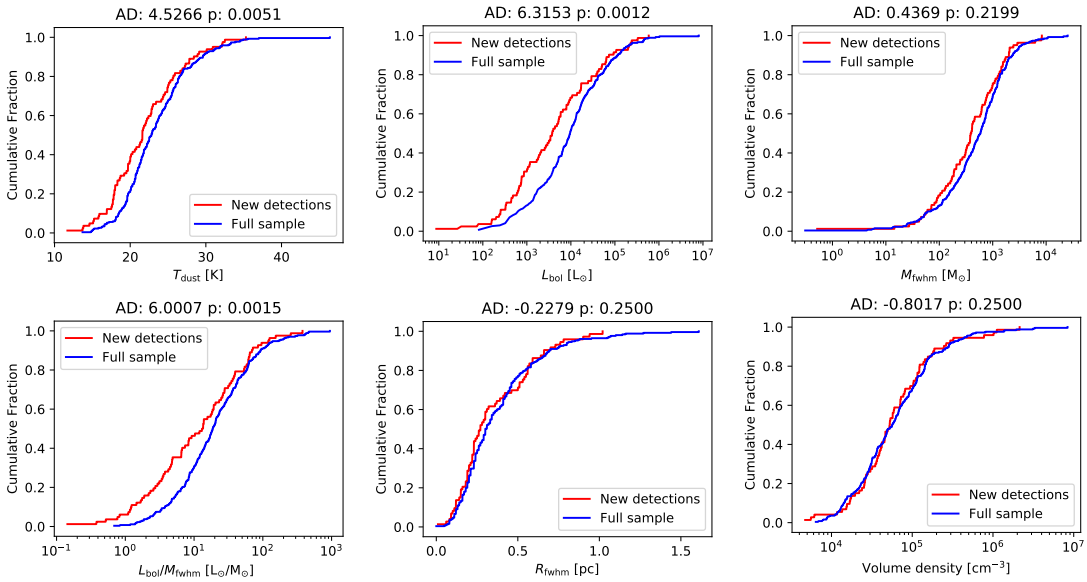

Figure 4.2: CDFs for various properties of ATLASGAL clumps associated with GLOSTAR methanol masers. We compare the sample clumps associated with new methanol maser detections (red) to the sample of clumps with associations to the full methanol maser catalogue (blue). The results of the Anderson-Darling (AD) test are shown above each plot. Adapted from Fig. 17 in Nguyen et al. (2022).

the subset of masers that have ATLASGAL CSC counterparts and are new detections. The cumulative distribution functions are shown in Fig. 4.2. In using Anderson-Darling tests, we find that only the distributions of dust clump bolometric luminosities are statistically different (3σ) between the newly detected maser population compared to the full sample.

We also compare the maser luminosity against the ATLASGAL bolometric luminosity, clump mass, and luminosity-to-mass ratio (L/M). We determine a minimum core mass for maser associated cores to be $\sim$10 $M_\odot$ which is consistent with the previous study by Ortiz-León et al. (2021) using masers in the Cygnus X region.

While some of the earliest detections of Class II methanol masers were made toward ultra-compact HII regions (Batrla et al. 1987; Menten et al. 1992), it was found that in fact very few of these methanol masers have radio continuum counterparts (Walsh et al. 1998; Beuther et al. 2002; Urquhart et al. 2013a, 2015; Hu et al. 2016; Billington et al. 2019). To further study the connection between 6.7 GHz methanol masers and radio continuum sources, we compare our maser catalogue with the GLOSTAR VLA D-configuration radio source catalogue and find a 12% association rate. This is smaller than previous studies (e.g., Hu et al. 2016) that find association rates of $\sim$30% towards UC HII regions. Our result is not unexpected as the resolution of the D-configuration continuum catalogue is not as well suited to sample UC HII and HC HII regions.

We calculate the luminosity function of our sample of methanol masers using distances determined from the Bayesian distance estimator (Reid et al. 2019) as well as

ATLASGAL clump distances that have been verified from HI self-absorption. We determine a completeness level of $6.9 \times 10^{-7}\,L_{\odot}$. We find a median luminosity of $3 \times 10^{-6}\,L_{\odot}$ which is in agreement with previous studies (e.g., Pandian et al. 2009).

4.5 Conclusions

With a typical noise level of $\sim$18 mJy beam^{-1}, we have conducted the most sensitive unbiased survey for methanol masers to date. We present the first study of 6.7 GHz CH_3OH masers that use GLOSTAR data in the Galactic plane. Methanol absorption sources have also been detected, and a systematic search is forthcoming. We detected 554 masers where 84 of them are new detections. We find that over 50 % of the new detections have fluxes of < 0.5 Jy. In searching for dust continuum associations, we used the 870 μm ATLASGAL compact source catalogue and found that 65% of the CH_3OH masers are associated with dense gas. Many of the newly detected maser have no associations. However, in comparing to the dust emission map instead, we are able to find associations with dust emission ($> 5\sigma$) that were below the sensitivity limit needed for sources to be included in the CSC. This gives us an expected higher association rate of 97%. Additionally, we found that newly detected masers in general have weaker maser emission and weaker associated dust emission. This might suggest that these sources are more distant or associated with less evolved stars.

In comparing the associated dust clump properties, we confirm the picture where 6.7 GHz methanol masers are associated exclusively with the early stages of high-mass star formation as there is a high correlation between methanol masers and dust emission and the high bolometric luminosities. We derived a L/M threshold for the onset of the methanol maser emission of $\sim 1\,L_{\odot}\,M_{\odot}^{-1}$, which is consistent with values determined by Ortiz-León et al. (2021).

Furthermore, we find that only 12% of the masers are coincident with radio continuum emission. While we are biased by the resolution of our data, the lack of association of 6.7 GHz methanol masers with radio continuum emission, however, indicates that these masers trace the earliest stages of high-mass star formation. We additionally compare the radio and maser flux distribution and find no correlation as a function of angular offset. This might indicate that the underlying mechanisms that power maser and continuum emission are unrelated.

Lastly, we have constructed a luminosity function from our sample of masers by using a broken power law. Our results agree with previous studies in that the distribution has a median luminosity $10^{-6}\,L_{\odot}$. We note, however, that while we can sample well the high-luminosity maser population, we find that we are sensitivity limited with respect to the lower-luminosity bins.

Chapter 5

GLOSTAR: Resolving regions of methanol maser emission and the search for variability

---

This chapter is will be submitted to the journal, Astronomy and Astrophysics titled **"A global view on star formation: The GLOSTAR Galactic plane survey. IX. Resolving regions of 6.7 GHz methanol maser emission and the search for variability in the Galactic longitude range of** $28^\circ < l < 36^\circ$**"** by:

H. Nguyen, M. R. Rugel, C. Murugeshan, K. M. Menten, A. Brunthaler, J. S. Urquhart, R. Dokara, S. A. Dzib, Y. Gong, S. Khan, S-N. X. Medina, G. N. Ortiz-León, W. Reich, F. Wyrowski, A. Y. Yang, H. Beuther, W. D. Cotton, and J. D. Pandian

in preparation

5.1 Overview

In Chapter 4, we presented the GLOSTAR methanol spectral line observations that were obtained with the VLA in the D-configuration. From this data set, we produced a catalogue of 6.7 GHz methanol maser detections. We compared these maser sources with the GLOSTAR radio continuum data from the same VLA configuration and found an association rate of ∼12% which is lower than previously reported in literature (∼30% e.g., Hu et al. 2016). This, however, is to be expected as the D-configuration is not well suited to probe the more compact HII regions such as UC HII regions or HC HII regions. Fortunately, the GLOSTAR project also observed the Milky Way in the B-configuration of the VLA which provides an order of magnitude higher angular resolution (∼1″). At this time, not all of the observations in this configuration are complete and so in this chapter, we present the B-configuration data for just the pilot region of GLOSTAR. In this way, we are better able to test the association of methanol masers with GLOSTAR radio continuum sources. Furthermore, in having observed these masers at a second point in time, we are able to search for maser sources that would be ideal for long term observations in order to study maser variability. The following chapter consists of the current manuscript titled above, which is in preparation and will be submitted to A&A.

5.2 Introduction

The $5_1 - 6_0 A^+$ CH_3OH (methanol) transition at 6.7 GHz was first detected in the interstellar medium by Menten (1991b). Second only to 22.2 GHz H_2O masers, it is one of the highest intensity and one of the most widespread maser lines observed (e.g., Caswell et al. 1995). In particular, radiatively pumped (Class II) CH_3OH masers have already proven to be one of the clearest signposts of high-mass star formation (HMSF) (Menten 1991b, 1993; Walsh et al. 1997, 1998; Minier et al. 2003; Xu et al. 2008). As such, many previous studies, both targeted (e.g., Menten 1991b; MacLeod et al. 1992; Caswell et al. 1995; Caswell 1996a; Ellingsen et al. 1996; van der Walt et al. 1996; Walsh et al. 1997; Ellingsen 2007; Yang et al. 2019b) and unbiased (Rickert et al. 2019; Pestalozzi et al. 2005; Pandian et al. 2007; Caswell et al. 2010; Green et al. 2010; Caswell et al. 2011; Green et al. 2012; Breen et al. 2015; Ortiz-León et al. 2021; Nguyen et al. 2022), have been performed to obtain a census of early high-mass star formation in the Milky Way.

This is one of the driving goals behind the Global View On Star Formation survey in the Milky Way (GLOSTAR) (Brunthaler et al. 2021). Using the Karl G. Jansky Very Large Array (VLA) in D- and B-configurations and the Effelsberg 100 m radio telescope, an unbiased survey was performed to identify and characterise star-forming regions in our local Galaxy.

The recent work in Nguyen et al. (2022) used the GLOSTAR data to produce a catalogue of the 6.7 GHz methanol masers in the region from $-2^\circ < l < 60^\circ$ and $|b| < 1^\circ$ in Galactic longitude and latitude respectively, using the D-configuration to detect 554 masers, of which 84 were new detections. Similarly, Ortiz-León et al. (2021) performed a search for methanol masers in the Cygnus X region with GLOSTAR data and detected 13 masers. Two of the masers are newly detected, and new velocity components were discovered towards a few known maser sources. Supplementing the VLA D-configuration data, Ortiz-León et al. (2021) also used the higher resolution B-configuration data to obtain better positional accuracy and established associations to radio continuum, (sub)millimetre, and infrared emission with a $\sim 1''$ accuracy.

Furthermore, our access to multiple epochs allows us to observe potential maser variability that is not yet well understood. Maser variability typically occurs with periods of ∼20 to 200 days and with sinusoidal patterns or intermittently with a quiescent phase (Goedhart et al. 2004; Szymczak et al. 2018; Olech et al. 2019). There are two kinds of models to explain the observed variability. The first explains the variation through cyclic variations in the seed photon flux from a colliding-wind binary (CWB; van der Walt et al. 2009, van der Walt 2011). The second type of model assumes changes in the temperature of the dust grains in the environment of the masing region. This affects the infrared radiation flux and thus the pump rate. There are multiple hypotheses for the origins of the changes in the temperature, such as periodic accretion from a circumbinary accretion disk (Araya et al. 2010), stellar pulsation (Inayoshi et al. 2013; Sanna et al. 2015), and spiral shock waves in the disk of a binary system (Parfenov & Sobolev 2014; Szymczak et al. 2018).

Here we present first results of the VLA B-configuration 6.7 GHz methanol obser-

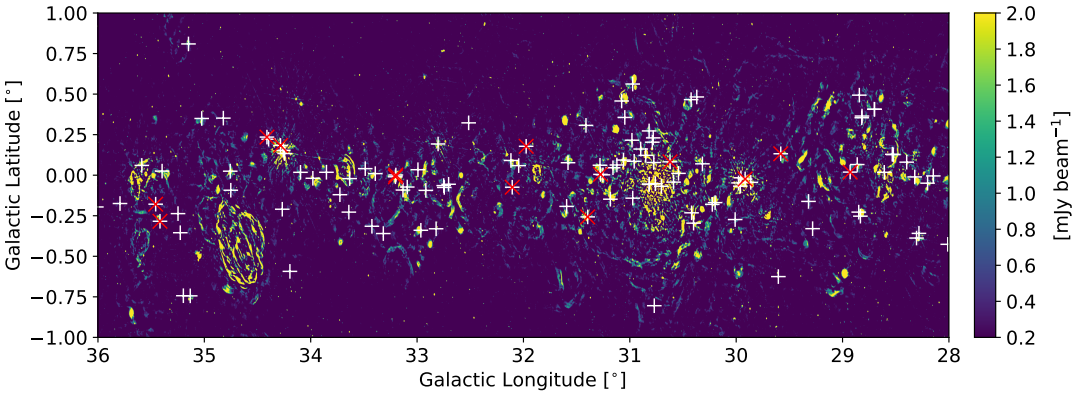

Figure 5.1: Methanol maser detections plotted as white crosses on top of the D-configuration continuum images from GLOSTAR where the flux has been limited to be between 0.2 and 2 mJy beam^{-1} for visibility. The red 'x's show the positions of all new methanol masers as discussed in Nguyen et al. (2022).

vations of the pilot region ($28° < l < 36°$, $|b| < 1°$). The B-configuration data allows a higher astrometric precision of the positions of the 6.7 GHz methanol masers covered in GLOSTAR and the separation of the maser emission into multiple maser sites. Moreover, these observations also provide an additional epoch for which maser variability studies can be performed. We structure this work as follows: In Sect. 5.3 we give a summary of the data used in this work along with its calibration and imaging. Section 5.4 details the production of our methanol maser catalogue and their general properties. Section 5.5 discusses our comparison with other surveys and associations with other wavelengths. We present the conclusions and summary in Sect. 5.6.

5.3 Observations and data reduction

Using the VLA interferometer and the Effelsberg 100 m single-dish telescope in the frequency range of 4–8 GHz, the GLOSTAR survey (Medina et al. 2019; Brunthaler et al. 2021) is an ongoing survey of the Galactic mid-plane from $-2° < l < 60°$ and $|b| < 1°$, and the Cygnus X star-forming complex. The VLA observations used in this work were conducted in D- and B-configuration with a typical angular resolution of $18''$ and $1.5''$ respectively at 6.7 GHz and focus only on the pilot region ($28° < l < 36°$ and $|b| < 1°$) which is shown in Fig. 5.1 with the D-configuration CH_3OH maser detections overlaid. In order to study various stages of early star formation, the survey aims to detect tracers of these stages using methanol, formaldehyde, and radio recombination lines as well as radio continuum data, in order to better understand the evolutionary process of massive stars. The full details of the survey techniques and specifications can be found in Brunthaler et al. (2021). The observations used in this work were carried out using ∼40 hours during the time period from April 2013 until January 2014 where the program IDs and details are summarised in Table 5.1.

Table 5.1: Summary of the VLA observations

Observing Date	Config.	Galactic coverage	Program ID	Calibrator
2013-04-09	D	$28° < l < 29°$; $\|b\| < 1.0°$	13A-334	J1804+0101
2013-09-29	B	$28° < l < 29°$; $\|b\| < 1.0°$	13A-334	J1804+0101
2013-04-06	D	$29° < l < 30°$; $\|b\| < 1.0°$	13A-334	J1804+0101
2013-11-04	B	$29° < l < 30°$; $\|b\| < 1.0°$	13A-334	J1804+0101
2013-04-11	D	$30° < l < 31°$; $\|b\| < 1.0°$	13A-334	J1804+0101
2014-01-10	B	$30° < l < 31°$; $\|b\| < 1.0°$	13A-334	J1804+0101
2013-04-15	D	$31° < l < 32°$; $\|b\| < 1.0°$	13A-334	J1804+0101
2013-10-03	B	$31° < l < 32°$; $\|b\| < 1.0°$	13A-334	J1804+0101
2013-04-16	D	$32° < l < 33°$; $\|b\| < 1.0°$	13A-334	J1804+0101
2013-11-03	B	$32° < l < 33°$; $\|b\| < 1.0°$	13A-334	J1804+0101
2013-04-20	D	$33° < l < 34°$; $\|b\| < 1.0°$	13A-334	J1804+0101
2013-10-02	B	$33° < l < 34°$; $\|b\| < 1.0°$	13A-334	J1804+0101
2013-04-29	D	$34° < l < 35°$; $\|b\| < 1.0°$	13A-334	J1804+0101
2014-01-05	B	$34° < l < 35°$; $\|b\| < 1.0°$	13A-334	J1804+0101
2013-05-02	D	$35° < l < 36°$; $\|b\| < 1.0°$	13A-334	J1804+0101
2014-01-04	B	$35° < l < 36°$; $\|b\| < 1.0°$	13A-334	J1804+0101

5.3.1 VLA data calibration

The calibration procedure is outlined in Sect. 2.2.2. We use a modified version of the VLA scripted pipeline[1] (version 1.3.8) for CASA[2] (version 4.6.0) which was adapted to work with spectral line data. The relevant changes are: no Hanning smoothing was performed on the first pass when producing the preliminary images to preserve the spectral resolution where possible; Hanning smoothing is performed on the sources that showed considerable Gibb's ringing after an initial inspection; the `rflag` flagging command, which is used to automatically remove RFI, was only applied to the calibration scans to avoid flagging spectral lines erroneously; `statwt` was not used to modify the statistical weights because that sometimes affects particularly bright sources. The complex gain calibrator used is J1804+0101, and the flux calibrator is 3C 286.

5.3.2 Spectral line data imaging

The methodology is the same as in Nguyen et al. (2022), we describe here the differences in parameters used during various stages of the data reduction. For the D-configuration, full *dirty* (un`CLEAN`ed) image cubes were produced for each longitude range in order to blindly search for methanol masers. Given the computing resources, this was already a heavy computational endeavour that took ∼200 days. Since the angular resolution of the B-configuration is one order of magnitude higher, this means that *dirty* images

[1] `https://science.nrao.edu/facilities/vla/data-processing/pipeline/scripted-pipeline`
[2] `https://casa.nrao.edu/`

would need more pixels to cover a similar spatial coverage and thus even more time. However, we do not need to image each longitude range in its entirety for the B-configuration data as wherever there is a maser detected in B-configuration, it should already have been detected in the D-configuration data. As such, we opt to only produce the final `CLEAN` images centred on the location of detected masers from the D-configuration data.

The imaging of the individual masers was performed using the `CLEAN` algorithm on small subsets of the data. The imaged cubes have a spatial coverage of $\sim 0.2^\circ \times 0.2^\circ$ or $\sim 0.06^\circ \times 0.06^\circ$ with a cell/pixel size of $2.5''$ and $0.2''$ for the D- and B-configuration respectively. The spectral coverage is $\Delta v \approx 55\,\mathrm{km\,s^{-1}}$ with channel widths of $0.18\,\mathrm{km\,s^{-1}}$. This is a spectral extent of 300 channels centred on the peak maser feature's velocity and spatial extents of 350×350 pixels or 750×750 pixels. The synthesized beams are on average $16'' \times 11''$ and $1.4'' \times 1.1''$ in the D- and B- configuration, respectively. The average 1σ root-mean-noise (rms) in emission-free channels is $0.018\,\mathrm{Jy\,beam^{-1}}$ per channel for both configurations. For deconvolution, a `CLEAN`ing threshold of $38\,\mathrm{mJy\,beam^{-1}}$ was chosen ($\sim 2\sigma$ of final cubes). Using the `tclean` task of CASA (version 5.4.0), the images were made with parameters: `gridder`='mosaic', `deconvolver`='hogbom', `weighting`='uniform', `restfreq`='6668.518 MHz', and a variable `niter`, which is the number of minor `CLEAN` cycles. The `niter` parameter was set to either 1000, 5000 or 10000 to reflect the need for more rigorous cleaning which is dependent on the strength of the maser involved. In imaging the D-configuration masers, we found that these iteration values optimised the automatic cleaning by maximising image fidelity while avoiding over-cleaning for masers and we adopt this procedure also for the B-configuration. The weighting parameter was set to 'uniform', since it gives a better angular resolution and thus more accurate positional information which is of high importance for the B-configuration data.

5.3.3 Complementary continuum data

A comparison of the D-configuration methanol maser catalogue with the GLOSTAR VLA D-configuration 5.8 GHz radio continuum catalogue was performed in Nguyen et al. (2022) to study their association rate. Here we focus on the B-configuration data using the GLOSTAR radio source catalogue from Dzib et al. (2022). As the goal of the B-configuration observations were to sample more compact sources, all radio emission on angular scales larger than $\approx 4\farcs13$ were discarded during the imaging process by excluding the shorter baselines. In this way, emission from poorly mapped extended structures that introduced artefacts in the images were rejected while having only a minor impact in the overall sensitivity. The images were convolved with a circular beam 1 arcsec. The mean measured noise in the images used is $60\,\mu\mathrm{Jy\,beam^{-1}}$, however, it can be higher in some areas where the extended emission was not properly recovered or around very bright radio sources that produce imperfectly cleaned sidelobe emission. The full details are found in Brunthaler et al. (2021) and Dzib et al. (2022).

5.3.4 Catalogue creation

To produce the D-configuration VLA methanol maser catalogue, a straightforward Search Extraction Code (SEC) was developed to produce a list of methanol maser candidates from the *dirty* cubes (see Nguyen et al. 2022, for the full details). The code uses as its main criteria a minimum signal-to-noise ratio (S/N) threshold and that the emission meets the S/N criteria for at least two channels in a row. There are additional filters to avoid false positives based on the proximity of tentative detections from other tentative detections. Once completed, the candidate list is visually inspected to produce a list of masers for individual `CLEAN`ing. The SEC is run again on the `CLEAN`ed images to identify lower intensity (weaker) masers that would have been missed due to its proximity to higher intensity (stronger) masers. A final catalogue of masers is compiled after a final visual inspection.

The same procedure is performed to produce the B-configuration VLA methanol maser catalogue. However, we run the SEC directly on the `CLEAN`ed images towards the positions of detected masers from the D-configuration catalogue.

Following the procedure done in Nguyen et al. (2022) to obtain the flux density of each maser source in the D-configuration, we similarly perform a 2D Gaussian fit of the brightness distribution for every channel whose peak intensity is above 4σ in the velocity range of the maser. The CASA task `imfit` was used on a 20×20 pixel box ($\sim 3\times$ the restoring beam) where the centre of the box was the pixel with maximum intensity. We visually verify the result of the source fits, as well as determine the individual peaks of each maser site. We refer to each velocity peak as a maser spot inside one maser site (Walsh et al. 2014). Table 5.2 lists a few examples of masers sites while the complete catalogue can be found in the Appendix.

The error in maser position can be determined by the astrometric uncertainty $\theta_{\rm res}/(2\times{\rm S/N})$, where $\theta_{\rm res}$ is the (VLA) restoring beam, and S/N is the ratio between source intensity and rms (Thompson et al. 2017). For the B-configurations, taking an average beamsize of $1.2''$, and a maser detection with S/N=10, the precision in position is $\approx 0\farcs06$. However, as discussed in Ortiz-León et al. (2021) and Nguyen et al. (2022), additional errors in the calibration process likely worsen the positional accuracy. As such, a better estimate of the positional errors can be obtained by comparing with very-long-baseline interferometry (VLBI) observations which is discussed in Section 5.5.1.

5.4 Survey results

5.4.1 Detections

In the area covered by the pilot region, we detected 116 CH_3OH masers in the D-configuration as presented in Nguyen et al. (2022). In making the D-configuration catalogue, we required that for a source to be detected, a minimum of two adjacent channels must meet our S/N threshold and as such, our estimated completeness level may be higher than the 4σ noise level. We have overlaid the detections on top of the GLOSTAR D-configuration continuum emission in Fig. 5.1 to provide an overview

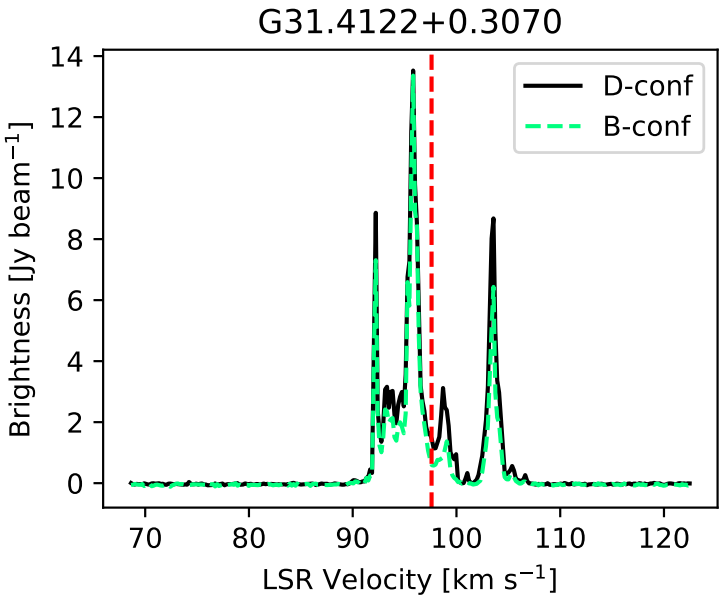

Figure 5.2: Spectra of 6.7 GHz methanol masers detected with GLOSTAR extracted at the peak pixel. The B-configuration data is the green dashed line while the D-configuration data is the black solid line. The vertical red dashed line indicates the ATLASGAL clump velocity (Urquhart et al. 2018b, 2022) in case of an associated 870 μm compact source catalogue (CSC) source.

of the area. These markers show the locations where the B-configuration cubes were focused on. From this, we have detected again every maser from the D-configuration catalogue with the B-configuration data. The properties of a few example detections are listed in Table 5.2, and we refer the reader to the Appendix for the full list of detections. Each maser source is identified by its galactic coordinates as its name. The equatorial coordinates for the maser spot with the highest peak flux, is given while the remaining maser spots (if any) are given as an offset to this main maser spot. This main maser spot is the main velocity component. The velocity of each maser spot as well as its peak flux and integrated flux are listed in the table. The fluxes were determined using 2D Gaussian fitting (see Section 5.3.4). Additionally, we report in Appendix C every velocity channel where emission was detected above the 4σ level for a given maser. We show in Fig. 5.2 the 6.7 GHz CH_3OH maser of G31.4122+0.3070 in both the D-configuration and B-configuration. The rest of the spectra are in Appendix C.

5.4.2 Flux densities

The brightest 6.7 GHz CH_3OH maser we detect in the pilot region using the B-configuration has a peak flux density of ∼148 Jy (G35.1973–0.7428). The weakest maser by comparison is 0.11 Jy for the source G34.8221+0.3518. The median flux is 3.8 Jy and we detect a total of 22 masers above 20 Jy. Of the 84 masers that were

newly detected using the D-configuration data, 17 are in the pilot region. Of these new detections, the B-configuration fluxes range from 0.12 Jy and 11.2 Jy corresponding to G34.2839+0.1837b and G32.1176+0.0906 respectively.

5.4.3 Luminosity

Given that all of the B-configuration maser sources were detected in D-configuration, the distances for all the masers were already discussed in Nguyen et al. (2022). This was done using a Bayesian distance estimator Reid et al. (2019) and using ATLASGAL sources which have had their distances checked for HI self-absorption (e.g., Schuller et al. 2009a; Urquhart et al. 2018b, 2022) in order to resolve the kinematic distance ambiguity (see e.g., Roman-Duval et al. 2009). As such, we use the same distances assigned to the associated maser source to calculate the luminosity for a given maser.

With the distances, the isotropic maser luminosity is estimated across all the velocity channels in which we have emission $> 4\sigma$. We use the velocity integrated flux density, $S_{\rm Int}$ in units of Jy km s^{-1} to determine the luminosity:

$$L_{\rm maser} = 4\pi D^2 S_{\rm Int} f/c \tag{5.1}$$

where D is the heliocentric distance to the source, f is the rest frequency of the maser line ($5_1 - 6_0{\rm A}^+$, 6668.5192 MHz) and c is the speed of light. The total velocity covered, $\Delta V_{\rm D}$, the estimated distance, the velocity integrated flux density, $S_{\rm Int}$, and the final isotropic maser luminosity, $L_{\rm maser}$, are listed for a few example sources in Table 5.3 and the rest are listed in the Appendix.

5.5 Discussion

5.5.1 Comparison with other maser surveys

The Methanol Multibeam (MMB) survey (Green et al. 2009) is an unbiased survey that covers a section of the Galactic plane ranging from $186^\circ \leq l \leq 60^\circ$ and $|b| < 2^\circ$. Using the Parkes 64 m radio telescope, the MMB made preliminary detections which are followed up using higher resolution interfermometers — the Australia Telescope Compact Array (ATCA) or the Multi-Element Radio Linked Interferometer Network (MERLIN, Thomasson 1986) — to improve the accuracy in their reported positions to be better than $< 1''$. The sensitivity of the survey is $\sim$0.2 Jy. The MMB catalogues $\sim$1000 sources (Caswell et al. 2010; Green et al. 2010; Caswell et al. 2011; Green et al. 2012; Breen et al. 2015), where 99 lie within the pilot region of the GLOSTAR data presented here. Of these, all of them were detected in our survey. As GLOSTAR is also an unbiased survey, it is useful to compare the catalogues resulting from these surveys.

We show the comparison in the GLOSTAR B-configuration and the MMB positions in Fig. 5.3. We use the equatorial coordinates of right ascension (RA) and declination (Dec.). The mean offsets are $\delta RA = -0.08 \pm 0.39$ arcsec and $\delta Dec. = -0.11 \pm 1.31$ arcsec. We see that there is a larger spread in the declination. This is due to the higher declination errors in the MMB catalogue. Otherwise, there is no

Table 5.2: Properties of methanol maser spots from B-configuration maps for a selection of sources.

Name	$\alpha/\Delta\alpha$	$\delta/\Delta\delta$	V_{LSR}	$S_{v,\,Peak}$	$S_{v,\,Int}$	Notes
	h:m:s/″	d:m:s/″	km s^{-1}	Jy beam^{-1}	Jy	
(1)	(2)	(3)	(4)	(5)	(6)	(7)
G29.2815–0.3295	18:45:56.8521	-3:23:56.312	92.26	3.46±0.03	3.55±0.05	YANG19
G29.2815–0.3295	0.09	0.13	91.72	0.13±0.02	0.17±0.04	
G29.2815–0.3295	0.03	0.01	91.90	0.30±0.02	0.32±0.04	
G29.2815–0.3295	0.01	-0.03	92.08	1.60±0.02	1.65±0.04	
G29.2815–0.3295	-0.01	-0.01	92.44	2.48±0.02	2.63±0.04	
G29.2815–0.3295	0.04	-0.03	92.62	0.77±0.02	0.79±0.04	
G29.2815–0.3295	0.02	0.01	92.80	0.57±0.02	0.63±0.04	
G29.2815–0.3295	0.01	-0.08	92.98	0.44±0.02	0.51±0.04	
G29.3197–0.1619	18:45:25.1509	-3:17:16.896	48.83	4.15±0.04	4.39±0.08	MMB
G29.3197–0.1619	0.08	0.22	42.17	0.17±0.02	0.23±0.05	
G29.3197–0.1619	-0.01	0.11	42.89	0.39±0.02	0.43±0.04	
G29.3197–0.1619	-0.04	0.08	43.07	0.96±0.02	0.97±0.04	
G29.3197–0.1619	-0.03	0.06	43.25	1.11±0.03	1.10±0.05	
G29.3197–0.1619	-0.05	-0.06	43.43	0.21±0.02	0.34±0.06	
G29.3197–0.1619	-0.07	0.12	43.61	0.31±0.02	0.24±0.03	
G29.3197–0.1619	0.01	0.07	43.79	0.14±0.02	0.08±0.02	
G29.3197–0.1619	0.04	0.05	44.15	0.15±0.02	0.22±0.05	
G29.3197–0.1619	-0.08	0.02	45.23	0.14±0.02	0.16±0.04	
G29.3197–0.1619	-0.02	-0.13	47.57	0.14±0.02	0.20±0.05	
G29.3197–0.1619	0.05	0.01	47.93	0.57±0.02	0.64±0.05	
G29.3197–0.1619	-0.00	-0.01	48.11	2.37±0.04	2.58±0.07	
G29.3197–0.1619	0.00	0.02	48.29	1.62±0.04	1.74±0.07	
G29.3197–0.1619	0.01	0.00	48.47	2.41±0.04	2.63±0.07	
G29.3197–0.1619	-0.00	0.01	48.65	2.43±0.03	2.57±0.06	
G29.3197–0.1619	0.01	-0.00	49.01	2.03±0.03	2.19±0.06	
G29.3197–0.1619	0.00	0.02	49.19	1.48±0.03	1.64±0.06	
G29.3197–0.1619	0.01	-0.01	49.37	1.41±0.03	1.47±0.06	
G29.3197–0.1619	0.03	0.05	49.55	0.08±0.02	0.29±0.09	
G29.3197–0.1619	-0.11	-0.05	50.09	0.55±0.02	0.57±0.04	
G29.3197–0.1619	-0.03	-0.01	50.27	0.35±0.03	0.44±0.06	
G29.5810+0.1323	18:44:50.9298	-2:55:17.744	31.88	0.31±0.02	0.40±0.04	NEW
G29.5810+0.1323	-0.29	-0.68	31.70	0.06±0.02	0.31±0.10	
G29.5810+0.1323	0.65	-1.11	32.06	0.05±0.01	0.36±0.11	

Notes. Column (1) gives the GLOSTAR source name based on the GLOSTAR Galactic coordinates. Columns (2) and (3) are the GLOSTAR equatorial coordinates of the position of the maser velocity component with the highest intensity. For sources with multiple components, we list their position offsets with respect to the component with the highest intensity. The position uncertainties are ″ (see Sect 5.5.1). Column (4) gives the LSR radial velocity of the peak of the component. Columns (5) and (6) give the peak and integrated fluxes at the peak velocity, given by (4). Column (7) Source references.

Table 5.3: Estimated distances and maser luminosities from B-configuration maps for the maser sources listed in Table 5.2. Refer to Table C.2 for a complete list of sources.

Name (glon, glat) (1)	$\Delta V_{\rm B}$ (km s^{-1}) (2)	Dist. (kpc) (3)	Note (4)	$S_{\rm Int}$ (Jy km s^{-1}) (5)	$L_{\rm maser,B}$ ($L_\odot$) (6)
G29.2815–0.3295	1.44	5.60±0.62	A	10.25±0.11	2.2×10^{-6}
G29.3197–0.1619	3.96	3.00±0.43	A	25.13±0.26	1.5×10^{-6}
G29.5809+0.1320	0.54	12.30±0.27	B	1.07±0.16	1.1×10^{-6}

Notes. Column (1) is the GLOSTAR source name. Column (2) gives the total velocity extent of maser emission above the local 4σ level. Column (3) gives the distance obtained from the Bayesian distance estimator (Reid et al. 2019) or from the ATLASGAL compact source catalogue (CSC) (Urquhart et al. 2018b, 2022) as marked in column (4) with a B or A respectively. Column (5) and (6) give the maser integrated flux and luminosity, respectively.

systematic offset in the astrometry with respect to the MMB catalogue for this smaller region of the GLOSTAR survey. However, the MMB does not have the same level of positional accuracy as the VLA in B-configuration so we use a different catalogue for comparison.

As mentioned in Section 5.3.4, ancillary maser observations with high precision positions would be able to give us a better measure of the precision of our B-configuration positions. To this end, we use the BeSSel survey (Brunthaler et al. 2011) to meet these goals. In particular, 16 of our sources have matching observations that were observed with the VLBA by Reid et al. (2019) which have milliarcsecond resolution, which exceeds by far our $\sim 1''$ resolution. A full comparison is not straightforward as our maser spots are mostly spatially unresolved in comparison to the BeSSel positions (see Appendix A from Ortiz-León et al. 2021), however, we can still use the reported positions from BeSSel to determine the offsets between the two measurements which is shown in Fig. 5.4. We obtain mean offsets of $0.01''$ and $0.04''$ for the RA and Dec. respectively with rms values of $0.03''$ and $0.05''$ which is smaller than that of the offsets with the MMB. The statistical error in the determined maser positions is given by $\theta_{\rm res}/(2 \times {\rm S/N})$, which is the astrometric uncertainty where $\theta_{\rm res}$ is the FWHM size of the restoring beam and S/N is the familiar signal-to-noise ratio. As such, for a typical B-configuration observation, the formal error for a 10σ detection given our noise level is $0.06''$. Taking into consideration our comparison with BeSSel, we take our positional errors to be $\sim 0.1''$.

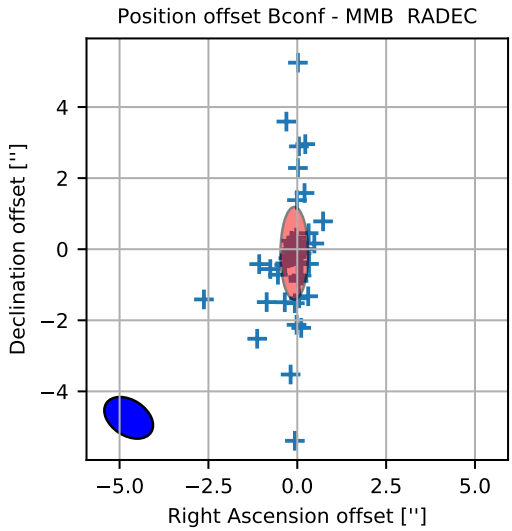

Figure 5.3: Comparison of the positions of matching MMB and GLOSTAR B-configuration methanol maser sources. The red shaded ellipse is centred on the mean offsets of $\delta RA = -0.08$ arcsec, and $\delta Dec. = 0.11$ arcsec. It shows the half-axes standard deviations in Galactic Longitude and Latitude which are 0.39 arcsec and 1.31 arcsec, respectively. The B-configuration beamsize is represented by the blue ellipse in the bottom left corner.

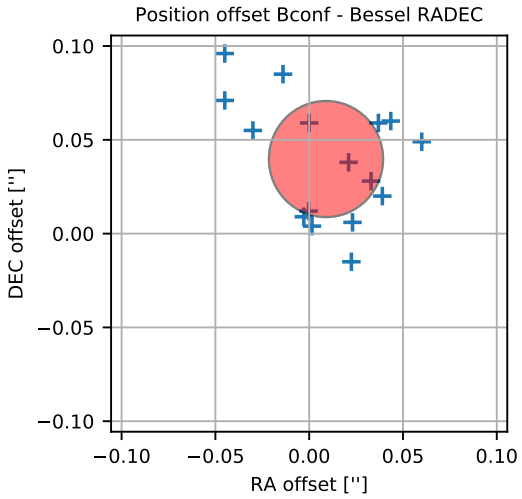

Figure 5.4: Comparison of the positions of matching BeSSel sources and GLOSTAR methanol maser sources. The red shaded ellipse is centred on the mean offsets of $\delta RA = 0.01$ arcsec, and $\delta Dec. = 0.04$ arcsec. It shows the half-axes standard deviations in right ascension and declination which are both 0.03 arcsec and 0.05 arcsec respectively.

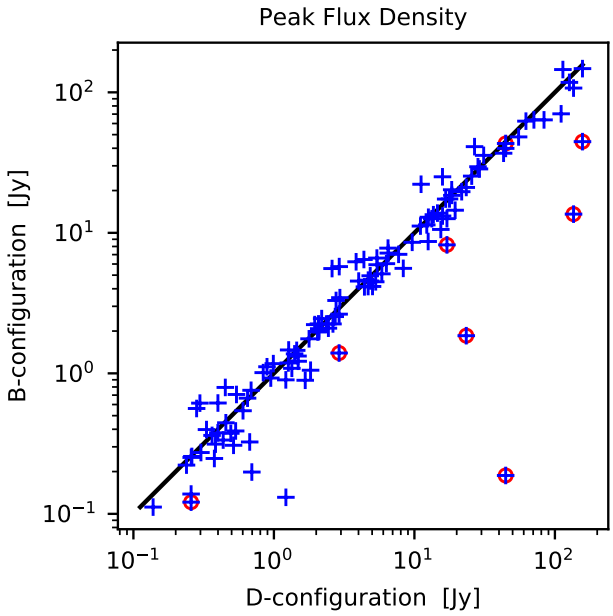

Figure 5.5: Comparison of GLOSTAR B-configuration vs. D-configuration peak flux densities for masers detected in both surveys. The black line indicates the 1:1 equality line. Red circles denote sources that have split into multiple components in the B-configuration maps.

5.5.2 Comparison between D and B configuration

Maser variability is not yet fully understood and thus comparing multiple epochs of data for a given maser would help to understand the general properties of maser variability. In the context of GLOSTAR, we have two epochs since the D-configuration and B-configuration data were taken as much as ∼8 months apart. As a sanity check, we first investigate if there are systemic differences between the fluxes of the masers from the two VLA configurations. To do this, we compare the fitted peak fluxes of each B-configuration maser's main velocity component (also its highest intensity component) to its D-configuration counterpart. We show in Fig. 5.5 this comparison between the peak fluxes. In general, there is no clear systematic deviation from equality, except for a few sources, giving us more confidence in detecting potential maser variability. The majority of the sources that differ largely from the equality line are the sources that are seen as two nearby masers in the B-configurationand have been resolved into multiple spatial components (highlighted with red circles in Fig. 5.5). We note that in this comparison, we used the D-configuration maser's main velocity component to compare with each of the resolved B-configuration masers' main velocity component. This leads to the large flux differences as we did not account for the different resolved B-configuration masers having different peak velocities. We investigate these masers that have been resolved into multiple components in Sect. 5.5.2.1 and account for the different velocity peaks in investigating maser variability in Sect. 5.5.4.

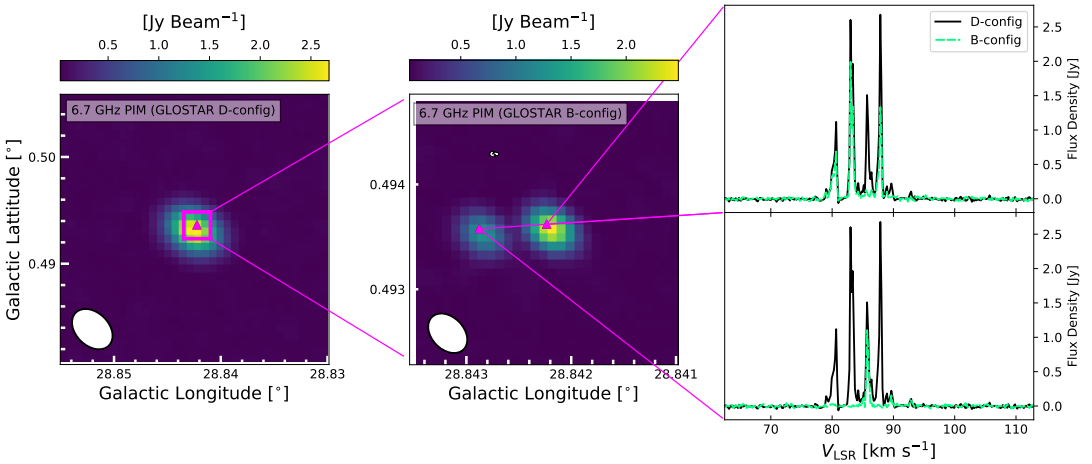

Figure 5.6: Presented are peak intensity maps (PIM) over the velocity range of the methanol maser source G28.8421+0.4938 and spectra obtained from VLA data. On the left is the VLA D-configuration data, which has an average beamsize of $\sim$ 18 arcsec. When observed in the B-configuration (with beamsize $\sim$ 1.5 arcsec, middle panel), one can see that the higher resolution allows us to resolve the maser into two sources. Viewing the spectra on the right, we see that the third peak at 85.7 km s^{-1} belongs only to the left source while the rest belong to the source on the right. The white contours mark the -3, 3, 5, and 7σ levels of the GLOSTAR radio continuum emission in their respective configurations.

5.5.2.1 Multiple components

As discussed above, we are able to resolve a few maser sources from the D-configuration into multiple maser sources in the B-configuration. We discuss briefly the results of these particular sources. An example figure is shown in Fig. 5.6 while the remainder are found in the Appendix C.1.

G28.8421+0.4938 has four main velocity peaks that we can see in the D-configuration data in Fig. 5.6. When seen in the B-configuration, we find that the velocity component at 85.69 km s^{-1} comes only from the western maser spot. This seems to be at the same velocity that an associated 22 GHz water maser also peaks (e.g., Szymczak et al. 2005). It is reported by Hu et al. (2016) that the source is associated with an UCHII region.

G29.9556–0.0156 is one of the masers, that are a part of the W43 high-mass star forming complex (along with G29.8621–0.0441, G31.2805+0.0617, and G31.5811+0.0769). Using trigonometric parallax from 12 GHz methanol and water maser emission, Zhang et al. (2014) found an average distance of 5.49 $\pm$ 0.4 kpc compared to the 4.90$\pm$, 0.7 kpc we used from ATLASGAL crossmatch. The spectra are shown in the top panel of

Fig. C.1. We find that the velocity component at 100.31 km s^{-1} comes solely from a southern maser spot that we resolved in the B-configuration data. Higher EVN observations by Surcis et al. (2019) were targeted towards the rotating disk of the associated protostar at VLBI scales which were distributed perpendicularly to the SiO outflow jet. They state that further observations would be required to determine if the methanol maser spots are exclusively associated with the rotating disk or if there are some associated with the outflowing gas.

G30.7880+0.2039 has two main maser spots. The strongest velocity feature is at 84.98 km s^{-1} which is not seen in the southern maser spot. The velocity feature at 75.8 km s^{-1} is seen in both maser spots and is not a sidelobe feature. However, it is clear that the southern source has a higher flux density at this position, making it distinct from the northern source.

G32.7443–0.0753 shows evidence for three main distinct maser spots. The northernmost component shows the 38.49 km s^{-1} component the strongest at roughly ∼40 Jy while it is $<$ 1 Jy for the other components. Conversely, the southern component is similarly strong but at the other velocities from 30-37 km s^{-1}. Most other observations seem to not detect the component at 44.07 km s^{-1} but was originally seen in the spectra by Caswell et al. (1995) also.

G34.2582+0.1534 is shown in the top panel of Fig. C.2. This source was observed by Slysh et al. (2001) using space-VLBI instruments targeting OH maser lines (1665 MHz and 1667 MHz) with 1 milliarcsecond resolution where they also detected multiple components. It is associated spatially with an UCHII region of the same name. The much weaker CH_3OH maser component is only seen in the north at 60.57 km s^{-1}, compared to the maser spot at 57.51km s^{-1}. It was similarly detected with two components by Breen et al. (2016) using the 12.2 GHz methanol maser line.

G34.2839+0.1837 is already one of the weaker sources that were detected in GLOSTAR at 0.25 Jy in the D-configuration. It is associated to a YSO matched from ATLASGAL (Urquhart et al. 2018b). We observe potentially two components split spatially and in velocity as the northern component is not detected at the peak velocity of 52.02 km s^{-1}. This target would benefit from even higher angular resolution data to better resolve the two components.

G35.1973–0.7428 was already shown to have two components by the MMB (Breen et al. 2015). Both components are relatively strong masers, but the strongest feature at 28.51 km s^{-1} is seen only in the southern component and is more than double the strength of its northern counterpart.

5.5.3 Association with radio continuum

As discussed in Nguyen et al. (2022), the relationship between methanol masers and radio emission from HII regions is still unclear. It has been proposed (e.g., Beuther et al. 2002) that one would not expect to see an association between them as HII regions are considered a later stage of a high mass star's development than the early protostar stage where methanol maser emission may be exhibited. However, HII regions are diverse and have classifications of their own. The more compact they are, the earlier the evolutionary stage and it may be possible for maser emission to be detected (Walsh et al. 1998; Yang et al. 2019a, 2021). A previous study by Hu et al. (2016) which used the VLA in C-configuration ($\theta_{\rm HPBW} \sim 3.5''$) in frequency range of 4–8 GHz has a comparable sensitivity ($\sim$45 μJy beam^{-1}) and showed an association rate of $\sim$30% between methanol masers and UC HII regions. In our previous work where we used the full GLOSTAR sample of D-configuration data, we found an association rate of $\sim$12%. This lower association rate is not unexpected as the angular scales we probed are not well suited for the more compact HII regions. We now, however, have access to the B-configuration data which has a higher angular resolution. We perform a similar analysis to see if new insights can be obtained for the pilot region.

Using an angular separation association of $1.5''$, we find 13 masers that have compact radio continuum source associations from a radio continuum catalogue produced by Dzib et al. (2022) using the BLOBCAT software package (Hales et al. 2012). This is in contrast to the D-configuration in the pilot region, where there were no associations. However, in visually inspecting the masers that have an association in the B-configuration, we do see associations in the D-configuration as well. An example is shown in Fig. 5.7 where the left panel shows the D-configuration radio continuum image and the right panel shows the zoomed in B-configuration image. This discrepancy can be attributed to a few possibilities. For some cases, the stringent cutoffs used to produce the D-configuration radio continuum catalogue where a high signal-to-noise ratio was required resulting in some of the weaker sources not meeting the chosen threshold. Furthermore, some sources show compact radio emission in the B-configurationbut extended emission in the D-configurationwhich may have been too far from the D-configurationradio continuum peak position. A third scenario is that there is a clear D-configuration radio continuum source that was missed in the original analysis. However, in comparing with the B-configuration continuum data, it gives more credibility to the detection of these radio sources.

Overall, our association rate is similar to our previous study (Nguyen et al. 2022) which considered the entire GLOSTAR coverage. As such, it is possible that the association rate of the B-configuration GLOSTAR catalogue for the full GLOSTAR survey would also increase. It reinforces the idea that we need high angular resolution and sensitivity to probe the hyper-compact (HC) HII regions to properly investigate the association between HII regions and methanol masers. Indeed, this has already been observed in the study by Yang et al. (2021) where their observational results have shown a maser detection rate of 100% when looking at a sample of HC HII regions. They further found that the detection rate decreases as HII regions evolve from HC HII regions

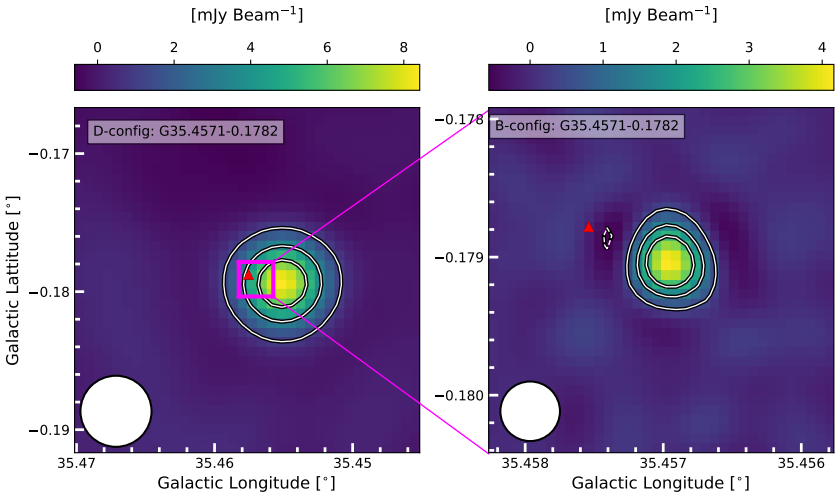

Figure 5.7: 5.8 GHz radio continuum cutouts of maser associated sources in the pilot region. The red triangle marks the position of detected masers in the region. *Left*: Cutout of 1.5×1.5 arcminute square from D-configuration data. *Right*: Cutout of 0.15×0.15 arcminute square from B-configuration data.

to UC HII regions.

5.5.4 Potential variability candidates

To study potential variability in the methanol maser flux we start with known variable masers that have been previously studied with many observations over a long period of time. However, in the pilot region, there are not many sources to choose from. From the literature, we find sources G30.4006–0.2958 and G33.6412–0.2276 to be known variable masers where we have data that has been analysed in both of GLOSTAR's D-configuration and B-configuration. To increase our sample size, we went outside of the pilot region and reduced some of the available VLA B-configuration data to include a few more sources, namely G9.6213+0.1961, G12.6807–0.1823, G12.8888–0.4892, G14.2298–0.5093, G22.3564+0.0663, and G37.5536+0.2007. We first analyse this sample to compare our data with known variable sources.

To obtain a meaningful comparison, we have smoothed the B-configuration data to the D-configuration beamsize and extracted the spectra from the same corresponding pixel. As usual, the pixel chosen is the pixel of greatest intensity at the strongest velocity feature of the maser. The spectra are shown in Figs. 5.8, 5.9, 5.10, and 5.11. The smoothing avoids the situation where the higher resolution data has resolved multiple maser spots where individual maser spots correspond to different velocity features. For example, in Fig. 5.9, we have shown the spectra of the D-configuration data, the smoothed B-configuration data, and the spectra from the B-configuration data at the positions of the individual maser spots, whereby looking only at these spectra, one would naively assume strong variability without taking into account the spatial po-

sitions of the maser. We note that the smoothing also introduces an increased noise level by a factor of ∼10. This behaviour is, however, expected as the noise in units of brightness temperature decreases with the square root of the beam area, but at the same time affects the conversion of brightness temperature to flux density as it is multiplied with the beam area. The end result is that the noise increases linearly with the beam size. To account for this, we do not consider peak fluxes of $< 1\,\mathrm{Jy\,beam^{-1}}$ as we cannot be sure that the variation in peak fluxes are not entirely due to the noise.

G9.6213+0.1961 has been observed extensively in the past, also because it is one of the brightest methanol masers observed to date (e.g., Goedhart et al. 2004, 2007; van der Walt et al. 2009, 2016). The mechanism powering the variability is still highly debated. A period of 244 days was found, where it was noted that the maximum amplitude of the variations also changes between periodic cycles. While many velocity components were previously studied, the main velocity component at $1.3\,\mathrm{km\,s^{-1}}$ shows an increase in the brightness by a factor of ∼1.24 while for the other components we detected in our data, the variation is negligible over a time span of 139 days between the two sets of GLOSTAR observations.

G12.6807–0.1823 was studied by Goedhart et al. (2004) and found to have a period of 307 days. The time between our observations is 232 days with the B-configuration data being observed first. For this maser, it is obvious that not all maser components vary the same way. We find that the velocity components at $51.91\,\mathrm{km\,s^{-1}}$, and $58.8\,\mathrm{km\,s^{-1}}$ have decreased by a factor of 1.2 and 1.3. Conversely, the velocity components at $57.5\,\mathrm{km\,s^{-1}}$, $58.4\,\mathrm{km\,s^{-1}}$, and $59.8\,\mathrm{km\,s^{-1}}$have increased by a factor of 1.2, 1.3, and 1.5 respectively.

G12.8888–0.4892 was studied by Goedhart et al. (2009) and was found to have one of the shorter periods of 29.5 days. This source was the example source of why smoothing the data is necessary. As this source was observed at the same time as G12.6807–0.1823, the time between observations is also 232 days. Only the weaker velocity component at $31.3\,\mathrm{km\,s^{-1}}$ showed an increase of a factor of 1.8.

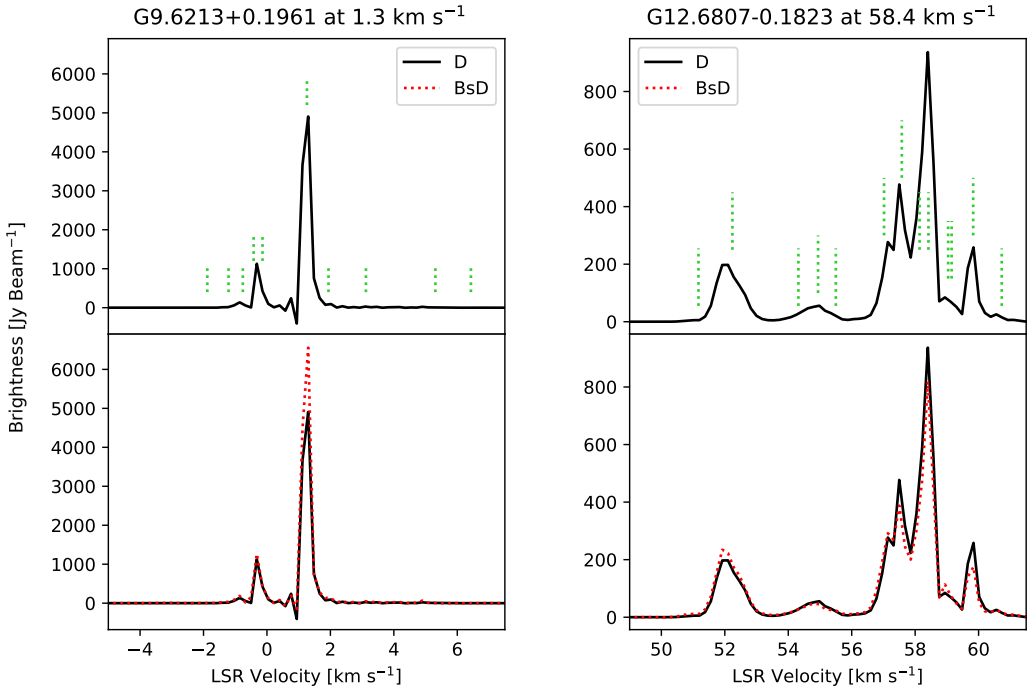

Figure 5.8: Comparison of the spectra taken from two epochs in GLOSTAR. In all frames, the D-configuration data (D - solid black) is shown and the smoothed B-configuration data (BsD - dashed red) is shown on top of the D-configuration for a clearer comparison. The green vertical dashed lines show the velocity components that were studied by the literature during long term observations of these maser sources.

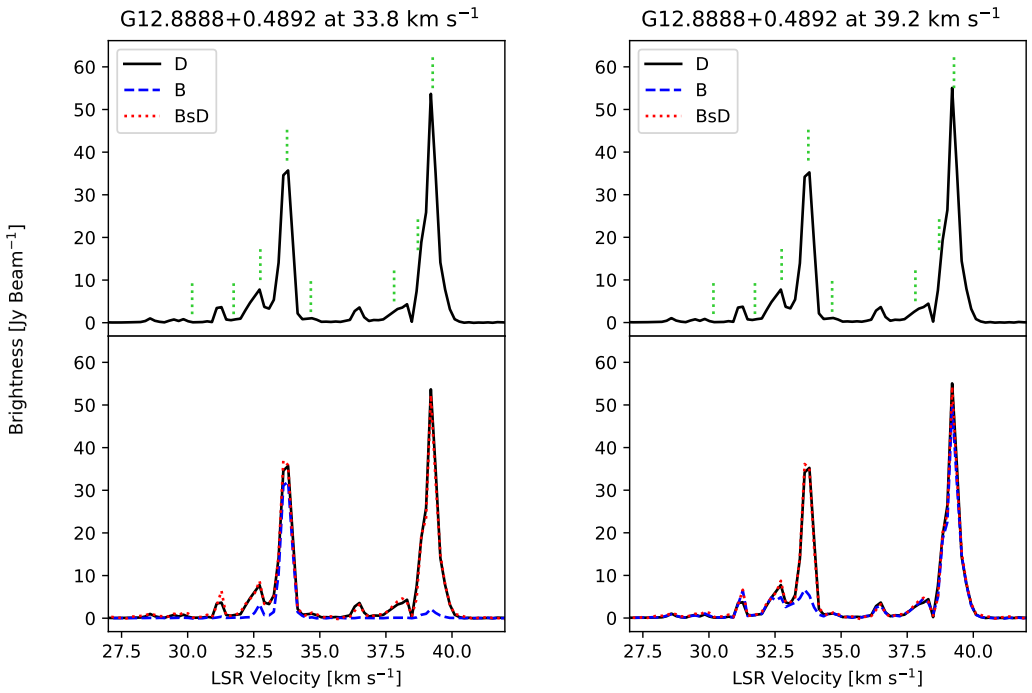

Figure 5.9: Continued from Fig. 5.8. In this case, we have plotted the unsmoothed B-configuration spectra from the unblended maser spots showing that the velocity peaks correspond to different spatial features and are not the true cause of the apparent variability.

G14.2298–0.5093 has the shortest periodicity at 23.9 days as studied by Sugiyama et al. (2017) with observations spanning 2013-01-05 to 2016-01-21. Our D-configuration observations take place 219 days after the B-configuration observations (2017-02-19 and 2016-07-15, respectively). This source is known to flare, where it fell to below the detection limit in the study of Sugiyama et al. (2017) ($3\sigma = 0.9$ Jy). Since our detection threshold is lower ($3\sigma = 0.054$ Jy), it was detected to have changed from 2.9 Jy to 0.3 Jy which is a decrease by a factor of ~ 10. The increase in noise in the smoothed spectra is not enough to account for this variation. Sugiyama et al. (2017) found that during flares, it could increase by a factor of more than 180 over a timescale of 2 days.

G22.3564+0.0663 has a period of 179.2 days, where it was seen that all the velocity components vary at the same time (Szymczak et al. 2011, 2015). In our case, the B-configuration data was taken 272 days after the D-configuration data where all of the velocity components increased. The factor by which they increased however was not uniform. The peak velocity component at 80.26 km s^{-1} increased by a factor of 2.2. The velocity components at 78.8 km s^{-1} and 83.3 km s^{-1} increased by a factor of 1.4 and 3.4 respectively. An interesting feature is for the velocity component at 81.51 km s^{-1} where the change is on the order of six times higher intensity. Not only that, but the peak seems to be shifted in velocity compared to the peak seen in the D-configuration.

G37.5536+0.2007 was studied by Araya et al. (2010) at the same time as a formaldehyde maser and found that while the two masers were spatially separated, they both flared in sync with a period of 237 days. We have a long time in between our two data points with a separation of 749 days. In our data, we see that the velocity component at 74.7 km s^{-1} seems to be the only component that has decreased over time while all the other components have increased (by a factor of $\sim$1.7), however, the peak flux for this velocity component for the smoothed data is ~ 1 Jy beam^{-1} which makes a comparison unreliable due to the increase in noise. Furthermore, the velocity components at 83.67 km s^{-1} and 84.93 km s^{-1} were not previously studied in detail.

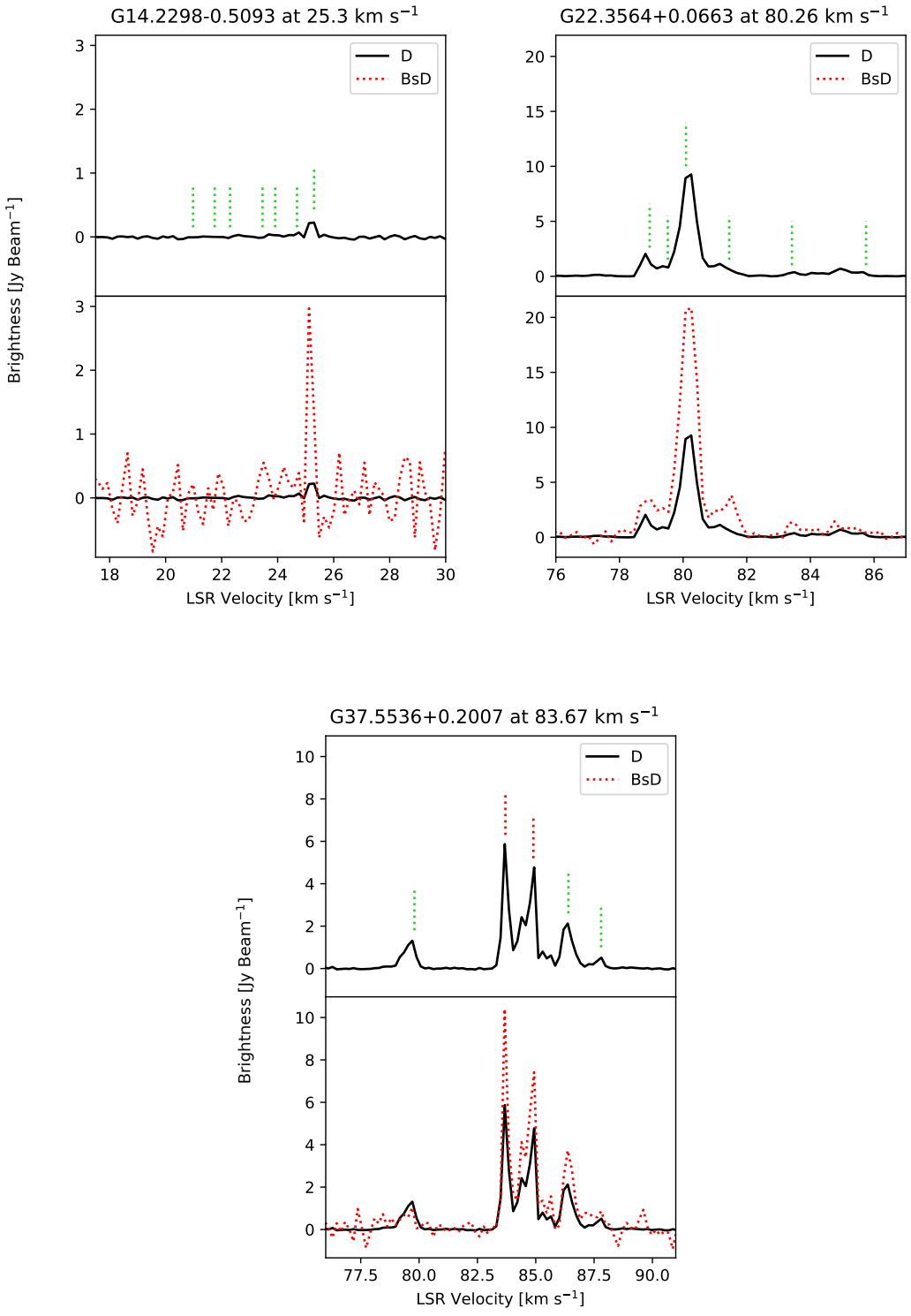

Figure 5.10: Continued from Fig. 5.8.

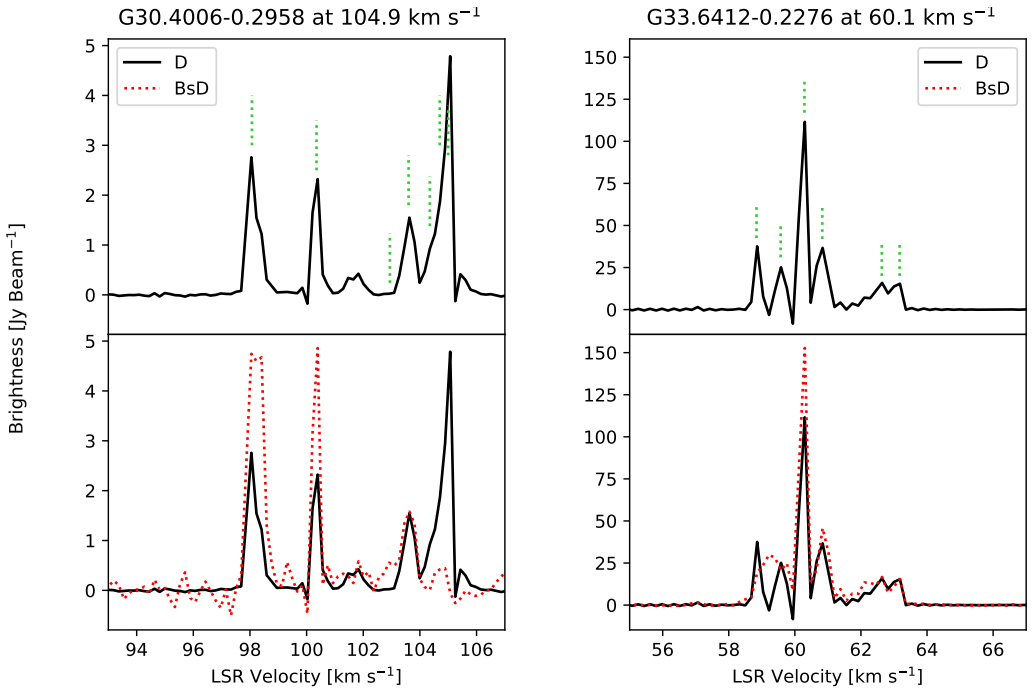

Figure 5.11: Continued from Fig. 5.8 for the masers found in the pilot region of GLOSTAR.

G30.4006–0.2958 shows a periodicity of 222.9 days (Olech et al. 2019). In their study, they found that the velocity components at 98.05 km s^{-1} and 100.39 km s^{-1} did not vary significantly but that the components at 103.63 km s^{-1} and 105.1 km s^{-1} varied by a factor $\sim$ 2. This is in contrast with our results where the first two velocity components are the ones that are varying by a factor $\sim$ 2. The velocity component at 103.63 km s^{-1} does not change significantly between our two data points which are separated by 274 days. Lastly, the velocity component at 105.1 km s^{-1} would not be considered to be detected as a peak at all in the B-configuration data whilst it is seen clearly in the D-configuration. As such, we see almost a 90% change in the intensity.

G33.6412–0.2276 was also studied by (Olech et al. 2019) where they could not make definitive conclusions about its periodicity. Their analysis showed only quasi-periodic variability over for a range of possible periods from 586 to 675 days. Our observations are 165 days apart. Kojima et al. (2017) also studied this maser, which is known to burst, and found that the bursts had periods ranging from 0.24 to 5 days. The velocity component that showed this bursting variability was at 59.57 km s^{-1}. In our data, the B-configuration data shows a different shape than the D-configuration, where two originally distinct peaks seem melded into one. The reason for this behaviour is unclear. The other velocity component that we can study at 60.84 km s^{-1} varies by a factor of 1.3 whilst the other components show negligible variability.

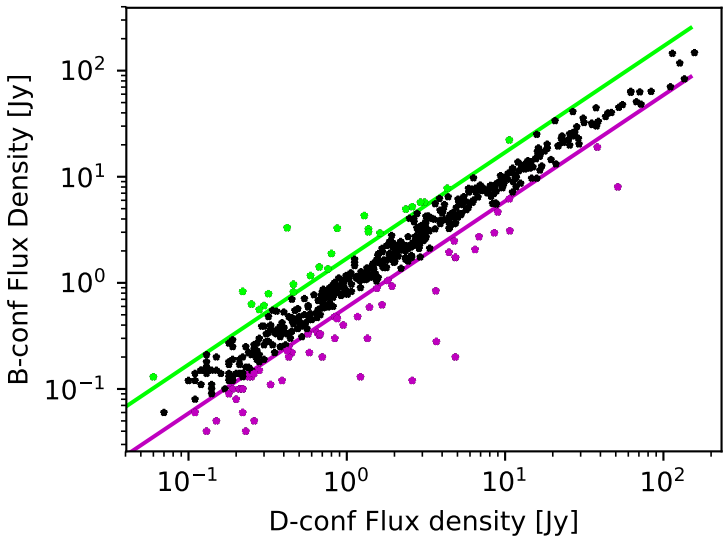

Figure 5.12: Comparison of the fitted fluxes for all main velocity components of all masers in D-configuration and their associated B-configuration velocity component. Given that all D-configuration data in the pilot region was obtained before the B-configuration, the green line shows the sources that increased in flux by a factor of 1.7, while the magenta line shows the threshold where it has decreased by the same factor.

From this sample, we can see that the study of maser variability is quite complicated as it requires many observations over a long period of time in order to determine a period for the variability. Furthermore, not all velocity components may vary, and not all components may vary at the same time. Even in this sample of known masers, having just our two data points, our observations may be at a phase where strong variability is not observed as we see that many of the velocity components changed only by a factor of ~ 1.7 on average. Nevertheless, we can use this as a minimum threshold to highlight maser sources in our full sample that would be ideal for long term observations as potential variable maser candidates. As a first approach, we search in each maser, all the detected velocity peaks. In doing so, we find velocity components from masers sources that show a variation of a factor 1.7 or more. We have plotted these results in Fig. 5.12 where the median ratio of all the compared components is 0.92. In contrast to Fig. 5.5, which only considered the main velocity peak, we have now included all the velocity components of a maser.

In Fig. 5.13 we show the distribution of the relative change for the peak fluxes of the main velocity components relative to the D-configuration epoch at their native resolutions, i.e, not smoothed. In fitting a Gaussian to the distribution we compute a mean of $-7.56 \pm 1.11\%$ and standard deviation of $20.01 \pm 1.11\%$ which is in agreement with our mean variation factor ($1.7 > 3\sigma$). In combination with our previous finding that the average ratio of the fluxes is 0.92, there is indeed a slight offset from what we would expect in that there are slightly more sources that have decreased in flux

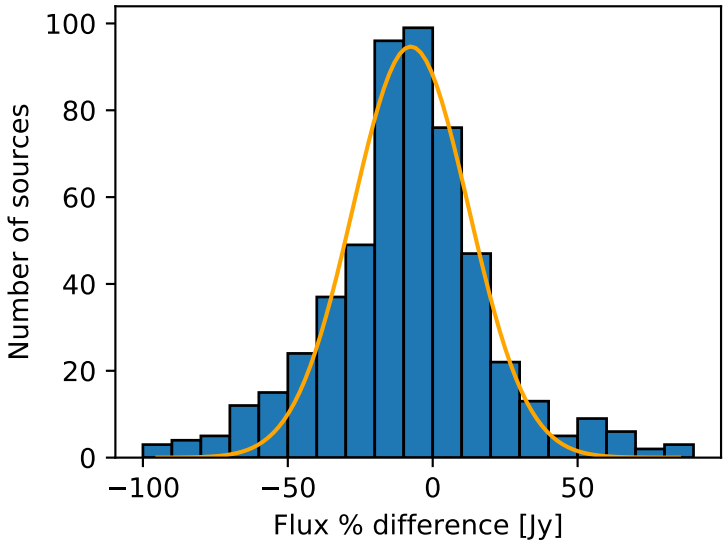

Figure 5.13: Distribution of the relative change for the fitted peaks relative to the D-configuration epoch. The normal distribution is described by a mean of $-7.56 \pm 1.11\%$ and standard deviation of $20.01 \pm 1.11\%$.

over time. One possible source of this discrepancy is that we have not performed yet the convolution of all the B-configuration data to the D-configuration beamsize for the full pilot region. As such, by excluding velocity components whose peak flux are $< 1\,\mathrm{Jy\,beam^{-1}}$ in consideration of the noise, we are left with 29 velocity components that fit our criteria. Of these, there are 16 velocity components that have increased and 13 that have decreased. Furthermore, the average flux ratio increases to 0.96, getting closer towards unity which is similar to the results found by Breen et al. (2015) when comparing their two epochs of data for the MMB. We propose these velocity components to be prime targets for additional long term observations and list them in Table 5.4.

Table 5.4: Velocity components with a variation factor >1.7.

Name	Velocity $\mathrm{km\,s^{-1}}$	$S_{\mathrm{p,D}}$ Jy	$S_{\mathrm{p,B}}$ Jy	Ratio
G28.6079+0.0180	106.33	0.42	3.3	7.9
G28.8621+0.0660	104.89	1.82	1.05	0.6
G28.3972+0.0803	68.74	0.59	1.17	2.0
G28.3972+0.0803	70.36	1.37	3.22	2.4
G28.3972+0.0803	72.16	1.62	2.94	1.8
G28.3972+0.0803	72.52	2.59	5.21	2.0
G28.3972+0.0803	80.8	3.1	5.75	1.9
G28.5228+0.1270	39.48	2.92	5.75	2.0
G29.9556–0.0156	97.79	4.42	1.94	0.4
G29.9556–0.0156	99.05	6.84	2.72	0.4
G30.7880+0.2039	75.8	10.71	3.09	0.3
G30.7880+0.2039	76.34	4.85	1.73	0.4
G30.2244–0.1803	111.23	4.31	7.78	1.8
G30.4006–0.2958	100.39	2.36	4.95	2.1
G32.0446+0.0593	94.06	8.55	2.96	0.3
G33.6412–0.2276	58.86	38.23	19.0	0.5
G33.3930+0.0097	107.46	0.8	1.89	2.4
G34.3957+0.2215	60.39	1.37	3.02	2.2
G34.3957+0.2215	61.29	0.76	1.35	1.8
G35.7927–0.1744	58.77	0.87	3.27	3.8
G35.7927–0.1744	59.49	0.67	1.41	2.1
G35.7927–0.1744	62.37	8.99	4.65	0.5
G35.7927–0.1744	62.91	1.29	4.3	3.3
G35.0248+0.3497	43.3	4.86	1.74	0.4
G35.0248+0.3497	46.18	4.77	2.48	0.5
G35.1327–0.7440	36.56	10.63	22.18	2.1
G35.1973–0.7428	27.07	6.46	2.06	0.3
G35.1973–0.7428	27.79	10.64	6.19	0.6
G35.1973–0.7428	28.87	51.51	8.01	0.2

5.6 Summary and Conclusions

In reducing the available GLOSTAR VLA B-configuration data, we have produced a catalogue of 6.7 GHz methanol masers for the GLOSTAR pilot region using higher angular resolution data. We calculate the fluxes, positions, and luminosities of the detected masers. With the benefit of this increased angular resolution, we are able to distinguish maser spots that were previously blended in the GLOSTAR VLA D-configuration data for 7 maser sources and show that certain velocity components are attributed to specific maser spots. Additionally, we compared our catalogue with the GLOSTAR radio continuum source catalogue for the B-configuration and found a similar association rate (12%) with our maser catalogue. This motivates the need for high angular resolution and high sensitivity to adequately investigate the association between methanol masers and HC HII regions. Furthermore, in having two epochs of observations, we used a small sample of known periodic masers to find a mean variation of a factor 1.7 for the velocity components of these masers. Using this threshold we produce a sample of more masers that would be ideal candidates for future long term monitoring projects of maser variability. Once more B-configuration data becomes available, we can provide better statistics in determining sources of potential variability.

Chapter 6

Concluding remarks

6.1 Summary

This PhD thesis presented an investigation into the environments of massive young stellar objects at two main periods of their evolution, the earliest stage and the final stage. Sources from the centre of the Milky Way as well as the majority of the 1st quadrant of our Galaxy were studied. To facilitate these studies, observations were taken using the VLA radio interferometer as part of the GLOSTAR survey. These observations were made possible due to the improvements made to the VLA by increasing its bandwidth and having a more flexible correlator. We used both radio spectral line and continuum data from GLOSTAR in conjunction with ancillary submillimetre data from ATLASGAL to identify regions of high-mass star formation and also to determine the properties of these regions and their tracers.

Part 1

The Central Molecular Zone is a ∼200 pc sized region around the Galactic Centre that is peculiar as it shows a star formation rate that is suppressed with respect to the available dense gas. To investigate the SFR in the CMZ, one can use the population of young stellar objects to characterise the SFR. If these infrared sources are indeed sites of current star formation, we expect them to be currently associated with HII regions, which can be seen at radio wavelengths.

As part of the GLOSTAR survey, D-configuration VLA data were obtained for the Galactic Centre, covering $-2^\circ < l < 2^\circ$ and $-1^\circ < b < 1^\circ$ with a frequency coverage of 4–8 GHz. We used these radio observations to search for radio counterparts of 334 2.2 μm infrared sources that have been identified as YSO candidates by Nandakumar et al. (2018). By using selection criteria, we matched this sample of YSOs with radio continuum sources and classified these radio sources as potential HII regions. An example of such an association is shown in the left panel of Fig. 6.1. Of the 334 YSO candidates, we found 35 with compact radio continuum counterparts. We also compare these YSO candidates with the 870 μm ATLASGAL survey and find that 94 YSOs are associated with dense dust condensations where 14 of these sources also have a GLOSTAR radio continuum counterpart. For those without both dust emission and radio emission, this lack of emission at these wavelengths suggests that they are potentially much older, having already dispersed their natal clouds. They are also perhaps not *high*-mass YSOs.

To characterise the radio sources that we do detect, we calculate their spectral indices and find that 11 are confirmed as HII regions. We also compared these radio sources to the WISE catalogue and found five without counterparts, making them potential new HII regions. We also determined the fluxes, sizes, and shapes of these HII regions allowing us to determine the Lyman continuum photon flux of the ionising zero-age-main-sequence star and determined its mass. We found masses between $10\,M_\odot < M_* < 40\,M_\odot$ and used their distribution (see right panel of Fig. 6.1) to estimate the total mass of all ZAMSs in the CMZ. In assuming an average formation timescale, we calculated their contribution to the SFR in the CMZ to be $0.04 \pm 0.02\,M_\odot\ \mathrm{yr}^{-1}$. This is consistent with the results of Nandakumar et al. (2018) as well as with other independent investigations that used different methods. However, our result is limited by an inherent bias, where we have used only the radio bright sources in our sample, neglecting possible star forming regions that are not yet radio bright. To account for this, we adapted the formulation of the SFR from Kauffmann et al. (2017a) and used the total ionising flux of HII regions to also estimate the SFR in the CMZ to be $0.068\,M_\odot\ \mathrm{yr}^{-1}$.

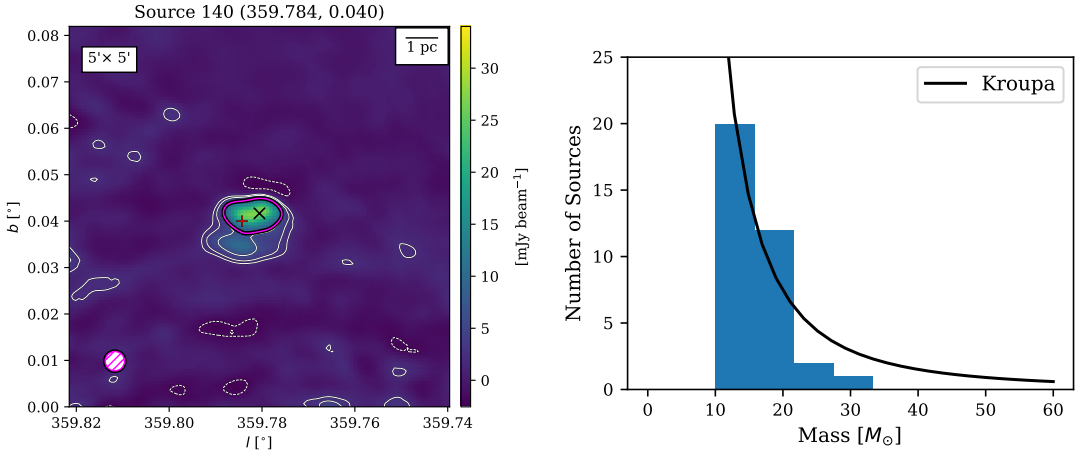

Figure 6.1: *Left*: Detection of a GLOSTAR 5.8 GHz counterpart for source 140 from Nandakumar et al. (2018). The GLOSTAR 5.8 GHz continuum map is shown in colour with positions of the peak radio emission and the YSO marked with a black X and red cross, respectively. White contours correspond to 3, 5, and $10\,\sigma$ ($\sigma = 0.634\,\mathrm{mJy\,beam}^{-1}$). The magenta contour outlines the area from which the flux density was calculated. The colour bar maximum was chosen to be 1.5× the peak intensity of the coinciding 5.8 GHz source. The beamsize is shown in magenta in the bottom left corner. Same as Fig. 3.1. *Right*: Mass distribution of calculated zero age main sequence (ZAMS) masses for the HII regions with associated YSOs. The black line represents the fitted Kroupa IMF (Kroupa 2001). Same as Fig. 3.2.

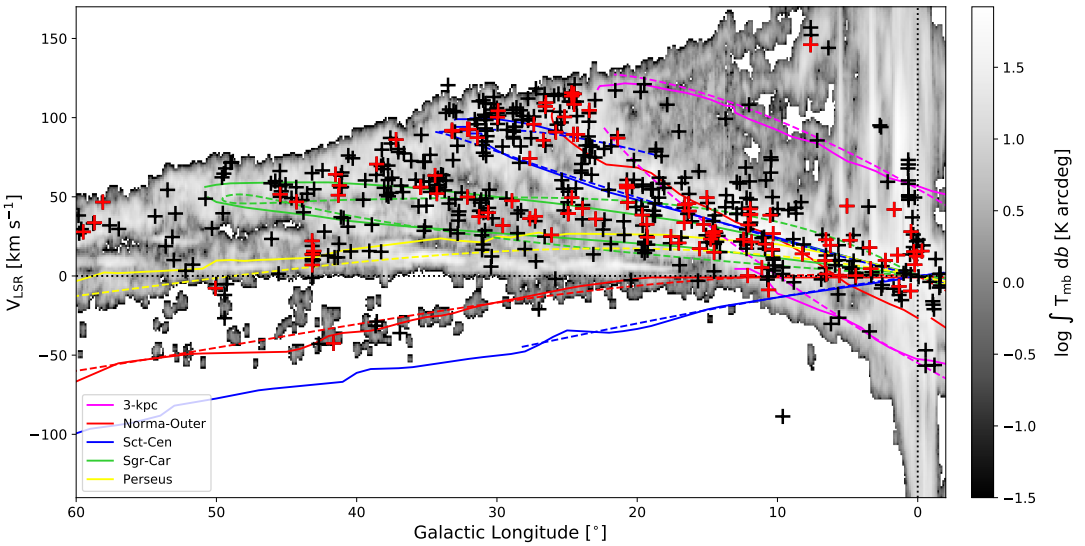

Figure 6.2: Distribution of detected 6.7 GHz methanol maser velocity with respect to Galactic longitude. Black crosses represent detections of known sources in the GLOSTAR survey and red crosses represent new detections. The dashed lines represent the updated spiral arm models of Taylor & Cordes (1993) as used in, e.g. Schuller et al. (2021) while the solid lines are the spiral arm descriptions from Reid et al. (2019). The background shows the CO emission from Dame et al. (2001). Same as Fig. 4.1.

Part 2

While the previous project looked at HII regions which are posited to be closer to the end stages of the MYSO evolution cycle, this project used spectral line data from GLOSTAR to look at sites of star formation associated with the earliest stages of the MYSO evolution. To this end, we have produced the most sensitive, unbiased survey of Class II 6.7 GHz CH_3OH masers to date in the region of $-2° < l < 60°$ in Galactic longitudes and $|b| < 1°$ in Galactic latitudes.

We developed a source extraction code to efficiently detect masers to address the challenges we faced due to the large datasets provided by the GLOSTAR survey. We detected a total of 554 masers, with 84 of them being new detections. Over 50 % of the new detections have fluxes of < 0.5 Jy which were detectable due to the improved sensitivity of GLOSTAR as compared to other unbiased surveys. We show an overview of their position relative to the spiral arms of the Milky Way in Fig. 6.2.

We compared our maser detections with the ATLASGAL Compact Source Catalogue and find that 65% of the CH_3OH masers are associated with dense gas. This leaves many of the newly detected masers unassociated, which is contrary to previous studies that show association rates $> 90\%$ (e.g., Billington et al. 2019). We rectify this discrepancy with a visual inspection and find that many of the new masers are associated with weak dust emission that is below the sensitivity required for inclusion in the ATLASGAL CSC, raising our true association rate to be 97% which is consistent

with other studies.

While it was shown in previous studies that ATLASGAL clump properties differ for different evolutionary stages (e.g., Urquhart et al. 2022, and that maser associated sources have higher dust temperatures, bolometric luminosities, and luminosity-to-mass ratios (Billington et al. 2019), we wanted to determine if the newly detected masers, were distinct from the total maser population as whole. Given that the newly detected masers often have weaker emission we compared the properties of their associated clump properties. Using an Anderson-Darling test (see Fig. 6.3), we find that only the bolometric luminosity of the dust clumps show a correlation (3σ) with the maser emission where the newly detected masers are weaker both in terms of their maser emission and associated dust emission. We made the hypothesis that weaker maser emission would trace earlier HMSF. However, given the lower range of maser luminosities and that the luminosity-to-mass ratio (a proxy for MYSO evolutionary stage) is consistent with the total maser population, this suggests that weaker masers do not necessarily trace earlier HMSF, but may trace less massive stars being formed.

Using the 5.8 GHz radio continuum D-configuration catalogue from GLOSTAR, we find that 12% of the masers are coincident with radio continuum emission (i.e. $< 12''$). This association rate is lower than previous studies ($\sim 30\%$ e.g., Hu et al. 2016) but can be accounted for when we note that the D-configuration catalogue is not optimised to sample UC HII regions and HC HII regions. However, when we compare the radio and maser flux distribution for sources that do have an association, we find no correlation as a function of angular offset. This suggests that the mechanisms powering maser and continuum emission are unrelated, despite their being a positional correlation.

The methanol maser luminosity function is of interest to HMSF as it is related to maser microphysics as well as the environment around the exciting massive YSO. However, lower luminosity ranges for the luminosity function to date have been under sampled. We used our sample of masers and a broken power law to construct a luminosity function. We determine a median luminosity $10^{-6}\,L_{\odot}$ for the distribution which is in agreement with previous studies. We sampled the high-luminosity maser population with success, but we find we are still limited with respect to the lower-luminosity bins.

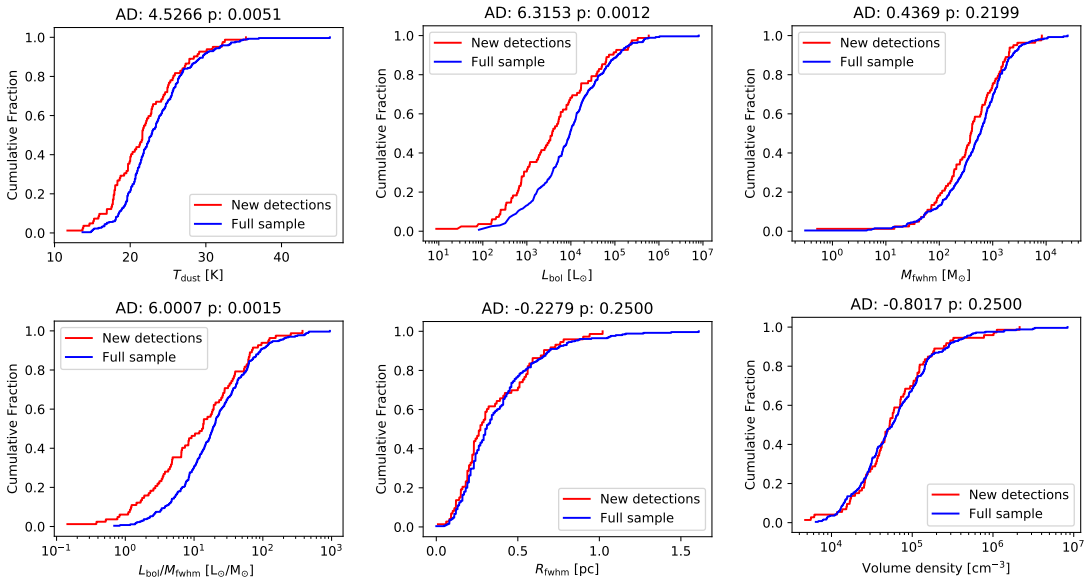

Figure 6.3: CDFs for various properties of ATLASGAL clumps associated with GLOSTAR methanol masers. We compare the sample clumps associated with new methanol maser detections (red) to the sample of clumps with associations to the full methanol maser catalogue (blue). The results of the Anderson-Darling (AD) test are shown above each plot. Same as Fig. 4.2.

Part 3

Given that the GLOSTAR survey also takes B-configuration data, this gives us access to higher resolution data of the methanol masers we detected in the D-configuration. We reduced and analysed these data for the pilot region of the GLOSTAR survey, namely $28° < l < 36°$ in Galactic longitude and $|b| < 1°$ in Galactic latitude. The aim of this follow-up project is two-fold:

- To provide better astrometry of the 6.7 GHz methanol masers we detected using the VLA in D-configuration and search for multiplicity.

- To determine potential candidates of methanol maser variability as we have access to two epochs of data within one survey.

To reduce the data, we follow the same procedure as outlined in Chapter 4. The data were calibrated in a similar fashion using CASA. However, full $2° \times 1°$ dirty cubes were not produced as they are even more computationally expensive as the higher angular resolution requires even more pixels for the same area coverage. Instead, we image only sub-cubes centred on the masers we detected in the D-configurationas any maser we are able to detect in the B-configuration should already have been detected in the D-configuration. We then used the source extraction code we developed to search for any maser that have now been resolved into multiple sources. We calculate

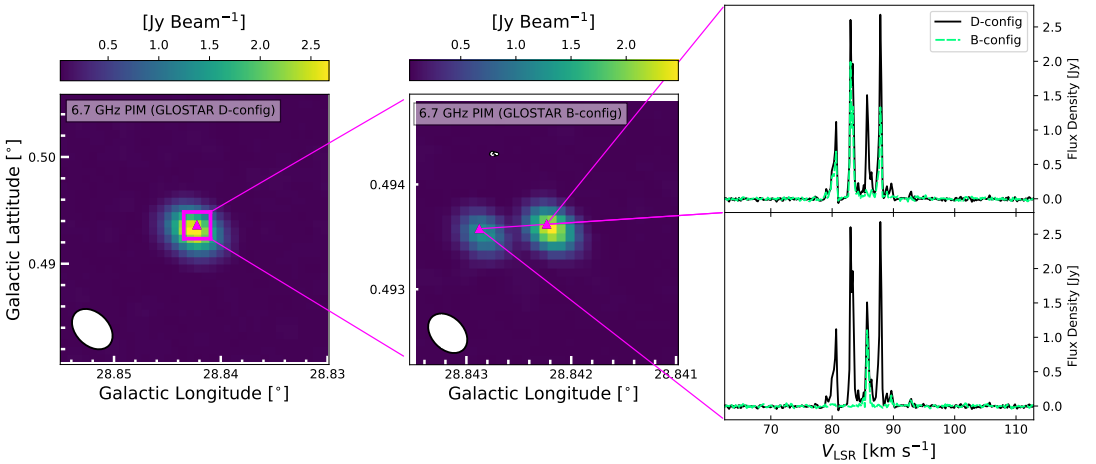

Figure 6.4: Presented are peak intensity maps (PIM) over the velocity range of the methanol maser source G28.8421+0.4938 and spectra obtained from VLA data. On the left is the VLA D-configuration data, which has an average beamsize of $\sim$ 18 arcsec. When observed in the B-configuration (with beamsize $\sim$ 1.5 arcsec, middle panel), one can see that the higher resolution allows us to resolve the maser into two sources. Viewing the spectra on the right, we see that the third peak at 85.7 km s^{-1} belongs only to the left source while the rest belong to the source on the right. The white contours mark the -3, 3, 5, and 7σ levels of the GLOSTAR radio continuum emission in their respective configurations. Same as Fig. 5.6.

maser properties such as their position, flux density, and luminosity for the 116 6.7 GHz methanol masers in the pilot region.

In our previous work, we reported positional uncertainties of $\sim$1.1 arcsecond. For the smaller sample size of the pilot region, we report positional uncertainties of $\sim$0.1 arcsecond after comparison with the BeSSel survey, which uses VLBI to obtain very high precision results. We then inspected the B-configuration maser images and found 7 masers that separated into multiple components when imaged at higher angular resolution. We are able to distinguish which velocity peaks correspond to which maser spots. An example of such a source is shown in Fig. 6.4.

Analogously to Nguyen et al. (2022), we searched for associations to HII regions using the radio continuum source catalogue from Dzib et al. (2022) which also uses the GLOSTAR VLA data in the B-configuration. We find a similar association rate and conclude that we would benefit from higher sensitivity radio continuum data in order to better detect UC HII regions and HC HII regions.

In having access to two data points in time, we are able to see how the brightness of the masers differ over time. We first look at a sample of known periodic masers and analyse the variation for the velocity components we are able to detect in our data. We first smooth the B-configuration images to the beam size of the D-configuration images. This increases the noise and so we only consider velocity components > 1 Jy beam^{-1}.

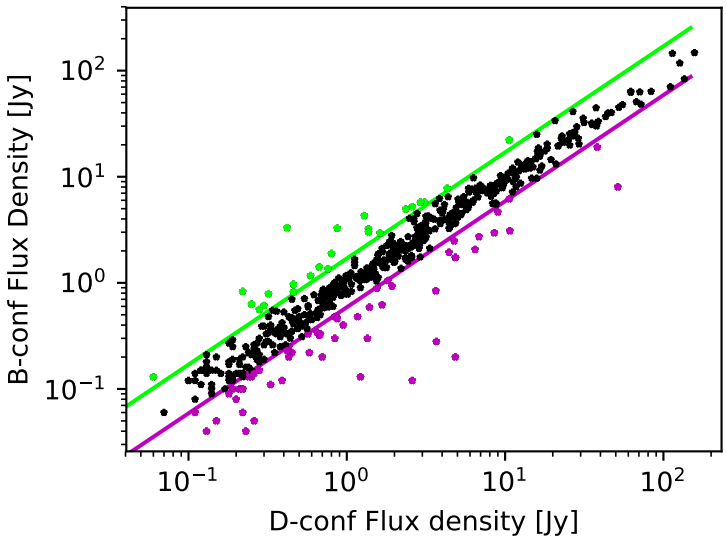

Figure 6.5: Comparison of the fitted fluxes for all main velocity components of all masers in D-configuration and their associated B-configuration velocity component. Given that all D-configuration data in the pilot region was obtained before the B-configuration, the red line shows the sources that increased in flux by a factor of 1.7, while the blue line shows the threshold where it has decreased by the same factor.

We find that for these known periodic masers, there is a mean variation of a factor 1.7 for the detected velocity components. We then looked at all the velocity components we detected in the B-configuration for the pilot region and compared the peak flux with their corresponding match in the D-configuration(as shown in Fig. 6.5). Based on this variation threshold, we find an average flux ratio ($S_{\mathrm{peak,B}}/S_{\mathrm{peak,D}}$) of 0.96 and detected 29 velocity components that would be potential sources of maser variability.

6.2 Outlook

This thesis focused on using modern radio wavelength data to better understand various phases of high-mass star formation. While we did our best to exploit the data to its fullest, there are interesting questions that we look forward to addressing in the future. When we first used the GLOSTAR radio continuum data to search for associations with the list of YSO candidates from Nandakumar et al. (2018), we performed this task visually and only analysed sources with simple and compact morphologies. As a next step, it would be useful to produce a full catalogue of radio continuum sources in the CMZ to better perform this analysis on a statistical basis. In this way, a more robust picture of the association of YSOs and developing HII regions can be formed.

Our 6.7 GHz methanol maser catalogue represents the most sensitive blind survey to date and has the best position accuracy. However, it only covers a portion of the Milky Way's plane. Naturally, a full coverage would provide a more complete picture of the masers in the Galaxy and thus a more complete census of the sites of exclusively early high-mass star formation. For the regions that are covered by GLOSTAR, once the reduction of the B-configuration data is completed, it will provide an upgrade in our measured positions as well as pinpoint sources of potential maser variability. For the sources we proposed as being variable methanol masers, dedicated long term observations would help to vindicate our assertion. Furthermore, methanol absorption can also be studied from the GLOSTAR data. Methanol absorption has been seen against radio continuum sources (e.g., Menten 1991b; Impellizzeri et al. 2008) but has also been detected against the CMB (e.g., Menten 1991b; Pandian et al. 2008; Ortiz-León et al. 2021). Having a catalogue of absorption detections would help to better understand the physical properties of this phenomenon. Pandian et al. (2008) did a modelling study to understand the conditions under which this absorption can occur. Having a larger sample size would allow for a more robust analysis. To this end we can use our source extraction code to search for this methanol absorption across a large area as part of the GLOSTAR survey.

Appendix A

GLOSTAR: Radio Continuum Detections of YSOs in the CMZ Paper

A&A 651, A88 (2021)
https://doi.org/10.1051/0004-6361/202140802

Astronomy & Astrophysics

A global view on star formation: The GLOSTAR Galactic plane survey

IV. Radio continuum detections of young stellar objects in the Galactic Centre region

H. Nguyen[1,⋆], M. R. Rugel[1], K. M. Menten[1], A. Brunthaler[1], S. A. Dzib[1], A. Y. Yang[1], J. Kauffmann[2], T. G. S. Pillai[3,1], G. Nandakumar[4,5], M. Schultheis[6], J. S. Urquhart[7], R. Dokara[1,⋆], Y. Gong[1], S-N. X. Medina[1], G. N. Ortiz-León[1], W. Reich[1], F. Wyrowski[1], H. Beuther[8], W. D. Cotton[9,10], T. Csengeri[11], J. D. Pandian[12], and N. Roy[13]

[1] Max-Planck-Institut für Radioastronomie, Auf dem Hügel 69, 53121 Bonn, Germany
e-mail: hnguyen@mpifr-bonn.mpg.de
[2] Haystack Observatory, Massachusetts Institute of Technology, 99 Millstone Road, Westford, MA 01886, USA
[3] Institute for Astrophysical Research, Boston University, Boston, MA 02215, USA
[4] Research School of Astronomy & Astrophysics, Australian National University, Canberra, ACT 2611, Australia
[5] ARC Centre of Excellence for All Sky Astrophysics in Three Dimensions (ASTRO-3D), Australia
[6] Laboratoire Lagrange, Université Côte d'Azur, Observatoire de la Côte d'Azur, CNRS, Bd de L'Observatoire, 06304 Nice, France
[7] Centre for Astrophysics and Planetary Science, University of Kent, Ingram Building, Canterbury, Kent CT2 7NH, UK
[8] Max Planck Institute for Astronomy, Königstuhl 17, 69117 Heidelberg, Germany
[9] National Radio Astronomy Observatory, 520 Edgemont Road, Charlottesville, VA 22903, USA
[10] South African Radio Astronomy Observatory, 2 Fir St, Black River Park, Observatory 7925, South Africa
[11] Laboratoire d'Astrophysique de Bordeaux, Univ. Bordeaux, CNRS, B18N, allée Geoffroy Saint-Hilaire, 33615 Pessac, France
[12] Department of Earth & Space Sciences, Indian Institute of Space Science and Technology, Trivandrum 695547, India
[13] Department of Physics, Indian Institute of Science, Bengaluru 560012, India

Received 12 March 2021 / Accepted 13 April 2021

ABSTRACT

Context. The Central Molecular Zone (CMZ), a ∼200 pc sized region around the Galactic Centre, is peculiar in that it shows a star formation rate (SFR) that is suppressed with respect to the available dense gas. To study the SFR in the CMZ, young stellar objects (YSOs) can be investigated. Here we present radio observations of 334 2.2 μm infrared sources that have been identified as YSO candidates.

Aims. Our goal is to investigate the presence of centimetre wavelength radio continuum counterparts to this sample of YSO candidates which we use to constrain the current SFR in the CMZ.

Methods. As part of the GLObal view on STAR formation (GLOSTAR) survey, D-configuration Very Large Array data were obtained for the Galactic Centre, covering $-2° < l < 2°$ and $-1° < b < 1°$ with a frequency coverage of 4–8 GHz. We matched YSOs with radio continuum sources based on selection criteria and classified these radio sources as potential HII regions and determined their physical properties.

Results. Of the 334 YSO candidates, we found 35 with radio continuum counterparts. We find that 94 YSOs are associated with dense dust condensations identified in the 870 μm ATLASGAL survey, of which 14 have a GLOSTAR counterpart. Of the 35 YSOs with radio counterparts, 11 are confirmed as HII regions based on their spectral indices and the literature. We estimated their Lyman continuum photon flux in order to estimate the mass of the ionising star. Combining these with known sources, the present-day SFR in the CMZ is calculated to be ∼0.068 $M_\odot$ yr^{-1}, which is ∼6.8% of the Galactic SFR. Candidate YSOs that lack radio counterparts may not have yet evolved to the stage of exhibiting an HII region or, conversely, are older and have dispersed their natal clouds. Since many lack dust emission, the latter is more likely. Our SFR estimate in the CMZ is in agreement with previous estimates in the literature.

Key words. Galaxy: center – Galaxy: stellar content – stars: formation – stars: massive – stars: pre-main sequence – HII regions

1. Introduction

The study of high-mass stars is vital to the understanding of the evolution of star formation in galaxies. They directly influence their surrounding environments by feeding energy through various feedback processes back into the interstellar medium (ISM). This can alter the efficiency of the remaining gas to form new stars and thus directly impact the evolution of their host galaxies. It is therefore important to understand the formation of high-mass stars themselves. Observations of star forming sites in our own galaxy, the Milky Way, are easier to resolve due to their proximity. Their study allows us to extend our understanding of

⋆ Member of the International Max Planck Research School (IMPRS) for Astronomy and Astrophysics at the Universities of Bonn and Cologne.

high-mass star formation (HMSF) to those in other galaxies as well (Kennicutt & Evans 2012).

The term massive young stellar object (MYSO) has been used for sources in a wide range of evolutionary stages. They start as objects that are still deeply embedded in their parental dense molecular cloud core and that are powered by accretion, often forming in clusters. Once nucleosynthesis commences, they start to ionise their surroundings (e.g., Zinnecker & Yorke 2007; Hoare et al. 2007; Breen et al. 2010), develop into hyper- and later ultra-compact HII regions that further evolve into compact HII regions (such as the Orion Nebula). The most luminous O-type stars therein clear their surroundings of obscuring dust and eventually make them and the much more numerous lower-mass members of the young stellar clusters, whose centres they occupy, visible (predominantly) in nearby parts of the Galaxy that do not suffer heavy line of sight and local visual extinction. The 1–2 million year old Orion Nebula Cluster (ONC; Genzel & Stutzki 1989) at a distance of only ∼400 pc (Menten et al. 2007; Kounkel et al. 2017) is a nearby prominent example. Observations of the earliest stages of development are difficult because of the embedded nature of YSOs, as well as by the comparatively short lifetime of massive stars and their short formation timescales (∼10^5 years). The HII region phase, however, gives a clear indication that, in particular, 'high-mass' star formation has recently occurred (Wood & Churchwell 1989).

High-mass star formation occurs in dense clumps within giant molecular clouds (GMCs). Thus, one would expect a high concentration in the so-called Central Molecular Zone (CMZ), which contains about 3–10% of the molecular material in our Galaxy (e.g., Güsten et al. 1989; Rodríguez-Fernández et al. 2004). The CMZ (Morris & Serabyn 1996) is a roughly ∼200 pc sized region that covers a range of $-0.^\circ7 < l < 1.^\circ8$ and $-0.^\circ3 < b < 0.^\circ2$ in Galactic coordinates at a distance of 8.2 kpc (GRAVITY Collaboration 2019)[1]. The CMZ's physical conditions are extreme in comparison to other GMCs in the Milky Way as the gas temperature, the pressure, and magnetic field strengths are a few to several orders of magnitude higher (Morris & Serabyn 1996). It is clear that the question of present-day star formation in the CMZ is an important one, in particular given the presence of a few massive star clusters, the Arches and the Quintuplet clusters, and the central cluster in the immediate vicinity of the super-massive black hole Sgr A* in the centre of the Galaxy (e.g., Cotera et al. 1996; Kobayashi et al. 1983). Theses clusters have ages of 2–4 Myr, while the massive '(mini-) starburst' region Sagittarius B2 (Sgr B2), which has a mass of $8 \times 10^6\,M_\odot$, is a prominent active star factory (Figer et al. 2002; Schneider et al. 2014; Lis & Goldsmith 1990; Schmiedeke et al. 2016). On the other hand, the infrared dark cloud M025+0.11, termed 'the Brick', contains a comparable, if not somewhat lower, mass to Sgr B2 (∼$10^5\,M_\odot$), but it shows few signs of active star formation (e.g., Lis & Menten 1998; Henshaw et al. 2019 and references therein). Recent observations by Walker et al. (2021) show unambiguous signs of low- to intermediate-mass star formation and potential evidence for future high-mass star formation, however, to a much lesser degree than Sgr B2.

The star formation rate (SFR) of galaxies has been shown empirically to follow the Kennicutt–Schmidt relation (Schmidt 1959; Kennicutt 1998), which infers a power law relation between the SFR per unit area and the total gas mass. One can further correlate the SFR with the amount of dense ($n > 10^4\,\mathrm{cm}^{-3}$) molecular gas in our Galaxy to also show a linear relation (e.g., Lada et al. 2010, 2012). Despite the amount of dense gas available, the SFR is a factor of 10–100 lower than expected in the CMZ and it does not follow the Kennicutt–Schmidt relation (e.g., Longmore et al. 2013; Csengeri et al. 2016), although it may have done so in the past (Kruijssen et al. 2014). Various investigations of the SFR in the CMZ have been performed using different methods such as YSO counting (e.g., Yusef-Zadeh et al. 2009; An et al. 2011; Immer et al. 2012b; Nandakumar et al. 2018), free-free emission (Longmore et al. 2013), and infrared luminosity (Barnes et al. 2017). Systematic uncertainties in various methods used for determining the SFR as the cause for the much lower value were ruled out by Barnes et al. (2017) as they obtained similar average SFRs by comparison of the above YSO counting and free-free emission measurements. Low SFRs have also been found in specific high-density clouds in the CMZ (e.g., Kauffmann et al. 2017; Lu et al. 2019b). While not applicable to clouds that already show traces of star formation at later stages, as in Sgr B2, some theoretical models suggest that the lower SFR is due to these clouds being in an early evolutionary stage where active star formation is not yet observable (see also, e.g., Kruijssen et al. 2014; Krumholz & Kruijssen 2015; Krumholz et al. 2017). In stark contrast, the mini-starburst region Sgr B2 is one of the most prolific star formation factories in the Galaxy (Ginsburg et al. 2018).

Various hypotheses exist for this difference in SFRs between the CMZ and typical star forming environments: On the one hand, the formation of high-mass stars may require a higher critical density threshold than that of low-mass stars (Krumholz & McKee 2008); on the other hand, the turbulent environment of the CMZ itself is increasing this density threshold (e.g., Kruijssen et al. 2014; Rathborne et al. 2014). Further studies of HMSF in the CMZ and the physical processes therein are therefore crucial for our understanding of star formation in our Galaxy as well as other galaxies. The question of why star formation in the CMZ is so unevenly distributed and why it is absent in so much of its volume is still open to this day. Obtaining a census of and characterising YSOs in the CMZ will help to address these points and is the focus of this paper.

Searching for YSOs is a direct way of identifying on-going and recent star formation and to determine the current SFR. The low number of YSOs identified in some parts of the Galactic Centre motivates new searches. Finding YSOs in the CMZ requires studies in multiple wavelengths. Very recently formed YSOs are surrounded by dense envelopes of gas and dust (Zinnecker & Yorke 2007) and as they begin to heat this nearby dust, the energy is re-emitted in the infrared regime and as such, most studies of YSOs have been performed with infrared photometry (Schuller et al. 2006; Yusef-Zadeh et al. 2009). However, the large and spatially variable extinction in the CMZ (A_V = 20–40 mag; Schultheis et al. 2009) can cause confusion regarding the identification of YSOs. Furthermore, the extinction in dense regions can be of the order of ∼100 mag making proper counts of forming stars impossible in these clusters, thus missing a large fraction of the stars currently forming. Studies classifying YSOs with near-infrared (NIR) photometry cannot identify YSOs uniquely since AGB stars, red giants, and even super giants can have similar photometric colour signatures similar to YSOs due to foreground extinction (Schultheis et al. 2003). To distinguish them, spectroscopic observations are required, with ambiguities in the classification schemes remaining even with this method (e.g., An et al. 2011; Immer et al. 2012b).

Recently, Nandakumar et al. (2018) presented a study aimed at identifying YSOs in the CMZ. They conducted *K*-band

[1] GRAVITY determines a geometric distance of 8178 ± 26 pc to the central super-massive black hole Sgr A*.

(2.2 μm) spectroscopic NIR observations of photometrically identified YSOs in the CMZ and detected 91 viable sources that they used to develop a new photometric YSO classification scheme that tries to eliminate contamination from late-type and evolved stars as those revealed by their spectroscopic observations. To estimate the SFR, a larger sample was needed and thus, in combining the photometric catalogue of YSO candidates from SIRIUS (J(1.25 μm), H(1.63 μm), and K_S(2.14 μm) filters; Nishiyama et al. 2006) and the point-source catalogue of the Spitzer IRAC survey (3.6–8.0 μm; Ramírez et al. 2008), they produced a final sample of 334 YSO candidates using their new classification scheme. The estimated masses from spectral energy distribution (SED) fitting models obtained from Robitaille (2017) range from 2.7 to 35 $M_\odot$ and furthermore peaks at ∼8 $M_\odot$, suggesting that >50% of these sources are already in the high-mass regime. To further investigate if these sources are indeed sites of HMSF, we used sub-millimetre and radio wavelengths to constrain the evolutionary stage.

In this paper, we used the sample of 334 YSO candidates from Nandakumar et al. (2018) to search for radio continuum counterparts at 4–8 GHz obtained with the *Karl G. Jansky* Very Large Array (VLA) as part of the GLObal view of STAR formation (GLOSTAR; Medina et al. 2019; Brunthaler et al. 2021) survey. Radio continuum sources can be signposts of free-free emission from HII regions. As of yet, it is unknown how many of the NIR-identified YSOs trace HII regions and so a census of the association between YSOs and HII regions would shed light on this. We produced a catalogue of radio continuum counterparts and investigated their nature by calculating their spectral indices. We used spectral indices to distinguish source types depending on whether the emission is thermal or non-thermal which helps to classify sources as bona fide HII regions or otherwise. We further determined the fraction of YSOs that have counterparts and physical reasons for the absence of an HII region. We also cross-matched these YSO candidates with the APEX Telescope Large Area Survey of the Galaxy (ATLASGAL; Schuller et al. 2009) 870 μm dust emission data, which trace the early natal environments of high-mass stars. If the YSO is still very young, we would expect to see it embedded in a compact cold dust envelope traced by sub-millimetre wavelengths. In this way, we investigated if there is any clear association of these YSOs with either the earliest or the latest stages of massive star formation in order to shed light on the complete spread of evolutionary stages of this census of YSOs. Lastly, we infer the SFR from the free-free emission of the HII regions detected in our field.

We structure this paper as follows: in Sect. 2 we give a short summary of the data used in this paper. Section 3 details our source selection criteria in finding radio continuum counterparts and the determination of their physical parameters needed to calculate the SFR. Section 4 discusses our comparison with other surveys and other prominent regions in the Galactic Centre and the properties of the YSO-sample with radio continuum counterparts as well as the SFR in the CMZ. We present the conclusions and summary in Sect. 5.

2. Observations

The GLOSTAR survey (Medina et al. 2019; Brunthaler et al. 2021) is an on-going survey with the VLA and the Effelsberg 100 m telescope between 4–8 GHz of the Galactic mid-plane from $-2° < l < 60°$ and $|b| < 1°$ as well as the Cygnus-X star-forming complex. VLA observations were mainly conducted in D- and B-configurations whose angular resolutions correspond to 18″ and 1.5″ at 5.8 GHz, respectively, to detect various tracers of different stages of early star formation using methanol, formaldehyde, and radio recombination lines as well as radio continuum to describe the stellar evolution process of massive stars.

This work is a targeted search for continuum sources towards YSOs identified with NIR photometry (Nandakumar et al. 2018) using only the continuum data obtained from the VLA in D-configuration for the Galactic Centre ($|l| < 1.5°$ and $|b| < 1°$). We briefly summarise the data properties (for details see, e.g., Medina et al. 2019; Brunthaler et al. 2021; Dzib et al., in prep.). Observing in the *C*-band (4–8 GHz), the correlator setup consists of two 1-GHz-wide sub-bands centred at 4.7 and 6.9 GHz. Each sub-band was further divided into eight intermediate frequency windows of 128 MHz with each window consisting of 64 channels with widths of 2 MHz. Approximately 2520 pointings were used to cover an area of $2° \times 4°$. Flux calibration was done using 3C 286 which was used as the band-pass calibrator and J1820-2528 as the phase calibrator. We used the Obit package (Cotton 2008) for the calibration as well as the imaging of the continuum data. The data were rearranged into nine different frequency bands (spectral windows) of a similar fractional bandwidth. Each pointing was first cleaned individually and then combined into a large mosaic for each frequency band. The final mosaic at the reference frequency was created by combining the individual, primary beam corrected images of each of the frequency bands.

The effective frequency of the averaged image is 5.8 GHz with a FWHM of 18″. The average noise level increases from ∼0.07 mJy beam^{-1} to ∼1 mJy beam^{-1} as one moves closer to the Galactic mid-plane, which is as expected since the majority of emission is in the plane of the disk such as the black hole in the centre of our galaxy. In comparison to other regions studied in GLOSTAR, emission-free regions typically have noise levels of around ∼0.06 mJy beam^{-1}, but they can steeply increase to ∼0.45 mJy beam^{-1} towards the Galactic mid-plane (Medina et al. 2019). We note that the VLA B-configuration and Effelsberg data have not yet been imaged and will be analysed in future works.

3. Results

3.1. 2.2 μm sources as equivalent ONCs in the CMZ

We would like to understand the nature of the 2.2 μm sources investigated in Nandakumar et al. (2018) but have the problem that they are far away and suffer from heavy extinction. As such, we make a comparison to a nearby known 2.2 μm star cluster. Due to its close distance of ∼400 pc (Menten et al. 2007; Kounkel et al. 2017; Großschedl et al. 2018), the ONC (Genzel & Stutzki 1989) is often used as the template environment for studying HMSF. It contains multiple massive stars that are easily detectable at this distance and also shows bright 2.2 μm and radio emission. The YSOs that we use as targets in our investigation are, however, located at a much farther distance of ∼8.2 kpc (GRAVITY Collaboration 2019) in the Galactic Centre. Therefore, to put the environment into perspective and to see how the YSO candidates compare to a cluster of massive stars similar to the ONC, we discuss what the ONC would look like if it was placed in the CMZ at similar infrared wavelengths.

The Cosmic Background Explorer[2] (COBE) space-based mission (Boggess et al. 1992) was developed to measure the diffuse infrared and microwave radiation from the early universe. The Diffuse Infrared Background Experiment's (DIRBE) objective is to search for Cosmic Infrared Background by making

[2] The National Aeronautics and Space Administration/Goddard Space Flight Center (NASA/GSFC).

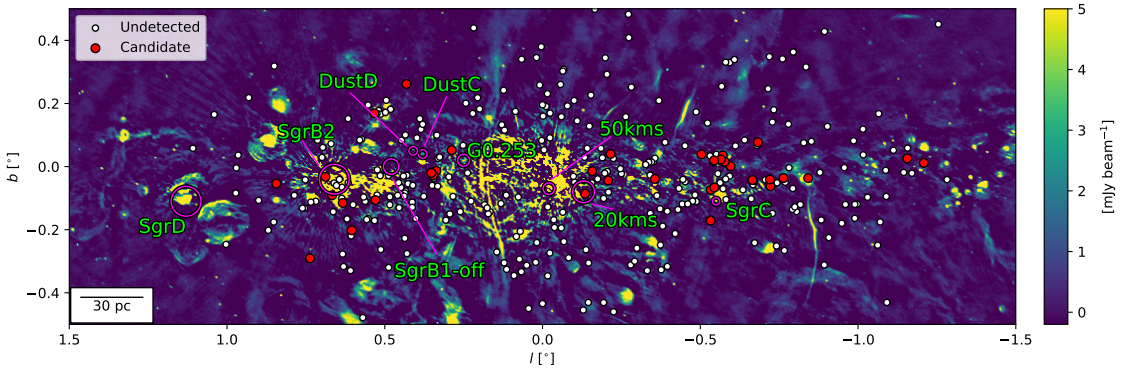

Fig. 1. GLOSTAR 5.8 GHz detections towards YSOs from Nandakumar et al. (2018, red circles). Non-detections are shown as white dots. The background image shows the GLOSTAR 5.8 GHz D-configuration continuum image restricted to the region studied by Nandakumar et al. (2018). The image has been clipped with minimum and maximum limits of −0.1 mJy beam^{-1} and 5 mJy beam^{-1}, respectively, to better emphasise visibility of the low intensity radio features. The main GMCs presented in the CMZ are highlighted with purple circles with effective radii from Kauffmann et al. (2017) and the references therein.

absolute brightness measurements of the diffuse infrared radiation in ten photometric bands from 1 to 300 µm. We obtained the map corresponding to 2.2 µm and plotted the intensities for each pixel near the ONC in Galactic coordinates (see Fig. 2). Given the size of a DIRBE pixel (0.32°) and the size of the ONC (∼5′), it is unclear which pixel is correctly associated. We carried out calculations for both the nearest singular pixel as well as the sum of all four surrounding pixels. The resultant peak flux and integrated flux density are 93.18 mJy and 630.22 mJy, respectively. Now if we were to place the ONC at a distance of 8.2 kpc, this woud scale the fluxes to 0.22 mJy and 1.49 mJy respectively, diminishing them by ∼400 times.

To compare to the YSO sample, we converted this photometric flux into photometric magnitude units given that $F_\nu = F_0 \times 10^{-m/2.5}$ where m is the magnitude, F_ν is the flux in Jy, and F_0 is the zero point for a given filter system (for 2.159 µm, $F_0 = 666.7$ where this corresponds to the K_S filter system used for the SIRIUS catalogue containing the YSOs). Using the conversion tool[3,4] for photometry, the resultant apparent magnitudes for the peak and integrated flux densities are 16.2 mag and 14.1 mag, respectively. When comparing with only the YSOs selected from spectroscopic KMOS observations (see Table 2 in Nandakumar et al. 2018), the magnitude values are at the lower range but are still possible to be observed, suggesting that KMOS would be able to observe ONC-like sources at the distance of the Galactic Centre.

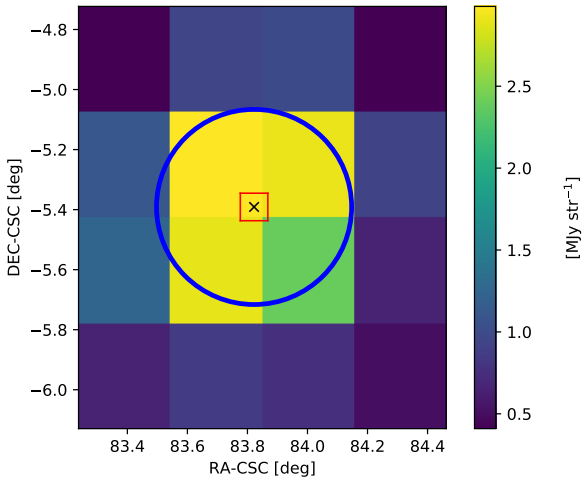

Fig. 2. COBE 2.2 µm data of the ONC plotted in equatorial coordinates (CSC; COBE quadrilateralised spherical cube projection). The × marker denotes the position of the ONC with the surrounding red square signifying a 5′ width, which is the estimated angular size of the ONC. The size of a DIRBE pixel is 0.32°. The blue circle highlights the four pixels selected for the flux determination.

3.2. GLOSTAR source selection

Nandakumar et al. (2018) provide a catalogue of 334 YSO candidates made with the new colour-colour diagram selection criteria aimed at disentangling YSOs from late-type stars. Using spectral line data, they first separated NIR sources as YSOs or cool, late-type stars through the absence of ^{12}CO (2,0) absorption and the presence of Brγ emission. They found that in a $H - K_S$ versus H − [8.0] colour-colour diagram, they could distinctly separate the two groups of stellar objects. This gives us a sample with very few contaminants even if not all of them have been spectroscopically identified as YSOs. Given this list of YSOs, we searched the GLOSTAR data to see if there are associations with 5.8 GHz continuum emission. The region that we study in this work is shown in Fig. 1, where we have also overlaid the complete sample of YSO candidates investigated and highlighted the sources coinciding with radio emission. One can already see that there is a statistical bias present from the YSOs as they are not evenly distributed across the Galactic Centre. We see that in some of the known massive star forming regions such as Sgr D, we do not find a large number of YSOs from Nandakumar et al. (2018). As such, we do not provide a complete census of all HII regions in this work.

[3] https://irsa.ipac.caltech.edu/data/SPITZER/docs/spitzermission/missionoverview/spitzertelescopehandbook/19/

[4] http://ssc.spitzer.caltech.edu/warmmission/propkit/pet/magtojy/index.html

We first investigated if there is a spatial coincidence between the YSO sample and the GLOSTAR continuum emission by using a radius for the angular separation of ∼10″, which is approximately equal to half of the GLOSTAR continuum data synthesised beamsize, corresponding to ∼0.4 pc at a distance of 8.2 kpc (GRAVITY Collaboration 2019). We find close to ∼100 YSOs which have potential 5.8 GHz counterparts that match this spatial selection criterion. We note that for certain extended regions (e.g., Sgr B2), it can be difficult to associate a single YSO to them. We used a sensitivity threshold to select the closest possible YSO as its counterpart, which is described below.

We examined the validity of these candidate radio sources by looking at their intensity, shape, and the likelihood of being a radio artefact. Taking the root-mean-square (rms) of a nearby emission-free region as the noise level, we considered sources that have peak pixel intensities of at least 5σ. To confirm the detection of the radio source, we used eight of the nine spectral windows from the GLOSTAR-VLA data since the ninth spectral window has a much higher noise level. We have kept sources that have clear and consistent structure in at least half of their spectral windows. The data can be strongly influenced by the strong emission from powerful sources in the Galactic Centre such as from Sgr A* that can lead to strong sidelobe effects. This can manifest as a false detection or a source appearing variable in intensity and shape across the multiple spectral windows. In general, the observed field is known to be extremely crowded and one needs to be wary of the surrounding environment of each source. The rms ranges from 0.351 mJy beam^{-1} to 11.914 mJy beam^{-1} with median and mean values of 0.709 mJy beam^{-1} and 1.558 mJy beam^{-1}, respectively. The lower noise value corresponds to regions which are located in emission-free regions far offset from strong emission sources and can act as a lower limit, while the higher end corresponds to the average environment of a strong emission source. For our investigation, we calculated the rms at each individual source separately.

With these criteria for a continuum detection, we removed roughly two-thirds of the candidates from our consideration as they do not meet our intensity detection threshold (continuum emission >5σ), are spatially separated with more than half a beam, have an unclear association with an extended continuum structure, or are most likely affected by sidelobes. The final list of 35 sources that we investigate further is given in Table A.1. For each radio source, we detail the position of the YSO and the position of peak intensity of the associated radio source as well as the peak intensity, S_p. We calculated the integrated flux density, $S_{\rm int}$, using 5σ contours or covering an area of at least a GLOSTAR beam size. This also serves to estimate an effective source diameter, $D_{\rm eff}$, where we assume the HII region is spherically symmetric. The rms used to define the detection limit for each source is also given in the table. We note that for sources 88, 230, 241, and 311, we made a manual integration contour. This was done as a 5σ contour does not perfectly capture just the emission of the local compact source we are interested in. In these cases, our flux estimation acts as a lower limit. The general shape of the radio sources are classified as compact (C; ∼66%), extended (E; ∼28%), or extended and complex (EC; ∼6%). An example source of our final sample is shown in Fig. 3 (and the rest in Fig. B.1). This illustrates an example association of a YSO candidate with an extended radio feature as it satisfies our criteria of being within 10″ of the continuum radio and within a 5σ contour. However, this is not always easily discernible for all of our sources. For example, sources 307 and 311 were

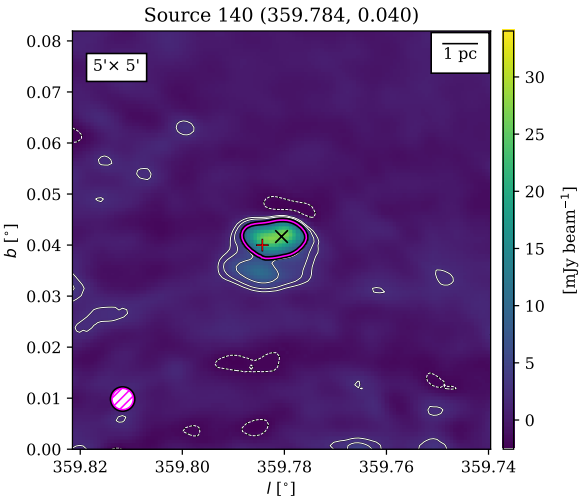

Fig. 3. Detection of a GLOSTAR 5.8 GHz counterpart for source 140 from Nandakumar et al. (2018). The GLOSTAR 5.8 GHz continuum map is shown in colour with positions of the peak radio emission and the YSO marked with a black X and red cross, respectively. White contours correspond to 3, 5, and 10σ (σ = 0.634 mJy beam^{-1}). The magenta contour outlines the area from which the flux density was calculated. The colour bar maximum was chosen to be 1.5× the peak intensity of the coinciding 5.8 GHz source. The beamsize is shown in magenta in the bottom left corner.

previously observed at 10.7 GHz with Effelsberg and listed as sources 40 and 41, respectively (Seiradakis et al. 1989). These single dish observations report higher flux densities of 28.5 Jy and 4.3 Jy, respectively, compared to our ∼0.2 Jy and ∼1.2 Jy. Furthermore, the sizes are of the order of 2 arcminutes compared to our arcsecond scale. The fact that these properties are so different from our higher angular resolution data indicates that for these sources in particular, they are sub-components of a larger and complex multi-component source. The Effelsberg data from (Seiradakis et al. 1989) capture the more extended emission that is resolved out at the angular resolution of our GLOSTAR-VLA data. This can be seen for other sources in our final sample as well, where the radio source we associate with our YSO candidate may be a part of a much more complicated multi-component source. For example, source 3 (see Fig. B.1) shows a continuum feature at 5σ above the local noise and is consistent in all the frequency bands of the GLOSTAR continuum data. However, it might not be a completely isolated and compact source as it is not distinctly 5σ above the local extended emission. In these cases, we recognise that the HII region associated with the YSO might actually be larger in some cases and would require higher resolution data to resolve the source.

We note that the distance to these radio counterparts is assumed to be the same as the YSOs placing them in the CMZ. Association with distance tracers such as HI absorption or the methanol maser to these radio sources as well as detected molecular lines for the YSOs would be needed to clearly determine their association along the line of sight.

3.3. Spectral index

We used the multiple spectral windows of the GLOSTAR observations at different frequencies to perform an estimate of the

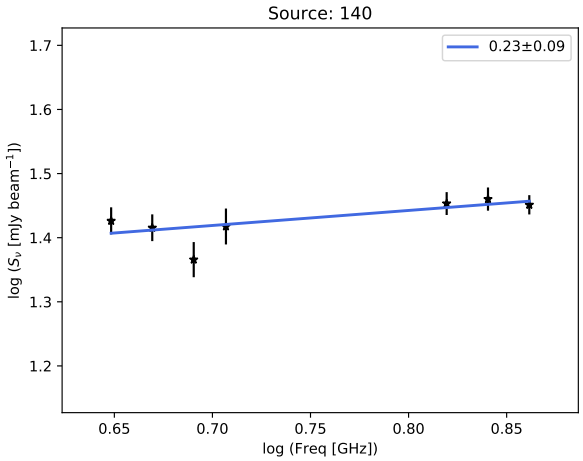

Fig. 4. Determination of the spectral index for source 140 (G359.784+0.040). Only frequency bands that meet the minimum threshold of 3σ are considered. The solid blue line shows the best-fit model determined by the linear regression. The fitted spectral index is indicated in the upper right corner. The frequencies range from 4.45 GHz to 7.2 GHz. The spectral indices of the full sample are shown in Appendix C.

spectral index of each continuum source. Following the same procedure for spectral index calculations as Bihr et al. (2016), we extracted the peak intensity from each individual frequency plane at the same position, using the peak pixel of the continuum emission in the averaged GLOSTAR image (see Fig. C.1). We used the intensity at the peak pixel, since the integrated emission may be more heavily impacted by the frequency-dependent spatial filtering of the interferometer. It should be noted that for some sources, the shape of the source is inconsistent in every spectral window. Some frequency planes show more extended features or disappear entirely. We therefore limit the number of frequency planes used for further analysis to those that have a peak intensity greater than 3σ, which we note is lower than the 5σ limit used for integrated flux calculations as each spectral window, from which we extracted the peak intensity, does not benefit from the decreased noise from combining all the frequency planes. We used this lower threshold for detection as each of the individual frequency planes has a lower signal-to-noise ratio (S/N) compared to the averaged image. From this, we extracted a set of peak intensities from which to estimate the spectral index. The possible missing flux, which is inherent to interferometric observations, may affect spectral indices of extended sources by frequency-dependant filtering. This is not further addressed here but will be in the future with the inclusion of GLOSTAR-Effelsberg observations. Assuming that the relationship between the flux and frequency is $S_\nu \propto \nu^\alpha$ where α is the spectral index and S_ν is the frequency-dependent intensity at the associated frequency ν, we used scipy's `curve_fit` to perform a linear fit of the data in log-space in order to obtain the slope, α (see Fig. 4), where the measured errors are only from the fitting procedure.

Using the spectral indices, we classified the continuum sources as HII regions depending on whether the emission is thermal or non-thermal. For indices between -0.1 and 2, the emission corresponds to thermal emission that is associated with HII regions or planetary nebulae (PNe). If it is steeply negative, that is ≤ 0.5, we consider it to be non-thermal, which means the emission is synchrotron in nature and could come from supernova remnants (SNR) or extra-galactic sources such as active galactic nuclei (AGN) (Condon 1984; Rodríguez et al. 2012; Dzib et al. 2013; Chakraborty et al. 2020). We record the values of the spectral indices in Table A.1. We conclude that we can only use the spectral indices to propose sources as HII region candidates since a larger frequency coverage with greater accuracy would be needed in order to truly constrain the spectral indices and thus their nature.

For 11 sources, the spectral index was in agreement with thermal emission as defined above. For three sources of our sample, we could not determine reliable spectral indices, as they had less than three spectral windows with a good enough S/N. Four sources show steeply negative spectral indices of $\simeq 0.5$, which we classify as non-thermal from our aforementioned definition. However, the errors are quite large and not sufficient to definitively exclude these candidates. The remaining 16 sources have values in between $-0.5 < \alpha < -0.1$ and are retained in the analysis that follows as HII region candidates.

4. Discussion

4.1. YSOs and their counterparts

To explore the nature of the YSOs, we discuss the properties of the sources that have a GLOSTAR-VLA radio continuum counterpart. Fig. 1 shows that while the majority of detections are in the Galactic mid-plane, which is also the case in Medina et al. (2019), there is no clear separation between the sources that have radio continuum counterparts and those that do not. We do a full comparison with HII region catalogues from Anderson et al. (2014), radio source catalogues from Becker et al. (1994) and Condon et al. (1998), and the MMB methanol maser catalogue from Caswell et al. (2010). The associations are shown in the last column of Table A.1.

We also performed a cross match for known sources in the literature. To date, the most complete and comprehensive catalogue of HII region candidates is presented in Anderson et al. (2014) by using sources from the all-sky Wide-Field Infrared Survey Explorer (WISE) satellite and investigating their mid-infrared (MIR) morphology[5], confirming candidates with existing literature. Of the ~8000 sources in their catalogue, ~450 are within our region of study. These were used to confirm the nature of the detected GLOSTAR sources. Of our 35 GLOSTAR sources, only six sources do not have a WISE counterpart and six are classified as, or are a part of, known HII regions by Anderson et al. (2014). The remaining 23 radio sources correspond to HII region candidates based on their MIR morphology. The strong correlation of the infrared WISE sources to our radio sources can be expected given that we selected these radio sources based on a catalogue of NIR sources. The six radio continuum sources without WISE counterparts have source IDs 66, 157, 230, 307, 315, and 323 as listed in Table A.1 and are potentially new HII regions due to the lack of associations, except for source 157, as it is likely associated with the '20 km s^{-1} cloud'. However, none of them show any methanol masers from the MMB, which suggests that these HII regions are at a later stage of HMSF.

Additionally, we searched for counterparts with the CMZoom survey (Battersby et al. 2020) as it searches the dust continuum at 1.3 mm for signs of compact substructures known to be sites of high mass star formation. We used the catalogue

[5] http://astro.phys.wvu.edu/wise/

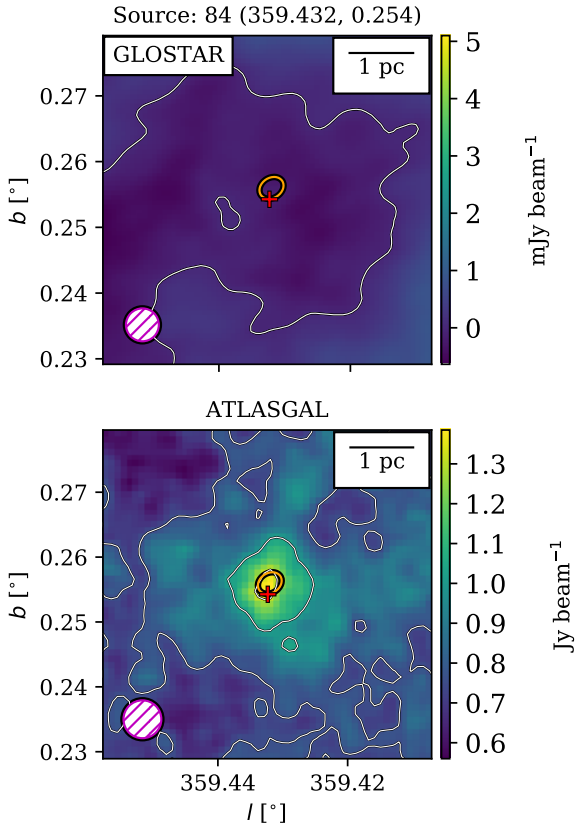

Fig. 5. Non-detection of GLOSTAR 5.8 GHz emission and detection of ATLASGAL 870 µm emission towards source 84 from Nandakumar et al. (2018). *Top*: GLOSTAR 5.8 GHz radio continuum $3' \times 3'$ zoom-in. A red cross denotes the location of the YSO, and the orange ellipse represents ATLASGAL sources from Contreras et al. (2013). The GLOSTAR beam size is shown in the bottom left corner. The white contour shows the 0.5 mJy beam^{-1} level, which is the average 5σ level for the GLOSTAR data. *Bottom*: ATLASGAL map, where the contours are dynamical contours (as formulated by Thompson et al. 2006).

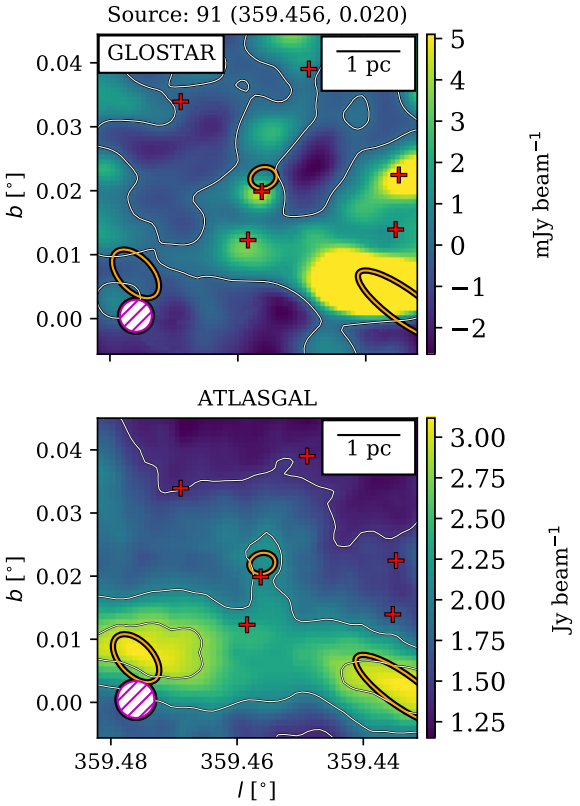

Fig. 6. Detections of GLOSTAR and ATLASGAL emission of source 91. Labels and markers are the same as in Fig. 5. The GLOSTAR image (top) instead has contours at 2.5 mJy beam^{-1}. It is the singular YSO candidate with both an ATLASGAL and potential GLOSTAR counterpart.

from Hatchfield et al. (2020) and find that of the 334 YSOs, only 22 have potential counterparts within 45″, where the angular separation criterion is chosen based on the CMZoom's upper sensitivity to structures on that scale. Of these 22 sources, only two also have a GLOSTAR counterpart, sources 307 and 311 from Nandakumar et al. (2018).

The recent study by Lu et al. (2019a) observed a smaller region of the CMZ also with the VLA in *C*-band, but with the interferometer in B-configuration, yielding a higher spatial resolution (∼1″). They detected 104 radio continuum sources of a varying natures. Our radio continuum sources 140 and 241 overlap with the sources C54 and C29 from Lu et al. (2019a), respectively, where C54 is a candidate ultra-compact HII region. However, a more in-depth analysis in the future with the upcoming higher resolution GLOSTAR-VLA data will provide a more complete comparison between the two data sets.

We additionally compared the YSO catalogue with the compact sources from ATLASGAL to investigate if the YSO is in the young protostar stage, as a young protostar needs to be embedded in compact dense gas, which is visible at submillimetre wavelengths. The earliest stages of HMSF can be observed in massive clumps of dust and gas that emit at the optically thin (sub)millimetre regime through their thermal emission. ATLASGAL (Schuller et al. 2009) observes thermal dust emission at 870 µm which aids in the study of the early natal environment of high-mass stars at their early prestellar stages. With a resolution of 19″ (FWHM), this unbiased survey has produced a catalogue of ∼10 000 dense and massive clumps (Contreras et al. 2013; Urquhart et al. 2014; Csengeri et al. 2014).

Comparing the GLOSTAR-VLA data with ATLASGAL can give insight into the nature of the observed potential HII regions as one would expect evolved dust clumps to have a radio continuum counterpart. However, of the ∼1000 compact sources from ATLASGAL in the CMZ area (Contreras et al. 2013), only eight have an angular separation of <10″ to a YSO candidate from Nandakumar et al. (2018) (see Fig. 5). Of these eight associations, YSO candidate 91 has a potential radio continuum counterpart at 5.8 GHz (see Fig. 6). At 870 µm, it has a peak intensity of 0.54 ± 0.23 Jy beam^{-1}, an integrated flux density of 1.89 ± 0.5 Jy, and a S/N of 8. While we expect that ultra-compact HII regions have both dust and radio emission, this source hardly classifies as an ultra-compact HII region as its physical properties (see Table A.2) do not meet the typical minimum requirements

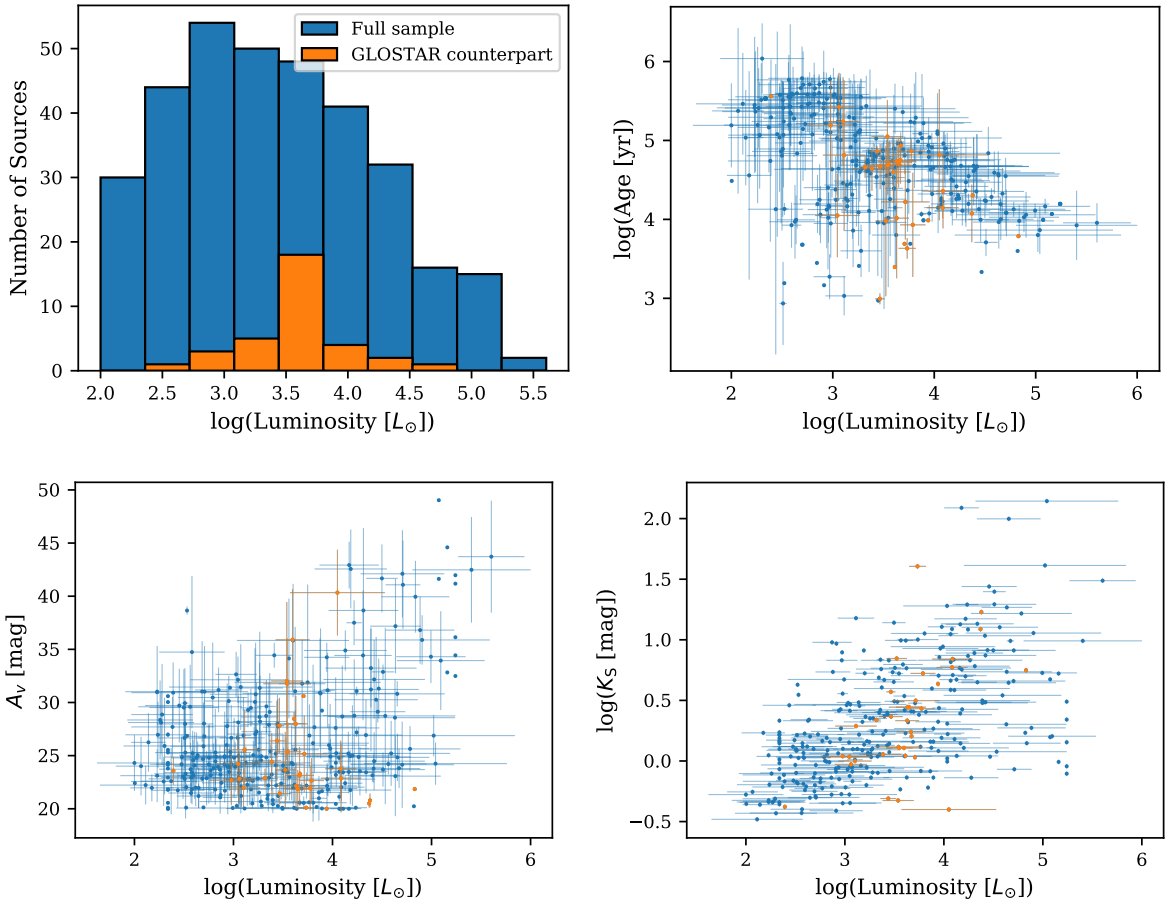

Fig. 7. Comparison of the bolometric luminosity of the YSOs to other properties (obtained from SED models Robitaille 2017 in the work done by Nandakumar et al. 2018). *Top left*: histogram of the YSO luminosity. *Top right*: estimated age of the YSO obtained from stellar evolution tracks. *Bottom left*: calculated extinction, A_v. *Bottom right*: brightness at photometric band, K_S. Shown in blue are all of the YSO sources which Nandakumar et al. (2018) used in their determination of the SFR, while orange denotes only the YSO sources that have a GLOSTAR counterpart.

(<0.1 pc; Kurtz 2002). Furthermore, Fig. 6 shows that the radio continuum source is offset from the main dust clump, suggesting that the HII region is of a more evolved state than the surrounding dense clumps. For the remaining seven sources that do not have a radio continuum counterpart, we suggest that these YSOs are not yet sufficiently evolved as we expect MYSOs to be IR-bright prior to being able to see the inner and developing HII region once it turns on (Motte et al. 2018).

This low YSO-ATLASGAL association rate is unexpected. Using the empirical mass-size relation (under the assumption that the sources fill the 19″ ATLASGAL beam; Urquhart et al. 2018), it is generally accepted that a cloud mass of 500–1000 $M_\odot$ is needed in order for at least one massive star to be formed in the cluster. This corresponds to peak intensities of 0.75–1.5 Jy beam^{-1}. In comparison to the typical noise of ATLASGAL in the CMZ of ~0.2 Jy beam^{-1}, we should be able to detect these kinds of clumps. However, given the extended nature of the dust emission seen in ATLASGAL and the limitations of source extraction, our original <10″ angular separation is likely insufficient to describe the full possible connection between our sample of YSOs and dust clouds. As such, we compare the positions of the full sample of YSO candidates to an emission map of ATLASGAL, which gives a total of 94 YSOs that lie in the dust features at 870 μm. Of these YSOs with GLOSTAR counterparts (35), 14 sources would then be classified as having an ATLASGAL association in this way. These sources having coincident associations are consistent with the picture that these YSOs are embedded in their natal dust envelopes. For the remaining sources without radio continuum or dust emission, it may be that they are instead associated with lower-mass dust clumps, suggesting that they may not be high-mass YSOs.

4.2. Properties of the YSO sub-sample

Of the 334 YSO sources we investigated to find GLOSTAR counterparts, we found 35 confident candidates. To determine if there are systematic effects, in Fig. 7 we plot a comparison of our selected sub-sample of YSOs to the full catalogue. We compared the modelled total stellar luminosities from Nandakumar et al. (2018) with their derived age, extinction in the *V*-band, and observed K_S photometric magnitude to determine if only the most powerful or luminous YSOs have radio-loud HII regions. The top left shows the distribution of the luminosities where the median luminosity of the full sample is of the order of ~ 10^3 $L_\odot$,

Table 1. Comparison of the GLOSTAR 5.8 GHz emission features from the dust ridge with literature, specifically Immer et al. (2012a).

Source	$S_{i,8.4\,\mathrm{GHz}}$ [a] [mJy]	$S_{i,5\,\mathrm{GHz}}$ [b] [mJy]	Θ_R [a] [″]	$S_{i,5.8\,\mathrm{GHz}}$ [mJy]	Θ_R [″]
A	180 ± 2	154	5.1	120 ± 10	15
B	9 ± 1	<9	1.8	16 ± 3	12
C	10 ± 1	<9	1.8	15 ± 3	15
D	145 ± 20	134	14.1 [b]	436 ± 42	30
E	886 ± 57	1417	32.0	1040 ± 10	33

Notes. Integrated flux densities as well as their angular radii, Θ_R, are shown. [a]From Immer et al. (2012a), [b]from Becker et al. (1994).

whereas the sample of sources with GLOSTAR counterparts have a slightly higher median value, but it does not seem to be strongly biased towards either the higher or lower limit of the distribution of the luminosities. We compare the luminosities with the calculated age of the YSOs in the top right corner of this figure and we see that our sub-sample covers only the young stars, $<10^5$ yr. This could explain the low association rate of the YSOs and GLOSTAR radio continuum data, as the YSOs would still be young and would not have reached the point of developing an HII region. However, these ages were calculated from SED model fitting (Robitaille 2017) where there can be large uncertainties for the age estimation. If they are truly in the early stages, one would expect to have a correlation with ATLASGAL sources. However, as explored in Sect. 4.1, there is limited ATLASGAL correlation, suggesting instead that these sources are either much older or are non-massive YSOs. As explained in the above section, we maintain that the noise level of ATLASGAL does not allow us to use the absence of sub-millimetre sources as a strict constraint on the evolutionary stage in this work.

Using an assumed distance in the ranges of 7–9 kpc for their SED models, Nandakumar et al. (2018) fitted values for the visual extinction, A_V, caused by the material along the line of sight from the Sun to the CMZ. We see that most of the sources fall under $A_V = 36$ mag and that there are no evident trends in comparing the luminosity with the photometric magnitude. In addition to the large uncertainties, the small sample size inhibits any defining conclusions from these results.

4.3. Notes on particular sources

4.3.1. The dust ridge

A known feature in the CMZ, the so-called dust ridge is a narrow string of massive clumps that connect the radio continuum sources G0.18–0.04 and Sgr B1 (Lis & Carlstrom 1994). Immer et al. (2012a) detected five radio continuum sources in *X*-band (labelled A-E) on the periphery of the dust ridge, likely hosting HMSF. This region is also covered in our GLOSTAR-VLA data in *C*-band. We make a comparison of this region between the *X*- and *C*-band studies and display the region and cutouts in Fig. 8 with the same angular size as in Immer et al. (2012a). The Immer et al. (2012a) observations were centred at 8.4 GHz using the VLA in CnB-hybrid configuration and have a restored elliptical Gaussian beam with FWHM of roughly $3\farcs6 \times 2\farcs5$. Compared to their VLA data, our D-configuration VLA data are much coarser and trace the more extended features that are likely resolved out in the Immer et al. (2012a) observations. We calculated effective radii and integrated flux densities and list them in Table 1 using CASA's `imfit` task which does Gaussian fitting of the sources. This was done to compare them with the Gaussian fitted results from Immer et al. (2012a). For sources A, B, and C, the source size is larger. Source D shows the most striking difference in terms of the flux and radius, which can be attributed to the fact that in our VLA D-configuration data, we have a much lower angular resolution and trace more extended features while the source has been resolved into multiple components in the work done by Immer et al. (2012a). It shows significant extended emission in a morphology that is offset from the position of the compact source (potentially cometary). Source E is of a comparable size in both this study and in Immer et al. (2012a). Upcoming comparison with GLOSTAR-VLA B configuration data can further our investigation of these sources.

Furthermore, to put our GLOSTAR-VLA data into perspective, we are interested in what the HII region associated with the ONC would look like at radio wavelengths if placed in the CMZ. Immer et al. (2012a), who present radio observations at similar frequencies but with higher resolution, show that the radio size of the Orion Nebula would only be slightly smaller than one of their radio sources (their Source E; see Fig. 8, lower-right panel). They also show that scaling the integrated flux density of the ONC to the distance of the CMZ would result in a value of 0.98 Jy, which is comparable to that of their Source E (see our Table 1). Inspecting our list of YSOs with radio counterparts (Table A.2), we find that YSO 234, with O7.5–O8, has a spectral type that is closest, if slightly later, than that of θ_1 C Ori (O7V), which is the star that provides most of the UV photons that excite the Orion Nebula. The radio flux we determine for this source, 0.44 Jy, is comparable and slightly lower than the 0.98 Jy quoted above as one might expect. As such, it is clear that we are able to detect the radio emission from Orion Nebula-like sources within the GLOSTAR-VLA data.

4.3.2. The Arches cluster

The Arches cluster, otherwise known as G0.121+0.017, is a massive ($7 \times 10^4\ M_\odot$) cluster of massive young (1–2 Myr) stars situated near the Galactic Centre that was identified by NIR imaging (e.g., Cotera et al. 1996; Figer et al. 2002). It has also been extensively studied at radio wavelengths (e.g., Lang et al. 2001, 2005; Yusef-Zadeh et al. 2002; Gallego-Calvente et al. 2021 and references therein) in which it shows clear filamentary 'arches' surrounding it. These are thought to be ionised by hot stars in the star cluster. High-resolution VLA observations (Lang et al. 2005) reveal ten radio sources on scales of $<0.5''$ that are believed to be due to stellar winds. With the D-configuration VLA data from our GLOSTAR-VLA survey, we do not currently see any convincing detection of the Arches cluster itself, but we do see the filamentary namesake arcs nearby as shown in Fig. 9. The NIR sources of the cluster are spread over $\lesssim 30''$, which is close to our beam size of $\sim 18''$. It is likely that the extended emission from these nearby HII regions or filaments confuse the point-like emission of the stellar cluster. Filtering out the extended emission during the imaging process may result in a higher sensitivity to compact radio sources at the location of the Arches cluster, but it is left for future analysis.

4.3.3. The Brick

G0.253+0.016, otherwise known as 'the Brick', is considered to be the prototypical infrared dark cloud (Lis & Menten 1998). It is one of the densest and most massive molecular

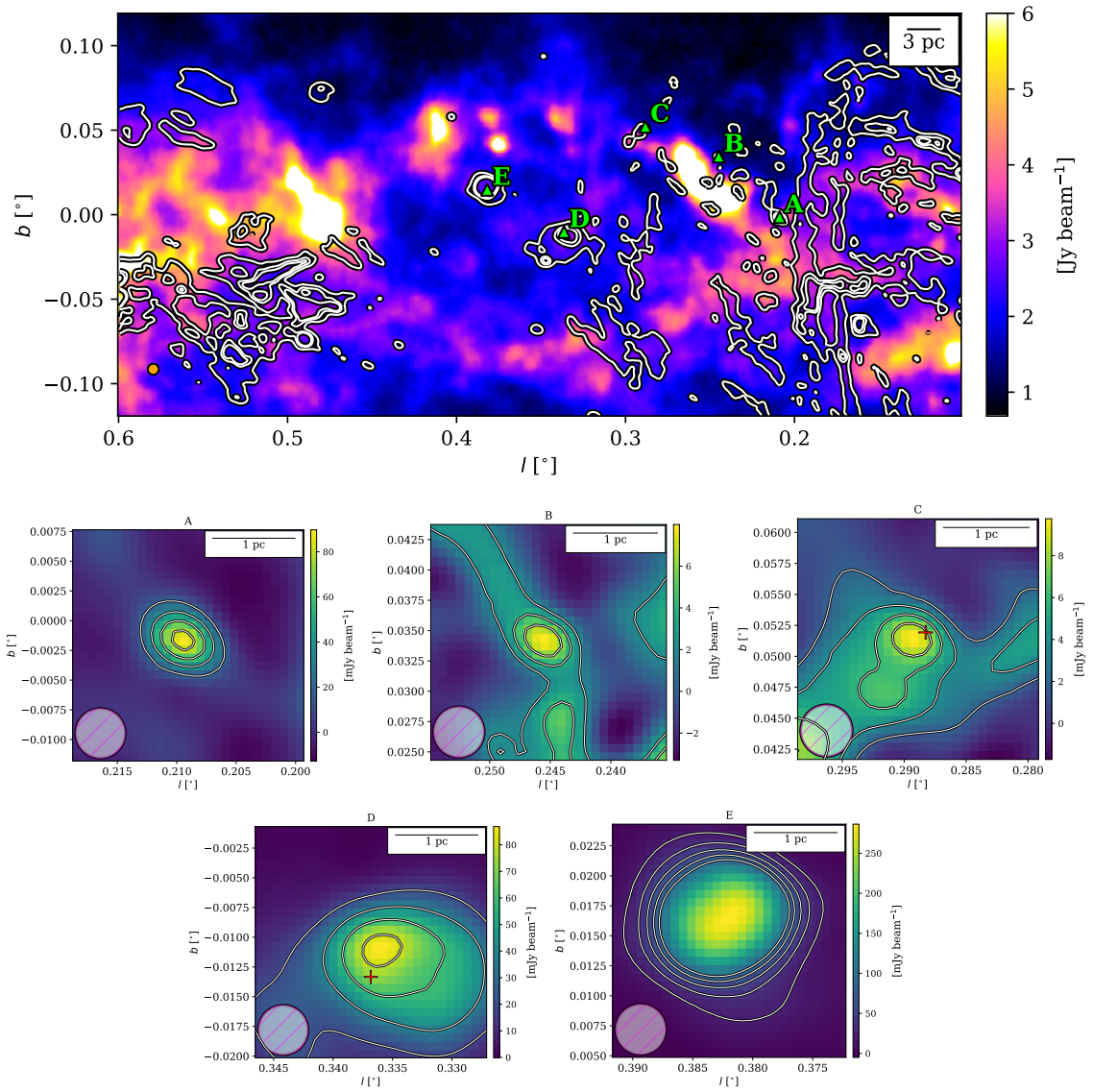

Fig. 8. Maps of the dust ridge presented similar to Fig. 5 in Immer et al. (2012a). *Top*: ATLASGAL 870 µm dust emission towards the dust ridge with GLOSTAR 5.8 GHz radio continuum contours overlaid with contour levels of 2%, 8%, and 13% of the maximum. *Bottom*: GLOSTAR VLA cutouts of sources A-E cut to a larger angular size compared to Immer et al. (2012a). For sources A, D, and E, the contours are from 10σ to 50σ in steps of 10σ. For sources B and C, the contour levels are 4σ, 12σ, and 20σ. Red crosses denote the positions of YSOs.

clouds within the Galaxy and the only one above $10^5\,M_\odot$ that does not show significant star formation (e.g., Henshaw et al. 2019 and references therein). We only find a radio continuum counterpart for one of the seven radio sources detected by Rodríguez & Zapata (2013) at 5.307 GHz and 20.943 GHz using the VLA in B- and C-configurations, respectively, where both have an approximate beamsize of ∼1″. The sources were determined to be HII regions or non-thermal sources of an unknown nature. These sources are displayed in Fig. 10 using their names from Rodríguez & Zapata (2013). Except for source J3, which is a known HII region also detected in other surveys (e.g., Anderson et al. 2014; Becker et al. 1994), the rest are not easily identifiable in our data. While it does not seem to be a result of sidelobe noise, it is unclear how to determine if these sources are detected above the local noise. However, with our own B-configuration data, we may be able to resolve these sources in future works.

4.4. Star formation in the CMZ

4.4.1. Mass estimation

Star formation activity is integral in the evolution, both chemically and structurally, of galaxies, and by extension, the

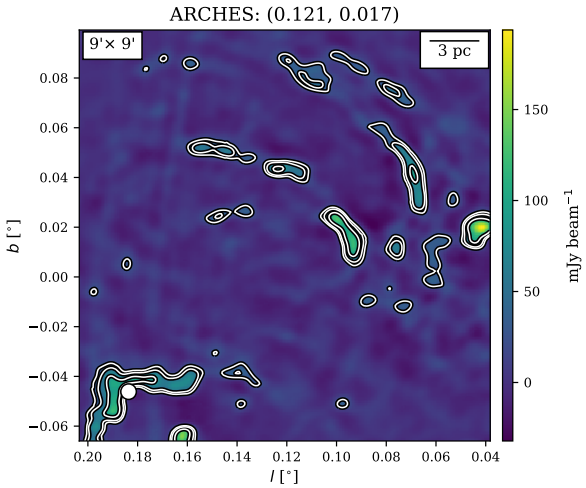

Fig. 9. GLOSTAR cutout of a $9' \times 9'$ area centred on the Arches cluster. Plotted in white contours are 3, 5, and 10 times the local rms (8 mJy beam^{-1}).

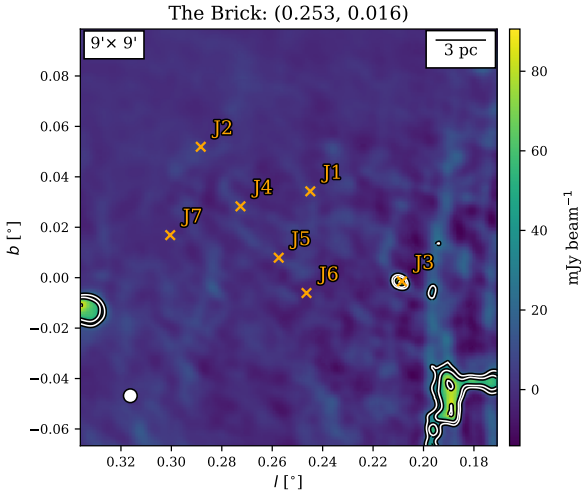

Fig. 10. GLOSTAR cutout of a $9' \times 9'$ area encompassing the region known as 'the Brick'. Plotted in white contours are 3, 5, and 10 times the local rms (8 mJy beam^{-1}). Labelled in orange are the positions and names of the seven radio sources found by Rodríguez & Zapata (2013) using the VLA B- and C-configuration.

large-scale structures of the universe. The rate at which the ISM is converted into stars (SFR) is thus an important quantity in studying star formation. Here we estimate a lower limit of the current SFR in the CMZ, given that the HII regions that we characterise are associated with YSOs that trace the early stages of star formation. In order to calculate the SFR in the CMZ from these HII regions, we need to estimate the masses of the individual zero-age-main-sequence (ZAMS) stars that are ionising the HII regions. Knowing the flux and the size of these radio sources, we can already calculate further properties as outlined in Immer et al. (2012a) where our main interest is the number of Lyman continuum photons, $N_{\rm Lyc}$, associated with each source as it can be used to determine the spectral type of a new-born star if we assume each HII region has only one star. This approximation generally holds as the most massive star dominates the contribution of Lyman continuum photons. We relate $N_{\rm Lyc}$ with our observables as follows:

$$\left[\frac{N_{\rm Lyc}}{\rm photons\,s^{-1}}\right] = 2.35\times10^{35}\left[\frac{S}{\rm Jy}\right]\left[\frac{T}{10^4\,\rm K}\right]^2\left[\frac{Dist}{\rm kpc}\right]^2 b(\nu,T)^5, \quad (1)$$

with

$$b(\nu,T) = 1 + 0.3195\log\left(\frac{T}{10^4\,\rm K}\right) - 0.213\log\left(\frac{\nu}{1\,\rm GHz}\right), \quad (2)$$

where S is the flux density, T is the electron temperature, $Dist$ is the distance to the source, ν is the frequency of the observation, and $b(\nu, T)$ is taken from Panagia & Walmsley (1978). To obtain this relation, we followed Tielens (2005) where they have related $N_{\rm Lyc}$ to the emission measure, EM, of an HII region assuming that it is an idealised ionised source with spherical geometry, assuming a constant electron density, $n_{\rm e}$, of the HII region:

$$EM = 4.3\times10^{-11}\left[\frac{n_{\rm e}}{10^3\,\rm cm^{-3}}\right]^{\frac{4}{3}}\left[\frac{N_{\rm Lyc}}{\rm photons\,s^{-1}}\right]^{\frac{1}{3}}\rm cm^{-6}\,pc, \quad (3)$$

and solved for $N_{\rm Lyc}$ by using expressions for EM and $n_{\rm e}$ from Panagia & Walmsley (1978):

$$EM = 5.638\times10^4\left[\frac{S}{\rm Jy}\right]\left[\frac{T}{10^4\,\rm K}\right]b(\nu,T)\theta_R^{-2}\,\rm cm^{-6}\,pc, \quad (4)$$

$$n_{\rm e} = 311.3\times\left[\frac{S}{\rm Jy}\right]^{0.5}\left[\frac{T}{10^4\,\rm K}\right]^{0.25}\left[\frac{Dist}{\rm kpc}\right]^{-0.5} b(\nu,T)^{-0.5}\theta_R^{-1.5}\,\rm cm^{-3}. \quad (5)$$

While S and θ_R (the angular radius of the source in arcminutes) were derived from the data, we assumed a temperature of 10^4 K and a distance of 8.2 kpc for all sources as they reside in the same general area of the CMZ.

Finally, following again Tielens (2005), we can estimate the mass, $M_{\rm HII}$, of the HII region within which the ionising star resides as

$$M_{\rm HII} \approx 1.6\times10^{-48}\left[\frac{n_{\rm e}}{10^3\,\rm cm^{-3}}\right]^{-1}\left[\frac{N_{\rm Lyc}}{\rm photons\,s^{-1}}\right]M_\odot. \quad (6)$$

In order to determine the SFR, we determined the mass of the ZAMS that are ionising the HII regions by interpolating the stellar masses given as a function of the Lyman continuum flux in Davies et al. (2011), as shown in Fig. 11. The derived masses of the stars range from 12 to 49 $M_\odot$ with a mean and median of 16.5 and 15 $M_\odot$, respectively. This corresponds to a spectral type range of B1 to O6 with a mean of B0-B0.5. Derived stellar properties are summarised in Table A.2.

We show the distribution of the masses of these stars in Fig. 12 , where masses $M_* < 10\,M_\odot$ and $M_* > 40\,M_\odot$ are not represented by our sample. The majority of the luminosity in a given star cluster comes from the massive stars, the majority of the mass of the star cluster, however, is distributed among the low mass stars. Our distribution clearly shows that we do not cover low mass stars and therefore need a way to infer the total mass of stars by interpolating the distribution of low mass stars. From this distribution of stellar masses, one can calculate the SFR. To do this we used an initial mass function (IMF; Salpeter 1955; Kroupa 2001) to obtain an estimate of the total mass. As our sample clearly does not represent all masses, especially the

lower masses, we used the IMF ($\xi(M)$) from Kroupa (2001) that better estimates the contribution of lower mass stars to the total stellar population and is given by

$$\xi(M) = \xi_{0,1} M^{-2.3} \text{ for } 0.5\,M_\odot \leq M \leq 120\,M_\odot \quad (7)$$

$$\xi(M) = \xi_{0,2} M^{-1.3} \text{ for } 0.08\,M_\odot \leq M \leq 0.5\,M_\odot \quad (8)$$

$$\xi(M) = \xi_{0,3} M^{-0.3} \text{ for } 0.01\,M_\odot \leq M \leq 0.08\,M_\odot \quad (9)$$

where $\xi_{0,1}$, $\xi_{0,2}$, and $\xi_{0,3}$ are scaling factors. Following the method detailed in Immer et al. (2012b), we determined the scaling factor $\xi_{0,1}$ by a non-linear least square fit to our data over the mass range $10\,M_\odot < M_* < 40\,M_\odot$ (Fig. 12). By requiring $\xi(M)$ to be continuous, we scaled $\xi_{0,2}$ and $\xi_{0,3}$ accordingly. For the scaling factors, we obtained $\xi_{0,1} = 6152$, $\xi_{0,2} = 12\,304$, and $\xi_{0,3} = 153\,807$.

The total mass of the stars was then calculated using

$$M_{tot} = \int_{0.01}^{120} M\xi(M)\mathrm{d}M, \quad (10)$$

where $\xi(M)\mathrm{d}M$ is the number of stars in the mass range of M and $M + \mathrm{d}M$ in units of $M_\odot$. Therefore we estimate the mass of all ZAMSs in the CMZ in the range of 0.01−120 $M_\odot$ to be ∼30 000 $M_\odot$. While this is the standard approach, we recognise that our sample is limited. Of all possible YSOs, we only selected those that have an associated HII region and, therefore, only the stars that are radio bright. This, however, is not representative of the total number of stars in the CMZ. Thus, we calculated the recent SFR in two methods to account for this bias.

4.4.2. Average SFR

First, we derived the SFR based on the estimated total mass of young stars. In order to calculate the SFR, we needed to determine the time over which the YSOs were formed. We estimated this using the average age of a YSO. YSOs need to be embedded in a surrounding envelope of dust in order to be visible in the mid-infrared (Wood & Churchwell 1989). This phase is only ∼10% of the full lifetime for a typical O or early B star and for an average B0 type star, this is ∼1 Myr (Wood & Churchwell 1989). As such, YSO candidates that are observed are at most ∼1 Myr in age. In following the more conservative estimation of the YSO timescale from Nandakumar et al. (2018) of 0.75 ± 0.25 Myr, we calculated the average ongoing SFR as $\dot{M}_{\rm SF} = M_{\rm tot}/\tau_{\rm YSO}$, where $\tau_{\rm YSO}$ is the considered timescale and $M_{\rm tot}$ is calculated in Sect. 4.4.1. We obtain a SFR of 0.04 ± 0.02 $M_\odot\,\mathrm{yr}^{-1}$, which is consistent with the results obtained with the YSO counting method by Nandakumar et al. (2018), which is interesting as we have a much smaller sample size. If we instead use the Salpeter IMF, we find a SFR of the order of ∼0.1 $M_\odot\,\mathrm{yr}^{-1}$. Given that we do not have a representative sample that covers low-mass stars, the Salpeter IMF especially may overestimate the SFR from our small sample and, in our case, the SFR is double what was estimated by a Kroupa IMF.

Secondly, we considered the total ionising flux from the HII regions and followed the statistical approach from Kauffmann et al. (2017) that relates the SFR to the number of HII regions. In their work, they also adopted a Kroupa (2001) IMF, where the power law covering the largest masses is $\alpha = 2.7$. The distribution has a mean stellar mass of $\langle m_* \rangle = 0.29\,M_\odot$. They derived a relationship between the number of cluster members of an HII region, which includes masses of 0.01 $M_\odot$ and greater, to the mass of the largest member as,

$$N_{\rm cl} = 20.5 \times (M_{\rm max}/M_\odot)^{1.7}. \quad (11)$$

The total mass in the given HII region is then $\langle m_* \rangle \times N_{\rm cl}$. To calculate the SFR contribution from a given HII region, we again need to consider an appropriate timescale over which this mass is produced. Following Kauffmann et al. (2017), we consider a timescale, $\tau_{\rm HII}$, of 1.1 Myr. This value is estimated based on the comparison of the ratio between the number of HII regions and the statistical estimate of the number of high-mass stars (here, the radio bright YSOs) and the ratio of their respective timescales. A more detailed discussion can be found in their appendix. Using this timescale, we calculated the SFR as $\dot{M}_{\rm SF} = \langle m_* \rangle \times N_{\rm cl}/\tau_{\rm HII}$. Using our sample of HII regions, we used our calculated masses to find the number of cluster members and then estimate the individual SFR. The sum of these rates provides a total ongoing SFR of 0.023 $M_\odot\,\mathrm{yr}^{-1}$. Knowing that the sample does not cover all possible HII regions within the CMZ, we used ancillary values compiled in Table 7 of Kauffmann et al. (2017) that considers the SFR in all the major GMCs in the CMZ. We made sure to exclude two sources that overlap with the Sgr B2 GMC, and one source with the '20 $\mathrm{km\,s}^{-1}$ cloud', and in these cases, we solely used the literature value. In this way, we provide an update on the SFR from Kauffmann et al. (2017) with a final estimate of ∼0.068 $M_\odot\,\mathrm{yr}^{-1}$.

Other estimates using YSO counting (Yusef-Zadeh et al. 2009; An et al. 2011; Immer et al. 2012a) estimate SFRs of at least a factor of two or more. A reference of calculated SFRs using different methods is summarised in Table 4 of Nandakumar et al. (2018). The numerous different methods for calculating the observed ongoing SFR is consistent in that they all point to a lower SFR than expected with respect to the available dense molecular gas present (e.g., 0.78 $M_\odot\,\mathrm{yr}^{-1}$; column density threshold, 0.41 $M_\odot\,\mathrm{yr}^{-1}$; volumetric star formation relations Longmore et al. 2013 also show lower SFR). While it is not yet known what the definitive reason for this deficiency of star formation is, Longmore et al. (2013) suggest turbulence as a possible counteracting component to gravitational collapse, which is supported from observations of the large velocity dispersions found in the clouds in the CMZ (Bally et al. 1987; Christopher et al. 2005; Shetty et al. 2012; Kauffmann et al. 2013; Mills et al. 2015; Rathborne et al. 2015). Kruijssen et al. (2014) discuss additional possible mechanisms that work on different size scales. On larger scales, episodic star formation from the accumulation of dense gas from spiral instabilities and the gas not being self-gravitating may explain the observed SFR and, on smaller scales, high turbulence likely drives up the volume density threshold needed to form stars. Alternatively, simulations by Sormani et al. (2020) suggest that the SFR might indeed be variable and that such variability is a reflection of changes in the mass of the CMZ instead of changes in the star formation efficiency.

5. Summary and conclusions

To investigate HMSF in the CMZ, one can use YSOs, that is to say tracers of on-going star formation to characterise the SFR. YSOs are observed indirectly from the re-emission of their energy from their surrounding natal dust cloud in the infrared. If these infrared sources are indeed sites of current star formation, we expect them to be currently associated with HII regions or for them to be in the future, which can be seen in the radio. We used a set of 334 YSOs that Nandakumar et al. (2018) selected

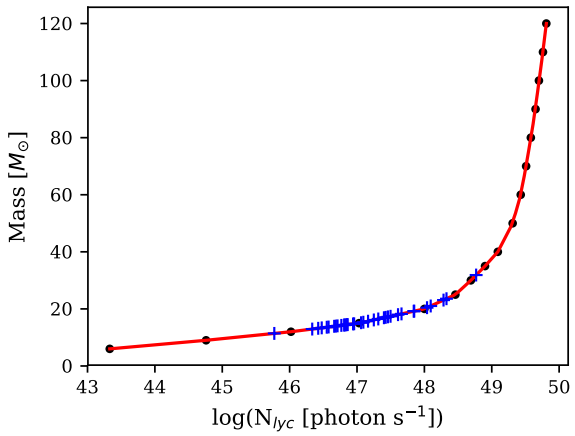

Fig. 11. ZAMS masses plotted against the Lyman continuum photon flux. The red line is interpolated from the data in Table 1 from Davies et al. (2011). The derived masses for the $N_{\rm Lyc}$ values determined in this work are highlighted as blue crosses.

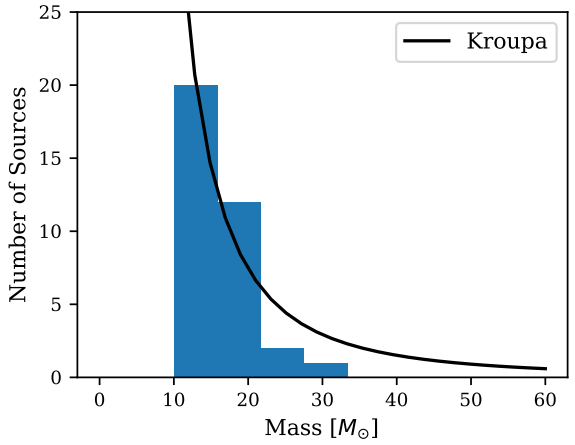

Fig. 12. Mass distribution of calculated ZAMS masses for the HII regions with associated YSOs. The black line represents the fitted Kroupa IMF (Kroupa 2001).

using a new colour-colour-diagram selection criterion as targets to look for radio sources to see how many of these YSO candidates have already formed an HII region. Using the GLOSTAR 5.8 GHz radio continuum data, we searched for YSO association candidates and obtain a final sample of 35 YSO sources that have a potential radio continuum counterpart. We also compared the YSO sample with ATLASGAL and find 94 coincident associations, with 14 having a GLOSTAR counterpart. For those without dust emission and radio emission, the lack of emission at these wavelengths suggests that they are potentially much older or are perhaps not high-mass YSOs. A cross-match of the 334 YSOs with the CMZoom survey showed 22 potential counterparts, and of these 22, two have radio counterparts in our data.

We used these 35 radio sources to estimate the SFR by first characterising their properties. We calculated their flux, size, shape, and their spectral indices. We also compared these radio sources to the WISE catalogue and found that there are six without WISE counterparts, where five of them are potential new HII regions. We determined the Lyman continuum photon flux of the ionising ZAMS and determined its mass. For our subsample, we found masses between $10\,M_\odot < M_* < 40\,M_\odot$. We calculated their contribution to the SFR in the CMZ to be $0.04 \pm 0.02\,M_\odot\,{\rm yr}^{-1}$, which is consistent with the results from Nandakumar et al. (2018) and other independent investigations that used different methods. However, we note the limitations in our approach of using, in essence, only the radio bright sources in our sample. We therefore adapted the formulation of the SFR from Kauffmann et al. (2017) and used the total ionising flux of HII regions to also estimate the SFR in the CMZ to be $0.068\,M_\odot\,{\rm yr}^{-1}$.

Acknowledgements. We would like to thank the anonymous referee for their useful comments. We would like to thank Denise Riquelme for a careful reading of the manuscript. H.N. is a member of the International Max-Planck Research School at the universities of Bonn and Cologne (IMPRS). This research was partially funded by the ERC Advanced Investigator Grant GLOSTAR (247078). Contributions from J.K. are in part supported by the National Science Foundation under Grant Number AST-1909097. H.B. acknowledges support from the European Research Council under the European Community's Horizon 2020 framework program (2014-2020) via the ERC Consolidator grant 'From Cloud to Star Formation (CSF)' (project number 648505). H.B. further acknowledges support from the Deutsche Forschungsgemeinschaft (DFG) via Sonderforschungsbereich (SFB) 881 'The Milky Way System' (sub-project B1). The National Radio Astronomy Observatory is a facility of the National Science Foundation, operated under a cooperative agreement by Associated Universities, Inc. It made use of information from the ATLASGAL database at `http://atlasgal.mpifr-bonn.mpg.de/cgi-bin/ATLASGAL_DATABASE.cgi` supported by the MPIfR in Bonn. This publication also makes use of data products from the Wide-field Infrared Survey Explorer (WISE) which is a joint project of the University of California, Los Angeles, and the Jet Propulsion Laboratory/California Institute of Technology, funded by the National Aeronautics and Space Administration. This research made use of Astropy (`http://www.astropy.org`), a community-developed core Python package for Astronomy (Astropy Collaboration 2013, 2018). This research has made use of the SIMBAD database, operated at CDS, Strasbourg, France.

References

An, D., Ramírez, S. V., Sellgren, K., et al. 2011, ApJ, 736, 133
Anderson, L. D., Bania, T. M., Balser, D. S., et al. 2014, ApJS, 212, 1
Astropy Collaboration (Robitaille, T. P., et al.) 2013, A&A , 558, A33
Astropy Collaboration (Price-Whelan, A. M., et al.) 2018, AJ, 156, 123
Bally, J., Stark, A. A., Wilson, R. W., & Henkel, C. 1987, ApJS, 65, 13
Barnes, A. T., Longmore, S. N., Battersby, C., et al. 2017, MNRAS, 469, 2263
Battersby, C., Keto, E., Walker, D., et al. 2020, ApJS, 249, 35
Becker, R. H., White, R. L., Helfand, D. J., & Zoonematkermani, S. 1994, ApJS, 91, 347
Bihr, S., Johnston, K. G., Beuther, H., et al. 2016, A&A, 588, A97
Boggess, N. W., Mather, J. C., Weiss, R., et al. 1992, ApJ, 397, 420
Breen, S. L., Ellingsen, S. P., Caswell, J. L., & Lewis, B. E. 2010, MNRAS, 401, 2219
Brunthaler, A., Menten, K. M., Dzib, S. A., et al. 2021, A&A, 651, A85 (Paper I)
Caswell, J. L., Fuller, G. A., Green, J. A., et al. 2010, MNRAS, 404, 1029
Chakraborty, A., Roy, N., Wang, Y., et al. 2020, MNRAS, 492, 2236
Christopher, M. H., Scoville, N. Z., Stolovy, S. R., & Yun, M. S. 2005, ApJ, 622, 346
Condon, J. J. 1984, ApJ, 287, 461
Condon, J. J., Cotton, W. D., Greisen, E. W., et al. 1998, AJ, 115, 1693
Contreras, Y., Schuller, F., Urquhart, J. S., et al. 2013, A&A, 549, A45
Cotera, A. S., Erickson, E. F., Colgan, S. W. J., et al. 1996, ApJ, 461, 750
Cotton, W. D. 2008, PASP, 120, 439
Csengeri, T., Urquhart, J. S., Schuller, F., et al. 2014, A&A, 565, A75
Csengeri, T., Weiss, A., Wyrowski, F., et al. 2016, A&A, 585, A104
Davies, B., Hoare, M. G., Lumsden, S. L., et al. 2011, MNRAS, 416, 972
Dzib, S. A., Loinard, L., Mioduszewski, A. J., et al. 2013, ApJ, 775, 63
Figer, D. F., Najarro, F., Gilmore, D., et al. 2002, ApJ, 581, 258
Gallego-Calvente, A. T., Schoedel, R., Alberdi, A., et al. 2021, A&A, 647, A110
Genzel, R., & Stutzki, J. 1989, ARA&A, 27, 41
Ginsburg, A., Bally, J., Barnes, A., et al. 2018, ApJ, 853, 171
GRAVITY Collaboration (Abuter, R., et al.) 2019, A&A, 625, L10
Großschedl, J. E., Alves, J., Meingast, S., et al. 2018, A&A, 619, A106

Güsten, R. 1989, in The Center of the Galaxy, ed. M. Morris, 136, 89
Hatchfield, H. P., Battersby, C., Keto, E., et al. 2020, ApJS, 251, 14
Henshaw, J. D., Ginsburg, A., Haworth, T. J., et al. 2019, MNRAS, 485, 2457
Hoare, M. G., Kurtz, S. E., Lizano, S., Keto, E., & Hofner, P. 2007, in Protostars and Planets V, eds. B. Reipurth, D. Jewitt, & K. Keil, 181
Immer, K., Schuller, F., Omont, A., & Menten, K. M. 2012a, A&A, 537, A121
Immer, K., Menten, K. M., Schuller, F., & Lis, D. C. 2012b, A&A, 548, A120
Kauffmann, J., Pillai, T., & Zhang, Q. 2013, ApJ, 765, L35
Kauffmann, J., Pillai, T., Zhang, Q., et al. 2017, A&A, 603, A89
Kennicutt, R. C. Jr. 1998, ApJ, 498, 541
Kennicutt, R. C., & Evans, N. J. 2012, ARA&A, 50, 531
Kobayashi, Y., Okuda, H., Sato, S., Jugaku, J., & Dyck, H. M. 1983, PASJ, 35, 101
Kounkel, M., Hartmann, L., Loinard, L., et al. 2017, ApJ, 834, 142
Kroupa, P. 2001, MNRAS, 322, 231
Kruijssen, J. M. D., Longmore, S. N., Elmegreen, B. G., et al. 2014, MNRAS, 440, 3370
Krumholz, M. R., & Kruijssen, J. M. D. 2015, MNRAS, 453, 739
Krumholz, M. R., & McKee, C. F. 2008, Nature, 451, 1082
Krumholz, M. R., Kruijssen, J. M. D., & Crocker, R. M. 2017, MNRAS, 466, 1213
Kurtz, S. 2002, in Hot Star Workshop III: The Earliest Phases of Massive Star Birth, ed. P. Crowther, ASP Conf. Ser., 267, 81
Lada, C. J., Lombardi, M., & Alves, J. F. 2010, ApJ, 724, 687
Lada, C. J., Forbrich, J., Lombardi, M., & Alves, J. F. 2012, ApJ, 745, 190
Lang, C. C., Goss, W. M., & Morris, M. 2001, AJ, 121, 2681
Lang, C., Johnson, K., Goss, W., & Rodriguez, L. 2005, AJ, 130
Lis, D. C., & Goldsmith, P. F. 1990, ApJ, 356, 195
Lis, D. C., & Carlstrom, J. E. 1994, ApJ, 424, 189
Lis, D. C., & Menten, K. M. 1998, ApJ, 507, 794
Longmore, S. N., Bally, J., Testi, L., et al. 2013, MNRAS, 429, 987
Lu, X., Zhang, Q., Kauffmann, J., et al. 2019a, ApJ, 872, 171
Lu, X., Mills, E. A. C., Ginsburg, A., et al. 2019b, ApJS, 244, 35
Medina, S. N. X., Urquhart, J. S., Dzib, S. A., et al. 2019, A&A, 627, A175
Menten, K. M., Reid, M. J., Forbrich, J., & Brunthaler, A. 2007, A&A, 474, 515
Mills, E. A. C., Butterfield, N., Ludovici, D. A., et al. 2015, ApJ, 805, 72
Morris, M., & Serabyn, E. 1996, ARA&A, 34, 645
Motte, F., Bontemps, S., & Louvet, F. 2018, ARA&A, 56, 41
Nandakumar, G., Schultheis, M., Feldmeier-Krause, A., et al. 2018, A&A, 609, A109
Nishiyama, S., Nagata, T., Kusakabe, N., et al. 2006, ApJ, 638, 839
Panagia, N. 1973, AJ, 78, 929
Panagia, N., & Walmsley, C. M. 1978, A&A, 70, 411
Purcell, C. R., Hoare, M. G., Cotton, W. D., et al. 2013, ApJS, 205, 1
Ramírez, S. V., Arendt, R. G., Sellgren, K., et al. 2008, ApJS, 175, 147
Rathborne, J. M., Longmore, S. N., Jackson, J. M., et al. 2014, ApJ, 786, 140
Rathborne, J. M., Longmore, S. N., Jackson, J. M., et al. 2015, ApJ, 802, 125
Robitaille, T. P. 2017, A&A, 600, A11
Rodríguez, L. F., & Zapata, L. A. 2013, ApJ, 767, L13
Rodríguez, L. F., González, R. F., Montes, G., et al. 2012, ApJ, 755, 152
Rodríguez-Fernández, N. J., Martín-Pintado, J., Fuente, A., & Wilson, T. L. 2004, A&A, 427, 217
Salpeter, E. E. 1955, ApJ, 121, 161
Sánchez Contreras, C., Báez-Rubio, A., Alcolea, J., Bujarrabal, V., & Martín-Pintado, J. 2017, A&A, 603, A67
Schmidt, M. 1959, ApJ, 129, 243
Schmiedeke, A., Schilke, P., Möller, T., et al. 2016, A&A, 588, A143
Schneider, F. R. N., Izzard, R. G., de Mink, S. E., et al. 2014, ApJ, 780, 117
Schuller, F., Omont, A., Glass, I. S., et al. 2006, A&A, 453, 535
Schuller, F., Menten, K. M., Contreras, Y., et al. 2009, A&A, 504, 415
Schultheis, M., Lançon, A., Omont, A., Schuller, F., & Ojha, D. K. 2003, A&A, 405, 531
Schultheis, M., Sellgren, K., Ramírez, S., et al. 2009, A&A, 495, 157
Seiradakis, J. H., Reich, W., Wielebinski, R., Lasenby, A. N., & Yusef-Zadeh, F. 1989, A&AS, 81, 291
Shetty, R., Beaumont, C. N., Burton, M. G., Kelly, B. C., & Klessen, R. S. 2012, MNRAS, 425, 720
Sormani, M. C., Tress, R. G., Glover, S. C. O., et al. 2020, MNRAS, 497, 5024
Thompson, M. A., Hatchell, J., Walsh, A. J., MacDonald, G. H., & Millar, T. J. 2006, A&A, 453, 1003
Tielens, A. G. G. M. 2005, The Physics and Chemistry of the Interstellar Medium (Cambridge Univ. Press)
Urquhart, J. S., Csengeri, T., Wyrowski, F., et al. 2014, A&A, 568, A41
Urquhart, J. S., König, C., Giannetti, A., et al. 2018, MNRAS, 473, 1059
Walker, D. L., Longmore, S. N., Bally, J., et al. 2021, MNRAS, 503, 77
Wood, D. O. S., & Churchwell, E. 1989, ApJ, 340, 265
Yusef-Zadeh, F., Law, C., Wardle, M., et al. 2002, ApJ, 570, 665
Yusef-Zadeh, F., Hewitt, J. W., Arendt, R. G., et al. 2009, ApJ, 702, 178
Zinnecker, H., & Yorke, H. W. 2007, ARA&A, 45, 481

Appendix A: Additional tables

Table A.1. Positions and integrated flux densities of the candidate YSO–5.8 GHz radio continuum associations.

Source ID	YSO		$\text{Cont}_{5.8\,\text{GHz}}$		S_p	S_{int}	δS_i	$\alpha(S \propto \nu^{\alpha})$	D_{eff}	Separation	rms	Q_{shape}	Catalogues
	l [°]	b [°]	l [°]	b [°]	[mJy beam^{-1}]	[mJy]	[mJy]		[″]	[″]	[mJy beam^{-1}]		
3	358.7918	0.0117	358.7920	0.0117	2.1	4.6	0.2	–	33.3	0.6	0.4	C	WC
5	358.8437	0.0259	358.8444	0.0257	19.5	27.6	0.3	−0.2 ± 0.03	37.5	2.9	0.8	C	WC,N
34	359.1581	−0.0363	359.1594	−0.0365	28.0	109.5	1.1	−0.3 ± 0.03	56.9	4.8	0.9	E	WK, N
44	359.2365	−0.0364	359.2389	−0.0361	11.0	11.2	0.1	−0.1 ± 0.12	24.3	8.8	1.3	E	WC
51	359.2777	−0.0618	359.2785	−0.0625	0.9	0.9	0.0	–	<18.0	3.6	0.3	C	WC
54	359.2796	−0.0407	359.2806	−0.0417	7.7	10.1	0.2	−0.2 ± 0.2	33.9	4.8	2.3	E	WQ,A
64	359.3347	−0.0425	359.3361	−0.0438	8.7	9.1	0.1	−0.3 ± 0.2	26.6	6.6	0.8	C	WC
66	359.3173	0.0771	359.3187	0.0764	2.7	3.4	0.1	0.5 ± 0.5	26.6	5.6	0.5	C	–
78	359.4288	0.0353	359.4292	0.0347	6.7	8.0	0.1	1.3 ± 0.3	29.0	2.5	0.9	EC	WC
80	359.4037	0.0016	359.4049	−0.0007	13.5	19.2	0.2	−0.4 ± 0.2	34.7	9.3	0.9	C	WC,A
82	359.4225	0.0152	359.4236	0.0146	7.8	11.1	0.2	−0.02 ± 0.36	33.5	4.7	0.8	C	WC
83	359.4348	0.0225	359.4319	0.0222	10.6	13.6	0.2	−0.5 ± 0.2	31.0	10.4 [(a)]	0.9	C	WC
87	359.4673	−0.1713	359.4687	−0.1715	53.2	169.7	1.8	0.3 ± 0.05	72.1	5.4	0.8	EC	WK,A
88	359.4665	−0.0735	359.4678	−0.0727	7.1	7.3	0.1	−2.3 ± 1.8	26.5	5.4	0.4	C	WC
89	359.4554	−0.0663	359.4576	−0.0667	9.5	10.1	0.2	0.5 ± 0.3	29.9	8.2	1.4	C	WC,A
91	359.4563	0.0199	359.4569	0.0194	4.3	5.2	0.1	–	27.6	2.9	0.5	C	WC,A
93	359.4964	0.0387	359.4962	0.0378	4.0	5.9	0.2	0.05 ± 0.31	32.5	3.2	0.9	C	WC
115	359.6436	−0.0389	359.6437	−0.0396	16.1	17.8	0.2	0.2 ± 0.2	30.8	2.4	1.6	C	WC
135	359.7919	−0.0439	359.7917	−0.0458	9.9	10.6	0.1	−0.1 ± 0.5	28.1	7.0	1.4	C	WC
140	359.7843	0.0400	359.7806	0.0417	39.5	71.0	0.7	0.2 ± 0.1	40.8	14.8 [(a)]	0.9	E	WK
147	359.8428	−0.0144	359.8444	−0.0139	14.6	22.6	0.2	−0.5 ± 0.8	30.8	6.4	1.6	C	WC
157	359.8651	−0.0860	359.8667	−0.0868	107.8	115.2	1.0	0.3 ± 0.2	34.3	6.3	1.3	C	A, [(b)]
230	0.2883	0.0519	0.2896	0.0514	9.7	15.9	0.1	−0.2 ± 0.2	19.7	5.1	2.1	E	A
234	0.3368	−0.0133	0.3358	−0.0108	89.2	330.0	3.0	−0.2 ± 0.05	63.0	9.9	1.9	E	WK,A
235	0.3466	−0.0271	0.3472	−0.0278	63.0	73.2	0.6	−0.1 ± 0.02	27.5	3.4	2.0	C	WC,A
241	0.3527	−0.0199	0.3554	−0.0201	12.5	14.0	0.1	−0.6 ± 0.23	25.4	9.8	1.7	C	WC,A
262	0.4314	0.2617	0.4319	0.2611	32.1	34.8	0.3	−0.2 ± 0.05	33.3	2.8	0.4	C	B
277	0.5294	−0.1061	0.5299	−0.1083	37.6	48.8	0.5	−0.3 ± 0.3	32.7	8.1	6.9	E	WC
284	0.5332	0.1687	0.5347	0.1694	31.2	44.6	0.5	−0.2 ± 0.1	39.0	6.2	0.9	C	WG,A
296	0.6050	−0.2017	0.6056	−0.2021	22.8	41.3	0.6	−0.4 ± 0.16	50.1	2.4	0.5	C	WC,N
299	0.6331	−0.1152	0.6354	−0.1139	97.1	298.2	2.6	−0.2 ± 0.2	55.5	9.4	3.4	E	WK
307	0.6673	−0.0911	0.6681	−0.0910	53.1	192.5	2.1	0.04 ± 0.19	55.3	2.6	4.9	E	A
311	0.6879	−0.0325	0.6896	−0.0343	909.2	1175.1	8.1	0.3 ± 0.042	28.2	8.9	11.9	E	WG,A
315	0.7369	−0.2908	0.7375	−0.2917	7.5	8.3	0.1	0.3 ± 0.2	26.8	3.7	0.4	C	–
323	0.8439	−0.0538	0.8458	−0.0549	22.6	38.9	0.4	0.1 ± 0.3	37.1	7.8	1.2	E	–

Notes. Grouped here are sources with a continuum detection and angular separation within a GLOSTAR beam. From left to right: source number and YSO Galactic coordinates from Nandakumar et al. (2018). The Galactic coordinates of the pixel with the peak intensity of the 5.8 GHz continuum (this work), the peak intensity (S_p), the integrated flux density (S_{int}) and error (δS_i; Purcell et al. 2013), and the spectral index (α). The effective diameter of the source (D_{eff}) was obtained by assuming a circle with an equivalent area to the area enclosed by the contour used for flux determination. The separation indicates the angular distance between the reported YSO position in Nandakumar et al. (2018) and the peak intensity position of the radio continuum source where we are constrained by the pixel size (2.5″). The root-mean-square (rms) indicates the noise level that was obtained from a nearby emission-free patch. The general morphology (Q_{shape}) of the source is classified as compact (C), extended (E), and extended & complicated (EC). Previous classifications and detections (catalogues) include WISE candidate (WC), radio quiet (WQ), group (WG), or known HII regions for nearby sources (WK; all Anderson et al. 2014), as well as sources with counterparts in the NVSS survey (Condon et al. 1998), Becker et al. (1994), or ATLASGAL (Sánchez Contreras et al. 2017). [(a)]Despite the slightly larger separation, the YSO lies well within the main 5.8 GHz emission peak. [(b)]Associated to the '20 km s^{-1} cloud'.

A&A 651, A88 (2021)

Table A.2. Physical parameters of the detected radio continuum sources that have candidate YSO associations (see Table A.1).

Source	$S_{5.8\,\mathrm{GHz}}$ [mJy]	D_{eff} [pc]	n_e [cm^{-3}]	EM [10^5 cm^{-6} pc]	N_{Lyc} [log(photon s^{-1})]	M_{HII} [$M_\odot$]	Spectral type (single ZAMS star [(a)])	M_* [$M_\odot$]
3	2.8	1.0	62	0.029	46.3	0.50	B0-B0.5	12.8
5	26.9	1.4	127	0.158	47.3	2.35	B0-B0.5	16.2
34	69.6	2.0	115	0.192	47.7	6.66	O9.5-B0	18.4
44	10.7	0.9	142	0.136	46.9	0.83	B0-B0.5	14.5
51	2.1	0.8	71	0.032	46.2	0.33	B0.5-B1	12.4
54	10.1	1.1	104	0.088	46.8	1.07	B0-B0.5	14.5
64	7.7	0.8	140	0.119	46.7	0.61	B0-B0.5	14.1
66	4.5	1.1	73	0.042	46.5	0.67	B0-B0.5	13.4
78	5.4	0.9	106	0.074	46.6	0.56	B0-B0.5	13.7
80	13.4	1.1	115	0.110	47.0	1.29	B0-B0.5	14.8
82	6.8	1.1	87	0.061	46.7	0.86	B0-B0.5	13.9
87	190.1	2.6	126	0.302	48.1	16.66	O8.5-O9	21.3
89	16.8	1.3	108	0.110	47.1	1.71	B0-B0.5	15.2
91	5.2	1.1	76	0.047	46.6	0.76	B0-B0.5	13.6
93	5.8	1.2	69	0.042	46.6	0.94	B0-B0.5	13.7
115	13.9	0.9	170	0.189	47.0	0.90	B0-B0.5	14.9
135	9.7	0.9	134	0.122	46.8	0.80	B0-B0.5	14.4
140	60.5	1.4	185	0.345	47.6	3.61	O9.5-B0	18.1
157	120.9	1.2	326	0.922	47.9	4.10	O9-O9.5	19.6
230	15.9	1.2	115	0.117	47.0	1.53	B0-B0.5	15.1
234	436.9	2.6	195	0.712	48.5	24.79	O7.5-O8	25.5
235	73.6	1.1	297	0.691	47.7	2.74	O9.5-B0	18.5
262	33.8	1.2	162	0.237	47.4	2.31	O9.5-B0	16.8
277	54.6	1.2	222	0.424	47.6	2.72	O9.5-B0	17.8
284	43.3	1.4	147	0.227	47.5	3.25	O9.5-B0	17.3
296	40.8	1.9	92	0.120	47.5	4.87	O9.5-B0	17.2
299	240.2	1.9	236	0.754	48.2	11.24	O8-O8.5	22.4
307	87.0	1.5	186	0.391	47.8	5.17	O9.5-B0	18.9
311	1010.2	1.2	951	7.775	48.8	11.77	O6-O6.5	33.7
315	7.3	0.9	117	0.092	46.7	0.69	B0-B0.5	14.0
323	37.8	1.3	153	0.228	47.4	2.74	O9.5-B0	17.0

Notes. From left to right: source ID, 5.8 GHz integrated flux ($S_{5.8\,\mathrm{GHz}}$), effective diameter (D_{eff}), electron number density (n_{e}), emission measure (EM), Lyman continuum photon flux (N_{Lyc}), HII region mass (M_{HII}), spectral type, and interpolated stellar mass from values (M_*) given by Davies et al. (2011). We calculated these values using the same caveat as in Immer et al. (2012a), where we assume radio sources are spherically symmetric HII regions. In our study, however, we adopted this assumption for extended sources as well, which have been marked in Table A.1. [(a)]Obtained from Panagia (1973).

Appendix B: GLOSTAR cutouts

Contained in this section are cutouts similar to Fig. 3 for the remaining sources in the selected sample using GLOSTAR-VLA 5.8 GHz D-configuration continuum data.

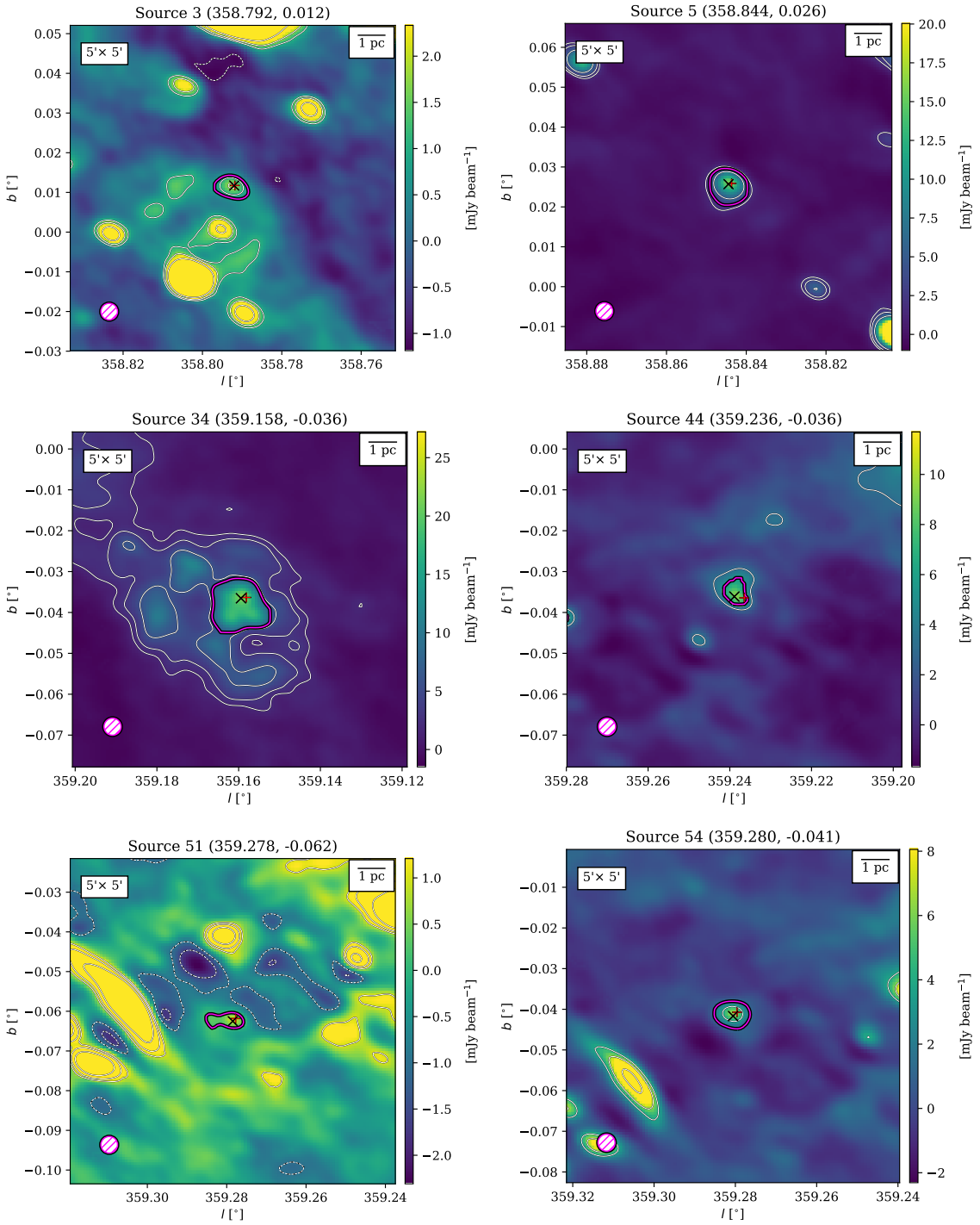

Fig. B.1. Same as Fig. 3, but for the remaining sources in Table A.1.

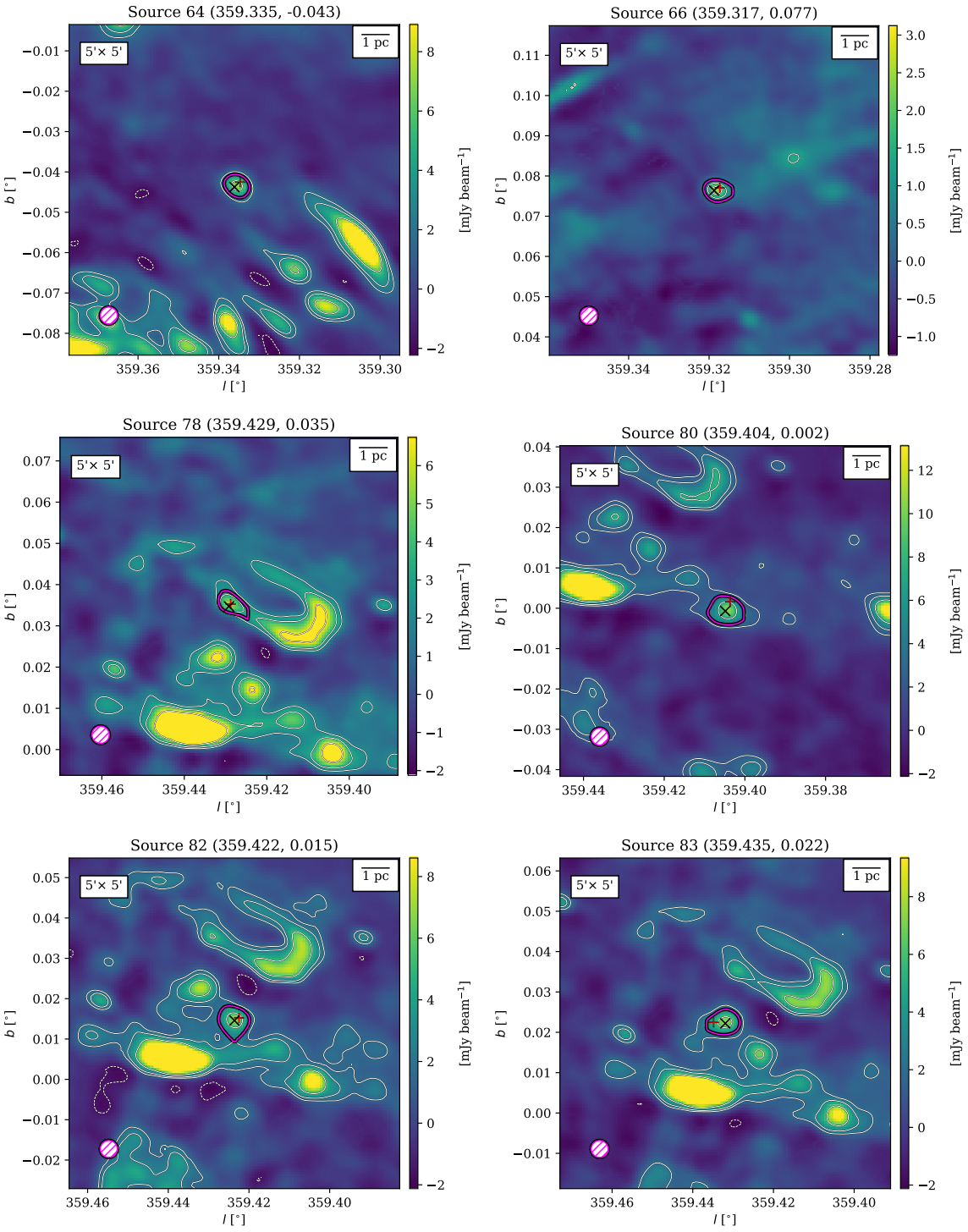

Fig. B.1. continued.

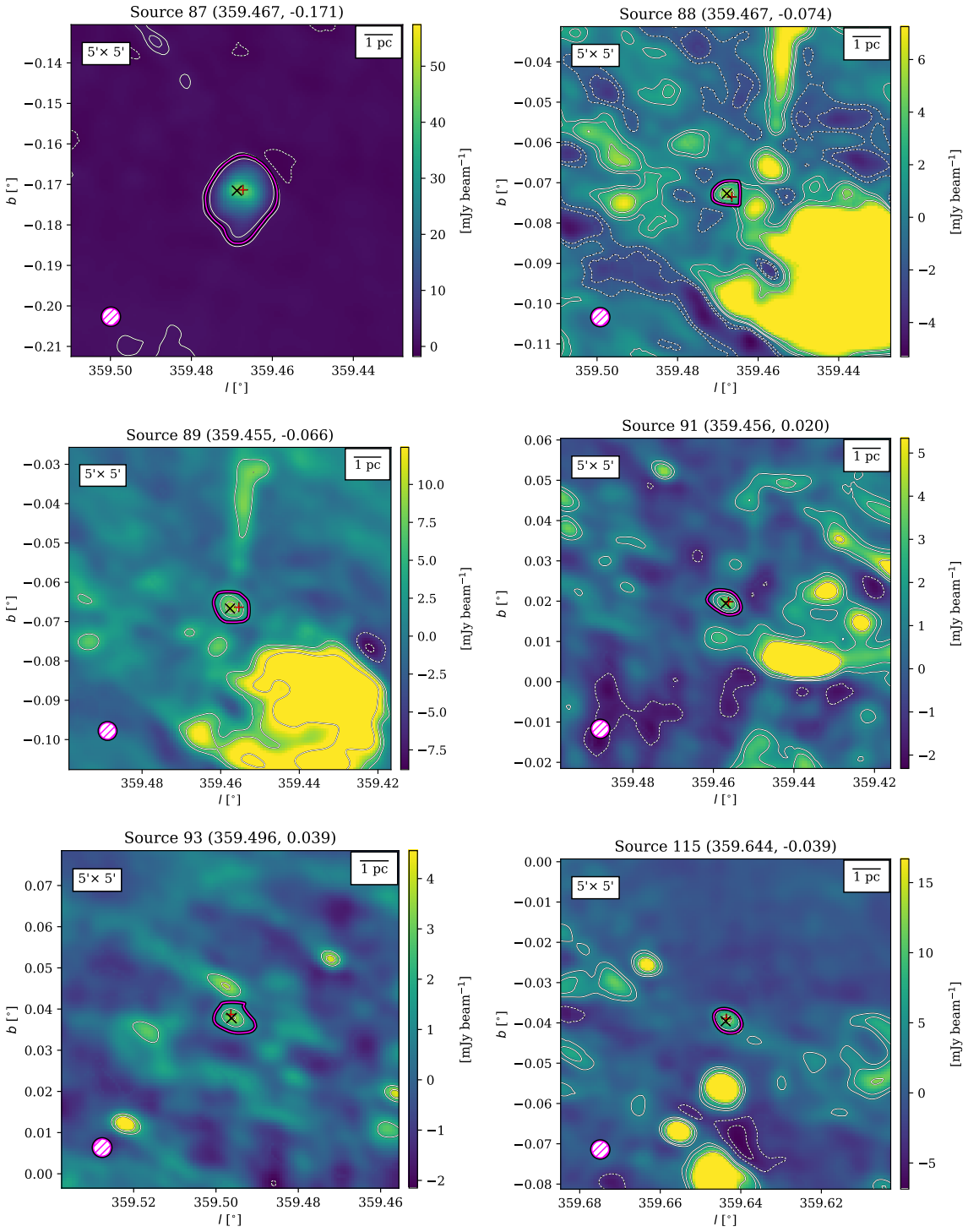

Fig. B.1. continued.

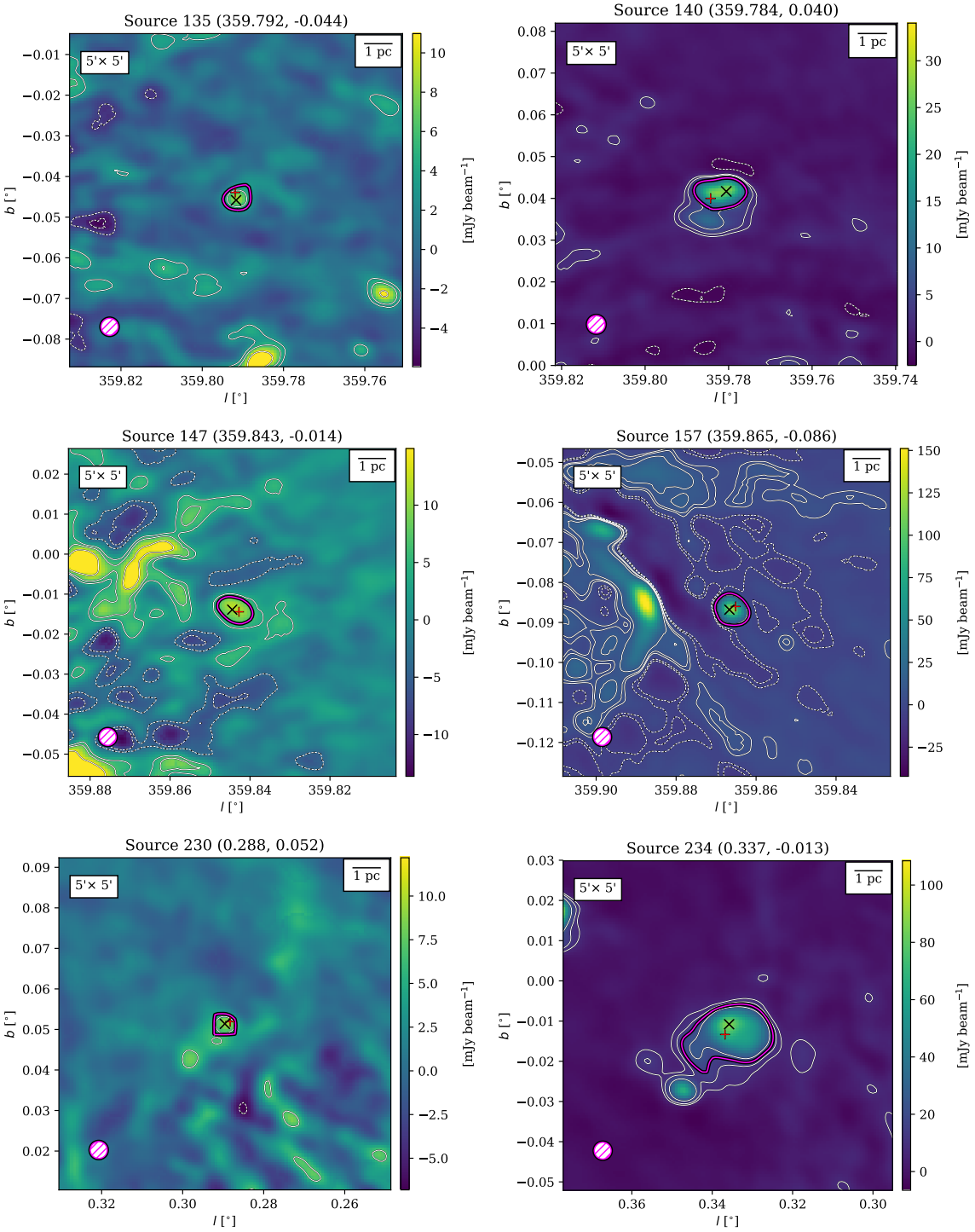

Fig. B.1. continued.

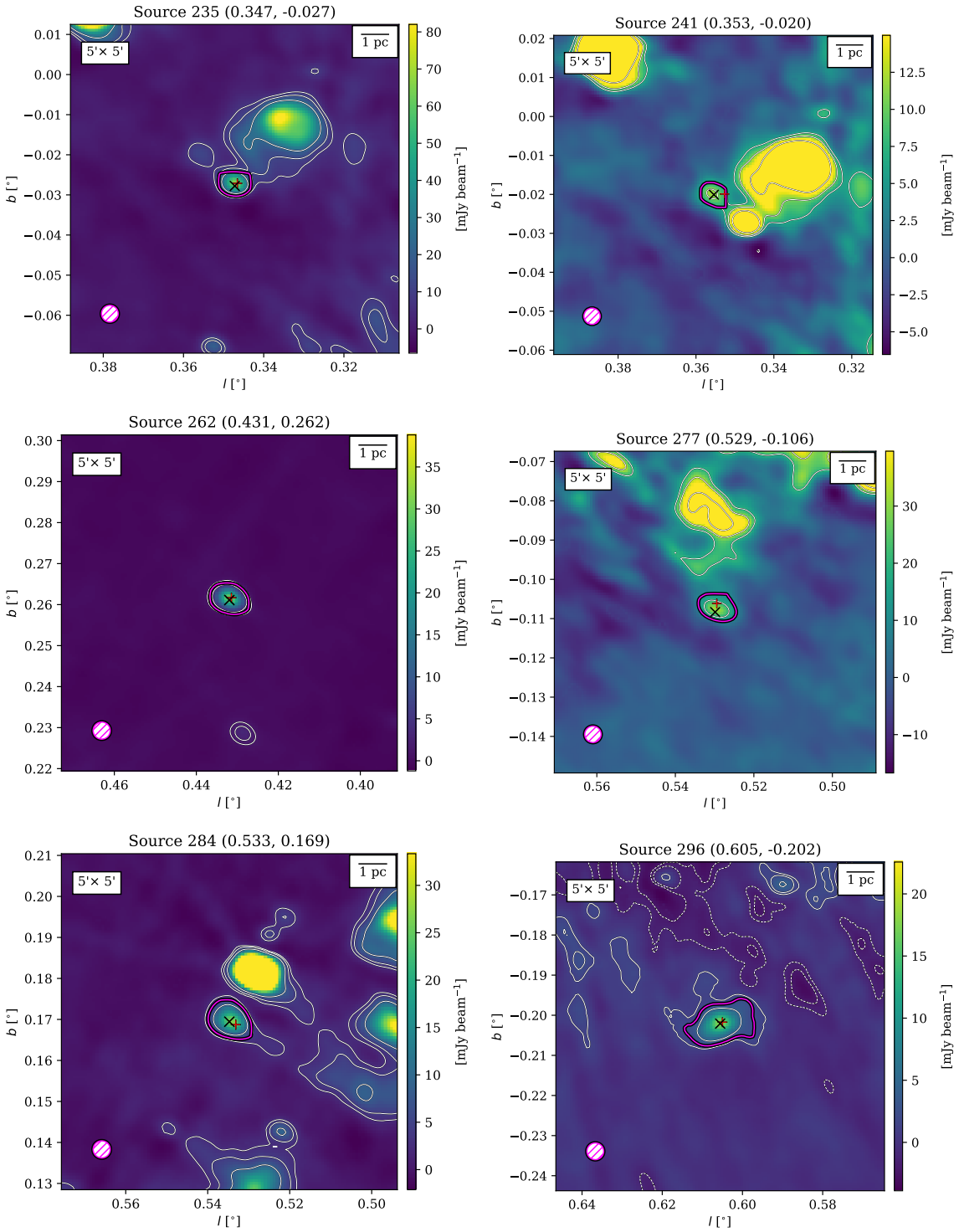

Fig. B.1. continued.

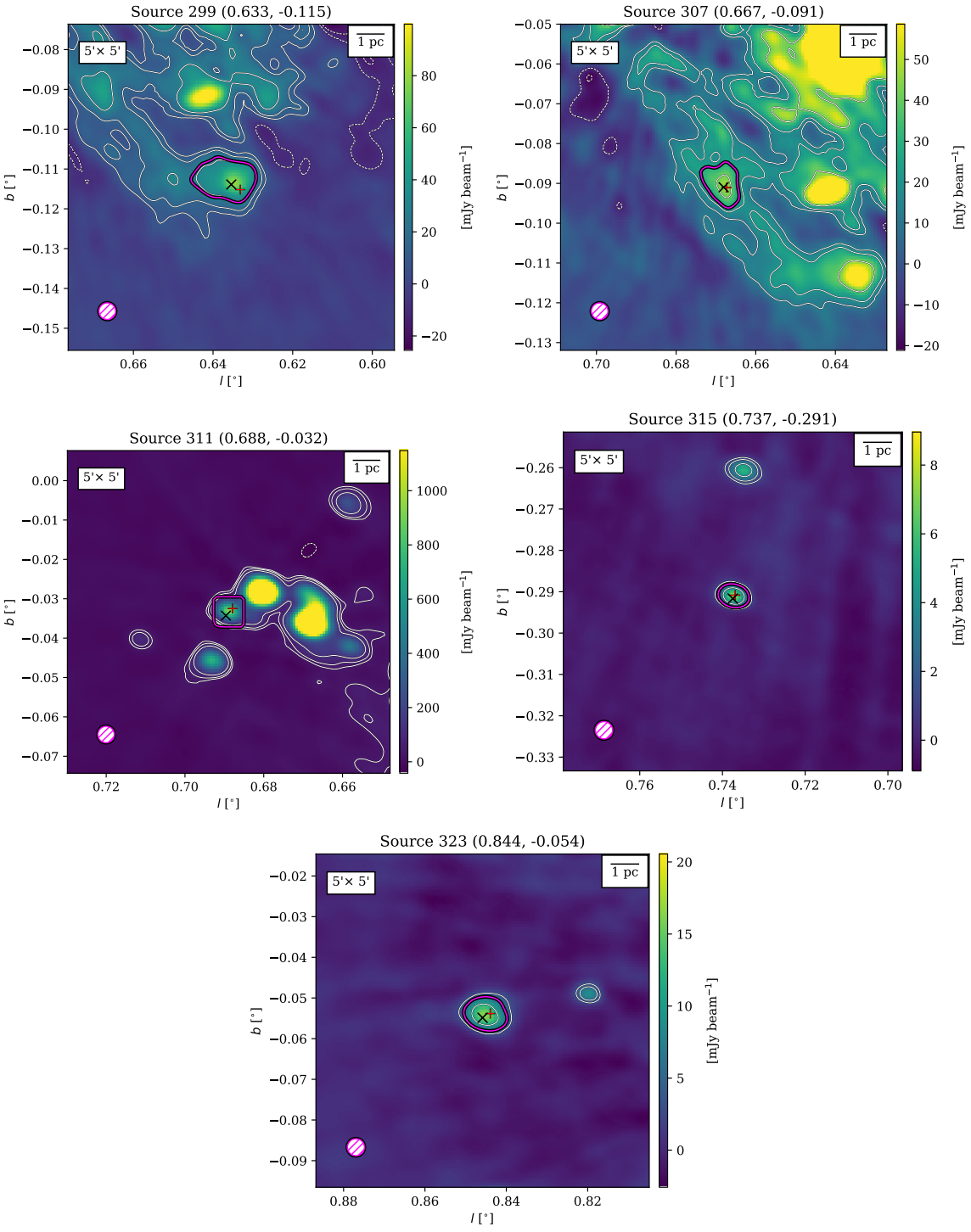

Fig. B.1. continued.

Appendix C: Other spectral index images

Here we provide an example of the different frequency channels used in the spectral index determination for a given source, which shows how the morphology is slightly different in each channel and therefore necessitates using only the peak flux for calculations.

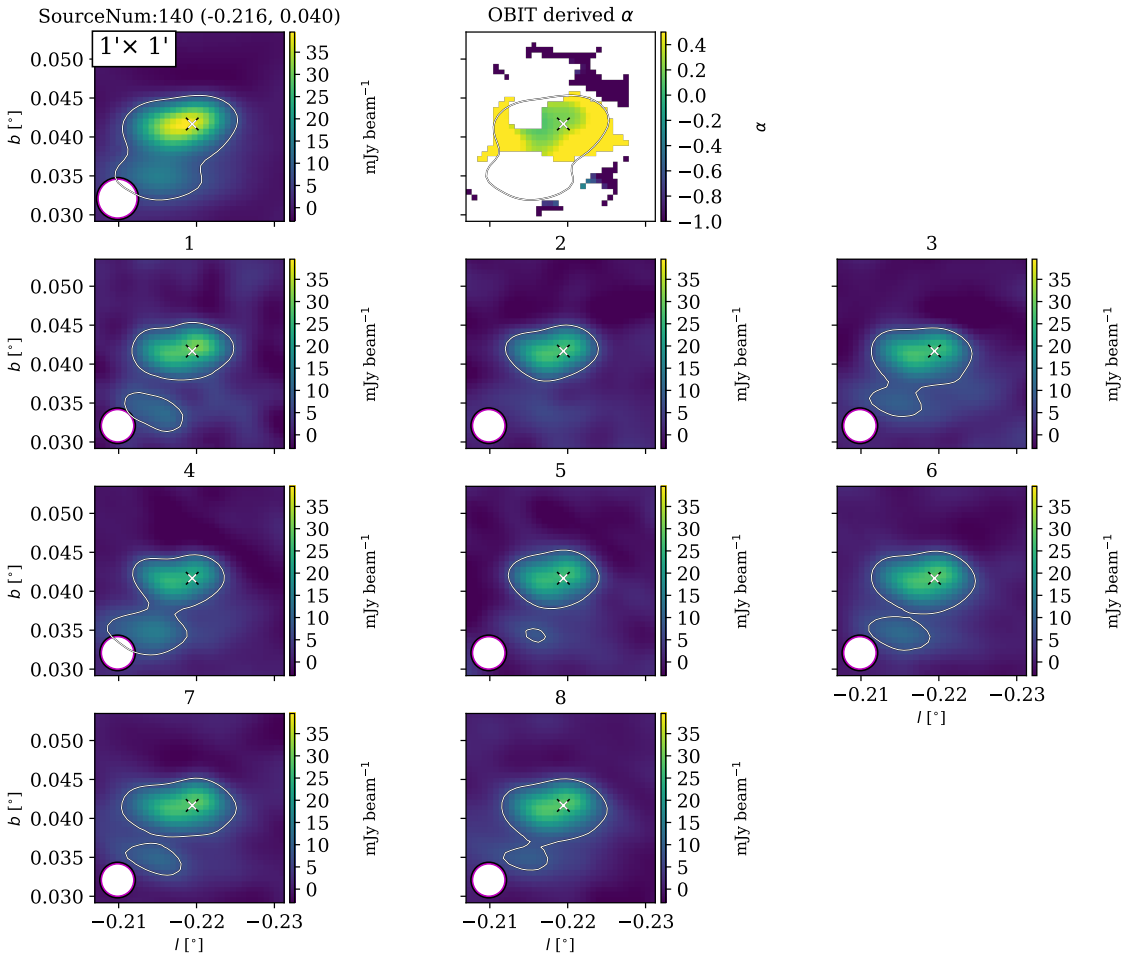

Fig. C.1. GLOSTAR continuum images of source 140 used for the determination of the spectral index. The *top-left image* is the combined image at 5.8 GHz, while the remaining 1–8 are from the individual frequency bands. Band 9 is omitted due to high noise. Shown also is the spectral index map produced by OBIT. The contour corresponds to the 5σ level of the combined image (7.608 mJy beam^{-1}) and used for comparison at each frequency. The combined contour is also overplotted atop the spectral index map. The 'x' marker denotes the position of the peak pixel from the combined image. The calculated spectral index for this source is $\alpha = 0.23 \pm 0.09$.

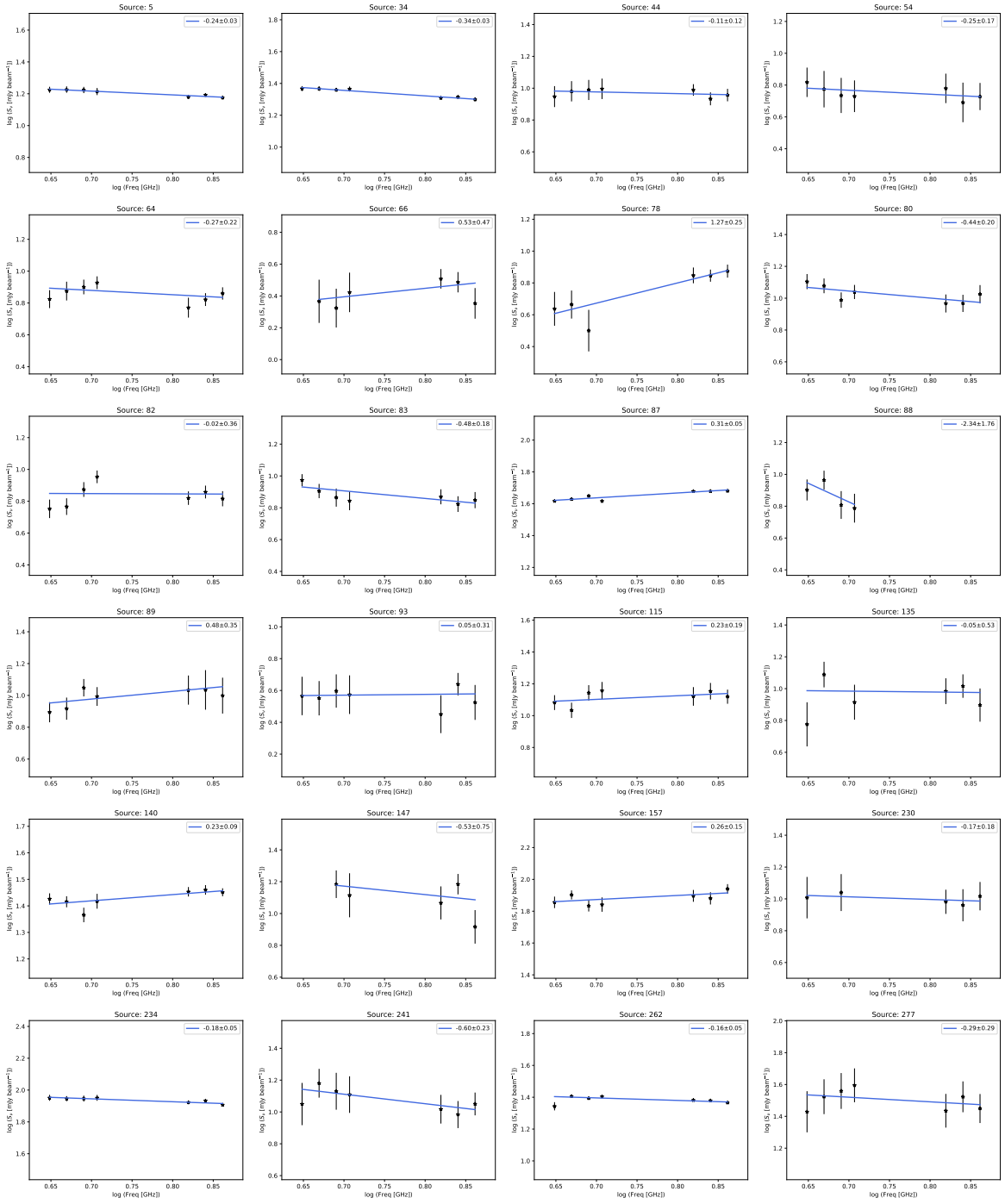

Fig. C.2. Linear fits of the peak brightness against frequency in logarithmic scale to determine the spectral index of a source. To better appreciate the error bars, all panels have a total range of 1 on the *y*-axis, centred on the mean brightness of that panel. The frequencies range from 4.45 GHz to 7.2 GHz.

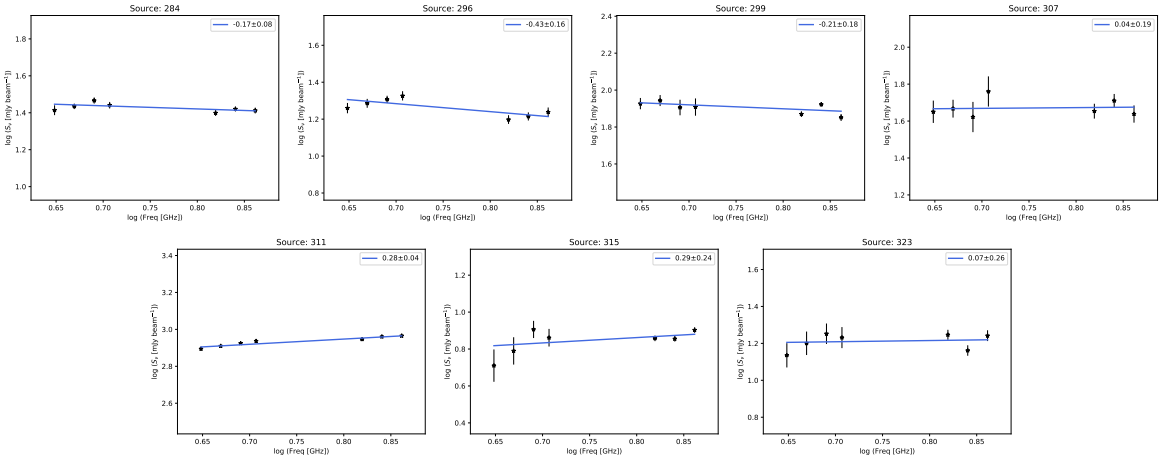

Fig. C.2. continued.

Appendix B

GLOSTAR: 6.7 GHz Methanol Maser Catalogue Paper

A&A 666, A59 (2022)
https://doi.org/10.1051/0004-6361/202244115

Astronomy & Astrophysics

A global view on star formation: The GLOSTAR Galactic plane survey

V. 6.7 GHz methanol maser catalogue*

H. Nguyen[1,**], M. R. Rugel[1], C. Murugeshan[2,1], K. M. Menten[1], A. Brunthaler[1], J. S. Urquhart[3], R. Dokara[1,**], S. A. Dzib[4,1], Y. Gong[1], S. Khan[1,**], S.-N. X. Medina[1], G. N. Ortiz-León[5,1], W. Reich[1], F. Wyrowski[1], A. Y. Yang[1], H. Beuther[6], W. D. Cotton[7,8], and J. D. Pandian[9]

[1] Max-Planck-Institut für Radioastronomie, Auf dem Hügel 69, 53121 Bonn, Germany
e-mail: hnguyen@mpifr-bonn.mpg.de
[2] CSIRO Space and Astronomy, PO Box 1130, Bentley, WA 6102, Australia
[3] Centre for Astrophysics and Planetary Science, University of Kent, Ingram Building, Canterbury, Kent CT2 7NH, UK
[4] IRAM, 300 rue de la piscine, 38406 Saint Martin d'Hères, France
[5] Instituto de Astronomía, Universidad Nacional Autónoma de México (UNAM), Apdo Postal 70-264, Ciudad de México, Mexico
[6] Max Planck Institute for Astronomy, Königstuhl 17, 69117 Heidelberg, Germany
[7] National Radio Astronomy Observatory, 520 Edgemont Road, Charlottesville, VA 22903, USA
[8] South African Radio Astronomy Observatory, 2 Fir St, Black River Park, Observatory 7925, South Africa
[9] Department of Earth & Space Sciences, Indian Institute of Space Science and Technology, Trivandrum 695547, India

Received 25 May 2022 / Accepted 17 July 2022

ABSTRACT

Class II methanol (CH_3OH) masers are amongst the clearest signposts of recent high-mass star formation (HMSF). A complete catalogue outlines the distribution of star formation in the Galaxy, the number of young star-forming cores, and the physical conditions of their environment, made possible by the Global View on Star Formation (GLOSTAR) survey. This blind survey of the radio regime of 4–8 GHz maps the Galactic mid-plane in the radio continuum, 6.7 GHz methanol line, the 4.8 GHz formaldehyde line, and several radio recombination lines. We present an analysis of the observations of the 6.7 GHz CH_3OH maser transition using data from the D-configuration of the Very Large Array (VLA). We analysed data covering Galactic longitudes from $-2° < l < 60°$ and Galactic latitudes of $|b| < 1°$. We detected a total of 554 methanol masers, out of which 84 are new, and we catalogued their positions, velocity components, and integrated fluxes. With a typical noise level of ~18 mJy beam^{-1}, this is the most sensitive unbiased methanol survey for methanol masers to date. We also searched for dust continuum and radio continuum associations, finding that 97% of the sources are associated with dust and 12% are associated with radio continuum emission.

Key words. masers – surveys – ISM: molecules – radio continuum: ISM – radio lines: ISM – stars: formation

1. Introduction

The Global View on Star Formation (GLOSTAR) survey (Brunthaler et al. 2021) is an unbiased survey observing the Galactic plane with the *Karl G. Jansky* Very Large Array (VLA) in D- and B-configurations and the Effelsberg 100 m radio telescope in order to find and characterise star-forming regions in the Milky Way. Thanks to its sensitivity and high angular resolution, the data contain a wealth of information that has already been used to catalogue new radio sources (Medina et al. 2019), identify supernova remnants (SNR; Dokara et al. 2021), and find new methanol (CH_3OH) masers in the Cygnus X region (Ortiz-León et al. 2021).

In studying high-mass star formation (HMSF), methanol masers have proven to be indispensable. Interstellar methanol maser emission was first discovered by Barrett et al. (1971) at 25 GHz towards Orion-KL. Since then, many other methanol maser lines have since been discovered, such as those at 6.7 and 12.2 GHz (Batrla et al. 1987; Menten 1991b). These are divided into two types based on their pumping mechanism: collisional (Class I: Batrla et al. 1987; Cragg et al. 1992; Voronkov et al. 2010, 2014; Leurini et al. 2016) or radiative (Class II: Menten 1991a,b; Caswell et al. 2010). In particular, Class II CH_3OH masers have already proven to be one of the clearest signposts of HMSF, with the 6.7 GHz transition being the brightest and most widespread in the Galaxy (Menten 1991b, 1993; Walsh et al. 1997, 1998). Second only to the 22.2 GHz H_2O maser in its intensity and abundance, methanol maser emission at 6.7 GHz is unique in that it exclusively traces high-mass star forming regions (Minier et al. 2003; Ellingsen 2006; Xu et al. 2008). The 6.7 GHz line from the $5_1-6_0A^+$ transition of the methanol molecule requires specific conditions in order to begin masing. These are met in the surrounding dust and gas of massive young stellar objects (MYSOs) with densities greater than 10^6 cm^{-3} and temperatures > 150 K (e.g. Sobolev & Deguchi 1994; Cragg et al. 2005) due to the intense

* Full Tables 2 and 3 are only available at the CDS via anonymous ftp to cdsarc.u-strasbg.fr (130.79.128.5) or via http://cdsarc.u-strasbg.fr/viz-bin/cat/J/A+A/666/A59

** Member of the International Max Planck Research School (IMPRS) for Astronomy and Astrophysics at the Universities of Bonn and Cologne.

radiation of the MYSOs. While some of the earliest detections of Class II methanol masers were made toward ultra-compact HII regions, namely, the archetypical W3(OH) (Batrla et al. 1987; Menten et al. 1992), it was found that in fact very few of these methanol masers have radio continuum counterparts (Walsh et al. 1998; Beuther et al. 2002; Urquhart et al. 2013, 2015; Hu et al. 2016; Billington et al. 2019). It is thus clear that most 6.7 GHz methanol masers probe MYSOs located in regions of recent high-mass star formation. Locating and studying them can provide further insights into the distribution of these regions in the Galaxy and characterise their properties.

Given their usefulness in the study of high-mass star formation, many targeted surveys (e.g. Menten 1991b; MacLeod et al. 1992; Caswell et al. 1995; Caswell 1996; Ellingsen et al. 1996; van der Walt et al. 1996; Walsh et al. 1997; Ellingsen 2007; Yang et al. 2019b) and unbiased surveys (Rickert et al. 2019; Pestalozzi et al. 2005; Pandian et al. 2007; Caswell et al. 2010, 2011; Green et al. 2010, 2012; Breen et al. 2015; Ortiz-León et al. 2021) have been performed, culminating in over 1000 Class II 6.7 GHz methanol masers being discovered in our Milky Way Galaxy. However, with the technological upgrades to the VLA (Perley et al. 2011), the methanol data from the GLOSTAR survey provides the most sensitive and unbiased catalogue to date.

Here, we report on the detection of 554 6.7 GHz methanol masers in the region of $l = -2°$ to 60° and $|b| =< 1°$ (see Fig. 1 for survey coverage), with 84 of these representing new detections. We used an automated search algorithm to search and verify all detections manually. We looked for associations at other wavelengths to identify the physical properties of the population of sources with detected maser emission and the differences in these properties for newly detected sources with respect to the total population.

In addition to the part of the Galactic plane listed above, the Cygnus X star formation complex was also covered by the GLOSTAR survey. The 6.7 GHz methanol maser content of Cygnus X was discussed in a recent article by Ortiz-León et al. (2021).

We structure this paper as follows: in Sect. 2, we give a summary of the data used in this paper along with its calibration and imaging. Section 3 describes the algorithm used to detect masers in the VLA data. Section 4 details the production of our methanol maser catalogue and their general properties. Section 5 discusses our comparison with other surveys and associations with other wavelengths. We present our conclusions and summary in Sect. 6.

2. Observations

The GLOSTAR survey (Medina et al. 2019; Brunthaler et al. 2021) is an ongoing survey with the VLA and the Effelsberg 100 m telescope between 4–8 GHz of the Galactic mid-plane, from $-2° < l < 60°$ and $|b| < 1°$, and the Cygnus X star-forming complex. The VLA observations used in this work were conducted in D-configuration with a typical angular resolution of 18″ at 6.7 GHz. Using methanol, formaldehyde, and radio recombination lines as well as radio continuum data, the survey aims to detect various tracers of different stages of early star formation in order to gain information on the start of the stellar evolution process of massive stars. The full details can be found in Brunthaler et al. (2021). The observations used in this work were carried out using ~300 h during the time period from December 2011 until April 2017, where the program IDs and details are summarised in Table 1. Observations that were

Table 1. Summary of the VLA observations.

Observing date D-conf.	Galactic coverage	Program ID	Calibrator
2014-10-05 [a]	$-2° < l < -1°$; $\|b\| < 1.0°$	14B-254	J1820-2528
2014-09-26 [a]	$-1° < l < 0°$; $\|b\| < 1.0°$	14B-254	J1820-2528
2014-09-28 [a]	$0° < l < 1°$; $\|b\| < 1.0°$	14B-254	J1820-2528
2016-01-09 [a]	$1° < l < 2°$; $\|b\| < 1.0°$	15B-175	J1820-2528
2016-01-17 [a]	$2° < l < 3°$; $\|b\| < 1.0°$	15B-175	J1820-2528
2016-01-21 [a]	$3° < l < 4°$; $\|b\| < 1.0°$	15B-175	J1820-2528
2016-01-22 [a]	$4° < l < 5°$; $\|b\| < 1.0°$	15B-175	J1820-2528
2016-01-16 [a]	$5° < l < 6°$; $\|b\| < 1.0°$	15B-175	J1820-2528
2017-04-03	$6° < l < 7°$; $\|b\| < 1.0°$	17A-197	J1820-2528
2017-03-31	$7° < l < 8°$; $\|b\| < 1.0°$	17A-197	J1820-2528
2017-02-20	$8° < l < 9°$; $\|b\| < 1.0°$	17A-197	J1820-2528
2016-01-24 [a]	$9° < l < 10°$; $\|b\| < 1.0°$	15B-175	J1820-2528
2013-05-16 [a]	$10° < l < 11°$; $\|b\| < 1.0°$	13A-334	J1811-2055
2013-05-17	$11° < l < 12°$; $\|b\| < 1.0°$	13A-334	J1825-0737
2017-03-06	$12° < l < 13°$; $\|b\| < 1.0°$	17A-197	J1825-0737
2017-04-04	$13° < l < 14°$; $\|b\| < 1.0°$	17A-197	J1825-0737
2017-02-19	$14° < l < 15°$; $\|b\| < 1.0°$	17A-197	J1825-0737
2014-07-14	$15° < l < 16°$; $\|b\| < 1.0°$	14A-420	J1825-0737
2014-07-24	$16° < l < 17°$; $\|b\| < 1.0°$	14A-420	J1825-0737
2014-08-05	$17° < l < 18°$; $\|b\| < 1.0°$	14A-420	J1825-0737
2014-08-14	$18° < l < 19°$; $\|b\| < 1.0°$	14A-420	J1825-0737
2014-07-12	$19° < l < 20°$; $\|b\| < 1.0°$	14A-420	J1825-0737
2014-07-23	$20° < l < 21°$; $\|b\| < 1.0°$	14A-420	J1825-0737
2014-07-28	$21° < l < 22°$; $\|b\| < 1.0°$	14A-420	J1825-0737
2014-07-27	$22° < l < 23°$; $\|b\| < 1.0°$	14A-420	J1825-0737
2014-08-26	$23° < l < 24°$; $\|b\| < 1.0°$	14A-420	J1825-0737
2014-07-16	$24° < l < 25°$; $\|b\| < 1.0°$	14A-420	J1825-0737
2014-07-29	$25° < l < 26°$; $\|b\| < 1.0°$	14A-420	J1825-0737
2014-08-13	$26° < l < 27°$; $\|b\| < 1.0°$	14A-420	J1825-0737
2014-08-28	$27° < l < 28°$; $\|b\| < 1.0°$	14A-420	J1825-0737
2013-04-09	$28° < l < 29°$; $\|b\| < 1.0°$	13A-334	J1804+0101
2013-04-06	$29° < l < 30°$; $\|b\| < 1.0°$	13A-334	J1804+0101
2013-04-11	$30° < l < 31°$; $\|b\| < 1.0°$	13A-334	J1804+0101
2013-04-15	$31° < l < 32°$; $\|b\| < 1.0°$	13A-334	J1804+0101
2013-04-16	$32° < l < 33°$; $\|b\| < 1.0°$	13A-334	J1804+0101
2013-04-20	$33° < l < 34°$; $\|b\| < 1.0°$	13A-334	J1804+0101
2013-04-29	$34° < l < 35°$; $\|b\| < 1.0°$	13A-334	J1804+0101
2013-05-02	$35° < l < 36°$; $\|b\| < 1.0°$	13A-334	J1804+0101
2014-07-07	$36° < l < 37°$; $\|b\| < 1.0°$	14A-420	J1907+0127
2014-07-04	$37° < l < 38°$; $\|b\| < 1.0°$	14A-420	J1907+0127
2014-08-01	$38° < l < 39°$; $\|b\| < 1.0°$	14A-420	J1907+0127
2014-08-25	$39° < l < 40°$; $\|b\| < 1.0°$	14A-420	J1907+0127
2014-08-07	$40° < l < 41°$; $\|b\| < 1.0°$	14A-420	J1907+0127
2014-07-21	$41° < l < 42°$; $\|b\| < 1.0°$	14A-420	J1907+0127
2014-07-09	$42° < l < 43°$; $\|b\| < 1.0°$	14A-420	J1907+0127
2014-07-17	$43° < l < 44°$; $\|b\| < 1.0°$	14A-420	J1907+0127
2014-08-03	$44° < l < 45°$; $\|b\| < 1.0°$	14A-420	J1907+0127
2014-06-29	$45° < l < 46°$; $\|b\| < 1.0°$	14A-420	J1907+0127
2015-11-25	$46° < l < 47°$; $\|b\| < 1.0°$	15B-175	J1922+1530
2015-11-13	$47° < l < 48°$; $\|b\| < 1.0°$	15B-175	J1922+1530
2015-11-21	$48° < l < 49°$; $\|b\| < 1.0°$	15B-175	J1922+1530
2015-11-14	$49° < l < 50°$; $\|b\| < 1.0°$	15B-175	J1922+1530
2015-11-22	$50° < l < 51°$; $\|b\| < 1.0°$	15B-175	J1922+1530
2015-11-11	$51° < l < 52°$; $\|b\| < 1.0°$	15B-175	J1922+1530
2015-11-20	$52° < l < 53°$; $\|b\| < 1.0°$	15B-175	J1922+1530
2015-11-10	$53° < l < 54°$; $\|b\| < 1.0°$	15B-175	J1922+1530
2015-11-27	$54° < l < 55°$; $\|b\| < 1.0°$	15B-175	J1922+1530
2015-12-17	$55° < l < 56°$; $\|b\| < 1.0°$	15B-175	J1922+1530
2015-11-28	$56° < l < 57°$; $\|b\| < 1.0°$	15B-175	J1925+2106
2015-11-08	$57° < l < 58°$; $\|b\| < 1.0°$	15B-175	J1925+2106
2011-12-15	$58° < l < 59°$; $\|b\| < 1.0°$	11B-168	J1931+2243
2011-12-29	$59° < l < 60°$; $\|b\| < 1.0°$	11B-168	J1931+2243

Notes. [a]These observations were conducted with the VLA in DnC configuration.

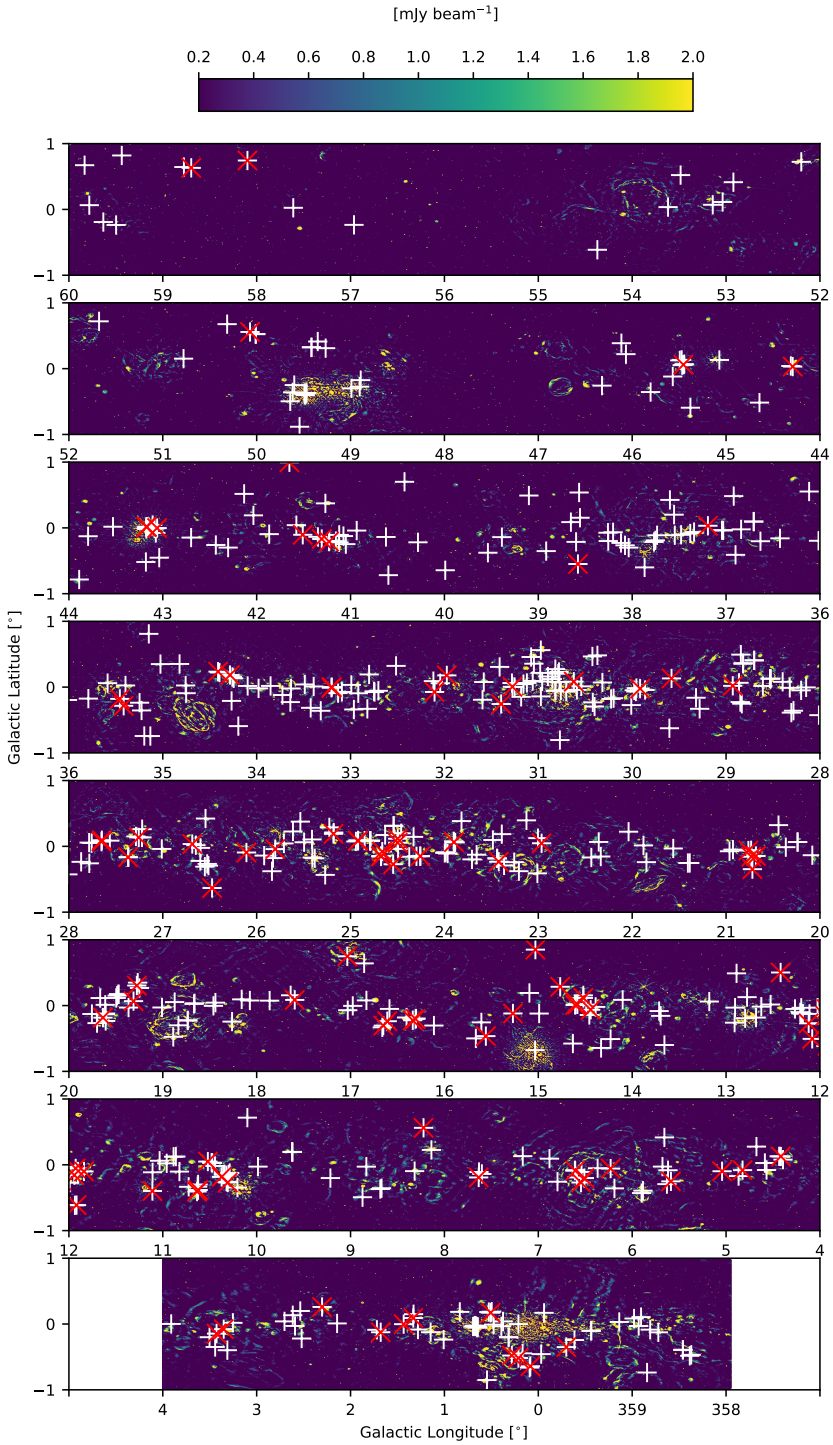

Fig. 1. Methanol maser detections plotted as white crosses on top of the D-configuration continuum images from GLOSTAR where the flux has been limited to be between 0.2 and 2 mJy beam^{-1} for visibility. The red "x"s show the positions of all new methanol masers as discussed in Sect. 4.5.

performed in the DnC hybrid configuration are marked in the table.

2.1. VLA data calibration

As detailed in Brunthaler et al. (2021), a modified version of the VLA scripted pipeline[1] (version 1.3.8) for CASA[2] (version 4.6.0) was adapted to work with spectral line data. We highlight the relevant changes here: no Hanning smoothing was performed on the first pass when producing the preliminary images to preserve the spectral resolution where possible; Hanning smoothing was performed on a select few sources after an initial inspection; the `rflag` flagging command was only applied to the calibration scans to avoid flagging spectral lines erroneously; `statwt` was not used to modify the statistical weights. The complex gain calibrators used for different fields include: J1804+0101, J1820-2528, J1811-2055, J1825-0737, J1907+0127, J1955+1530, J1925+2106, and J1931+2243, and the flux calibrators are 3C 286 and 3C48.

2.2. Spectral line data imaging

To process the spectral line data, we imaged it in two steps. We first produced a so-called "dirty" image (or unCLEANed), which is simply the direct Fourier transform of the *uv* data with the `tclean` task in CASA. We search these cubes for preliminary sources. We then properly carried out a `CLEAN` process on smaller sub-cubes centred on these sources to search for additional sources. This approach was chosen to address the computation limitations imposed by the sheer volume of data used. With the available computing resources at the time, it would take a month to produce a $2^\circ \times 1^\circ$ CLEANed data cube for the methanol data, where a dirty image would take only three days.

2.2.1. Imaging "dirty" cubes

Using the CASA task `tclean`, we were able to produce preliminary, mosaicked, and primary beam corrected images with the following task parameters: `niter`=0, a cube size (`imsize`) of 2500 × 2500 pixels, and a pixel size (`cell`) of 2.5″ for the D-configuration data. The number of channels (`nchan`) and the rest frequency (`restfreq`) were set to 1800 channels and 6668.518 MHz, respectively. We used a "natural" `weighting` parameter for better sensitivity in detecting sources. On average, the 1σ root-mean-square (rms) noise in the line free channels of the dirty cubes is found to be ∼18 mJy beam^{-1} for a single channel (0.18 km s^{-1}), which is better than the estimated noise for a single pointing of ∼40 mJy beam^{-1} based on a 15-s integration time. This is due to the mapping strategy where each field has been overlapped by six neighbouring fields, resulting in sensitivities that are at least a factor of two better. The achieved sensitivity is about a factor of 2 better than previous VLA targeted surveys (e.g. Hu et al. 2016). We were able to detect weak and isolated masers in the "dirty" image itself, which contributes to savings in computational time. Weak masers that are in the vicinity of strong masers and with similar velocity may be missed, but will be found in the next stage of our imaging approach.

2.2.2. Imaging of individual masers

In order to find weaker masers that are hidden in the side lobes of stronger masers, we used the `CLEAN` algorithm on small subsets of the data. We selected, on average, 16 pointings that cover the positions of sources detected from the "dirty" images. They were split out for further imaging and deconvolution to make smaller cubes (∼$0.2^\circ \times 0.2^\circ$, Δv ∼55 km s^{-1}). These sub-cubes were then imaged with a cell (pixel) size of 2.5″ and the imaging was restricted to the velocity ranges over which significant signal was detected. The sub-cubes have a spatial extent of 350 × 350 pixels and spectral extents of 300 channels centred on the peak velocity. Included at the beginning and end of the 300 channels, there are line free channels to estimate the spectral noise. For deconvolution, a `CLEAN`ing threshold of 38 mJy beam^{-1} was chosen (∼2σ of final cubes). Using the `tclean` task of CASA (version 5.4.0), the images were made with parameters: `gridder`="mosaic", `deconvolver`="hogbom", `weighting`="uniform", and a variable `niter`. The number of minor `CLEAN` cycles was set to either 1000, 5000 or 10 000 depending on the strength of the maser involved. These iteration values were found to optimize the automatic cleaning for many sources by maximizing image fidelity while avoiding over-cleaning. The weighting parameter was set to "uniform," since it gives a better angular resolution and thus more accurate positional information.

2.3. Complementary continuum data

In addition to the methanol line data, we also used GLOSTAR-VLA radio 5.8 GHz continuum data to search for associations with methanol masers. Radio sources such as ultra-compact HII regions (UCHII) are a clear indicator of HMSF, however, their relationship with methanol masers is not yet fully understood. Thus, a study of the associations and the physical properties of these sources may give valuable insights into the overall formation process of high-mass stars in this stage of their evolution. The full analysis of continuum maps in the D-configuration and B-configuration will be presented in forthcoming papers (Medina et al., in prep; Dzib et al., in prep.; Yang et al., in prep.), while the D-configuration continuum catalogue for the pilot region is already complete (Medina et al. 2019). We also make use of the Co-Ordinated Radio "N" Infrared Survey for High-mass star formation (CORNISH, Hoare et al. 2012; Purcell et al. 2013), which uses the VLA in the B and BnA-configuration at 5 GHz, to supplement our comparisons.

3. Source extraction

Here we give a technical description of the algorithm used for automatically selecting maser candidates from the "dirty" images. A description of the final catalogue is given in Sect. 4.1.

3.1. Source extraction code

As explained in Sect. 2.2, given the computational challenge of imaging and deconvolving large mosaics, we adopted an approach of searching for the methanol masers in the dirty images. We wrote a simple source extraction code (SEC; Murugeshan 2015; Nguyen 2015) to deal specifically with this data in a rapid manner. This SEC was written to detect methanol masers that have high brightness values in comparison to the surrounding noise. It was also adapted for absorption searches (see Brunthaler et al. 2021). It takes the "dirty" or fully `CLEAN`ed images as input. The code was first used on the "dirty" images to produce a preliminary catalogue of detections which were verified by visual inspection. The verified detections were `CLEAN`ed over a small spatial and spectral extent (see Sect. 2.2.2). The code

[1] https://science.nrao.edu/facilities/vla/data-processing/pipeline/scripted-pipeline
[2] https://casa.nrao.edu/

was then used again on these sub-cubes to find any other masers that were previously not detected on account of their proximity to stronger sources.

The code scans through the images, saving the coordinates where the brightness meets two criteria. The first and foremost is that the emission surpasses a certain signal-to-noise ratio (S/N) threshold. Secondly, we require that the emission is above this threshold for at least two consecutive channels. If these two criteria are satisfied, the code considers such a detection as real.

We selected a 50×50 pixel "box" to start. Beginning from the first channel, the root mean square (rms) of the box is calculated by the code. This is then chosen to be the noise within the box. Next, the code selects the pixel with the maximum flux. The ratio between the maximum flux and the rms of the box then defines the S/N. This is done iteratively for each channel within the boundaries of the 50×50 pixel box for the entire spectral extent of the given image. For a given channel, where the S/N is above a user-defined threshold, we check if it continues for at least another contiguous channel in order to satisfy our main criteria described above. If it also passes through three additional selection filters (defined below), it qualifies as a potential source. We then record the pixel coordinates, right ascension (RA), declination (DEC), channel range, peak flux, the associated channel of the peak flux, and the S/N. The code moves onto the next spatial box and repeats the search along the spectral axis. After its completion, a catalogue of the potential sources is produced. As a final check, we always verify each source visually. A flow diagram illustrating the algorithm is presented in the top of Fig. 2 and an illustration of the physical movements of the search algorithm is shown in the bottom. In order to reduce false detections and repeated detections, we describe the aforementioned filters used to improve the quality of detections:

First filter (F1). This filter checks if the current potential detection is within 200 pixels from the previous detection and also appears in the same channel range. If these conditions are met, it checks if the S/N of current detection is greater than the previous detection. If this is the case, the current detection is updated as the true detection and its coordinates kept as a reference.

Second filter (F2). The next filter checks if the current detection is within 200 pixels of the previous detection, but appears in a different channel range. Since side lobe artefacts appear in the same channel range as the source, we consider the detection a potential source if the channel ranges are different. This helps to differentiate multiple sources within the same box.

Third filter (F3). The final filter checks if the current detection is more than 200 pixels away from any previous detection. An angular separation of 200 pixels (~8.3′) is chosen as typically this is the largest extent of any side lobe feature. If this criterion is met, the code selects the pixel as a potential source.

We chose a S/N value of 6 when searching through the "dirty" images. This choice is based on the general statistics of the cube in order to balance dismissing artefacts as well as picking up weak sources. For the `CLEAN`ed sub-cubes, we used a lower S/N value of 4 as it was found to be the most efficient in detecting the generally weaker sources that were initially hidden in the side lobes of the nearby stronger sources.

Since the algorithm picks out just one maximum in a given box, it is possible that real but weaker sources are missed if they lie in the same box. It was found that a box size of 50 pixels (corresponding to ~2′ ; in comparison, the primary beam of the VLA at 6.7 GHz is 6.5′) substantially minimizes the run time without losing too many additional sources. Furthermore, because we are using a "dirty" image, there are noisy structures in the neighbourhood of strong sources. In the direct vicinity of a potential strong source, the code will reliably pick out the pixel coordinates of the real source as side lobe features will never have a higher flux than the actual source. The spillage of side lobe features into adjacent boxes is mitigated by the utilisation of the filters defined above.

Given the simple nature of the algorithm, the code can be easily parallelized. The parallelization is done by splitting the

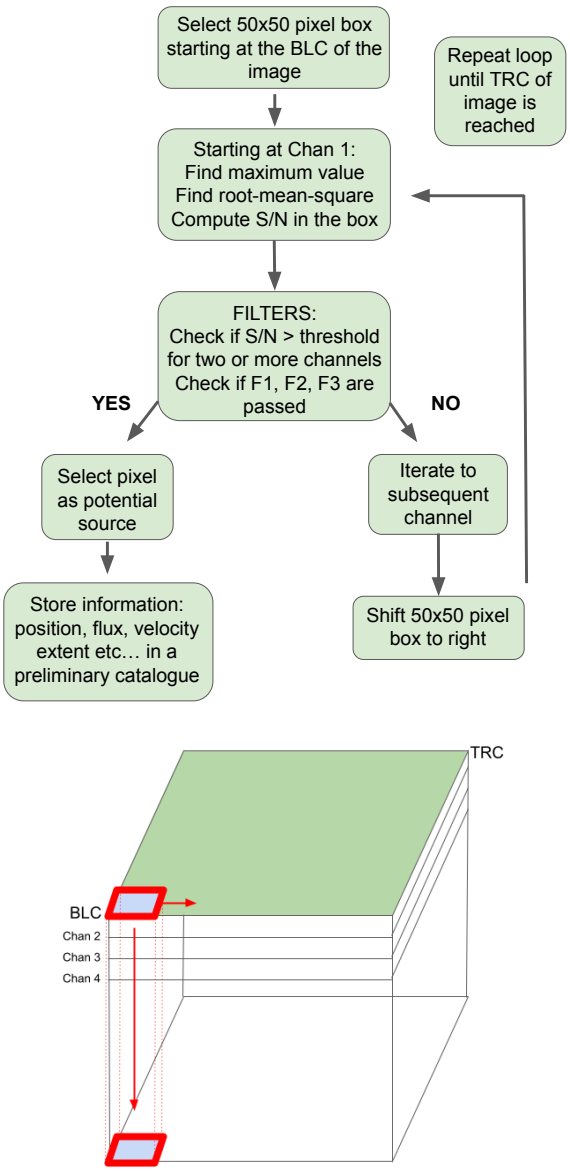

Fig. 2. Algorithm flow chart for the Source Extraction Code (SEC) which details the selection of the positions and channels of maser candidates based on the signal-to-noise ratio S/N (*top panel*; for details, see Sect. 3). Illustration of the process used by the SEC (*bottom panel*). A 50×50 pixel box that starts from the bottom left corner (BLC) iterates first through channels to detect sources until it reaches the top right corner (TRC).

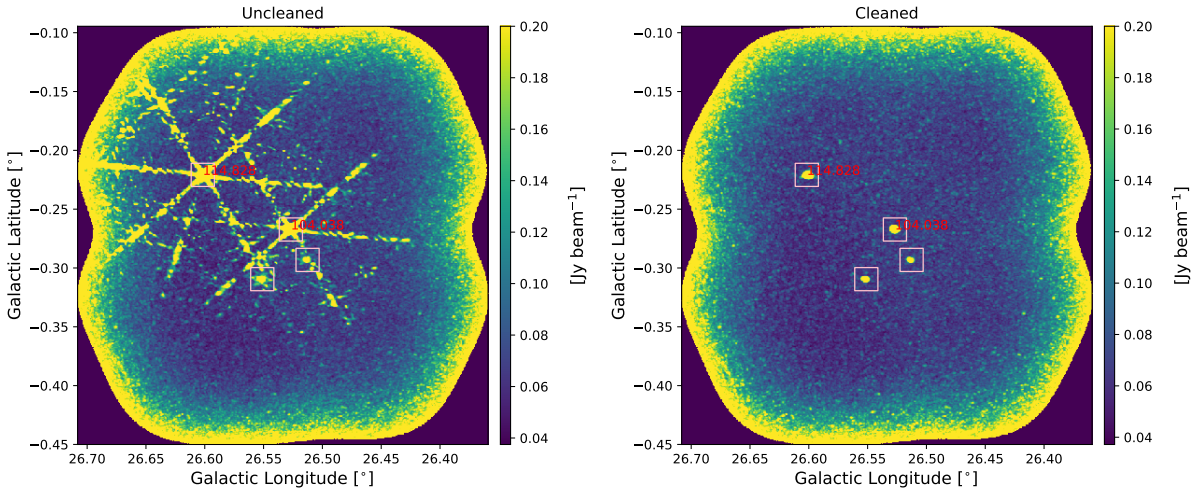

Fig. 3. Example of the Source Extraction Code (SEC) on unCLEANed and CLEANed data sub-cubes. *Left*: example peak intensity map of a dirty sub-cube towards $l = 26.5270$ deg, $b = -0.2674$ deg which is an example of the data used when making preliminary detection catalogues with our SEC. Velocities of known sources are shown in red text, while pink squares highlight the final source detections. In this "dirty" image, the bottom two sources would not have been detected. *Right*: once we CLEAN the image, we can see how the two bottom sources would indeed be detected by our SEC and, as such, illustrates how running the SEC again on the cleaned sub-cubes can lead to new detections.

spatial extent of the image into smaller patches. The code is then run individually on each of these patches. Each process creates its own search catalogue, which is then combined when all processes are finished. For a strong source, side lobe artefacts can spill over onto the next patch and be picked up in a different catalogue. We resolve this through a visual verification.

3.2. Catalogue creation

After performing the initial pass with the SEC on the "dirty" images, we carried out a cross-check with all known masers in the survey range in case there are weaker known sources that do not pass our initial noise threshold criterion. We further inspected all the potential SEC detections, looking at their spectra and moment maps. We examined the positions, velocities, and intensities of the detections to decide which SEC candidates are to be considered real. We visually checked for any velocity features that have very large offsets from other velocity features along the line of sight to also be considered as a new maser. From this, we compile a list of candidates for further cleaning.

For these maser candidates, we made smaller CLEAN images (as described in Sect. 2.2). We ran our SEC code with modified settings (box size of 5 pixels and no filters) in order to pick up weaker sources that would have been hidden by a nearby strong source. We visually inspected each cube at the end to ensure that we picked up all possible masers in the data. In Fig. 3, we give an example of two new methanol maser detections that were not found in the 'dirty' image cube due to the presence of nearby strong sources.

From this final visual inspection, we compiled a final list of detections. As we were interested in determining the methanol masers' properties, we performed a 2D Gaussian fit of the brightness distribution in each channel whose peak intensity is above 4σ. We used the CASA task `imfit` on a 14×14 pixel box ($\sim 2\times$ the restoring beam), which is centred on the pixel with maximum intensity. As discussed in Ortiz-León et al. (2021), the error in maser position is determined by the astrometric uncertainty $\theta_{\rm res}/(2\times{\rm S/N})$, where $\theta_{\rm res}$ is the (VLA) restoring beam, and S/N is the ratio between source intensity and rms (Thompson et al. 2017). Given that the average beam size in the D-configuration methanol maps across the whole Galactic plane is 15″, and a maser detection with S/N=10, the precision in position is $\approx 0\farcs7$. We further discuss the reliability of our position measurements in Sect. 4.5. We visually verified the result of the source fits and determined the peaks of each maser site. We refer to each velocity peak as a maser spot inside one maser site (Walsh et al. 2014). A few examples of these, including new maser sites, are listed in Table 2, while the complete catalogue can be found at the CDS. The positions for all emission channels of a given maser site are given as an offset to the position of the maser spot with the strongest emission within the maser site.

4. Results

4.1. Detections

We detected a total of 554 CH_3OH maser emission and 6 cases of methanol absorption in the range of GLOSTAR survey coverage ($-2° < l < 60°$, $|b| \leq 1°$; see Ortiz-León et al. 2021 for the 13 masers found in the Cygnus X region, or the CDS table for all 567 GLOSTAR masers). Of these detections, we have determined 84 ($\sim$15%) of them to be new detections. As we require that for a source to be detected, a minimum of two adjacent channels must meet our S/N threshold, our estimated completeness level may be higher than the 4σ noise level. We overlay the detections on top of the GLOSTAR D-configuration continuum emission in Fig. 1 and display their spatial distributions in Figs. 4 and 5. We note that within the GLOSTAR Galactic longitude range, the CH_3OH 6.7 GHz maser source distribution seems to peak towards $l = 30°$, which is not surprising given the multiple crossings of spiral arms of the Milky Way, as is evident from Fig. 6. The distribution in Galactic latitude is presented in Fig. 5, which shows that the majority of sources are in the range of $|b| \leq 0.5°$.

Table 2. Properties of methanol maser spots from D-configuration maps for a selection of sources.

Name	$\alpha/\Delta\alpha$ (h:m:s/″)	$\delta/\Delta\delta$ (d:m:s/″)	$V_{\rm LSR}$ (km s^{-1})	$S_{v,\rm Peak}$ (Jy beam^{-1})	$S_{v,\rm Int}$ (Jy)	Notes
(1)	(2)	(3)	(4)	(5)	(6)	(7)
G35.2260–0.3544	18:56:53.2332	+01:52:47.068	59.49	0.38 ± 0.02	0.39 ± 0.04	YANG19
G35.2260–0.3544	–0.17	–0.34	59.13	0.12 ± 0.02	0.16 ± 0.04	
G35.2260–0.3544	0.27	0.03	59.31	0.20 ± 0.02	0.19 ± 0.03	
G35.2260–0.3544	1.32	0.84	59.67	0.14 ± 0.02	0.23 ± 0.04	
G35.2476–0.2365	18:56:30.3917	+01:57:08.664	72.25	1.40 ± 0.02	1.47 ± 0.03	MMB
G35.2476–0.2365	–1.30	1.68	71.53	0.12 ± 0.02	0.14 ± 0.03	
G35.2476–0.2365	–0.91	–0.42	71.89	0.08 ± 0.02	0.10 ± 0.03	
G35.2476–0.2365	0.12	0.16	72.43	1.34 ± 0.02	1.33 ± 0.04	
G35.2476–0.2365	2.08	1.03	72.79	0.10 ± 0.02	0.22 ± 0.05	
G35.3974+0.0252	18:55:50.7873	+02:12:18.699	89.07	0.36 ± 0.01	0.36 ± 0.02	MMB
G35.3974+0.0252	–2.04	–2.05	88.89	0.12 ± 0.01	0.15 ± 0.03	
G35.3974+0.0252	–0.29	0.39	89.25	0.27 ± 0.02	0.32 ± 0.03	
G35.3974+0.0252	0.76	–0.28	89.43	0.19 ± 0.02	0.25 ± 0.04	
G35.3974+0.0252	0.76	–0.50	89.61	0.11 ± 0.02	0.14 ± 0.04	
G35.4166–0.2839	18:56:59.0536	+02:04:54.463	56.11	1.67 ± 0.02	1.69 ± 0.03	NEW
G35.4166–0.2839	–0.05	–0.49	55.75	0.21 ± 0.01	0.23 ± 0.02	
G35.4166–0.2839	0.00	–0.02	55.93	0.73 ± 0.01	0.72 ± 0.03	
G35.4166–0.2839	0.17	–0.07	56.29	1.35 ± 0.02	1.35 ± 0.03	
G35.4166–0.2839	–0.04	-0.20	56.47	0.48 ± 0.02	0.55 ± 0.04	
G35.4571–0.1782	18:56:41.0152	+02:09:57.411	56.11	0.26 ± 0.02	0.31 ± 0.05	NEW
G35.4571–0.1782	–1.16	0.92	54.67	0.12 ± 0.02	0.21 ± 0.04	
G35.4571–0.1782	–0.08	–0.11	54.85	0.19 ± 0.02	0.30 ± 0.05	
G35.4571–0.1782	–1.41	–2.16	55.21	0.09 ± 0.01	0.17 ± 0.04	
G35.4571–0.1782	1.16	0.48	55.39	0.11 ± 0.01	0.09 ± 0.02	
G35.4571–0.1782	–0.66	0.20	55.57	0.24 ± 0.02	0.32 ± 0.04	
G35.4571–0.1782	–1.01	0.30	55.75	0.20 ± 0.02	0.21 ± 0.04	
G35.4571–0.1782	–2.15	–0.36	55.93	0.23 ± 0.02	0.27 ± 0.04	
G35.4571–0.1782	–0.45	–0.46	56.29	0.17 ± 0.02	0.21 ± 0.04	
G35.4571–0.1782	–2.15	–2.03	56.65	0.12 ± 0.02	0.18 ± 0.04	

Notes. Column (1) gives the GLOSTAR source name based on the GLOSTAR Galactic coordinates. Columns (2) and (3) are the GLOSTAR equatorial coordinates of the position of the maser velocity component with the highest intensity. For sources with multiple components, we list their position offsets with respect to the component with the highest intensity. The position uncertainties are ∼1.1″ (see Sect. 4.5). Column (4) gives the LSR radial velocity of the peak of the component. Columns (5) and (6) give the peak and integrated fluxes at the peak velocity, given by Col. (4). Column (7): Source references.

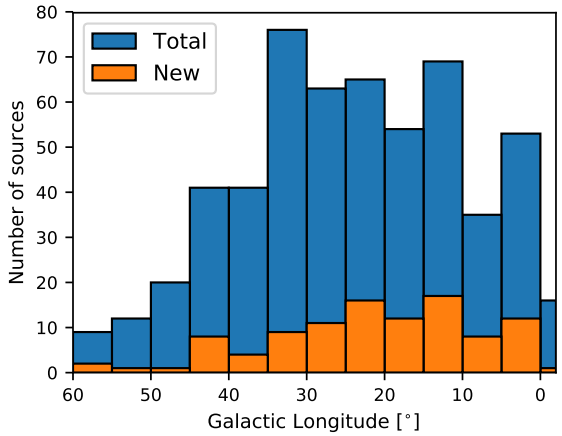

Fig. 4. Distribution of detected masers along Galactic longitude. The bin width used is 5° from l = 60° to 0° and 2° for the last bin.

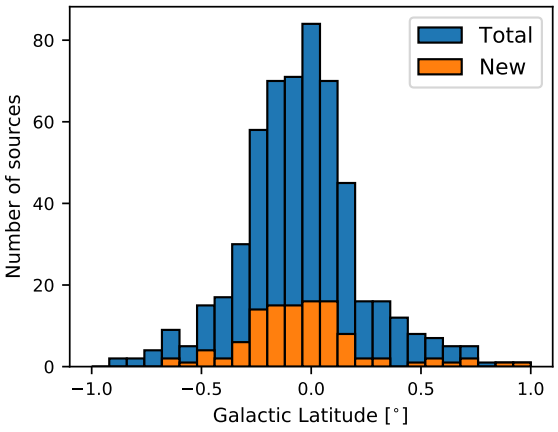

Fig. 5. Distribution of detected masers along Galactic latitude. The bin width used is 0.08°.

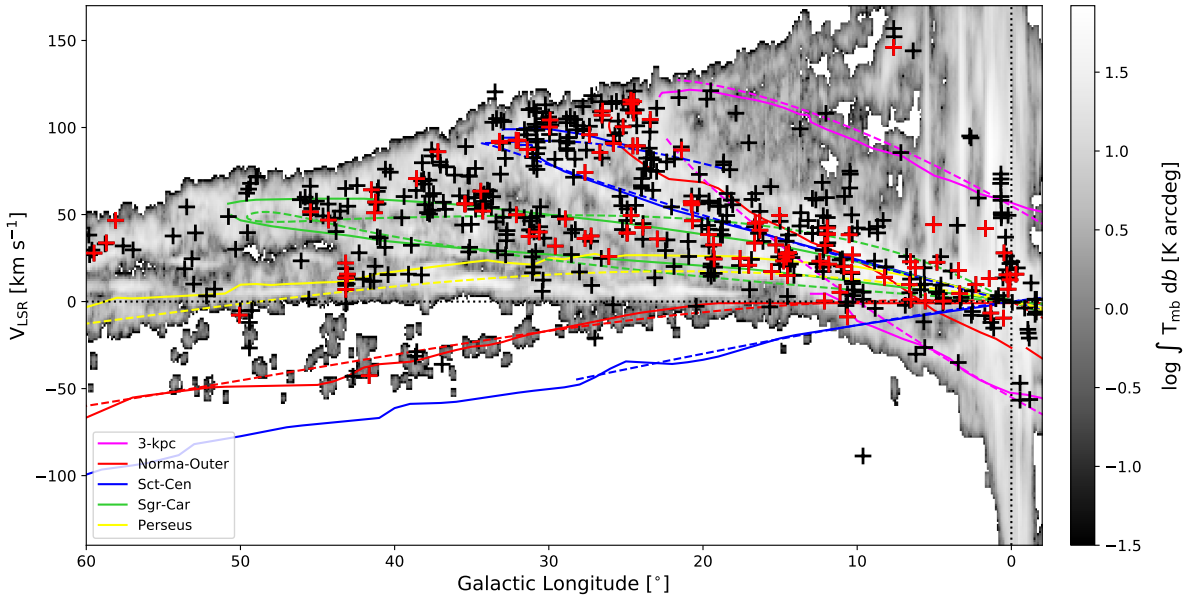

Fig. 6. Distribution of detected 6.7 GHz methanol maser velocity with respect to Galactic longitude. Black crosses represent detections of known sources in the GLOSTAR survey and red crosses represent new detections. The coloured spiral arms are as follows: magenta is 3 kpc, red is Norma-Outer, blue is Scutum Centaurus, green is Sagittarius Carina, and yellow is Perseus. The dashed lines represent the updated spiral arm models of Taylor & Cordes (1993) as used in, e.g. Schuller et al. (2021) while the solid lines are the spiral arm descriptions from Reid et al. (2019). The background shows the CO emission from Dame et al. (2001).

The properties of a few example detections are listed in Table 2, and we refer to the catalogue at the CDS for the full list of detections. We identify each maser source by its galactic coordinates. The equatorial coordinates for the maser spot with the highest peak flux, which is the main velocity component, is given while the remaining maser spots (if any) are given as an offset to this main maser spot. The velocity of each maser spot as well as its peak flux and integrated flux are listed in the table. The fluxes were determined using 2D Gaussian fitting (see Sect. 3.2). Additionally, we report in the online catalogues every velocity channel where emission was detected above the 4σ level for a given maser.

4.2. Flux densities

The brightest 6.7 GHz CH_3OH maser that we detected is the well-known example of G9.6213+0.1961, with a peak flux density of ~5700 Jy. This source is known not only as the methanol maser that reaches the highest flux density, but also, given its distance of 5.2 kpc, it has the highest line luminosity (Sanna et al. 2015). Conversely, the weakest maser we detect is the source G25.1772+0.2111 with a peak flux density of ~0.09 Jy. For the newly detected masers, the fluxes range from 0.16 Jy to 5.4 Jy. The median peak flux density of the newly detected masers is 0.47 Jy. The surface density of new detections across the survey coverage is ~0.8 masers per sq. degree. We detected a total of 80 masers above 20 Jy, none of which are new detections.

4.3. Distance determination

To calculate the luminosity of a maser source, the distance information is required. This can be obtained from the peak velocity of the maser and comparing it to a Galactic rotation curve. However, there is an inherent kinematic distance ambiguity that affects all sources within the Solar Circle (see Roman-Duval et al. 2009 for an overview). To resolve this, we used the distances obtained from associated ATLASGAL 870 µm emission sources (Schuller et al. 2009) from the compact source catalogue (Urquhart et al. 2018, 2022) as they have been individually checked for HI self-absorption. However, not every maser source has a dust clump association from ATLASGAL and in these cases, we used the Bayesian distance estimator from Reid et al. (2019) to help resolve the kinematic distance ambiguity. We show the distribution of our maser sample overlaid on an artist's impression of the Milky Way[3] in Fig. 7. We note that this method is biased to the location of the spiral arms, which can be seen by its very smooth distribution along curves.

4.4. Luminosity

The luminosity is estimated across all the velocity channels in which we have emission of $>4\sigma$. In this way, we used the line flux, that is, the velocity integrated flux density, $S_{\rm Int}$ in units of Jy km s^{-1} to determine the luminosity:

$$L_{\rm maser} = 4\pi D^2 S_{\rm Int} f/c, \quad (1)$$

where D is the heliocentric distance to the source, f is the rest frequency of the maser line ($5_1 - 6_0A^+$, 6668.5192 MHz), and c is the speed of light. The total velocity covered, $\Delta V_{\rm D}$, the estimated distance, the velocity integrated flux density, $S_{\rm Int}$, and the final isotropic maser luminosity, $L_{\rm maser}$, are listed for a few example sources in Table 3 and the rest are listed in a catalogue at the CDS. As mentioned by previous studies (Breen et al. 2011; Billington et al. 2019; Ortiz-León et al. 2021), a positive trend

[3] https://photojournal.jpl.nasa.gov/catalog/PIA19341

Table 3. Estimated distances and maser luminosities from D-configuration maps for the maser sources listed in Table 2.

Name (glon, glat) (1)	ΔV_D (km s^{-1}) (2)	Dist. (kpc) (3)	Note (4)	S_{Int} (Jy km s^{-1}) (5)	$L_{maser,D}$ ($L_\odot$) (6)
G35.2260–0.3544	0.72	9.43 ± 0.36	B	0.96 ± 0.07	5.8×10^{-7}
G35.2476–0.2365	0.90	4.84 ± 0.61	B	3.26 ± 0.08	5.2×10^{-7}
G35.3974+0.0252	0.90	5.90 ± 0.54	A	1.22 ± 0.07	2.86×10^{-7}
G35.4166–0.2839	0.90	3.20 ± 0.37	A	4.53 ± 0.07	3.13×10^{-7}
G35.4571–0.1782	1.80	4.10 ± 0.38	A	2.27 ± 0.13	2.58×10^{-7}

Notes. Refer to the online table for a complete list of sources. Column (1) is the GLOSTAR source name. Column (2) gives the total velocity extent of maser emission above the local 4σ level. Column (3) gives the distance obtained from the Bayesian distance estimator (Reid et al. 2019) or from the ATLASGAL compact source catalogue (CSC) (Urquhart et al. 2018, 2022) as marked in Col. (4) with a B or A respectively. Columns (5) and (6) give the maser integrated flux and luminosity, respectively.

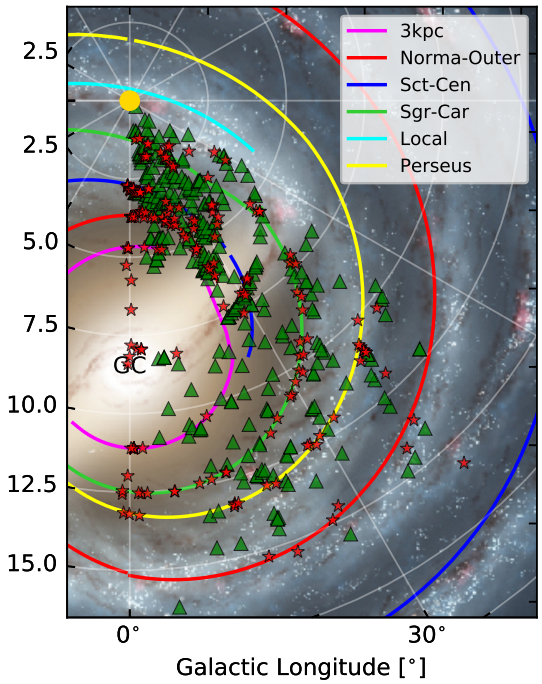

Fig. 7. Distances of 6.7 GHz methanol masers from GLOSTAR D-configuration VLA observations plotted on top an artist's rendition of the Milky Way. We used the distance estimator (Reid et al. 2019) to assign the near or far distance to a source (red stars) except for maser sources with an ATLASGAL dust clump association, for which we used the reported distance from Urquhart et al. (2018, 2022), shown as a green triangle.

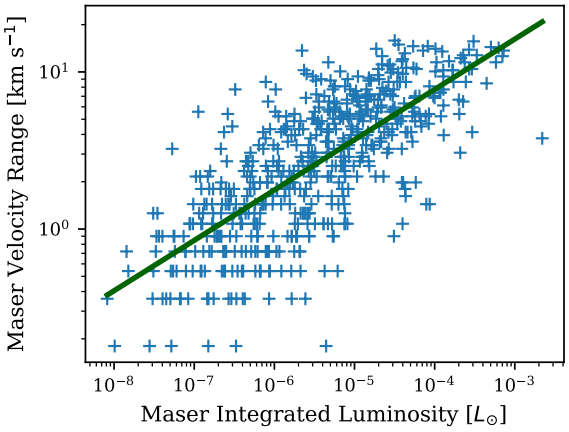

Fig. 8. Total velocity range of maser emission vs. integrated maser luminosity as blue crosses. Here, we see a positive trend. The green line represents a power law fit to the data with an exponent of 0.32 ± 0.01. A Spearman correlation test yields a rank coefficient of $r = 0.74$ and p-value $\ll 0.0013$, which indicates a positive correlation and is consistent with previous studies using a smaller sample (e.g. Ortiz-León et al. 2021).

between the total velocity width, ΔV_D, of a maser source and its maser luminosity is shown in Fig. 8. Given that we can take the velocity range of a maser as a proxy for line complexity, that is, for many components, it might naively be expected that stronger sources are more complex. However, it could also be that for weaker sources, there may be other velocity components, however, if these components do not meet the S/N threshold, they are thus not considered. We have fit a power law in the form of $\Delta V_D \propto L_{maser}^{\alpha}$ to the relation and found $\alpha = 0.32 \pm 0.01$, which supports the positive trend we see (a Spearman correlation test yields a coefficient $r = 0.74$ and p-value $\ll 0.0013$, which strongly supports the correlation).

4.5. Comparison with other maser surveys

The Arecibo Methanol Maser Galactic Plane Survey (AMMGPS, Pandian et al. 2007), using the 305 m Arecibo radio telescope to cover the ranges of $35.2° \leq l \leq 53.7°$ and $|b| \leq 0.41°$, detected 86 masers. The survey has an rms noise level of ~85 mJy in each spectral channel after Hanning smoothing and averaging both polarizations. Of these masers, only G35.374+0.018 at 96.9 km s^{-1} and G36.952–0.245 at 61.7 km s^{-1} were not detected by our survey. This may be due to the time variability of methanol masers, making these sources candidates for long term observations.

The Methanol Multibeam (MMB) survey (Green et al. 2009) is a comprehensive, unbiased survey that covers a large portion of the Galactic plane, ranging from $186° \leq l \leq 60°$ and $|b| < 2°$.

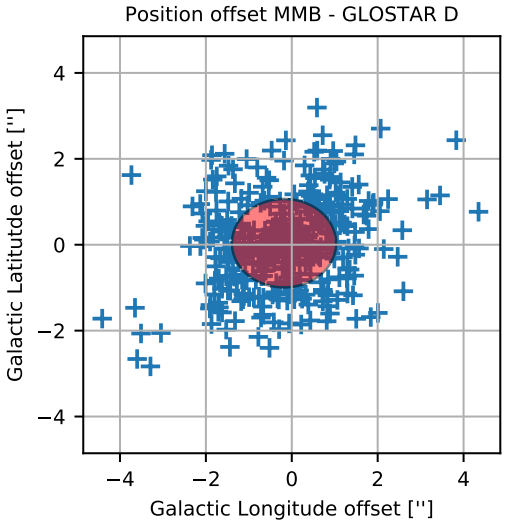

Fig. 9. Comparison of the positions of matching MMB and GLOSTAR methanol maser sources. The red shaded ellipse is centred on the mean offsets of $\delta l = -0.18$ arcsec, and $\delta b = 0.04$ arcsec. It shows the half-axes standard deviations in Galactic Longitude and Latitude, which are 1.21 arcsec and 1.03 arcsec, respectively.

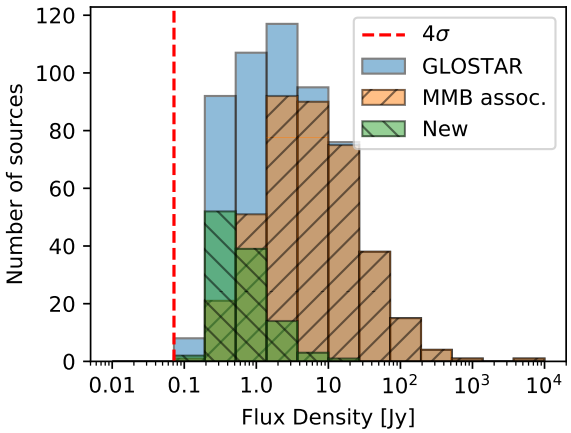

Fig. 10. Flux distribution of detected masers. The vertical dashed red line corresponds to the average 4σ noise level for the methanol D-configuration data (~70 mJy beam^{-1}). We show the full set of GLOSTAR fluxes, as well as the subset with MMB associations, and all new detections. As expected, the bulk of the new detections peaks at lower flux densities.

It uses the Parkes 64 m radio telescope to make preliminary detections which are followed up on using the higher resolution interfermometers: Australia Telescope Compact Array (ATCA) or Multi-Element Radio Linked Interferometer Network (MERLIN, Thomasson 1986) to improve the accuracy in their reported positions to be better than <1″. The survey sensitivity is ~0.2 Jy. Of the ~1000 sources in their complete catalogue (Caswell et al. 2010, 2011; Green et al. 2010, 2012; Breen et al. 2015), 404 lie within the GLOSTAR data presented here. Of these, 394 were detected in our survey. As GLOSTAR is an unbiased survey, it is useful to compare the catalogues resulting from these surveys.

To augment our comparison, we also used the Yang et al. (2019b) catalogue of 6.7 GHz CH_3OH masers that were obtained through a targeted search towards sources from the Wide Field Infrared Survey Explorer (WISE) point source catalogue using the 65 m Shanghai Tianama Radio Telescope (TMRT). These surveys were used to help in the identification of our SEC detections (presented in Sect. 3) where weak sources that were close to the 4σ threshold were conclusively kept as a detection given matching coordinates and velocities. This resulted in 113 detections that were not detected by Yang et al. (2019b). There are some masers from Yang et al. (2019b) that were undetected in the GLOSTAR survey, with the majority having fluxes below our sensitivity limit. While the sensitivity of the observations done by Yang et al. (2019b) with the TMRT is 1.5 Jy K^{-1}, their catalogue also includes weaker masers that were previously included in the literature.

We carried out a final check with the webtool, Maserdb[4] (Ladeyschikov et al. 2019), which is an online collection of catalogues of many maser species (e.g. OH, H_2O). We find that our catalogue has 84 new 6.7 GHz CH_3OH maser emission sources (see Fig. 1).

Next, we compared the GLOSTAR and the MMB positions. In Fig. 9, we show the position offsets to the GLOSTAR D-configuration detections. The mean offsets are $\delta l = -0.18 \pm 1.21$ arcsec and $\delta b = 0.04 \pm 1.03$ arcsec. This indicates that there are no systematic offsets in the astrometry with respect to the MMB catalogue. However, the standard deviation of the offsets suggests that the astrometric uncertainty is closer to ~1.1 arcseconds, which is slightly higher than the statistical uncertainties of 0.7″ determined for a 10σ detection.

We show in Fig. 10 the flux distributions of the GLOSTAR methanol maser detections. We highlight the subset of sources that have a MMB counterpart as well as the subset of new sources. In comparison with the MMB catalogue, we directly see that our increased sensitivity finds new, weaker sources. However, there are 74 sources above the survey cube detection threshold of 0.7 Jy that we would have expected to be detected by the MMB. There are several possible reasons for this. Given that these observations were taken years apart, it could be the result of variability, making these sources possible candidates for long term observations. Furthermore, close to 30 of these sources are situated near bright sources and as such, they were not able to be initially resolved by the MMB in their blind survey. Examples of these are shown in Appendix A.

For masers with counterparts in both surveys, we compared the peak fluxes in Fig. 11. The fluxes do not show a systematic difference. G9.6211+0.1956 is already known to be a periodic Class II CH_3OH maser with a period of ~244 days (e.g. Goedhart et al. 2007; van der Walt et al. 2009)[5]. We detected two main velocity components for this source at the known velocity of 1.3 km s^{-1} and at a new velocity of −88.7 km s^{-1}. Given the large difference in velocity, we consider these to be distinct entries in our catalogue. Both of these spatially coincide with the known MMB maser at the same position. The component at 1.3 km s^{-1} has a high peak flux density of >5700 Jy beam^{-1} in both the GLOSTAR and the MMB

[4] maserdb.net

[5] In periodic methanol masers, certain velocity components show periodic variability with a wide range of periods, ranging from 20 to >500 days. As discussed in a future publication, the several epochs at which the GLOSTAR data were taken and comparison with MMB spectra will lead to the detection of new candidates of these interesting sources (e.g. Goedhart et al. 2018, and references therein).

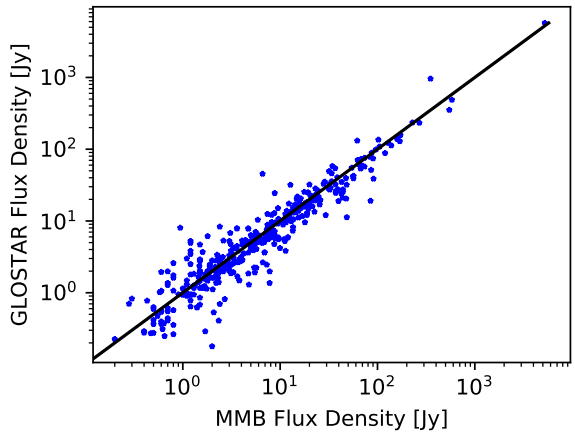

Fig. 11. Comparison of GLOSTAR vs. MMB peak flux densities for masers detected in both surveys. The black line indicates the 1:1 equality line. Red circles denote sources for which the percent difference was greater than 50%.

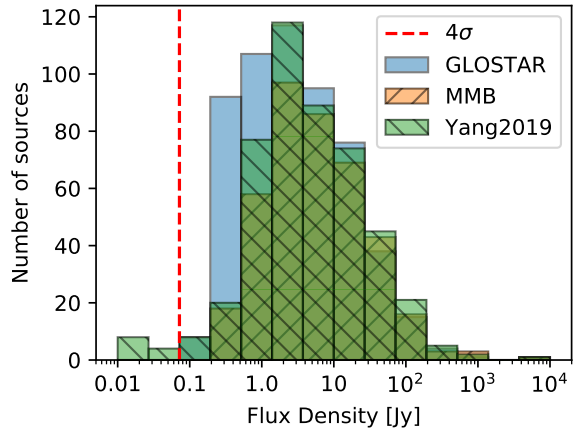

Fig. 12. Flux distribution of masers as reported in the GLOSTAR, the MMB (Green et al. 2009) and the Yang et al. (2019b) catalogues. The vertical dashed red line corresponds to the average 4σ noise level for the GLOSTAR methanol D-configuration data (~70 mJy beam^{-1}). The sources of the other surveys that were not detected in the GLOSTAR survey are well below the sensitivity level of our unbiased search.

spectra with a matching velocity, which corresponds to the velocity of the host source. As such we consider this the true association for the following analysis. The component at the velocity of −88.7 km s^{-1} is much weaker with a peak flux density ~1 Jy beam^{-1}. Emission at this velocity seems to not yet have been detected towards this source and deserves further study.

In Fig. 12, we compare the flux distributions between the GLOSTAR, MMB, and Yang et al. (2019b) catalogues for masers within the GLOSTAR survey coverage. It is evident that there are masers below our detection threshold that were not detected. The detection comparison between the three maser surveys is shown in Fig. 13 and details how many masers have been detected by each survey and their overlap. There are 44 sources that we did not detect, but that were detected by Yang et al. (2019b) or by both Yang et al. (2019b) and the MMB. Of these, 14 have reported fluxes below our sensitivity limit. Variability may also

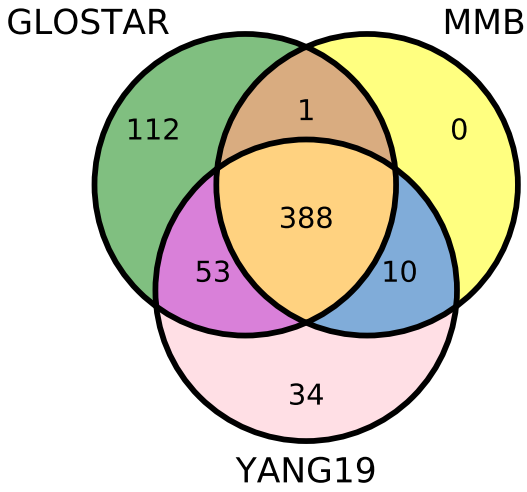

Fig. 13. Venn diagram presenting the overlap between the GLOSTAR methanol maser catalogue, the MMB (Green et al. 2009) and the Yang et al. (2019b) catalogues over the same region as GLOSTAR. We detected 112 masers that had not been detected by the MMB or the Yang et al. (2019b) catalogues, while we did not detect 44 known masers.

account for some of the other non-detections, however, long term observations would be needed to confirm this nature of maser activity. We also see that while there are some known masers that we do not detect, the majority of our new detections are in the lower flux bins as expected.

4.6. Absorption detections

While detections of the 6.7 GHz $5_1 - 6_0A^+$ CH_3OH line are widespread, the absorption detections are comparatively more sparse. Only a few studies have confirmed the 6.7 GHz line in absorption thus far (e.g. Menten 1991b; Pandian et al. 2008; Impellizzeri et al. 2008; Ortiz-León et al. 2021; Yang et al. 2022). Absorption in this line can occur towards radio continuum emission and the cosmic microwave background (CMB). In conjunction with maser emission detections, we are also sensitive enough to detect absorption features and indeed we find a few absorption sources (listed in Table 4), where an example is shown in Fig. 14. A systematic search had not yet been performed and thus a comprehensive list of all absorption detections is not presented in this work. An in-depth analysis of the absorption sources detected in the GLOSTAR data will be performed in a future work, for which we will use the complete GLOSTAR D-configuration continuum source catalogue (Medina et al., in prep.) to check for methanol in absorption.

5. Discussion

5.1. Association with ATLASGAL sources

Methanol masers are known tracers of star formation and the Class II 6.7 GHz methanol maser is thought to exclusively trace the early stages of HMSF (Minier et al. 2003; Ellingsen 2006; Xu et al. 2008). Recently, Billington et al. (2019) used the MMB and ATLASGAL surveys to do a comprehensive study on the physical environments of the regions these masers originate from. They used newly available distances and luminosities to compare with the clump properties as determined in ATLASGAL and JPS

Table 4. Examples of absorption features detected.

Common name	α (h:m:s)	δ (d:m:s)	$v_{\rm Peak}$ (km s^{-1})	$S_{\rm Peak}$ (Jy beam^{-1})
Sgr B2	17:47:18.71	–28:22:53.54	70.4	–2.0
G08.67-0.36	18:06:19.02	–21:37:30.29	35.6	–0.2
G10.62-0.38	18:10:28.62	–19:55:48.40	–1.3	–0.4
G012.81-0.20	18:14:13.95	–17:55:38.31	36.0	–1.6
G34.26+0.16	18:53:18.03	01:15:00.09	59.7	–0.2
W49	19:10:12.97	09:06:10.98	12.55	–0.3

Notes. The source is listed with equatorial coordinates (J2000), the peak velocity feature, and the peak flux density.

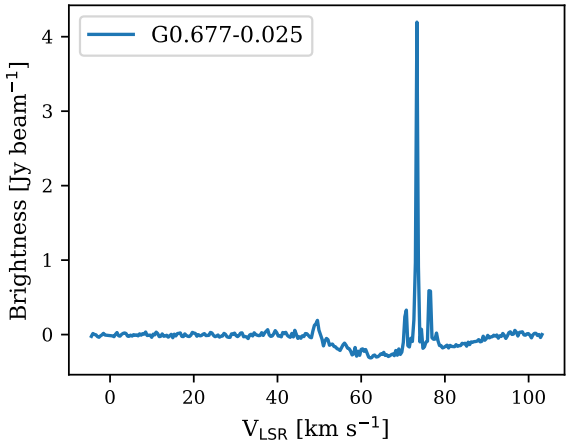

Fig. 14. CH_3OH 6.7 GHz spectra of the maser source G0.677-0.025 near Sagittarius B2. Broad absorption can be seen between the velocity range of 50 km s^{-1} and 90 km s^{-1}.

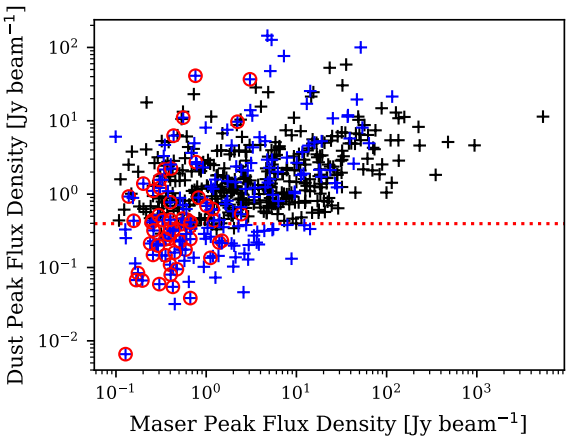

Fig. 15. CH_3OH 6.7 GHz maser peak flux density compared to 870 µm dust emission extracted from ATLASGAL maps towards the maser position. Black crosses correspond to sources that were matched to the ATLASGAL compact source catalogue (CSC). The remaining sources are marked in blue. The red dashed line corresponds to the ATLASGAL 6σ noise level and the red circles highlight the new masers found in this work.

(JCMT Plane Survey: Moore et al. 2015; Eden et al. 2017) to determine correlations for maser associated sources. As seen in previous studies (e.g. Urquhart et al. 2013, 2015; Billington et al. 2019), there is a ubiquitous association with the MMB masers and dust continuum sources (99%), strongly correlating these masers with the earlier stages of HMSF. Billington et al. (2019) determined that values of clump masses and radii are not indicative of a clump having a 6.7 GHz methanol maser, whereas the measurement of clump density may be able to make this indication. Furthermore, these authors determined a lower density threshold of $n(H_2) \geq 10^{4.1}$ cm^{-3} for the "turning on" of maser emission. As such, with our sample, especially our new weaker detections, it is interesting to see whether these correlations hold.

We performed a cross-matching with ATLASGAL sources using an emission map and distance threshold of 12″, which is three times the pointing uncertainty of ATLASGAL and was determined from analysing the surface density distribution of matches. We use the ATLASGAL CSC from $l = 3°$ to 60° as the source properties for sources in the region of the Galactic centre are not at the same confidence level. We find 363 associations within 12″ (~65%) between GLOSTAR masers and the ATLASGAL compact source catalogue (CSC; Urquhart et al. 2018, 2022) for which the dust clump properties (e.g. clump mass, clump temperature, bolometric luminosity) were calculated. The ~65% association with dust emission is lower than expected from the studies mentioned above. For masers without an ATLASGAL CSC association, it is possible that they are still are associated with dust as they could be associated with more distant clumps well below the ATLASGAL threshold. They could also be situated at a closer heliocentric distance to us, but are instead associated with low-mass clumps.

To address this discrepancy, we visually inspected ATLASGAL cutouts centred on the positions of the masers (examples can be found in Appendix B), using dust continuum contours from 1σ to 5σ. We took this approach as the ATLASGAL CSC uses a threshold of at least 6σ for the sources they report, but there are still many potential dust continuum sources below this limit. In this way, we find that there are an additional 72 maser sources that show compact dust emission above 3σ. There are a further 93 maser sources that can be associated to an extended ATLASGAL feature above 6σ and 7 maser sources that are offset slightly further than 12″. As such, we find that only 18 maser sources have no dust continuum emission, which corresponds to a methanol maser and dust continuum association of ~97%. The result is in agreement with previous studies (e.g. Billington et al. 2019). From Fig. 15, we find that there seems to be a cluster of new maser detections that are centred on the lower end of the dust emission around the 6σ noise level of ATLASGAL.

We compare the velocities of the maser's median velocity and the velocities of the matched dust clumps in Fig. 16. The ATLASGAL velocities were assigned by matching clump positions with observations of molecular line transitions from multiple molecular line surveys (see Urquhart et al. 2018, Sect. 2.1 for details). A linear fit yields a slope and y-intercept of 1.00 ± 0.13 and 0.01 ± 0.75, respectively, and with Spearman's rank coefficient of $r = 0.98$ and p-value $\ll 0.0013$ supporting the positive correlation. In fitting a Gaussian to the distribution of the velocity offsets, we find a mean offset of 0.49 ± 0.18 km s^{-1} and dispersion of 3.69 ± 0.1 km s^{-1}. The result is in agreement with the results from Billington et al. (2019), who compared the total MMB sample with corresponding ATLASGAL sources, where they used sources with offsets of <3σ. There are three sources, however, with

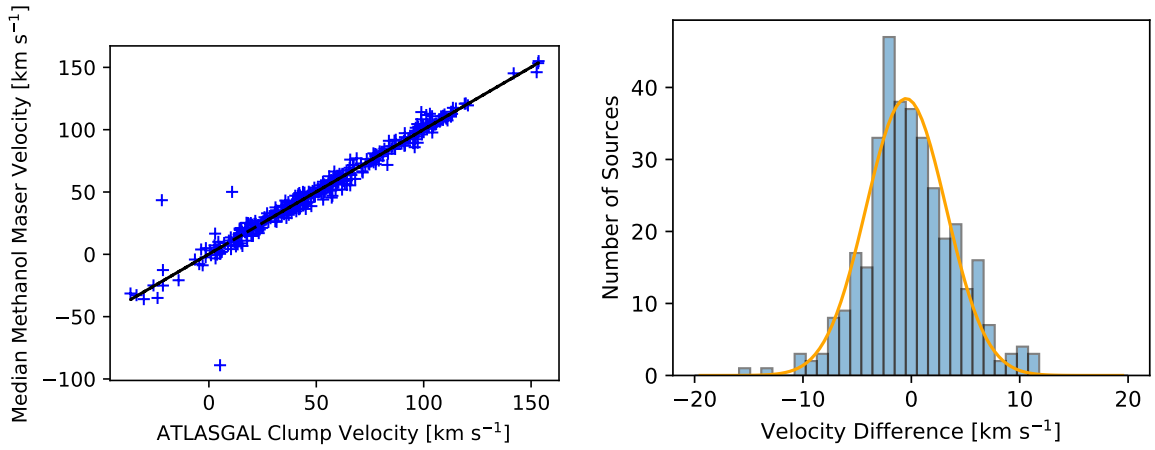

Fig. 16. Comparison of the velocities of the methanol masers and their associated dust clumps. *Left*: the median methanol maser velocity plotted as a function of the ATLASGAL clump velocity for sources with an association to an ATLASGAL compact source catalogue (CSC) source. The black line is the fitted linear result, with a Spearman's rank coefficient of $r = 0.98$ and p-value $\ll 0.0013$. *Right*: distribution of the offsets between the median methanol maser velocities and the molecular line velocities from ATLASGAL. Fitting the distribution with a Gaussian yields a mean of 0.49 ± 0.18 km s^{-1} and standard deviation of 3.69 ± 0.1 km s^{-1}. We use 3σ (11 km s^{-1}) as a confidence threshold to identify outliers.

greater velocity offsets: G3.5022−0.2005, G9.6211+0.1956, and G10.3563−0.1484. These were all previously detected in the MMB, with G3.5022−0.2005 being associated with millimetre dust continuum (Rosolowsky et al. 2010) and G10.3563−0.1484 associated with a YSO candidate (Deharveng et al. 2015). G9.6211+0.1956 is associated with the well-studied HII region of similar name, where its shock fronts have been studied (e.g. Liu et al. 2017, and references therein). As mentioned in Sect. 4.5, there are two sources in our catalogue with vastly different velocities associated with this ATLASGAL source. The maser at 1.3 km s^{-1} is consistent with the well-studied clump velocity. This other velocity component at −88.7 km s^{-1} would be an interesting target for future studies.

We show the cumulative distribution functions (CDFs) of the clumps associated with GLOSTAR masers and clumps associated with just the new detections in Fig. 17 for different associated clump properties such as dust temperature, bolometric luminosity, clump mass, luminosity to mass ratio, clump size, and H_2 density. A comparison of a sample of 364 maser associated clumps with that of 45 clumps associated with newly detected GLOSTAR masers. Urquhart et al. (2022) shows CDFs (in their Fig. 7) that compares the clump properties for different evolutionary stages of ATLASGAL sources, indeed demonstrating that it is possible to distinguish evolutionary stages on the basis of certain properties. Furthermore, Billington et al. (2019) compared the properties of ATLASGAL clumps with the subset that have MMB methanol maser associations. They found that maser associated sources have higher dust temperatures, bolometric luminosities, and luminosity-to-mass ratios, which is expected as these are regions in the process of developing high-mass stars (see Fig. 10 from Billington et al. 2019). In contrast to these works, we investigate the ATLASGAL sample of sources that have GLOSTAR methanol maser associations with the subset of those that are newly detected masers. We perform Anderson-Darling tests for all CDFs instead of Kolmogorov–Smirnov tests as the Anderson-Darling test is more sensitive to changes at the boundaries, which is the subset of our sample that we are more interested in, given that most of our newly detected masers are weaker. The results are shown on the plots in Fig. 17. Clump luminosity is the only statistically different sample to the 3σ level (p-value < 0.0013), while dust temperature and luminosity-to-mass ratio are significant only to the 2σ level (p-value < 0.05). In obtaining more clump properties for the masers without an ATLASGAL CSC counterpart, it will help improve the determination of the significance of the Anderson-Darling tests on these properties. Furthermore, we see that for the dust temperature, bolometric luminosity of the clump, and luminosity-to-mass ratio, the mean properties for the new maser detections are slightly lower, but they do extend to similar limits on the high end as the general population of masers. It is reasonable to naively expect this as lower luminosity masers may trace earlier stages of development.

We also compare the 6.7 GHz methanol maser luminosity to the dust clump properties of luminosity and mass in the left and middle panels of Fig. 18. To test whether these two dust clump properties are correlated to the maser luminosity, we performed a Spearman's rank correlation test that yields values of $r = 0.28$ and $r = 0.18$ respectively (with p-value $\ll 0.0013$) and so, there is a weak but significant correlation. The left panels of Fig. 18 shows the comparison between maser and clump luminosities and the distribution of the clump luminosities, where we have plotted (for reference) the dust core luminosity value of $\sim$200 $L_\odot$ as found by Ortiz-León et al. (2021) to be the lower limit of methanol maser associated clumps in the Cygnus X region. There are a few sources in our sample that show luminosities lower than this. The sharp cut-off does lie, however, close to this value and not around 10^3 $L_\odot$, as estimated by Bourke et al. (2005). Our results are in agreement with other recent studies such as Ortiz-León et al. (2021), who used similar data but for a small sample in the Cygnus X region, Paulson & Pandian (2020), who used a sample of 320 MMB masers, and Billington et al. (2019) who used a sample of 958 methanol masers from the MMB.

The middle panel in Fig. 18 similarly shows the investigation using the ATLASGAL full width at half maximum (FWHM) masses (mass within 50% of the 870 μm contour) for the clumps. Ortiz-León et al. (2021) determined the minimum core mass in Cygnus X for maser associated cores to be $\sim$10 $M_\odot$,

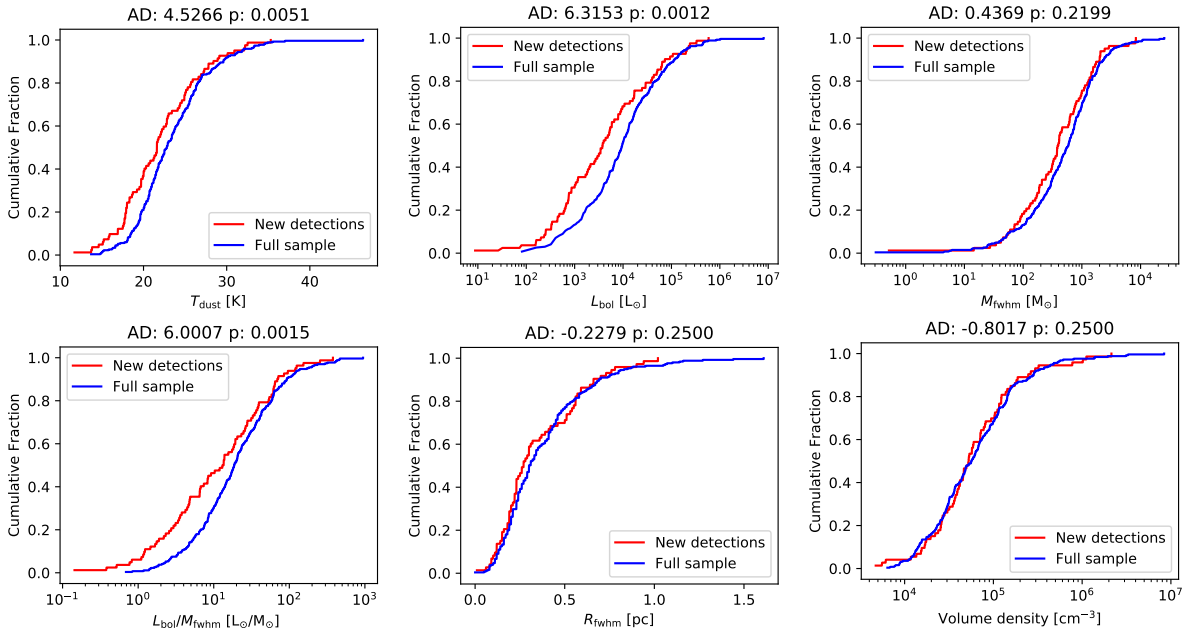

Fig. 17. CDFs for various properties of ATLASGAL clumps associated with GLOSTAR methanol masers. We compare the sample clumps associated with new methanol maser detections (red) to the sample of clumps with associations to the full methanol maser catalogue (blue). The results of the Anderson-Darling (AD) test are shown above each plot.

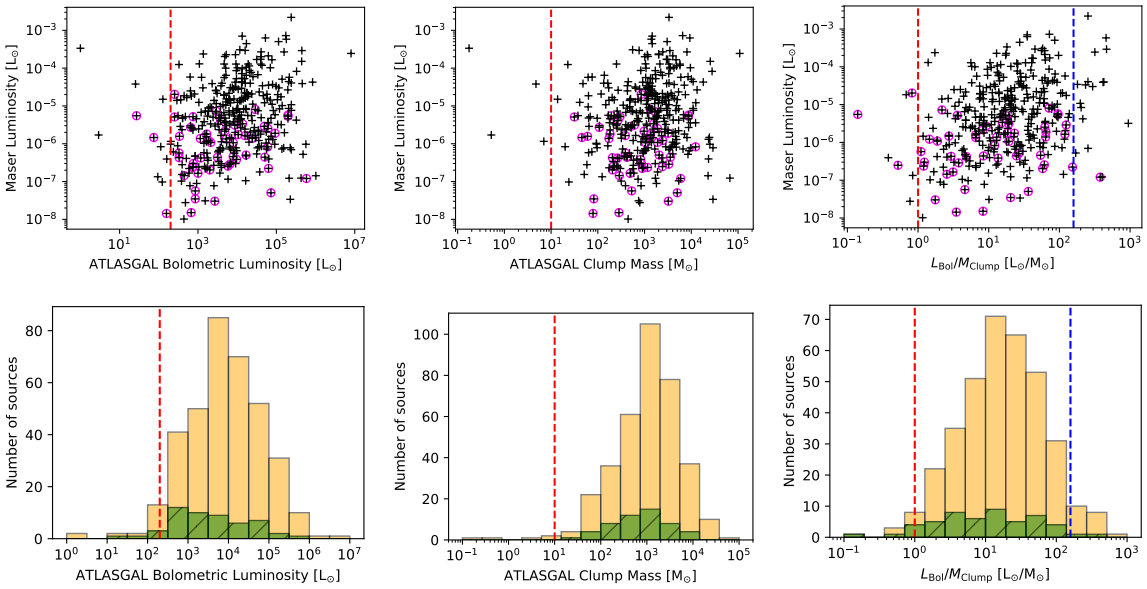

Fig. 18. Maser-integrated luminosity measured in D-configuration GLOSTAR data as a function of ATLASGAL clump properties shown in the *top row*: Bolometric luminosity (*left*), FWHM mass (*middle*), and luminosity-to-mass ratio (*right*). The black crosses represent masers with ATLASGAL compact source catalogue (CSC) counterparts, while the crosses surrounded by magenta circles highlight masers that were newly detected as part of the GLOSTAR survey. The *bottom row* shows the distribution of ATLASGAL molecular clump properties for the new masers (hatched green) in comparison to the full sample (yellow) of clumps associated with masers. The red-dashed lines denote the lower limits of the respective properties determined by Ortiz-León et al. (2021). The blue-dashed line denotes the upper bound at which maser emission is expected to decline due to the disruption of the physical conditions required for maser emission (e.g. expanding HII regions and dispersion of the host clump; Walsh et al. 1997, 1998; van der Walt et al. 2003).

while Billington et al. (2019) used the FWHM clump masses of the ATLASGAL sample to estimate a lower limit of $\sim 17\,M_\odot$. Paulson & Pandian (2020) determined a value similar to that reported by Ortiz-León et al. (2021) of $11\,M_\odot$ for their sample. These clump values are sufficient to produce high-mass stars if one assumes a 10% star formation efficiency. We used the FWHM clump masses of ATLASGAL and find a minimum mass of $0.175\,M_\odot$. Rather than being the true lower limit, we see that it is likely an exception, since all but four data points have clump masses above the lower limit estimated by Ortiz-León et al. (2021). Since we use masses from the same sample as Billington et al. (2019), we similarly see a cut-off at around $\sim 17\,M_\odot$ but the first percentile of the mass is $\sim 10\,M_\odot$.

In combining the clump properties of luminosity and mass, the luminosity-to-mass ratio (L/M) has been shown to serve as a statistical indicator of the evolutionary stage of high-mass star forming clumps (Molinari et al. 2008). Furthermore, Billington et al. (2019) found a weak correlation between the L/M ratio of maser associated clumps and maser integrated luminosity. In the right part of Fig. 18, we find a Spearman's rank coefficient of $r = 0.3$ with p-value $\ll 0.0013$, which suggests that there is a weak correlation between the properties. We find that 90% of the data points lie between the values of $1\,L_\odot\,M_\odot^{-1}$ and $10^{2.2}\,L_\odot\,M_\odot^{-1}$. These values estimate the lower and upper limits of the L/M ratio, which depict the onset of maser emission and the decline of the maser due to the formation of the HII region having disruptive effects on the maser's environment. Our results are in agreement with previous studies (e.g. Breen et al. 2010; Billington et al. 2019, 2020; Ortiz-León et al. 2021).

We also highlight the dust clumps that are associated with newly detected masers in Fig. 18. Contrary to our hypothesis that the newly detected and weak masers would strongly trace the earliest stages of high-mass star forming clumps, we see that except for clump luminosity, the histograms shown in Fig. 18 have similar shapes. Furthermore, the Anderson–Darling tests in Fig. 17, save for the bolometric luminosity, show no significant correlation between the samples to the 3σ level. We note that many newly detected masers have low maser luminosity ($<10^{-6}\,L_\odot$) and the lack of a strong correlation of this sample is in agreement with Paulson & Pandian (2020); this suggests that other properties, such as gas density and gas temperature, are perhaps more important factors for the maser luminosity than the dust clump bolometric luminosity. However, there are some of new masers we report (53) that have ATLASGAL associations, but for which we do not have the clump properties and, as stated above, which are generally associated with lower 870 μm emission dust clumps. As this is a significant portion of our new detections, the outcome of the sample comparison presented here may differ once we obtain the host clump properties for these masers in future works. The results presented here are in agreement with previous results (e.g. Billington et al. 2019) as the majority of the values are derived from known methanol maser and ATLASGAL clump associations.

5.2. Association with radio continuum

In general, we do not expect to see a close relationship between methanol masers and radio emission from HII regions, as the latter is a more developed stage of HMSF where methanol maser emission begins to decline (e.g. Beuther et al. 2002). However, this may not necessarily be the case with regard to the properties and early evolution of the more compact HII regions, (i.e. hypercompact (HC) and ultra-compact (UC) HII regions) as proposed, for instance, by Walsh et al. (1998); Yang et al. (2019a, 2021).

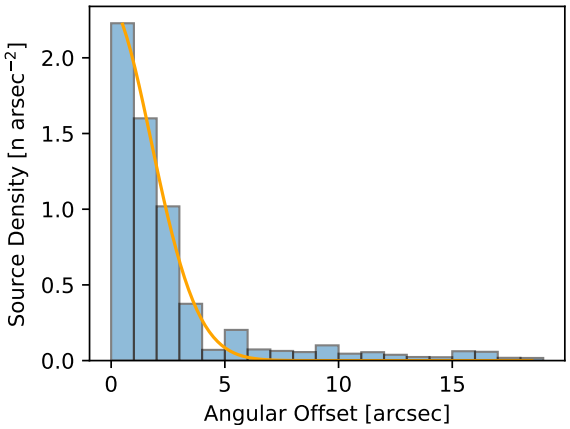

Fig. 19. Surface density plot of the offset of GLOSTAR radio continuum sources associated with GLOSTAR 6.7 GHz methanol masers.

These more compact HII regions are younger sites of HMSF and may still have maser emission in their surroundings as they evolve. This is supported by the observational results seen in Yang et al. (2021) from the largest sample of HC HII regions showing a maser detection rate of 100%, and the detection rate decreases as HII regions evolve from HC HII regions to UC HII regions. However, radio continuum emission at this stage is difficult to detect due to the compactness of the optically thick free-free radiation of HC HII, which results in low fluxes.

We attempted a search for associations of masers with the 5.8 GHz GLOSTAR D-configuration continuum (from $3° < l < 60°$). We find there to be 111 sources within $20''$, which is the size of the VLA D-array beam dropping to 64 when we use an angular distance threshold of $6''$. This threshold value corresponds to the 3σ level of the distribution shown in the source surface density plot in Fig. 19. This 12% association rate is smaller than that reported by Hu et al. (2016), with a better sensitivity of ~ 45 μJy beam^{-1} in the Galactic mid-plane for the radio continuum data; these authors found that ~30% of masers were associated with UC HII regions. This is not unexpected as the resolution of the D-configuration continuum catalogue is not as well suited to sampling UC HII and HC HII regions. The lack of association of 6.7 GHz methanol masers with radio continuum, however, indicates that these masers trace the earliest stages of high mass star formation.

We show (again) in Fig. 20 the flux distribution of the masers and their associations to continuum sources. By comparing the fraction of masers with an associated continuum source for each flux bin, there seems to be a trend in that the association with continuum sources increases with maser flux density. In Fig. 21, we show instead the flux distribution of the continuum sources to see if weaker radio sources (that are HII regions) are more correlated with methanol masers as it is possible to attribute weaker sources to younger stages of development. Despite the low association rate, we see that a Kolmogorov–Smirnov test of the distribution (bottom panel of Fig. 21) results in a p-value of $\ll 0.0013$, showing that there is a correlation with the continuum source flux for sources that have methanol maser associations. We see that radio sources with methanol masers are significantly brighter than the general population of radio sources.

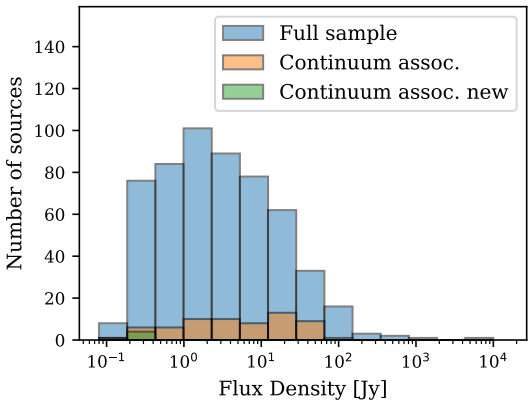

Fig. 20. As Fig. 10 except for subsets of GLOSTAR maser detections that have GLOSTAR D-configuration continuum source detections.

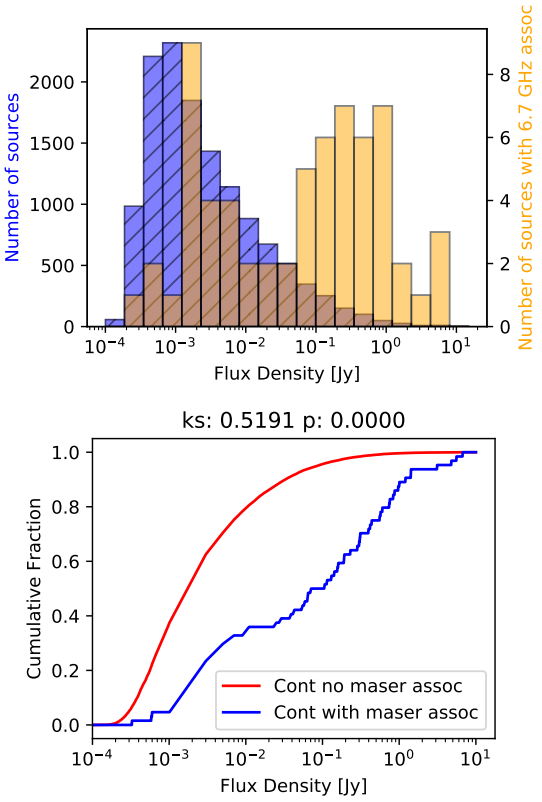

Fig. 21. Flux density comparison between maser associated continuum sources and those without. *Top*: blue hatched histogram shows the flux distribution of the GLOSTAR D-configuration continuum sources (Medina et al. 2019, and in prep.). The orange histogram shows the distribution of the radio sources that are associated with GLOSTAR 6.7 GHz methanol masers and has been rescaled for better visibility (the axis is indicated on the right). *Bottom*: CDFs for the flux density of radio continuum sources that have 6.7 GHz methanol maser associations (blue) and those without (red). The result of the Kolmogorov-Smirnov test is reported above the figure and indicates that both distributions are distinct, with continuum sources associated with methanol masers typically being stronger than the overall distribution of continuum sources.

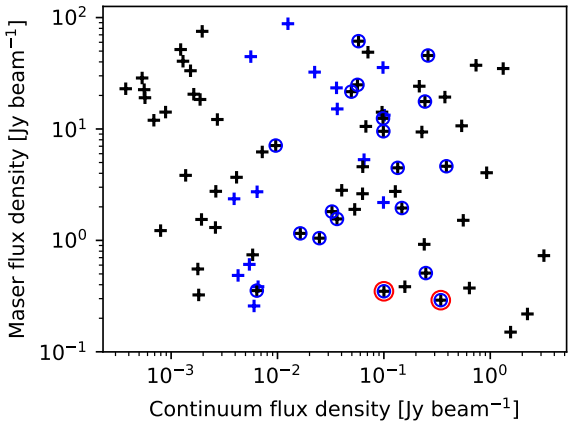

Fig. 22. Maser flux density against radio continuum flux density. Black crosses correspond to GLOSTAR D-configuration values for the radio continuum whereas blue crosses correspond to CORNISH B-configuration values. Blue circles show the sources that have counterparts in both continuum catalogues, but are plotted with the GLOSTAR flux density. Red circles denote sources that are new maser detections.

The true nature of the radio continuum sources, however, can be something other than HII regions, as they might be planetary nebulae, for instance, or they may even be extragalactic in origin. Following Medina et al. (2019), who determined that for the GLOSTAR D-configuration sensitivity there would be a source density of 0.0172 arcmin^2, this suggests that there would be ~7600 extragalactic sources of this sort, which is close to 60% of the sources in the catalogue. As such, we need to take into account the likelihood of an extragalactic background source being inside our matching radius. This is given by $N_{\rm bg}$ = (source density) × (search area). We used a search radius of 6 arcsec around the maser positions, which means that the estimated number of background sources is then $N_{\rm bg} \ll 1$. This implies that line-of-sight associations between GLOSTAR 6.7 GHz masers and GLOSTAR 5.8 GHz radio-continuum sources have a low probability of being purely coincidental. We also used the CORNISH catalogue to supplement our comparison. They have classified their sources which helps us to determine the nature of the continuum sources we have associated with our methanol masers. We find that 34 masers have CORNISH counterparts, which are all labelled as UC HII regions. Of these associations, 15 do not have GLOSTAR D-configuration radio catalogue counterparts. These are likely involved in extended emission seen through the D-configuration . Conversely, 45 sources have GLOSTAR radio counterparts but no CORNISH counterparts. A future analysis of the sources' spectral index can provide further insight on the astrophysical nature of the remaining continuum sources (Medina et al., in prep.).

We show in Fig. 22 the maser flux density as a function of continuum flux density, using the CORNISH catalogue to supplement the GLOSTAR radio continuum catalogue, where we used the flux from GLOSTAR where available. The Spearman's rank coefficient is $r = -0.11$, with a p-value = 0.32, thereby showing no correlation between the properties. As discussed above, we know that there is a positional correlation between radio sources and methanol masers, however in Fig. 23, we do not see any relation between the flux of a maser and its proximity to the radio continuum source (Kolmogorov–Smirnovtest results

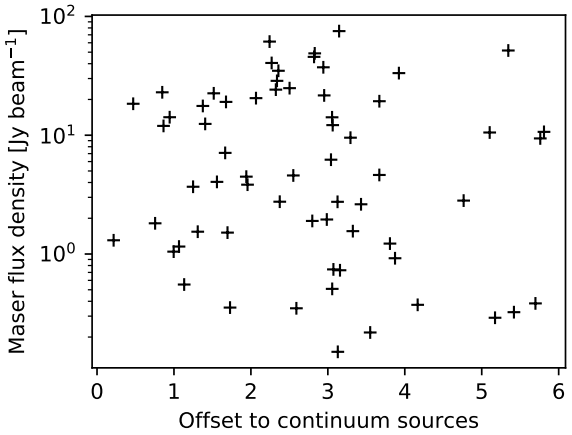

Fig. 23. Methanol maser flux as a function of offset to the peak flux position of its associated radio continuum source.

of $r = -0.11$ and p-value = 0.3). If the methanol maser was intimately connected with the radio source, one would expect to see increasing maser strength with decreasing position offset. Given that the maser flux and continuum flux show no correlation and that there is no correlation with maser flux and position offset, this suggests that the mechanisms powering the two kinds of sources are unrelated as expected, despite there being a positional correlation.

5.3. Luminosity function

Given that the 6.7 GHz methanol maser is a tracer of HMSF, a luminosity function of these sources would allow us to compare the amount of HMSF in the Milky Way and other nearby Galaxies. Studies have shown that the luminosity function for these masers cannot be fit by a single power law but may be fit with a broken power law (Pestalozzi et al. 2007; Pandian et al. 2009; Green & McClure-Griffiths 2011). As discussed in Sect. 4.3, we have allocated distances to the maser sources using a Bayesian distance estimator as well as ATLASGAL clump velocities. However, if we were to use only the sources with an ATLASGAL association to determine the luminosity function, we would be biased towards sources with higher luminosities. This is evident in Fig. 24, which shows a clear fractional difference in the number of sources in the lower luminosity bins compared to the full sample to ATLASGAL CSC only sources. While a CDF of these two samples would show that they are not statistically distinct, which is to be expected, we do find that in examining the right panel of Fig. 24, we see that there is a statistical difference in maser properties between the sources with ATLASGAL counterparts and those without (Kolmogorov–Smirnov test result of $r = 0.74$ and p-value $\ll 0.0013$). As such, we chose to use the full sample. In Fig. 25, we plot the luminosity as a function of heliocentric distance. As expected, the new maser detections cover the lower luminosity ranges for a given distance. This also allows us to determine the completeness level. Given a minimum flux, we can calculate the minimum luminosity of a maser we can detect for a given heliocentric distance. This, in turn, can be turned around to give the maximum distance at which a maser of a given luminosity can be detected. Then, within the limits of the survey coverage, the fraction of the Milky Way disk covered at a given distance will give us the completeness that has been normalised over the survey area. This is shown in the luminosity function in Fig. 26. We find that we are 100% complete at $6.9 \times 10^{-7}\,L_\odot$.

We also find that the median luminosity is $3 \times 10^{-6}\,L_\odot$ and this is in agreement with previous studies (e.g. Pandian et al. 2009) that report that the distribution peaks around $10^{-6}\,L_\odot$. Our sample size is about six times greater than that of Pandian et al. (2007, 2009) and, therefore, our median luminosity is statistically more robust. To characterise the luminosity function, we used only the luminosity bins for above which we are complete. We simultaneously fit two power laws and found indexes of 0.08 ± 0.05 for the lower luminosity range and -0.66 ± 0.05 for the higher luminosity range where the turnover has been determined to be $\sim 2{\times}10^{-5}\,L_\odot$. However, we see that while it is possible to fit a broken power law to the data, we do not sample well the lower luminosities, as our 100% completeness is around $6.9 \times 10^{-7}\,L_\odot$.

6. Summary and conclusions

In this work, we conduct the most sensitive, unbiased survey of Class II 6.7 GHz CH_3OH masers to date in the region covered by the GLOSTAR survey in the Galactic plane. A total of 554 masers were detected, with 84 of them being new detections. Over 50 % of the new detections have fluxes of <0.5 Jy and it was possible to detect them thanks to the improved sensitivity of GLOSTAR as compared to other unbiased surveys. A summary of the main results of this work are as follows:

- In a comparing with the ATLASGAL Compact Source Catalogue (CSC), we find that 65% of the CH_3OH masers are associated with dense gas, with many of the newly detected masers remaining unassociated. However, a visual inspection reveals a much higher association rate of 97%, indicating that many of the new masers are associated with weak dust emission that is below the sensitivity required for inclusion in the ATLASGAL CSC.
- The newly detected masers are weaker both in terms of their maser emission and associated dust emission. This might indicate they are either more distant than the previously detected masers or could be associated with lower mass stars or less evolved stars. Given the lower range of maser luminosities and the fact that the L/M distribution of the new masers is consistent with the previous masers, this indicates that they are more likely to be associated with lower-mass stars.
- The high correlation between methanol masers and dust emission and the high bolometric luminosities are consistent with the picture of methanol masers being associated with the early stages of high-mass star formation. We derived an L/M threshold for the onset of the methanol maser emission of $\sim 1\,L_\odot\,M_\odot^{-1}$, which is consistent with values determined by Ortiz-León et al. (2021) based on a study of the Cygnus X region with GLOSTAR data as well as a previous work on the MMB catalogue carried out by Billington et al. (2019).
- We find that 12% of the masers are coincident with radio continuum emission (i.e. <12″) but in comparing the radio and maser flux distribution, we find no correlation as a function of angular offset. This suggests that the mechanisms powering maser and continuum emission are unrelated.
- We used our sample of masers to construct a luminosity function using a broken power law. Our results agree with previous studies in that the distribution has a median luminosity $10^{-6}\,L_\odot$. We sampled the high-luminosity maser

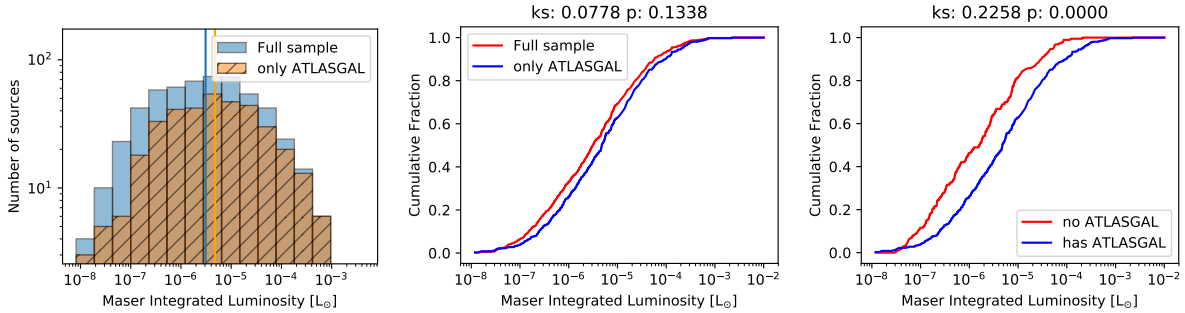

Fig. 24. Comparison of the luminosities of sources with and without association with ATLASGAL sources. *Left*: shown is the distribution of the luminosities. The median value is $3.1 \times 10^{-6}\,L_\odot$ for the full sample and $4.7 \times 10^{-6}\,L_\odot$ and the subset of detections peaks that have ATLASGAL compact source catalogue (CSC) associations. *Middle*: CDF comparing the full sample of luminosities to the subset of sources that are associated with ATLASGAL where the two samples are not distinct. *Right*: CDF comparing the sample of luminosities without an ATLASGAL association to those with where they are seen to be statistically distinct.

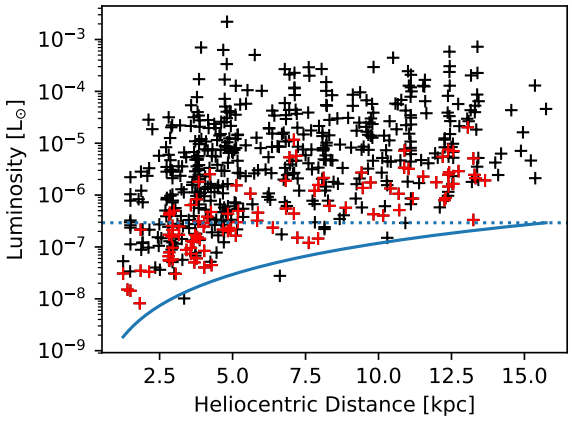

Fig. 25. Maser integrated luminosity as a function of heliocentric distance marked as black crosses where red crosses highlight the new maser detections from this work. The blue curve denotes the 5σ luminosity threshold and the dotted blue line corresponds to the completeness level of 100%.

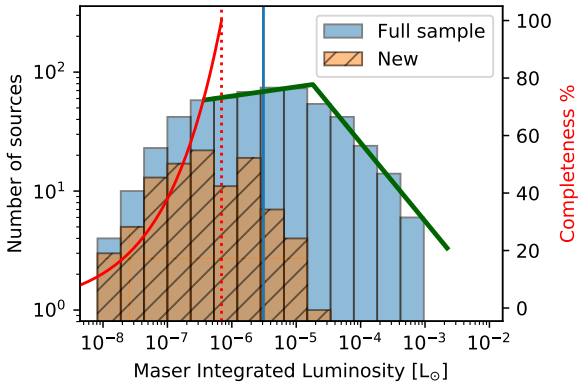

Fig. 26. Distribution of luminosities derived. The blue vertical line represents the median value of $3.1 \times 10^{-6}\,L_\odot$. The subset of new detections peaks at a lower luminosity as expected. The red curve corresponds to the completeness level with values on the right axis, and the dotted red line indicates the level of 100% completeness. The two green lines represent the broken power law fit with powers of 0.08 ± 0.05 for the lower luminosity range and -0.66 ± 0.05 for the upper luminosity range.

population with success, but we find we are limited with respect to the lower-luminosity bins.

This work is the first step in our study of 6.7 GHz CH_3OH masers using GLOSTAR data in the Galactic plane. Methanol absorption sources have also been detected and a systematic search is forthcoming. Further study of the properties of these masers would be best served with higher resolution data that we will present in future works.

Acknowledgements. We would like to thank the anonymous referee for their useful comments. H.N. is a member of the International Max-Planck Research School at the universities of Bonn and Cologne (IMPRS). This research was partially funded by the ERC Advanced Investigator Grant GLOSTAR (247078). H.B. acknowledges support from the European Research Council under the European Community's Horizon 2020 framework program (2014–2020) via the ERC Consolidator grant 'From Cloud to Star Formation (CSF)' (project number 648505). H.B. further acknowledges support from the Deutsche Forschungsgemeinschaft (DFG) via Sonderforschungsbereich (SFB) 881 "The Milky Way System" (sub-project B1). The National Radio Astronomy Observatory is a facility of the National Science Foundation, operated under a cooperative agreement by Associated Universities, Inc. This research made use of information from the ATLASGAL database at http://atlasgal.mpifr-bonn.mpg.de/cgi-bin/ATLASGAL_DATABASE.cgi supported by the MPIfR in Bonn. This research made use of Astropy (http://www.astropy.org), a community-developed core Python package for Astronomy (Astropy Collaboration 2013, 2018). This research has made use of the SIMBAD database, operated at CDS, Strasbourg, France.

References

Astropy Collaboration (Robitaille, T. P., et al.) 2013, A&A, 558, A33
Astropy Collaboration (Price-Whelan, A. M., et al.) 2018, AJ, 156, 123
Barrett, A. H., Schwartz, P. R., & Waters, J. W. 1971, ApJ, 168, L101
Batrla, W., Matthews, H. E., Menten, K. M., & Walmsley, C. M. 1987, Nature, 326, 49
Beuther, H., Walsh, A., Schilke, P., et al. 2002, A&A, 390, 289
Billington, S. J., Urquhart, J. S., König, C., et al. 2019, MNRAS, 490, 2779
Billington, S. J., Urquhart, J. S., König, C., et al. 2020, MNRAS, 499, 2744
Bourke, T. L., Hyland, A. R., & Robinson, G. 2005, ApJ, 625, 883
Breen, S. L., Ellingsen, S. P., Caswell, J. L., & Lewis, B. E. 2010, MNRAS, 401, 2219
Breen, S. L., Ellingsen, S. P., Caswell, J. L., et al. 2011, ApJ, 733, 80
Breen, S. L., Fuller, G. A., Caswell, J. L., et al. 2015, MNRAS, 450, 4109
Brunthaler, A., Menten, K. M., Dzib, S. A., et al. 2021, A&A, 651, A85
Caswell, J. L. 1996, MNRAS, 283, 606
Caswell, J. L., Vaile, R. A., Ellingsen, S. P., Whiteoak, J. B., & Norris, R. P. 1995, MNRAS, 272, 96
Caswell, J. L., Fuller, G. A., Green, J. A., et al. 2010, MNRAS, 404, 1029

Caswell, J. L., Fuller, G. A., Green, J. A., et al. 2011, MNRAS, 417, 1964
Cragg, D. M., Johns, K. P., Godfrey, P. D., & Brown, R. D. 1992, MNRAS, 259, 203
Cragg, D. M., Sobolev, A., & Godfrey, P. D. 2005, MNRAS, 360, 533
Dame, T. M., Hartmann, D., & Thaddeus, P. 2001, ApJ, 547, 792
Deharveng, L., Zavagno, A., Samal, M. R., et al. 2015, A&A, 582, A1
Dokara, R., Brunthaler, A., Menten, K. M., et al. 2021, A&A, 651, A86
Eden, D. J., Moore, T. J. T., Plume, R., et al. 2017, MNRAS, 469, 2163
Ellingsen, S. P. 2006, ApJ, 638, 241
Ellingsen, S. P. 2007, MNRAS, 377, 571
Ellingsen, S. P., von Bibra, M. L., McCulloch, P. M., et al. 1996, MNRAS, 280, 378
Goedhart, S., Gaylard, M. J., & van der Walt, D. J. 2007, in Astrophysical Masers and their Environments, eds. J. M. Chapman, & W. A. Baan, 242, 97
Goedhart, S., van Rooyen, R., van der Walt, D. J., et al. 2018, in Astrophysical Masers: Unlocking the Mysteries of the Universe, eds. A. Tarchi, M. J. Reid, & P. Castangia, 336, 225
Green, J. A., & McClure-Griffiths, N. M. 2011, MNRAS, 417, 2500
Green, J. A., Caswell, J. L., Fuller, G. A., et al. 2009, MNRAS, 392, 783
Green, J. A., Caswell, J. L., Fuller, G. A., et al. 2010, MNRAS, 409, 913
Green, J. A., Caswell, J. L., Fuller, G. A., et al. 2012, MNRAS, 420, 3108
Hoare, M. G., Purcell, C. R., Churchwell, E. B., et al. 2012, PASP, 124, 939
Hu, B., Menten, K. M., Wu, Y., et al. 2016, ApJ, 833, 18
Impellizzeri, C. M. V., Henkel, C., Roy, A. L., & Menten, K. M. 2008, A&A, 484, L43
Ladeyschikov, D. A., Bayandina, O. S., & Sobolev, A. M. 2019, AJ, 158, 233
Leurini, S., Menten, K. M., & Walmsley, C. M. 2016, A&A, 592, A31
Liu, T., Lacy, J., Li, P. S., et al. 2017, ApJ, 849, 25
MacLeod, G. C., Gaylard, M. J., & Nicolson, G. D. 1992, MNRAS, 254, 1P
Medina, S. N. X., Urquhart, J. S., Dzib, S. A., et al. 2019, A&A, 627, A175
Menten, K. M. 1991a, in Astronomical Society of the Pacific Conference Series, Atoms, Ions and Molecules: New Results in Spectral Line Astrophysics, eds. A. D. Haschick, & P. T. P. Ho, 16, 119
Menten, K. M. 1991b, ApJ, 380, L75
Menten, K. M. 1993, in Astrophysical Masers, eds. A. W. Clegg, & G. E. Nedoluha (Berlin, Heidelberg: Springer Berlin Heidelberg), 199
Menten, K. M., Reid, M. J., Pratap, P., Moran, J. M., & Wilson, T. L. 1992, ApJ, 401, L39
Minier, V., Burton, M. G., Wong, T., Purcell, C., & Hill, T. 2003, in IAU Symposium, 221
Molinari, S., Pezzuto, S., Cesaroni, R., et al. 2008, A&A, 481, 345
Moore, T. J. T., Plume, R., Thompson, M. A., et al. 2015, MNRAS, 453, 4264
Murugeshan, C. 2015, Master's thesis, University of Bonn, Germany
Nguyen, H. 2015, Master's thesis, University of Bonn, Germany
Ortiz-León, G. N., Menten, K. M., Brunthaler, A., et al. 2021, A&A, 651, A87
Pandian, J. D., Goldsmith, P. F., & Deshpande, A. A. 2007, ApJ, 656, 255
Pandian, J. D., Leurini, S., Menten, K. M., Belloche, A., & Goldsmith, P. F. 2008, A&A, 489, 1175
Pandian, J. D., Menten, K. M., & Goldsmith, P. F. 2009, ApJ, 706, 1609
Paulson, S. T., & Pandian, J. D. 2020, MNRAS, 492, 1335
Perley, R. A., Chandler, C. J., Butler, B. J., & Wrobel, J. M. 2011, ApJ, 739, L1
Pestalozzi, M. R., Minier, V., & Booth, R. S. 2005, A&A, 432, 737
Pestalozzi, M. R., Chrysostomou, A., Collett, J. L., et al. 2007, A&A, 463, 1009
Purcell, C. R., Hoare, M. G., Cotton, W. D., et al. 2013, ApJS, 205, 1
Reid, M. J., Menten, K. M., Brunthaler, A., et al. 2019, ApJ, 885, 131
Rickert, M., Yusef-Zadeh, F., & Ott, J. 2019, MNRAS, 482, 5349
Roman-Duval, J., Jackson, J. M., Heyer, M., et al. 2009, ApJ, 699, 1153
Rosolowsky, E., Dunham, M. K., Ginsburg, A., et al. 2010, ApJS, 188, 123
Sanna, A., Menten, K. M., Carrasco-González, C., et al. 2015, ApJ, 804, L2
Schuller, F., Menten, K. M., Contreras, Y., et al. 2009, A&A, 504, 415
Schuller, F., Urquhart, J. S., Csengeri, T., et al. 2021, MNRAS, 500, 3064
Sobolev, A. M., & Deguchi, S. 1994, A&A, 291, 569
Taylor, J. H., & Cordes, J. M. 1993, ApJ, 411, 674
Thomasson, P. 1986, QJRAS, 27, 413
Thompson, A. R., Moran, J. M., & Swenson, George W., J. 2017, Interferometry and Synthesis in Radio Astronomy, 3rd edn
Urquhart, J. S., Moore, T. J. T., Schuller, F., et al. 2013, MNRAS, 431, 1752
Urquhart, J. S., Moore, T. J. T., Menten, K. M., et al. 2015, MNRAS, 446, 3461
Urquhart, J. S., König, C., Giannetti, A., et al. 2018, MNRAS, 473, 1059
Urquhart, J. S., Wells, M. R. A., Pillai, T., et al. 2022, MNRAS, 510, 3389
van der Walt, D. J., Retief, S. J. P., Gaylard, M. J., & MacLeod, G. C. 1996, MNRAS, 282, 1085
van der Walt, D. J., Churchwell, E., Gaylard, M. J., & Goedhart, S. 2003, MNRAS, 341, 270
van der Walt, D. J., Goedhart, S., & Gaylard, M. J. 2009, MNRAS, 398, 961
Voronkov, M. A., Caswell, J. L., Ellingsen, S. P., & Sobolev, A. M. 2010, MNRAS, 405, 2471
Voronkov, M. A., Caswell, J. L., Ellingsen, S. P., Green, J. A., & Breen, S. L. 2014, MNRAS, 439, 2584
Walsh, A. J., Hyland, A. R., Robinson, G., & Burton, M. G. 1997, MNRAS, 291, 261
Walsh, A. J., Burton, M. G., Hyland, A. R., & Robinson, G. 1998, MNRAS, 301, 640
Walsh, A. J., Purcell, C. R., Longmore, S. N., et al. 2014, MNRAS, 442, 2240
Xu, Y., Li, J. J., Hachisuka, K., et al. 2008, A&A, 485, 729
Yang, A. Y., Thompson, M. A., Tian, W. W., et al. 2019a, MNRAS, 482, 2681
Yang, K., Chen, X., Shen, Z.-Q., et al. 2019b, ApJS, 241, 18
Yang, A. Y., Urquhart, J. S., Thompson, M. A., et al. 2021, A&A, 645, A110
Yang, W. J., Menten, K. M., Yang, A. Y., et al. 2022, A&A, 658, A192

A&A 666, A59 (2022)

Appendix A: The strongest new sources

Cutouts of the strongest new 6.7 GHz CH_3OH maser detections at their respective peak velocities. We visually inspected these sources that should have been detected by the MMB given their high fluxes. While some sources were probably missed previously due to its proximity to a stronger maser source, it is likely maser variability that plays a role in their previous non-detection.

Appendix B: Association of masers with weaker ATLASGAL emission

We visually inspected all maser positions that were not automatically matched with an ATLASGAL CSC counterpart for dust emission and find that most of them are still associated with dust.

Appendix C: The spectra of CH_3OH masers

Here, we present the spectra for each maser source.

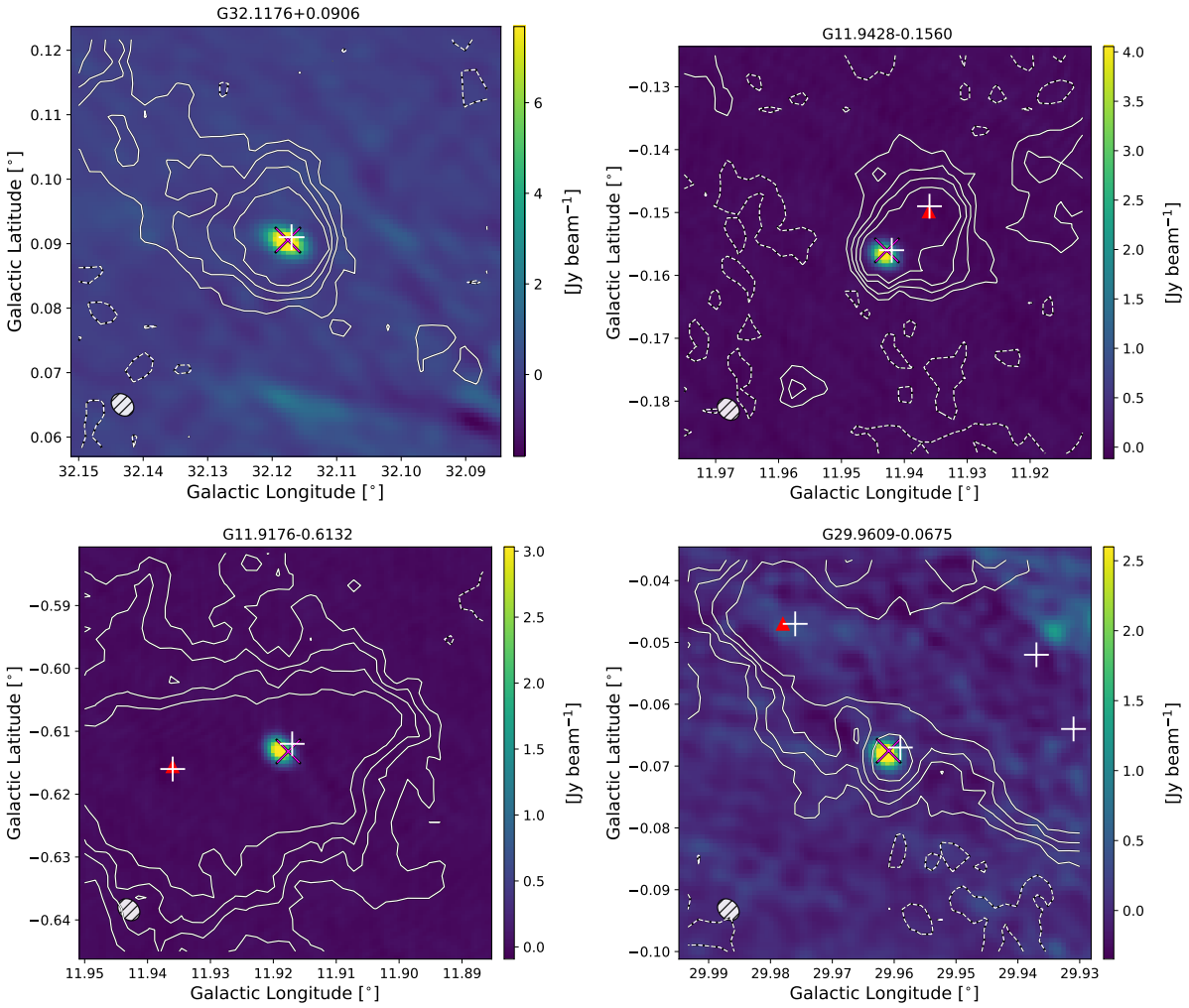

Fig. A.1: GLOSTAR 6.7 GHz emission maps at the velocity of the maser emission peak of the ten strongest new masers, denoted by the magenta 'X'. Red triangles denote the position of known MMB masers. The flux levels were limited to 75% of the maser peak to better illustrate low intensity features. The white "+" signs show the positions of known compact ATLASGAL sources and the white contours are from the ATLASGAL 870 μm dust emission map with contour levels at -3, 3, 5, 7, and 10 σ noise levels.

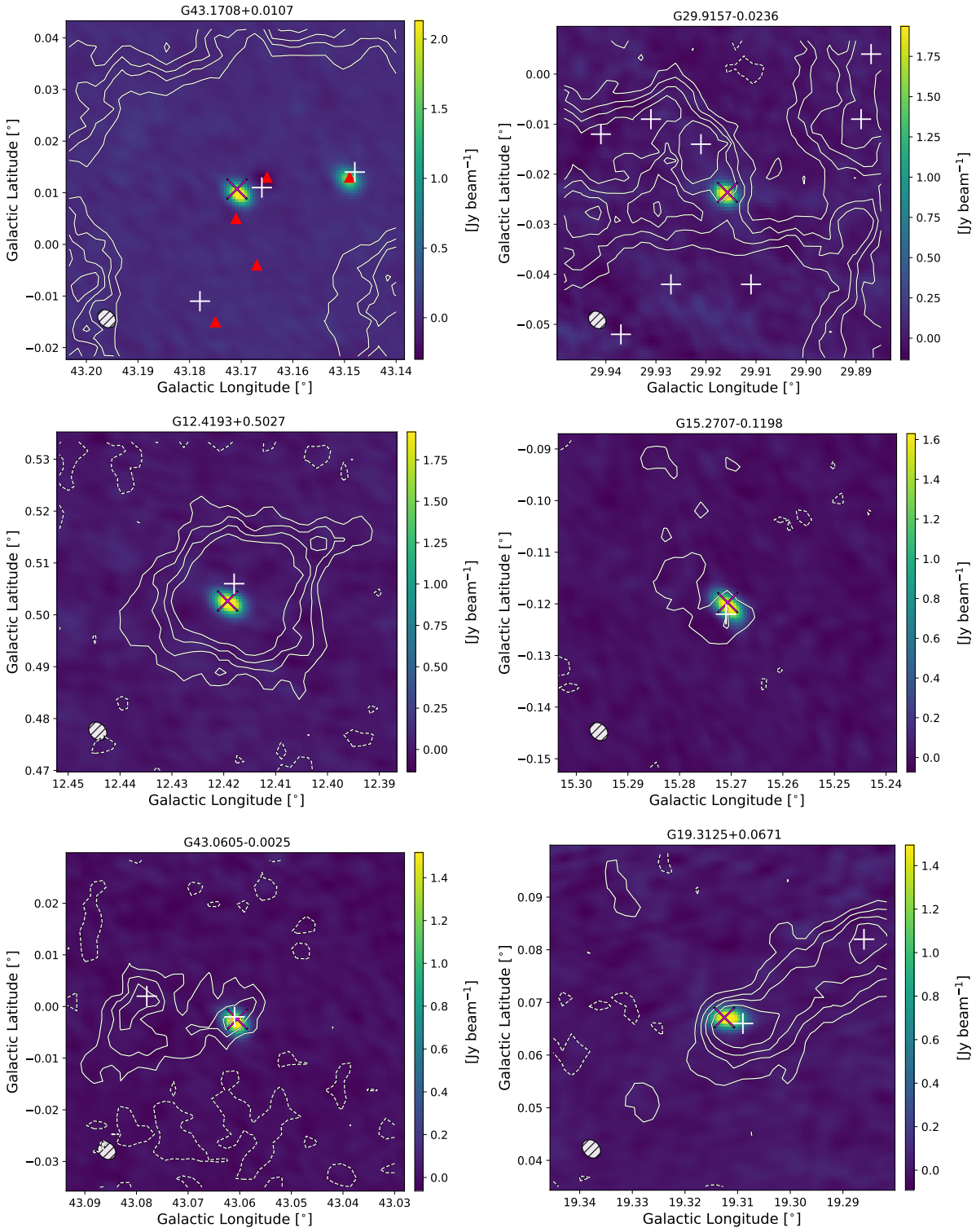

Fig. A.2: Fig. A.1. continued.

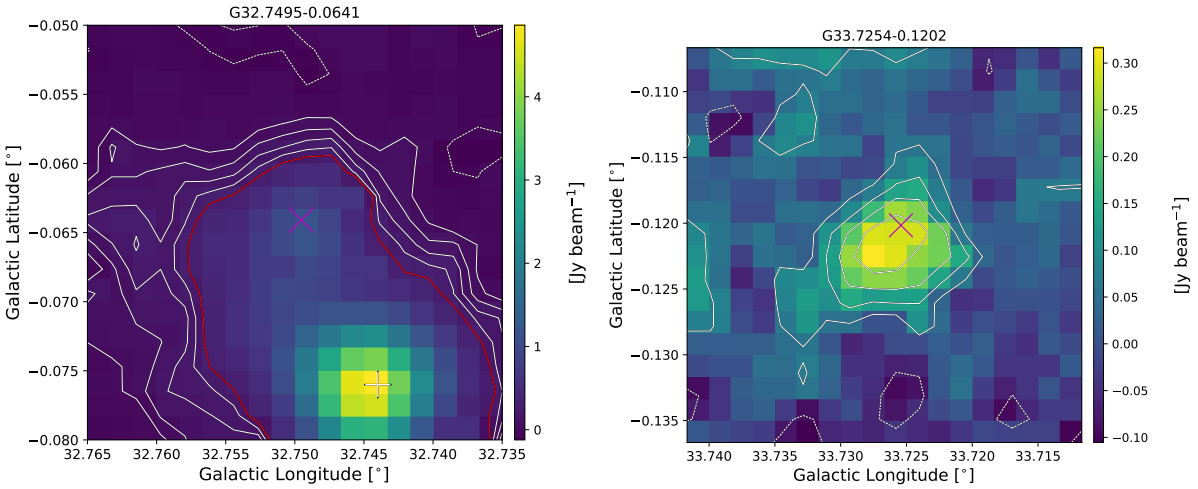

Fig. B.1: ATLASGAL 870 μm dust continuum cutouts centred on the position of a given maser, shown as a magenta 'X'. The white '+' is the position of an ATLASGAL compact source from the compact source catalogue (CSC). The white contours are the ATLASGAL 1, 2, 3, and 4σ levels, where the red contour is the 5σ level. The left panel shows an example where it is clear that the methanol maser is associated with dust emission above 5σ, but farther than the 12″ used for the association. The right panel shows an example of a weak compact source that shows a maser association, but was not considered for the ATLASGAL CSC. However, the association with the maser makes a strong argument for the veracity of the weak compact source.

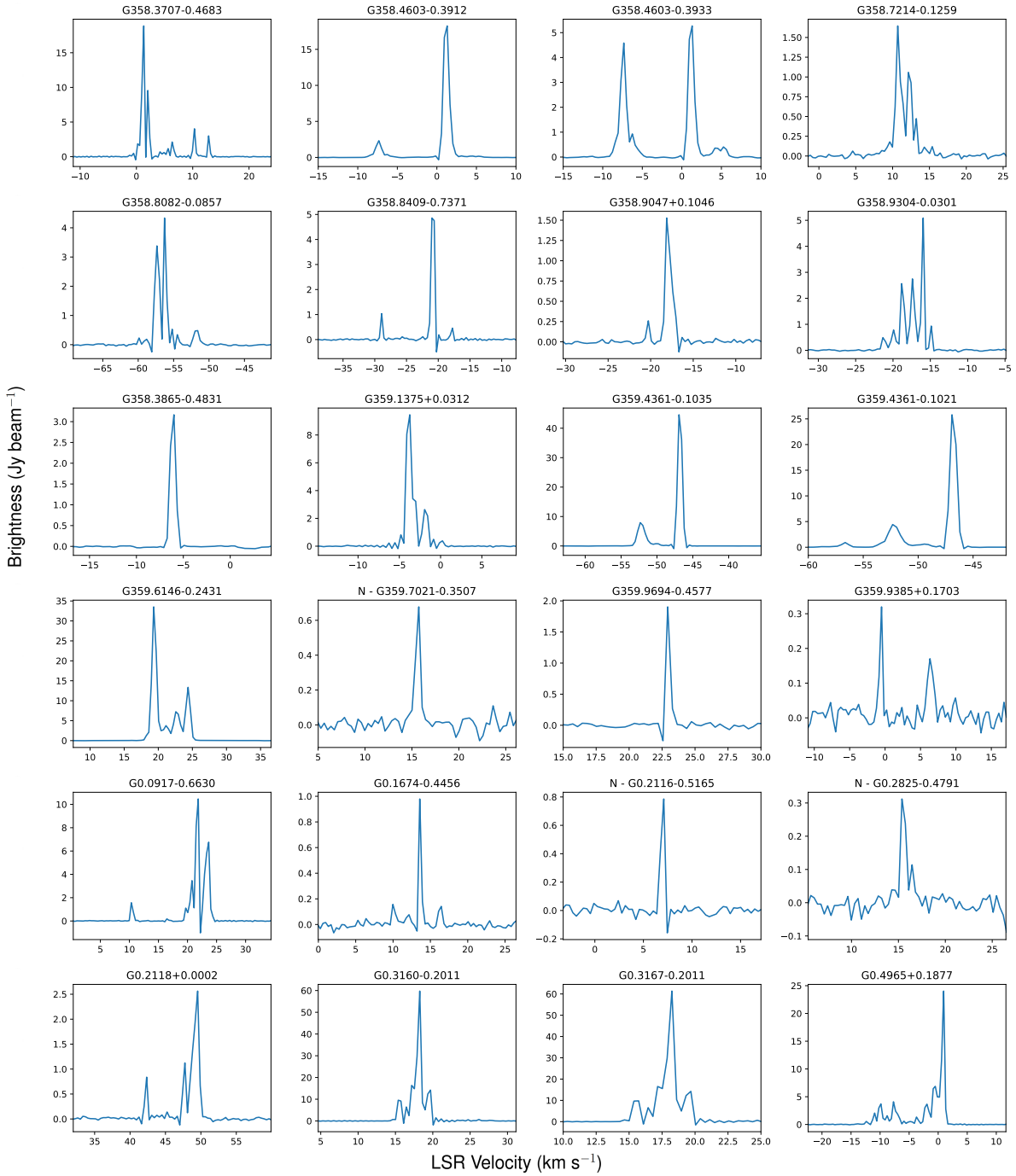

Fig. C.1: Spectra of 6.7 GHz methanol masers detected with GLOSTAR extracted at the peak pixel. The red dashed line indicates the ATLASGAL clump velocity (Urquhart et al. 2018, 2022) in case of an associated 870 μm compact source catalog (CSC) source.

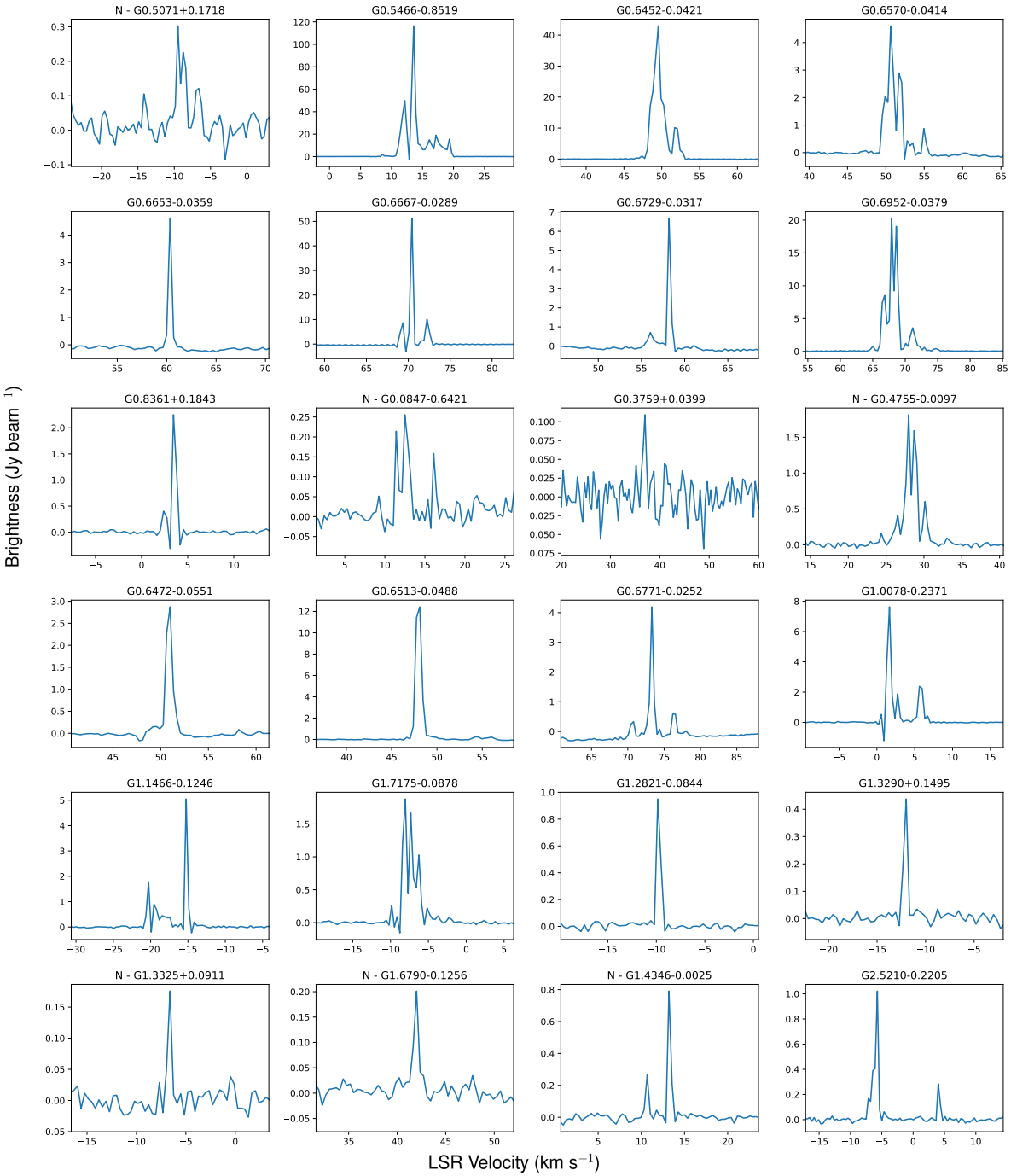

Fig. C.2: Fig. C.1. continued.

Fig. C.3: Fig. C.1. continued.

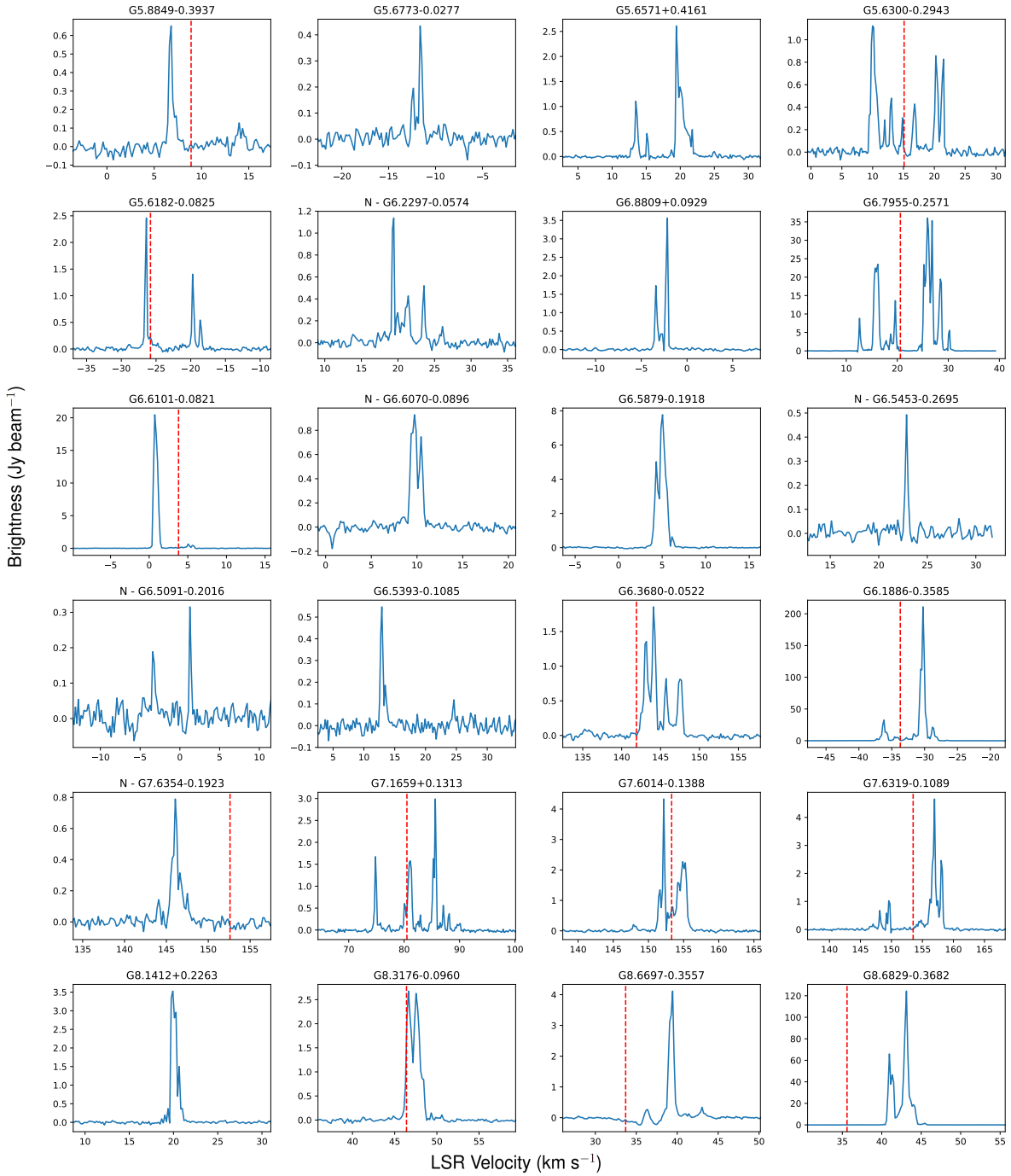

Fig. C.4: Fig. C.1. continued.

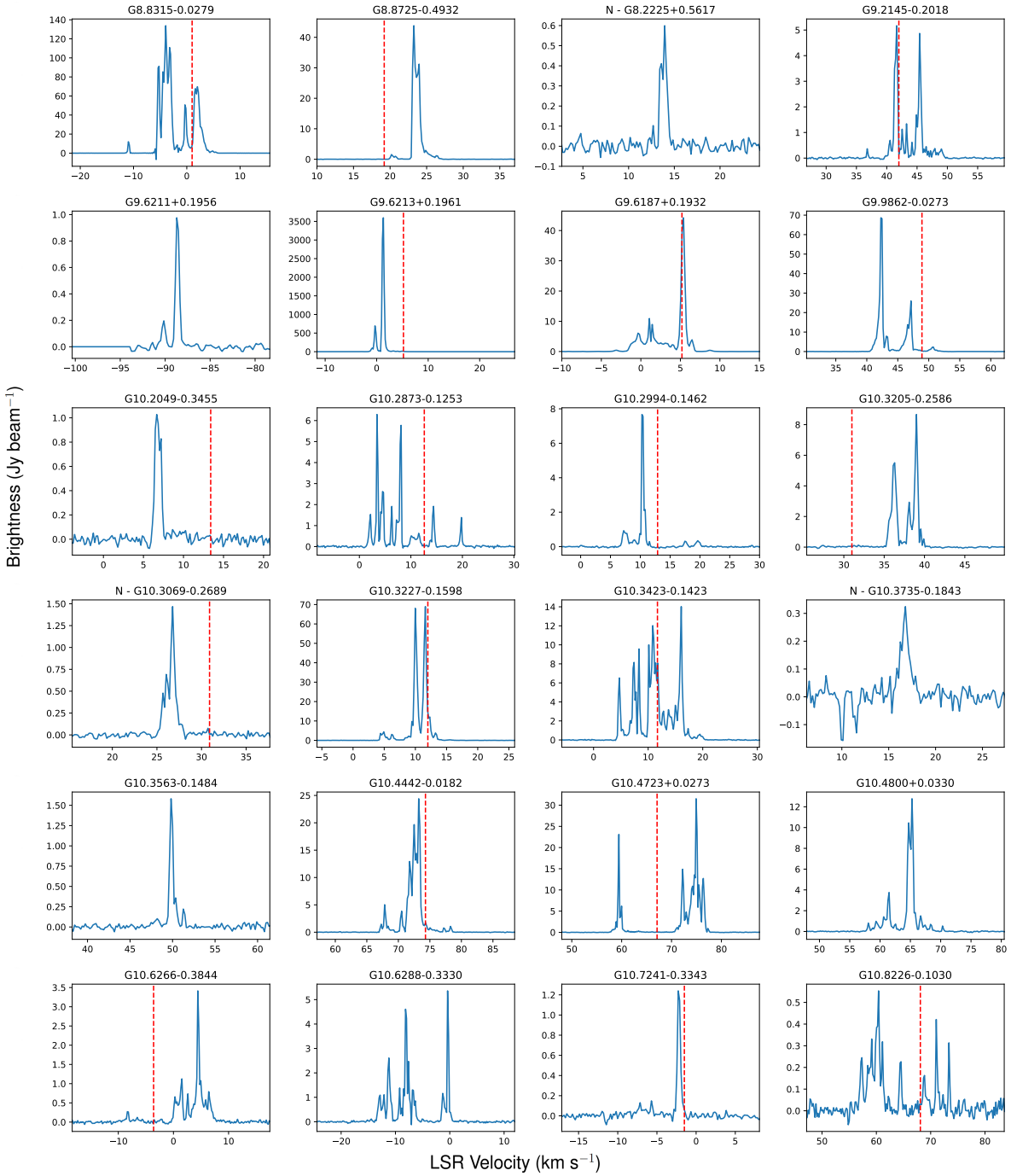

Fig. C.5: Fig. C.1. continued.

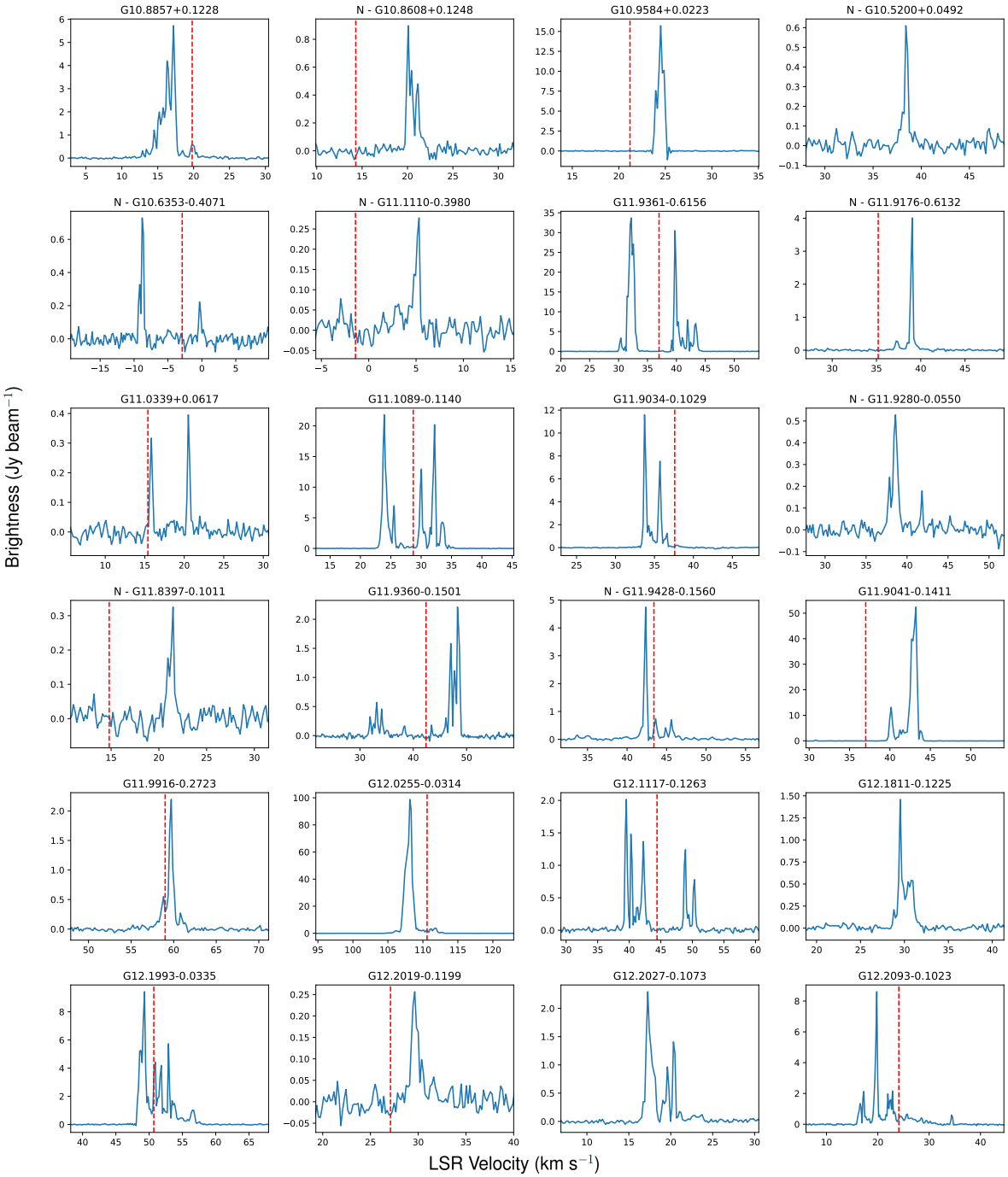

Fig. C.6: Fig. C.1. continued.

Fig. C.7: Fig. C.1. continued.

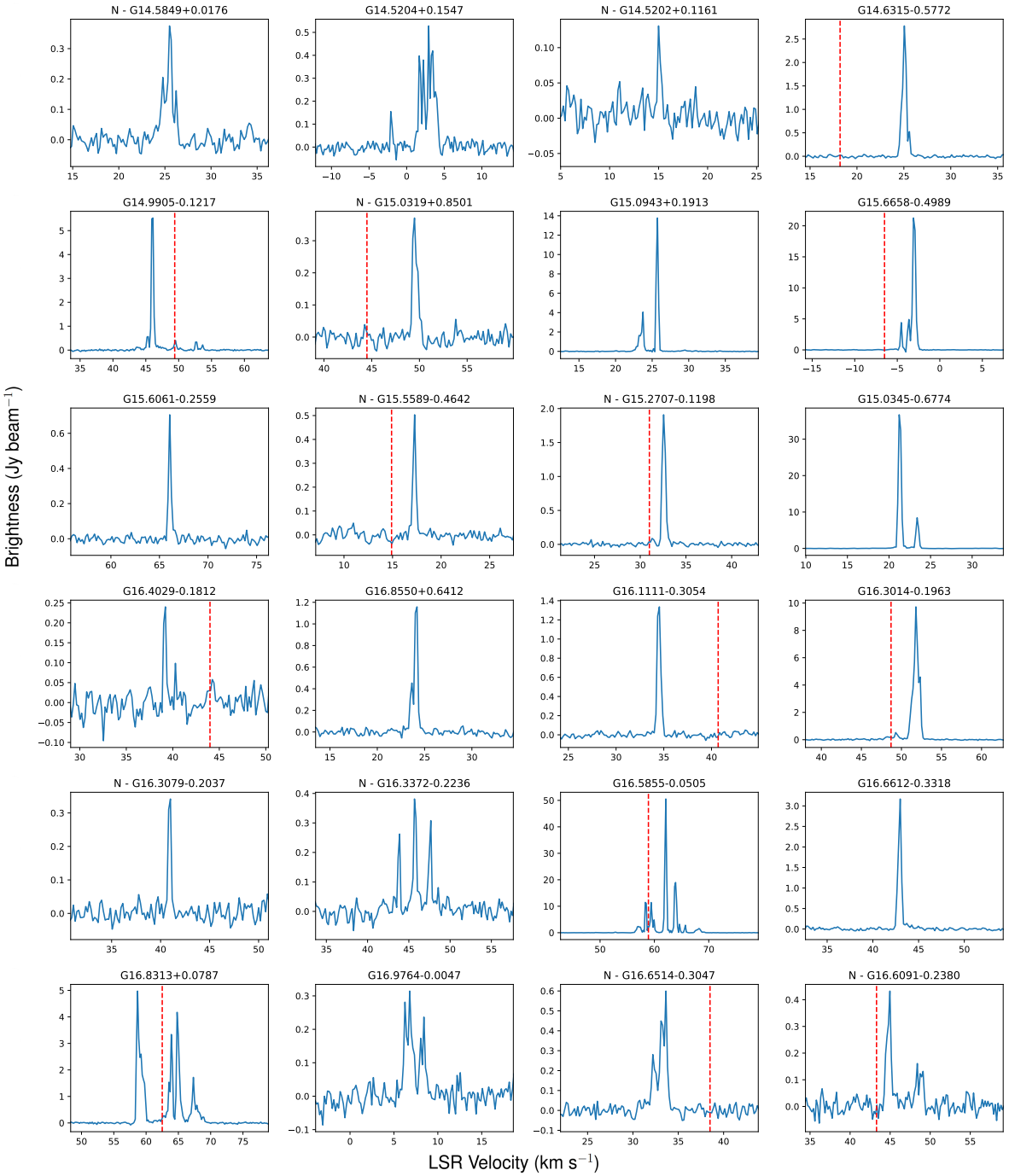

Fig. C.8: Fig. C.1. continued.

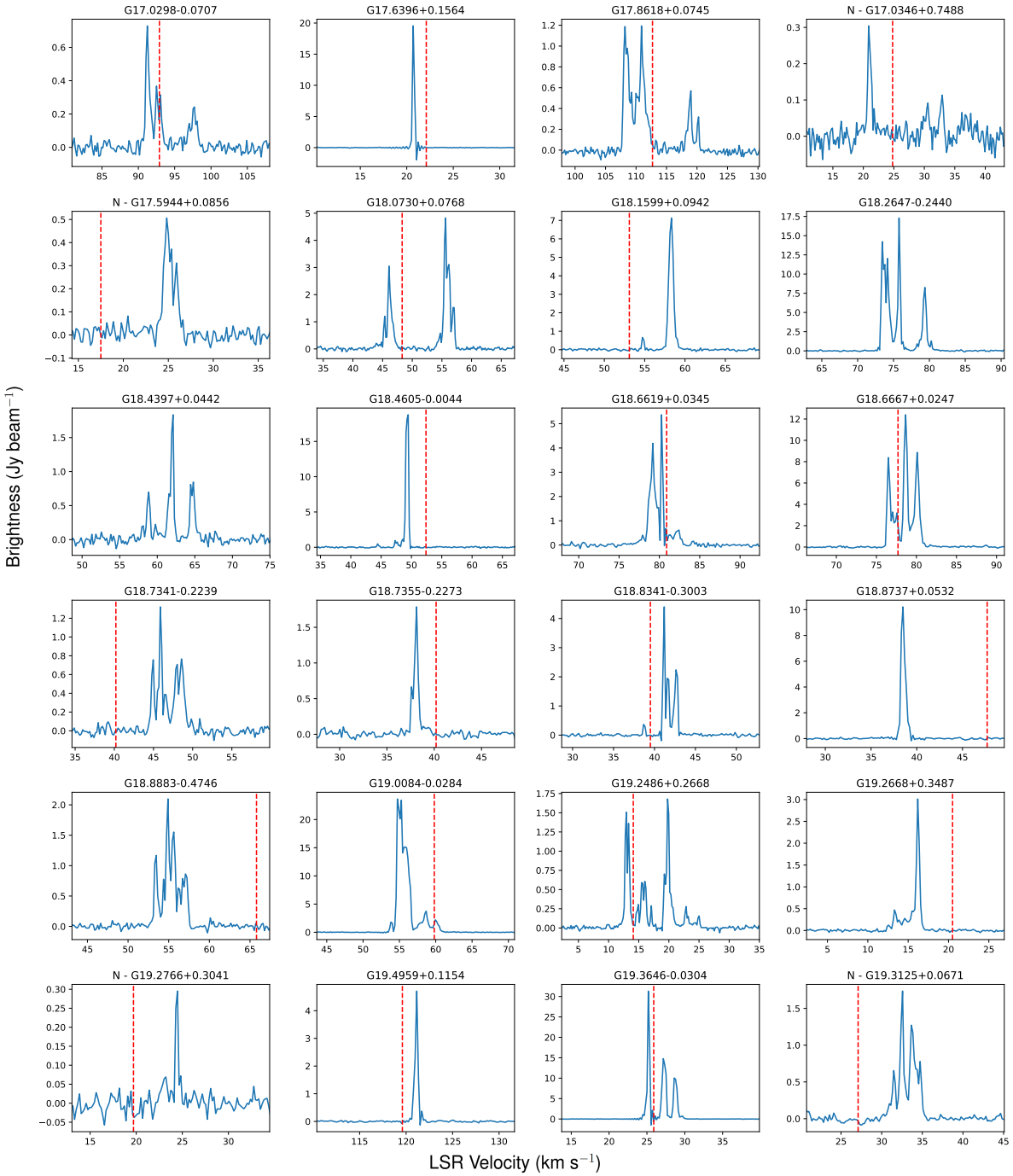

Fig. C.9: Fig. C.1. continued.

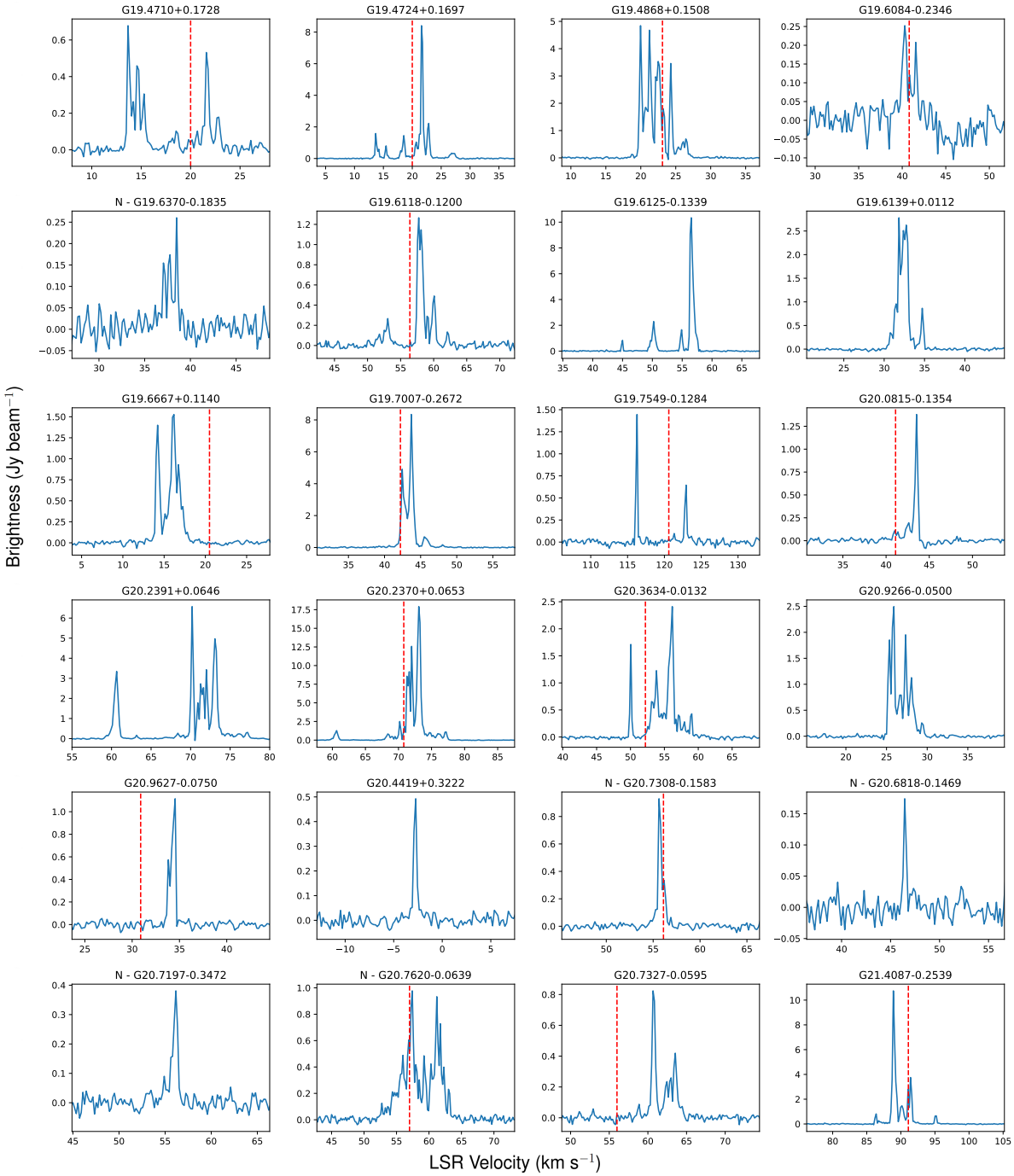

Fig. C.10: Fig. C.1. continued.

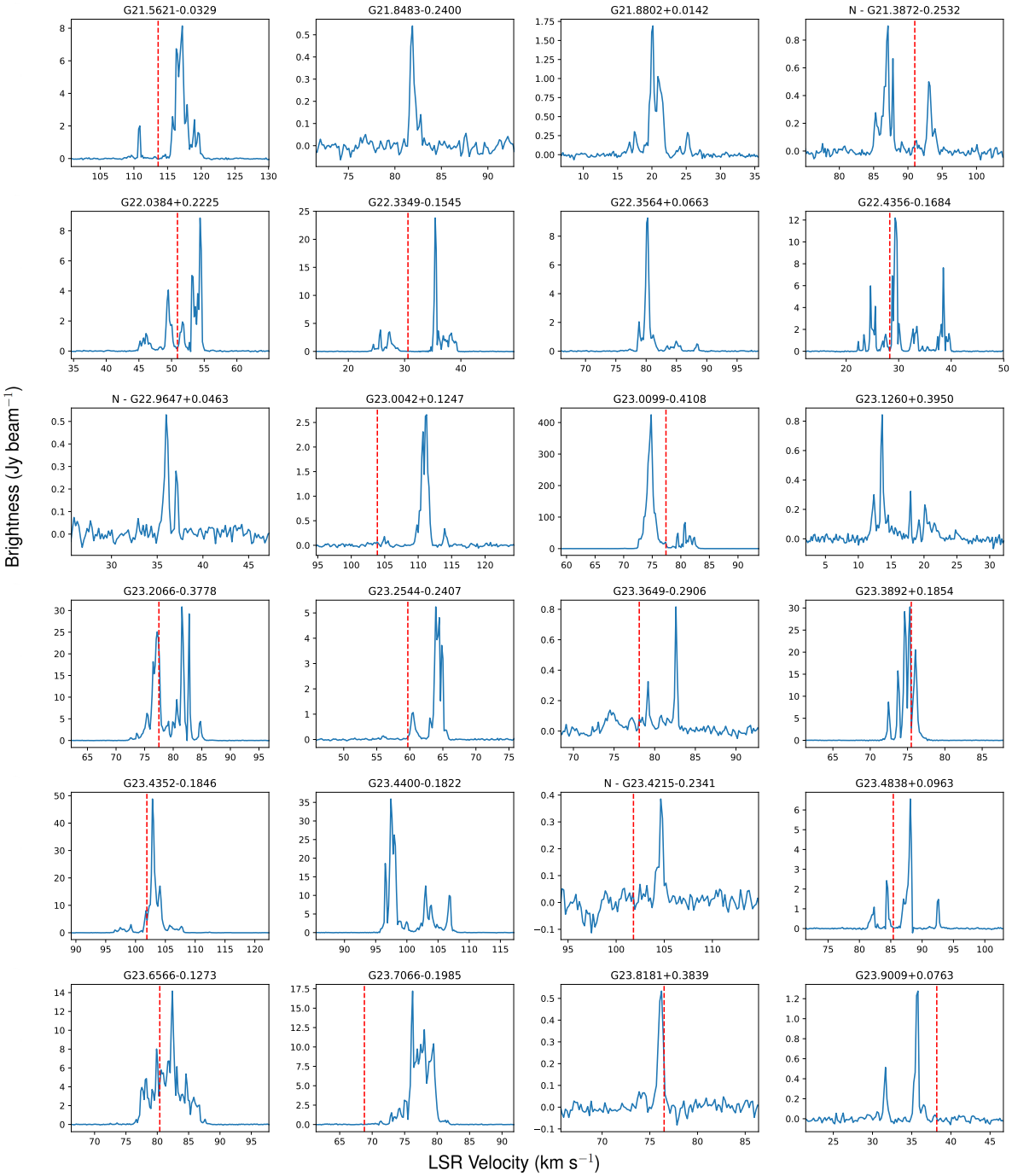

Fig. C.11: Fig. C.1. continued.

Fig. C.12: Fig. C.1. continued.

Fig. C.13: Fig. C.1. continued.

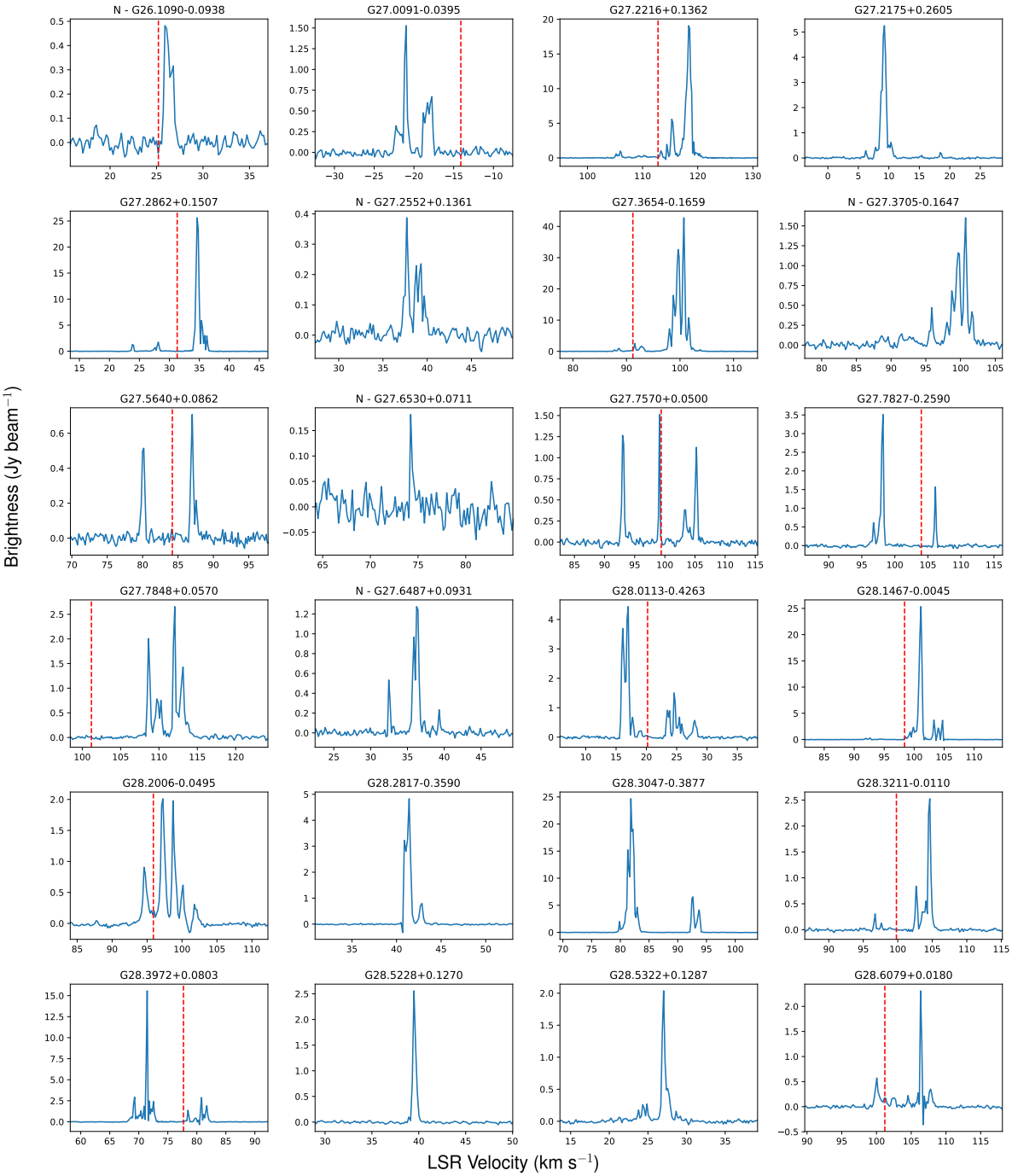

Fig. C.14: Fig. C.1. continued.

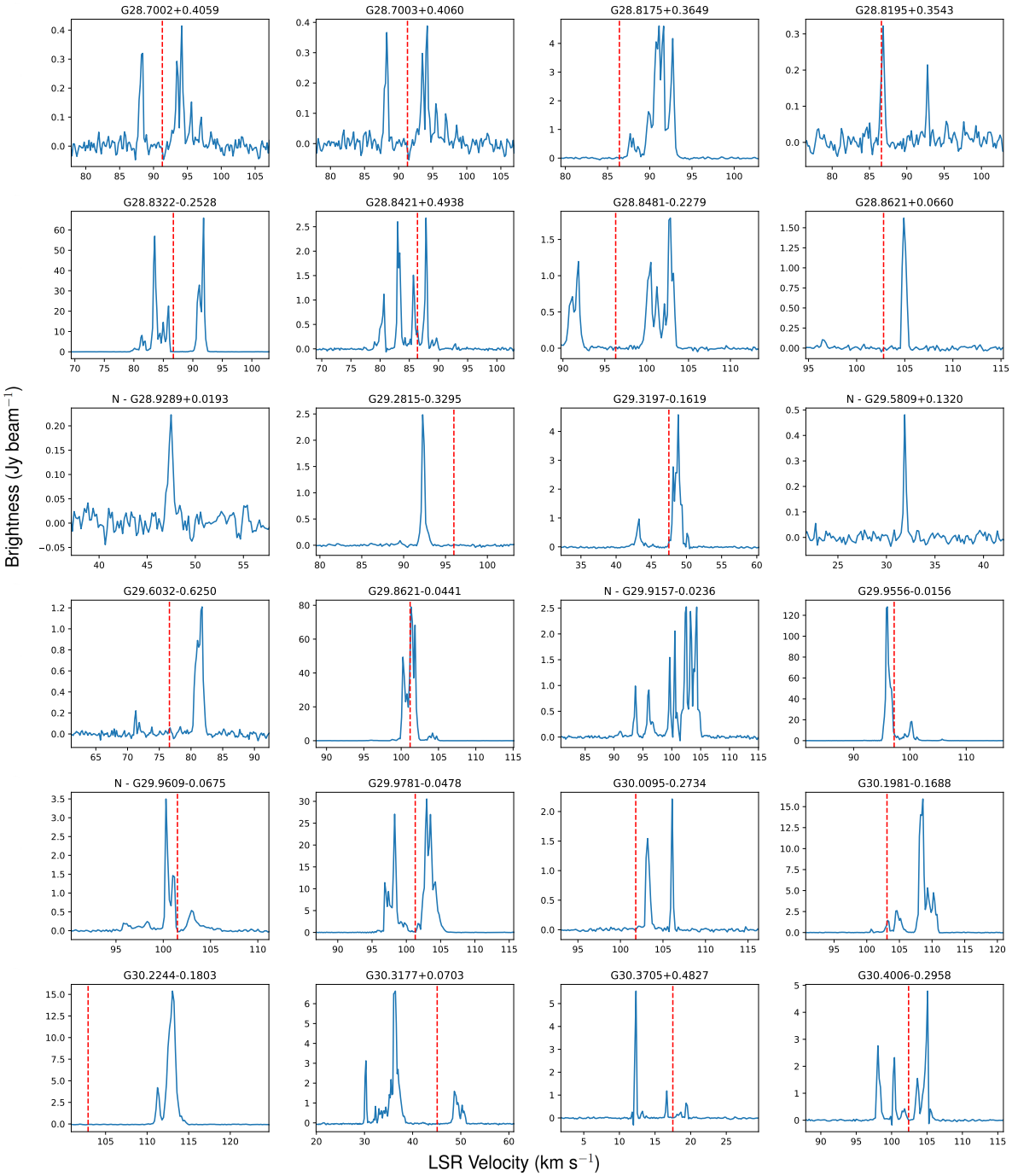

Fig. C.15: Fig. C.1. continued.

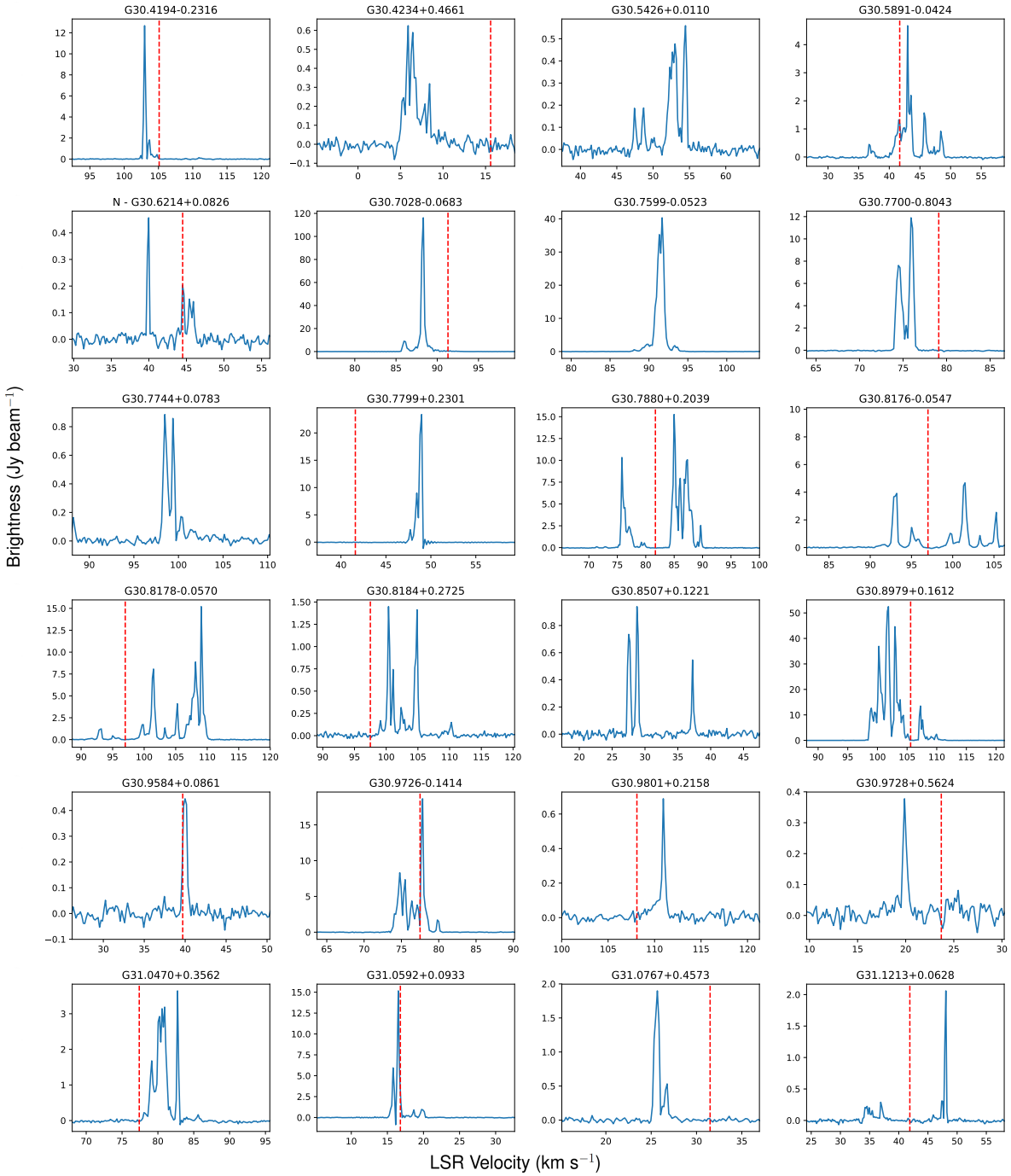

Fig. C.16: Fig. C.1. continued.

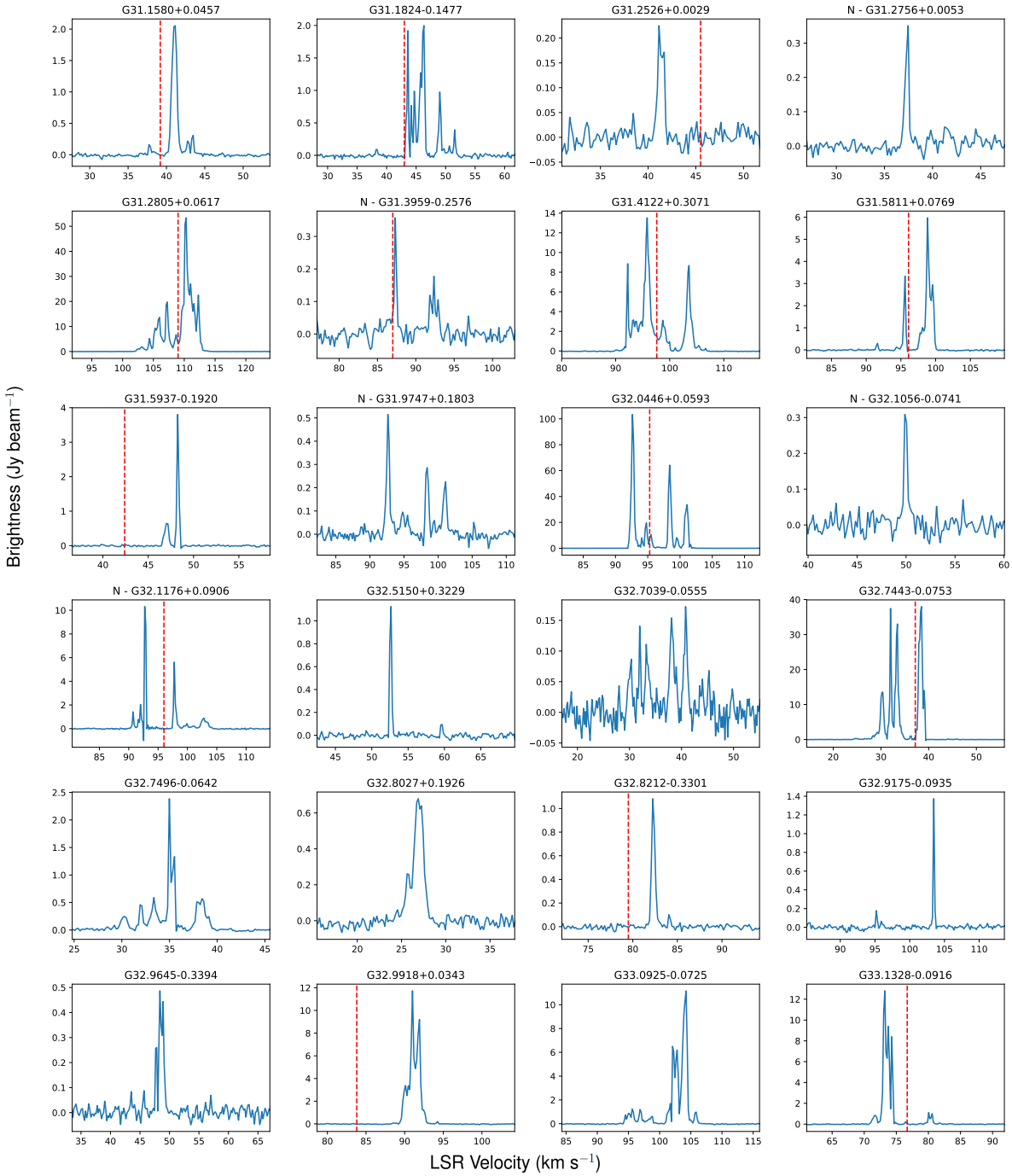

Fig. C.17: Fig. C.1. continued.

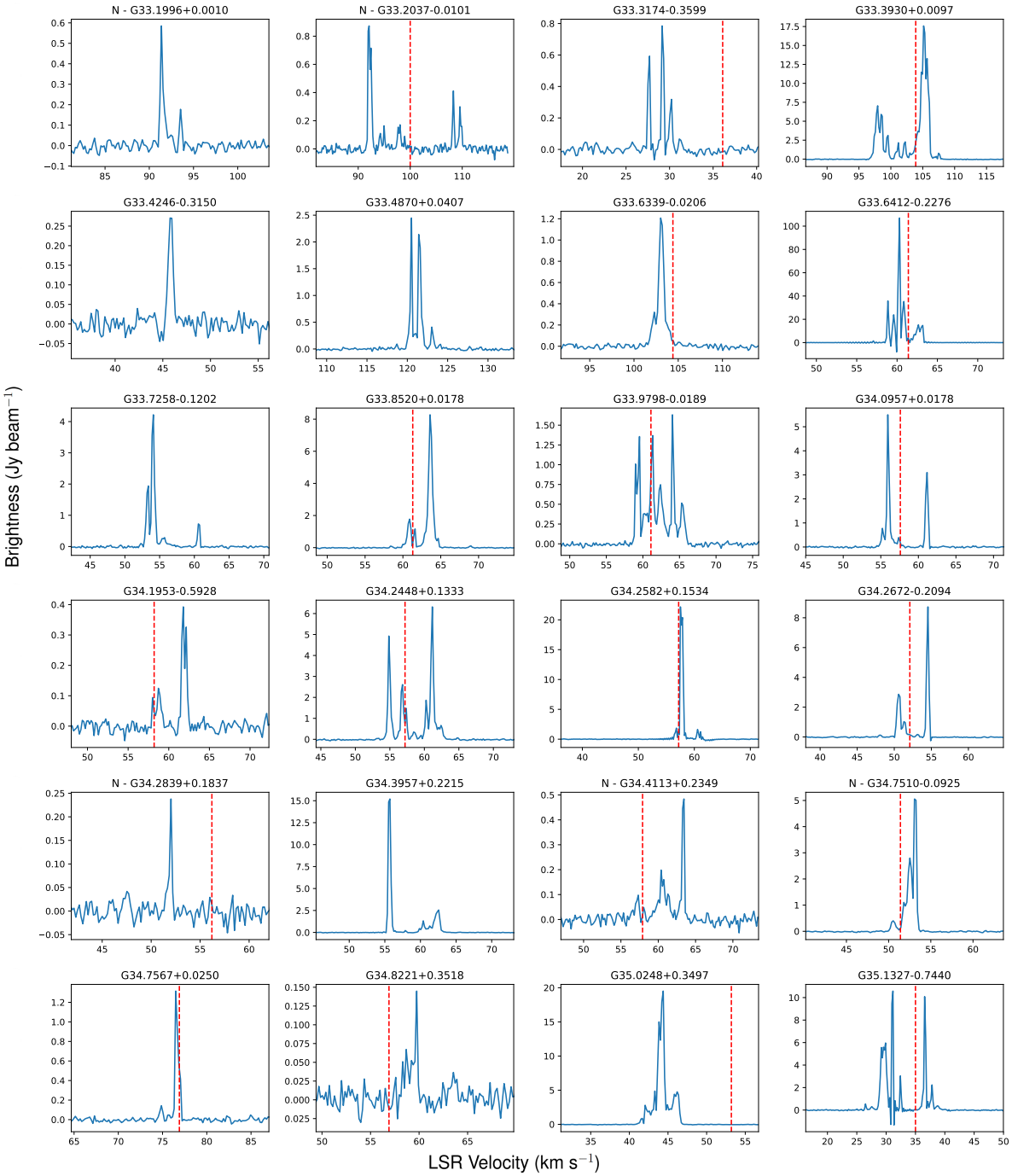

Fig. C.18: Fig. C.1. continued.

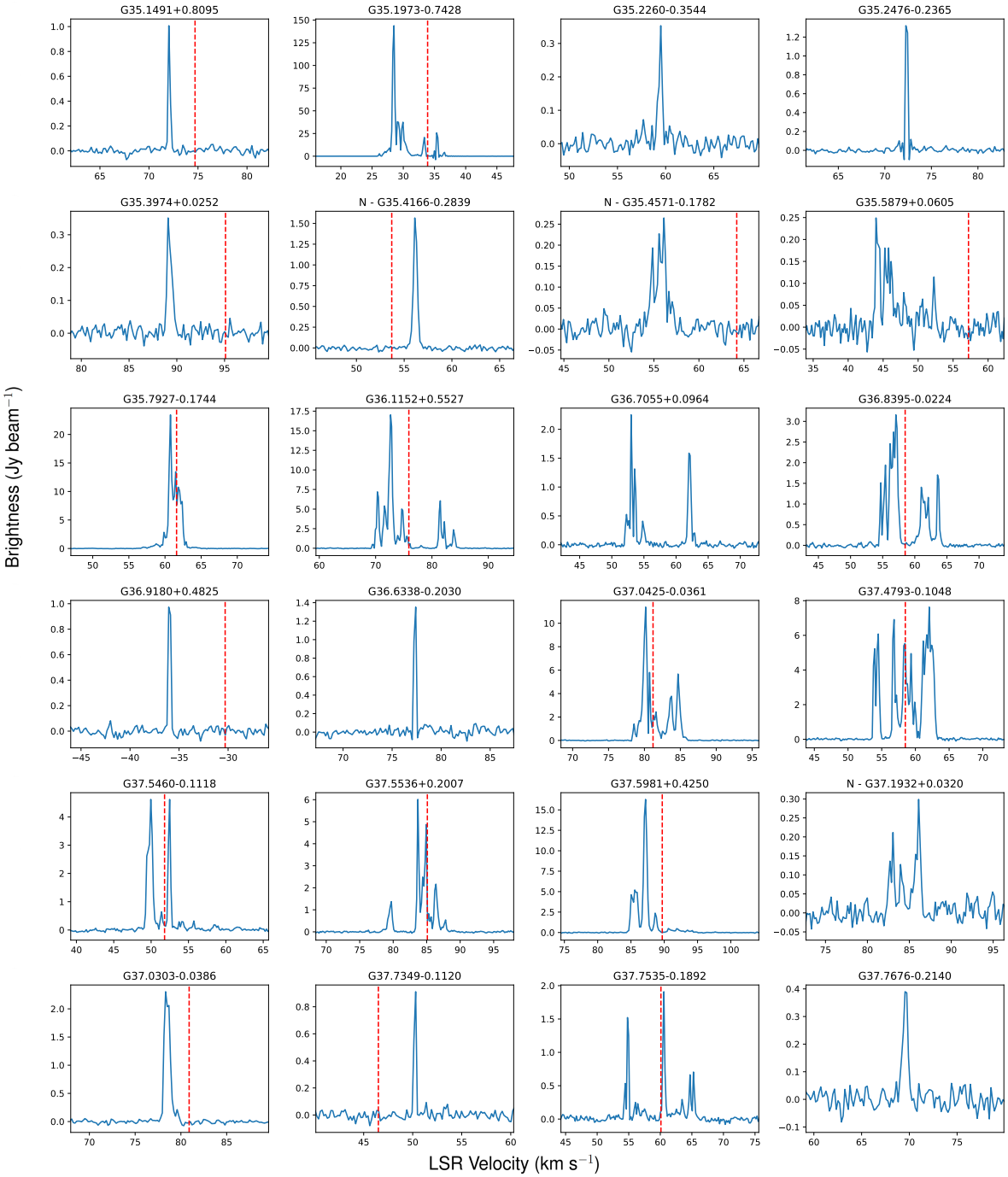

Fig. C.19: Fig. C.1. continued.

Fig. C.20: Fig. C.1. continued.

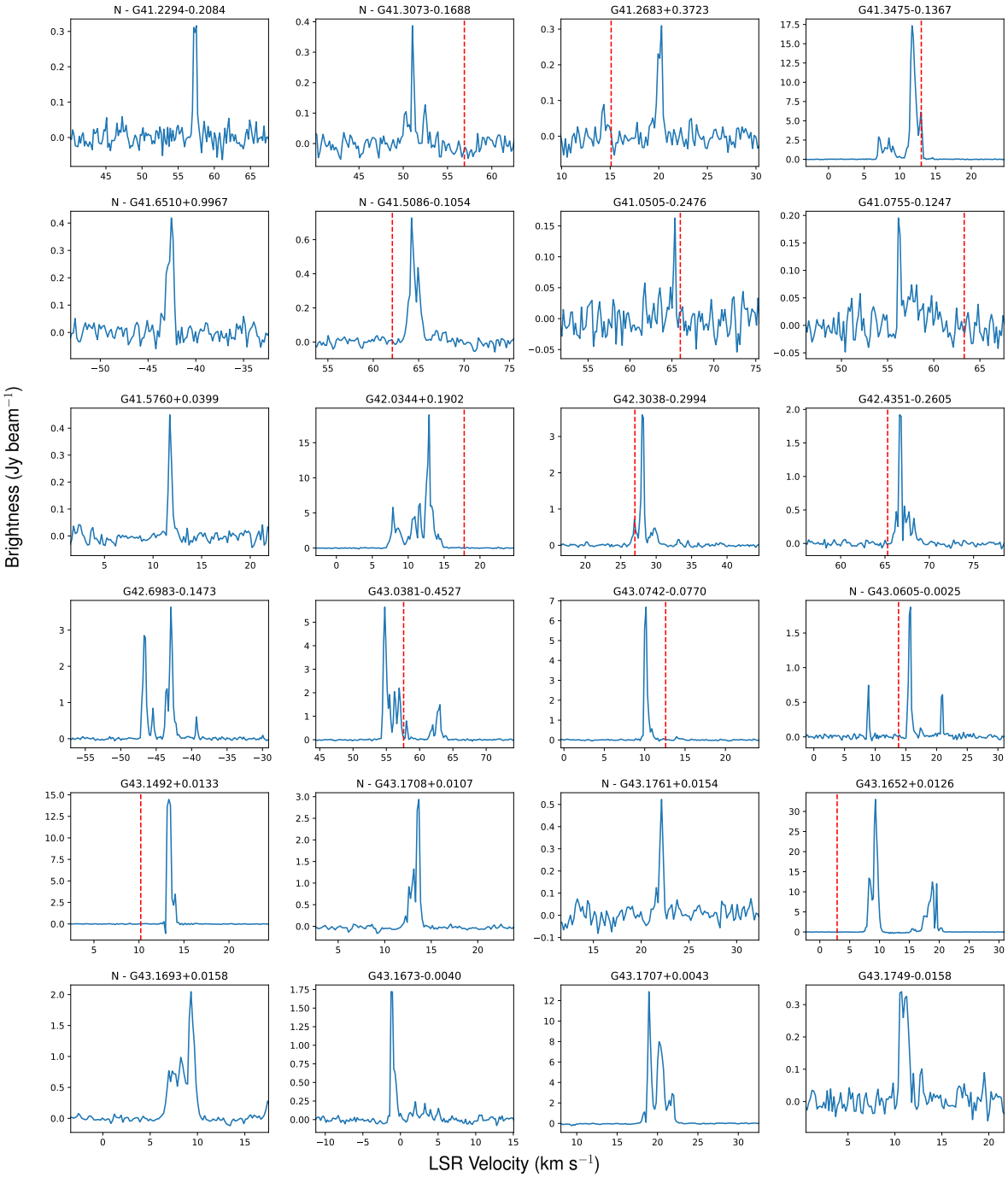

Fig. C.21: Fig. C.1. continued.

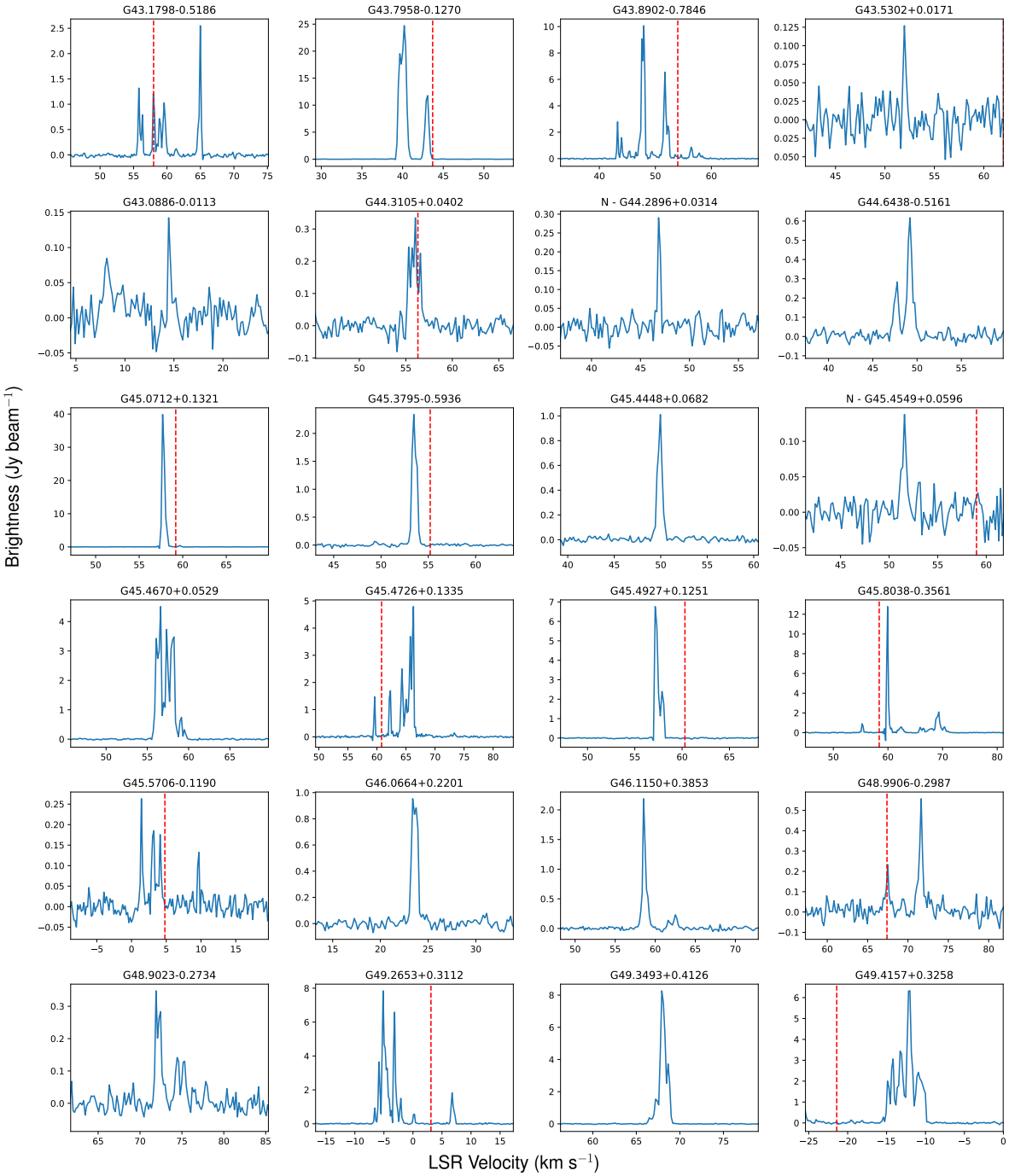

Fig. C.22: Fig. C.1. continued.

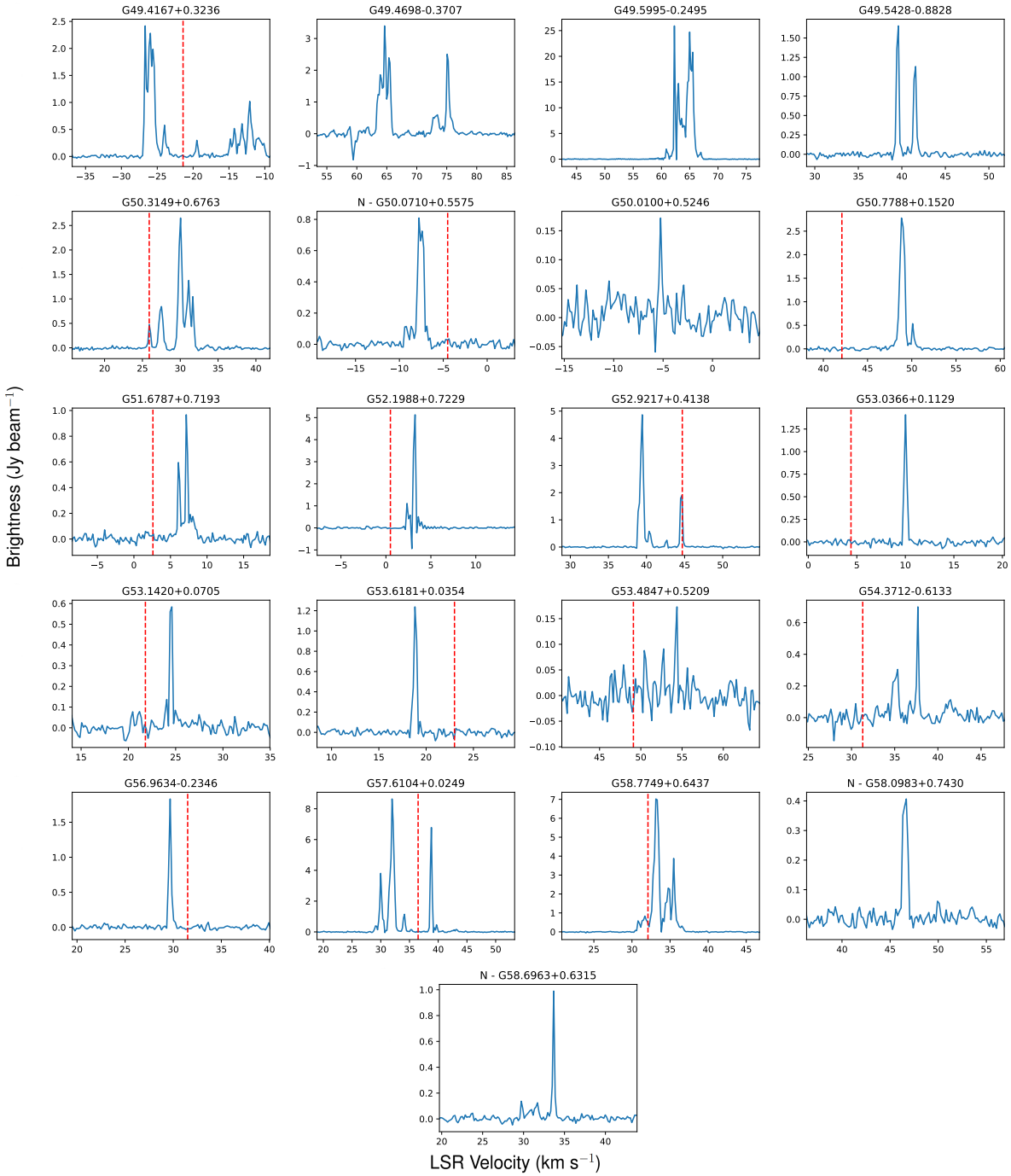

Fig. C.23: Fig. C.1. continued.

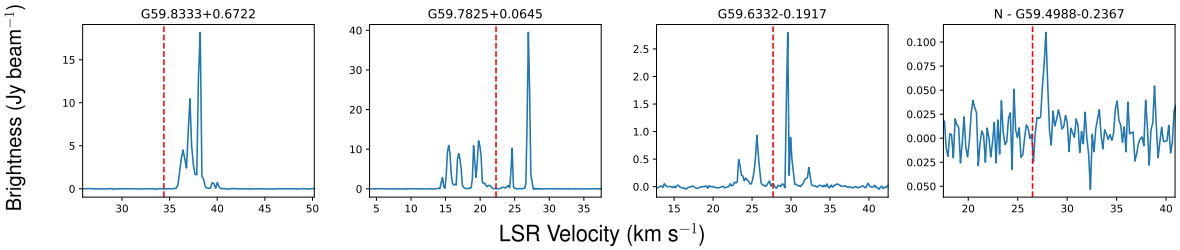

Fig. C.24: Fig. C.1. continued.

Appendix C

Chapter 5 Appendix

C.1 Sources with multiple components

GLOSTAR 6.7 GHz methanol masers that show multiple maser spots when viewed with the higher angular resolution B-configuration data are included here.

C.2 Methanol masers with continuum counterparts

Shown are the radio continuum counterparts for the methanol masers in the pilot region in both the D-configuration and the B-configuration starting with Fig. 5.7.

C.3 The spectra of CH_3H masers in B- and D-configuration

Here, we present the spectra for each maser source in the pilot region using the B-configuration data compared to the D-configuration data.

C.4 Tables of maser properties

Shown are the full versions of Table 5.2 of the individual maser spot properties in the B-configuration and Table 5.3 of the calculated maser luminosities in Table C.1 and Table C.2 respectively.

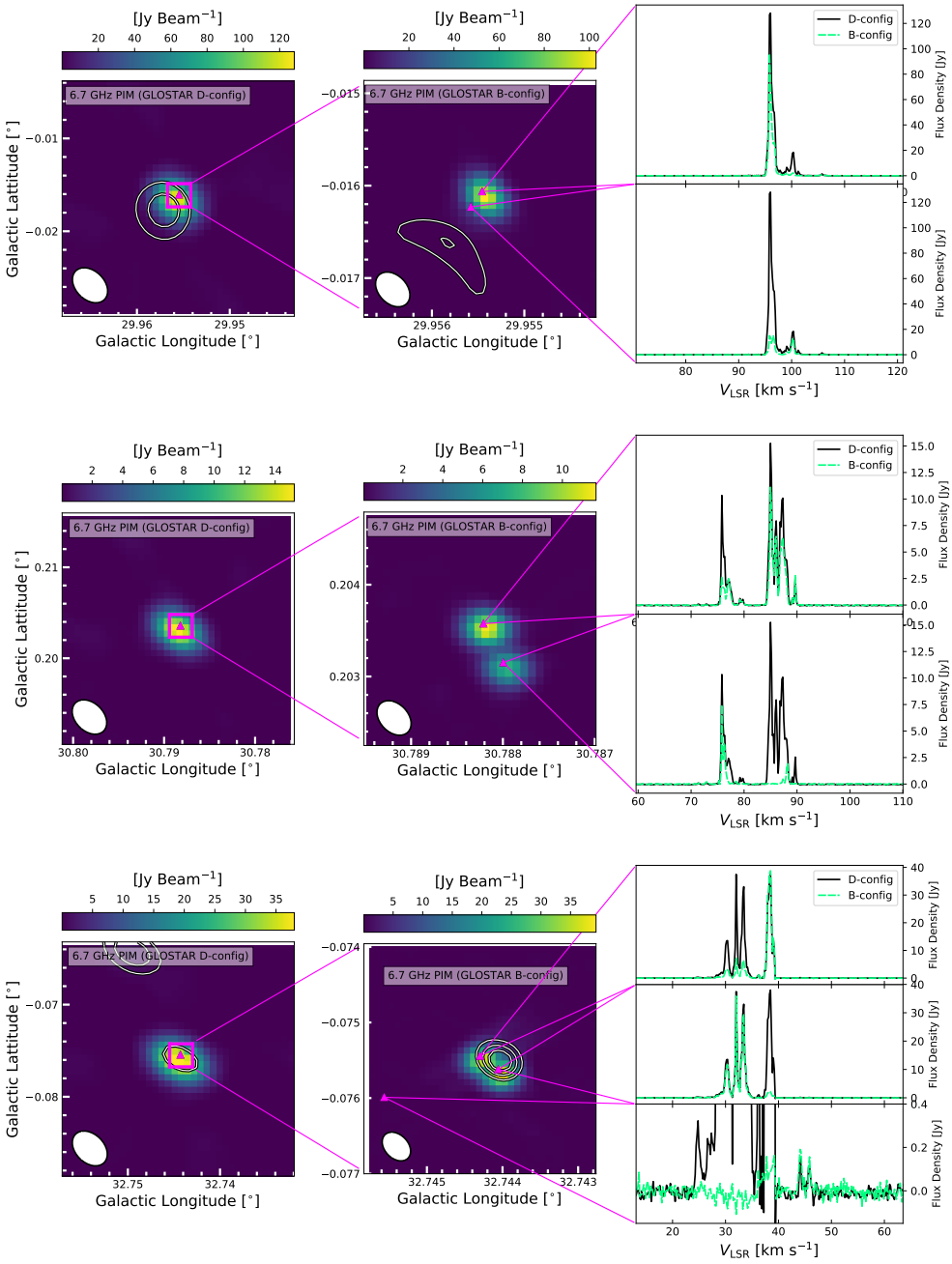

Figure C.1: More examples similar to Fig. 5.6 for sources G29.9556–0.0156, G30.7880+0.2039, and G32.7443–0.0753.

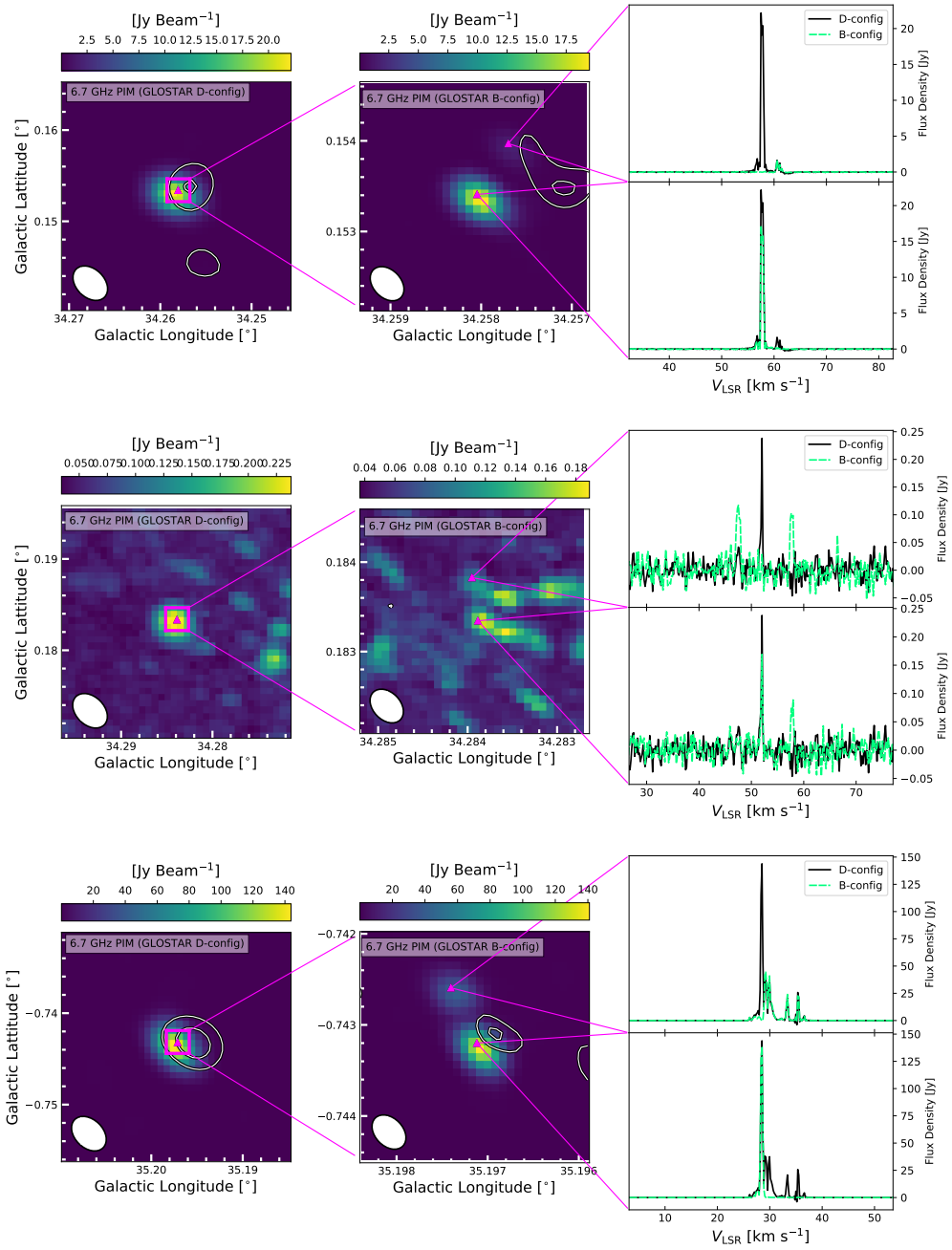

Figure C.2: Continued from Fig. C.1 for sources G34.2582+0.1534, G34.2839+0.1837, and G35.1973–0.7428.

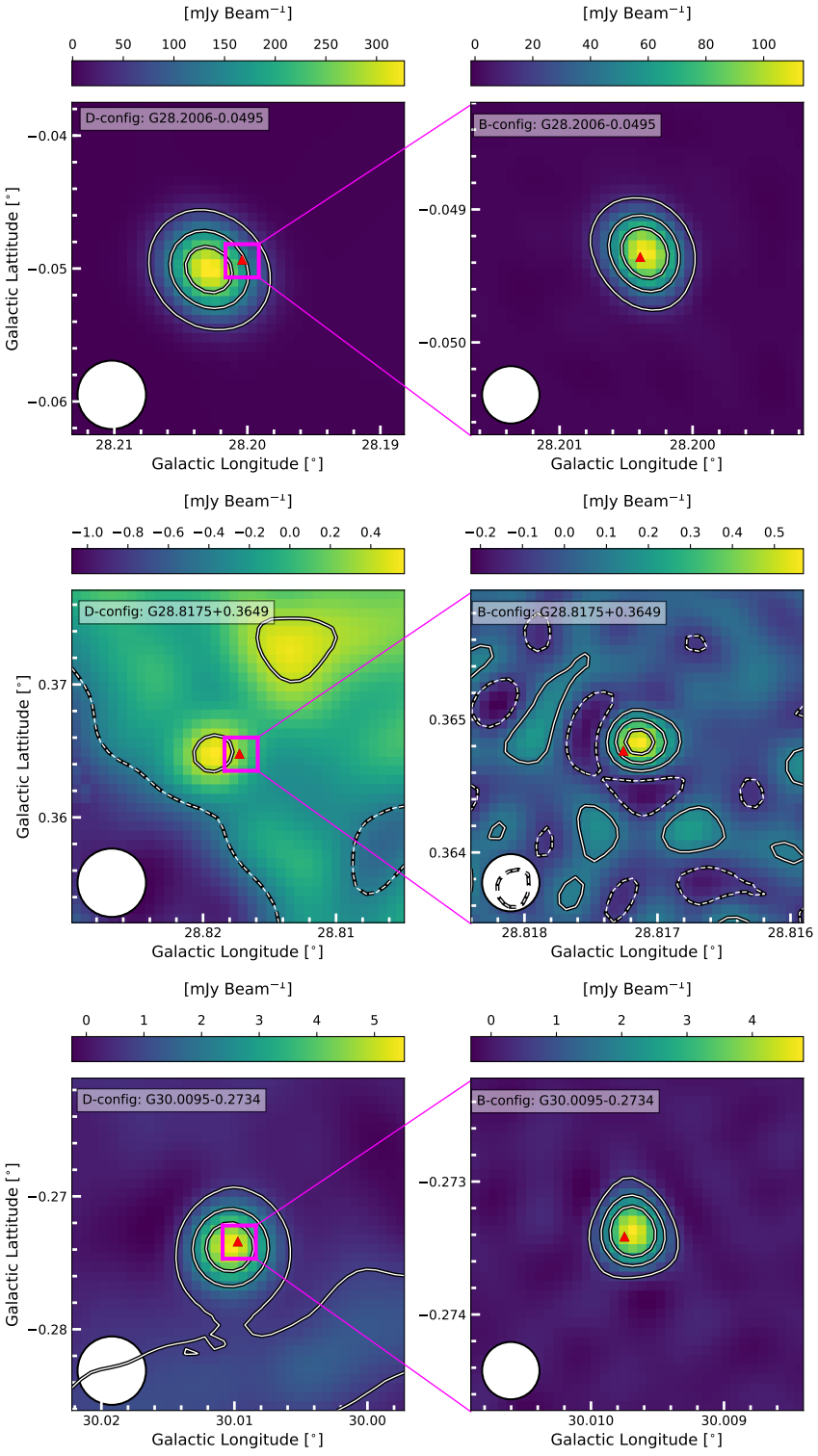

Figure C.3: Continued from Fig. 5.7.

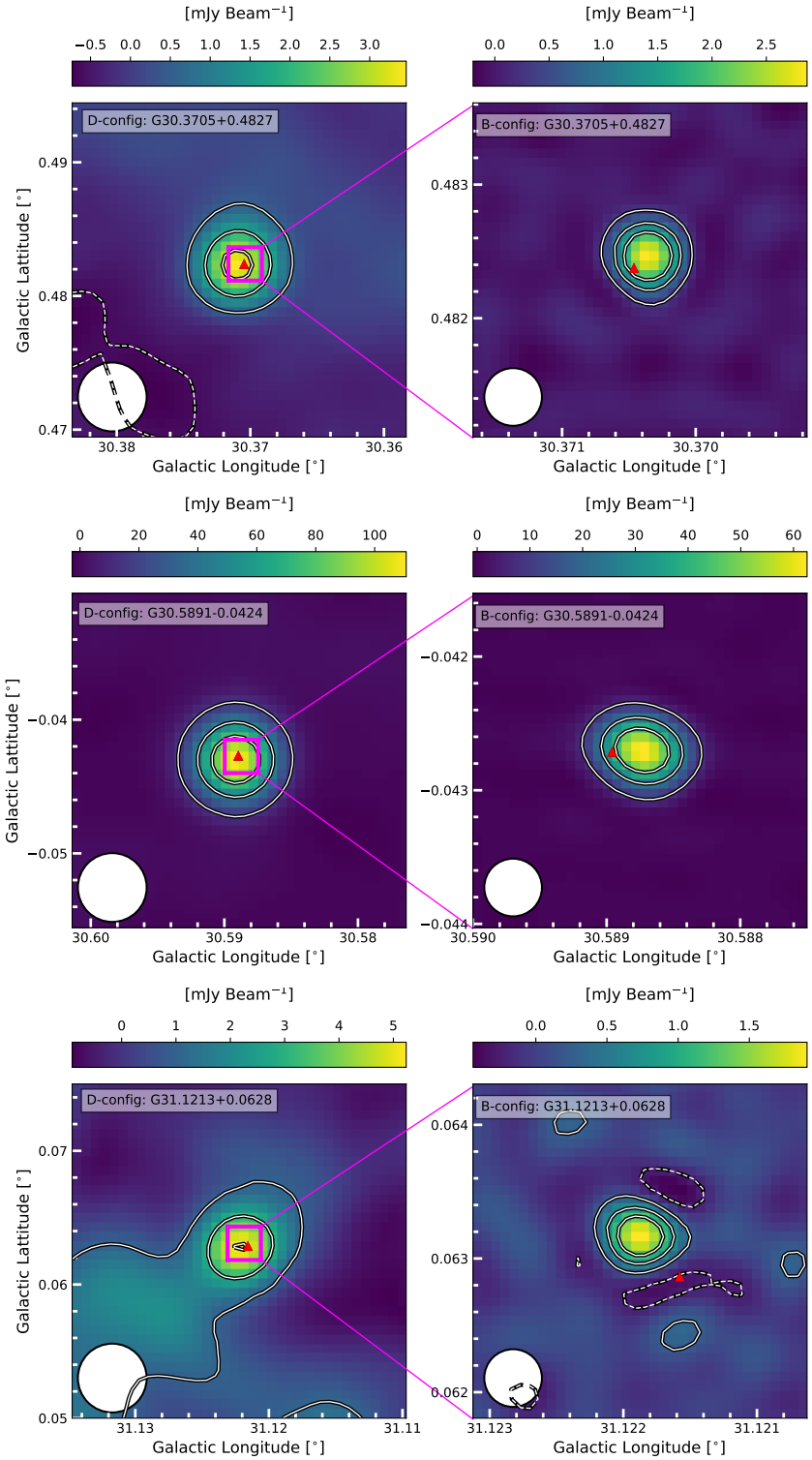

Figure C.4: Continued from Fig. 5.7.

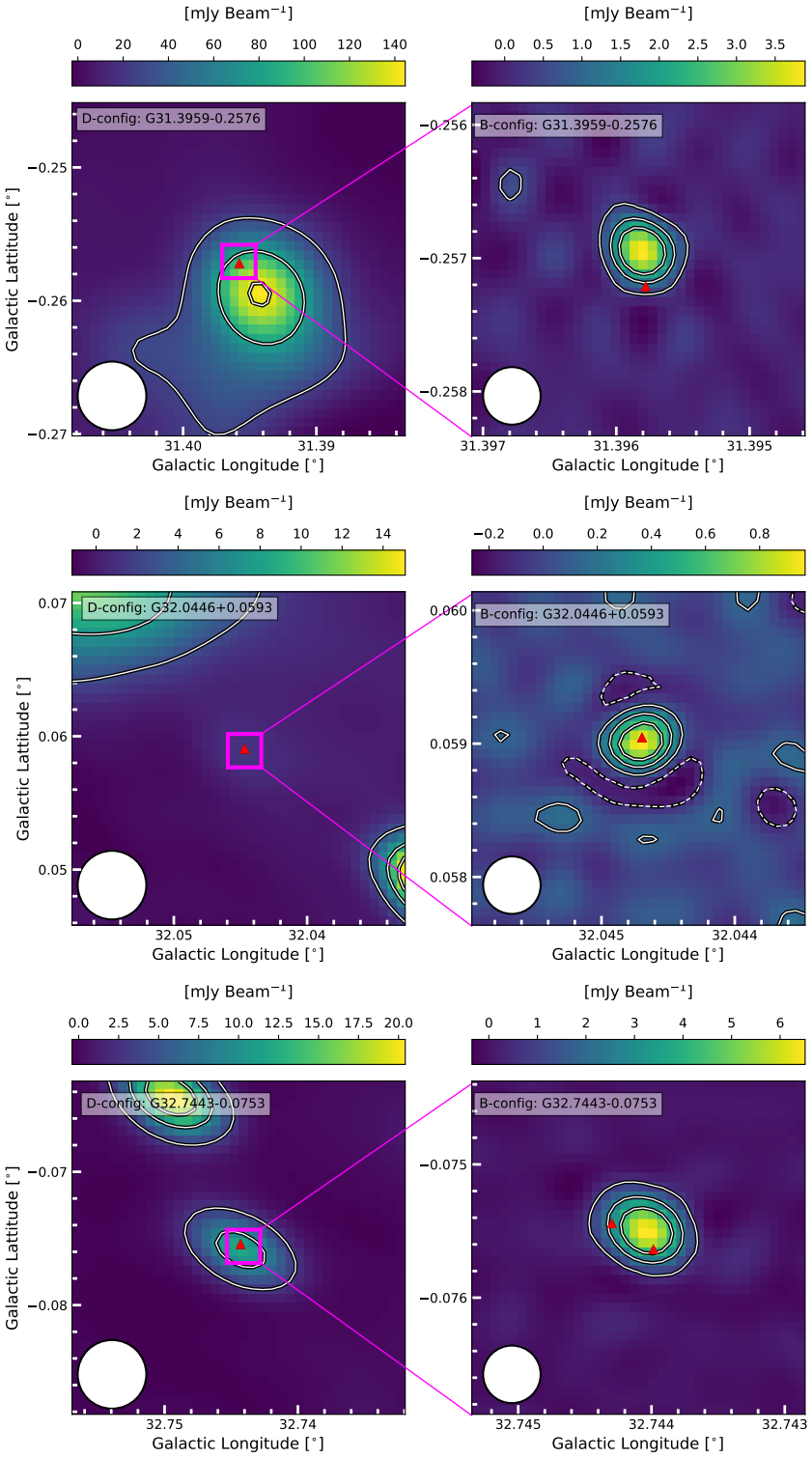

Figure C.5: Continued from Fig. 5.7.

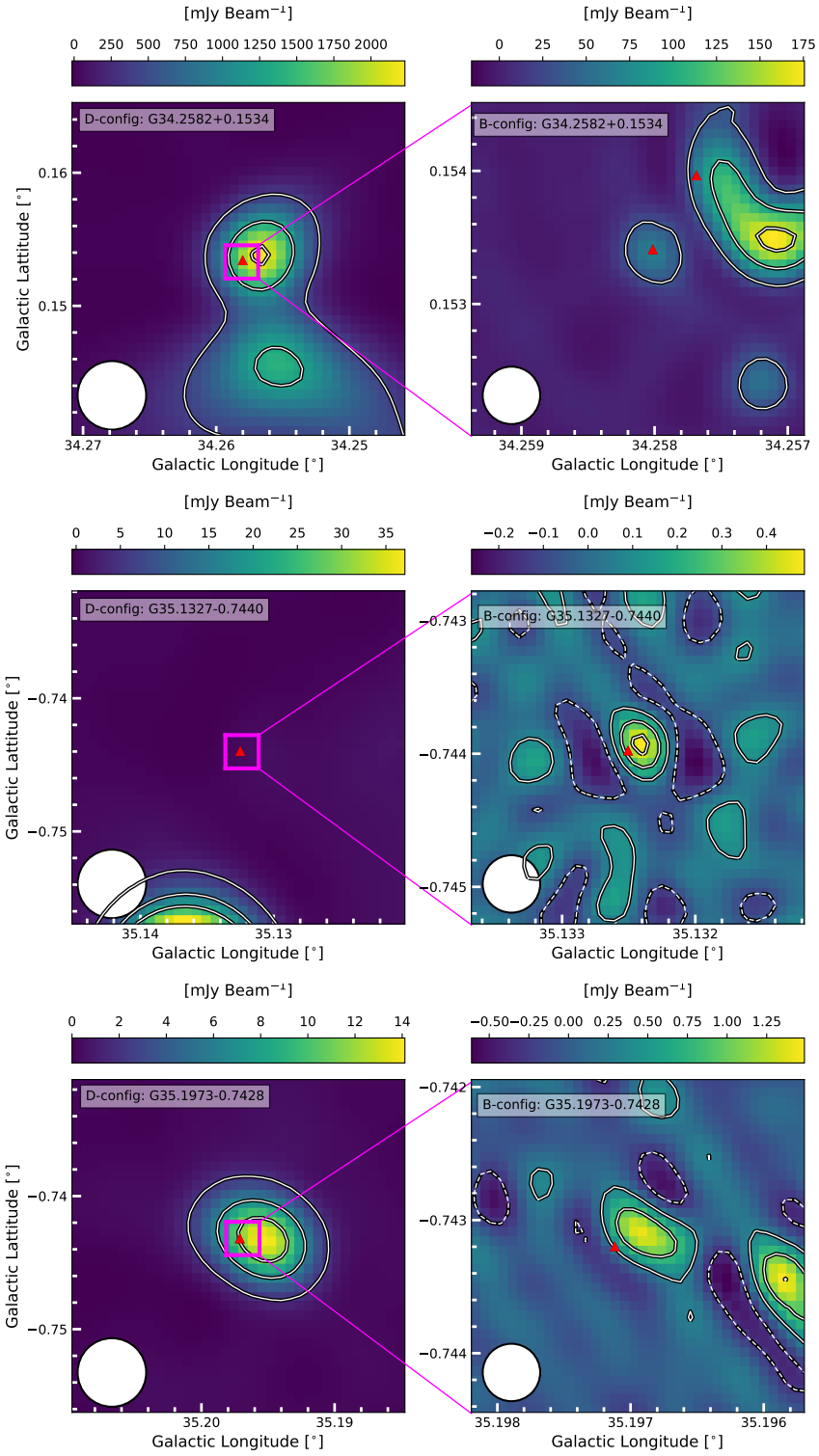

Figure C.6: Continued from Fig. 5.7.

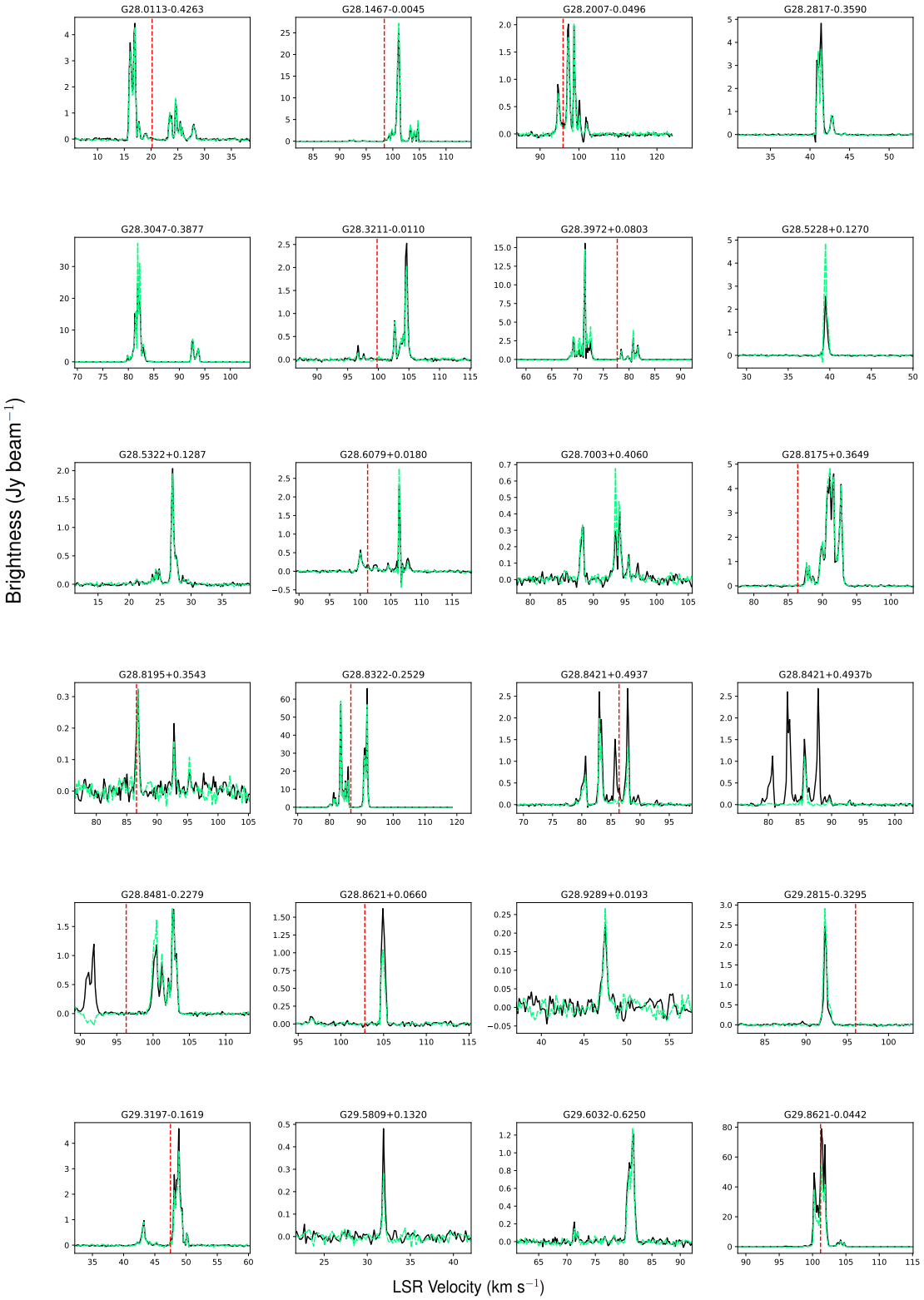

Figure C.7: Spectra of 6.7 GHz methanol masers detected with GLOSTAR extracted at the peak pixel. The B-configuration data is the green-dashed line while the D-configuration data is the black solid line. The vertical red dashed line indicates the ATLASGAL clump velocity (Urquhart et al. 2018b, 2022) in case of an associated 870 μm compact source catalogue (CSC) source.

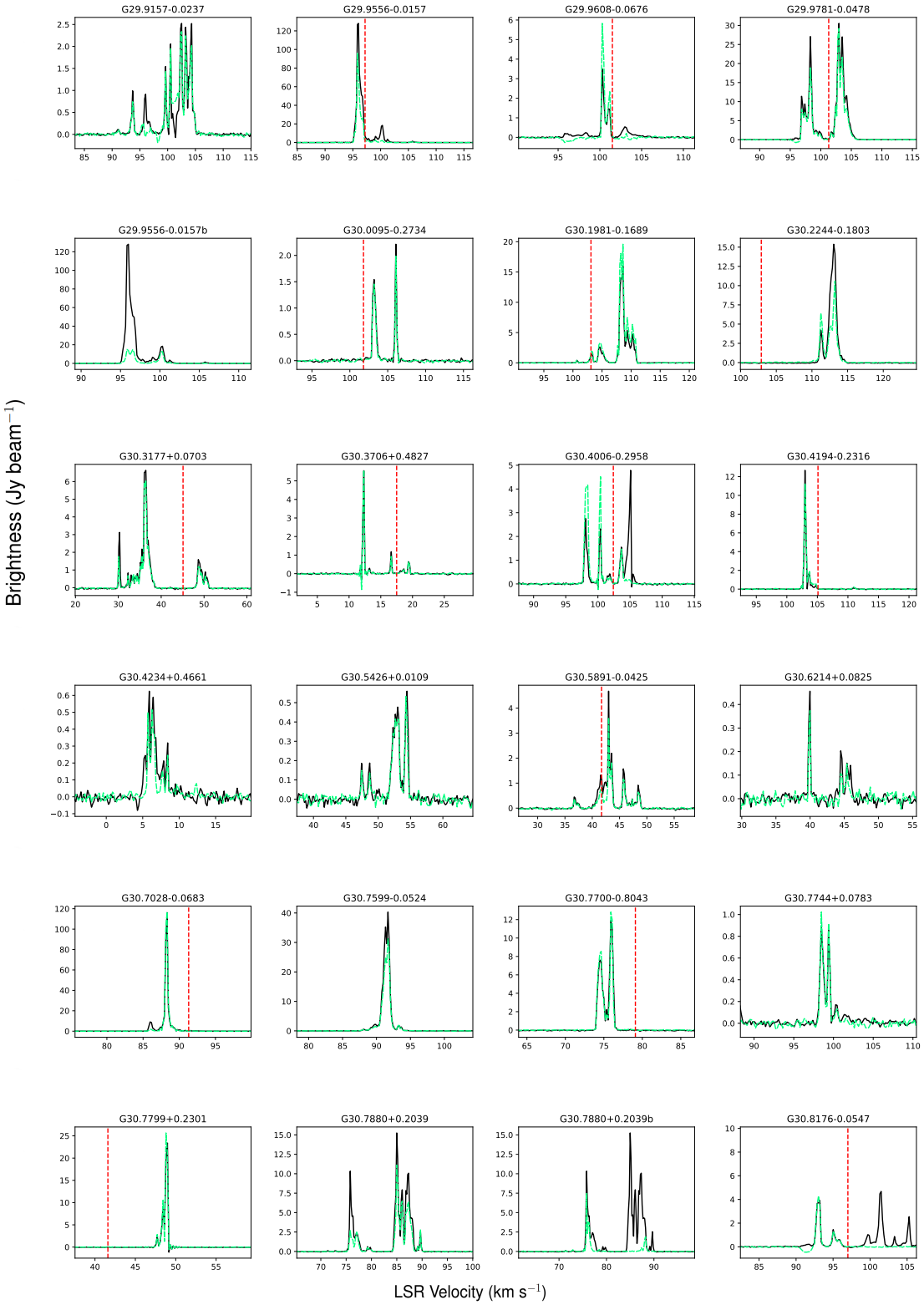

Figure C.8: Continued from Fig. C.7.

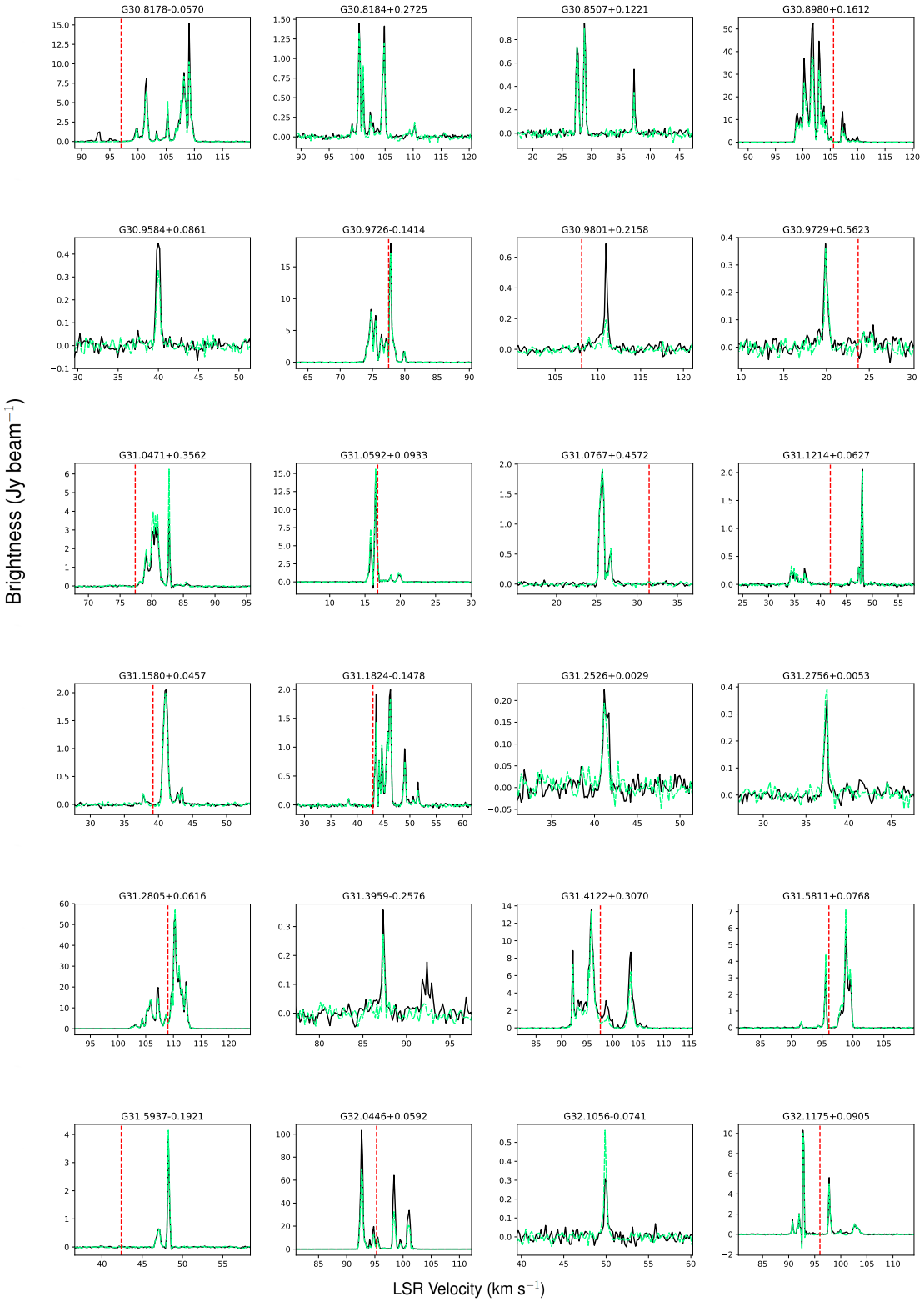

Figure C.9: Continued from Fig. C.7.

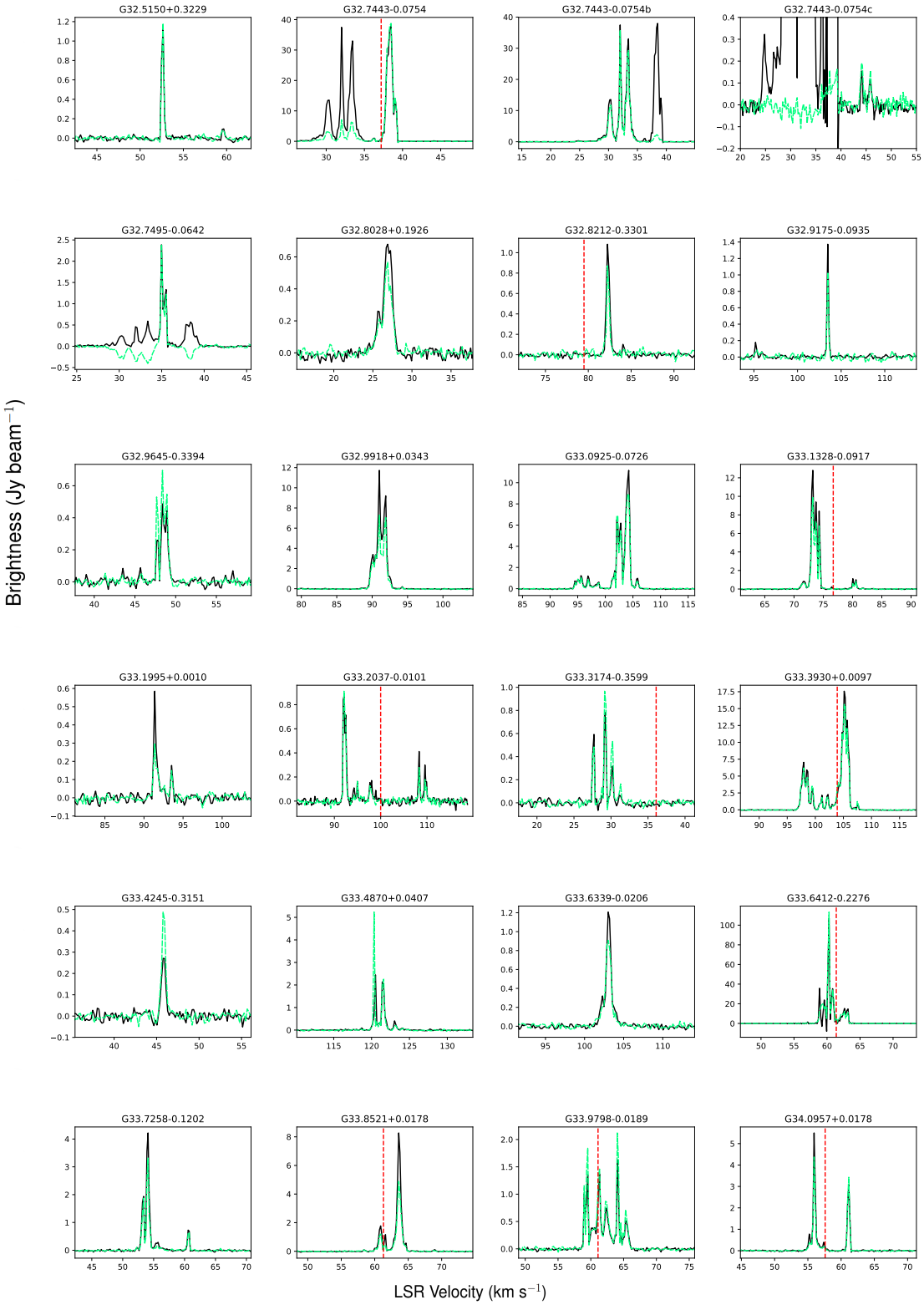

Figure C.10: Continued from Fig. C.7.

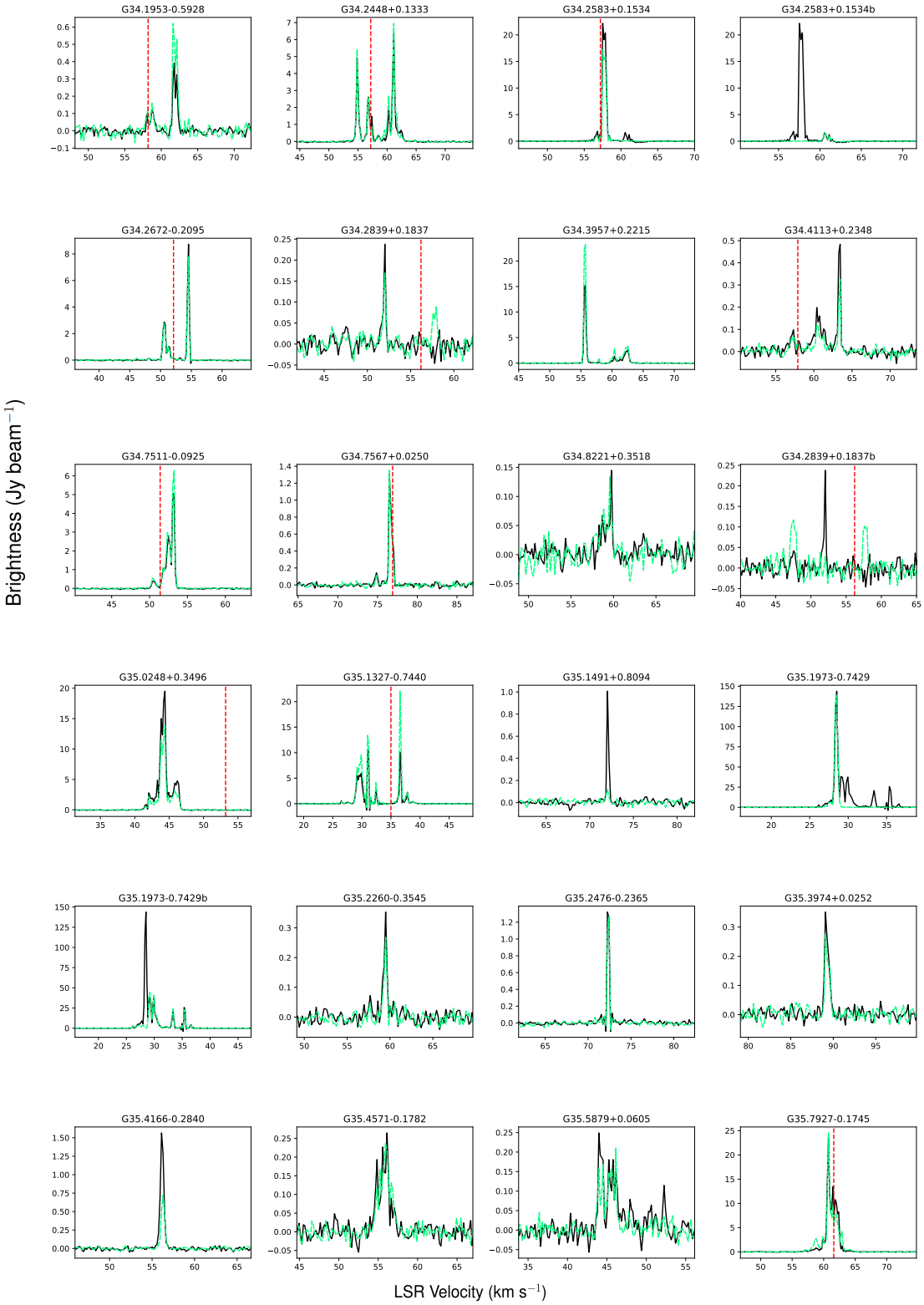

Figure C.11: Continued from Fig. C.7.

Table C.1: The complete version of Table 5.2.

Name	$\alpha/\Delta\alpha$	$\delta/\Delta\delta$	V_{LSR}	$S_{v,\,Peak}$	$S_{v,\,Int}$	Notes
	h:m:s/″	d:m:s/″	km s^{-1}	Jy beam^{-1}	Jy	
(1)	(2)	(3)	(4)	(5)	(6)	(7)
G28.6079+0.0180	18:43:28.5227	-3:50:22.850	106.33	3.30±0.03	3.43±0.06	MMB
G28.6079+0.0180	0.46	0.27	99.49	0.06±0.01	0.19±0.06	
G28.6079+0.0180	0.13	0.15	99.67	0.18±0.02	0.18±0.03	
G28.6079+0.0180	0.11	0.14	99.85	0.41±0.01	0.40±0.02	
G28.6079+0.0180	0.18	0.02	100.03	0.50±0.02	0.51±0.03	
G28.6079+0.0180	0.15	0.09	100.21	0.22±0.02	0.40±0.05	
G28.6079+0.0180	-0.01	0.15	100.39	0.20±0.02	0.25±0.03	
G28.6079+0.0180	0.02	-0.04	100.57	0.23±0.01	0.21±0.02	
G28.6079+0.0180	-0.01	0.07	100.75	0.11±0.01	0.12±0.03	
G28.6079+0.0180	-0.12	0.00	101.11	0.10±0.02	0.13±0.04	
G28.6079+0.0180	0.13	-0.05	101.29	0.15±0.01	0.10±0.02	
G28.6079+0.0180	0.04	-0.07	102.37	0.10±0.02	0.21±0.05	
G28.6079+0.0180	0.18	0.28	102.55	0.09±0.01	0.07±0.02	
G28.6079+0.0180	0.02	-0.13	102.73	0.08±0.02	0.23±0.07	
G28.6079+0.0180	0.24	0.10	103.09	0.08±0.02	0.14±0.04	
G28.6079+0.0180	0.04	0.02	104.53	0.21±0.02	0.22±0.03	
G28.6079+0.0180	0.11	-0.00	104.71	0.09±0.01	0.30±0.06	
G28.6079+0.0180	0.00	0.03	106.51	1.63±0.02	1.69±0.04	
G28.6079+0.0180	-0.06	0.05	106.87	0.18±0.02	0.26±0.04	
G28.6079+0.0180	-0.03	-0.19	107.59	0.22±0.02	0.26±0.04	
G28.6079+0.0180	0.02	0.08	107.77	0.30±0.02	0.35±0.04	
G28.6079+0.0180	0.69	-0.04	107.95	0.05±0.02	0.10±0.04	
G28.6079+0.0180	0.34	0.29	108.13	0.09±0.02	0.09±0.03	
G28.7003+0.4065	18:42:15.5642	-3:34:46.822	93.47	0.79±0.02	0.75±0.03	MMB
G28.7003+0.4065	-0.00	0.04	87.89	0.30±0.01	0.27±0.02	
G28.7003+0.4065	-0.04	-0.06	88.07	0.31±0.01	0.29±0.02	
G28.7003+0.4065	0.04	-0.06	88.25	0.37±0.02	0.43±0.03	
G28.7003+0.4065	-0.00	-0.08	88.43	0.19±0.01	0.20±0.02	
G28.7003+0.4065	-0.09	-0.10	93.11	0.04±0.01	0.28±0.08	
G28.7003+0.4065	0.04	-0.06	93.29	0.26±0.01	0.22±0.02	
G28.7003+0.4065	0.02	0.05	93.65	0.35±0.02	0.35±0.03	
G28.7003+0.4065	0.01	-0.20	93.83	0.16±0.02	0.16±0.03	
G28.7003+0.4065	-0.02	-0.07	94.01	0.55±0.02	0.59±0.03	
G28.7003+0.4065	0.00	0.04	94.19	0.47±0.02	0.51±0.03	
G28.7003+0.4065	-0.11	0.32	94.37	0.10±0.02	0.31±0.07	
G28.7003+0.4065	0.62	0.59	94.55	0.03±0.01	0.53±0.17	
G28.7003+0.4065	0.03	0.04	95.45	0.15±0.01	0.15±0.03	
G28.7003+0.4065	0.32	0.67	95.63	0.07±0.01	0.35±0.08	
G28.8175+0.3649	18:42:37.3481	-3:29:40.907	91.09	5.93±0.03	6.02±0.05	MMB
G28.8175+0.3649	-0.11	-0.06	87.67	1.25±0.03	1.28±0.05	
G28.8175+0.3649	-0.04	-0.06	88.03	0.99±0.03	1.09±0.05	
G28.8175+0.3649	-0.08	0.02	88.21	0.33±0.02	0.43±0.05	
G28.8175+0.3649	-0.13	-0.03	88.57	0.41±0.03	0.59±0.08	
G28.8175+0.3649	-0.05	-0.02	88.75	0.23±0.02	0.37±0.04	

Continuation
of Table C.1

Name	$\alpha/\Delta\alpha$ h:m:s/″	$\delta/\Delta\delta$ d:m:s/″	V_{LSR} km s^{-1}	$S_{v,\,Peak}$ Jy beam^{-1}	$S_{v,\,Int}$ Jy	Notes
(1)	(2)	(3)	(4)	(5)	(6)	(7)
G28.8175+0.3649	-0.18	0.10	88.93	0.07±0.01	0.16±0.04	
G28.8175+0.3649	0.04	0.10	89.11	0.13±0.01	0.16±0.03	
G28.8175+0.3649	0.01	0.05	89.29	0.10±0.01	0.11±0.03	
G28.8175+0.3649	-0.10	-0.00	89.47	0.48±0.02	0.49±0.03	
G28.8175+0.3649	0.04	-0.03	89.65	1.53±0.02	1.57±0.03	
G28.8175+0.3649	-0.00	-0.02	89.83	1.87±0.02	1.93±0.04	
G28.8175+0.3649	-0.01	-0.03	90.01	2.19±0.02	2.25±0.04	
G28.8175+0.3649	0.01	-0.01	90.19	1.36±0.02	1.39±0.03	
G28.8175+0.3649	-0.02	-0.00	90.37	1.68±0.02	1.67±0.04	
G28.8175+0.3649	0.01	-0.02	90.55	3.96±0.02	4.02±0.04	
G28.8175+0.3649	0.00	-0.01	90.73	5.13±0.02	5.23±0.04	
G28.8175+0.3649	0.00	0.00	90.91	5.46±0.02	5.54±0.04	
G28.8175+0.3649	0.00	-0.00	91.27	4.47±0.03	4.51±0.05	
G28.8175+0.3649	-0.00	-0.00	91.45	5.21±0.02	5.33±0.04	
G28.8175+0.3649	-0.00	-0.01	91.63	5.45±0.02	5.63±0.04	
G28.8175+0.3649	-0.03	-0.01	91.81	1.89±0.02	1.96±0.03	
G28.8175+0.3649	0.00	0.01	91.99	1.29±0.02	1.31±0.03	
G28.8175+0.3649	-0.00	-0.00	92.17	1.25±0.02	1.29±0.04	
G28.8175+0.3649	-0.00	-0.01	92.35	2.13±0.03	2.20±0.05	
G28.8175+0.3649	-0.01	0.01	92.53	3.29±0.02	3.28±0.04	
G28.8175+0.3649	-0.00	0.00	92.71	5.13±0.03	5.20±0.05	
G28.8175+0.3649	-0.02	0.01	92.89	2.91±0.02	2.95±0.04	
G28.8175+0.3649	-0.02	-0.02	93.07	0.52±0.02	0.56±0.04	
G28.8175+0.3649	-0.04	0.22	93.25	0.12±0.02	0.26±0.06	
G28.8195+0.3543	18:42:39.8201	-3:29:51.561	86.82	0.40±0.02	0.41±0.03	MMB
G28.8195+0.3543	0.16	0.24	86.46	0.10±0.01	0.12±0.03	
G28.8195+0.3543	0.11	0.19	86.64	0.21±0.02	0.26±0.03	
G28.8195+0.3543	0.04	0.27	87.00	0.19±0.02	0.21±0.03	
G28.8195+0.3543	-0.05	0.12	92.76	0.17±0.02	0.38±0.07	
G28.8195+0.3543	0.15	0.26	95.28	0.11±0.02	0.19±0.05	
G28.8322–0.2528	18:44:51.0880	-3:45:48.372	83.53	63.69±0.20	64.90±0.35	MMB
G28.8322–0.2528	-0.33	0.52	79.39	0.06±0.02	0.30±0.10	
G28.8322–0.2528	-0.05	-0.05	79.57	0.32±0.04	0.54±0.09	
G28.8322–0.2528	-0.04	-0.11	79.75	0.37±0.04	0.74±0.11	
G28.8322–0.2528	-0.06	-0.02	79.93	0.97±0.06	1.34±0.13	
G28.8322–0.2528	-0.06	-0.02	80.11	1.90±0.05	2.14±0.10	
G28.8322–0.2528	-0.07	-0.04	80.29	1.22±0.05	1.45±0.09	
G28.8322–0.2528	-0.07	-0.04	80.47	1.01±0.05	1.26±0.10	
G28.8322–0.2528	-0.06	-0.02	80.65	1.10±0.06	1.43±0.12	
G28.8322–0.2528	-0.07	-0.03	80.83	0.98±0.05	1.22±0.10	
G28.8322–0.2528	-0.02	-0.03	81.01	1.74±0.05	1.88±0.09	
G28.8322–0.2528	-0.03	-0.04	81.19	4.57±0.06	4.73±0.12	
G28.8322–0.2528	-0.03	-0.03	81.37	5.51±0.06	5.74±0.11	
G28.8322–0.2528	-0.03	-0.03	81.55	2.25±0.05	2.41±0.10	

Continuation
of Table C.1

Name	$\alpha/\Delta\alpha$ h:m:s/″	$\delta/\Delta\delta$ d:m:s/″	V_{LSR} km s^{-1}	$S_{v,\,Peak}$ Jy beam^{-1}	$S_{v,\,Int}$ Jy	Notes
(1)	(2)	(3)	(4)	(5)	(6)	(7)
G28.8322–0.2528	-0.02	-0.02	81.73	4.29±0.06	4.46±0.10	
G28.8322–0.2528	-0.03	-0.02	81.91	4.88±0.05	5.05±0.09	
G28.8322–0.2528	-0.02	0.00	82.09	0.77±0.05	1.00±0.11	
G28.8322–0.2528	-0.03	-0.01	82.27	0.42±0.04	0.89±0.13	
G28.8322–0.2528	-0.00	0.00	82.45	0.83±0.05	1.04±0.11	
G28.8322–0.2528	0.02	0.02	82.63	1.16±0.05	1.37±0.10	
G28.8322–0.2528	-0.01	-0.00	82.81	1.87±0.05	2.07±0.10	
G28.8322–0.2528	-0.00	-0.01	82.99	6.13±0.07	6.25±0.13	
G28.8322–0.2528	0.02	-0.00	83.17	13.90±0.13	13.95±0.23	
G28.8322–0.2528	0.01	-0.01	83.35	46.45±0.19	47.25±0.33	
G28.8322–0.2528	-0.03	-0.01	83.71	34.74±0.17	35.25±0.30	
G28.8322–0.2528	-0.07	0.00	83.89	20.64±0.14	20.71±0.24	
G28.8322–0.2528	-0.06	0.01	84.07	6.17±0.09	6.22±0.16	
G28.8322–0.2528	-0.08	0.00	84.25	8.10±0.09	8.23±0.15	
G28.8322–0.2528	-0.09	0.01	84.43	9.88±0.08	10.09±0.15	
G28.8322–0.2528	-0.09	0.01	84.61	3.70±0.07	3.83±0.12	
G28.8322–0.2528	-0.12	0.05	84.97	17.28±0.12	17.57±0.21	
G28.8322–0.2528	-0.19	0.13	85.33	4.77±0.07	4.89±0.12	
G28.8322–0.2528	-0.21	0.15	85.51	6.30±0.08	6.35±0.14	
G28.8322–0.2528	-0.21	0.14	85.69	14.73±0.12	14.77±0.22	
G28.8322–0.2528	-0.21	0.14	85.87	22.54±0.14	22.81±0.25	
G28.8322–0.2528	-0.19	0.11	86.05	4.53±0.06	4.46±0.10	
G28.8322–0.2528	-0.08	0.03	86.41	0.14±0.02	0.11±0.03	
G28.8322–0.2528	0.05	-0.56	90.01	0.13±0.02	0.53±0.11	
G28.8322–0.2528	0.10	-0.29	90.19	0.38±0.04	0.54±0.09	
G28.8322–0.2528	0.16	-0.31	90.37	1.88±0.05	1.98±0.08	
G28.8322–0.2528	0.17	-0.30	90.55	5.13±0.08	5.19±0.13	
G28.8322–0.2528	0.16	-0.30	90.73	21.41±0.14	21.46±0.25	
G28.8322–0.2528	0.16	-0.30	90.91	30.05±0.17	30.10±0.30	
G28.8322–0.2528	0.15	-0.30	91.09	31.98±0.17	32.20±0.30	
G28.8322–0.2528	0.14	-0.30	91.27	23.82±0.15	23.81±0.26	
G28.8322–0.2528	0.11	-0.29	91.45	17.29±0.15	17.28±0.26	
G28.8322–0.2528	0.11	-0.29	91.63	35.32±0.18	35.71±0.31	
G28.8322–0.2528	0.10	-0.28	91.81	62.88±0.21	64.02±0.38	
G28.8322–0.2528	0.10	-0.29	91.99	18.54±0.12	18.58±0.22	
G28.8322–0.2528	0.08	-0.28	92.17	4.67±0.07	4.67±0.11	
G28.8322–0.2528	0.09	-0.30	92.35	2.59±0.06	2.80±0.10	
G28.8322–0.2528	0.27	-0.20	92.71	0.09±0.02	0.47±0.10	
G28.8322–0.2528	0.51	-0.26	93.97	0.05±0.02	0.31±0.12	
G28.8322–0.2528	0.31	0.12	94.33	0.09±0.02	0.07±0.03	
G28.8322–0.2528	0.98	-3.10	114.49	0.04±0.01	0.37±0.13	
G28.8421+0.4938	18:42:12.5412	-3:24:48.815	82.99	2.64±0.02	2.62±0.04	MMB
G28.8421+0.4938	0.60	-0.33	78.85	0.07±0.01	0.37±0.09	
G28.8421+0.4938	0.01	0.13	79.03	0.10±0.02	0.24±0.05	

Continuation
of Table C.1

Name	$\alpha/\Delta\alpha$ h:m:s/″	$\delta/\Delta\delta$ d:m:s/″	V_{LSR} km s^{-1}	$S_{v,\,Peak}$ Jy beam^{-1}	$S_{v,\,Int}$ Jy	Notes
(1)	(2)	(3)	(4)	(5)	(6)	(7)
G28.8421+0.4938	0.17	0.12	79.57	0.11±0.02	0.21±0.05	
G28.8421+0.4938	-0.09	0.02	79.75	0.13±0.02	0.17±0.03	
G28.8421+0.4938	-0.07	0.06	79.93	0.48±0.02	0.52±0.03	
G28.8421+0.4938	-0.10	-0.00	80.11	0.53±0.02	0.55±0.03	
G28.8421+0.4938	-0.09	0.07	80.29	0.55±0.01	0.53±0.03	
G28.8421+0.4938	-0.05	-0.08	80.47	0.72±0.02	0.73±0.03	
G28.8421+0.4938	-0.10	0.00	80.65	1.07±0.02	1.15±0.03	
G28.8421+0.4938	-0.12	-0.01	80.83	0.28±0.02	0.35±0.03	
G28.8421+0.4938	-0.01	0.01	82.81	0.64±0.02	0.64±0.04	
G28.8421+0.4938	0.01	0.00	83.17	1.38±0.03	1.39±0.05	
G28.8421+0.4938	-0.00	-0.01	83.35	1.78±0.02	1.80±0.03	
G28.8421+0.4938	-0.00	0.02	83.53	0.72±0.02	0.74±0.03	
G28.8421+0.4938	-0.07	-0.12	83.71	0.21±0.02	0.35±0.04	
G28.8421+0.4938	0.11	-0.19	83.89	0.09±0.02	0.14±0.04	
G28.8421+0.4938	-0.07	0.10	84.07	0.13±0.01	0.10±0.02	
G28.8421+0.4938	0.29	-0.08	84.25	0.05±0.01	0.43±0.13	
G28.8421+0.4938	-0.22	-0.29	84.79	0.06±0.01	0.11±0.04	
G28.8421+0.4938	0.03	-0.20	86.41	0.12±0.02	0.20±0.06	
G28.8421+0.4938	-0.00	-0.16	86.59	0.11±0.02	0.18±0.04	
G28.8421+0.4938	0.05	-0.19	87.13	0.08±0.02	0.20±0.06	
G28.8421+0.4938	0.05	-0.16	87.31	0.25±0.02	0.31±0.03	
G28.8421+0.4938	-0.05	-0.09	87.49	0.45±0.02	0.55±0.04	
G28.8421+0.4938	-0.02	-0.13	87.67	0.61±0.02	0.59±0.03	
G28.8421+0.4938	-0.02	-0.11	87.85	1.75±0.02	1.77±0.04	
G28.8421+0.4938	-0.04	-0.10	88.03	1.33±0.02	1.31±0.03	
G28.8421+0.4938	0.23	-0.37	88.75	0.04±0.01	0.20±0.06	
G28.8421+0.4938	-0.03	-0.24	88.93	0.14±0.01	0.14±0.03	
G28.8429+0.4936	18:42:12.6212	-3:24:46.827	85.69	1.40±0.03	1.43±0.05	G28.8421+0.4938b
G28.8429+0.4936	-0.13	-0.23	85.15	0.10±0.02	0.39±0.09	
G28.8429+0.4936	0.01	0.03	85.51	0.38±0.03	0.45±0.06	
G28.8429+0.4936	-0.02	0.02	85.87	1.03±0.02	1.09±0.03	
G28.8429+0.4936	0.01	-0.00	86.05	0.44±0.02	0.58±0.05	
G28.8429+0.4936	1.17	0.95	86.23	0.03±0.01	0.82±0.29	
G28.8429+0.4936	-0.17	-0.09	89.47	0.09±0.02	0.18±0.05	
G28.8429+0.4936	-0.02	0.05	89.65	0.21±0.01	0.23±0.03	
G28.8429+0.4936	0.57	0.51	92.71	0.06±0.01	0.28±0.07	
G28.8429+0.4936	-0.08	0.14	92.89	0.10±0.02	0.10±0.03	
G28.8481–0.2279	18:44:47.4594	-3:44:17.163	102.64	1.76±0.06	2.06±0.12	MMB
G28.8481–0.2279	0.21	-0.07	99.22	0.06±0.02	0.17±0.06	
G28.8481–0.2279	0.68	-0.29	99.40	0.06±0.02	0.15±0.06	
G28.8481–0.2279	0.13	0.02	99.58	0.10±0.02	0.57±0.14	
G28.8481–0.2279	0.03	0.05	99.76	0.33±0.04	0.75±0.11	
G28.8481–0.2279	0.05	-0.03	99.94	0.83±0.06	1.23±0.13	
G28.8481–0.2279	0.06	-0.00	100.12	1.19±0.05	1.53±0.11	

Continuation
of Table C.1

Name	$\alpha/\Delta\alpha$ h:m:s/″	$\delta/\Delta\delta$ d:m:s/″	V_{LSR} km s^{-1}	$S_{v,\,Peak}$ Jy beam^{-1}	$S_{v,\,Int}$ Jy	Notes
(1)	(2)	(3)	(4)	(5)	(6)	(7)
G28.8481–0.2279	0.07	-0.02	100.30	1.23±0.05	1.40±0.09	
G28.8481–0.2279	0.05	-0.04	100.48	1.55±0.05	1.79±0.10	
G28.8481–0.2279	0.06	-0.05	100.66	0.48±0.05	0.77±0.12	
G28.8481–0.2279	0.04	-0.08	100.84	0.34±0.04	0.76±0.13	
G28.8481–0.2279	0.09	-0.01	101.02	0.60±0.06	1.01±0.15	
G28.8481–0.2279	0.06	-0.01	101.20	0.90±0.07	1.40±0.15	
G28.8481–0.2279	0.06	-0.00	101.38	0.52±0.05	0.96±0.15	
G28.8481–0.2279	0.07	0.02	101.56	0.29±0.03	0.40±0.07	
G28.8481–0.2279	-0.08	-0.11	101.74	0.11±0.02	0.32±0.06	
G28.8481–0.2279	-0.03	-0.05	101.92	0.21±0.03	0.31±0.06	
G28.8481–0.2279	0.04	0.01	102.10	0.42±0.05	0.81±0.12	
G28.8481–0.2279	0.03	0.02	102.28	0.17±0.03	0.72±0.13	
G28.8481–0.2279	-0.01	-0.09	102.46	0.42±0.05	1.06±0.17	
G28.8481–0.2279	-0.01	-0.02	102.82	1.63±0.06	1.95±0.12	
G28.8481–0.2279	-0.00	-0.03	103.00	0.84±0.06	1.16±0.12	
G28.8481–0.2279	0.00	-0.01	103.18	0.84±0.06	1.16±0.13	
G28.8481–0.2279	0.03	0.02	103.36	0.46±0.05	0.83±0.13	
G28.8621+0.0660	18:43:46.2196	-3:35:29.809	104.89	1.05±0.02	1.03±0.03	MMB
G28.8621+0.0660	-0.00	0.00	104.71	0.81±0.02	0.88±0.04	
G28.8621+0.0660	-0.00	-0.03	105.07	0.68±0.02	0.75±0.03	
G28.8621+0.0660	0.04	0.03	105.25	0.35±0.02	0.34±0.03	
G28.0113–0.4263	18:43:57.9674	-4:34:24.114	17.00	4.61±0.03	4.70±0.06	MMB
G28.0113–0.4263	0.12	0.02	15.74	0.30±0.02	0.30±0.03	
G28.0113–0.4263	0.01	0.03	15.92	2.58±0.02	2.64±0.04	
G28.0113–0.4263	0.01	0.01	16.10	3.61±0.03	3.63±0.05	
G28.0113–0.4263	0.02	0.02	16.28	3.00±0.03	2.96±0.05	
G28.0113–0.4263	-0.00	0.02	16.46	1.86±0.02	1.83±0.04	
G28.0113–0.4263	0.01	-0.03	16.64	1.83±0.03	1.77±0.05	
G28.0113–0.4263	0.00	0.01	16.82	3.93±0.03	3.97±0.05	
G28.0113–0.4263	-0.01	-0.01	17.18	1.68±0.02	1.73±0.04	
G28.0113–0.4263	0.01	0.04	17.54	0.40±0.02	0.40±0.03	
G28.0113–0.4263	0.08	0.13	17.72	0.68±0.02	0.67±0.04	
G28.0113–0.4263	0.14	0.10	17.90	0.38±0.02	0.41±0.03	
G28.0113–0.4263	0.00	0.09	18.80	0.15±0.02	0.39±0.08	
G28.0113–0.4263	-0.33	0.04	18.98	0.08±0.02	0.39±0.11	
G28.0113–0.4263	0.04	0.10	19.16	0.23±0.02	0.20±0.03	
G28.0113–0.4263	0.09	0.05	23.30	0.71±0.02	0.70±0.03	
G28.0113–0.4263	0.10	0.03	23.48	1.04±0.02	1.08±0.04	
G28.0113–0.4263	0.16	0.01	23.66	0.65±0.02	0.65±0.03	
G28.0113–0.4263	0.10	-0.05	23.84	0.76±0.02	0.80±0.03	
G28.0113–0.4263	0.22	-0.04	24.20	0.10±0.02	0.11±0.04	
G28.0113–0.4263	-0.27	0.38	24.38	0.04±0.02	0.28±0.13	
G28.0113–0.4263	0.14	-0.01	24.56	1.56±0.02	1.62±0.04	
G28.0113–0.4263	0.11	-0.00	24.74	1.18±0.02	1.19±0.04	

Continuation
of Table C.1

Name	$\alpha/\Delta\alpha$ h:m:s/″	$\delta/\Delta\delta$ d:m:s/″	V_{LSR} km s^{-1}	$S_{v,\,Peak}$ Jy beam^{-1}	$S_{v,\,Int}$ Jy	Notes
(1)	(2)	(3)	(4)	(5)	(6)	(7)
G28.0113–0.4263	0.12	-0.00	24.92	0.37±0.02	0.38±0.03	
G28.0113–0.4263	0.16	0.20	25.10	0.22±0.02	0.30±0.05	
G28.0113–0.4263	0.21	0.02	25.28	0.33±0.02	0.32±0.03	
G28.0113–0.4263	0.13	0.02	25.46	0.58±0.02	0.63±0.04	
G28.0113–0.4263	0.29	0.15	25.64	0.09±0.01	0.23±0.05	
G28.0113–0.4263	0.09	-0.04	25.82	0.45±0.02	0.44±0.04	
G28.0113–0.4263	0.14	-0.15	26.00	0.17±0.02	0.21±0.04	
G28.0113–0.4263	0.14	-0.02	27.62	0.23±0.02	0.25±0.04	
G28.0113–0.4263	0.10	-0.00	27.80	0.40±0.02	0.49±0.04	
G28.0113–0.4263	0.14	-0.01	27.98	0.50±0.02	0.57±0.04	
G28.0113–0.4263	0.12	0.02	28.16	0.36±0.02	0.36±0.03	
G28.0113–0.4263	0.17	-0.07	28.34	0.26±0.02	0.24±0.03	
G28.0113–0.4263	0.26	-0.21	28.52	0.09±0.01	0.16±0.04	
G28.9285+0.0191	18:44:03.4968	-3:33:13.537	47.48	0.26±0.02	0.29±0.05	NEW
G28.9285+0.0191	-0.18	-0.20	47.12	0.07±0.01	0.12±0.04	
G28.9285+0.0191	0.05	0.07	47.30	0.13±0.02	0.21±0.05	
G28.9285+0.0191	0.09	0.03	47.66	0.19±0.02	0.17±0.03	
G28.1467–0.0045	18:42:42.5894	-4:15:35.119	101.12	29.54±0.19	30.60±0.35	MMB
G28.1467–0.0045	-0.55	-0.48	91.76	0.07±0.02	0.34±0.10	
G28.1467–0.0045	-0.26	-0.24	91.94	0.13±0.02	0.40±0.08	
G28.1467–0.0045	0.06	-0.23	92.48	0.19±0.02	0.20±0.03	
G28.1467–0.0045	-0.04	-0.13	92.66	0.26±0.02	0.34±0.03	
G28.1467–0.0045	0.01	-0.11	94.28	0.06±0.01	0.28±0.09	
G28.1467–0.0045	-0.01	0.09	98.24	0.07±0.02	0.09±0.03	
G28.1467–0.0045	0.17	-0.14	98.42	0.14±0.02	0.21±0.05	
G28.1467–0.0045	-0.01	-0.13	98.60	0.50±0.02	0.51±0.04	
G28.1467–0.0045	-0.06	-0.05	98.78	0.40±0.02	0.42±0.04	
G28.1467–0.0045	0.06	-0.13	98.96	0.40±0.02	0.37±0.03	
G28.1467–0.0045	0.03	-0.08	99.14	0.93±0.02	0.95±0.04	
G28.1467–0.0045	0.04	-0.06	99.32	1.89±0.03	1.97±0.05	
G28.1467–0.0045	0.23	-0.75	99.50	0.07±0.02	0.42±0.14	
G28.1467–0.0045	0.03	-0.06	99.68	2.25±0.04	2.38±0.06	
G28.1467–0.0045	0.02	-0.05	99.86	2.91±0.03	3.00±0.06	
G28.1467–0.0045	0.03	-0.06	100.04	1.43±0.03	1.43±0.05	
G28.1467–0.0045	0.02	-0.04	100.22	1.99±0.03	2.00±0.05	
G28.1467–0.0045	0.03	-0.06	100.40	1.66±0.04	1.67±0.06	
G28.1467–0.0045	0.02	-0.05	100.58	5.05±0.06	5.07±0.11	
G28.1467–0.0045	0.01	-0.02	100.76	12.44±0.11	12.76±0.19	
G28.1467–0.0045	0.01	-0.01	100.94	25.33±0.17	26.27±0.31	
G28.1467–0.0045	-0.02	0.03	101.30	15.83±0.13	16.30±0.24	
G28.1467–0.0045	-0.01	-0.00	101.48	2.80±0.04	2.91±0.08	
G28.1467–0.0045	0.03	-0.11	101.84	0.45±0.03	0.59±0.05	
G28.1467–0.0045	-0.16	-0.20	102.20	0.13±0.02	0.20±0.06	
G28.1467–0.0045	-0.12	-0.05	102.56	0.09±0.02	0.39±0.10	

Continuation
of Table C.1

Name	$\alpha/\Delta\alpha$ h:m:s/″	$\delta/\Delta\delta$ d:m:s/″	V_{LSR} km s^{-1}	$S_{v,\,Peak}$ Jy beam^{-1}	$S_{v,\,Int}$ Jy	Notes
(1)	(2)	(3)	(4)	(5)	(6)	(7)
G28.1467–0.0045	0.02	-0.13	102.92	0.32±0.03	0.46±0.07	
G28.1467–0.0045	0.09	-0.12	103.10	1.27±0.03	1.28±0.05	
G28.1467–0.0045	0.08	-0.10	103.28	3.93±0.05	4.04±0.08	
G28.1467–0.0045	0.10	-0.10	103.46	2.49±0.04	2.52±0.06	
G28.1467–0.0045	0.04	-0.04	103.82	0.79±0.02	0.82±0.04	
G28.1467–0.0045	0.03	-0.05	104.00	2.72±0.04	2.79±0.07	
G28.1467–0.0045	0.05	-0.06	104.18	1.76±0.03	1.87±0.06	
G28.1467–0.0045	-0.05	-0.12	104.36	0.30±0.02	0.29±0.04	
G28.1467–0.0045	0.06	-0.06	104.54	1.45±0.03	1.45±0.06	
G28.1467–0.0045	0.04	-0.07	104.72	4.91±0.05	5.06±0.08	
G28.2006–0.0495	18:42:58.1005	-4:13:57.524	98.69	2.45±0.04	2.60±0.07	MMB
G28.2006–0.0495	0.53	-0.31	94.01	0.11±0.02	0.11±0.03	
G28.2006–0.0495	0.64	-0.25	94.19	0.10±0.02	0.47±0.09	
G28.2006–0.0495	0.49	-0.40	94.37	0.32±0.02	0.43±0.04	
G28.2006–0.0495	0.48	-0.44	94.55	0.91±0.03	1.11±0.05	
G28.2006–0.0495	0.48	-0.41	94.73	0.81±0.03	1.02±0.06	
G28.2006–0.0495	0.38	-0.36	94.91	0.51±0.02	0.64±0.05	
G28.2006–0.0495	0.35	-0.32	95.09	0.32±0.02	0.51±0.05	
G28.2006–0.0495	0.29	-0.38	95.27	0.14±0.02	0.43±0.08	
G28.2006–0.0495	0.46	-0.32	95.45	0.13±0.02	0.39±0.08	
G28.2006–0.0495	0.53	-0.60	95.63	0.13±0.02	0.43±0.07	
G28.2006–0.0495	0.19	-0.65	95.81	0.08±0.02	0.31±0.08	
G28.2006–0.0495	0.14	-0.30	95.99	0.10±0.02	0.29±0.07	
G28.2006–0.0495	0.04	-0.20	96.17	0.12±0.02	0.20±0.04	
G28.2006–0.0495	0.08	-0.32	96.35	0.14±0.02	0.25±0.05	
G28.2006–0.0495	-0.00	-0.27	96.53	0.16±0.02	0.39±0.06	
G28.2006–0.0495	0.05	-0.25	96.71	0.34±0.02	0.50±0.05	
G28.2006–0.0495	0.18	-0.40	96.89	0.80±0.03	0.94±0.05	
G28.2006–0.0495	0.28	-0.45	97.07	2.09±0.03	2.33±0.05	
G28.2006–0.0495	0.30	-0.47	97.25	2.17±0.03	2.43±0.06	
G28.2006–0.0495	0.23	-0.42	97.43	1.44±0.03	1.69±0.05	
G28.2006–0.0495	0.23	-0.42	97.61	0.99±0.03	1.17±0.05	
G28.2006–0.0495	0.26	-0.44	97.79	0.50±0.02	0.63±0.05	
G28.2006–0.0495	0.32	-0.40	97.97	0.13±0.02	0.28±0.06	
G28.2006–0.0495	-0.04	-0.35	98.15	0.11±0.02	0.25±0.05	
G28.2006–0.0495	0.68	-0.84	98.33	0.06±0.02	0.30±0.09	
G28.2006–0.0495	0.02	-0.06	98.51	0.77±0.03	1.04±0.07	
G28.2006–0.0495	0.00	0.00	98.87	1.46±0.03	1.57±0.05	
G28.2006–0.0495	0.00	0.06	99.05	1.00±0.02	1.19±0.05	
G28.2006–0.0495	0.01	0.02	99.23	0.48±0.02	0.61±0.05	
G28.2006–0.0495	0.48	-0.15	99.41	0.10±0.01	0.30±0.06	
G28.2006–0.0495	0.62	-0.30	99.59	0.07±0.02	0.23±0.08	
G28.2006–0.0495	0.68	-0.56	99.77	0.21±0.03	0.46±0.09	
G28.2006–0.0495	0.65	-0.66	99.95	0.58±0.03	0.68±0.05	

Continuation
of Table C.1

Name	$\alpha/\Delta\alpha$ h:m:s/″	$\delta/\Delta\delta$ d:m:s/″	V_{LSR} km s^{-1}	$S_{v,\,Peak}$ Jy beam^{-1}	$S_{v,\,Int}$ Jy	Notes
(1)	(2)	(3)	(4)	(5)	(6)	(7)
G28.2006–0.0495	0.67	-0.51	100.13	0.52±0.02	0.58±0.05	
G28.2006–0.0495	0.76	-0.55	100.31	0.24±0.03	0.36±0.06	
G28.2006–0.0495	0.85	-0.39	100.49	0.09±0.02	0.29±0.08	
G28.2006–0.0495	0.78	-0.48	101.57	0.11±0.02	0.26±0.06	
G28.2006–0.0495	0.85	-0.44	101.75	0.11±0.02	0.52±0.12	
G28.2006–0.0495	0.67	-0.52	101.93	0.27±0.02	0.30±0.04	
G28.2006–0.0495	0.62	-0.60	102.11	0.14±0.02	0.29±0.07	
G28.2006–0.0495	0.71	-0.43	102.29	0.11±0.02	0.17±0.04	
G28.2006–0.0495	0.90	-0.24	102.47	0.05±0.01	0.21±0.07	
G28.2006–0.0495	0.35	-0.83	119.03	0.04±0.02	0.28±0.11	
G28.2820–0.3585	18:44:13.2568	-4:18:04.817	41.41	4.15±0.03	4.15±0.05	MMB
G28.2820–0.3585	-0.00	-0.02	40.87	2.12±0.02	2.07±0.04	
G28.2820–0.3585	0.00	-0.00	41.05	4.02±0.03	4.00±0.04	
G28.2820–0.3585	-0.01	-0.03	41.23	1.50±0.03	1.47±0.04	
G28.2820–0.3585	-0.01	-0.01	41.59	2.03±0.02	2.06±0.04	
G28.2820–0.3585	-0.08	0.01	42.49	0.23±0.02	0.36±0.05	
G28.2820–0.3585	-0.07	-0.05	42.67	0.91±0.02	0.95±0.03	
G28.2820–0.3585	-0.05	-0.07	42.85	0.76±0.02	0.79±0.03	
G28.2820–0.3585	-0.18	-0.07	43.03	0.24±0.02	0.26±0.03	
G28.3047–0.3877	18:44:21.9666	-4:17:39.892	81.83	41.06±0.09	42.83±0.17	MMB
G28.3047–0.3877	-0.19	0.23	79.49	0.07±0.02	0.44±0.14	
G28.3047–0.3877	0.06	0.18	79.67	1.04±0.03	1.19±0.06	
G28.3047–0.3877	0.00	0.19	79.85	2.27±0.03	2.39±0.05	
G28.3047–0.3877	0.00	0.18	80.03	1.41±0.02	1.58±0.05	
G28.3047–0.3877	-0.03	0.12	80.21	0.32±0.02	0.43±0.05	
G28.3047–0.3877	-0.01	0.13	80.39	1.89±0.02	1.98±0.04	
G28.3047–0.3877	-0.02	0.07	80.57	1.48±0.03	1.58±0.05	
G28.3047–0.3877	0.01	-0.03	80.75	1.92±0.03	1.96±0.05	
G28.3047–0.3877	0.01	0.02	80.93	4.40±0.03	4.56±0.06	
G28.3047–0.3877	0.01	0.02	81.11	4.70±0.05	4.72±0.08	
G28.3047–0.3877	0.00	0.01	81.29	11.53±0.06	11.70±0.11	
G28.3047–0.3877	0.01	0.00	81.47	17.27±0.06	17.91±0.12	
G28.3047–0.3877	-0.01	-0.04	81.65	4.85±0.06	4.55±0.11	
G28.3047–0.3877	0.00	-0.02	82.01	16.62±0.08	16.72±0.14	
G28.3047–0.3877	0.01	-0.01	82.19	33.69±0.09	34.99±0.16	
G28.3047–0.3877	0.01	-0.01	82.37	20.85±0.07	21.61±0.12	
G28.3047–0.3877	-0.00	0.08	82.55	2.05±0.04	1.96±0.07	
G28.3047–0.3877	-0.00	0.03	82.73	3.99±0.03	4.07±0.06	
G28.3047–0.3877	-0.01	0.02	82.91	6.14±0.04	6.31±0.08	
G28.3047–0.3877	-0.01	0.06	83.09	4.89±0.04	5.02±0.07	
G28.3047–0.3877	-0.03	0.14	83.27	3.40±0.03	3.49±0.05	
G28.3047–0.3877	-0.01	0.20	83.45	0.92±0.02	0.97±0.04	
G28.3047–0.3877	-0.06	0.07	83.63	0.24±0.03	0.45±0.08	
G28.3047–0.3877	-0.04	0.37	83.81	0.09±0.01	0.08±0.02	

Continuation
of Table C.1

Name	$\alpha/\Delta\alpha$ h:m:s/″	$\delta/\Delta\delta$ d:m:s/″	V_{LSR} km s^{-1}	$S_{v,\,Peak}$ Jy beam^{-1}	$S_{v,\,Int}$ Jy	Notes
(1)	(2)	(3)	(4)	(5)	(6)	(7)
G28.3047–0.3877	-0.03	0.09	83.99	0.12±0.02	0.53±0.12	
G28.3047–0.3877	0.00	-0.04	84.17	0.10±0.02	0.38±0.09	
G28.3047–0.3877	-0.46	-0.13	84.35	0.08±0.02	0.61±0.13	
G28.3047–0.3877	-0.18	-0.35	84.53	0.08±0.01	0.37±0.08	
G28.3047–0.3877	-0.09	0.09	84.71	0.09±0.02	0.28±0.08	
G28.3047–0.3877	0.19	0.03	92.27	2.77±0.03	2.88±0.06	
G28.3047–0.3877	0.19	0.03	92.45	6.78±0.05	6.84±0.09	
G28.3047–0.3877	0.19	0.03	92.63	7.38±0.05	7.46±0.08	
G28.3047–0.3877	0.19	0.03	92.81	3.89±0.03	3.95±0.06	
G28.3047–0.3877	0.19	0.09	92.99	0.98±0.02	1.04±0.05	
G28.3047–0.3877	0.18	0.02	93.17	1.55±0.03	1.59±0.05	
G28.3047–0.3877	0.18	0.05	93.35	2.07±0.02	2.12±0.04	
G28.3047–0.3877	0.18	0.05	93.53	3.53±0.03	3.59±0.06	
G28.3047–0.3877	0.18	0.05	93.71	4.41±0.03	4.54±0.06	
G28.3047–0.3877	0.19	0.06	93.89	2.31±0.03	2.40±0.05	
G28.3211–0.0110	18:43:03.1180	-4:06:27.140	104.62	2.25±0.03	2.26±0.04	MMB
G28.3211–0.0110	-0.45	0.11	96.52	0.19±0.02	0.25±0.04	
G28.3211–0.0110	-0.65	0.09	96.70	0.39±0.02	0.47±0.04	
G28.3211–0.0110	-0.64	0.10	97.60	0.14±0.03	0.27±0.08	
G28.3211–0.0110	-0.11	0.02	102.28	0.06±0.02	0.38±0.14	
G28.3211–0.0110	0.11	-0.01	102.46	0.24±0.02	0.35±0.05	
G28.3211–0.0110	-0.04	-0.01	102.64	0.93±0.03	0.98±0.06	
G28.3211–0.0110	-0.04	-0.02	102.82	0.54±0.02	0.60±0.04	
G28.3211–0.0110	-0.10	0.21	103.18	0.13±0.02	0.21±0.05	
G28.3211–0.0110	-0.01	0.00	103.36	0.24±0.02	0.27±0.04	
G28.3211–0.0110	0.11	0.03	103.54	0.33±0.03	0.44±0.06	
G28.3211–0.0110	0.04	0.02	103.72	0.54±0.03	0.54±0.04	
G28.3211–0.0110	-0.00	0.02	103.90	0.40±0.03	0.44±0.05	
G28.3211–0.0110	0.01	0.01	104.08	0.61±0.02	0.59±0.04	
G28.3211–0.0110	0.02	-0.06	104.26	0.28±0.03	0.35±0.05	
G28.3211–0.0110	-0.01	-0.00	104.44	1.99±0.03	2.08±0.05	
G28.3211–0.0110	-0.06	-0.04	104.80	0.74±0.03	0.80±0.05	
G28.3211–0.0110	0.01	-0.03	104.98	0.35±0.02	0.35±0.03	
G28.3211–0.0110	-0.42	-0.42	105.16	0.08±0.02	0.61±0.15	
G28.3972+0.0803	18:42:51.9823	-3:59:54.490	71.44	17.40±0.04	18.21±0.06	MMB
G28.3972+0.0803	0.25	-0.12	68.20	0.07±0.02	0.32±0.09	
G28.3972+0.0803	-0.02	-0.13	68.38	0.61±0.02	0.63±0.04	
G28.3972+0.0803	0.09	-0.09	68.56	0.45±0.02	0.48±0.03	
G28.3972+0.0803	-0.02	-0.13	68.74	1.17±0.02	1.18±0.03	
G28.3972+0.0803	-0.01	-0.12	68.92	0.41±0.02	0.43±0.03	
G28.3972+0.0803	0.00	-0.13	69.10	3.49±0.02	3.54±0.03	
G28.3972+0.0803	0.01	-0.12	69.28	3.63±0.02	3.62±0.04	
G28.3972+0.0803	-0.02	-0.11	69.46	0.91±0.02	0.91±0.03	
G28.3972+0.0803	-0.03	-0.10	69.64	0.56±0.02	0.55±0.03	

Continuation
of Table C.1

Name	$\alpha/\Delta\alpha$ h:m:s/″	$\delta/\Delta\delta$ d:m:s/″	V_{LSR} km s^{-1}	$S_{v,\,Peak}$ Jy beam^{-1}	$S_{v,\,Int}$ Jy	Notes
(1)	(2)	(3)	(4)	(5)	(6)	(7)
G28.3972+0.0803	0.03	-0.11	69.82	1.27±0.02	1.27±0.03	
G28.3972+0.0803	-0.02	-0.12	70.00	0.60±0.02	0.58±0.03	
G28.3972+0.0803	0.02	-0.09	70.18	2.82±0.02	2.90±0.03	
G28.3972+0.0803	0.04	-0.11	70.36	3.22±0.03	3.30±0.05	
G28.3972+0.0803	0.03	-0.08	70.54	0.68±0.02	0.74±0.04	
G28.3972+0.0803	0.02	-0.15	70.72	0.79±0.02	0.79±0.03	
G28.3972+0.0803	0.02	-0.10	70.90	2.41±0.02	2.49±0.04	
G28.3972+0.0803	-0.03	-0.31	71.08	0.72±0.02	0.63±0.04	
G28.3972+0.0803	0.00	-0.02	71.26	10.64±0.03	11.05±0.06	
G28.3972+0.0803	-0.01	0.01	71.62	1.90±0.02	1.93±0.04	
G28.3972+0.0803	0.01	-0.02	71.80	4.01±0.02	4.16±0.04	
G28.3972+0.0803	0.01	-0.02	71.98	2.46±0.02	2.50±0.04	
G28.3972+0.0803	-0.00	-0.04	72.16	2.94±0.02	2.97±0.04	
G28.3972+0.0803	-0.00	0.03	72.34	2.73±0.02	2.77±0.04	
G28.3972+0.0803	0.01	0.06	72.52	5.21±0.02	5.32±0.04	
G28.3972+0.0803	0.01	0.08	72.70	2.34±0.02	2.38±0.03	
G28.3972+0.0803	-0.00	0.08	72.88	0.75±0.02	0.83±0.04	
G28.3972+0.0803	-0.22	-0.34	77.74	0.09±0.02	0.30±0.07	
G28.3972+0.0803	-0.10	-0.50	77.92	0.08±0.01	0.17±0.04	
G28.3972+0.0803	-0.16	-0.11	78.10	0.11±0.02	0.21±0.04	
G28.3972+0.0803	-0.13	-0.18	78.28	0.32±0.02	0.34±0.03	
G28.3972+0.0803	-0.10	-0.13	78.46	1.53±0.02	1.57±0.03	
G28.3972+0.0803	-0.16	-0.09	78.64	0.64±0.02	0.68±0.03	
G28.3972+0.0803	-0.08	-0.05	79.54	0.42±0.02	0.40±0.03	
G28.3972+0.0803	-0.10	-0.07	79.72	0.45±0.02	0.47±0.03	
G28.3972+0.0803	-0.09	-0.07	79.90	0.63±0.02	0.67±0.03	
G28.3972+0.0803	-0.06	-0.04	80.26	0.18±0.02	0.23±0.03	
G28.3972+0.0803	-0.18	-0.00	80.62	2.18±0.02	2.26±0.04	
G28.3972+0.0803	-0.15	-0.03	80.80	5.75±0.02	5.93±0.04	
G28.3972+0.0803	-0.06	-0.11	81.16	1.05±0.02	1.14±0.04	
G28.3972+0.0803	-0.08	-0.10	81.34	0.60±0.02	0.59±0.03	
G28.3972+0.0803	-0.08	-0.12	81.52	1.16±0.02	1.14±0.03	
G28.3972+0.0803	-0.07	-0.11	81.70	2.24±0.02	2.24±0.04	
G28.3972+0.0803	-0.08	-0.08	81.88	0.55±0.02	0.56±0.03	
G28.3972+0.0803	-0.11	-0.12	82.06	0.18±0.02	0.19±0.03	
G28.3972+0.0803	0.01	-0.28	82.24	0.08±0.02	0.17±0.05	
G28.5228+0.1270	18:42:55.8843	-3:51:55.437	39.48	5.75±0.03	5.74±0.05	MMB
G28.5228+0.1270	0.01	0.12	38.94	0.18±0.02	0.22±0.03	
G28.5228+0.1270	-0.00	0.00	39.30	2.81±0.02	2.81±0.03	
G28.5228+0.1270	0.00	0.02	39.66	2.07±0.02	2.07±0.04	
G28.5228+0.1270	-0.02	0.03	39.84	1.54±0.02	1.57±0.04	
G28.5228+0.1270	0.26	0.37	40.02	0.07±0.02	0.42±0.11	
G28.5322+0.1287	18:42:56.4996	-3:51:21.584	27.03	1.98±0.02	2.04±0.03	MMB
G28.5322+0.1287	0.01	-0.20	21.27	0.06±0.01	0.19±0.06	

Continuation
of Table C.1

Name	$\alpha/\Delta\alpha$ h:m:s/″	$\delta/\Delta\delta$ d:m:s/″	V_{LSR} km s^{-1}	$S_{v,\,Peak}$ Jy beam^{-1}	$S_{v,\,Int}$ Jy	Notes
(1)	(2)	(3)	(4)	(5)	(6)	(7)
G28.5322+0.1287	-0.02	0.09	23.79	0.14±0.01	0.13±0.02	
G28.5322+0.1287	-0.00	0.06	24.33	0.27±0.01	0.27±0.02	
G28.5322+0.1287	0.06	-0.06	24.51	0.07±0.01	0.06±0.02	
G28.5322+0.1287	0.01	-0.02	24.69	0.15±0.02	0.17±0.03	
G28.5322+0.1287	0.03	-0.12	24.87	0.23±0.02	0.35±0.04	
G28.5322+0.1287	0.20	-0.32	25.05	0.05±0.01	0.42±0.09	
G28.5322+0.1287	0.06	-0.02	26.67	0.19±0.02	0.15±0.03	
G28.5322+0.1287	0.01	-0.01	26.85	1.29±0.01	1.30±0.03	
G28.5322+0.1287	0.01	-0.00	27.21	0.89±0.01	0.89±0.03	
G28.5322+0.1287	-0.01	-0.04	27.39	0.45±0.02	0.48±0.03	
G28.5322+0.1287	-0.03	0.02	27.57	0.42±0.02	0.49±0.03	
G28.5322+0.1287	0.03	-0.08	27.75	0.44±0.02	0.43±0.03	
G28.5322+0.1287	-0.02	-0.06	27.93	0.16±0.02	0.15±0.03	
G28.5322+0.1287	0.02	-0.13	28.83	0.10±0.01	0.08±0.02	
G28.5322+0.1287	0.39	-0.15	29.55	0.08±0.02	0.14±0.04	
G29.9556–0.0163	18:46:03.7889	-2:39:22.121	100.31	13.59±0.16	14.19±0.30	G29.9556–0.0156b
G29.9556–0.0163	-0.17	-0.09	99.23	2.38±0.11	3.53±0.26	
G29.9556–0.0163	-0.11	-0.03	99.41	1.55±0.08	2.19±0.18	
G29.9556–0.0163	-0.05	-0.02	99.59	1.93±0.08	2.34±0.16	
G29.9556–0.0163	-0.03	0.01	99.77	3.46±0.09	3.85±0.18	
G29.9556–0.0163	-0.03	0.01	99.95	7.52±0.13	8.04±0.24	
G29.9556–0.0163	-0.01	0.02	100.13	13.30±0.17	13.78±0.30	
G29.9556–0.0163	-0.02	0.00	100.49	5.99±0.12	6.32±0.21	
G29.9556–0.0163	-0.04	-0.05	100.67	1.17±0.08	1.50±0.17	
G29.9556–0.0163	-0.05	-0.02	100.85	0.51±0.06	0.90±0.15	
G29.9556–0.0163	0.33	0.03	101.03	0.52±0.06	0.90±0.16	
G29.9556–0.0163	0.38	0.13	101.21	0.98±0.10	1.48±0.22	
G29.9556–0.0163	0.42	0.08	101.39	0.59±0.07	0.87±0.17	
G29.9556–0.0163	0.27	0.31	101.57	0.25±0.05	0.34±0.11	
G29.2815–0.3295	18:45:56.8521	-3:23:56.312	92.26	3.46±0.03	3.55±0.05	YAN19
G29.2815–0.3295	0.09	0.13	91.72	0.13±0.02	0.17±0.04	
G29.2815–0.3295	0.03	0.01	91.90	0.30±0.02	0.32±0.04	
G29.2815–0.3295	0.01	-0.03	92.08	1.60±0.02	1.65±0.04	
G29.2815–0.3295	-0.01	-0.01	92.44	2.48±0.02	2.63±0.04	
G29.2815–0.3295	0.04	-0.03	92.62	0.77±0.02	0.79±0.04	
G29.2815–0.3295	0.02	0.01	92.80	0.57±0.02	0.63±0.04	
G29.2815–0.3295	0.01	-0.08	92.98	0.44±0.02	0.51±0.04	
G29.3197–0.1619	18:45:25.1509	-3:17:16.896	48.83	4.15±0.04	4.39±0.08	MMB
G29.3197–0.1619	0.08	0.22	42.17	0.17±0.02	0.23±0.05	
G29.3197–0.1619	-0.01	0.11	42.89	0.39±0.02	0.43±0.04	
G29.3197–0.1619	-0.04	0.08	43.07	0.96±0.02	0.97±0.04	
G29.3197–0.1619	-0.03	0.06	43.25	1.11±0.03	1.10±0.05	
G29.3197–0.1619	-0.05	-0.06	43.43	0.21±0.02	0.34±0.06	
G29.3197–0.1619	-0.07	0.12	43.61	0.31±0.02	0.24±0.03	

Continuation
of Table C.1

Name	$\alpha/\Delta\alpha$ h:m:s/″	$\delta/\Delta\delta$ d:m:s/″	V_{LSR} km s^{-1}	$S_{v,\,Peak}$ Jy beam^{-1}	$S_{v,\,Int}$ Jy	Notes
(1)	(2)	(3)	(4)	(5)	(6)	(7)
G29.3197–0.1619	0.01	0.07	43.79	0.14±0.02	0.08±0.02	
G29.3197–0.1619	0.04	0.05	44.15	0.15±0.02	0.22±0.05	
G29.3197–0.1619	-0.08	0.02	45.23	0.14±0.02	0.16±0.04	
G29.3197–0.1619	-0.02	-0.13	47.57	0.14±0.02	0.20±0.05	
G29.3197–0.1619	0.05	0.01	47.93	0.57±0.02	0.64±0.05	
G29.3197–0.1619	-0.00	-0.01	48.11	2.37±0.04	2.58±0.07	
G29.3197–0.1619	0.00	0.02	48.29	1.62±0.04	1.74±0.07	
G29.3197–0.1619	0.01	0.00	48.47	2.41±0.04	2.63±0.07	
G29.3197–0.1619	-0.00	0.01	48.65	2.43±0.03	2.57±0.06	
G29.3197–0.1619	0.01	-0.00	49.01	2.03±0.03	2.19±0.06	
G29.3197–0.1619	0.00	0.02	49.19	1.48±0.03	1.64±0.06	
G29.3197–0.1619	0.01	-0.01	49.37	1.41±0.03	1.47±0.06	
G29.3197–0.1619	0.03	0.05	49.55	0.08±0.02	0.29±0.09	
G29.3197–0.1619	-0.11	-0.05	50.09	0.55±0.02	0.57±0.04	
G29.3197–0.1619	-0.03	-0.01	50.27	0.35±0.03	0.44±0.06	
G29.5810+0.1323	18:44:50.9298	-2:55:17.744	31.88	0.31±0.02	0.40±0.04	NEW
G29.5810+0.1323	-0.29	-0.68	31.70	0.06±0.02	0.31±0.10	
G29.5810+0.1323	0.65	-1.11	32.06	0.05±0.01	0.36±0.11	
G29.6036–0.6252	18:47:35.4033	-3:14:50.024	81.56	1.47±0.03	1.58±0.05	MMB
G29.6036–0.6252	-0.18	-0.25	71.12	0.08±0.02	0.23±0.07	
G29.6036–0.6252	0.08	-0.09	71.30	0.14±0.02	0.20±0.04	
G29.6036–0.6252	0.13	-0.13	71.84	0.12±0.02	0.09±0.02	
G29.6036–0.6252	0.03	-0.10	80.48	0.33±0.02	0.47±0.05	
G29.6036–0.6252	0.08	0.09	80.66	0.54±0.02	0.66±0.05	
G29.6036–0.6252	-0.02	-0.04	80.84	0.78±0.02	0.85±0.04	
G29.6036–0.6252	-0.03	-0.04	81.02	0.93±0.02	0.97±0.04	
G29.6036–0.6252	-0.01	0.02	81.20	0.71±0.02	0.76±0.04	
G29.6036–0.6252	-0.00	-0.05	81.38	0.94±0.02	0.94±0.04	
G29.6036–0.6252	0.02	0.00	81.74	1.20±0.02	1.29±0.04	
G29.6036–0.6252	-0.00	-0.04	81.92	0.55±0.02	0.58±0.03	
G29.6036–0.6252	-0.02	-0.01	82.10	0.24±0.02	0.28±0.05	
G29.8621–0.0441	18:45:59.5687	-2:45:06.527	101.30	63.68±0.53	68.55±0.99	MMB
G29.8621–0.0441	-0.74	-0.16	98.78	0.12±0.03	0.62±0.18	
G29.8621–0.0441	-0.51	-0.22	98.96	0.16±0.03	0.80±0.20	
G29.8621–0.0441	0.03	0.20	99.50	0.16±0.03	0.97±0.18	
G29.8621–0.0441	-0.12	0.07	99.68	0.30±0.04	1.68±0.28	
G29.8621–0.0441	-0.26	-0.04	99.86	0.43±0.07	2.04±0.40	
G29.8621–0.0441	0.00	0.00	100.04	4.32±0.28	5.50±0.58	
G29.8621–0.0441	-0.01	0.03	100.22	45.05±0.47	48.30±0.88	
G29.8621–0.0441	0.01	0.03	100.40	23.31±0.40	25.02±0.73	
G29.8621–0.0441	0.00	0.04	100.58	19.98±0.37	21.83±0.69	
G29.8621–0.0441	0.01	0.03	100.76	20.31±0.35	21.95±0.65	
G29.8621–0.0441	0.01	0.03	100.94	16.52±0.34	17.83±0.62	
G29.8621–0.0441	0.00	0.02	101.12	29.14±0.45	31.11±0.82	

Continuation
of Table C.1

Name	$\alpha/\Delta\alpha$ h:m:s/″	$\delta/\Delta\delta$ d:m:s/″	V_{LSR} km s^{-1}	$S_{v,\,Peak}$ Jy beam^{-1}	$S_{v,\,Int}$ Jy	Notes
(1)	(2)	(3)	(4)	(5)	(6)	(7)
G29.8621–0.0441	0.00	-0.01	101.48	45.62±0.48	49.06±0.89	
G29.8621–0.0441	0.00	-0.01	101.66	34.58±0.47	37.22±0.88	
G29.8621–0.0441	-0.01	-0.02	101.84	48.19±0.50	51.55±0.91	
G29.8621–0.0441	-0.03	-0.07	102.02	14.45±0.28	16.10±0.53	
G29.8621–0.0441	-0.02	-0.09	102.20	4.86±0.17	6.22±0.35	
G29.8621–0.0441	0.14	-0.22	102.38	0.56±0.07	1.85±0.30	
G29.8621–0.0441	0.10	-0.12	102.56	0.53±0.06	1.43±0.22	
G29.8621–0.0441	0.22	0.63	102.92	0.23±0.07	1.09±0.38	
G29.8621–0.0441	0.21	-0.26	103.10	0.32±0.06	0.94±0.24	
G29.8621–0.0441	0.15	-0.12	103.28	0.56±0.07	1.43±0.25	
G29.8621–0.0441	0.02	-0.12	103.46	0.38±0.08	0.64±0.19	
G29.8621–0.0441	-0.05	-0.11	103.64	1.20±0.12	2.36±0.34	
G29.8621–0.0441	-0.10	-0.20	103.82	2.11±0.13	3.30±0.30	
G29.8621–0.0441	-0.07	-0.20	104.00	1.66±0.13	3.04±0.35	
G29.8621–0.0441	-0.11	-0.19	104.18	4.41±0.16	5.73±0.33	
G29.8621–0.0441	-0.08	-0.19	104.36	1.95±0.13	3.19±0.31	
G29.8621–0.0441	-0.10	-0.32	104.54	0.63±0.07	1.46±0.23	
G29.8621–0.0441	-0.12	-0.21	104.72	2.59±0.12	3.58±0.27	
G29.8621–0.0441	-0.02	-0.24	104.90	0.56±0.07	1.59±0.25	
G29.8621–0.0441	0.26	-0.16	105.08	0.08±0.02	0.21±0.08	
G29.9157–0.0236	18:46:00.9597	-2:41:41.821	102.50	2.10±0.15	3.30±0.35	NEW
G29.9157–0.0236	-0.14	0.01	93.32	0.24±0.03	0.37±0.07	
G29.9157–0.0236	-0.09	0.04	93.50	0.35±0.04	0.63±0.10	
G29.9157–0.0236	-0.02	0.04	93.68	0.48±0.07	1.87±0.34	
G29.9157–0.0236	-0.14	0.07	93.86	0.35±0.05	1.48±0.26	
G29.9157–0.0236	-0.03	-0.01	99.44	0.60±0.10	1.10±0.25	
G29.9157–0.0236	-0.08	-0.04	99.62	1.20±0.15	2.31±0.40	
G29.9157–0.0236	-0.78	-0.64	99.80	0.41±0.10	1.56±0.46	
G29.9157–0.0236	-0.39	0.68	100.34	1.11±0.32	4.29±1.53	
G29.9157–0.0236	-0.23	0.28	100.52	1.56±0.28	6.08±1.37	
G29.9157–0.0236	-0.37	0.71	100.70	0.85±0.19	4.25±1.12	
G29.9157–0.0236	-0.39	0.74	100.88	0.82±0.17	3.78±0.93	
G29.9157–0.0236	-0.37	0.73	101.06	0.89±0.21	4.51±1.23	
G29.9157–0.0236	-0.24	0.72	101.60	1.01±0.25	5.29±1.53	
G29.9157–0.0236	-0.23	0.66	101.78	1.07±0.26	5.47±1.59	
G29.9157–0.0236	-0.37	0.63	101.96	1.04±0.23	4.91±1.29	
G29.9157–0.0236	-0.11	0.14	102.14	0.70±0.10	4.00±0.68	
G29.9157–0.0236	-0.04	0.01	102.32	1.93±0.16	3.68±0.43	
G29.9157–0.0236	0.12	-0.04	102.68	0.60±0.12	1.59±0.41	
G29.9157–0.0236	0.18	0.04	103.04	0.74±0.17	2.15±0.66	
G29.9157–0.0236	0.05	0.05	103.22	2.01±0.18	3.35±0.44	
G29.9157–0.0236	0.14	0.03	103.40	1.16±0.17	2.81±0.57	
G29.9157–0.0236	0.19	0.01	103.58	0.64±0.14	1.89±0.54	
G29.9157–0.0236	0.06	-0.01	103.76	0.67±0.11	2.39±0.49	

Continuation
of Table C.1

Name	$\alpha/\Delta\alpha$ h:m:s/″	$\delta/\Delta\delta$ d:m:s/″	V_{LSR} km s^{-1}	$S_{v,\,Peak}$ Jy beam^{-1}	$S_{v,\,Int}$ Jy	Notes
(1)	(2)	(3)	(4)	(5)	(6)	(7)
G29.9157–0.0236	-0.06	-0.05	103.94	0.73±0.10	2.92±0.50	
G29.9157–0.0236	-0.04	-0.02	104.12	1.31±0.15	3.80±0.57	
G29.9157–0.0236	-0.04	-0.01	104.30	1.60±0.16	3.60±0.49	
G29.9157–0.0236	-0.05	-0.05	104.48	0.48±0.07	1.65±0.31	
G29.9157–0.0236	-0.05	0.04	104.66	0.32±0.05	1.83±0.33	
G29.9157–0.0236	-0.01	0.10	104.84	0.28±0.04	1.29±0.24	
G29.9157–0.0236	0.13	-0.14	105.02	0.10±0.02	0.42±0.12	
G29.9556–0.0156	18:46:03.7397	-2:39:22.234	95.81	107.25±0.29	109.30±0.51	MMB
G29.9556–0.0156	0.18	-0.42	94.91	0.20±0.03	0.40±0.09	
G29.9556–0.0156	0.14	-0.07	95.09	0.85±0.09	1.60±0.23	
G29.9556–0.0156	0.02	-0.03	95.27	11.29±0.15	11.84±0.28	
G29.9556–0.0156	0.02	-0.03	95.45	12.39±0.19	13.15±0.34	
G29.9556–0.0156	-0.00	-0.01	95.63	42.99±0.25	43.96±0.45	
G29.9556–0.0156	0.00	0.01	95.99	83.52±0.36	87.46±0.65	
G29.9556–0.0156	0.01	0.00	96.17	53.57±0.31	55.93±0.57	
G29.9556–0.0156	0.11	0.02	96.35	36.10±0.38	42.15±0.73	
G29.9556–0.0156	0.24	0.02	96.53	30.34±0.36	38.89±0.74	
G29.9556–0.0156	0.15	0.00	96.71	29.82±0.36	37.04±0.73	
G29.9556–0.0156	0.03	-0.01	96.89	23.29±0.24	25.58±0.45	
G29.9556–0.0156	0.29	-0.06	97.07	3.92±0.14	5.71±0.32	
G29.9556–0.0156	0.30	-0.06	97.25	2.47±0.12	3.99±0.30	
G29.9556–0.0156	0.27	-0.18	97.43	1.56±0.11	2.82±0.30	
G29.9556–0.0156	0.13	-0.19	97.61	1.26±0.10	2.29±0.26	
G29.9556–0.0156	0.09	-0.17	97.79	1.94±0.10	2.68±0.22	
G29.9556–0.0156	0.05	-0.22	97.97	0.93±0.12	1.82±0.34	
G29.9556–0.0156	-0.02	-0.28	98.51	0.68±0.13	1.86±0.48	
G29.9556–0.0156	0.11	-0.14	98.69	0.97±0.10	2.19±0.31	
G29.9556–0.0156	0.20	-0.13	98.87	1.08±0.08	2.41±0.26	
G29.9556–0.0156	0.27	-0.07	99.05	2.72±0.11	4.35±0.26	
G29.9556–0.0156	0.57	0.03	99.23	2.38±0.11	3.53±0.26	
G29.9556–0.0156	-0.07	-0.26	105.17	0.16±0.03	0.24±0.08	
G29.9556–0.0156	0.00	-0.19	105.35	0.29±0.03	0.31±0.05	
G29.9556–0.0156	0.02	-0.12	105.53	0.55±0.04	0.58±0.07	
G29.9556–0.0156	0.01	-0.13	105.71	0.59±0.05	0.92±0.12	
G29.9556–0.0156	0.01	-0.25	105.89	0.29±0.03	0.53±0.08	
G29.9556–0.0156	0.16	-0.31	106.07	0.24±0.02	0.25±0.04	
G29.9556–0.0156	-0.00	-0.20	106.25	0.24±0.02	0.17±0.03	
G29.9556–0.0156	0.04	-0.18	106.43	0.11±0.02	0.32±0.08	
G29.9556–0.0156	0.16	-0.33	106.61	0.08±0.02	0.22±0.08	
G29.9609–0.0675	18:46:15.3691	-2:40:28.774	100.27	6.22±0.18	6.79±0.34	HU16
G29.9609–0.0675	0.00	0.01	100.45	4.27±0.14	4.71±0.27	
G29.9609–0.0675	0.05	-0.08	100.63	0.69±0.08	1.06±0.20	
G29.9609–0.0675	-0.01	0.01	100.81	0.76±0.06	1.05±0.14	
G29.9609–0.0675	0.00	0.03	100.99	1.66±0.07	1.95±0.13	

Continuation
of Table C.1

Name	$\alpha/\Delta\alpha$ h:m:s/″	$\delta/\Delta\delta$ d:m:s/″	V_{LSR} km s^{-1}	$S_{v,\,Peak}$ Jy beam^{-1}	$S_{v,\,Int}$ Jy	Notes
(1)	(2)	(3)	(4)	(5)	(6)	(7)
G29.9609–0.0675	0.01	0.02	101.17	2.42±0.08	2.82±0.16	
G29.9609–0.0675	0.30	0.40	101.35	0.22±0.05	0.72±0.19	
G29.9781–0.0478	18:46:12.9607	-2:39:01.356	102.96	35.60±0.36	36.72±0.64	MMB
G29.9781–0.0478	0.02	0.11	96.84	9.71±0.23	10.35±0.43	
G29.9781–0.0478	0.04	0.08	97.02	7.93±0.18	8.59±0.33	
G29.9781–0.0478	0.06	0.08	97.20	6.69±0.14	7.21±0.27	
G29.9781–0.0478	0.06	0.08	97.38	8.20±0.15	8.83±0.27	
G29.9781–0.0478	0.06	0.08	97.56	6.81±0.13	7.39±0.25	
G29.9781–0.0478	0.05	0.07	97.74	5.42±0.13	5.99±0.24	
G29.9781–0.0478	0.02	0.07	97.92	7.16±0.15	7.79±0.27	
G29.9781–0.0478	-0.01	0.09	98.10	15.68±0.23	16.49±0.42	
G29.9781–0.0478	-0.02	0.10	98.28	24.18±0.31	25.15±0.55	
G29.9781–0.0478	-0.02	0.10	98.46	17.40±0.24	18.29±0.44	
G29.9781–0.0478	-0.02	0.08	98.64	5.31±0.13	5.88±0.24	
G29.9781–0.0478	0.00	0.08	98.82	1.69±0.09	2.30±0.20	
G29.9781–0.0478	0.02	0.04	99.00	1.71±0.10	2.26±0.21	
G29.9781–0.0478	0.01	0.09	99.18	2.24±0.10	2.65±0.19	
G29.9781–0.0478	0.01	0.07	99.36	2.17±0.10	2.79±0.21	
G29.9781–0.0478	0.03	0.01	99.54	0.86±0.09	1.62±0.25	
G29.9781–0.0478	0.02	0.04	99.72	1.37±0.11	2.10±0.25	
G29.9781–0.0478	0.01	0.07	99.90	1.63±0.13	2.27±0.27	
G29.9781–0.0478	-0.13	-0.21	100.08	0.63±0.14	1.96±0.55	
G29.9781–0.0478	-0.21	-0.04	100.80	0.18±0.04	0.31±0.10	
G29.9781–0.0478	0.10	-0.07	101.52	0.44±0.06	1.01±0.18	
G29.9781–0.0478	0.06	-0.06	101.70	1.77±0.10	2.45±0.23	
G29.9781–0.0478	0.07	-0.04	101.88	1.29±0.09	1.94±0.22	
G29.9781–0.0478	0.08	-0.04	102.06	0.65±0.06	1.09±0.16	
G29.9781–0.0478	0.10	-0.04	102.24	4.12±0.11	4.62±0.21	
G29.9781–0.0478	0.09	-0.04	102.42	9.48±0.14	10.20±0.26	
G29.9781–0.0478	0.03	-0.01	102.60	7.20±0.19	7.78±0.35	
G29.9781–0.0478	0.01	0.00	102.78	32.49±0.34	33.67±0.62	
G29.9781–0.0478	0.01	0.00	103.14	16.24±0.28	17.02±0.50	
G29.9781–0.0478	0.00	-0.00	103.32	23.09±0.30	24.03±0.54	
G29.9781–0.0478	0.00	-0.00	103.50	26.16±0.31	27.25±0.55	
G29.9781–0.0478	0.01	0.00	103.68	16.93±0.23	17.78±0.43	
G29.9781–0.0478	0.00	0.00	103.86	8.58±0.16	9.29±0.30	
G29.9781–0.0478	0.00	-0.00	104.04	9.46±0.16	10.16±0.30	
G29.9781–0.0478	0.00	0.00	104.22	9.85±0.16	10.61±0.30	
G29.9781–0.0478	0.00	-0.00	104.40	7.85±0.14	8.52±0.26	
G29.9781–0.0478	-0.00	-0.00	104.58	4.85±0.11	5.28±0.20	
G29.9781–0.0478	-0.00	0.00	104.76	3.69±0.10	4.25±0.20	
G29.9781–0.0478	-0.00	-0.00	104.94	2.09±0.09	2.66±0.19	
G29.9781–0.0478	-0.01	0.00	105.12	1.23±0.08	1.68±0.17	
G29.9781–0.0478	-0.00	0.02	105.30	0.78±0.07	1.35±0.17	

Continuation
of Table C.1

Name	$\alpha/\Delta\alpha$ h:m:s/″	$\delta/\Delta\delta$ d:m:s/″	V_{LSR} km s^{-1}	$S_{v,\,Peak}$ Jy beam^{-1}	$S_{v,\,Int}$ Jy	Notes
(1)	(2)	(3)	(4)	(5)	(6)	(7)
G29.9781–0.0478	0.01	-0.01	105.48	0.55±0.05	0.97±0.13	
G29.9781–0.0478	-0.07	-0.19	105.66	0.19±0.03	0.46±0.10	
G30.5891–0.0424	18:47:18.8813	-2:06:16.750	42.99	4.48±0.03	4.62±0.05	MMB
G30.5891–0.0424	0.06	-0.10	36.51	0.09±0.02	0.21±0.06	
G30.5891–0.0424	-0.09	-0.23	36.69	0.48±0.02	0.52±0.03	
G30.5891–0.0424	-0.08	-0.26	36.87	0.36±0.02	0.34±0.03	
G30.5891–0.0424	-0.02	-0.08	37.05	0.15±0.02	0.15±0.03	
G30.5891–0.0424	-0.30	-0.08	37.23	0.08±0.02	0.19±0.07	
G30.5891–0.0424	0.01	-0.14	37.41	0.20±0.02	0.25±0.04	
G30.5891–0.0424	-0.47	-0.36	37.59	0.05±0.02	0.36±0.12	
G30.5891–0.0424	-0.26	0.19	40.29	0.17±0.02	0.24±0.04	
G30.5891–0.0424	-0.07	-0.08	40.47	0.11±0.02	0.14±0.04	
G30.5891–0.0424	-0.21	0.02	40.65	0.37±0.02	0.43±0.03	
G30.5891–0.0424	-0.24	0.21	40.83	0.41±0.02	0.44±0.03	
G30.5891–0.0424	-0.23	0.09	41.01	0.62±0.02	0.75±0.03	
G30.5891–0.0424	-0.35	0.06	41.19	0.69±0.02	0.86±0.04	
G30.5891–0.0424	-0.11	0.01	41.37	0.82±0.02	0.90±0.04	
G30.5891–0.0424	-0.15	0.09	41.55	1.14±0.02	1.30±0.04	
G30.5891–0.0424	-0.20	0.02	41.73	1.02±0.02	1.22±0.04	
G30.5891–0.0424	-0.16	0.03	41.91	0.52±0.02	0.62±0.04	
G30.5891–0.0424	-0.50	0.08	42.09	0.74±0.02	0.83±0.03	
G30.5891–0.0424	-0.49	0.14	42.27	1.05±0.02	1.14±0.04	
G30.5891–0.0424	-0.38	0.18	42.45	1.03±0.02	1.13±0.04	
G30.5891–0.0424	-0.38	0.22	42.63	1.09±0.02	1.12±0.03	
G30.5891–0.0424	-0.03	0.03	42.81	1.00±0.02	1.07±0.04	
G30.5891–0.0424	0.01	-0.03	43.17	1.49±0.02	1.52±0.04	
G30.5891–0.0424	-0.01	-0.00	43.35	1.48±0.02	1.48±0.04	
G30.5891–0.0424	0.01	-0.02	43.53	2.23±0.02	2.33±0.04	
G30.5891–0.0424	0.01	0.00	43.71	1.01±0.02	1.12±0.04	
G30.5891–0.0424	0.04	0.14	43.89	0.16±0.01	0.20±0.03	
G30.5891–0.0424	-0.03	-0.06	45.51	0.43±0.02	0.50±0.04	
G30.5891–0.0424	-0.01	0.01	45.69	1.42±0.02	1.53±0.04	
G30.5891–0.0424	0.01	-0.01	45.87	1.28±0.02	1.36±0.04	
G30.5891–0.0424	0.00	-0.04	46.05	0.52±0.02	0.59±0.03	
G30.5891–0.0424	-0.01	-0.03	46.23	0.37±0.03	0.44±0.05	
G30.5891–0.0424	-0.00	0.12	46.41	0.11±0.02	0.20±0.05	
G30.5891–0.0424	-0.07	-0.12	46.59	0.22±0.01	0.22±0.03	
G30.5891–0.0424	-0.02	-0.03	46.77	0.21±0.02	0.18±0.03	
G30.5891–0.0424	-0.16	-0.04	46.95	0.11±0.02	0.16±0.04	
G30.5891–0.0424	0.04	0.05	47.13	0.08±0.01	0.09±0.03	
G30.5891–0.0424	0.01	-0.04	47.31	0.42±0.02	0.51±0.04	
G30.5891–0.0424	0.13	-0.11	47.49	0.11±0.02	0.13±0.04	
G30.5891–0.0424	0.06	-0.12	47.67	0.17±0.02	0.18±0.03	
G30.5891–0.0424	0.06	0.10	47.85	0.22±0.02	0.27±0.03	

Continuation
of Table C.1

Name	$\alpha/\Delta\alpha$ h:m:s/″	$\delta/\Delta\delta$ d:m:s/″	V_{LSR} km s^{-1}	$S_{v,\,Peak}$ Jy beam^{-1}	$S_{v,\,Int}$ Jy	Notes
(1)	(2)	(3)	(4)	(5)	(6)	(7)
G30.5891–0.0424	0.03	0.07	48.03	0.20±0.02	0.30±0.05	
G30.5891–0.0424	-0.01	0.02	48.21	0.26±0.02	0.33±0.04	
G30.5891–0.0424	-0.03	-0.02	48.39	0.78±0.02	0.84±0.04	
G30.5891–0.0424	-0.01	-0.03	48.57	0.72±0.02	0.77±0.03	
G30.5891–0.0424	-0.02	-0.03	48.75	0.46±0.02	0.52±0.03	
G30.6218+0.0824	18:46:55.7481	-2:01:06.033	39.98	0.37±0.02	0.44±0.05	NEW
G30.6218+0.0824	-0.15	-0.13	39.80	0.29±0.02	0.31±0.03	
G30.6218+0.0824	-0.19	0.27	44.48	0.13±0.02	0.18±0.04	
G30.6218+0.0824	-0.13	0.11	44.66	0.12±0.02	0.14±0.03	
G30.6218+0.0824	-0.03	-0.12	45.38	0.15±0.02	0.20±0.03	
G30.6218+0.0824	-0.81	0.46	45.56	0.05±0.01	0.31±0.11	
G30.7028–0.0683	18:47:36.7955	-2:00:54.244	88.30	117.73±0.53	124.20±0.96	MMB
G30.7028–0.0683	-0.69	0.43	85.60	0.27±0.04	0.59±0.13	
G30.7028–0.0683	-0.69	0.40	85.78	4.08±0.07	4.32±0.13	
G30.7028–0.0683	-0.71	0.38	85.96	10.79±0.09	11.14±0.17	
G30.7028–0.0683	-0.70	0.39	86.14	9.37±0.09	9.76±0.16	
G30.7028–0.0683	-0.69	0.36	86.32	3.08±0.08	3.51±0.15	
G30.7028–0.0683	-0.68	0.38	86.50	1.59±0.07	2.12±0.16	
G30.7028–0.0683	-0.51	0.35	86.68	0.39±0.05	1.54±0.25	
G30.7028–0.0683	-0.73	0.46	86.86	0.40±0.04	0.69±0.11	
G30.7028–0.0683	-0.37	0.23	87.04	0.47±0.06	1.50±0.23	
G30.7028–0.0683	-0.73	0.43	87.22	1.95±0.06	2.23±0.12	
G30.7028–0.0683	-0.30	0.17	87.40	3.33±0.09	5.39±0.22	
G30.7028–0.0683	-0.62	0.40	87.58	1.89±0.09	2.88±0.20	
G30.7028–0.0683	-0.06	0.00	87.76	8.63±0.13	10.24±0.26	
G30.7028–0.0683	-0.01	0.00	87.94	13.24±0.17	14.28±0.31	
G30.7028–0.0683	-0.01	-0.02	88.12	100.79±0.42	105.28±0.77	
G30.7028–0.0683	0.01	0.05	88.48	27.88±0.22	30.02±0.40	
G30.7028–0.0683	0.00	0.05	88.66	12.01±0.15	13.16±0.27	
G30.7028–0.0683	0.03	0.33	88.84	4.85±0.10	5.74±0.19	
G30.7028–0.0683	-0.05	0.18	89.02	5.91±0.10	7.12±0.20	
G30.7028–0.0683	-0.06	0.26	89.20	2.53±0.09	3.34±0.20	
G30.7028–0.0683	-0.05	0.09	89.38	2.80±0.09	3.46±0.18	
G30.7028–0.0683	-0.54	0.85	89.56	0.18±0.04	1.59±0.39	
G30.7028–0.0683	-0.19	0.12	89.74	1.14±0.09	2.12±0.25	
G30.7028–0.0683	-0.73	0.44	89.92	1.18±0.07	1.21±0.13	
G30.7599–0.0523	18:47:39.7226	-1:57:24.888	91.68	36.87±0.27	37.28±0.47	MMB
G30.7599–0.0523	2.99	-0.49	88.26	4.08±0.32	7.97±0.88	
G30.7599–0.0523	0.03	-0.41	89.16	0.38±0.09	2.66±0.73	
G30.7599–0.0523	-0.08	-0.02	89.34	0.94±0.10	1.47±0.25	
G30.7599–0.0523	-0.06	0.04	89.52	1.33±0.07	1.64±0.14	
G30.7599–0.0523	-0.05	-0.02	89.70	1.65±0.08	2.05±0.16	
G30.7599–0.0523	-0.05	0.01	89.88	1.67±0.09	2.17±0.19	
G30.7599–0.0523	-0.04	-0.01	90.06	1.33±0.08	1.75±0.18	

Continuation
of Table C.1

Name	$\alpha/\Delta\alpha$ h:m:s/″	$\delta/\Delta\delta$ d:m:s/″	V_{LSR} km s^{-1}	$S_{v,\,Peak}$ Jy beam^{-1}	$S_{v,\,Int}$ Jy	Notes
(1)	(2)	(3)	(4)	(5)	(6)	(7)
G30.7599–0.0523	-0.03	-0.01	90.24	1.80±0.07	2.13±0.14	
G30.7599–0.0523	-0.02	-0.04	90.42	2.04±0.07	2.30±0.13	
G30.7599–0.0523	-0.02	-0.02	90.60	6.35±0.08	6.51±0.15	
G30.7599–0.0523	-0.02	-0.01	90.78	11.81±0.12	12.04±0.21	
G30.7599–0.0523	-0.02	-0.01	90.96	16.08±0.16	16.18±0.28	
G30.7599–0.0523	-0.02	-0.01	91.14	24.00±0.22	24.24±0.38	
G30.7599–0.0523	-0.02	-0.01	91.32	30.01±0.25	30.44±0.44	
G30.7599–0.0523	-0.01	-0.01	91.50	27.43±0.24	27.89±0.42	
G30.7599–0.0523	0.00	-0.00	91.86	31.18±0.23	31.68±0.41	
G30.7599–0.0523	-0.00	-0.00	92.04	12.01±0.14	12.29±0.25	
G30.7599–0.0523	-0.00	0.00	92.22	4.43±0.09	4.73±0.17	
G30.7599–0.0523	-0.03	0.03	92.40	1.56±0.07	1.88±0.15	
G30.7599–0.0523	-0.02	-0.01	92.58	0.91±0.07	1.32±0.17	
G30.7599–0.0523	0.17	-0.00	92.76	0.39±0.05	0.48±0.10	
G30.7599–0.0523	0.13	0.04	92.94	0.51±0.07	0.70±0.14	
G30.7599–0.0523	0.08	0.00	93.12	1.65±0.07	1.83±0.13	
G30.7599–0.0523	0.02	0.00	93.30	2.46±0.07	2.74±0.14	
G30.7599–0.0523	0.00	0.05	93.48	0.70±0.06	1.26±0.17	
G30.7599–0.0523	-0.00	-0.01	93.66	1.13±0.06	1.47±0.14	
G30.7599–0.0523	-0.02	0.03	93.84	0.41±0.04	0.50±0.07	
G30.7599–0.0523	0.03	0.02	94.02	0.12±0.02	0.15±0.04	
G30.7599–0.0523	-0.09	0.29	94.20	0.11±0.02	0.22±0.06	
G30.7700–0.8043	18:50:21.5375	-2:17:27.525	75.90	12.91±0.06	13.39±0.10	MMB
G30.7700–0.8043	0.01	0.15	73.92	0.16±0.02	0.11±0.02	
G30.7700–0.8043	0.02	-0.05	74.10	3.93±0.04	4.02±0.07	
G30.7700–0.8043	0.02	-0.05	74.28	6.70±0.04	6.84±0.08	
G30.7700–0.8043	0.02	-0.04	74.46	8.28±0.05	8.42±0.08	
G30.7700–0.8043	0.01	-0.04	74.64	8.56±0.05	8.80±0.09	
G30.7700–0.8043	0.01	-0.02	74.82	4.45±0.04	4.56±0.08	
G30.7700–0.8043	-0.00	0.01	75.00	3.11±0.03	3.23±0.06	
G30.7700–0.8043	0.01	-0.02	75.18	1.10±0.02	1.11±0.04	
G30.7700–0.8043	-0.00	0.01	75.36	1.73±0.03	1.84±0.05	
G30.7700–0.8043	-0.07	0.01	75.54	1.32±0.02	1.43±0.05	
G30.7700–0.8043	0.01	0.01	75.72	3.34±0.03	3.42±0.06	
G30.7700–0.8043	0.00	-0.00	76.08	12.02±0.05	12.51±0.09	
G30.7700–0.8043	-0.01	0.00	76.26	2.70±0.03	2.67±0.06	
G30.7700–0.8043	-0.04	-0.03	76.44	0.29±0.02	0.20±0.02	
G30.7700–0.8043	-0.08	0.09	76.62	0.07±0.02	0.29±0.08	
G30.7700–0.8043	-0.23	0.13	76.80	0.11±0.02	0.07±0.02	
G30.7744+0.0783	18:47:13.3824	-1:53:03.948	98.46	1.17±0.04	1.28±0.07	MMB
G30.7744+0.0783	0.07	0.01	98.28	0.55±0.03	0.51±0.04	
G30.7744+0.0783	0.02	0.04	98.64	0.70±0.03	0.68±0.05	
G30.7744+0.0783	0.12	0.05	98.82	0.49±0.03	0.55±0.05	
G30.7744+0.0783	0.07	0.40	99.00	0.11±0.02	0.37±0.10	

Continuation
of Table C.1

Name	$\alpha/\Delta\alpha$ h:m:s/″	$\delta/\Delta\delta$ d:m:s/″	V_{LSR} km s^{-1}	$S_{v,\,Peak}$ Jy beam^{-1}	$S_{v,\,Int}$ Jy	Notes
(1)	(2)	(3)	(4)	(5)	(6)	(7)
G30.7744+0.0783	0.24	0.44	99.18	0.17±0.02	0.27±0.05	
G30.7744+0.0783	0.01	0.02	99.36	1.03±0.03	1.16±0.05	
G30.7744+0.0783	0.08	0.01	99.54	0.58±0.03	0.59±0.05	
G30.7744+0.0783	0.03	0.39	100.26	0.09±0.02	0.43±0.14	
G30.7744+0.0783	0.53	0.13	100.44	0.11±0.03	0.31±0.09	
G30.7799+0.2301	18:46:41.5091	-1:48:36.862	48.79	28.51±0.16	29.96±0.28	MMB
G30.7799+0.2301	0.03	0.04	47.53	0.33±0.02	0.36±0.04	
G30.7799+0.2301	-0.00	0.01	47.71	3.17±0.03	3.32±0.05	
G30.7799+0.2301	0.10	0.03	47.89	0.19±0.02	0.15±0.03	
G30.7799+0.2301	0.01	0.01	48.07	1.13±0.03	1.10±0.05	
G30.7799+0.2301	-0.00	0.02	48.25	4.83±0.06	4.90±0.10	
G30.7799+0.2301	-0.01	0.00	48.43	11.74±0.10	12.38±0.17	
G30.7799+0.2301	0.03	0.01	48.61	1.41±0.04	1.40±0.07	
G30.7799+0.2301	-0.00	-0.00	48.97	22.98±0.12	24.52±0.23	
G30.7799+0.2301	-0.01	-0.07	49.33	0.68±0.02	0.81±0.04	
G30.7882+0.2036	18:46:48.0864	-1:48:53.887	84.98	12.61±0.03	12.97±0.06	MMB, G30.7880+0.2039
G30.7882+0.2036	0.03	0.04	75.26	0.11±0.01	0.11±0.01	
G30.7882+0.2036	0.04	-0.05	75.44	0.11±0.00	0.10±0.01	
G30.7882+0.2036	0.02	0.07	75.62	1.80±0.02	1.84±0.04	
G30.7882+0.2036	0.05	0.03	75.80	3.09±0.12	3.47±0.22	
G30.7882+0.2036	0.01	0.06	75.98	2.02±0.04	2.11±0.07	
G30.7882+0.2036	0.03	0.03	76.16	1.88±0.07	2.09±0.14	
G30.7882+0.2036	0.03	0.06	76.34	1.73±0.07	1.94±0.14	
G30.7882+0.2036	-0.00	0.10	76.52	0.70±0.02	0.74±0.04	
G30.7882+0.2036	-0.02	0.07	76.70	1.12±0.02	1.15±0.03	
G30.7882+0.2036	-0.01	0.11	76.88	2.50±0.02	2.58±0.03	
G30.7882+0.2036	-0.01	0.10	77.06	3.06±0.02	3.12±0.04	
G30.7882+0.2036	-0.01	0.11	77.24	2.64±0.02	2.62±0.03	
G30.7882+0.2036	-0.02	0.09	77.42	1.41±0.01	1.45±0.02	
G30.7882+0.2036	-0.02	0.07	77.60	0.88±0.00	0.87±0.01	
G30.7882+0.2036	-0.04	0.15	77.78	0.41±0.00	0.37±0.01	
G30.7882+0.2036	-0.01	-0.10	77.96	0.12±0.01	0.13±0.01	
G30.7882+0.2036	0.04	0.09	79.04	0.27±0.00	0.29±0.01	
G30.7882+0.2036	0.02	-0.01	79.22	0.58±0.00	0.57±0.01	
G30.7882+0.2036	0.05	0.04	79.40	0.38±0.00	0.35±0.01	
G30.7882+0.2036	0.13	0.10	79.58	0.31±0.01	0.29±0.02	
G30.7882+0.2036	-0.07	-0.01	79.76	0.37±0.01	0.37±0.01	
G30.7882+0.2036	0.02	0.12	79.94	0.29±0.01	0.28±0.01	
G30.7882+0.2036	-0.06	0.21	80.12	0.08±0.01	0.08±0.01	
G30.7882+0.2036	0.15	-0.14	83.90	0.09±0.01	0.09±0.02	
G30.7882+0.2036	-0.08	0.11	84.26	0.22±0.01	0.23±0.01	
G30.7882+0.2036	0.01	0.00	84.44	1.26±0.01	1.28±0.03	
G30.7882+0.2036	0.00	0.03	84.62	2.93±0.02	2.94±0.04	

Continuation
of Table C.1

Name	$\alpha/\Delta\alpha$ h:m:s/″	$\delta/\Delta\delta$ d:m:s/″	V_{LSR} km s^{-1}	$S_{v,\,Peak}$ Jy beam^{-1}	$S_{v,\,Int}$ Jy	Notes
(1)	(2)	(3)	(4)	(5)	(6)	(7)
G30.7882+0.2036	-0.01	0.01	84.80	5.52±0.03	5.62±0.05	
G30.7882+0.2036	-0.00	-0.00	85.16	10.56±0.03	10.78±0.05	
G30.7882+0.2036	-0.00	0.00	85.34	5.54±0.03	5.65±0.05	
G30.7882+0.2036	-0.01	-0.01	85.52	4.38±0.02	4.40±0.04	
G30.7882+0.2036	0.00	0.03	85.70	3.21±0.03	3.23±0.05	
G30.7882+0.2036	0.00	0.01	85.88	7.04±0.03	7.14±0.05	
G30.7882+0.2036	0.01	0.01	86.06	7.34±0.03	7.47±0.06	
G30.7882+0.2036	-0.01	-0.01	86.24	3.77±0.03	3.78±0.05	
G30.7882+0.2036	-0.01	0.04	86.42	1.04±0.01	0.98±0.02	
G30.7882+0.2036	0.01	0.02	86.60	1.79±0.01	1.78±0.02	
G30.7882+0.2036	0.01	0.01	86.78	5.65±0.02	5.73±0.04	
G30.7882+0.2036	0.00	0.00	86.96	5.83±0.03	5.86±0.05	
G30.7882+0.2036	-0.01	0.00	87.14	6.91±0.03	7.03±0.05	
G30.7882+0.2036	0.00	-0.00	87.32	7.17±0.04	7.26±0.06	
G30.7882+0.2036	0.00	0.01	87.50	5.53±0.03	5.69±0.06	
G30.7882+0.2036	0.01	0.01	87.68	4.35±0.03	4.43±0.05	
G30.7882+0.2036	0.03	0.03	87.86	3.60±0.03	3.65±0.06	
G30.7882+0.2036	0.01	-0.01	88.04	2.66±0.06	2.81±0.10	
G30.7882+0.2036	0.04	-0.01	88.22	1.17±0.06	1.35±0.11	
G30.7882+0.2036	0.11	-0.26	88.40	0.18±0.02	0.23±0.05	
G30.7882+0.2036	0.03	-0.03	88.94	0.08±0.01	0.04±0.01	
G30.7882+0.2036	0.02	0.01	89.12	0.75±0.00	0.78±0.01	
G30.7882+0.2036	0.06	0.08	89.30	0.24±0.01	0.26±0.01	
G30.7882+0.2036	0.04	0.03	89.48	0.58±0.00	0.61±0.01	
G30.7882+0.2036	0.02	0.04	89.66	3.15±0.01	3.23±0.02	
G30.7882+0.2036	0.07	-0.01	89.84	0.57±0.01	0.47±0.01	
G30.7882+0.2036	-0.03	0.36	90.02	0.09±0.01	0.12±0.01	
G30.7880+0.2031	18:46:48.1535	-1:48:55.277	75.80	8.21±0.08	8.66±0.14	G30.7880+0.2039b
G30.7880+0.2031	-0.01	0.11	71.48	0.10±0.01	0.14±0.01	
G30.7880+0.2031	-0.17	0.08	72.74	0.19±0.00	0.21±0.01	
G30.7880+0.2031	0.04	0.06	72.92	0.24±0.01	0.27±0.01	
G30.7880+0.2031	0.06	0.05	75.26	0.32±0.00	0.36±0.01	
G30.7880+0.2031	0.02	0.02	75.62	1.13±0.04	1.25±0.08	
G30.7880+0.2031	-0.01	-0.01	75.98	2.50±0.05	2.68±0.08	
G30.7880+0.2031	-0.02	0.03	76.16	4.30±0.05	4.50±0.09	
G30.7880+0.2031	-0.03	0.01	76.34	4.14±0.04	4.35±0.07	
G30.7880+0.2031	-0.01	-0.02	76.52	1.47±0.02	1.56±0.03	
G30.7880+0.2031	0.00	-0.01	76.70	0.79±0.02	0.94±0.05	
G30.7880+0.2031	-0.10	0.05	78.32	0.18±0.01	0.16±0.01	
G30.7880+0.2031	-0.08	0.05	78.50	0.31±0.01	0.29±0.02	
G30.7880+0.2031	0.03	0.04	88.04	1.62±0.08	2.01±0.16	
G30.7880+0.2031	0.05	-0.03	88.22	1.99±0.04	2.15±0.07	
G30.7880+0.2031	0.06	-0.04	88.40	0.80±0.01	0.85±0.02	
G30.7880+0.2031	0.08	0.01	88.58	0.23±0.00	0.23±0.01	

Continuation
of Table C.1

Name	$\alpha/\Delta\alpha$ h:m:s/″	$\delta/\Delta\delta$ d:m:s/″	V_{LSR} km s^{-1}	$S_{v,\,Peak}$ Jy beam^{-1}	$S_{v,\,Int}$ Jy	Notes
(1)	(2)	(3)	(4)	(5)	(6)	(7)
G30.8176–0.0547	18:47:46.5085	-1:54:24.216	93.02	4.55±0.07	4.86±0.12	MMB
G30.8176–0.0547	-0.18	0.04	92.48	0.25±0.04	0.43±0.10	
G30.8176–0.0547	-0.04	-0.02	92.66	2.11±0.05	2.45±0.11	
G30.8176–0.0547	-0.02	-0.03	92.84	3.85±0.06	4.15±0.11	
G30.8176–0.0547	-0.01	-0.03	93.20	3.66±0.07	4.02±0.13	
G30.8176–0.0547	-0.05	-0.02	93.38	0.58±0.05	0.84±0.11	
G30.8176–0.0547	0.09	0.41	93.56	0.12±0.03	0.50±0.17	
G30.8176–0.0547	0.19	0.27	94.64	0.18±0.02	0.25±0.06	
G30.8176–0.0547	0.04	0.14	94.82	0.50±0.06	0.89±0.15	
G30.8176–0.0547	0.08	0.13	95.00	1.39±0.04	1.62±0.08	
G30.8176–0.0547	0.14	0.13	95.18	1.09±0.05	1.41±0.10	
G30.8176–0.0547	0.06	0.06	95.36	0.62±0.05	0.92±0.11	
G30.8176–0.0547	0.13	0.16	95.54	0.38±0.04	0.86±0.13	
G30.8176–0.0547	0.04	0.18	95.72	0.59±0.05	0.88±0.10	
G30.8176–0.0547	-0.02	0.14	95.90	0.54±0.04	0.91±0.11	
G30.8176–0.0547	-0.06	0.14	96.08	0.25±0.03	0.65±0.11	
G30.8176–0.0547	0.14	-0.01	96.26	0.12±0.02	0.09±0.03	
G30.0095–0.2734	18:47:04.7107	-2:43:31.141	106.06	2.24±0.02	2.33±0.04	MMB
G30.0095–0.2734	0.07	-0.07	103.00	1.14±0.02	1.28±0.04	
G30.0095–0.2734	0.09	-0.09	103.18	1.51±0.02	1.54±0.04	
G30.0095–0.2734	0.10	-0.11	103.36	1.10±0.02	1.13±0.04	
G30.0095–0.2734	0.10	-0.04	103.54	0.34±0.02	0.39±0.04	
G30.0095–0.2734	0.15	0.20	103.90	0.07±0.01	0.17±0.04	
G30.0095–0.2734	0.05	0.10	105.88	0.21±0.02	0.26±0.04	
G30.0095–0.2734	0.07	0.01	106.24	0.43±0.02	0.40±0.03	
G30.8178–0.0570	18:47:46.9720	-1:54:26.345	109.03	10.57±0.10	11.02±0.18	MMB
G30.8178–0.0570	0.04	0.23	98.77	0.08±0.02	0.23±0.07	
G30.8178–0.0570	0.13	-0.22	98.95	0.07±0.02	0.20±0.07	
G30.8178–0.0570	0.23	0.03	99.13	0.15±0.02	0.34±0.07	
G30.8178–0.0570	0.22	0.17	99.31	0.32±0.04	0.71±0.11	
G30.8178–0.0570	0.18	0.10	99.49	0.63±0.05	0.98±0.11	
G30.8178–0.0570	0.13	-0.01	99.67	1.51±0.05	1.86±0.11	
G30.8178–0.0570	0.14	-0.02	99.85	1.39±0.05	1.79±0.11	
G30.8178–0.0570	0.14	-0.18	100.03	0.24±0.04	0.79±0.15	
G30.8178–0.0570	0.15	-0.07	100.21	0.24±0.03	1.02±0.18	
G30.8178–0.0570	0.16	-0.01	100.39	0.34±0.04	0.76±0.13	
G30.8178–0.0570	0.14	-0.06	100.57	0.47±0.04	0.75±0.10	
G30.8178–0.0570	0.21	0.13	100.75	0.36±0.04	0.60±0.10	
G30.8178–0.0570	0.12	0.03	100.93	1.11±0.04	1.38±0.09	
G30.8178–0.0570	0.11	0.07	101.11	2.45±0.05	2.71±0.09	
G30.8178–0.0570	0.12	0.08	101.29	5.83±0.06	6.19±0.11	
G30.8178–0.0570	0.11	0.08	101.47	6.53±0.07	6.94±0.13	
G30.8178–0.0570	0.10	0.09	101.65	3.66±0.06	3.95±0.10	
G30.8178–0.0570	0.06	0.09	101.83	1.56±0.04	1.79±0.08	

Continuation
of Table C.1

Name	$\alpha/\Delta\alpha$ h:m:s/″	$\delta/\Delta\delta$ d:m:s/″	V_{LSR} km s^{-1}	$S_{v,\,Peak}$ Jy beam^{-1}	$S_{v,\,Int}$ Jy	Notes
(1)	(2)	(3)	(4)	(5)	(6)	(7)
G30.8178–0.0570	0.04	0.05	102.01	0.33±0.04	0.59±0.11	
G30.8178–0.0570	-0.17	0.06	103.09	0.34±0.04	0.82±0.13	
G30.8178–0.0570	-0.19	0.11	103.27	1.16±0.04	1.45±0.08	
G30.8178–0.0570	-0.22	0.03	103.45	0.52±0.04	0.73±0.09	
G30.8178–0.0570	-0.21	-0.06	103.63	0.16±0.02	0.23±0.05	
G30.8178–0.0570	-0.17	-0.22	104.17	0.20±0.02	0.36±0.06	
G30.8178–0.0570	-0.44	-0.08	104.35	0.18±0.03	1.19±0.23	
G30.8178–0.0570	-0.36	-0.16	104.53	0.22±0.04	1.37±0.29	
G30.8178–0.0570	-0.25	0.05	104.71	0.20±0.03	0.96±0.20	
G30.8178–0.0570	-0.12	-0.14	104.89	0.49±0.04	0.78±0.10	
G30.8178–0.0570	-0.06	-0.10	105.07	1.84±0.04	2.00±0.07	
G30.8178–0.0570	-0.06	-0.08	105.25	5.46±0.05	5.79±0.09	
G30.8178–0.0570	-0.05	-0.12	105.43	0.77±0.05	1.00±0.10	
G30.8178–0.0570	0.34	-0.67	105.61	0.08±0.02	0.44±0.12	
G30.8178–0.0570	-0.09	-0.11	105.79	0.06±0.01	0.27±0.08	
G30.8178–0.0570	0.20	-0.12	106.15	0.09±0.02	0.23±0.06	
G30.8178–0.0570	0.12	0.07	106.33	0.23±0.03	0.40±0.07	
G30.8178–0.0570	-0.07	-0.01	106.51	0.51±0.04	0.68±0.08	
G30.8178–0.0570	-0.06	-0.03	106.69	1.64±0.05	1.86±0.09	
G30.8178–0.0570	-0.07	-0.04	106.87	1.31±0.04	1.62±0.09	
G30.8178–0.0570	-0.02	-0.03	107.05	1.44±0.05	1.61±0.09	
G30.8178–0.0570	-0.05	-0.01	107.23	2.41±0.04	2.65±0.08	
G30.8178–0.0570	-0.03	-0.02	107.41	2.52±0.05	2.84±0.10	
G30.8178–0.0570	-0.05	-0.04	107.59	5.51±0.06	5.88±0.11	
G30.8178–0.0570	-0.05	-0.05	107.77	4.33±0.06	4.58±0.11	
G30.8178–0.0570	-0.04	-0.01	107.95	7.54±0.07	7.89±0.13	
G30.8178–0.0570	-0.04	-0.01	108.13	8.79±0.08	9.11±0.14	
G30.8178–0.0570	-0.04	-0.00	108.31	6.19±0.07	6.49±0.13	
G30.8178–0.0570	-0.04	-0.01	108.49	4.21±0.06	4.46±0.11	
G30.8178–0.0570	-0.06	-0.03	108.67	1.10±0.05	1.38±0.10	
G30.8178–0.0570	-0.01	0.00	108.85	3.39±0.06	3.70±0.11	
G30.8178–0.0570	-0.01	0.00	109.21	8.25±0.08	8.65±0.15	
G30.8178–0.0570	-0.00	0.01	109.39	3.17±0.05	3.32±0.09	
G30.8178–0.0570	-0.00	-0.00	109.57	2.29±0.05	2.51±0.09	
G30.8178–0.0570	-0.01	0.01	109.75	1.21±0.04	1.33±0.07	
G30.8178–0.0570	-0.04	0.02	109.93	0.42±0.04	0.66±0.10	
G30.8186+0.2729	18:46:36.5959	-1:45:22.485	100.35	1.33±0.02	1.37±0.04	MMB
G30.8186+0.2729	0.02	-0.04	99.09	0.15±0.02	0.21±0.04	
G30.8186+0.2729	0.49	-0.30	99.27	0.08±0.02	0.20±0.08	
G30.8186+0.2729	0.24	0.23	99.99	0.10±0.02	0.37±0.10	
G30.8186+0.2729	0.05	-0.05	100.17	0.53±0.02	0.57±0.04	
G30.8186+0.2729	0.04	-0.01	100.53	1.08±0.02	1.14±0.04	
G30.8186+0.2729	-0.32	-0.12	100.89	0.11±0.02	0.26±0.05	
G30.8186+0.2729	0.01	-0.02	101.07	0.90±0.02	0.89±0.03	

Continuation
of Table C.1

Name	$\alpha/\Delta\alpha$ h:m:s/″	$\delta/\Delta\delta$ d:m:s/″	V_{LSR} km s^{-1}	$S_{v,\,Peak}$ Jy beam^{-1}	$S_{v,\,Int}$ Jy	Notes
(1)	(2)	(3)	(4)	(5)	(6)	(7)
G30.8186+0.2729	0.04	-0.32	102.33	0.28±0.02	0.41±0.04	
G30.8186+0.2729	0.06	-0.30	102.51	0.11±0.02	0.58±0.12	
G30.8186+0.2729	0.30	-0.88	102.69	0.05±0.01	0.52±0.15	
G30.8186+0.2729	0.21	-0.34	102.87	0.08±0.02	0.26±0.07	
G30.8186+0.2729	-0.39	0.27	103.41	0.06±0.02	0.16±0.06	
G30.8186+0.2729	0.21	0.16	103.77	0.03±0.01	0.40±0.12	
G30.8186+0.2729	0.09	-0.22	104.31	0.32±0.02	0.32±0.03	
G30.8186+0.2729	0.10	-0.15	104.49	0.64±0.02	0.65±0.04	
G30.8186+0.2729	0.05	-0.14	104.67	0.96±0.03	1.01±0.05	
G30.8186+0.2729	0.12	-0.15	104.85	1.24±0.02	1.29±0.04	
G30.8186+0.2729	0.10	-0.11	105.03	0.51±0.03	0.53±0.05	
G30.8186+0.2729	-0.20	-0.20	109.35	0.05±0.02	0.23±0.08	
G30.8186+0.2729	0.02	-0.28	110.07	0.08±0.02	0.09±0.03	
G30.8186+0.2729	0.22	-0.21	110.25	0.18±0.02	0.24±0.04	
G30.8186+0.2729	0.33	-0.26	110.43	0.06±0.01	0.51±0.14	
G30.8508+0.1225	18:47:12.2574	-1:47:46.579	28.78	0.93±0.02	0.88±0.04	MMB
G30.8508+0.1225	-0.01	0.01	27.34	0.42±0.02	0.53±0.05	
G30.8508+0.1225	-0.01	-0.12	27.52	0.73±0.03	0.69±0.05	
G30.8508+0.1225	-0.05	-0.01	27.70	0.59±0.02	0.58±0.04	
G30.8508+0.1225	0.07	-0.16	27.88	0.20±0.02	0.17±0.03	
G30.8508+0.1225	0.61	-0.24	28.42	0.06±0.02	0.21±0.07	
G30.8508+0.1225	0.09	-0.04	28.60	0.33±0.02	0.39±0.04	
G30.8508+0.1225	0.04	-0.01	28.96	0.63±0.02	0.58±0.04	
G30.8508+0.1225	0.08	0.30	29.14	0.11±0.02	0.09±0.03	
G30.8508+0.1225	-0.24	0.01	37.06	0.14±0.02	0.14±0.04	
G30.8508+0.1225	0.01	-0.12	37.24	0.33±0.02	0.34±0.04	
G30.8979+0.1612	18:47:09.1254	-1:44:12.620	101.66	48.17±0.34	49.19±0.61	MMB
G30.8979+0.1612	-0.15	-0.16	98.24	0.10±0.02	0.15±0.05	
G30.8979+0.1612	0.30	-0.03	98.42	0.07±0.02	0.20±0.07	
G30.8979+0.1612	-0.07	-0.04	98.60	4.16±0.08	4.29±0.14	
G30.8979+0.1612	-0.05	-0.03	98.78	11.07±0.17	11.53±0.31	
G30.8979+0.1612	-0.05	-0.03	98.96	11.79±0.18	12.12±0.31	
G30.8979+0.1612	-0.04	-0.02	99.14	8.14±0.14	8.49±0.25	
G30.8979+0.1612	-0.02	-0.01	99.32	7.66±0.14	8.06±0.24	
G30.8979+0.1612	-0.02	-0.02	99.50	10.27±0.16	10.71±0.30	
G30.8979+0.1612	-0.01	-0.02	99.68	9.75±0.15	10.04±0.26	
G30.8979+0.1612	-0.02	-0.01	99.86	6.76±0.13	7.11±0.23	
G30.8979+0.1612	-0.01	-0.01	100.04	15.13±0.22	15.40±0.38	
G30.8979+0.1612	-0.01	-0.02	100.22	33.25±0.31	34.06±0.55	
G30.8979+0.1612	-0.01	-0.02	100.40	26.81±0.28	27.32±0.50	
G30.8979+0.1612	-0.01	-0.01	100.58	18.07±0.24	18.40±0.43	
G30.8979+0.1612	-0.01	-0.01	100.76	17.00±0.22	17.42±0.40	
G30.8979+0.1612	-0.01	-0.02	100.94	10.96±0.17	11.29±0.30	
G30.8979+0.1612	-0.00	-0.01	101.12	8.74±0.15	8.99±0.27	

Continuation
of Table C.1

Name	$\alpha/\Delta\alpha$ h:m:s/″	$\delta/\Delta\delta$ d:m:s/″	V_{LSR} km s^{-1}	$S_{v,\,Peak}$ Jy beam^{-1}	$S_{v,\,Int}$ Jy	Notes
(1)	(2)	(3)	(4)	(5)	(6)	(7)
G30.8979+0.1612	-0.00	-0.01	101.30	12.58±0.20	12.83±0.36	
G30.8979+0.1612	-0.00	-0.01	101.48	37.72±0.30	38.55±0.53	
G30.8979+0.1612	0.00	0.00	101.84	47.71±0.34	48.75±0.60	
G30.8979+0.1612	0.00	0.00	102.02	24.04±0.26	24.50±0.45	
G30.8979+0.1612	0.00	0.00	102.20	8.81±0.15	9.15±0.27	
G30.8979+0.1612	-0.03	0.02	102.38	1.20±0.08	1.42±0.16	
G30.8979+0.1612	0.01	0.01	102.56	5.63±0.10	6.12±0.19	
G30.8979+0.1612	0.02	0.02	102.74	6.00±0.17	6.12±0.30	
G30.8979+0.1612	0.02	0.01	102.92	40.24±0.32	41.06±0.56	
G30.8979+0.1612	0.01	0.02	103.10	38.36±0.29	38.86±0.51	
G30.8979+0.1612	0.03	0.02	103.28	9.38±0.20	9.48±0.35	
G30.8979+0.1612	0.01	0.02	103.46	16.11±0.19	16.53±0.34	
G30.8979+0.1612	0.03	0.03	103.64	8.53±0.18	8.71±0.32	
G30.8979+0.1612	0.02	0.02	103.82	16.86±0.19	17.41±0.34	
G30.8979+0.1612	0.02	0.03	104.00	4.85±0.14	5.09±0.24	
G30.8979+0.1612	0.01	0.02	104.18	9.17±0.14	9.52±0.24	
G30.8979+0.1612	0.02	0.02	104.36	9.45±0.13	9.76±0.23	
G30.8979+0.1612	-0.00	0.03	104.54	2.08±0.09	2.33±0.17	
G30.8979+0.1612	0.03	0.01	104.72	0.68±0.06	1.09±0.15	
G30.8979+0.1612	0.02	-0.00	104.90	0.87±0.07	1.37±0.16	
G30.8979+0.1612	0.01	0.03	105.08	2.34±0.07	2.80±0.14	
G30.8979+0.1612	0.06	0.06	105.26	0.54±0.06	1.22±0.19	
G30.8979+0.1612	0.24	0.06	105.44	0.10±0.02	0.36±0.09	
G30.8979+0.1612	0.02	0.65	106.34	0.07±0.02	0.38±0.13	
G30.8979+0.1612	0.08	-0.20	106.70	0.16±0.03	0.43±0.11	
G30.8979+0.1612	0.02	0.20	106.88	0.26±0.03	0.43±0.08	
G30.8979+0.1612	-0.08	0.21	107.06	8.78±0.13	9.17±0.24	
G30.8979+0.1612	-0.08	0.21	107.24	12.03±0.18	12.44±0.32	
G30.8979+0.1612	-0.09	0.17	107.42	4.86±0.12	5.39±0.22	
G30.8979+0.1612	-0.15	0.11	107.60	6.93±0.11	7.44±0.20	
G30.8979+0.1612	-0.11	0.15	107.78	2.57±0.08	2.96±0.15	
G30.8979+0.1612	-0.05	0.23	107.96	1.05±0.06	1.50±0.14	
G30.8979+0.1612	-0.06	0.13	108.14	0.38±0.04	0.75±0.12	
G30.8979+0.1612	-0.10	0.18	108.32	0.89±0.06	1.28±0.13	
G30.8979+0.1612	-0.07	0.29	108.50	0.22±0.04	0.82±0.17	
G30.8979+0.1612	-0.24	0.07	108.68	0.22±0.04	0.77±0.16	
G30.8979+0.1612	-0.20	0.07	108.86	0.39±0.05	0.94±0.17	
G30.8979+0.1612	-0.11	0.04	109.04	1.12±0.07	1.54±0.15	
G30.8979+0.1612	-0.11	0.04	109.22	0.76±0.07	1.36±0.18	
G30.8979+0.1612	-0.14	0.01	109.40	0.42±0.05	1.02±0.16	
G30.8979+0.1612	-0.16	-0.03	109.58	0.36±0.04	0.61±0.09	
G30.8979+0.1612	-0.15	0.06	109.76	0.59±0.06	1.07±0.15	
G30.8979+0.1612	-0.11	0.04	109.94	1.81±0.07	2.08±0.13	
G30.8979+0.1612	-0.09	0.11	110.12	0.42±0.06	0.97±0.18	

Continuation
of Table C.1

Name	$\alpha/\Delta\alpha$ h:m:s/″	$\delta/\Delta\delta$ d:m:s/″	V_{LSR} km s^{-1}	$S_{v,\,Peak}$ Jy beam^{-1}	$S_{v,\,Int}$ Jy	Notes
(1)	(2)	(3)	(4)	(5)	(6)	(7)
G30.8979+0.1612	-0.11	0.09	110.30	0.27±0.03	0.50±0.08	
G30.9591+0.0859	18:47:31.9248	-1:43:00.119	39.98	0.44±0.02	0.43±0.03	MMB
G30.9591+0.0859	0.17	0.35	39.62	0.16±0.02	0.15±0.03	
G30.9591+0.0859	0.05	0.24	39.80	0.39±0.02	0.42±0.03	
G30.9591+0.0859	0.14	0.26	40.16	0.43±0.02	0.47±0.03	
G30.9591+0.0859	0.32	-0.08	41.42	0.03±0.01	0.32±0.11	
G30.9726–0.1414	18:48:22.0473	-1:48:30.701	77.83	19.63±0.14	21.01±0.26	MMB
G30.9726–0.1414	0.22	-0.12	73.15	0.04±0.01	0.59±0.18	
G30.9726–0.1414	0.47	0.11	73.33	0.09±0.02	0.26±0.07	
G30.9726–0.1414	0.28	0.09	73.69	0.11±0.02	0.38±0.10	
G30.9726–0.1414	0.22	0.11	73.87	0.70±0.03	0.83±0.05	
G30.9726–0.1414	0.22	0.13	74.05	2.81±0.04	3.00±0.08	
G30.9726–0.1414	0.23	0.13	74.23	2.95±0.05	3.14±0.09	
G30.9726–0.1414	0.24	0.14	74.41	3.91±0.06	4.12±0.11	
G30.9726–0.1414	0.24	0.14	74.59	6.24±0.07	6.53±0.13	
G30.9726–0.1414	0.24	0.14	74.77	9.52±0.09	10.00±0.16	
G30.9726–0.1414	0.24	0.14	74.95	7.04±0.08	7.38±0.14	
G30.9726–0.1414	0.24	0.13	75.13	2.05±0.05	2.14±0.09	
G30.9726–0.1414	0.25	0.14	75.31	6.01±0.07	6.34±0.13	
G30.9726–0.1414	0.25	0.15	75.49	7.87±0.08	8.28±0.15	
G30.9726–0.1414	0.25	0.16	75.67	2.76±0.05	2.95±0.09	
G30.9726–0.1414	0.38	0.21	75.85	0.42±0.03	0.60±0.07	
G30.9726–0.1414	0.18	0.11	76.03	0.64±0.03	0.80±0.06	
G30.9726–0.1414	0.04	0.05	76.21	3.81±0.05	4.25±0.10	
G30.9726–0.1414	0.02	0.08	76.39	4.47±0.06	4.89±0.12	
G30.9726–0.1414	0.04	0.11	76.57	3.34±0.05	3.72±0.10	
G30.9726–0.1414	0.07	0.16	76.75	1.69±0.04	1.96±0.08	
G30.9726–0.1414	0.09	0.15	76.93	3.38±0.05	3.89±0.10	
G30.9726–0.1414	0.04	0.07	77.11	3.73±0.06	4.20±0.10	
G30.9726–0.1414	0.03	0.02	77.29	3.33±0.04	3.66±0.08	
G30.9726–0.1414	-0.02	0.09	77.47	0.88±0.04	0.97±0.08	
G30.9726–0.1414	0.00	0.00	77.65	14.74±0.10	15.72±0.17	
G30.9726–0.1414	0.00	0.01	78.01	7.23±0.07	7.67±0.13	
G30.9726–0.1414	0.00	-0.00	78.19	3.65±0.06	3.81±0.10	
G30.9726–0.1414	0.00	0.02	78.37	2.97±0.05	3.18±0.10	
G30.9726–0.1414	-0.00	0.02	78.55	2.13±0.03	2.25±0.06	
G30.9726–0.1414	0.04	0.02	78.73	0.29±0.02	0.36±0.04	
G30.9726–0.1414	-0.02	0.00	78.91	0.19±0.02	0.32±0.05	
G30.9726–0.1414	-0.11	0.41	79.45	0.06±0.01	0.28±0.07	
G30.9726–0.1414	0.16	0.11	79.63	0.32±0.02	0.40±0.05	
G30.9726–0.1414	0.22	0.11	79.81	1.69±0.03	1.85±0.06	
G30.9726–0.1414	0.20	0.14	79.99	1.99±0.04	2.14±0.07	
G30.9726–0.1414	0.24	0.26	80.17	0.19±0.02	0.22±0.03	
G30.9726–0.1414	-0.53	0.03	80.35	0.06±0.02	0.16±0.07	

Continuation
of Table C.1

Name	$\alpha/\Delta\alpha$ h:m:s/″	$\delta/\Delta\delta$ d:m:s/″	V_{LSR} km s^{-1}	$S_{v,\,Peak}$ Jy beam^{-1}	$S_{v,\,Int}$ Jy	Notes
(1)	(2)	(3)	(4)	(5)	(6)	(7)
G30.9801+0.2158	18:47:06.4722	-1:38:19.939	110.92	0.20±0.02	0.28±0.05	MMB
G30.9801+0.2158	-0.81	-1.03	110.56	0.05±0.01	0.21±0.07	
G30.9801+0.2158	0.53	0.09	110.74	0.08±0.02	0.35±0.10	
G30.9801+0.2158	0.44	-0.85	111.10	0.08±0.02	0.29±0.08	
G30.9728+0.5624	18:45:51.6903	-1:29:13.287	19.88	0.34±0.02	0.47±0.05	MMB
G30.9728+0.5624	-0.05	0.01	19.70	0.07±0.02	0.15±0.05	
G30.9728+0.5624	-0.05	0.02	20.06	0.25±0.02	0.30±0.03	
G30.9728+0.5624	-0.08	-0.10	20.24	0.14±0.02	0.18±0.03	
G30.1981–0.1688	18:47:03.0720	-2:30:36.240	108.58	20.26±0.11	21.46±0.20	MMB
G30.1981–0.1688	-0.09	-0.13	100.66	0.44±0.02	0.52±0.05	
G30.1981–0.1688	-0.11	-0.16	100.84	0.20±0.02	0.24±0.04	
G30.1981–0.1688	0.03	-0.08	101.74	0.08±0.02	0.31±0.08	
G30.1981–0.1688	-0.20	0.03	102.46	0.05±0.01	0.44±0.13	
G30.1981–0.1688	-0.06	-0.03	102.64	0.19±0.02	0.21±0.04	
G30.1981–0.1688	-0.13	-0.06	102.82	0.68±0.03	0.81±0.05	
G30.1981–0.1688	-0.12	-0.07	103.00	1.14±0.03	1.22±0.06	
G30.1981–0.1688	-0.09	-0.06	103.18	2.11±0.04	2.17±0.07	
G30.1981–0.1688	-0.11	-0.05	103.36	1.99±0.04	2.06±0.07	
G30.1981–0.1688	-0.16	-0.06	103.54	0.30±0.02	0.40±0.05	
G30.1981–0.1688	-0.64	-0.21	103.72	0.08±0.02	0.68±0.18	
G30.1981–0.1688	-0.21	-0.06	103.90	0.15±0.03	0.61±0.14	
G30.1981–0.1688	-0.16	-0.13	104.08	0.16±0.02	0.36±0.07	
G30.1981–0.1688	-0.14	-0.04	104.26	1.23±0.02	1.36±0.05	
G30.1981–0.1688	-0.08	-0.07	104.44	3.16±0.05	3.38±0.09	
G30.1981–0.1688	-0.02	-0.10	104.62	3.43±0.06	3.59±0.10	
G30.1981–0.1688	-0.05	-0.08	104.80	3.32±0.05	3.49±0.10	
G30.1981–0.1688	-0.08	-0.06	104.98	2.52±0.05	2.61±0.08	
G30.1981–0.1688	-0.14	-0.05	105.16	2.17±0.04	2.31±0.08	
G30.1981–0.1688	-0.07	-0.03	105.34	1.35±0.03	1.42±0.05	
G30.1981–0.1688	-0.12	-0.04	105.52	0.92±0.02	1.01±0.05	
G30.1981–0.1688	-0.09	-0.03	105.70	0.51±0.03	0.66±0.05	
G30.1981–0.1688	-0.17	-0.04	105.88	0.32±0.03	0.40±0.06	
G30.1981–0.1688	-0.60	-0.74	106.06	0.05±0.01	0.60±0.19	
G30.1981–0.1688	0.20	-0.46	106.24	0.06±0.01	0.60±0.15	
G30.1981–0.1688	0.01	-0.05	107.32	0.11±0.01	0.09±0.02	
G30.1981–0.1688	-0.03	0.04	107.50	0.49±0.02	0.53±0.04	
G30.1981–0.1688	0.03	-0.01	107.68	2.90±0.04	3.09±0.07	
G30.1981–0.1688	-0.01	0.04	107.86	1.32±0.04	1.34±0.08	
G30.1981–0.1688	0.02	-0.01	108.04	16.66±0.10	17.28±0.18	
G30.1981–0.1688	-0.00	0.00	108.22	18.67±0.11	19.89±0.19	
G30.1981–0.1688	0.02	-0.01	108.40	14.18±0.10	14.62±0.18	
G30.1981–0.1688	0.01	-0.00	108.76	8.41±0.08	8.78±0.15	
G30.1981–0.1688	0.02	0.00	108.94	4.06±0.06	4.14±0.11	
G30.1981–0.1688	0.03	-0.01	109.12	3.65±0.06	3.76±0.10	

Continuation
of Table C.1

Name	$\alpha/\Delta\alpha$ h:m:s/″	$\delta/\Delta\delta$ d:m:s/″	V_{LSR} km s^{-1}	$S_{v,\,Peak}$ Jy beam^{-1}	$S_{v,\,Int}$ Jy	Notes
(1)	(2)	(3)	(4)	(5)	(6)	(7)
G30.1981–0.1688	0.02	0.00	109.30	7.64±0.08	7.97±0.14	
G30.1981–0.1688	0.02	-0.00	109.48	6.16±0.08	6.36±0.14	
G30.1981–0.1688	0.02	-0.00	109.66	4.56±0.06	4.59±0.11	
G30.1981–0.1688	0.03	0.00	109.84	3.45±0.05	3.56±0.09	
G30.1981–0.1688	0.02	-0.02	110.02	3.96±0.06	3.98±0.10	
G30.1981–0.1688	0.02	0.00	110.20	6.48±0.07	6.76±0.13	
G30.1981–0.1688	0.02	-0.01	110.38	5.20±0.08	5.36±0.13	
G30.1981–0.1688	0.02	0.00	110.56	3.36±0.05	3.56±0.10	
G30.1981–0.1688	0.03	-0.01	110.74	4.05±0.07	4.28±0.12	
G30.1981–0.1688	0.03	-0.06	110.92	0.83±0.03	0.88±0.05	
G30.2244–0.1803	18:47:08.3008	-2:29:29.270	113.21	13.18±0.12	13.40±0.20	MMB
G30.2244–0.1803	0.31	0.22	109.97	0.15±0.03	0.34±0.11	
G30.2244–0.1803	0.25	0.09	110.15	0.29±0.04	0.55±0.12	
G30.2244–0.1803	0.20	0.22	110.33	0.25±0.04	0.50±0.11	
G30.2244–0.1803	0.26	0.15	110.51	0.22±0.03	0.32±0.08	
G30.2244–0.1803	0.06	0.11	110.69	0.39±0.04	0.45±0.07	
G30.2244–0.1803	0.05	0.01	110.87	0.66±0.02	0.72±0.05	
G30.2244–0.1803	0.01	-0.00	111.05	3.28±0.04	3.37±0.08	
G30.2244–0.1803	0.01	-0.00	111.23	7.78±0.08	7.98±0.14	
G30.2244–0.1803	0.01	0.01	111.41	6.00±0.07	6.08±0.12	
G30.2244–0.1803	0.02	0.00	111.59	2.26±0.04	2.35±0.07	
G30.2244–0.1803	0.02	0.03	111.77	1.29±0.03	1.40±0.05	
G30.2244–0.1803	-0.02	-0.01	111.95	0.84±0.02	0.93±0.04	
G30.2244–0.1803	-0.00	0.02	112.13	1.80±0.03	1.89±0.06	
G30.2244–0.1803	0.00	0.01	112.31	3.81±0.05	3.87±0.08	
G30.2244–0.1803	0.00	0.01	112.49	5.59±0.06	5.61±0.11	
G30.2244–0.1803	0.00	-0.00	112.67	5.90±0.07	5.95±0.12	
G30.2244–0.1803	0.01	0.01	112.85	5.16±0.06	5.25±0.11	
G30.2244–0.1803	0.01	-0.00	113.03	9.68±0.10	9.90±0.17	
G30.2244–0.1803	0.01	0.01	113.39	6.41±0.07	6.56±0.12	
G30.2244–0.1803	0.01	0.00	113.57	2.75±0.04	2.87±0.08	
G30.2244–0.1803	-0.00	0.00	113.75	2.20±0.03	2.29±0.06	
G30.2244–0.1803	-0.00	0.01	113.93	1.00±0.03	1.10±0.05	
G30.2244–0.1803	0.02	0.03	114.11	0.40±0.03	0.58±0.07	
G30.2244–0.1803	0.01	0.09	114.29	0.17±0.02	0.25±0.05	
G30.2244–0.1803	-0.06	0.04	114.47	0.25±0.02	0.32±0.04	
G30.2244–0.1803	-0.39	-0.37	114.65	0.07±0.02	0.31±0.09	
G30.3177+0.0703	18:46:25.0249	-2:17:41.037	36.42	7.03±0.05	7.31±0.08	MMB
G30.3177+0.0703	-0.03	0.08	29.94	0.70±0.02	0.67±0.03	
G30.3177+0.0703	-0.01	0.01	30.12	2.08±0.03	2.17±0.05	
G30.3177+0.0703	-0.07	0.03	30.30	0.84±0.02	0.89±0.04	
G30.3177+0.0703	0.09	0.34	31.92	0.09±0.02	0.39±0.10	
G30.3177+0.0703	0.05	0.16	32.10	0.20±0.02	0.18±0.03	
G30.3177+0.0703	-0.01	0.01	32.28	0.79±0.02	0.91±0.04	

Continuation
of Table C.1

Name	$\alpha/\Delta\alpha$ h:m:s/″	$\delta/\Delta\delta$ d:m:s/″	V_{LSR} km s^{-1}	$S_{v,\,Peak}$ Jy beam^{-1}	$S_{v,\,Int}$ Jy	Notes
(1)	(2)	(3)	(4)	(5)	(6)	(7)
G30.3177+0.0703	-0.02	0.02	32.46	0.36±0.02	0.39±0.03	
G30.3177+0.0703	-0.35	-0.42	32.82	0.08±0.02	0.34±0.08	
G30.3177+0.0703	0.02	-0.05	33.00	0.30±0.02	0.38±0.04	
G30.3177+0.0703	-0.05	0.11	33.18	0.38±0.02	0.43±0.03	
G30.3177+0.0703	-0.02	0.02	33.36	0.77±0.02	0.80±0.03	
G30.3177+0.0703	-0.02	-0.00	33.54	0.87±0.02	0.92±0.03	
G30.3177+0.0703	0.01	0.07	33.72	0.28±0.02	0.31±0.03	
G30.3177+0.0703	-0.04	0.03	33.90	0.62±0.02	0.65±0.03	
G30.3177+0.0703	0.01	-0.00	34.08	0.80±0.02	0.81±0.03	
G30.3177+0.0703	0.05	-0.04	34.26	0.41±0.02	0.40±0.03	
G30.3177+0.0703	0.03	0.03	34.44	0.78±0.02	0.82±0.03	
G30.3177+0.0703	-0.03	0.03	34.62	0.46±0.01	0.50±0.03	
G30.3177+0.0703	-0.01	0.02	34.80	0.25±0.01	0.26±0.03	
G30.3177+0.0703	-0.02	0.02	34.98	0.75±0.02	0.80±0.03	
G30.3177+0.0703	-0.01	0.05	35.16	1.43±0.02	1.53±0.03	
G30.3177+0.0703	-0.00	-0.03	35.34	1.16±0.02	1.24±0.04	
G30.3177+0.0703	-0.02	0.03	35.52	2.17±0.03	2.22±0.05	
G30.3177+0.0703	-0.01	-0.00	35.70	1.25±0.03	1.29±0.05	
G30.3177+0.0703	0.01	0.00	35.88	1.64±0.03	1.71±0.05	
G30.3177+0.0703	0.00	0.01	36.06	6.84±0.05	7.15±0.08	
G30.3177+0.0703	0.00	0.01	36.24	6.67±0.05	6.89±0.08	
G30.3177+0.0703	-0.00	0.01	36.60	4.90±0.04	5.05±0.07	
G30.3177+0.0703	0.01	0.00	36.78	2.55±0.03	2.57±0.05	
G30.3177+0.0703	0.01	0.00	36.96	2.76±0.03	2.82±0.06	
G30.3177+0.0703	-0.00	-0.01	37.14	2.02±0.03	2.07±0.05	
G30.3177+0.0703	-0.00	0.02	37.32	1.43±0.03	1.49±0.05	
G30.3177+0.0703	-0.00	0.01	37.50	1.24±0.02	1.31±0.04	
G30.3177+0.0703	0.00	-0.02	37.68	0.96±0.02	1.05±0.04	
G30.3177+0.0703	-0.02	-0.06	37.86	0.63±0.02	0.73±0.04	
G30.3177+0.0703	0.03	0.00	38.04	0.45±0.02	0.52±0.03	
G30.3177+0.0703	-0.08	0.09	38.22	0.46±0.02	0.54±0.04	
G30.3177+0.0703	-0.09	0.01	38.40	0.17±0.02	0.29±0.05	
G30.3177+0.0703	-0.02	0.04	48.30	0.20±0.02	0.30±0.04	
G30.3177+0.0703	-0.09	0.09	48.48	0.84±0.02	0.92±0.04	
G30.3177+0.0703	-0.12	0.09	48.66	1.69±0.03	1.75±0.05	
G30.3177+0.0703	-0.08	0.07	48.84	1.55±0.03	1.65±0.05	
G30.3177+0.0703	-0.11	0.06	49.02	1.48±0.02	1.54±0.04	
G30.3177+0.0703	-0.10	0.04	49.20	0.94±0.02	1.04±0.04	
G30.3177+0.0703	-0.10	0.05	49.38	1.14±0.02	1.21±0.04	
G30.3177+0.0703	-0.10	0.13	49.56	0.96±0.02	1.03±0.04	
G30.3177+0.0703	-0.06	0.04	49.74	0.34±0.02	0.40±0.04	
G30.3177+0.0703	-0.10	0.10	49.92	0.26±0.02	0.25±0.03	
G30.3177+0.0703	-0.10	0.06	50.10	0.55±0.02	0.54±0.03	
G30.3177+0.0703	-0.08	0.11	50.28	0.97±0.02	0.98±0.04	

Continuation
of Table C.1

Name	$\alpha/\Delta\alpha$ h:m:s/″	$\delta/\Delta\delta$ d:m:s/″	V_{LSR} km s^{-1}	$S_{v,\,Peak}$ Jy beam^{-1}	$S_{v,\,Int}$ Jy	Notes
(1)	(2)	(3)	(4)	(5)	(6)	(7)
G30.3177+0.0703	-0.09	0.06	50.46	0.58±0.02	0.59±0.03	
G30.3177+0.0703	-0.12	0.12	50.64	0.63±0.02	0.66±0.03	
G30.3177+0.0703	-0.10	0.10	50.82	0.44±0.02	0.48±0.03	
G30.3177+0.0703	-0.09	-0.02	51.00	0.21±0.02	0.23±0.04	
G30.3705+0.4827	18:45:02.7282	-2:03:33.814	12.33	6.03±0.03	6.22±0.05	MMB
G30.3705+0.4827	0.01	-0.04	11.79	0.49±0.01	0.49±0.03	
G30.3705+0.4827	-0.01	-0.01	12.15	3.18±0.02	3.28±0.04	
G30.3705+0.4827	0.06	0.04	12.69	0.13±0.02	0.25±0.05	
G30.3705+0.4827	-0.12	-0.02	13.05	0.24±0.02	0.18±0.02	
G30.3705+0.4827	0.07	0.31	13.23	0.19±0.02	0.25±0.04	
G30.3705+0.4827	-0.12	0.22	16.47	0.24±0.02	0.18±0.02	
G30.3705+0.4827	-0.11	0.21	16.65	1.27±0.02	1.29±0.03	
G30.3705+0.4827	-0.04	0.37	16.83	0.11±0.02	0.22±0.05	
G30.3705+0.4827	-0.75	-0.34	17.91	0.06±0.01	0.12±0.04	
G30.3705+0.4827	-0.31	-0.21	18.09	0.09±0.01	0.13±0.03	
G30.3705+0.4827	-0.28	0.10	18.27	0.12±0.02	0.16±0.04	
G30.3705+0.4827	-0.17	0.10	18.45	0.19±0.02	0.17±0.03	
G30.3705+0.4827	0.02	0.16	18.63	0.26±0.01	0.27±0.02	
G30.3705+0.4827	-0.44	0.06	18.99	0.07±0.01	0.10±0.03	
G30.3705+0.4827	-0.01	0.13	19.35	0.72±0.02	0.78±0.04	
G30.3705+0.4827	-0.02	0.12	19.53	0.57±0.02	0.57±0.03	
G30.4006–0.2958	18:47:52.2991	-2:23:16.060	100.39	4.95±0.03	4.97±0.05	MMB
G30.4006–0.2958	0.08	-0.04	97.69	0.23±0.02	0.27±0.03	
G30.4006–0.2958	0.02	0.02	97.87	2.26±0.02	2.29±0.03	
G30.4006–0.2958	0.03	0.04	98.05	4.50±0.03	4.53±0.04	
G30.4006–0.2958	0.02	0.03	98.23	4.61±0.03	4.56±0.05	
G30.4006–0.2958	0.03	0.05	98.41	4.73±0.02	4.72±0.04	
G30.4006–0.2958	0.00	0.01	98.59	1.24±0.02	1.23±0.03	
G30.4006–0.2958	-0.03	-0.09	98.77	0.32±0.01	0.32±0.03	
G30.4006–0.2958	-0.04	-0.00	98.95	0.22±0.01	0.22±0.03	
G30.4006–0.2958	-0.06	0.46	99.13	0.06±0.01	0.12±0.03	
G30.4006–0.2958	0.51	0.47	99.49	0.03±0.01	0.31±0.10	
G30.4006–0.2958	-0.23	0.55	99.67	0.05±0.01	0.16±0.05	
G30.4006–0.2958	-0.04	-0.01	99.85	0.24±0.01	0.24±0.02	
G30.4006–0.2958	0.00	-0.00	100.21	3.09±0.02	3.11±0.04	
G30.4006–0.2958	-0.05	-0.05	100.57	0.24±0.02	0.22±0.03	
G30.4006–0.2958	0.01	-0.02	100.75	0.36±0.01	0.39±0.02	
G30.4006–0.2958	-0.66	0.30	101.11	0.03±0.01	0.32±0.10	
G30.4006–0.2958	-0.11	-0.02	101.29	0.12±0.02	0.15±0.03	
G30.4006–0.2958	0.02	0.11	101.47	0.30±0.02	0.39±0.04	
G30.4006–0.2958	0.04	0.14	101.65	0.20±0.01	0.26±0.03	
G30.4006–0.2958	0.03	0.13	101.83	0.33±0.01	0.36±0.03	
G30.4006–0.2958	0.06	0.15	102.01	0.18±0.02	0.21±0.03	
G30.4006–0.2958	0.04	0.07	102.19	0.17±0.02	0.19±0.03	

Continuation
of Table C.1

Name	$\alpha/\Delta\alpha$ h:m:s/″	$\delta/\Delta\delta$ d:m:s/″	V_{LSR} km s^{-1}	$S_{v,\,Peak}$ Jy beam^{-1}	$S_{v,\,Int}$ Jy	Notes
(1)	(2)	(3)	(4)	(5)	(6)	(7)
G30.4006–0.2958	0.01	0.18	103.27	0.36±0.02	0.37±0.04	
G30.4006–0.2958	0.02	0.11	103.45	1.08±0.02	1.13±0.04	
G30.4006–0.2958	0.02	0.13	103.63	1.81±0.02	1.85±0.04	
G30.4006–0.2958	0.03	0.11	103.81	1.15±0.02	1.14±0.04	
G30.4006–0.2958	0.06	0.06	103.99	0.25±0.01	0.23±0.02	
G30.4006–0.2958	0.12	-0.00	104.17	0.13±0.01	0.15±0.03	
G30.4006–0.2958	0.22	0.06	104.35	0.27±0.02	0.25±0.04	
G30.4006–0.2958	-0.05	0.32	104.53	0.11±0.02	0.31±0.06	
G30.4006–0.2958	0.10	0.32	104.71	0.25±0.02	0.27±0.03	
G30.4006–0.2958	0.12	0.27	104.89	0.27±0.01	0.26±0.02	
G30.4006–0.2958	-0.01	0.19	105.07	0.20±0.01	0.18±0.02	
G30.4194–0.2316	18:47:40.7617	-2:20:30.887	102.96	13.46±0.05	13.73±0.10	MMB
G30.4194–0.2316	-0.02	-0.03	102.42	0.48±0.02	0.48±0.04	
G30.4194–0.2316	-0.00	-0.00	102.78	5.54±0.04	5.58±0.06	
G30.4194–0.2316	0.00	-0.01	103.14	7.50±0.04	7.56±0.07	
G30.4194–0.2316	0.03	-0.02	103.32	0.86±0.02	0.87±0.04	
G30.4194–0.2316	-0.00	-0.02	103.50	1.67±0.02	1.72±0.04	
G30.4194–0.2316	-0.00	-0.02	103.68	2.27±0.03	2.33±0.05	
G30.4194–0.2316	-0.00	-0.04	103.86	0.70±0.02	0.71±0.04	
G30.4194–0.2316	-0.00	-0.05	104.04	0.82±0.02	0.84±0.03	
G30.4194–0.2316	-0.01	-0.01	104.22	0.56±0.01	0.59±0.03	
G30.4194–0.2316	-0.03	-0.04	104.40	0.66±0.01	0.69±0.03	
G30.4194–0.2316	-0.01	-0.13	104.58	0.57±0.01	0.55±0.02	
G30.4194–0.2316	-0.01	-0.12	104.76	0.70±0.02	0.68±0.03	
G30.4194–0.2316	0.01	-0.05	104.94	0.23±0.02	0.22±0.03	
G30.4194–0.2316	-0.15	-0.33	110.70	0.13±0.01	0.32±0.05	
G30.4194–0.2316	-0.05	-0.08	110.88	0.25±0.02	0.38±0.05	
G30.4194–0.2316	0.01	-0.17	111.06	0.21±0.02	0.26±0.03	
G30.4194–0.2316	-0.12	-0.20	111.24	0.06±0.01	0.17±0.05	
G30.4236+0.4659	18:45:12.0831	-2:01:10.707	6.26	0.67±0.02	0.72±0.03	MMB
G30.4236+0.4659	0.00	-0.01	5.72	0.63±0.01	0.72±0.03	
G30.4236+0.4659	-0.02	0.01	5.90	0.34±0.01	0.35±0.02	
G30.4236+0.4659	-0.09	-0.03	6.08	0.26±0.01	0.30±0.03	
G30.4236+0.4659	-0.04	-0.01	6.44	0.51±0.01	0.51±0.02	
G30.4236+0.4659	-0.00	0.00	6.62	0.48±0.01	0.51±0.02	
G30.4236+0.4659	-0.00	0.03	6.80	0.14±0.01	0.12±0.02	
G30.4236+0.4659	-0.04	0.12	7.52	0.13±0.01	0.12±0.02	
G30.4236+0.4659	-0.06	0.02	7.70	0.24±0.01	0.20±0.02	
G30.4236+0.4659	0.04	0.03	7.88	0.15±0.01	0.12±0.02	
G30.4236+0.4659	-0.10	-0.05	8.24	0.12±0.01	0.19±0.03	
G30.4236+0.4659	-0.01	0.04	8.42	0.33±0.02	0.38±0.03	
G30.4236+0.4659	0.06	-0.17	9.68	0.10±0.01	0.05±0.02	
G30.4236+0.4659	0.30	-0.11	9.86	0.05±0.01	0.17±0.05	
G30.5423+0.0111	18:47:02.2600	-2:07:17.749	54.27	0.54±0.02	0.60±0.03	MMB

Continuation
of Table C.1

Name	$\alpha/\Delta\alpha$ h:m:s/″	$\delta/\Delta\delta$ d:m:s/″	V_{LSR} km s^{-1}	$S_{v,\,Peak}$ Jy beam^{-1}	$S_{v,\,Int}$ Jy	Notes
(1)	(2)	(3)	(4)	(5)	(6)	(7)
G30.5423+0.0111	-0.30	-0.26	47.43	0.13±0.02	0.24±0.05	
G30.5423+0.0111	-0.13	0.02	47.61	0.07±0.02	0.08±0.03	
G30.5423+0.0111	-0.03	0.07	48.69	0.12±0.02	0.17±0.04	
G30.5423+0.0111	0.09	-0.27	51.93	0.12±0.02	0.34±0.07	
G30.5423+0.0111	0.09	0.28	52.11	0.16±0.02	0.38±0.07	
G30.5423+0.0111	0.02	0.08	52.29	0.35±0.02	0.38±0.04	
G30.5423+0.0111	0.01	0.06	52.47	0.32±0.02	0.36±0.04	
G30.5423+0.0111	0.02	0.11	52.65	0.45±0.02	0.48±0.03	
G30.5423+0.0111	0.01	-0.02	52.83	0.39±0.02	0.41±0.03	
G30.5423+0.0111	0.09	0.04	53.01	0.43±0.02	0.45±0.03	
G30.5423+0.0111	0.03	0.04	53.19	0.41±0.02	0.48±0.04	
G30.5423+0.0111	0.26	0.25	53.37	0.06±0.01	0.34±0.09	
G30.5423+0.0111	-0.02	-0.01	54.09	0.23±0.02	0.30±0.04	
G30.5423+0.0111	0.05	0.04	54.45	0.45±0.02	0.45±0.03	
G30.5423+0.0111	-0.02	-0.08	54.63	0.17±0.01	0.14±0.02	
G31.3958–0.2572	18:49:33.0845	-1:29:04.187	87.31	0.31±0.02	0.41±0.03	NEW
G31.3958–0.2572	-0.20	-0.06	87.49	0.16±0.02	0.27±0.05	
G31.4122+0.3071	18:47:34.2756	-1:12:45.769	95.81	13.82±0.16	16.66±0.32	MMB
G31.4122+0.3071	0.02	-0.24	91.31	0.11±0.02	0.42±0.10	
G31.4122+0.3071	0.11	-0.70	91.49	0.07±0.02	0.58±0.16	
G31.4122+0.3071	0.15	-0.35	91.67	0.26±0.03	0.35±0.05	
G31.4122+0.3071	0.13	-0.53	91.85	0.31±0.02	0.37±0.05	
G31.4122+0.3071	0.14	0.05	92.03	4.57±0.05	4.95±0.08	
G31.4122+0.3071	0.15	0.07	92.21	7.85±0.07	8.66±0.13	
G31.4122+0.3071	0.20	-0.27	92.39	2.46±0.04	3.03±0.08	
G31.4122+0.3071	0.21	-0.57	92.57	1.68±0.03	1.91±0.07	
G31.4122+0.3071	0.23	-0.56	92.75	1.39±0.03	1.51±0.05	
G31.4122+0.3071	0.20	-0.48	92.93	1.84±0.04	2.16±0.07	
G31.4122+0.3071	0.19	-0.44	93.11	2.82±0.04	3.46±0.08	
G31.4122+0.3071	0.19	-0.54	93.29	3.08±0.04	3.47±0.08	
G31.4122+0.3071	0.19	-0.53	93.47	2.52±0.04	2.95±0.07	
G31.4122+0.3071	0.18	-0.55	93.65	2.68±0.04	3.31±0.08	
G31.4122+0.3071	0.17	-0.55	93.83	2.70±0.04	3.37±0.08	
G31.4122+0.3071	0.17	-0.52	94.01	1.85±0.04	2.44±0.08	
G31.4122+0.3071	0.13	-0.47	94.19	1.58±0.03	2.17±0.06	
G31.4122+0.3071	0.14	-0.51	94.37	2.16±0.04	3.02±0.08	
G31.4122+0.3071	0.15	-0.57	94.55	2.52±0.04	3.33±0.08	
G31.4122+0.3071	0.18	-0.64	94.73	2.61±0.04	3.28±0.08	
G31.4122+0.3071	0.18	-0.65	94.91	2.36±0.04	3.09±0.09	
G31.4122+0.3071	0.05	-0.28	95.09	2.33±0.04	3.43±0.09	
G31.4122+0.3071	-0.06	0.02	95.27	7.07±0.08	8.15±0.15	
G31.4122+0.3071	-0.01	-0.01	95.45	6.05±0.10	7.64±0.21	
G31.4122+0.3071	-0.02	0.00	95.63	10.54±0.13	12.83±0.26	
G31.4122+0.3071	0.02	0.02	95.99	9.22±0.09	10.44±0.17	

Continuation
of Table C.1

Name	$\alpha/\Delta\alpha$ h:m:s/″	$\delta/\Delta\delta$ d:m:s/″	V_{LSR} km s^{-1}	$S_{v,\,Peak}$ Jy beam^{-1}	$S_{v,\,Int}$ Jy	Notes
(1)	(2)	(3)	(4)	(5)	(6)	(7)
G31.4122+0.3071	0.06	-0.03	96.17	8.46±0.12	10.42±0.24	
G31.4122+0.3071	0.12	-0.07	96.35	4.73±0.11	6.63±0.25	
G31.4122+0.3071	0.06	0.11	96.53	3.20±0.04	3.76±0.08	
G31.4122+0.3071	0.08	0.12	96.71	2.51±0.04	3.04±0.09	
G31.4122+0.3071	0.10	0.12	96.89	2.06±0.04	2.58±0.07	
G31.4122+0.3071	0.20	0.08	97.07	1.61±0.04	2.33±0.08	
G31.4122+0.3071	0.31	-0.11	97.25	1.19±0.03	1.88±0.08	
G31.4122+0.3071	0.54	-0.42	97.43	1.32±0.03	1.96±0.07	
G31.4122+0.3071	0.61	-0.54	97.61	1.25±0.03	1.73±0.07	
G31.4122+0.3071	0.58	-0.42	97.79	0.96±0.03	1.52±0.07	
G31.4122+0.3071	0.50	-0.25	97.97	0.84±0.03	1.38±0.07	
G31.4122+0.3071	0.46	-0.16	98.15	1.00±0.03	1.74±0.09	
G31.4122+0.3071	0.57	-0.33	98.33	1.19±0.04	1.97±0.09	
G31.4122+0.3071	0.70	-0.52	98.51	2.21±0.04	2.63±0.09	
G31.4122+0.3071	0.75	-0.58	98.69	3.18±0.04	3.43±0.07	
G31.4122+0.3071	0.63	-0.30	98.87	2.08±0.05	3.00±0.11	
G31.4122+0.3071	0.47	0.03	99.05	2.00±0.04	2.88±0.09	
G31.4122+0.3071	0.52	-0.12	99.23	1.49±0.04	2.32±0.09	
G31.4122+0.3071	0.67	-0.45	99.41	1.02±0.03	1.33±0.07	
G31.4122+0.3071	0.73	-0.61	99.59	0.97±0.03	1.11±0.05	
G31.4122+0.3071	0.78	-0.64	99.77	1.01±0.02	1.11±0.04	
G31.4122+0.3071	0.88	-0.73	99.95	0.90±0.03	0.99±0.05	
G31.4122+0.3071	0.82	-0.75	100.13	0.27±0.02	0.34±0.05	
G31.4122+0.3071	0.91	-0.55	100.85	0.13±0.02	0.30±0.07	
G31.4122+0.3071	0.89	-0.62	101.03	0.22±0.02	0.26±0.04	
G31.4122+0.3071	0.65	-0.05	102.47	0.74±0.02	0.90±0.04	
G31.4122+0.3071	0.54	0.03	102.65	1.23±0.03	1.38±0.05	
G31.4122+0.3071	0.53	0.07	102.83	1.99±0.04	2.18±0.07	
G31.4122+0.3071	0.52	0.07	103.01	3.15±0.04	3.31±0.07	
G31.4122+0.3071	0.50	0.09	103.19	5.75±0.05	5.96±0.09	
G31.4122+0.3071	0.51	0.07	103.37	8.29±0.07	8.70±0.13	
G31.4122+0.3071	0.50	0.08	103.55	10.22±0.07	10.65±0.12	
G31.4122+0.3071	0.50	0.09	103.73	4.80±0.06	4.86±0.10	
G31.4122+0.3071	0.51	0.09	103.91	3.55±0.04	3.59±0.08	
G31.4122+0.3071	0.51	0.10	104.09	3.18±0.04	3.30±0.07	
G31.4122+0.3071	0.51	0.10	104.27	2.17±0.03	2.18±0.05	
G31.4122+0.3071	0.50	0.10	104.45	0.90±0.02	0.91±0.04	
G31.4122+0.3071	0.56	0.11	104.63	0.35±0.02	0.41±0.04	
G31.4122+0.3071	0.55	0.03	104.81	0.18±0.02	0.22±0.04	
G31.4122+0.3071	0.61	0.11	104.99	0.22±0.02	0.31±0.05	
G31.4122+0.3071	0.45	0.04	105.17	0.37±0.02	0.50±0.05	
G31.4122+0.3071	0.48	0.08	105.35	0.45±0.03	0.57±0.05	
G31.4122+0.3071	0.53	0.09	105.53	0.33±0.02	0.35±0.04	
G31.4122+0.3071	0.75	0.25	105.71	0.11±0.02	0.33±0.09	

Continuation
of Table C.1

Name	$\alpha/\Delta\alpha$ h:m:s/″	$\delta/\Delta\delta$ d:m:s/″	V_{LSR} km s^{-1}	$S_{v,\,\mathrm{Peak}}$ Jy beam^{-1}	$S_{v,\,\mathrm{Int}}$ Jy	Notes
(1)	(2)	(3)	(4)	(5)	(6)	(7)
G31.5811+0.0769	18:48:41.9463	-1:10:02.553	98.82	7.79±0.03	8.24±0.05	MMB
G31.5811+0.0769	0.01	-0.11	91.44	0.18±0.02	0.29±0.05	
G31.5811+0.0769	0.01	-0.06	91.62	0.39±0.02	0.50±0.05	
G31.5811+0.0769	-0.09	-0.09	94.32	0.20±0.02	0.29±0.05	
G31.5811+0.0769	-0.08	0.27	94.50	0.09±0.02	0.33±0.08	
G31.5811+0.0769	-0.10	-0.12	95.22	0.36±0.02	0.44±0.04	
G31.5811+0.0769	-0.12	-0.09	95.40	2.04±0.03	2.16±0.05	
G31.5811+0.0769	-0.11	-0.08	95.58	5.55±0.03	5.67±0.05	
G31.5811+0.0769	-0.19	-0.08	95.76	0.62±0.02	0.79±0.05	
G31.5811+0.0769	-0.15	-0.07	97.56	0.69±0.02	0.73±0.03	
G31.5811+0.0769	-0.18	-0.06	97.74	0.96±0.02	1.04±0.04	
G31.5811+0.0769	-0.10	-0.12	97.92	1.44±0.02	1.49±0.04	
G31.5811+0.0769	-0.08	-0.04	98.10	1.67±0.02	1.72±0.04	
G31.5811+0.0769	-0.07	-0.05	98.28	1.46±0.02	1.54±0.04	
G31.5811+0.0769	-0.08	-0.04	98.46	1.73±0.03	1.81±0.05	
G31.5811+0.0769	-0.04	-0.01	98.64	3.85±0.03	4.04±0.05	
G31.5811+0.0769	0.02	0.00	99.00	5.18±0.03	5.52±0.06	
G31.5811+0.0769	0.03	-0.01	99.18	3.43±0.03	3.58±0.05	
G31.5811+0.0769	0.04	-0.03	99.36	3.03±0.02	3.15±0.04	
G31.5811+0.0769	0.02	-0.03	99.54	3.76±0.03	3.92±0.05	
G31.5811+0.0769	0.04	-0.03	99.72	2.52±0.03	2.62±0.05	
G31.5811+0.0769	0.08	-0.01	99.90	0.49±0.02	0.63±0.05	
G31.5937–0.1920	18:49:40.8926	-1:16:43.117	48.25	4.54±0.02	4.68±0.04	MMB
G31.5937–0.1920	-0.00	-0.05	46.63	0.23±0.02	0.29±0.04	
G31.5937–0.1920	-0.03	0.01	46.81	0.33±0.02	0.34±0.03	
G31.5937–0.1920	-0.01	0.05	46.99	0.69±0.01	0.71±0.03	
G31.5937–0.1920	0.01	0.04	47.17	0.68±0.01	0.66±0.02	
G31.5937–0.1920	0.02	-0.14	47.35	0.09±0.01	0.08±0.02	
G31.5937–0.1920	-0.02	-0.04	48.07	0.50±0.02	0.49±0.03	
G31.5937–0.1920	-0.03	-0.01	48.43	1.53±0.02	1.54±0.03	
G31.0470+0.3562	18:46:43.8523	-1:30:54.268	82.73	6.46±0.03	6.70±0.06	MMB
G31.0470+0.3562	-0.05	-0.02	77.87	0.07±0.02	0.19±0.06	
G31.0470+0.3562	0.14	-0.03	78.05	0.19±0.02	0.23±0.03	
G31.0470+0.3562	0.12	0.02	78.23	0.26±0.01	0.21±0.02	
G31.0470+0.3562	-0.13	-0.09	78.41	0.12±0.02	0.20±0.04	
G31.0470+0.3562	0.01	0.03	78.59	0.20±0.02	0.24±0.03	
G31.0470+0.3562	0.06	-0.01	78.77	0.61±0.02	0.60±0.03	
G31.0470+0.3562	0.04	0.02	78.95	1.50±0.02	1.52±0.04	
G31.0470+0.3562	0.06	0.02	79.13	1.96±0.02	1.99±0.04	
G31.0470+0.3562	0.07	0.01	79.31	1.34±0.02	1.28±0.03	
G31.0470+0.3562	0.05	0.02	79.49	1.19±0.02	1.20±0.03	
G31.0470+0.3562	0.04	0.02	79.67	1.06±0.02	1.08±0.04	
G31.0470+0.3562	0.05	0.02	79.85	1.62±0.02	1.61±0.04	
G31.0470+0.3562	0.05	-0.00	80.03	3.46±0.02	3.52±0.04	

Continuation
of Table C.1

Name	$\alpha/\Delta\alpha$ h:m:s/″	$\delta/\Delta\delta$ d:m:s/″	V_{LSR} km s^{-1}	$S_{v,\,Peak}$ Jy beam^{-1}	$S_{v,\,Int}$ Jy	Notes
(1)	(2)	(3)	(4)	(5)	(6)	(7)
G31.0470+0.3562	0.05	0.02	80.21	4.04±0.03	4.16±0.05	
G31.0470+0.3562	0.04	0.01	80.39	2.81±0.03	2.88±0.05	
G31.0470+0.3562	0.05	0.00	80.57	3.85±0.03	3.94±0.06	
G31.0470+0.3562	0.05	0.00	80.75	3.05±0.03	3.06±0.05	
G31.0470+0.3562	0.03	0.00	80.93	3.88±0.03	3.97±0.05	
G31.0470+0.3562	0.04	-0.01	81.11	2.16±0.03	2.20±0.04	
G31.0470+0.3562	0.05	-0.01	81.29	1.13±0.02	1.16±0.03	
G31.0470+0.3562	0.04	-0.02	81.47	0.33±0.02	0.33±0.03	
G31.0470+0.3562	-0.11	0.04	81.65	0.41±0.02	0.46±0.03	
G31.0470+0.3562	-0.06	-0.17	81.83	0.19±0.02	0.26±0.03	
G31.0470+0.3562	-0.09	-0.48	82.01	0.06±0.02	0.12±0.05	
G31.0470+0.3562	0.01	0.07	82.37	0.29±0.02	0.35±0.04	
G31.0470+0.3562	-0.00	0.01	82.55	1.07±0.02	1.03±0.03	
G31.0470+0.3562	0.02	0.02	82.91	0.56±0.02	0.50±0.03	
G31.0470+0.3562	-0.00	-0.12	84.53	0.08±0.02	0.11±0.03	
G31.0470+0.3562	-0.03	0.05	85.25	0.14±0.02	0.27±0.05	
G31.0470+0.3562	0.09	0.01	85.43	0.21±0.02	0.22±0.03	
G31.0470+0.3562	0.70	-0.19	85.61	0.04±0.01	0.35±0.12	
G31.0592+0.0933	18:47:41.3368	-1:37:26.433	16.51	17.43±0.08	17.94±0.14	MMB
G31.0592+0.0933	-0.01	0.01	15.25	0.66±0.02	0.68±0.04	
G31.0592+0.0933	-0.04	0.01	15.43	0.88±0.03	0.87±0.05	
G31.0592+0.0933	-0.00	0.03	15.61	2.97±0.04	3.08±0.07	
G31.0592+0.0933	-0.02	0.02	15.79	8.34±0.05	8.55±0.09	
G31.0592+0.0933	-0.01	0.01	15.97	4.44±0.04	4.51±0.07	
G31.0592+0.0933	-0.00	0.01	16.33	7.43±0.06	7.62±0.10	
G31.0592+0.0933	0.00	-0.00	16.69	7.35±0.05	7.53±0.09	
G31.0592+0.0933	0.00	-0.02	16.87	2.12±0.03	2.18±0.06	
G31.0592+0.0933	-0.03	-0.04	17.23	0.21±0.03	0.38±0.07	
G31.0592+0.0933	-0.05	0.00	17.59	0.40±0.02	0.49±0.04	
G31.0592+0.0933	0.07	-0.04	17.95	0.22±0.02	0.24±0.04	
G31.0592+0.0933	-0.09	-0.16	18.31	0.10±0.02	0.14±0.04	
G31.0592+0.0933	0.06	0.08	18.49	0.35±0.02	0.51±0.04	
G31.0592+0.0933	0.05	-0.00	18.67	1.09±0.02	1.12±0.04	
G31.0592+0.0933	0.10	-0.13	18.85	0.24±0.02	0.21±0.04	
G31.0592+0.0933	-0.08	-0.23	19.39	0.11±0.02	0.50±0.10	
G31.0592+0.0933	0.05	0.00	19.57	0.59±0.02	0.71±0.04	
G31.0592+0.0933	0.08	0.00	19.75	1.45±0.03	1.44±0.05	
G31.0592+0.0933	0.07	0.00	19.93	1.22±0.02	1.23±0.04	
G31.0592+0.0933	0.08	0.01	20.11	0.91±0.02	1.00±0.03	
G31.0767+0.4573	18:46:25.4349	-1:26:33.508	25.68	1.97±0.03	1.99±0.05	MMB
G31.0767+0.4573	0.15	0.17	25.14	0.12±0.02	0.26±0.05	
G31.0767+0.4573	0.02	-0.03	25.32	1.22±0.02	1.30±0.04	
G31.0767+0.4573	0.01	-0.01	25.50	1.65±0.02	1.68±0.04	
G31.0767+0.4573	-0.03	-0.02	25.86	1.61±0.03	1.70±0.05	

Continuation
of Table C.1

Name	$\alpha/\Delta\alpha$ h:m:s/″	$\delta/\Delta\delta$ d:m:s/″	V_{LSR} km s^{-1}	$S_{v,\,Peak}$ Jy beam^{-1}	$S_{v,\,Int}$ Jy	Notes
(1)	(2)	(3)	(4)	(5)	(6)	(7)
G31.0767+0.4573	-0.31	0.57	26.04	0.06±0.01	0.40±0.11	
G31.0767+0.4573	0.06	0.31	26.22	0.16±0.02	0.27±0.04	
G31.0767+0.4573	-0.10	0.22	26.40	0.16±0.02	0.20±0.03	
G31.0767+0.4573	0.04	0.05	26.58	0.36±0.02	0.46±0.04	
G31.0767+0.4573	0.02	0.04	26.76	0.59±0.02	0.68±0.04	
G31.0767+0.4573	0.16	0.67	26.94	0.03±0.01	0.37±0.15	
G31.1213+0.0628	18:47:54.6711	-1:34:57.096	48.07	2.08±0.03	2.17±0.06	MMB
G31.1213+0.0628	0.01	0.29	34.21	0.16±0.01	0.16±0.02	
G31.1213+0.0628	-0.13	0.24	34.39	0.42±0.01	0.41±0.02	
G31.1213+0.0628	-0.03	0.22	34.57	0.19±0.02	0.20±0.03	
G31.1213+0.0628	-0.06	0.33	34.75	0.19±0.02	0.25±0.04	
G31.1213+0.0628	0.04	0.21	34.93	0.29±0.02	0.41±0.05	
G31.1213+0.0628	-0.07	0.28	35.29	0.22±0.02	0.28±0.04	
G31.1213+0.0628	-0.05	0.27	35.47	0.21±0.02	0.19±0.02	
G31.1213+0.0628	-0.06	0.34	35.65	0.24±0.02	0.23±0.03	
G31.1213+0.0628	-0.21	0.18	36.19	0.08±0.01	0.23±0.06	
G31.1213+0.0628	-0.07	0.01	36.91	0.18±0.02	0.49±0.08	
G31.1213+0.0628	-0.14	0.27	37.09	0.19±0.01	0.16±0.02	
G31.1213+0.0628	-0.38	-0.52	37.27	0.06±0.01	0.19±0.05	
G31.1213+0.0628	0.01	0.44	37.45	0.16±0.02	0.21±0.04	
G31.1213+0.0628	0.20	-0.37	45.73	0.05±0.01	0.23±0.07	
G31.1213+0.0628	0.02	0.27	45.91	0.13±0.02	0.19±0.04	
G31.1213+0.0628	0.01	0.03	47.35	0.30±0.02	0.36±0.03	
G31.1213+0.0628	-0.00	-0.02	47.53	0.30±0.02	0.35±0.03	
G31.1213+0.0628	0.02	-0.00	47.89	1.21±0.02	1.25±0.04	
G31.1580+0.0457	18:48:02.3286	-1:33:27.219	40.96	2.25±0.03	2.26±0.06	MMB
G31.1580+0.0457	-0.01	-0.08	37.72	0.20±0.02	0.25±0.03	
G31.1580+0.0457	0.15	0.12	37.90	0.15±0.02	0.19±0.04	
G31.1580+0.0457	-0.03	0.05	40.42	0.34±0.02	0.33±0.04	
G31.1580+0.0457	0.02	-0.00	40.60	0.98±0.03	1.07±0.05	
G31.1580+0.0457	0.02	0.01	40.78	1.61±0.03	1.63±0.05	
G31.1580+0.0457	0.00	0.01	41.14	2.24±0.03	2.23±0.06	
G31.1580+0.0457	0.02	-0.01	41.32	1.48±0.03	1.60±0.05	
G31.1580+0.0457	0.00	-0.01	41.50	0.68±0.02	0.76±0.04	
G31.1580+0.0457	0.02	0.30	41.86	0.07±0.02	0.26±0.09	
G31.1580+0.0457	0.00	0.24	42.58	0.09±0.01	0.06±0.02	
G31.1580+0.0457	-0.07	-0.10	42.76	0.14±0.02	0.13±0.03	
G31.1580+0.0457	0.01	-0.17	42.94	0.19±0.02	0.17±0.03	
G31.1580+0.0457	-0.07	-0.19	43.12	0.06±0.02	0.07±0.03	
G31.1580+0.0457	0.06	0.06	43.30	0.20±0.02	0.28±0.04	
G31.1580+0.0457	0.02	0.08	43.48	0.36±0.02	0.46±0.04	
G31.1824–0.1477	18:48:46.4100	-1:37:28.112	46.31	2.00±0.04	2.12±0.06	MMB
G31.1824–0.1477	-0.46	-0.80	38.39	0.07±0.01	0.33±0.07	
G31.1824–0.1477	0.02	0.06	43.25	0.43±0.02	0.45±0.03	

Continuation
of Table C.1

Name	$\alpha/\Delta\alpha$ h:m:s/″	$\delta/\Delta\delta$ d:m:s/″	V_{LSR} km s^{-1}	$S_{v,\,Peak}$ Jy beam^{-1}	$S_{v,\,Int}$ Jy	Notes
(1)	(2)	(3)	(4)	(5)	(6)	(7)
G31.1824–0.1477	-0.03	-0.00	43.43	0.77±0.02	0.78±0.04	
G31.1824–0.1477	-0.02	-0.01	43.61	1.58±0.03	1.68±0.05	
G31.1824–0.1477	-0.08	-0.11	43.79	0.36±0.02	0.37±0.04	
G31.1824–0.1477	-0.05	-0.03	44.15	0.85±0.02	0.95±0.03	
G31.1824–0.1477	-0.04	-0.05	44.33	0.34±0.01	0.37±0.03	
G31.1824–0.1477	-0.10	0.02	44.51	0.21±0.02	0.27±0.03	
G31.1824–0.1477	-0.03	-0.05	44.69	1.10±0.03	1.23±0.05	
G31.1824–0.1477	-0.06	0.00	44.87	0.76±0.02	0.80±0.04	
G31.1824–0.1477	-0.00	-0.16	45.05	0.28±0.02	0.34±0.04	
G31.1824–0.1477	-0.06	-0.08	45.23	0.20±0.02	0.30±0.04	
G31.1824–0.1477	-0.03	-0.00	45.41	0.53±0.02	0.64±0.04	
G31.1824–0.1477	-0.03	-0.04	45.59	1.06±0.02	1.14±0.05	
G31.1824–0.1477	-0.04	-0.02	45.77	1.38±0.03	1.47±0.06	
G31.1824–0.1477	-0.03	-0.05	45.95	1.03±0.03	1.06±0.05	
G31.1824–0.1477	-0.03	0.01	46.13	1.83±0.04	1.90±0.06	
G31.1824–0.1477	0.01	0.02	46.49	0.98±0.03	1.06±0.05	
G31.1824–0.1477	0.01	-0.14	46.67	0.03±0.01	0.36±0.16	
G31.1824–0.1477	-0.16	-0.26	48.65	0.14±0.02	0.20±0.04	
G31.1824–0.1477	0.07	-0.10	48.83	0.36±0.02	0.46±0.05	
G31.1824–0.1477	0.02	-0.10	49.01	0.79±0.02	0.80±0.03	
G31.1824–0.1477	0.06	-0.09	49.19	0.51±0.02	0.58±0.03	
G31.1824–0.1477	0.00	-0.09	51.35	0.10±0.02	0.21±0.05	
G31.1824–0.1477	-0.02	-0.13	51.53	0.26±0.02	0.36±0.04	
G31.1824–0.1477	-0.20	-0.72	51.71	0.06±0.01	0.15±0.04	
G31.2527+0.0025	18:48:21.9201	-1:29:36.239	41.14	0.22±0.02	0.26±0.04	YAN19
G31.2527+0.0025	-0.04	0.17	40.96	0.15±0.02	0.19±0.04	
G31.2527+0.0025	-0.06	0.05	41.32	0.17±0.02	0.21±0.04	
G31.2527+0.0025	-0.06	0.22	41.50	0.13±0.02	0.17±0.04	
G31.2756+0.0053	18:48:23.8758	-1:28:18.567	37.46	0.38±0.02	0.41±0.04	NEW
G31.2756+0.0053	0.05	-0.07	37.10	0.16±0.02	0.19±0.03	
G31.2756+0.0053	0.07	0.05	37.28	0.36±0.02	0.36±0.03	
G31.2756+0.0053	0.10	-0.03	37.64	0.11±0.02	0.11±0.03	
G31.2805+0.0617	18:48:12.3794	-1:26:30.659	110.29	62.38±0.27	67.23±0.49	MMB
G31.2805+0.0617	0.11	0.13	102.19	0.21±0.03	0.73±0.14	
G31.2805+0.0617	0.04	0.18	102.37	0.77±0.05	1.16±0.12	
G31.2805+0.0617	0.04	0.15	102.55	1.15±0.05	1.46±0.10	
G31.2805+0.0617	0.03	0.19	102.73	0.98±0.04	1.23±0.09	
G31.2805+0.0617	0.02	0.23	102.91	1.79±0.05	2.05±0.09	
G31.2805+0.0617	0.01	0.23	103.09	2.34±0.05	2.56±0.10	
G31.2805+0.0617	0.03	0.19	103.27	1.64±0.06	1.97±0.12	
G31.2805+0.0617	0.05	0.13	103.45	1.06±0.06	1.46±0.13	
G31.2805+0.0617	0.05	0.12	103.63	0.74±0.06	1.20±0.13	
G31.2805+0.0617	0.04	0.11	103.81	0.64±0.04	0.95±0.10	
G31.2805+0.0617	0.10	0.09	103.99	0.45±0.04	0.75±0.11	

Continuation
of Table C.1

Name	$\alpha/\Delta\alpha$ h:m:s/″	$\delta/\Delta\delta$ d:m:s/″	V_{LSR} km s^{-1}	$S_{v,\,Peak}$ Jy beam^{-1}	$S_{v,\,Int}$ Jy	Notes
(1)	(2)	(3)	(4)	(5)	(6)	(7)
G31.2805+0.0617	0.04	0.15	104.17	3.02±0.06	3.21±0.10	
G31.2805+0.0617	0.04	0.20	104.35	6.73±0.07	7.01±0.13	
G31.2805+0.0617	0.03	0.20	104.53	3.31±0.06	3.47±0.11	
G31.2805+0.0617	0.08	0.10	104.71	1.41±0.05	1.68±0.10	
G31.2805+0.0617	0.06	0.10	104.89	2.00±0.06	2.17±0.10	
G31.2805+0.0617	0.08	-0.00	105.07	7.97±0.09	8.38±0.17	
G31.2805+0.0617	0.08	-0.00	105.25	10.93±0.12	11.44±0.21	
G31.2805+0.0617	0.11	0.03	105.43	10.04±0.12	10.55±0.22	
G31.2805+0.0617	0.11	0.01	105.61	11.71±0.14	12.50±0.25	
G31.2805+0.0617	0.10	-0.06	105.79	15.07±0.15	15.54±0.27	
G31.2805+0.0617	0.11	-0.08	105.97	14.97±0.15	15.40±0.26	
G31.2805+0.0617	0.11	-0.07	106.15	7.82±0.10	8.04±0.17	
G31.2805+0.0617	0.10	-0.08	106.33	6.64±0.08	6.91±0.15	
G31.2805+0.0617	0.10	-0.07	106.51	5.34±0.07	5.59±0.13	
G31.2805+0.0617	0.11	0.00	106.69	5.08±0.07	5.43±0.13	
G31.2805+0.0617	0.17	0.09	106.87	6.09±0.10	6.66±0.18	
G31.2805+0.0617	0.24	0.24	107.05	19.95±0.17	21.06±0.31	
G31.2805+0.0617	0.27	0.27	107.23	24.17±0.18	24.97±0.32	
G31.2805+0.0617	0.15	0.04	107.41	10.60±0.13	11.27±0.23	
G31.2805+0.0617	0.09	-0.05	107.59	5.97±0.08	6.29±0.15	
G31.2805+0.0617	-0.11	-0.11	107.77	3.50±0.06	4.07±0.12	
G31.2805+0.0617	-0.13	-0.08	107.95	2.79±0.06	3.32±0.12	
G31.2805+0.0617	-0.02	-0.04	108.13	1.31±0.06	1.64±0.12	
G31.2805+0.0617	-0.01	0.03	108.31	3.13±0.06	3.48±0.12	
G31.2805+0.0617	-0.16	-0.07	108.49	5.67±0.08	6.46±0.15	
G31.2805+0.0617	-0.12	-0.08	108.67	7.66±0.10	8.93±0.19	
G31.2805+0.0617	0.08	0.05	108.85	4.81±0.09	5.67±0.16	
G31.2805+0.0617	-0.03	0.02	109.03	2.95±0.07	3.72±0.14	
G31.2805+0.0617	0.03	0.05	109.21	3.93±0.08	4.82±0.16	
G31.2805+0.0617	0.01	0.04	109.39	7.06±0.13	8.89±0.25	
G31.2805+0.0617	-0.06	-0.03	109.57	16.02±0.20	20.82±0.42	
G31.2805+0.0617	-0.10	-0.02	109.75	20.26±0.20	24.01±0.39	
G31.2805+0.0617	0.12	0.01	109.93	12.17±0.19	17.39±0.42	
G31.2805+0.0617	0.07	0.02	110.11	55.10±0.28	67.43±0.55	
G31.2805+0.0617	0.08	-0.04	110.47	37.33±0.21	40.00±0.39	
G31.2805+0.0617	0.05	-0.03	110.65	29.00±0.19	30.61±0.35	
G31.2805+0.0617	0.01	-0.04	110.83	26.03±0.20	28.24±0.36	
G31.2805+0.0617	-0.01	-0.03	111.01	32.36±0.20	35.02±0.37	
G31.2805+0.0617	0.01	-0.03	111.19	22.65±0.18	24.48±0.34	
G31.2805+0.0617	-0.10	-0.04	111.37	18.47±0.17	20.19±0.32	
G31.2805+0.0617	-0.22	-0.06	111.55	22.89±0.18	24.50±0.32	
G31.2805+0.0617	-0.15	-0.03	111.73	16.72±0.16	18.05±0.30	
G31.2805+0.0617	-0.10	0.01	111.91	10.27±0.13	11.09±0.24	
G31.2805+0.0617	-0.19	0.00	112.09	16.80±0.17	17.66±0.31	

Continuation
of Table C.1

Name	$\alpha/\Delta\alpha$ h:m:s/″	$\delta/\Delta\delta$ d:m:s/″	V_{LSR} km s^{-1}	$S_{v,\,Peak}$ Jy beam^{-1}	$S_{v,\,Int}$ Jy	Notes
(1)	(2)	(3)	(4)	(5)	(6)	(7)
G31.2805+0.0617	-0.24	0.02	112.27	26.05±0.19	26.95±0.34	
G31.2805+0.0617	-0.22	0.03	112.45	15.18±0.16	15.71±0.28	
G31.2805+0.0617	-0.21	0.05	112.63	5.57±0.08	5.91±0.14	
G31.2805+0.0617	-0.22	0.07	112.81	3.50±0.06	3.67±0.10	
G31.2805+0.0617	-0.28	0.10	112.99	0.67±0.04	0.89±0.08	
G31.2805+0.0617	-0.28	0.08	113.17	0.38±0.05	0.80±0.14	
G31.2805+0.0617	-0.43	0.13	113.35	0.22±0.03	0.35±0.07	
G31.2805+0.0617	-0.32	0.07	113.53	0.30±0.03	0.60±0.09	
G31.2805+0.0617	-0.44	-0.26	113.71	0.14±0.02	0.16±0.04	
G31.2805+0.0617	-0.35	0.10	113.89	0.19±0.03	0.30±0.06	
G32.8027+0.1926	18:50:30.9803	-0:01:39.020	26.89	0.76±0.02	0.73±0.04	MMB
G32.8027+0.1926	0.10	0.01	25.27	0.07±0.01	0.21±0.06	
G32.8027+0.1926	0.06	-0.23	25.45	0.10±0.02	0.17±0.05	
G32.8027+0.1926	-0.03	0.04	25.63	0.24±0.02	0.26±0.04	
G32.8027+0.1926	-0.03	0.02	25.81	0.27±0.02	0.32±0.03	
G32.8027+0.1926	-0.00	-0.15	25.99	0.23±0.02	0.29±0.04	
G32.8027+0.1926	-0.04	0.09	26.17	0.19±0.02	0.28±0.04	
G32.8027+0.1926	-0.06	-0.15	26.35	0.33±0.02	0.29±0.03	
G32.8027+0.1926	-0.01	0.02	26.53	0.58±0.02	0.60±0.04	
G32.8027+0.1926	-0.01	-0.03	26.71	0.66±0.02	0.75±0.04	
G32.8027+0.1926	-0.01	0.06	27.07	0.53±0.02	0.58±0.04	
G32.8027+0.1926	-0.01	-0.05	27.25	0.53±0.02	0.58±0.04	
G32.8027+0.1926	-0.01	0.04	27.43	0.41±0.02	0.47±0.04	
G32.8027+0.1926	0.15	0.05	27.61	0.25±0.02	0.37±0.04	
G32.8027+0.1926	0.01	0.07	27.79	0.16±0.02	0.26±0.06	
G32.8212–0.3301	18:52:24.6919	-0:14:57.744	82.23	0.90±0.03	1.02±0.05	MMB
G32.8212–0.3301	-0.08	0.04	81.87	0.08±0.02	0.37±0.11	
G32.8212–0.3301	0.09	-0.12	82.05	0.14±0.03	0.32±0.08	
G32.8212–0.3301	-0.00	-0.02	82.41	0.64±0.03	0.63±0.05	
G32.9175–0.0935	18:51:44.6899	-0:03:19.758	103.45	1.22±0.03	1.19±0.05	MMB
G32.9175–0.0935	0.72	-0.44	103.63	0.11±0.02	0.65±0.14	
G32.9645–0.3394	18:52:42.3514	-0:07:33.837	48.38	0.71±0.02	0.78±0.04	MMB
G32.9645–0.3394	0.01	-0.02	47.66	0.55±0.02	0.53±0.03	
G32.9645–0.3394	0.08	-0.00	47.84	0.39±0.02	0.39±0.04	
G32.9645–0.3394	0.04	0.09	48.20	0.46±0.02	0.48±0.03	
G32.9645–0.3394	0.07	0.02	48.56	0.34±0.02	0.47±0.05	
G32.9645–0.3394	0.07	-0.00	48.74	0.43±0.01	0.42±0.02	
G32.9645–0.3394	0.04	0.02	48.92	0.57±0.02	0.55±0.03	
G32.9645–0.3394	0.11	-0.02	49.10	0.22±0.02	0.30±0.04	
G32.9645–0.3394	0.30	0.28	49.28	0.05±0.01	0.29±0.10	
G32.9918+0.0338	18:51:25.5834	00:04:06.919	91.00	8.68±0.04	8.95±0.07	MMB
G32.9918+0.0338	-0.14	-0.20	89.38	0.15±0.02	0.18±0.03	
G32.9918+0.0338	0.03	-0.07	89.56	0.25±0.02	0.26±0.04	
G32.9918+0.0338	-0.02	-0.02	89.74	1.92±0.02	1.88±0.04	

Continuation
of Table C.1

Name	$\alpha/\Delta\alpha$ h:m:s/″	$\delta/\Delta\delta$ d:m:s/″	V_{LSR} km s^{-1}	$S_{v,\,Peak}$ Jy beam^{-1}	$S_{v,\,Int}$ Jy	Notes
(1)	(2)	(3)	(4)	(5)	(6)	(7)
G32.9918+0.0338	-0.02	-0.01	89.92	2.70±0.03	2.66±0.05	
G32.9918+0.0338	-0.01	-0.01	90.10	3.22±0.03	3.26±0.06	
G32.9918+0.0338	-0.03	-0.00	90.28	2.62±0.03	2.71±0.05	
G32.9918+0.0338	-0.02	-0.02	90.46	3.97±0.03	4.05±0.05	
G32.9918+0.0338	-0.03	-0.04	90.64	3.69±0.03	3.69±0.06	
G32.9918+0.0338	-0.00	-0.00	90.82	4.90±0.05	4.94±0.08	
G32.9918+0.0338	-0.00	0.00	91.18	4.15±0.03	4.18±0.05	
G32.9918+0.0338	-0.01	0.01	91.36	4.07±0.03	4.05±0.05	
G32.9918+0.0338	-0.01	0.01	91.54	3.92±0.03	4.00±0.06	
G32.9918+0.0338	-0.02	0.01	91.72	7.00±0.05	7.21±0.08	
G32.9918+0.0338	-0.02	0.01	91.90	8.61±0.04	8.93±0.08	
G32.9918+0.0338	-0.02	0.00	92.08	2.91±0.03	2.93±0.05	
G32.9918+0.0338	-0.02	0.01	92.26	1.07±0.02	1.09±0.04	
G32.9918+0.0338	0.02	0.03	92.44	0.99±0.02	0.99±0.04	
G32.9918+0.0338	0.01	-0.00	92.62	0.67±0.02	0.68±0.04	
G32.9918+0.0338	-0.10	-0.19	92.80	0.06±0.01	0.23±0.06	
G32.9918+0.0338	-0.05	0.07	94.24	0.19±0.02	0.20±0.03	
G32.0446+0.0593	18:49:36.5582	-0:45:45.944	92.62	70.32±0.20	72.43±0.35	MMB
G32.0446+0.0593	0.50	0.24	91.00	0.08±0.02	0.10±0.04	
G32.0446+0.0593	-0.18	-0.32	91.90	0.06±0.02	0.38±0.15	
G32.0446+0.0593	0.01	0.00	92.08	4.05±0.06	4.11±0.11	
G32.0446+0.0593	0.00	0.00	92.26	17.48±0.14	17.95±0.26	
G32.0446+0.0593	0.00	-0.00	92.44	36.20±0.17	37.02±0.31	
G32.0446+0.0593	-0.00	-0.00	92.80	61.44±0.19	62.99±0.35	
G32.0446+0.0593	-0.01	0.00	92.98	16.82±0.12	17.02±0.22	
G32.0446+0.0593	-0.01	0.02	93.16	7.01±0.08	7.17±0.15	
G32.0446+0.0593	0.01	0.02	93.34	5.28±0.07	5.60±0.13	
G32.0446+0.0593	-0.01	0.03	93.52	1.37±0.05	1.57±0.10	
G32.0446+0.0593	0.00	-0.00	93.70	1.74±0.05	1.94±0.09	
G32.0446+0.0593	0.02	-0.00	93.88	1.02±0.05	1.21±0.10	
G32.0446+0.0593	0.03	0.03	94.06	2.96±0.05	3.18±0.09	
G32.0446+0.0593	0.02	-0.02	94.24	1.43±0.05	1.70±0.10	
G32.0446+0.0593	0.01	-0.07	94.42	1.33±0.06	1.78±0.14	
G32.0446+0.0593	0.02	-0.14	94.60	10.08±0.11	11.01±0.21	
G32.0446+0.0593	0.03	-0.07	94.78	13.17±0.12	13.92±0.22	
G32.0446+0.0593	0.04	-0.04	94.96	4.27±0.08	4.72±0.15	
G32.0446+0.0593	0.03	-0.10	95.14	1.92±0.06	2.17±0.11	
G32.0446+0.0593	-0.00	-0.27	95.32	6.44±0.08	6.89±0.14	
G32.0446+0.0593	0.01	-0.18	95.50	8.98±0.08	9.55±0.16	
G32.0446+0.0593	0.04	-0.07	95.68	3.18±0.06	3.54±0.12	
G32.0446+0.0593	0.07	-0.03	95.86	0.76±0.05	1.09±0.11	
G32.0446+0.0593	0.05	0.09	96.04	0.35±0.04	0.74±0.12	
G32.0446+0.0593	0.06	0.06	96.22	0.27±0.03	0.39±0.06	
G32.0446+0.0593	0.09	0.03	96.40	0.49±0.04	0.95±0.13	

Continuation
of Table C.1

Name	$\alpha/\Delta\alpha$ h:m:s/″	$\delta/\Delta\delta$ d:m:s/″	V_{LSR} km s^{-1}	$S_{v,\,Peak}$ Jy beam^{-1}	$S_{v,\,Int}$ Jy	Notes
(1)	(2)	(3)	(4)	(5)	(6)	(7)
G32.0446+0.0593	0.08	-0.03	96.58	0.62±0.04	0.87±0.10	
G32.0446+0.0593	0.12	0.07	96.76	0.73±0.05	1.00±0.10	
G32.0446+0.0593	0.23	0.11	96.94	0.22±0.04	1.03±0.21	
G32.0446+0.0593	0.19	0.17	97.12	0.30±0.04	0.63±0.10	
G32.0446+0.0593	0.18	0.10	97.30	0.16±0.02	0.57±0.10	
G32.0446+0.0593	0.17	0.28	97.48	0.32±0.04	0.54±0.10	
G32.0446+0.0593	0.27	0.41	98.02	4.75±0.08	4.92±0.14	
G32.0446+0.0593	0.28	0.41	98.20	35.01±0.17	36.12±0.31	
G32.0446+0.0593	0.28	0.42	98.38	50.78±0.20	52.47±0.35	
G32.0446+0.0593	0.28	0.42	98.56	34.17±0.17	35.05±0.31	
G32.0446+0.0593	0.28	0.42	98.74	14.30±0.12	14.62±0.21	
G32.0446+0.0593	0.26	0.41	98.92	2.12±0.04	2.22±0.08	
G32.0446+0.0593	0.34	0.47	99.10	0.15±0.03	0.93±0.24	
G32.0446+0.0593	0.24	0.42	99.28	2.75±0.06	3.02±0.10	
G32.0446+0.0593	0.24	0.43	99.46	8.32±0.09	8.75±0.16	
G32.0446+0.0593	0.26	0.43	99.64	6.25±0.07	6.56±0.13	
G32.0446+0.0593	0.27	0.42	99.82	2.02±0.05	2.24±0.09	
G32.0446+0.0593	0.26	0.40	100.00	0.60±0.04	0.70±0.07	
G32.0446+0.0593	0.17	0.44	100.18	0.23±0.03	0.66±0.11	
G32.0446+0.0593	0.24	0.45	100.36	2.01±0.05	2.22±0.09	
G32.0446+0.0593	0.23	0.42	100.54	4.54±0.07	4.64±0.13	
G32.0446+0.0593	0.24	0.43	100.72	22.29±0.15	23.04±0.27	
G32.0446+0.0593	0.25	0.43	100.90	31.58±0.18	32.49±0.31	
G32.0446+0.0593	0.25	0.42	101.08	30.95±0.17	31.82±0.31	
G32.0446+0.0593	0.25	0.42	101.26	20.75±0.14	21.35±0.25	
G32.0446+0.0593	0.27	0.44	101.62	2.50±0.06	2.79±0.11	
G32.0446+0.0593	-0.05	0.28	101.80	0.13±0.02	0.21±0.05	
G32.0446+0.0593	0.11	0.32	101.98	0.23±0.03	0.57±0.09	
G32.0446+0.0593	0.22	0.39	102.16	0.18±0.02	0.29±0.05	
G32.1052–0.0743	18:50:11.6672	-0:46:11.046	49.87	0.61±0.02	0.67±0.04	NEW
G32.1052–0.0743	0.29	0.23	49.51	0.08±0.01	0.08±0.03	
G32.1052–0.0743	-0.00	0.35	49.69	0.09±0.02	0.36±0.08	
G32.1052–0.0743	0.04	-0.02	50.05	0.30±0.02	0.33±0.04	
G32.1052–0.0743	0.15	0.70	50.23	0.06±0.01	0.22±0.06	
G32.1176+0.0906	18:49:37.7520	-0:41:00.197	92.71	11.18±0.08	11.81±0.14	HU16
G32.1176+0.0906	0.10	-0.27	90.37	0.06±0.02	0.20±0.08	
G32.1176+0.0906	0.08	-0.04	90.55	0.40±0.03	0.59±0.07	
G32.1176+0.0906	0.01	0.00	90.73	1.39±0.03	1.50±0.05	
G32.1176+0.0906	0.01	-0.03	90.91	0.51±0.02	0.59±0.04	
G32.1176+0.0906	0.42	-0.77	91.27	0.04±0.01	0.41±0.14	
G32.1176+0.0906	-0.02	0.01	91.63	0.84±0.03	0.94±0.05	
G32.1176+0.0906	-0.03	-0.10	91.81	0.55±0.03	0.64±0.06	
G32.1176+0.0906	-0.02	0.03	91.99	2.18±0.03	2.31±0.05	
G32.1176+0.0906	0.04	0.05	92.17	0.94±0.04	0.98±0.07	

Continuation
of Table C.1

Name	$\alpha/\Delta\alpha$ h:m:s/″	$\delta/\Delta\delta$ d:m:s/″	V_{LSR} km s^{-1}	$S_{v,\,Peak}$ Jy beam^{-1}	$S_{v,\,Int}$ Jy	Notes
(1)	(2)	(3)	(4)	(5)	(6)	(7)
G32.1176+0.0906	-0.30	-0.26	92.35	0.13±0.05	0.64±0.29	
G32.1176+0.0906	-0.00	-0.01	92.89	10.12±0.07	10.55±0.12	
G32.1176+0.0906	-0.02	-0.00	93.25	0.19±0.03	0.12±0.04	
G32.1176+0.0906	-0.01	-0.00	97.57	1.82±0.03	1.83±0.05	
G32.1176+0.0906	-0.03	-0.01	97.75	5.64±0.05	5.86±0.08	
G32.1176+0.0906	-0.03	-0.00	97.93	2.63±0.04	2.75±0.08	
G32.1176+0.0906	-0.04	-0.05	98.11	1.09±0.04	1.19±0.08	
G32.1176+0.0906	-0.29	-0.50	99.19	0.06±0.02	0.15±0.06	
G32.1176+0.0906	0.09	-0.02	99.37	0.15±0.02	0.12±0.03	
G32.1176+0.0906	-0.33	-0.60	99.55	0.09±0.03	0.28±0.12	
G32.1176+0.0906	0.23	-0.25	99.91	0.32±0.03	0.49±0.07	
G32.1176+0.0906	0.49	-0.58	100.09	0.06±0.01	0.62±0.17	
G32.1176+0.0906	0.04	-1.18	102.07	0.04±0.01	0.55±0.18	
G32.1176+0.0906	-0.24	0.18	102.25	0.09±0.02	0.59±0.16	
G32.1176+0.0906	-0.02	-0.04	102.43	0.64±0.04	0.89±0.08	
G32.1176+0.0906	0.02	-0.08	102.61	1.09±0.03	1.18±0.06	
G32.1176+0.0906	0.00	-0.03	102.79	0.96±0.03	1.11±0.07	
G32.1176+0.0906	0.02	-0.08	102.97	0.66±0.02	0.73±0.05	
G32.1176+0.0906	-0.01	-0.06	103.15	0.74±0.03	0.81±0.05	
G32.1176+0.0906	0.04	-0.03	103.33	0.63±0.03	0.68±0.05	
G32.1176+0.0906	-0.01	-0.02	103.51	0.46±0.03	0.68±0.07	
G32.1176+0.0906	0.10	0.03	103.69	0.14±0.02	0.66±0.12	
G32.1176+0.0906	0.00	-0.11	103.87	0.12±0.02	0.29±0.07	
G32.1176+0.0906	-0.06	0.03	104.05	0.15±0.02	0.17±0.04	
G32.5150+0.3229	18:49:31.7355	-0:13:26.191	52.65	1.19±0.04	1.36±0.08	MMB
G32.5150+0.3229	-0.01	-0.01	52.47	0.68±0.03	0.80±0.05	
G32.5150+0.3229	0.05	-0.04	52.83	0.17±0.02	0.19±0.04	
G32.7443–0.0753	18:51:21.8532	-0:12:05.255	38.49	39.90±0.32	40.72±0.56	MMB
G32.7443–0.0753	0.06	-0.06	36.15	0.84±0.02	0.97±0.05	
G32.7443–0.0753	0.06	-0.03	36.33	1.09±0.02	1.19±0.03	
G32.7443–0.0753	0.00	-0.13	36.69	0.16±0.02	0.26±0.04	
G32.7443–0.0753	-0.12	-0.05	37.05	0.33±0.02	0.37±0.03	
G32.7443–0.0753	0.05	-0.01	37.41	2.84±0.05	3.11±0.09	
G32.7443–0.0753	0.08	0.01	37.59	3.31±0.04	3.35±0.08	
G32.7443–0.0753	0.02	0.01	37.77	12.35±0.15	12.54±0.27	
G32.7443–0.0753	0.01	0.00	37.95	31.16±0.28	31.59±0.49	
G32.7443–0.0753	0.01	-0.00	38.13	32.14±0.27	32.83±0.48	
G32.7443–0.0753	0.01	-0.00	38.31	38.58±0.31	39.42±0.54	
G32.7443–0.0753	-0.01	0.00	38.67	26.21±0.23	26.56±0.41	
G32.7443–0.0753	-0.02	0.01	38.85	9.99±0.12	10.06±0.22	
G32.7443–0.0753	-0.09	0.01	39.03	15.56±0.18	15.95±0.31	
G32.7443–0.0753	-0.08	0.01	39.21	11.11±0.14	11.45±0.24	
G32.7440–0.0756	18:51:21.8648	-0:12:06.314	32.01	43.25±0.36	44.74±0.64	G32.7443-0.0753b
G32.7440–0.0756	-0.03	0.34	24.45	0.14±0.01	0.10±0.01	

Continuation
of Table C.1

Name	$\alpha/\Delta\alpha$ h:m:s/″	$\delta/\Delta\delta$ d:m:s/″	V_{LSR} km s^{-1}	$S_{v,\,Peak}$ Jy beam^{-1}	$S_{v,\,Int}$ Jy	Notes
(1)	(2)	(3)	(4)	(5)	(6)	(7)
G32.7440–0.0756	-0.06	0.31	24.63	0.22±0.02	0.27±0.03	
G32.7440–0.0756	-0.11	0.28	24.81	0.31±0.01	0.36±0.03	
G32.7440–0.0756	-0.02	0.22	24.99	0.19±0.02	0.23±0.03	
G32.7440–0.0756	-0.06	0.36	25.17	0.12±0.02	0.16±0.04	
G32.7440–0.0756	-0.05	0.22	25.89	0.10±0.02	0.09±0.03	
G32.7440–0.0756	0.12	0.58	26.43	0.08±0.02	0.28±0.09	
G32.7440–0.0756	0.04	0.07	26.61	0.22±0.02	0.23±0.04	
G32.7440–0.0756	-0.02	0.08	26.79	0.17±0.02	0.11±0.02	
G32.7440–0.0756	0.04	0.14	26.97	0.21±0.01	0.18±0.02	
G32.7440–0.0756	-0.17	0.03	27.15	0.17±0.02	0.23±0.03	
G32.7440–0.0756	-0.12	0.07	27.33	0.28±0.02	0.40±0.05	
G32.7440–0.0756	-0.19	0.10	27.51	0.22±0.02	0.39±0.07	
G32.7440–0.0756	-0.02	0.24	27.69	0.22±0.02	0.25±0.03	
G32.7440–0.0756	-0.12	0.11	27.87	0.18±0.01	0.21±0.03	
G32.7440–0.0756	-0.06	0.04	28.05	0.34±0.02	0.35±0.03	
G32.7440–0.0756	-0.07	0.19	28.23	0.83±0.02	0.95±0.05	
G32.7440–0.0756	-0.05	0.18	28.41	1.22±0.03	1.36±0.06	
G32.7440–0.0756	-0.05	0.15	28.59	0.70±0.03	0.80±0.06	
G32.7440–0.0756	-0.05	0.15	28.77	1.43±0.03	1.60±0.06	
G32.7440–0.0756	-0.06	0.14	28.95	1.42±0.04	1.52±0.08	
G32.7440–0.0756	-0.07	0.13	29.13	2.17±0.04	2.34±0.07	
G32.7440–0.0756	-0.09	0.10	29.31	2.17±0.04	2.30±0.07	
G32.7440–0.0756	-0.08	0.08	29.49	2.00±0.04	2.05±0.07	
G32.7440–0.0756	-0.05	0.12	29.67	2.59±0.05	2.81±0.10	
G32.7440–0.0756	-0.06	0.10	29.85	6.64±0.10	6.93±0.17	
G32.7440–0.0756	-0.07	0.10	30.03	12.75±0.15	12.99±0.26	
G32.7440–0.0756	-0.05	0.06	30.21	14.74±0.17	15.25±0.30	
G32.7440–0.0756	-0.01	0.05	30.39	14.82±0.18	15.45±0.33	
G32.7440–0.0756	-0.01	0.10	30.57	10.24±0.13	10.64±0.23	
G32.7440–0.0756	-0.02	0.13	30.75	3.79±0.07	4.07±0.13	
G32.7440–0.0756	0.00	0.11	30.93	1.91±0.04	2.13±0.08	
G32.7440–0.0756	-0.02	0.12	31.11	1.33±0.03	1.55±0.06	
G32.7440–0.0756	-0.05	0.08	31.29	0.46±0.03	0.54±0.05	
G32.7440–0.0756	-0.01	0.01	31.47	3.52±0.06	3.66±0.11	
G32.7440–0.0756	0.02	-0.01	31.65	6.08±0.09	6.41±0.17	
G32.7440–0.0756	-0.01	0.02	31.83	10.31±0.16	10.65±0.28	
G32.7440–0.0756	-0.03	0.02	32.19	19.71±0.20	20.58±0.36	
G32.7440–0.0756	-0.06	0.08	32.37	5.13±0.09	5.24±0.17	
G32.7440–0.0756	-0.03	0.05	32.55	5.74±0.08	6.16±0.14	
G32.7440–0.0756	-0.03	0.07	32.73	2.64±0.08	2.74±0.14	
G32.7440–0.0756	0.01	0.02	32.91	15.94±0.16	16.81±0.28	
G32.7440–0.0756	0.00	0.03	33.09	15.73±0.19	16.41±0.35	
G32.7440–0.0756	-0.01	0.02	33.27	34.66±0.29	36.02±0.52	
G32.7440–0.0756	0.00	0.02	33.45	35.52±0.31	37.06±0.56	

Continuation
of Table C.1

Name	$\alpha/\Delta\alpha$ h:m:s/″	$\delta/\Delta\delta$ d:m:s/″	V_{LSR} km s^{-1}	$S_{v,\,Peak}$ Jy beam^{-1}	$S_{v,\,Int}$ Jy	Notes
(1)	(2)	(3)	(4)	(5)	(6)	(7)
G32.7440–0.0756	0.01	0.01	33.63	15.99±0.19	16.52±0.34	
G32.7440–0.0756	0.01	0.04	33.81	13.79±0.15	14.41±0.27	
G32.7440–0.0756	-0.04	0.04	33.99	4.08±0.08	4.26±0.15	
G32.7440–0.0756	-0.06	0.08	34.17	4.38±0.05	4.65±0.09	
G32.7440–0.0756	-0.04	0.14	34.35	1.61±0.04	1.99±0.08	
G32.7440–0.0756	-0.05	0.12	34.53	1.67±0.03	1.91±0.05	
G32.7440–0.0756	-0.11	0.10	34.71	0.63±0.02	0.76±0.04	
G32.7440–0.0756	-0.10	0.14	34.89	0.43±0.02	0.60±0.04	
G32.7455–0.0760	18:51:22.1089	-0:12:02.093	44.07	0.19±0.02	0.27±0.03	G32.7443-0.0753c
G32.7455–0.0760	0.04	0.12	43.89	0.11±0.02	0.15±0.04	
G32.7455–0.0760	-0.18	-0.09	44.25	0.18±0.02	0.35±0.05	
G32.7455–0.0760	-0.10	-0.19	44.43	0.09±0.02	0.20±0.05	
G32.7455–0.0760	0.21	0.04	45.69	0.13±0.01	0.11±0.02	
G32.7455–0.0760	0.08	-0.01	45.87	0.17±0.01	0.15±0.02	
G32.7455–0.0760	-0.18	0.15	46.05	0.12±0.01	0.12±0.02	
G32.7496–0.0642	18:51:19.9994	-0:11:29.450	34.98	2.54±0.08	2.93±0.15	MMB
G32.7496–0.0642	-0.32	-0.02	34.80	0.26±0.05	0.86±0.19	
G32.7496–0.0642	-0.01	-0.03	35.16	0.95±0.07	1.31±0.15	
G32.7496–0.0642	0.04	-0.05	35.34	0.62±0.06	1.16±0.16	
G32.7496–0.0642	0.02	0.02	35.52	1.23±0.06	1.65±0.13	
G33.6412–0.2276	18:53:32.5640	00:31:39.230	60.30	145.28±0.26	152.78±0.46	MMB
G33.6412–0.2276	0.03	-0.03	56.88	0.37±0.04	0.68±0.10	
G33.6412–0.2276	-0.06	0.03	57.06	0.57±0.04	0.85±0.10	
G33.6412–0.2276	-0.09	-0.19	57.24	0.11±0.02	0.30±0.08	
G33.6412–0.2276	-0.03	-0.05	58.32	1.06±0.04	1.22±0.08	
G33.6412–0.2276	-0.06	0.04	58.50	2.15±0.05	2.41±0.10	
G33.6412–0.2276	-0.05	-0.02	58.68	3.91±0.06	4.09±0.12	
G33.6412–0.2276	-0.06	0.01	58.86	19.00±0.13	19.21±0.23	
G33.6412–0.2276	-0.06	0.01	59.04	22.90±0.15	23.19±0.27	
G33.6412–0.2276	-0.06	0.01	59.22	28.79±0.17	29.26±0.30	
G33.6412–0.2276	-0.06	-0.00	59.40	27.02±0.16	27.54±0.28	
G33.6412–0.2276	-0.07	0.01	59.58	19.84±0.14	20.15±0.26	
G33.6412–0.2276	-0.06	0.00	59.76	24.10±0.15	24.58±0.27	
G33.6412–0.2276	-0.12	0.01	59.94	8.18±0.10	8.18±0.17	
G33.6412–0.2276	-0.01	-0.00	60.12	76.91±0.24	80.10±0.44	
G33.6412–0.2276	-0.02	0.01	60.48	13.47±0.15	13.51±0.26	
G33.6412–0.2276	-0.00	-0.01	60.66	21.30±0.15	21.60±0.27	
G33.6412–0.2276	-0.01	0.00	60.84	44.55±0.18	45.91±0.33	
G33.6412–0.2276	-0.01	0.01	61.02	30.73±0.16	31.45±0.28	
G33.6412–0.2276	0.04	0.08	61.20	3.86±0.07	3.82±0.12	
G33.6412–0.2276	0.03	0.03	61.38	8.81±0.07	9.04±0.12	
G33.6412–0.2276	0.00	0.07	61.56	2.00±0.05	2.04±0.09	
G33.6412–0.2276	0.02	0.01	61.74	6.33±0.06	6.61±0.11	
G33.6412–0.2276	0.04	0.06	61.92	6.24±0.07	6.32±0.13	

Continuation
of Table C.1

Name	$\alpha/\Delta\alpha$ h:m:s/″	$\delta/\Delta\delta$ d:m:s/″	V_{LSR} km s^{-1}	$S_{v,\,Peak}$ Jy beam^{-1}	$S_{v,\,Int}$ Jy	Notes
(1)	(2)	(3)	(4)	(5)	(6)	(7)
G33.6412–0.2276	0.05	0.07	62.10	12.48±0.10	12.77±0.18	
G33.6412–0.2276	0.05	0.07	62.28	12.20±0.11	12.48±0.19	
G33.6412–0.2276	0.01	0.04	62.46	11.15±0.11	11.35±0.19	
G33.6412–0.2276	-0.01	0.01	62.64	16.15±0.11	16.61±0.19	
G33.6412–0.2276	-0.02	-0.00	62.82	6.78±0.09	6.84±0.16	
G33.6412–0.2276	-0.02	0.00	63.00	10.56±0.09	10.77±0.17	
G33.6412–0.2276	0.01	0.05	63.18	14.73±0.10	15.19±0.19	
G33.6412–0.2276	0.02	0.12	63.54	0.29±0.04	0.68±0.12	
G33.7258–0.1202	18:53:18.7831	00:39:04.957	54.09	4.13±0.04	4.22±0.08	MMB
G33.7258–0.1202	0.53	-0.12	52.29	0.05±0.01	0.38±0.12	
G33.7258–0.1202	-0.09	0.15	52.83	0.13±0.02	0.23±0.05	
G33.7258–0.1202	0.01	-0.04	53.01	0.85±0.02	0.94±0.04	
G33.7258–0.1202	0.01	-0.00	53.19	1.60±0.02	1.59±0.04	
G33.7258–0.1202	0.03	-0.00	53.37	2.25±0.02	2.29±0.04	
G33.7258–0.1202	-0.03	-0.08	53.55	0.29±0.02	0.25±0.03	
G33.7258–0.1202	-0.01	-0.03	53.73	0.54±0.02	0.53±0.04	
G33.7258–0.1202	0.01	0.01	53.91	3.06±0.03	3.10±0.06	
G33.7258–0.1202	0.00	-0.00	54.27	1.53±0.02	1.56±0.04	
G33.7258–0.1202	-0.02	0.03	54.45	0.95±0.02	1.00±0.03	
G33.7258–0.1202	0.25	0.45	54.63	0.10±0.02	0.14±0.04	
G33.7258–0.1202	0.17	-0.17	54.99	0.06±0.01	0.07±0.02	
G33.7258–0.1202	-0.03	-0.36	55.17	0.07±0.01	0.14±0.04	
G33.7258–0.1202	-0.30	0.32	55.35	0.04±0.01	0.27±0.09	
G33.7258–0.1202	-0.14	0.09	55.53	0.14±0.02	0.35±0.06	
G33.7258–0.1202	-0.01	0.07	55.71	0.15±0.02	0.16±0.03	
G33.7258–0.1202	0.07	-0.07	55.89	0.07±0.01	0.04±0.01	
G33.7258–0.1202	0.24	-0.05	56.07	0.06±0.02	0.14±0.05	
G33.7258–0.1202	-0.18	-0.33	56.25	0.05±0.01	0.16±0.04	
G33.7258–0.1202	0.44	0.16	60.39	0.11±0.02	0.28±0.07	
G33.7258–0.1202	0.03	0.05	60.57	0.76±0.02	0.86±0.04	
G33.7258–0.1202	0.04	0.08	60.75	0.79±0.02	0.87±0.04	
G33.8520+0.0178	18:53:03.1384	00:49:37.283	63.58	5.59±0.03	5.62±0.06	MMB
G33.8520+0.0178	0.15	0.01	58.36	0.11±0.01	0.11±0.02	
G33.8520+0.0178	-0.03	0.05	60.16	0.23±0.02	0.24±0.03	
G33.8520+0.0178	-0.01	0.06	60.34	0.17±0.02	0.17±0.03	
G33.8520+0.0178	0.03	0.08	60.52	0.41±0.01	0.41±0.02	
G33.8520+0.0178	-0.02	0.01	60.70	1.21±0.02	1.23±0.03	
G33.8520+0.0178	-0.02	0.02	60.88	1.41±0.02	1.45±0.04	
G33.8520+0.0178	-0.04	0.01	61.06	0.76±0.02	0.80±0.03	
G33.8520+0.0178	0.04	-0.00	61.42	0.49±0.02	0.52±0.04	
G33.8520+0.0178	0.01	0.02	61.60	0.48±0.02	0.50±0.03	
G33.8520+0.0178	0.13	0.06	61.96	0.13±0.02	0.14±0.03	
G33.8520+0.0178	0.04	-0.32	62.14	0.12±0.02	0.08±0.02	
G33.8520+0.0178	0.05	-0.02	62.50	0.11±0.02	0.12±0.04	

Continuation
of Table C.1

Name	$\alpha/\Delta\alpha$ h:m:s/″	$\delta/\Delta\delta$ d:m:s/″	V_{LSR} km s^{-1}	$S_{v,\,Peak}$ Jy beam^{-1}	$S_{v,\,Int}$ Jy	Notes
(1)	(2)	(3)	(4)	(5)	(6)	(7)
G33.8520+0.0178	0.11	0.05	62.68	0.30±0.02	0.36±0.03	
G33.8520+0.0178	0.03	0.04	62.86	0.67±0.02	0.67±0.03	
G33.8520+0.0178	-0.00	-0.00	63.04	0.90±0.02	0.91±0.04	
G33.8520+0.0178	-0.00	0.00	63.22	1.72±0.02	1.71±0.04	
G33.8520+0.0178	0.01	0.00	63.40	3.67±0.03	3.72±0.04	
G33.8520+0.0178	-0.01	-0.01	63.76	4.56±0.03	4.66±0.06	
G33.8520+0.0178	0.00	-0.02	63.94	2.81±0.02	2.86±0.04	
G33.8520+0.0178	0.01	-0.06	64.12	1.53±0.02	1.57±0.03	
G33.8520+0.0178	0.00	0.01	64.30	0.58±0.02	0.61±0.03	
G33.8520+0.0178	0.04	-0.08	64.48	0.43±0.02	0.46±0.03	
G33.8520+0.0178	0.05	-0.06	64.66	0.37±0.01	0.37±0.02	
G33.9798–0.0189	18:53:25.0189	00:55:25.911	64.03	2.22±0.02	2.34±0.04	MMB
G33.9798–0.0189	-0.01	0.07	58.99	1.27±0.02	1.31±0.03	
G33.9798–0.0189	-0.06	-0.04	59.17	0.28±0.02	0.23±0.03	
G33.9798–0.0189	0.01	0.02	59.35	1.51±0.02	1.51±0.03	
G33.9798–0.0189	-0.01	0.02	59.53	1.96±0.02	2.01±0.04	
G33.9798–0.0189	0.01	-0.09	59.89	0.31±0.02	0.38±0.04	
G33.9798–0.0189	-0.08	-0.01	60.07	0.36±0.02	0.41±0.04	
G33.9798–0.0189	-0.02	-0.04	60.25	0.35±0.02	0.38±0.04	
G33.9798–0.0189	-0.08	0.03	60.43	0.41±0.02	0.48±0.05	
G33.9798–0.0189	0.01	0.14	60.61	0.38±0.02	0.40±0.04	
G33.9798–0.0189	-0.06	0.01	60.79	0.41±0.02	0.40±0.04	
G33.9798–0.0189	-0.05	-0.05	60.97	0.74±0.02	0.75±0.04	
G33.9798–0.0189	-0.02	0.01	61.15	1.42±0.02	1.43±0.04	
G33.9798–0.0189	-0.03	0.00	61.33	1.56±0.02	1.62±0.04	
G33.9798–0.0189	-0.02	0.02	61.51	0.61±0.02	0.67±0.04	
G33.9798–0.0189	0.05	0.13	61.69	0.27±0.02	0.33±0.04	
G33.9798–0.0189	0.06	0.07	61.87	0.25±0.02	0.30±0.03	
G33.9798–0.0189	0.04	0.06	62.05	0.51±0.02	0.57±0.04	
G33.9798–0.0189	0.03	-0.00	62.23	0.95±0.02	0.89±0.03	
G33.9798–0.0189	0.02	0.03	62.41	0.90±0.02	0.99±0.05	
G33.9798–0.0189	0.02	0.04	62.59	0.67±0.02	0.67±0.04	
G33.9798–0.0189	0.04	0.08	62.77	0.47±0.02	0.47±0.03	
G33.9798–0.0189	0.05	0.09	62.95	0.32±0.02	0.35±0.03	
G33.9798–0.0189	0.09	0.08	63.13	0.25±0.02	0.26±0.03	
G33.9798–0.0189	-0.12	0.23	63.31	0.13±0.02	0.38±0.08	
G33.9798–0.0189	0.04	-0.42	63.49	0.09±0.02	0.13±0.04	
G33.9798–0.0189	-0.04	0.13	63.67	0.27±0.01	0.28±0.03	
G33.9798–0.0189	-0.06	-0.07	63.85	0.23±0.02	0.29±0.03	
G33.9798–0.0189	0.00	0.01	64.21	1.71±0.02	1.80±0.03	
G33.9798–0.0189	0.72	0.46	64.39	0.06±0.02	0.29±0.11	
G33.9798–0.0189	0.04	0.06	64.57	0.51±0.02	0.51±0.03	
G33.9798–0.0189	0.02	0.00	64.93	0.30±0.02	0.32±0.03	
G33.9798–0.0189	-0.01	-0.13	65.11	0.22±0.01	0.30±0.03	

Continuation
of Table C.1

Name	$\alpha/\Delta\alpha$ h:m:s/″	$\delta/\Delta\delta$ d:m:s/″	V_{LSR} km s^{-1}	$S_{v,\,Peak}$ Jy beam^{-1}	$S_{v,\,Int}$ Jy	Notes
(1)	(2)	(3)	(4)	(5)	(6)	(7)
G33.9798–0.0189	-0.02	0.04	65.29	0.77±0.02	0.82±0.03	
G33.9798–0.0189	-0.07	0.01	65.47	0.59±0.01	0.59±0.03	
G33.9798–0.0189	0.02	-0.02	65.65	0.39±0.02	0.40±0.03	
G33.9798–0.0189	-0.14	0.17	65.83	0.11±0.02	0.29±0.06	
G33.0925–0.0725	18:51:59.4049	00:06:34.087	104.22	11.39±0.13	11.61±0.22	MMB
G33.0925–0.0725	0.00	0.16	94.32	0.16±0.02	0.27±0.05	
G33.0925–0.0725	-0.03	0.01	94.50	0.73±0.02	0.80±0.05	
G33.0925–0.0725	-0.02	-0.07	94.68	0.45±0.02	0.46±0.04	
G33.0925–0.0725	-0.01	-0.07	94.86	0.79±0.02	0.81±0.04	
G33.0925–0.0725	0.02	-0.05	95.04	1.04±0.02	1.09±0.04	
G33.0925–0.0725	-0.04	-0.05	95.22	0.82±0.02	0.85±0.04	
G33.0925–0.0725	0.06	0.00	95.40	0.54±0.02	0.55±0.04	
G33.0925–0.0725	-0.01	-0.08	95.58	1.32±0.02	1.42±0.05	
G33.0925–0.0725	0.00	0.01	95.76	0.92±0.02	1.01±0.05	
G33.0925–0.0725	-0.03	-0.00	95.94	0.33±0.02	0.37±0.03	
G33.0925–0.0725	0.16	-0.13	96.12	0.13±0.02	0.20±0.04	
G33.0925–0.0725	-0.04	-0.08	96.30	0.12±0.02	0.16±0.04	
G33.0925–0.0725	0.14	0.43	96.48	0.06±0.02	0.29±0.10	
G33.0925–0.0725	-0.00	-0.05	96.66	0.30±0.02	0.39±0.05	
G33.0925–0.0725	-0.01	-0.05	96.84	1.07±0.02	1.11±0.04	
G33.0925–0.0725	-0.02	-0.01	97.02	0.80±0.02	0.85±0.04	
G33.0925–0.0725	-0.02	-0.12	97.20	0.25±0.02	0.26±0.03	
G33.0925–0.0725	0.02	0.00	97.38	0.25±0.02	0.27±0.03	
G33.0925–0.0725	-0.04	0.01	97.56	0.22±0.02	0.23±0.04	
G33.0925–0.0725	-0.01	-0.25	97.74	0.14±0.02	0.13±0.03	
G33.0925–0.0725	0.02	-0.03	97.92	0.22±0.02	0.21±0.04	
G33.0925–0.0725	0.02	-0.01	98.10	0.27±0.02	0.41±0.05	
G33.0925–0.0725	0.03	0.05	98.28	0.27±0.02	0.34±0.05	
G33.0925–0.0725	-0.03	0.04	98.46	0.37±0.02	0.34±0.03	
G33.0925–0.0725	-0.03	-0.10	98.64	0.56±0.02	0.57±0.04	
G33.0925–0.0725	0.01	-0.01	98.82	0.67±0.02	0.72±0.04	
G33.0925–0.0725	0.05	-0.09	99.00	0.29±0.02	0.24±0.03	
G33.0925–0.0725	-0.11	-0.31	99.36	0.06±0.02	0.26±0.08	
G33.0925–0.0725	0.03	-0.15	100.98	0.21±0.02	0.34±0.05	
G33.0925–0.0725	0.01	-0.01	101.16	0.78±0.02	0.84±0.04	
G33.0925–0.0725	0.08	-0.02	101.34	1.18±0.03	1.33±0.05	
G33.0925–0.0725	0.04	0.00	101.52	1.12±0.03	1.14±0.04	
G33.0925–0.0725	0.05	-0.02	101.70	1.80±0.02	1.87±0.04	
G33.0925–0.0725	0.04	-0.06	102.06	8.04±0.08	8.34±0.14	
G33.0925–0.0725	0.03	-0.06	102.24	8.06±0.10	8.24±0.17	
G33.0925–0.0725	0.07	-0.04	102.42	3.91±0.05	3.99±0.09	
G33.0925–0.0725	0.04	-0.05	102.60	5.08±0.06	5.18±0.10	
G33.0925–0.0725	0.06	-0.03	102.78	6.43±0.07	6.59±0.13	
G33.0925–0.0725	0.06	-0.02	102.96	4.51±0.06	4.60±0.10	

Continuation
of Table C.1

Name	$\alpha/\Delta\alpha$ h:m:s/″	$\delta/\Delta\delta$ d:m:s/″	V_{LSR} km s^{-1}	$S_{v,\,Peak}$ Jy beam^{-1}	$S_{v,\,Int}$ Jy	Notes
(1)	(2)	(3)	(4)	(5)	(6)	(7)
G33.0925–0.0725	0.04	-0.09	103.14	0.42±0.02	0.34±0.04	
G33.0925–0.0725	0.02	-0.01	103.32	2.14±0.03	2.13±0.06	
G33.0925–0.0725	-0.00	-0.00	103.50	4.07±0.06	4.10±0.10	
G33.0925–0.0725	0.00	0.00	103.68	7.79±0.09	7.93±0.15	
G33.0925–0.0725	0.01	-0.00	103.86	10.05±0.11	10.27±0.19	
G33.0925–0.0725	0.00	0.00	104.04	11.21±0.12	11.55±0.21	
G33.0925–0.0725	0.00	0.00	104.40	7.85±0.08	7.97±0.15	
G33.0925–0.0725	-0.00	0.01	104.58	1.54±0.03	1.55±0.05	
G33.0925–0.0725	-0.02	0.01	104.76	0.42±0.02	0.45±0.04	
G33.0925–0.0725	-0.00	0.06	104.94	0.41±0.02	0.67±0.05	
G33.0925–0.0725	-0.15	0.04	105.12	0.11±0.02	0.26±0.07	
G33.0925–0.0725	0.08	0.01	105.48	0.32±0.02	0.30±0.03	
G33.0925–0.0725	0.03	0.02	105.66	0.84±0.02	0.85±0.04	
G33.0925–0.0725	0.00	0.01	105.84	0.83±0.03	0.86±0.05	
G33.0925–0.0725	-0.01	0.04	106.02	0.52±0.02	0.49±0.04	
G33.0925–0.0725	0.04	-0.15	106.20	0.16±0.02	0.25±0.05	
G33.1328–0.0916	18:52:07.8248	00:08:12.383	73.20	12.61±0.07	13.21±0.13	MMB
G33.1328–0.0916	0.04	-0.07	70.86	0.24±0.03	0.20±0.04	
G33.1328–0.0916	-0.00	0.01	71.04	0.29±0.02	0.35±0.05	
G33.1328–0.0916	0.03	0.05	71.22	0.44±0.03	0.50±0.06	
G33.1328–0.0916	0.01	-0.01	71.40	0.73±0.02	0.69±0.04	
G33.1328–0.0916	-0.01	0.03	71.58	0.90±0.03	0.91±0.04	
G33.1328–0.0916	0.01	0.03	71.76	0.80±0.03	0.83±0.06	
G33.1328–0.0916	0.04	0.02	71.94	0.61±0.03	0.71±0.05	
G33.1328–0.0916	0.05	-0.03	72.12	0.13±0.02	0.14±0.05	
G33.1328–0.0916	0.02	0.01	72.30	0.16±0.02	0.32±0.06	
G33.1328–0.0916	-0.04	-0.10	72.48	0.29±0.03	0.41±0.06	
G33.1328–0.0916	0.01	-0.00	72.66	1.18±0.03	1.28±0.06	
G33.1328–0.0916	0.01	0.02	72.84	2.82±0.04	2.87±0.08	
G33.1328–0.0916	0.01	0.01	73.02	10.16±0.06	10.51±0.10	
G33.1328–0.0916	-0.03	-0.08	73.38	6.11±0.06	6.50±0.11	
G33.1328–0.0916	-0.01	-0.01	73.56	5.97±0.05	6.30±0.08	
G33.1328–0.0916	-0.02	-0.07	73.74	8.97±0.08	9.24±0.14	
G33.1328–0.0916	-0.01	-0.07	73.92	5.72±0.04	5.85±0.07	
G33.1328–0.0916	0.09	0.06	74.10	1.28±0.03	1.23±0.05	
G33.1328–0.0916	-0.03	-0.08	74.28	8.46±0.06	8.81±0.11	
G33.1328–0.0916	-0.00	-0.07	74.46	3.67±0.04	3.82±0.06	
G33.1328–0.0916	-0.07	0.08	74.64	0.22±0.03	0.25±0.05	
G33.1328–0.0916	-0.20	0.12	74.82	0.13±0.02	0.26±0.06	
G33.1328–0.0916	-0.19	-0.13	79.68	0.14±0.02	0.23±0.06	
G33.1328–0.0916	-0.28	-0.38	79.86	0.14±0.03	0.21±0.07	
G33.1328–0.0916	-0.30	-0.36	80.04	1.11±0.03	1.13±0.05	
G33.1328–0.0916	-0.08	0.05	80.22	0.32±0.03	0.34±0.05	
G33.1328–0.0916	-0.07	0.11	80.40	0.72±0.02	0.70±0.04	

Continuation
of Table C.1

Name	$\alpha/\Delta\alpha$ h:m:s/″	$\delta/\Delta\delta$ d:m:s/″	V_{LSR} km s^{-1}	$S_{v,\,Peak}$ Jy beam^{-1}	$S_{v,\,Int}$ Jy	Notes
(1)	(2)	(3)	(4)	(5)	(6)	(7)
G33.1328–0.0916	-0.09	0.05	80.58	1.24±0.03	1.23±0.05	
G33.1328–0.0916	0.11	0.23	80.76	0.21±0.03	0.34±0.08	
G33.1328–0.0916	0.32	-0.02	80.94	0.14±0.02	0.41±0.09	
G33.1999+0.0011	18:51:55.3543	00:14:20.187	91.36	0.32±0.02	0.36±0.03	NEW
G33.1999+0.0011	-0.07	-0.10	91.18	0.19±0.02	0.15±0.02	
G33.1999+0.0011	0.10	-0.01	91.54	0.14±0.02	0.28±0.05	
G33.1999+0.0011	0.06	-0.13	91.72	0.16±0.02	0.19±0.03	
G33.1999+0.0011	-0.05	-0.32	91.90	0.09±0.02	0.13±0.04	
G33.1999+0.0011	0.17	-0.07	92.62	0.05±0.01	0.19±0.06	
G33.1999+0.0011	0.22	-0.15	93.52	0.09±0.02	0.34±0.09	
G33.1999+0.0011	0.05	-0.39	93.70	0.04±0.01	0.26±0.11	
G33.2037–0.0101	18:51:58.1213	00:14:14.370	92.08	1.11±0.02	1.11±0.04	NEW
G33.2037–0.0101	-0.01	-0.05	91.90	0.81±0.02	0.82±0.03	
G33.2037–0.0101	-0.00	-0.03	92.26	0.91±0.02	0.84±0.03	
G33.2037–0.0101	-0.01	-0.02	92.44	0.82±0.02	0.84±0.04	
G33.2037–0.0101	-0.01	-0.06	92.62	0.23±0.01	0.21±0.02	
G33.2037–0.0101	0.22	-0.16	92.80	0.04±0.01	0.19±0.08	
G33.2037–0.0101	0.08	-0.04	94.96	0.18±0.02	0.24±0.04	
G33.2037–0.0101	-0.08	0.05	95.14	0.10±0.02	0.11±0.03	
G33.2037–0.0101	0.07	-0.07	97.66	0.14±0.02	0.11±0.03	
G33.2037–0.0101	-0.04	-0.02	97.84	0.14±0.01	0.09±0.02	
G33.2037–0.0101	0.86	-0.73	98.02	0.04±0.01	0.24±0.09	
G33.2037–0.0101	0.04	0.04	108.28	0.34±0.02	0.34±0.04	
G33.2037–0.0101	-0.01	-0.02	108.46	0.14±0.02	0.13±0.03	
G33.2037–0.0101	-0.03	-0.01	109.54	0.21±0.02	0.27±0.04	
G33.2037–0.0101	-0.12	-0.13	109.72	0.12±0.02	0.16±0.03	
G33.2037–0.0101	-0.07	-0.11	109.90	0.19±0.01	0.11±0.02	
G33.3174–0.3599	18:53:25.2990	00:10:43.904	29.14	1.01±0.02	1.08±0.03	MMB
G33.3174–0.3599	-0.03	-0.01	27.52	0.42±0.02	0.47±0.03	
G33.3174–0.3599	-0.04	-0.06	27.70	0.47±0.02	0.59±0.04	
G33.3174–0.3599	-0.05	-0.22	28.78	0.13±0.01	0.13±0.02	
G33.3174–0.3599	-0.04	-0.01	29.32	0.88±0.02	0.94±0.04	
G33.3174–0.3599	-0.10	0.03	29.86	0.08±0.02	0.06±0.02	
G33.3174–0.3599	-0.01	-0.00	30.04	0.46±0.02	0.47±0.03	
G33.3174–0.3599	-0.07	-0.06	30.22	0.55±0.02	0.59±0.04	
G33.3174–0.3599	-0.04	-0.49	30.40	0.04±0.02	0.19±0.09	
G33.3174–0.3599	0.03	0.07	31.30	0.16±0.02	0.21±0.03	
G33.3930+0.0097	18:52:14.6420	00:24:52.486	105.12	18.48±0.17	19.23±0.31	MMB
G33.3930+0.0097	-0.04	0.14	96.66	0.10±0.02	0.12±0.04	
G33.3930+0.0097	-0.14	0.17	96.84	0.19±0.03	0.64±0.12	
G33.3930+0.0097	0.00	0.09	97.02	0.74±0.03	0.82±0.05	
G33.3930+0.0097	0.03	0.15	97.20	1.01±0.04	1.11±0.07	
G33.3930+0.0097	0.02	0.12	97.38	4.05±0.07	4.20±0.13	
G33.3930+0.0097	0.03	0.10	97.56	4.80±0.09	4.96±0.15	

Continuation
of Table C.1

Name	$\alpha/\Delta\alpha$ h:m:s/″	$\delta/\Delta\delta$ d:m:s/″	V_{LSR} km s^{-1}	$S_{v,\,Peak}$ Jy beam^{-1}	$S_{v,\,Int}$ Jy	Notes
(1)	(2)	(3)	(4)	(5)	(6)	(7)
G33.3930+0.0097	0.02	0.11	97.74	5.74±0.10	5.87±0.17	
G33.3930+0.0097	0.02	0.11	97.92	7.63±0.10	7.79±0.18	
G33.3930+0.0097	0.02	0.11	98.10	4.86±0.08	4.91±0.15	
G33.3930+0.0097	0.01	0.10	98.28	4.10±0.08	4.23±0.14	
G33.3930+0.0097	0.02	0.11	98.46	5.73±0.09	5.98±0.16	
G33.3930+0.0097	0.01	0.11	98.64	5.85±0.09	6.06±0.15	
G33.3930+0.0097	0.02	0.08	98.82	1.26±0.05	1.31±0.08	
G33.3930+0.0097	0.01	0.14	99.00	1.39±0.03	1.49±0.06	
G33.3930+0.0097	0.00	0.12	99.18	1.39±0.04	1.40±0.07	
G33.3930+0.0097	0.03	0.10	99.36	4.22±0.07	4.32±0.12	
G33.3930+0.0097	0.02	0.11	99.54	4.22±0.07	4.33±0.12	
G33.3930+0.0097	-0.01	0.10	99.72	1.34±0.04	1.42±0.07	
G33.3930+0.0097	-0.13	0.09	99.90	0.14±0.02	0.41±0.09	
G33.3930+0.0097	-0.26	-0.38	100.26	0.05±0.01	0.27±0.07	
G33.3930+0.0097	0.06	0.12	100.44	0.05±0.01	0.20±0.07	
G33.3930+0.0097	0.05	-0.03	100.62	0.68±0.03	0.81±0.06	
G33.3930+0.0097	0.04	-0.03	100.80	1.03±0.03	1.10±0.05	
G33.3930+0.0097	0.04	-0.00	100.98	1.11±0.03	1.26±0.07	
G33.3930+0.0097	0.03	-0.01	101.16	2.03±0.04	2.26±0.08	
G33.3930+0.0097	0.00	-0.02	101.34	0.43±0.03	0.51±0.05	
G33.3930+0.0097	0.04	-0.00	101.52	0.22±0.02	0.31±0.05	
G33.3930+0.0097	-0.25	0.05	101.70	0.09±0.02	0.21±0.06	
G33.3930+0.0097	0.04	-0.00	101.88	0.86±0.03	0.95±0.05	
G33.3930+0.0097	0.01	0.02	102.06	2.11±0.05	2.32±0.09	
G33.3930+0.0097	-0.00	0.07	102.24	2.22±0.05	2.41±0.08	
G33.3930+0.0097	-0.02	0.17	102.42	0.74±0.03	0.88±0.07	
G33.3930+0.0097	-0.24	0.41	102.60	0.11±0.03	0.43±0.12	
G33.3930+0.0097	-0.34	0.35	102.78	0.13±0.02	0.49±0.11	
G33.3930+0.0097	-0.04	0.08	102.96	0.78±0.03	0.87±0.05	
G33.3930+0.0097	-0.04	0.14	103.14	0.73±0.03	0.77±0.05	
G33.3930+0.0097	-0.03	0.06	103.32	0.76±0.03	0.90±0.06	
G33.3930+0.0097	-0.03	0.03	103.50	0.95±0.03	1.01±0.06	
G33.3930+0.0097	-0.03	0.02	103.68	1.73±0.04	1.84±0.07	
G33.3930+0.0097	-0.02	0.02	103.86	3.58±0.06	3.72±0.11	
G33.3930+0.0097	-0.03	0.01	104.04	5.02±0.09	5.21±0.16	
G33.3930+0.0097	-0.02	0.02	104.22	4.83±0.09	4.93±0.16	
G33.3930+0.0097	-0.03	-0.00	104.40	4.26±0.08	4.37±0.14	
G33.3930+0.0097	-0.02	-0.01	104.58	5.51±0.09	5.67±0.16	
G33.3930+0.0097	-0.02	-0.02	104.76	13.73±0.14	14.28±0.25	
G33.3930+0.0097	-0.01	-0.02	104.94	12.42±0.13	12.97±0.23	
G33.3930+0.0097	0.01	0.00	105.30	18.02±0.19	18.99±0.33	
G33.3930+0.0097	0.03	-0.00	105.48	9.33±0.12	9.72±0.22	
G33.3930+0.0097	0.00	0.00	105.66	14.14±0.16	14.87±0.28	
G33.3930+0.0097	-0.00	-0.00	105.84	9.12±0.13	9.45±0.23	

Continuation
of Table C.1

Name	$\alpha/\Delta\alpha$ h:m:s/″	$\delta/\Delta\delta$ d:m:s/″	V_{LSR} km s^{-1}	$S_{v,\,Peak}$ Jy beam^{-1}	$S_{v,\,Int}$ Jy	Notes
(1)	(2)	(3)	(4)	(5)	(6)	(7)
G33.3930+0.0097	-0.01	-0.00	106.02	7.70±0.10	8.01±0.18	
G33.3930+0.0097	0.01	0.02	106.20	0.52±0.04	0.57±0.08	
G33.3930+0.0097	0.02	0.01	106.38	0.32±0.03	0.41±0.05	
G33.3930+0.0097	0.10	0.17	106.56	0.09±0.02	0.16±0.04	
G33.3930+0.0097	-0.06	0.11	106.74	0.18±0.02	0.17±0.03	
G33.3930+0.0097	-0.08	0.05	106.92	0.28±0.02	0.27±0.03	
G33.3930+0.0097	-0.10	0.05	107.10	0.18±0.02	0.28±0.05	
G33.3930+0.0097	-0.18	-0.01	107.46	1.89±0.03	2.04±0.06	
G33.3930+0.0097	-0.21	0.02	107.64	1.19±0.03	1.28±0.06	
G33.3930+0.0097	-0.08	0.50	107.82	0.07±0.02	0.24±0.09	
G33.3930+0.0097	-0.34	0.06	108.00	0.14±0.02	0.13±0.03	
G33.4246–0.3150	18:53:27.4566	00:17:41.877	45.76	0.56±0.02	0.52±0.03	YAN19
G33.4246–0.3150	-0.17	0.01	45.40	0.09±0.02	0.22±0.06	
G33.4246–0.3150	-0.02	-0.03	45.58	0.24±0.01	0.23±0.02	
G33.4246–0.3150	0.01	0.05	45.94	0.52±0.02	0.49±0.03	
G33.4246–0.3150	-0.01	-0.02	46.12	0.24±0.02	0.17±0.02	
G33.4870+0.0407	18:52:18.3912	00:30:45.448	120.31	5.57±0.07	5.88±0.12	MMB
G33.4870+0.0407	-0.10	0.04	120.13	0.25±0.04	0.28±0.07	
G33.4870+0.0407	0.07	1.03	120.49	0.12±0.03	0.15±0.08	
G33.4870+0.0407	0.01	-0.04	120.67	0.38±0.02	0.41±0.04	
G33.4870+0.0407	-0.13	-0.02	120.85	0.09±0.02	0.34±0.08	
G33.4870+0.0407	0.02	0.07	121.03	0.34±0.02	0.47±0.05	
G33.4870+0.0407	-0.06	0.13	121.21	0.17±0.02	0.18±0.04	
G33.4870+0.0407	-0.01	-0.01	121.39	2.15±0.05	2.24±0.08	
G33.4870+0.0407	-0.00	0.00	121.57	2.40±0.05	2.49±0.08	
G33.4870+0.0407	-0.07	0.04	121.75	0.62±0.03	0.67±0.06	
G33.4870+0.0407	-0.04	0.04	121.93	0.17±0.03	0.29±0.07	
G33.4870+0.0407	-0.07	-0.33	122.11	0.06±0.01	0.37±0.09	
G33.4870+0.0407	0.02	0.01	123.01	0.20±0.02	0.19±0.04	
G33.4870+0.0407	-0.08	0.02	123.19	0.18±0.02	0.31±0.06	
G33.4870+0.0407	0.32	-0.30	123.37	0.06±0.01	0.13±0.04	
G33.6338–0.0210	18:52:47.5629	00:36:54.210	103.00	1.09±0.02	1.07±0.04	MMB
G33.6338–0.0210	0.09	-0.23	101.56	0.09±0.02	0.09±0.03	
G33.6338–0.0210	0.07	0.56	101.74	0.05±0.02	0.28±0.10	
G33.6338–0.0210	-0.01	0.08	102.10	0.22±0.02	0.19±0.03	
G33.6338–0.0210	-0.09	0.01	102.28	0.28±0.02	0.23±0.03	
G33.6338–0.0210	-0.08	0.05	102.46	0.27±0.02	0.30±0.04	
G33.6338–0.0210	-0.03	0.07	102.64	0.51±0.02	0.59±0.04	
G33.6338–0.0210	-0.01	0.02	102.82	0.99±0.02	1.04±0.04	
G33.6338–0.0210	0.01	0.03	103.18	0.97±0.02	1.02±0.03	
G33.6338–0.0210	-0.02	0.03	103.36	0.77±0.02	0.80±0.03	
G33.6338–0.0210	-0.05	0.04	103.54	0.29±0.02	0.34±0.04	
G33.6338–0.0210	-0.15	-0.05	103.72	0.11±0.02	0.15±0.04	
G33.6338–0.0210	0.05	-0.15	103.90	0.16±0.02	0.16±0.03	

Continuation of Table C.1

Name	$\alpha/\Delta\alpha$ h:m:s/″	$\delta/\Delta\delta$ d:m:s/″	V_{LSR} km s^{-1}	$S_{v,\,Peak}$ Jy beam^{-1}	$S_{v,\,Int}$ Jy	Notes
(1)	(2)	(3)	(4)	(5)	(6)	(7)
G33.6338–0.0210	0.17	0.26	104.08	0.08±0.02	0.08±0.03	
G34.7510–0.0925	18:55:05.2196	+01:34:36.206	53.24	6.61±0.04	6.74±0.07	MMB, BAR09
G34.7510–0.0925	0.04	-0.05	50.18	0.13±0.02	0.10±0.02	
G34.7510–0.0925	0.06	-0.03	50.36	0.59±0.02	0.55±0.03	
G34.7510–0.0925	0.10	-0.01	50.54	0.48±0.02	0.57±0.03	
G34.7510–0.0925	0.08	-0.01	50.72	0.36±0.02	0.47±0.04	
G34.7510–0.0925	-0.05	-0.11	50.90	0.20±0.02	0.35±0.04	
G34.7510–0.0925	0.10	-0.20	51.26	0.05±0.02	0.29±0.11	
G34.7510–0.0925	0.01	0.08	51.44	0.12±0.01	0.23±0.04	
G34.7510–0.0925	-0.00	0.02	51.62	0.66±0.02	0.72±0.04	
G34.7510–0.0925	0.00	-0.00	51.80	1.15±0.02	1.15±0.04	
G34.7510–0.0925	0.01	-0.00	51.98	0.97±0.03	1.08±0.06	
G34.7510–0.0925	0.02	0.03	52.16	1.62±0.02	1.67±0.04	
G34.7510–0.0925	0.01	-0.00	52.34	3.11±0.02	3.23±0.04	
G34.7510–0.0925	0.01	0.02	52.52	3.05±0.02	3.11±0.04	
G34.7510–0.0925	0.01	0.00	52.70	2.45±0.02	2.51±0.04	
G34.7510–0.0925	0.01	-0.01	52.88	1.41±0.03	1.45±0.05	
G34.7510–0.0925	0.00	0.00	53.06	5.83±0.04	5.96±0.08	
G34.7510–0.0925	0.01	-0.05	53.42	1.05±0.02	1.09±0.04	
G34.7567+0.0250	18:54:40.7388	+01:38:06.387	76.48	1.46±0.02	1.56±0.04	MMB
G34.7567+0.0250	-0.11	0.21	74.86	0.16±0.02	0.22±0.04	
G34.7567+0.0250	-0.03	-0.04	76.66	0.82±0.02	0.86±0.03	
G34.7567+0.0250	-0.02	0.02	76.84	0.67±0.02	0.65±0.03	
G34.7567+0.0250	-0.02	0.13	77.02	0.28±0.02	0.31±0.03	
G34.8212+0.3520	18:53:37.8769	+01:50:30.623	59.57	0.11±0.02	0.17±0.04	MMB
G34.8212+0.3520	0.61	0.55	58.85	0.05±0.02	0.38±0.18	
G34.2839+0.1837	18:53:14.9825	+01:17:13.296	47.34	0.12±0.01	0.13±0.03	G34.2839+0.1837b
G34.2839+0.1837	-0.19	-0.44	46.98	0.04±0.01	0.23±0.07	
G34.2839+0.1837	-0.02	0.03	47.16	0.09±0.01	0.16±0.04	
G34.2839+0.1837	-0.36	-0.08	47.52	0.07±0.02	0.31±0.09	
G34.2839+0.1837	-0.02	-0.52	47.70	0.06±0.01	0.31±0.08	
G34.2839+0.1837	0.14	-0.86	47.88	0.06±0.02	0.20±0.06	
G34.0957+0.0178	18:53:29.9037	+01:02:38.681	55.93	5.11±0.04	5.22±0.07	MMB
G34.0957+0.0178	0.09	-0.41	54.85	0.05±0.01	0.23±0.09	
G34.0957+0.0178	-0.07	-0.07	55.03	0.16±0.02	0.24±0.05	
G34.0957+0.0178	-0.05	-0.08	55.21	0.48±0.01	0.45±0.02	
G34.0957+0.0178	-0.01	-0.09	55.39	0.39±0.01	0.40±0.03	
G34.0957+0.0178	-0.03	-0.15	55.57	0.28±0.01	0.33±0.03	
G34.0957+0.0178	-0.01	-0.05	55.75	1.51±0.02	1.56±0.03	
G34.0957+0.0178	0.00	-0.00	56.11	2.49±0.02	2.57±0.04	
G34.0957+0.0178	0.02	-0.03	56.29	0.53±0.02	0.55±0.03	
G34.0957+0.0178	-0.03	0.00	56.47	0.32±0.02	0.40±0.03	
G34.0957+0.0178	0.01	-0.04	56.65	0.23±0.01	0.26±0.03	

Continuation
of Table C.1

Name	$\alpha/\Delta\alpha$ h:m:s/″	$\delta/\Delta\delta$ d:m:s/″	V_{LSR} km s^{-1}	$S_{v,\,Peak}$ Jy beam^{-1}	$S_{v,\,Int}$ Jy	Notes
(1)	(2)	(3)	(4)	(5)	(6)	(7)
G34.0957+0.0178	-0.10	-0.15	56.83	0.17±0.01	0.24±0.03	
G34.0957+0.0178	0.15	-0.12	57.01	0.12±0.01	0.17±0.03	
G34.0957+0.0178	0.05	-0.09	57.19	0.12±0.02	0.22±0.04	
G34.0957+0.0178	-0.05	-0.15	57.37	0.23±0.02	0.29±0.04	
G34.0957+0.0178	-0.10	0.08	57.55	0.12±0.01	0.14±0.03	
G34.0957+0.0178	-0.03	-0.25	60.79	0.28±0.01	0.31±0.03	
G34.0957+0.0178	-0.03	-0.19	60.97	2.83±0.02	2.91±0.04	
G34.0957+0.0178	-0.04	-0.18	61.15	4.26±0.02	4.28±0.04	
G34.0957+0.0178	-0.04	-0.15	61.33	1.45±0.01	1.42±0.03	
G34.1953–0.5928	18:55:51.2179	00:51:13.474	61.60	0.61±0.02	0.72±0.04	O14
G34.1953–0.5928	0.04	-0.28	58.18	0.12±0.02	0.23±0.05	
G34.1953–0.5928	-0.08	0.08	58.72	0.16±0.02	0.22±0.04	
G34.1953–0.5928	-0.17	0.12	58.90	0.14±0.02	0.10±0.03	
G34.1953–0.5928	0.32	-0.04	61.42	0.08±0.02	0.44±0.10	
G34.1953–0.5928	0.07	-0.02	61.78	0.53±0.02	0.61±0.04	
G34.1953–0.5928	-0.01	-0.05	61.96	0.35±0.02	0.34±0.03	
G34.1953–0.5928	0.01	0.05	62.14	0.54±0.02	0.53±0.04	
G34.1953–0.5928	-0.01	-0.05	62.32	0.17±0.03	0.37±0.08	
G34.2448+0.1333	18:53:21.4536	+01:13:45.981	61.15	7.18±0.06	7.33±0.10	MMB
G34.2448+0.1333	-0.08	0.01	54.49	0.22±0.03	0.45±0.09	
G34.2448+0.1333	-0.04	-0.01	54.67	2.02±0.03	2.10±0.06	
G34.2448+0.1333	-0.04	-0.01	54.85	5.71±0.04	5.97±0.08	
G34.2448+0.1333	-0.03	-0.02	55.03	2.96±0.03	3.06±0.06	
G34.2448+0.1333	-0.02	-0.00	55.21	1.19±0.02	1.23±0.04	
G34.2448+0.1333	0.03	-0.04	55.39	0.51±0.02	0.59±0.04	
G34.2448+0.1333	0.39	-0.34	55.57	0.05±0.02	0.23±0.09	
G34.2448+0.1333	-0.26	0.25	55.93	0.05±0.01	0.16±0.05	
G34.2448+0.1333	0.03	0.21	56.11	0.12±0.02	0.20±0.05	
G34.2448+0.1333	-0.04	-0.07	56.29	0.26±0.02	0.33±0.04	
G34.2448+0.1333	-0.07	-0.05	56.47	0.57±0.02	0.62±0.04	
G34.2448+0.1333	-0.08	0.01	56.65	2.79±0.03	2.91±0.06	
G34.2448+0.1333	-0.07	0.01	56.83	2.73±0.03	2.82±0.05	
G34.2448+0.1333	-0.03	0.02	57.01	1.00±0.02	1.00±0.04	
G34.2448+0.1333	-0.04	-0.05	57.19	0.57±0.03	0.73±0.05	
G34.2448+0.1333	-0.16	0.15	57.37	1.04±0.05	1.08±0.09	
G34.2448+0.1333	-0.04	0.09	58.27	0.29±0.03	0.42±0.07	
G34.2448+0.1333	-0.04	-0.02	58.45	0.34±0.03	0.52±0.06	
G34.2448+0.1333	-0.15	-0.01	58.63	0.30±0.03	0.48±0.08	
G34.2448+0.1333	-0.81	-0.15	58.81	0.05±0.02	0.42±0.13	
G34.2448+0.1333	0.17	0.10	59.17	0.05±0.01	0.42±0.11	
G34.2448+0.1333	0.02	0.10	59.35	0.34±0.02	0.52±0.05	
G34.2448+0.1333	-0.03	-0.05	59.53	0.67±0.02	0.78±0.05	
G34.2448+0.1333	0.02	-0.03	59.71	0.22±0.02	0.40±0.06	
G34.2448+0.1333	-0.01	0.03	59.89	0.69±0.02	0.81±0.05	

Continuation
of Table C.1

Name	$\alpha/\Delta\alpha$ h:m:s/″	$\delta/\Delta\delta$ d:m:s/″	V_{LSR} km s^{-1}	$S_{v,\,\mathrm{Peak}}$ Jy beam^{-1}	$S_{v,\,\mathrm{Int}}$ Jy	Notes
(1)	(2)	(3)	(4)	(5)	(6)	(7)
G34.2448+0.1333	-0.01	-0.00	60.07	1.41±0.03	1.55±0.06	
G34.2448+0.1333	-0.02	0.03	60.25	2.79±0.03	3.01±0.07	
G34.2448+0.1333	-0.02	0.02	60.43	1.74±0.03	1.82±0.05	
G34.2448+0.1333	0.00	-0.01	60.61	0.35±0.03	0.40±0.05	
G34.2448+0.1333	0.02	-0.07	60.79	0.69±0.03	0.78±0.06	
G34.2448+0.1333	0.01	0.00	60.97	3.72±0.04	3.78±0.06	
G34.2448+0.1333	0.00	-0.01	61.33	3.19±0.03	3.25±0.06	
G34.2448+0.1333	-0.00	-0.00	61.51	1.58±0.03	1.60±0.05	
G34.2448+0.1333	-0.00	-0.02	61.69	1.68±0.02	1.76±0.05	
G34.2448+0.1333	0.03	-0.08	61.87	0.35±0.03	0.45±0.06	
G34.2448+0.1333	0.03	-0.08	62.05	0.22±0.02	0.37±0.06	
G34.2448+0.1333	0.06	-0.28	62.23	0.12±0.02	0.62±0.12	
G34.2448+0.1333	0.03	-0.07	62.41	0.33±0.03	0.60±0.09	
G34.2448+0.1333	-0.02	-0.02	62.59	0.17±0.03	0.49±0.10	
G34.2448+0.1333	-0.05	0.01	62.77	0.11±0.02	0.22±0.05	
G34.2448+0.1333	-0.19	-0.20	62.95	0.06±0.01	0.26±0.07	
G34.2448+0.1333	-0.04	0.09	64.75	0.10±0.01	0.07±0.02	
G34.2582+0.1534	18:53:18.6450	+01:15:00.356	57.51	21.04±0.11	22.07±0.20	MMB
G34.2582+0.1534	-0.09	-0.51	56.07	0.14±0.02	0.49±0.08	
G34.2582+0.1534	-0.18	-0.56	56.43	0.34±0.03	0.85±0.10	
G34.2582+0.1534	0.08	-0.29	56.61	0.77±0.05	1.35±0.13	
G34.2582+0.1534	-0.08	-0.38	56.79	0.93±0.06	1.89±0.17	
G34.2582+0.1534	-0.65	-1.59	56.97	0.50±0.03	0.48±0.05	
G34.2582+0.1534	0.03	-0.07	57.15	0.99±0.04	1.45±0.10	
G34.2582+0.1534	-0.48	-1.50	57.33	0.28±0.03	0.34±0.06	
G34.2582+0.1534	-0.00	0.01	57.69	18.81±0.09	19.18±0.16	
G34.2582+0.1534	0.01	0.01	57.87	19.43±0.10	20.08±0.17	
G34.2582+0.1534	-0.01	0.01	58.05	9.55±0.06	9.86±0.11	
G34.2582+0.1534	0.51	-0.01	58.23	0.07±0.02	0.40±0.16	
G34.2582+0.1534	0.02	-0.07	58.41	1.00±0.03	1.22±0.05	
G34.2582+0.1534	0.21	-0.17	58.77	0.23±0.02	0.35±0.05	
G34.2582+0.1534	0.20	-0.08	58.95	0.14±0.02	0.33±0.07	
G34.2582+0.1534	0.23	-0.25	59.13	0.12±0.02	0.30±0.07	
G34.2582+0.1534	0.34	-0.35	59.31	0.23±0.03	0.50±0.09	
G34.2582+0.1534	0.18	-0.11	59.49	0.15±0.03	0.29±0.08	
G34.2582+0.1534	0.21	-0.50	59.67	0.16±0.03	0.46±0.11	
G34.2582+0.1534	0.42	0.36	60.03	0.09±0.02	0.49±0.14	
G34.2577+0.1540	18:53:18.4875	+01:15:00.176	60.57	1.85±0.03	1.82±0.05	G34.2582+0.1534b
G34.2577+0.1540	0.02	0.20	60.39	0.69±0.01	0.63±0.02	
G34.2577+0.1540	0.01	-0.18	60.75	0.95±0.02	0.91±0.03	
G34.2577+0.1540	0.03	-0.08	60.93	0.33±0.02	0.23±0.03	
G34.2577+0.1540	0.09	-0.12	61.11	1.06±0.03	1.19±0.05	
G34.2577+0.1540	0.24	0.07	61.29	0.21±0.02	0.13±0.02	
G34.2577+0.1540	0.15	-0.04	61.47	0.50±0.02	0.41±0.02	

Continuation
of Table C.1

Name	$\alpha/\Delta\alpha$ h:m:s/″	$\delta/\Delta\delta$ d:m:s/″	V_{LSR} km s^{-1}	$S_{v,\,Peak}$ Jy beam^{-1}	$S_{v,\,Int}$ Jy	Notes
(1)	(2)	(3)	(4)	(5)	(6)	(7)
G34.2577+0.1540	0.08	0.16	61.65	0.15±0.01	0.07±0.02	
G34.2672–0.2094	18:54:37.2519	+01:05:33.631	54.54	8.56±0.04	8.74±0.07	MMB
G34.2672–0.2094	-0.15	-0.06	46.08	0.17±0.02	0.23±0.05	
G34.2672–0.2094	-0.15	0.12	46.26	0.11±0.02	0.17±0.04	
G34.2672–0.2094	-0.07	0.22	48.06	0.14±0.02	0.20±0.05	
G34.2672–0.2094	0.06	-0.09	48.24	0.11±0.02	0.13±0.03	
G34.2672–0.2094	-0.07	-0.03	50.22	0.83±0.02	0.91±0.04	
G34.2672–0.2094	-0.08	-0.07	50.40	2.42±0.03	2.54±0.05	
G34.2672–0.2094	-0.08	-0.04	50.58	3.13±0.03	3.19±0.06	
G34.2672–0.2094	-0.09	-0.05	50.76	2.71±0.03	2.81±0.05	
G34.2672–0.2094	-0.02	-0.06	50.94	0.68±0.02	0.68±0.03	
G34.2672–0.2094	-0.06	0.04	51.12	0.62±0.02	0.67±0.03	
G34.2672–0.2094	-0.03	0.09	51.30	1.14±0.02	1.21±0.03	
G34.2672–0.2094	-0.04	0.08	51.48	0.80±0.02	0.93±0.05	
G34.2672–0.2094	-0.05	0.04	51.66	0.12±0.02	0.17±0.04	
G34.2672–0.2094	-0.06	-0.15	51.84	0.23±0.02	0.19±0.03	
G34.2672–0.2094	-0.10	0.15	52.02	0.25±0.02	0.27±0.04	
G34.2672–0.2094	-0.13	-0.07	52.20	0.11±0.02	0.12±0.03	
G34.2672–0.2094	-0.06	-0.03	54.18	0.40±0.02	0.38±0.03	
G34.2672–0.2094	0.00	0.01	54.36	5.25±0.03	5.35±0.06	
G34.2672–0.2094	-0.01	-0.01	54.72	2.01±0.03	2.00±0.04	
G34.2839+0.1837	18:53:15.0784	+01:17:12.292	52.02	0.14±0.02	0.27±0.06	NEW
G34.2839+0.1837	0.09	-0.23	51.84	0.05±0.01	0.23±0.07	
G34.2839+0.1837	-0.25	0.02	52.20	0.07±0.01	0.12±0.04	
G34.3957+0.2215	18:53:19.0938	+01:24:13.804	55.71	25.06±0.14	26.27±0.26	MMB
G34.3957+0.2215	-0.16	-0.05	54.99	0.06±0.01	0.35±0.09	
G34.3957+0.2215	-0.01	0.00	55.35	3.31±0.03	3.39±0.05	
G34.3957+0.2215	0.00	0.01	55.53	24.00±0.12	24.84±0.22	
G34.3957+0.2215	-0.01	0.00	55.89	8.96±0.06	9.21±0.11	
G34.3957+0.2215	-0.04	-0.03	56.07	1.31±0.03	1.40±0.05	
G34.3957+0.2215	-0.04	-0.08	56.25	0.30±0.02	0.47±0.05	
G34.3957+0.2215	0.03	0.01	56.43	0.25±0.02	0.30±0.03	
G34.3957+0.2215	-0.33	-0.04	56.61	0.08±0.01	0.43±0.09	
G34.3957+0.2215	-0.02	-0.04	56.79	0.24±0.02	0.26±0.03	
G34.3957+0.2215	-0.15	-0.02	56.97	0.09±0.02	0.22±0.05	
G34.3957+0.2215	0.03	-0.07	57.69	0.08±0.02	0.24±0.06	
G34.3957+0.2215	0.00	-0.16	57.87	0.83±0.02	0.90±0.04	
G34.3957+0.2215	0.23	-0.49	58.05	0.06±0.02	0.48±0.16	
G34.3957+0.2215	-0.11	0.12	59.49	0.08±0.01	0.12±0.04	
G34.3957+0.2215	-0.07	0.13	59.67	0.28±0.02	0.34±0.04	
G34.3957+0.2215	0.01	0.04	59.85	0.97±0.02	1.03±0.04	
G34.3957+0.2215	-0.01	0.02	60.03	0.79±0.02	0.92±0.04	
G34.3957+0.2215	-0.01	-0.10	60.21	1.52±0.03	1.59±0.05	
G34.3957+0.2215	-0.02	-0.09	60.39	3.02±0.03	3.10±0.06	

Continuation
of Table C.1

Name	$\alpha/\Delta\alpha$ h:m:s/″	$\delta/\Delta\delta$ d:m:s/″	V_{LSR} km s^{-1}	$S_{v,\,Peak}$ Jy beam^{-1}	$S_{v,\,Int}$ Jy	Notes
(1)	(2)	(3)	(4)	(5)	(6)	(7)
G34.3957+0.2215	-0.00	-0.10	60.57	1.04±0.02	1.12±0.04	
G34.3957+0.2215	0.01	-0.04	60.75	0.52±0.02	0.52±0.03	
G34.3957+0.2215	-0.01	-0.02	60.93	0.74±0.01	0.75±0.03	
G34.3957+0.2215	-0.05	-0.03	61.11	0.82±0.02	0.84±0.04	
G34.3957+0.2215	-0.02	0.01	61.29	1.35±0.02	1.39±0.04	
G34.3957+0.2215	-0.06	-0.02	61.47	1.12±0.02	1.16±0.04	
G34.3957+0.2215	-0.06	0.03	61.65	1.09±0.02	1.16±0.04	
G34.3957+0.2215	-0.05	0.03	61.83	1.95±0.02	2.04±0.04	
G34.3957+0.2215	-0.06	0.03	62.01	2.33±0.03	2.40±0.05	
G34.3957+0.2215	-0.05	0.02	62.19	3.31±0.03	3.44±0.06	
G34.3957+0.2215	-0.05	0.03	62.37	3.29±0.03	3.34±0.06	
G34.3957+0.2215	-0.04	0.03	62.55	3.76±0.04	3.91±0.07	
G34.3957+0.2215	-0.03	0.04	62.73	1.88±0.03	1.94±0.05	
G34.3957+0.2215	0.01	0.15	62.91	0.34±0.02	0.44±0.04	
G34.3957+0.2215	0.06	-0.04	63.09	0.20±0.02	0.28±0.04	
G34.3957+0.2215	-0.00	0.06	63.27	0.09±0.02	0.12±0.04	
G34.4113+0.2349	18:53:18.0031	+01:25:25.503	63.44	0.39±0.02	0.45±0.03	NEW
G34.4113+0.2349	-0.12	-0.21	60.38	0.10±0.02	0.37±0.10	
G34.4113+0.2349	-0.07	0.24	60.56	0.13±0.02	0.27±0.05	
G34.4113+0.2349	0.46	0.48	60.74	0.05±0.01	0.24±0.08	
G34.4113+0.2349	0.05	-0.02	61.10	0.06±0.01	0.28±0.09	
G34.4113+0.2349	-0.00	-0.05	63.26	0.23±0.02	0.28±0.04	
G35.4574–0.1786	18:56:40.9716	+02:09:57.252	55.93	0.25±0.02	0.31±0.03	NEW
G35.4574–0.1786	0.04	-0.23	54.67	0.05±0.01	0.13±0.05	
G35.4574–0.1786	0.12	-0.06	54.85	0.12±0.01	0.14±0.02	
G35.4574–0.1786	0.33	0.28	55.03	0.04±0.01	0.16±0.06	
G35.4574–0.1786	0.07	0.05	55.21	0.18±0.01	0.25±0.03	
G35.4574–0.1786	0.06	-0.09	55.39	0.10±0.01	0.10±0.02	
G35.4574–0.1786	0.02	-0.00	55.57	0.16±0.01	0.19±0.03	
G35.4574–0.1786	-0.07	-0.06	55.75	0.22±0.01	0.23±0.02	
G35.4574–0.1786	-0.03	-0.10	56.11	0.23±0.01	0.25±0.03	
G35.4574–0.1786	-0.01	0.03	56.29	0.19±0.01	0.17±0.02	
G35.4574–0.1786	0.12	-0.22	56.65	0.11±0.02	0.20±0.04	
G35.4574–0.1786	0.12	0.02	56.83	0.11±0.01	0.11±0.02	
G35.4574–0.1786	0.19	0.16	57.01	0.07±0.01	0.06±0.02	
G35.5879+0.0605	18:56:04.2214	+02:23:28.249	46.14	0.27±0.02	0.28±0.03	MMB
G35.5879+0.0605	-0.01	-0.06	43.80	0.08±0.02	0.13±0.05	
G35.5879+0.0605	-0.02	0.08	43.98	0.26±0.02	0.21±0.03	
G35.5879+0.0605	-0.33	-0.56	44.16	0.07±0.02	0.16±0.05	
G35.5879+0.0605	0.19	-0.94	44.34	0.09±0.02	0.21±0.06	
G35.5879+0.0605	0.01	0.03	44.52	0.21±0.02	0.25±0.04	
G35.5879+0.0605	0.01	0.07	44.88	0.09±0.02	0.21±0.05	
G35.5879+0.0605	-0.06	0.04	45.24	0.20±0.02	0.37±0.05	
G35.5879+0.0605	0.03	-0.05	45.42	0.14±0.02	0.31±0.05	

Continuation
of Table C.1

Name	$\alpha/\Delta\alpha$ h:m:s/″	$\delta/\Delta\delta$ d:m:s/″	V_{LSR} km s^{-1}	$S_{v,\,Peak}$ Jy beam^{-1}	$S_{v,\,Int}$ Jy	Notes
(1)	(2)	(3)	(4)	(5)	(6)	(7)
G35.5879+0.0605	0.11	-0.09	45.60	0.12±0.02	0.37±0.07	
G35.5879+0.0605	-0.11	-0.04	45.78	0.10±0.02	0.43±0.10	
G35.5879+0.0605	-0.08	0.09	45.96	0.12±0.02	0.12±0.03	
G35.7927–0.1744	18:57:16.8929	+02:27:58.062	60.75	25.35±0.30	26.80±0.54	MMB
G35.7927–0.1744	-0.00	0.16	56.79	0.12±0.02	0.19±0.05	
G35.7927–0.1744	-0.18	0.07	56.97	0.26±0.02	0.50±0.07	
G35.7927–0.1744	-0.16	0.06	57.15	0.49±0.02	0.64±0.04	
G35.7927–0.1744	-0.19	0.24	57.33	0.24±0.02	0.31±0.04	
G35.7927–0.1744	-0.08	0.12	57.51	0.18±0.02	0.24±0.05	
G35.7927–0.1744	-0.09	-0.05	57.69	0.19±0.02	0.36±0.06	
G35.7927–0.1744	-0.13	0.06	57.87	0.62±0.02	0.70±0.05	
G35.7927–0.1744	-0.11	0.05	58.05	0.95±0.03	1.02±0.05	
G35.7927–0.1744	-0.13	0.06	58.23	1.25±0.03	1.33±0.05	
G35.7927–0.1744	-0.14	0.03	58.41	1.74±0.03	1.81±0.06	
G35.7927–0.1744	-0.14	0.03	58.59	2.83±0.05	2.99±0.10	
G35.7927–0.1744	-0.14	0.02	58.77	3.27±0.06	3.40±0.12	
G35.7927–0.1744	-0.13	0.03	58.95	2.62±0.05	2.81±0.09	
G35.7927–0.1744	-0.13	0.02	59.13	1.49±0.03	1.63±0.06	
G35.7927–0.1744	-0.14	0.02	59.31	1.00±0.03	1.09±0.05	
G35.7927–0.1744	-0.12	0.04	59.49	1.41±0.03	1.56±0.06	
G35.7927–0.1744	-0.10	0.02	59.67	1.15±0.04	1.23±0.07	
G35.7927–0.1744	-0.03	0.01	59.85	3.25±0.05	3.48±0.09	
G35.7927–0.1744	0.00	0.04	60.03	1.83±0.05	2.00±0.09	
G35.7927–0.1744	-0.03	-0.04	60.21	1.97±0.04	2.11±0.08	
G35.7927–0.1744	0.00	0.03	60.39	2.28±0.06	2.42±0.10	
G35.7927–0.1744	-0.01	-0.01	60.57	13.48±0.15	14.40±0.28	
G35.7927–0.1744	0.00	-0.00	60.93	13.65±0.16	14.45±0.29	
G35.7927–0.1744	-0.00	0.01	61.11	8.51±0.13	8.87±0.24	
G35.7927–0.1744	0.00	0.01	61.29	7.29±0.10	7.61±0.18	
G35.7927–0.1744	0.01	0.00	61.47	9.69±0.15	10.17±0.27	
G35.7927–0.1744	0.02	0.01	61.65	5.49±0.10	5.80±0.18	
G35.7927–0.1744	0.00	0.00	61.83	8.00±0.11	8.36±0.21	
G35.7927–0.1744	0.01	0.01	62.01	7.85±0.13	8.21±0.24	
G35.7927–0.1744	0.01	0.01	62.19	6.16±0.10	6.43±0.18	
G35.7927–0.1744	0.01	0.00	62.37	4.65±0.09	4.97±0.16	
G35.7927–0.1744	0.01	-0.00	62.55	2.01±0.05	2.08±0.09	
G35.7927–0.1744	0.02	-0.05	62.73	3.45±0.06	3.66±0.12	
G35.7927–0.1744	0.01	-0.07	62.91	4.30±0.07	4.55±0.13	
G35.7927–0.1744	0.03	-0.07	63.09	1.14±0.04	1.19±0.07	
G35.7927–0.1744	-0.01	-0.02	63.27	0.53±0.03	0.60±0.05	
G35.7927–0.1744	0.12	-0.07	63.45	0.20±0.02	0.39±0.07	
G35.7927–0.1744	0.05	-0.09	63.63	0.39±0.02	0.48±0.05	
G35.7927–0.1744	0.12	-0.03	63.81	0.25±0.02	0.33±0.05	
G35.7927–0.1744	-0.04	-0.06	63.99	0.48±0.02	0.61±0.05	

Continuation
of Table C.1

Name	$\alpha/\Delta\alpha$ h:m:s/″	$\delta/\Delta\delta$ d:m:s/″	V_{LSR} km s^{-1}	$S_{v,\,Peak}$ Jy beam^{-1}	$S_{v,\,Int}$ Jy	Notes
(1)	(2)	(3)	(4)	(5)	(6)	(7)
G35.7927–0.1744	0.01	-0.06	64.17	0.44±0.02	0.56±0.05	
G35.7927–0.1744	0.00	-0.12	64.35	0.43±0.02	0.49±0.04	
G35.7927–0.1744	-0.03	-0.25	64.53	0.13±0.02	0.29±0.06	
G35.7927–0.1744	-0.01	-0.12	64.71	0.18±0.02	0.32±0.05	
G35.0248+0.3497	18:54:00.6579	+02:01:19.186	44.38	14.49±0.08	15.12±0.14	MMB
G35.0248+0.3497	-0.03	0.22	41.32	0.13±0.02	0.31±0.07	
G35.0248+0.3497	-0.01	0.08	41.50	0.54±0.02	0.64±0.04	
G35.0248+0.3497	-0.08	0.04	41.68	0.46±0.02	0.60±0.05	
G35.0248+0.3497	-0.03	-0.01	41.86	0.37±0.03	0.47±0.05	
G35.0248+0.3497	-0.04	0.05	42.04	2.43±0.04	2.57±0.07	
G35.0248+0.3497	-0.02	0.04	42.22	1.69±0.04	1.78±0.07	
G35.0248+0.3497	0.00	0.04	42.40	1.03±0.02	1.10±0.04	
G35.0248+0.3497	-0.02	-0.00	42.58	1.20±0.03	1.32±0.06	
G35.0248+0.3497	-0.01	0.03	42.76	0.85±0.02	0.90±0.05	
G35.0248+0.3497	-0.00	0.02	42.94	1.52±0.03	1.62±0.06	
G35.0248+0.3497	-0.00	-0.01	43.12	1.17±0.03	1.33±0.06	
G35.0248+0.3497	-0.02	0.00	43.30	1.74±0.03	1.82±0.06	
G35.0248+0.3497	-0.02	0.03	43.48	1.58±0.03	1.61±0.06	
G35.0248+0.3497	-0.02	0.08	43.66	6.97±0.06	7.14±0.10	
G35.0248+0.3497	-0.01	0.07	43.84	12.36±0.07	12.73±0.13	
G35.0248+0.3497	-0.01	0.04	44.02	9.70±0.07	10.05±0.13	
G35.0248+0.3497	-0.00	0.01	44.20	12.28±0.07	12.79±0.12	
G35.0248+0.3497	-0.00	0.01	44.56	5.10±0.06	5.38±0.10	
G35.0248+0.3497	0.04	0.11	44.74	1.58±0.04	1.68±0.07	
G35.0248+0.3497	0.03	0.09	44.92	2.25±0.03	2.37±0.06	
G35.0248+0.3497	0.03	0.11	45.10	1.27±0.03	1.38±0.05	
G35.0248+0.3497	0.00	0.01	45.28	1.85±0.03	2.02±0.06	
G35.0248+0.3497	-0.00	-0.00	45.46	2.10±0.04	2.28±0.07	
G35.0248+0.3497	-0.01	0.02	45.64	2.61±0.04	2.81±0.08	
G35.0248+0.3497	-0.01	0.01	45.82	3.25±0.04	3.43±0.08	
G35.0248+0.3497	-0.04	0.06	46.00	2.83±0.04	2.99±0.08	
G35.0248+0.3497	-0.09	0.14	46.18	2.48±0.04	2.65±0.07	
G35.0248+0.3497	-0.07	0.12	46.36	2.83±0.04	3.04±0.07	
G35.0248+0.3497	-0.04	0.05	46.54	1.43±0.03	1.64±0.06	
G35.0248+0.3497	-0.20	0.11	46.72	0.25±0.03	0.39±0.06	
G35.0248+0.3497	-0.03	0.26	46.90	0.07±0.01	0.11±0.03	
G35.1327–0.7440	18:58:06.1392	+01:37:07.503	36.56	22.18±0.29	22.54±0.52	MMB
G35.1327–0.7440	-0.20	-0.16	28.82	0.97±0.16	1.58±0.40	
G35.1327–0.7440	-0.09	0.00	29.00	3.90±0.15	4.45±0.29	
G35.1327–0.7440	-0.09	-0.02	29.18	7.15±0.19	7.94±0.36	
G35.1327–0.7440	-0.12	-0.03	29.36	6.11±0.17	6.59±0.32	
G35.1327–0.7440	-0.11	-0.08	29.54	7.76±0.14	8.01±0.26	
G35.1327–0.7440	-0.11	-0.08	29.72	7.85±0.15	8.00±0.27	
G35.1327–0.7440	-0.10	-0.07	29.90	9.74±0.18	10.11±0.33	

Continuation
of Table C.1

Name	$\alpha/\Delta\alpha$ h:m:s/″	$\delta/\Delta\delta$ d:m:s/″	V_{LSR} km s^{-1}	$S_{v,\,Peak}$ Jy beam^{-1}	$S_{v,\,Int}$ Jy	Notes
(1)	(2)	(3)	(4)	(5)	(6)	(7)
G35.1327–0.7440	-0.12	-0.06	30.08	5.34±0.14	5.34±0.25	
G35.1327–0.7440	-0.13	-0.05	30.26	4.24±0.13	4.33±0.22	
G35.1327–0.7440	-0.20	0.06	30.44	0.98±0.11	0.97±0.19	
G35.1327–0.7440	-0.17	-0.04	30.62	1.82±0.10	1.99±0.18	
G35.1327–0.7440	-0.14	-0.08	30.98	13.88±0.22	13.96±0.39	
G35.1327–0.7440	-0.13	-0.08	31.16	12.04±0.21	12.04±0.38	
G35.1327–0.7440	-0.15	-0.08	31.52	1.21±0.06	1.55±0.12	
G35.1327–0.7440	-0.26	-0.06	31.88	0.34±0.05	0.73±0.15	
G35.1327–0.7440	-0.17	0.03	32.24	0.65±0.06	0.64±0.10	
G35.1327–0.7440	-0.12	-0.12	32.42	4.24±0.07	4.34±0.13	
G35.1327–0.7440	-0.13	-0.12	32.60	2.07±0.06	2.33±0.11	
G35.1327–0.7440	-0.21	0.01	32.96	0.55±0.05	0.78±0.12	
G35.1327–0.7440	0.04	0.27	35.66	0.20±0.05	0.31±0.12	
G35.1327–0.7440	-0.08	0.06	35.84	0.30±0.03	0.34±0.05	
G35.1327–0.7440	-0.09	-0.00	36.02	0.63±0.05	0.99±0.13	
G35.1327–0.7440	-0.10	0.03	36.20	0.89±0.06	1.17±0.12	
G35.1327–0.7440	-0.02	-0.01	36.38	4.83±0.12	4.88±0.22	
G35.1327–0.7440	0.00	-0.00	36.74	12.05±0.21	12.17±0.37	
G35.1327–0.7440	-0.03	0.03	36.92	1.12±0.08	1.26±0.14	
G35.1327–0.7440	0.02	-0.03	37.10	0.64±0.06	1.15±0.16	
G35.1327–0.7440	0.06	0.02	37.28	0.34±0.04	0.76±0.12	
G35.1327–0.7440	0.01	0.04	37.46	1.06±0.06	1.48±0.13	
G35.1327–0.7440	0.03	-0.04	37.64	1.56±0.07	1.81±0.13	
G35.1327–0.7440	0.02	-0.00	37.82	2.14±0.07	2.36±0.13	
G35.1327–0.7440	-0.01	0.07	38.00	0.69±0.07	1.03±0.15	
G35.1327–0.7440	0.12	-0.16	38.18	0.16±0.03	0.34±0.09	
G35.1327–0.7440	0.03	0.22	38.36	0.17±0.03	0.45±0.09	
G35.1327–0.7440	0.02	0.21	38.54	0.43±0.04	0.75±0.12	
G35.1327–0.7440	-0.04	0.33	38.72	0.39±0.05	0.79±0.14	
G35.1327–0.7440	0.19	0.03	38.90	0.29±0.04	0.79±0.14	
G35.1327–0.7440	0.05	0.26	39.08	0.12±0.02	0.17±0.05	
G35.1489+0.8092	18:52:36.0231	+02:20:31.143	72.02	0.13±0.02	0.25±0.05	YAN19
G35.1489+0.8092	-0.02	0.31	71.84	0.07±0.02	0.18±0.05	
G35.1971–0.7432	18:58:13.0557	+01:40:35.715	28.51	147.52±0.76	153.33±1.38	MMB, G35.1973-0.7428
G35.1971–0.7432	-0.39	0.29	25.99	0.32±0.02	0.55±0.06	
G35.1971–0.7432	-0.33	0.29	26.35	0.28±0.02	0.52±0.06	
G35.1971–0.7432	-0.28	-0.09	26.53	0.13±0.01	0.33±0.03	
G35.1971–0.7432	-0.37	0.27	26.71	0.45±0.05	1.22±0.18	
G35.1971–0.7432	-0.58	0.68	26.89	0.58±0.07	2.37±0.35	
G35.1971–0.7432	-0.08	0.06	27.07	2.06±0.09	2.74±0.20	
G35.1971–0.7432	-0.14	0.12	27.25	1.09±0.09	1.82±0.24	
G35.1971–0.7432	-0.02	0.04	27.43	5.72±0.08	6.30±0.16	
G35.1971–0.7432	0.01	0.05	27.61	6.49±0.08	7.03±0.16	

Continuation
of Table C.1

Name	$\alpha/\Delta\alpha$	$\delta/\Delta\delta$	V_{LSR}	$S_{v,\,Peak}$	$S_{v,\,Int}$	Notes
	h:m:s/″	d:m:s/″	km s^{-1}	Jy beam^{-1}	Jy	
(1)	(2)	(3)	(4)	(5)	(6)	(7)
G35.1971–0.7432	-0.03	0.04	27.79	6.19±0.10	6.78±0.18	
G35.1971–0.7432	-0.08	0.04	27.97	2.38±0.11	2.91±0.23	
G35.1971–0.7432	-0.01	0.00	28.15	41.84±0.33	43.50±0.60	
G35.1971–0.7432	-0.01	-0.00	28.33	136.25±0.82	141.07±1.49	
G35.1971–0.7432	-0.00	0.00	28.69	63.76±0.36	66.29±0.66	
G35.1971–0.7432	-0.03	0.05	28.87	8.01±0.32	9.46±0.64	
G35.1974–0.7426	18:58:12.9574	+01:40:37.626	29.23	44.57±0.21	47.03±0.38	G35.1973-0.7428b
G35.1974–0.7426	0.03	-0.01	25.81	0.12±0.00	0.17±0.00	
G35.1974–0.7426	-0.08	0.01	25.99	0.70±0.01	0.78±0.03	
G35.1974–0.7426	-0.01	-0.01	26.17	2.95±0.02	3.07±0.04	
G35.1974–0.7426	-0.07	0.02	26.35	0.65±0.02	0.73±0.04	
G35.1974–0.7426	-0.06	-0.02	26.53	0.38±0.01	0.44±0.02	
G35.1974–0.7426	-0.03	-0.01	26.71	1.43±0.02	1.56±0.04	
G35.1974–0.7426	-0.01	-0.01	26.89	2.50±0.02	2.65±0.04	
G35.1974–0.7426	-0.03	-0.02	27.07	3.56±0.04	3.81±0.08	
G35.1974–0.7426	-0.04	-0.04	27.25	3.63±0.03	3.89±0.06	
G35.1974–0.7426	-0.01	-0.09	27.43	1.81±0.05	2.16±0.11	
G35.1974–0.7426	-0.01	-0.13	27.61	1.67±0.05	2.02±0.10	
G35.1974–0.7426	-0.07	-0.10	27.79	3.05±0.06	3.37±0.11	
G35.1974–0.7426	-0.07	-0.08	27.97	3.61±0.04	3.93±0.07	
G35.1974–0.7426	0.09	0.03	28.87	11.74±0.12	12.64±0.22	
G35.1974–0.7426	0.07	0.03	29.05	41.84±0.25	44.49±0.47	
G35.1974–0.7426	-0.07	-0.05	29.41	34.38±0.15	35.69±0.28	
G35.1974–0.7426	-0.04	-0.07	29.59	11.34±0.08	11.86±0.14	
G35.1974–0.7426	-0.12	-0.13	29.77	30.91±0.20	31.62±0.35	
G35.1974–0.7426	-0.12	-0.11	29.95	44.20±0.23	45.27±0.42	
G35.1974–0.7426	-0.11	-0.12	30.13	19.43±0.15	19.77±0.26	
G35.1974–0.7426	-0.10	-0.13	30.31	17.43±0.12	17.92±0.21	
G35.1974–0.7426	-0.11	-0.14	30.49	14.07±0.09	14.49±0.17	
G35.1974–0.7426	-0.13	-0.11	30.67	7.95±0.06	8.26±0.11	
G35.1974–0.7426	-0.13	-0.15	30.85	4.71±0.04	4.95±0.08	
G35.1974–0.7426	-0.09	-0.19	31.03	3.24±0.03	3.42±0.05	
G35.1974–0.7426	-0.10	-0.20	31.21	0.92±0.02	0.98±0.04	
G35.1974–0.7426	-0.04	-0.18	31.39	0.67±0.01	0.78±0.03	
G35.1974–0.7426	0.00	-0.21	31.57	0.61±0.02	0.77±0.05	
G35.1974–0.7426	0.07	-0.15	31.75	0.64±0.02	0.79±0.04	
G35.1974–0.7426	0.09	-0.18	31.93	0.84±0.02	0.98±0.04	
G35.1974–0.7426	0.07	-0.13	32.11	1.35±0.02	1.49±0.03	
G35.1974–0.7426	0.05	-0.14	32.29	2.11±0.02	2.20±0.03	
G35.1974–0.7426	0.04	-0.17	32.47	0.89±0.02	0.94±0.03	
G35.1974–0.7426	0.04	-0.13	32.65	0.63±0.01	0.69±0.02	
G35.1974–0.7426	-0.04	-0.09	32.83	0.51±0.01	0.57±0.02	
G35.1974–0.7426	-0.02	-0.02	33.01	2.84±0.04	2.87±0.08	
G35.1974–0.7426	-0.08	-0.03	33.19	15.56±0.10	15.93±0.18	

Continuation
of Table C.1

Name	$\alpha/\Delta\alpha$ h:m:s/″	$\delta/\Delta\delta$ d:m:s/″	V_{LSR} km s^{-1}	$S_{v,\,Peak}$ Jy beam^{-1}	$S_{v,\,Int}$ Jy	Notes
(1)	(2)	(3)	(4)	(5)	(6)	(7)
G35.1974–0.7426	-0.07	-0.04	33.37	24.60±0.11	25.22±0.21	
G35.1974–0.7426	-0.06	-0.08	33.55	8.23±0.06	8.33±0.11	
G35.1974–0.7426	-0.02	-0.10	33.73	0.56±0.02	0.54±0.03	
G35.1974–0.7426	-0.02	-0.21	33.91	0.61±0.01	0.71±0.03	
G35.1974–0.7426	-0.03	-0.26	34.27	0.38±0.01	0.38±0.01	
G35.1974–0.7426	-0.07	-0.30	34.63	0.63±0.01	0.72±0.02	
G35.1974–0.7426	-0.07	-0.32	34.99	3.84±0.03	4.00±0.05	
G35.1974–0.7426	-0.09	-0.31	35.35	26.96±0.17	27.40±0.30	
G35.1974–0.7426	-0.09	-0.31	35.53	25.76±0.15	26.18±0.26	
G35.1974–0.7426	-0.07	-0.33	35.89	1.76±0.02	1.79±0.03	
G35.1974–0.7426	-0.09	-0.32	36.25	1.00±0.02	1.06±0.03	
G35.1974–0.7426	-0.11	-0.29	36.43	1.40±0.02	1.44±0.03	
G35.1974–0.7426	-0.10	-0.30	36.61	4.59±0.03	4.70±0.05	
G35.1974–0.7426	-0.08	-0.32	36.97	0.56±0.01	0.63±0.02	
G35.1974–0.7426	-0.11	-0.34	37.33	0.27±0.01	0.30±0.01	
G35.2260–0.3544	18:56:53.2156	+01:52:47.498	59.49	0.25±0.02	0.33±0.04	YAN19
G35.2260–0.3544	-0.22	0.77	59.13	0.06±0.01	0.26±0.07	
G35.2260–0.3544	0.02	0.08	59.31	0.12±0.02	0.16±0.04	
G35.2260–0.3544	0.14	-0.49	59.67	0.04±0.01	0.53±0.17	
G35.2476–0.2365	18:56:30.3879	+01:57:08.863	72.43	1.38±0.02	1.41±0.03	MMB
G35.2476–0.2365	0.37	0.05	71.89	0.06±0.02	0.15±0.05	
G35.2476–0.2365	0.02	-0.06	72.25	1.13±0.02	1.22±0.04	
G35.3971+0.0253	18:55:50.7799	+02:12:19.043	89.07	0.36±0.02	0.35±0.03	MMB
G35.3971+0.0253	0.05	0.08	89.25	0.27±0.02	0.24±0.03	
G35.3971+0.0253	-0.07	0.12	89.43	0.28±0.01	0.25±0.02	
G35.3971+0.0253	-0.04	-0.00	89.61	0.24±0.02	0.20±0.03	
G35.3971+0.0253	-0.31	0.00	89.79	0.08±0.02	0.07±0.03	
G35.4170–0.2840	18:56:59.0634	+02:04:54.541	56.29	0.89±0.02	0.89±0.03	NEW
G35.4170–0.2840	-0.05	0.17	55.93	0.19±0.02	0.20±0.03	
G35.4170–0.2840	0.03	0.01	56.11	0.62±0.02	0.65±0.04	
G35.4170–0.2840	0.03	-0.01	56.47	0.56±0.02	0.60±0.03	
G35.4170–0.2840	0.06	0.10	56.65	0.13±0.02	0.13±0.04	

Table C.2: The complete version of Table 5.3.

Name (glon, glat) (1)	$\Delta V_{\rm B}$ (km s^{-1}) (2)	Dist. (kpc) (3)	Note (4)	$S_{\rm Int}$ (Jy km s^{-1}) (5)	$L_{\rm maser,B}$ ($L_\odot$) (6)
G28.6079+0.0180	4.14	5.00±0.50	AGAL	9.82±0.19	1.7×10^{-6}
G28.7003+0.4060	2.70	4.70±0.34	AGAL	5.39±0.24	8.0×10^{-7}
G28.8175+0.3649	5.40	4.70±0.34	AGAL	68.80±0.23	1.0×10^{-5}
G28.8195+0.3543	1.08	4.70±0.34	AGAL	1.57±0.11	2.3×10^{-7}
G28.8322–0.2528	9.90	5.00±1.04	AGAL	588.79±1.32	9.9×10^{-5}
G28.8421+0.4938	5.40	4.70±0.34	AGAL	18.60±0.26	2.8×10^{-6}
G28.8421+0.4938b	1.80	4.70±0.34	AGAL	5.55±0.33	8.3×10^{-7}
G28.8481–0.2279	4.32	5.70±0.64	AGAL	23.28±0.58	5.1×10^{-6}
G28.8621+0.0660	0.72	5.00±0.47	AGAL	3.00±0.07	5.1×10^{-7}
G28.0113-0.4263	6.48	1.90±0.43	AGAL	37.03±0.30	9.0×10^{-7}
G28.9289+0.0193	0.72	10.71±0.36	BAYE	0.80±0.08	6.2×10^{-7}
G28.1467–0.0045	6.66	6.30±0.94	AGAL	132.62±0.67	3.6×10^{-5}
G28.2006–0.0495	7.92	6.30±0.90	AGAL	29.44±0.43	7.9×10^{-6}
G28.2817–0.3590	1.62	7.70±3.29	BAYE	16.11±0.12	6.4×10^{-6}
G28.3047–0.3877	7.20	4.37±0.33	BAYE	232.06±0.54	3.0×10^{-5}
G28.3211–0.0110	3.42	6.30±0.90	AGAL	12.23±0.29	3.3×10^{-6}
G28.3972+0.0803	8.28	4.30±0.28	AGAL	95.75±0.27	1.2×10^{-5}
G28.5228+0.1270	1.08	10.75±0.38	BAYE	12.83±0.14	1.0×10^{-5}
G28.5322+0.1287	3.06	12.50±0.27	BAYE	7.74±0.15	8.2×10^{-6}
G29.9556–0.0156b	2.52	4.90±0.45	AGAL	60.23±0.78	9.8×10^{-6}
G29.2815–0.3295	1.44	5.60±0.62	AGAL	10.25±0.11	2.2×10^{-6}
G29.3197–0.1619	3.96	3.00±0.43	AGAL	25.13±0.26	1.5×10^{-6}
G29.5809+0.1320	0.54	12.30±0.27	BAYE	1.07±0.16	1.1×10^{-6}
G29.6032–0.6250	2.34	4.40±0.26	AGAL	8.89±0.16	1.2×10^{-6}
G29.8621–0.0441	5.94	4.90±0.63	AGAL	438.18±2.98	7.1×10^{-5}
G29.9157–0.0236	5.58	7.10±0.76	BAYE	88.59±4.31	3.0×10^{-5}
G29.9556–0.0156	5.76	4.90±0.45	AGAL	504.49±2.09	8.2×10^{-5}
G29.9609–0.0675	1.26	4.90±0.70	AGAL	19.09±0.57	3.1×10^{-6}
G29.9781–0.0478	7.92	4.90±0.70	AGAL	381.02±2.19	6.2×10^{-5}
G30.5891–0.0424	8.46	11.50±0.43	AGAL	34.58±0.29	3.1×10^{-5}
G30.6214+0.0826	1.08	11.40±0.43	AGAL	1.58±0.14	1.4×10^{-6}
G30.7028–0.0683	4.50	4.90±0.87	AGAL	367.41±1.63	6.0×10^{-5}
G30.7599–0.0523	5.40	7.13±0.77	BAYE	239.99±1.68	8.2×10^{-5}
G30.7700–0.8043	3.06	4.40±0.43	AGAL	72.92±0.27	9.5×10^{-6}
G30.7744+0.0783	1.80	7.23±0.73	BAYE	6.15±0.24	2.2×10^{-6}
G30.7799+0.2301	1.80	2.60±0.43	AGAL	78.90±0.43	3.6×10^{-6}
G30.7880+0.2039	9.90	4.90±1.72	AGAL	144.81±0.42	2.3×10^{-5}
G30.7880+0.2039b	3.06	4.90±1.72	AGAL	30.62±0.28	5.0×10^{-6}
G30.8176–0.0547	3.06	4.90±0.70	AGAL	25.74±0.46	4.2×10^{-6}
G30.0095–0.2734	1.44	4.90±0.70	AGAL	7.49±0.11	1.2×10^{-6}
G30.8178–0.0570	9.90	4.90±0.70	AGAL	133.86±0.86	2.2×10^{-5}
G30.8184+0.2725	4.14	4.90±0.70	AGAL	12.22±0.35	2.0×10^{-6}
G30.8507+0.1221	1.98	1.92±0.27	BAYE	4.60±0.14	1.1×10^{-7}
G30.8979+0.1612	11.34	4.90±0.70	AGAL	621.62±2.30	1.0×10^{-4}

Continuation of Table C.2

Name (glon, glat) (1)	$\Delta V_{\rm B}$ (km s^{-1}) (2)	Dist. (kpc) (3)	Note (4)	$S_{\rm Int}$ (Jy km s^{-1}) (5)	$L_{\rm maser,B}$ ($L_\odot$) (6)
G30.9584+0.0861	0.90	11.80±0.43	AGAL	1.77±0.13	1.7×10^{-6}
G30.9726–0.1414	6.84	4.90±0.26	AGAL	144.25±0.66	2.3×10^{-5}
G30.9801+0.2158	0.72	4.90±0.70	AGAL	1.12±0.15	1.8×10^{-7}
G30.9729+0.5624	0.72	12.39±0.30	BAYE	1.10±0.08	1.1×10^{-6}
G30.1981–0.1688	8.28	4.90±0.22	AGAL	173.69±0.74	2.8×10^{-5}
G30.2244–0.1803	4.86	4.90±0.70	AGAL	85.12±0.51	1.4×10^{-5}
G30.3177+0.0703	9.90	2.80±0.43	AGAL	74.38±0.34	3.9×10^{-6}
G30.3705+0.4827	3.06	1.10±0.54	AGAL	14.66±0.15	1.2×10^{-7}
G30.4006–0.2958	6.12	4.90±0.70	AGAL	35.67±0.25	5.8×10^{-6}
G30.4194–0.2316	3.24	4.90±0.33	AGAL	37.66±0.20	6.1×10^{-6}
G30.4234+0.4661	2.52	1.10±0.54	AGAL	4.46±0.10	3.6×10^{-8}
G30.5426+0.0110	2.88	10.42±0.34	BAYE	5.59±0.18	4.1×10^{-6}
G31.3959–0.2576	0.36	4.90±0.70	AGAL	0.68±0.06	1.1×10^{-7}
G31.4122+0.3071	12.78	4.90±0.41	AGAL	228.26±0.88	3.7×10^{-5}
G31.5811+0.0769	3.96	4.90±0.99	AGAL	50.48±0.23	8.2×10^{-6}
G31.5937–0.1920	1.44	2.10±0.13	AGAL	8.78±0.09	2.6×10^{-7}
G31.0470+0.3562	5.76	4.90±0.70	AGAL	45.97±0.26	7.5×10^{-6}
G31.0592+0.0933	3.78	13.20±0.54	AGAL	60.93±0.31	7.2×10^{-5}
G31.0767+0.4573	1.98	12.30±0.49	AGAL	9.31±0.22	9.5×10^{-6}
G31.1213+0.0628	3.42	11.40±0.43	AGAL	7.96±0.19	7.0×10^{-6}
G31.1580+0.0457	2.88	2.50±0.43	AGAL	11.76±0.19	5.0×10^{-7}
G31.1824–0.1477	4.86	2.70±0.43	AGAL	20.40±0.28	1.0×10^{-6}
G31.2526+0.0029	0.72	2.80±0.43	AGAL	0.83±0.08	4.4×10^{-8}
G31.2756+0.0053	0.72	2.14±0.26	BAYE	1.06±0.07	3.3×10^{-8}
G31.2805+0.0617	11.88	4.90±0.67	AGAL	756.14±1.89	1.2×10^{-4}
G32.8027+0.1926	2.70	12.03±0.28	BAYE	6.16±0.17	6.0×10^{-6}
G32.8212–0.3301	0.72	5.10±0.28	AGAL	2.34±0.16	4.1×10^{-7}
G32.9175–0.0935	0.36	6.86±0.60	BAYE	1.83±0.15	5.8×10^{-7}
G32.9645–0.3394	1.62	2.56±0.26	BAYE	4.21±0.15	1.9×10^{-7}
G32.9918+0.0343	3.78	9.20±0.55	AGAL	67.05±0.25	3.8×10^{-5}
G32.0446+0.0593	10.08	5.10±0.38	AGAL	583.46±1.35	1.0×10^{-4}
G32.1056–0.0741	0.90	10.16±0.37	BAYE	1.66±0.12	1.2×10^{-6}
G32.1176+0.0906	6.12	5.10±0.40	AGAL	52.89±0.59	9.3×10^{-6}
G32.5150+0.3229	0.54	10.28±0.66	BAYE	2.35±0.10	1.7×10^{-6}
G32.7443–0.0753	2.70	7.90±1.02	AGAL	230.37±1.24	9.7×10^{-5}
G32.7443–0.0753b	9.72	7.90±1.02	AGAL	340.74±1.48	1.4×10^{-4}
G32.7443–0.0753c	1.26	7.90±1.02	AGAL	1.35±0.09	5.7×10^{-7}
G32.7496–0.0642	0.90	2.15±0.24	BAYE	7.92±0.35	2.5×10^{-7}
G33.6412–0.2276	5.76	7.60±1.19	AGAL	621.52±1.25	2.4×10^{-4}
G33.7258–0.1202	4.14	9.79±0.38	BAYE	19.53±0.25	1.3×10^{-5}
G33.8520+0.0178	4.32	10.50±0.43	AGAL	29.29±0.17	2.2×10^{-5}
G33.9798–0.0189	6.66	2.90±0.10	AGAL	25.56±0.26	1.5×10^{-6}
G33.0925–0.0725	10.08	6.83±0.58	BAYE	118.68±0.62	3.7×10^{-5}
G33.1328–0.0916	5.58	9.40±0.43	AGAL	79.80±0.40	4.8×10^{-5}

Continuation of Table C.2

Name (glon, glat) (1)	$\Delta V_{\rm B}$ (km s^{-1}) (2)	Dist. (kpc) (3)	Note (4)	$S_{\rm Int}$ (Jy km s^{-1}) (5)	$L_{\rm maser,B}$ ($L_\odot$) (6)
G33.1996+0.0010	1.44	6.83±0.56	BAYE	1.90±0.17	6.0×10^{-7}
G33.2037–0.0101	2.88	8.80±2.40	AGAL	5.81±0.17	3.0×10^{-6}
G33.3174–0.3599	1.80	2.20±0.43	AGAL	4.72±0.13	1.5×10^{-7}
G33.3930+0.0097	11.16	8.80±2.43	AGAL	218.16±1.02	1.1×10^{-4}
G33.4246–0.3150	0.90	2.51±0.18	BAYE	1.64±0.08	7.0×10^{-8}
G33.4870+0.0407	2.70	6.80±1.40	BAYE	14.40±0.28	4.5×10^{-6}
G33.6339–0.0206	2.52	8.80±2.40	AGAL	6.36±0.16	3.3×10^{-6}
G34.7510–0.0925	3.24	3.10±0.43	AGAL	31.27±0.22	2.0×10^{-6}
G34.7567+0.0250	0.90	4.80±0.41	AGAL	3.59±0.07	5.6×10^{-7}
G34.8221+0.3518	0.36	3.40±0.43	AGAL	0.55±0.18	4.3×10^{-8}
G34.2839+0.1837b	1.08	2.90±0.10	AGAL	1.34±0.16	7.6×10^{-8}
G34.0957+0.0178	3.60	2.90±0.10	AGAL	22.20±0.18	1.3×10^{-6}
G34.1953–0.5928	1.62	3.60±0.43	AGAL	3.57±0.16	3.1×10^{-7}
G34.2448+0.1333	7.74	2.90±0.10	AGAL	56.61±0.45	3.2×10^{-6}
G34.2582+0.1534	3.60	2.90±0.10	AGAL	82.38±0.53	4.7×10^{-6}
G34.2582+0.1534b	1.44	2.90±0.10	AGAL	5.39±0.09	3.1×10^{-7}
G34.2672–0.2094	3.60	3.10±0.47	AGAL	30.87±0.20	2.0×10^{-6}
G34.2839+0.1837	0.54	2.90±0.10	AGAL	0.63±0.10	3.6×10^{-8}
G34.3957+0.2215	6.48	9.82±0.39	BAYE	100.71±0.48	6.6×10^{-5}
G34.4113+0.2349	1.08	2.90±0.10	AGAL	1.89±0.17	1.1×10^{-7}
G35.4571–0.1782	2.34	4.10±0.43	AGAL	2.30±0.12	2.6×10^{-7}
G35.5879+0.0605	2.16	10.40±0.27	AGAL	3.07±0.19	2.2×10^{-6}
G35.7927–0.1744	8.10	8.80±1.03	AGAL	163.46±0.99	8.5×10^{-5}
G35.0248+0.3497	5.76	2.30±0.22	AGAL	106.08±0.44	3.8×10^{-6}
G35.1327–0.7440	7.02	2.20±0.20	AGAL	151.20±1.41	4.9×10^{-6}
G35.1491+0.8095	0.36	4.80±0.43	AGAL	0.43±0.07	6.7×10^{-8}
G35.1973–0.7428	2.88	2.20±0.22	AGAL	446.23±2.40	1.5×10^{-5}
G35.1973–0.7428b	9.54	2.20±0.22	AGAL	458.38±1.14	1.5×10^{-5}
G35.2260–0.3544	0.72	9.43±0.36	BAYE	1.28±0.20	7.7×10^{-7}
G35.2476–0.2365	0.54	4.84±0.61	BAYE	2.78±0.07	4.4×10^{-7}
G35.3974+0.0252	0.90	5.90±0.54	AGAL	1.11±0.06	2.6×10^{-7}
G35.4166–0.2839	0.90	3.20±0.43	AGAL	2.47±0.07	1.7×10^{-7}

Bibliography

Aguirre, J. E., Ginsburg, A. G., Dunham, M. K., et al. 2011, ApJS, 192, 4 (Cited on page 38.)

André, P. 2002, Ap&SS, 281, 51 (Cited on page 4.)

Araya, E. D., Hofner, P., Goss, W. M., et al. 2010, ApJ, 717, L133 (Cited on pages 64 and 82.)

Barnes, A. T., Longmore, S. N., Battersby, C., et al. 2017, MNRAS, 469, 2263 (Cited on page 20.)

Barrett, A. H., Ho, P., & Martin, R. N. 1975, ApJ, 198, L119 (Cited on page 8.)

Barrett, A. H., Schwartz, P. R., & Waters, J. W. 1971a, ApJ, 168, L101 (Cited on page 8.)

Barrett, A. H., Schwartz, P. R., & Waters, J. W. 1971b, ApJ, 168, L101 (Cited on page 57.)

Batrla, W., Matthews, H. E., Menten, K. M., & Walmsley, C. M. 1987, Nature, 326, 49 (Cited on pages 8, 57 and 60.)

Becker, R. 1990, Ph.D. Thesis (Cited on page 38.)

Becker, R. H., White, R. L., Helfand, D. J., & Zoonematkermani, S. 1994, ApJS, 91, 347 (Cited on pages 7 and 38.)

Beuther, H., Bihr, S., Rugel, M., et al. 2016, A&A, 595, A32 (Cited on page 38.)

Beuther, H., Leurini, S., Schilke, P., et al. 2007, AAP, 466, 1065 (Cited on page 4.)

Beuther, H., Walsh, A., Schilke, P., et al. 2002, A&A, 390, 289 (Cited on pages 60 and 77.)

Bihr, S., Beuther, H., Ott, J., et al. 2015, A&A, 580, A112 (Cited on page 38.)

Billington, S. J., Urquhart, J. S., König, C., et al. 2019, MNRAS, 490, 2779 (Cited on pages 9, 58, 60, 91 and 92.)

Boggess, N. W., Mather, J. C., Weiss, R., et al. 1992, ApJ, 397, 420 (Cited on page 52.)

Bonnell, I. A. & Bate, M. R. 2006, MNRAS, 370, 488 (Cited on page 4.)

Breen, S. L., Ellingsen, S. P., Caswell, J. L., et al. 2016, MNRAS, 459, 4066 (Cited on page 76.)

Breen, S. L., Fuller, G. A., Caswell, J. L., et al. 2015, MNRAS, 450, 4109 (Cited on pages 18, 19, 57, 64, 70, 76 and 86.)

Brunthaler, A., Menten, K. M., Dzib, S. A., et al. 2021, A&A, 651, A85 (Cited on pages 38, 40, 41, 42, 43, 45, 46, 58, 64, 65 and 67.)

Brunthaler, A., Reid, M. J., Menten, K. M., et al. 2011, Astronomische Nachrichten, 332, 461 (Cited on page 72.)

Carey, S. J., Noriega-Crespo, A., Mizuno, D. R., et al. 2009, PASP, 121, 76 (Cited on page 38.)

Caswell, J. L. 1996a, MNRAS, 283, 606 (Cited on pages 19, 57 and 64.)

Caswell, J. L. 1996b, MNRAS, 283, 606 (Cited on page 19.)

Caswell, J. L., Fuller, G. A., Green, J. A., et al. 2010, MNRAS, 404, 1029 (Cited on pages 18, 19, 57, 64 and 70.)

Caswell, J. L., Fuller, G. A., Green, J. A., et al. 2011, MNRAS, 417, 1964 (Cited on pages 18, 19, 57, 64 and 70.)

Caswell, J. L., Vaile, R. A., Ellingsen, S. P., Whiteoak, J. B., & Norris, R. P. 1995, MNRAS, 272, 96 (Cited on pages 8, 17, 57, 64 and 76.)

Cesaroni, R., Pestalozzi, M., Beltrán, M. T., et al. 2015, A&A, 579, A71 (Cited on page 40.)

Cheung, A. C., Rank, D. M., Townes, C. H., Thornton, D. D., & Welch, W. J. 1969, Nature, 221, 626 (Cited on page 8.)

Churchwell, E., Babler, B. L., Meade, M. R., et al. 2009, PASP, 121, 213 (Cited on page 38.)

Clark, B. G. 1980, A&A, 89, 377 (Cited on page 49.)

Clark, P. C., Glover, S. C. O., Ragan, S. E., Shetty, R., & Klessen, R. S. 2013, ApJ, 768, L34 (Cited on page 20.)

Cohen, R. J. 1989, Reports on Progress in Physics, 52, 881 (Cited on page 17.)

Cotton, W. D. 2008, PASP, 120, 439 (Cited on page 46.)

Cragg, D. M., Johns, K. P., Godfrey, P. D., & Brown, R. D. 1992, MNRAS, 259, 203 (Cited on pages 15 and 57.)

Crowther, P. A., Schnurr, O., Hirschi, R., et al. 2010, MNRAS, 408, 731 (Cited on page 4.)

Csengeri, T., Urquhart, J. S., Schuller, F., et al. 2014, A&A, 565, A75 (Cited on page 38.)

Dame, T. M., Hartmann, D., & Thaddeus, P. 2001, ApJ, 547, 792 (Cited on pages 59 and 91.)

Davies, B., Hoare, M. G., Lumsden, S. L., et al. 2011, Monthly Notices of the Royal Astronomical Society, 416, 972 (Cited on page 53.)

Deharveng, L., Schuller, F., Anderson, L. D., et al. 2010, A&A, 523, A6 (Cited on page 2.)

Dokara, R., Brunthaler, A., Menten, K. M., et al. 2021, arXiv e-prints, arXiv:2103.06267 (Cited on page 41.)

Draine, B. T. 2011, Physics of the Interstellar and Intergalactic Medium (41 William Street, Princeton, new Jersey 08540: Princeton University Press) (Cited on page 10.)

Dzib, S. A., Yang, A. Y., Urquhart, J. S., et al. 2022, arXiv e-prints, arXiv:2210.00560 (Cited on pages 41, 67, 77 and 94.)

Eden, D. J., Moore, T. J. T., Plume, R., et al. 2017, MNRAS, 469, 2163 (Cited on page 38.)

Elia, D., Molinari, S., Schisano, E., et al. 2017, MNRAS, 471, 100 (Cited on page 38.)

Elitzur, M. 1982, Rev. Mod. Phys., 54, 1225 (Cited on pages 10, 15 and 17.)

Ellingsen, S. P. 2006, ApJ, 638, 241 (Cited on pages 8 and 57.)

Ellingsen, S. P. 2007, MNRAS, 377, 571 (Cited on pages 18, 57 and 64.)

Ellingsen, S. P., von Bibra, M. L., McCulloch, P. M., et al. 1996, MNRAS, 280, 378 (Cited on pages 19, 57 and 64.)

Event Horizon Telescope Collaboration, Akiyama, K., Alberdi, A., et al. 2022, ApJ, 930, L12 (Cited on page 25.)

Event Horizon Telescope Collaboration, Akiyama, K., Alberdi, A., et al. 2019, ApJ, 875, L1 (Cited on page 25.)

Ferrière, K., Gillard, W., & Jean, P. 2007, A&A, 467, 611 (Cited on page 20.)

Figer, D. F., Najarro, F., Gilmore, D., et al. 2002, ApJ, 581, 258 (Cited on page 20.)

Gao, Y. & Solomon, P. M. 2004, ApJ, 606, 271 (Cited on page 21.)

Garay, G., Rodriguez, L. F., Moran, J. M., & Churchwell, E. 1993, ApJ, 418, 368 (Cited on page 7.)

Gaylard, M. J. & MacLeod, G. C. 1993, MNRAS, 262, 43 (Cited on page 17.)

Ginsburg, A., Henkel, C., Ao, Y., et al. 2016, A&A, 586, A50 (Cited on page 20.)

Goedhart, S., Gaylard, M. J., & van der Walt, D. J. 2004, MNRAS, 355, 553 (Cited on pages 64 and 79.)

Goedhart, S., Gaylard, M. J., & van der Walt, D. J. 2007, in Astrophysical Masers and their Environments, ed. J. M. Chapman & W. A. Baan, Vol. 242, 97–101 (Cited on page 79.)

Goedhart, S., Langa, M. C., Gaylard, M. J., & Van Der Walt, D. J. 2009, MNRAS, 398, 995 (Cited on page 79.)

Gravity Collaboration, Abuter, R., Amorim, A., et al. 2019, A&A, 625, L10 (Cited on page 20.)

Green, J. A., Caswell, J. L., Fuller, G. A., et al. 2009, MNRAS, 392, 783 (Cited on pages 19, 58 and 70.)

Green, J. A., Caswell, J. L., Fuller, G. A., et al. 2010, MNRAS, 409, 913 (Cited on pages 18, 19, 57, 64 and 70.)

Green, J. A., Caswell, J. L., Fuller, G. A., et al. 2012, MNRAS, 420, 3108 (Cited on pages 18, 19, 57, 64 and 70.)

Green, J. A., Caswell, J. L., Fuller, G. A., et al. 2008, MNRAS, 385, 948 (Cited on page 19.)

Greisen, E. W. 2003, Information Handling in Astronomy - Historical Vistas ed. A. Heck, 109, Vol. 285 (Springer) (Cited on page 46.)

Habing, H. J. & Israel, F. P. 1979, ARA&A, 17, 345 (Cited on page 7.)

Hales, C. A., Murphy, T., Curran, J. R., et al. 2012, Monthly Notices of the Royal Astronomical Society, 425, 979 (Cited on page 77.)

Han, J. L., Reich, W., Sun, X. H., et al. 2015, Highlights of Astronomy, 16, 394 (Cited on page 38.)

Henshaw, J. D., Barnes, A. T., Battersby, C., et al. 2022, arXiv e-prints, arXiv:2203.11223 (Cited on page 20.)

Hoare, M. G., Purcell, C. R., Churchwell, E. B., et al. 2012, PASP, 124, 939 (Cited on page 38.)

Högbom, J. A. 1974, A&AS, 15, 417 (Cited on pages 36 and 48.)

Hu, B., Menten, K. M., Wu, Y., et al. 2016, The Astrophysical Journal, 833, 18 (Cited on pages 60, 63, 75, 77 and 92.)

Impellizzeri, C. M. V., Henkel, C., Roy, A. L., & Menten, K. M. 2008, A&A, 484, L43 (Cited on page 96.)

Inayoshi, K., Sugiyama, K., Hosokawa, T., Motogi, K., & Tanaka, K. E. I. 2013, ApJ, 769, L20 (Cited on page 64.)

Irabor, T., Hoare, M. G., Oudmaijer, R. D., et al. 2018, MNRAS, 480, 2423 (Cited on page 40.)

Jenkins, F. & White, H. 2001, Fundamentals of Optics, 4th ed. (McGraw-Hill, New York), chap. 13 (Cited on page 31.)

Kahn, F. D. 1974, A&A, 37, 149 (Cited on page 3.)

Kalcheva, I. E., Hoare, M. G., Urquhart, J. S., et al. 2018, A&A, 615, A103 (Cited on page 40.)

Kauffmann, J., Pillai, T., Zhang, Q., et al. 2017a, A&A, 603, A89 (Cited on pages 21, 54 and 90.)

Kauffmann, J., Pillai, T., Zhang, Q., et al. 2017b, A&A, 603, A90 (Cited on page 20.)

Klein, T. 2014, Lecture notes. Radio astronomy, tools, applications and impacts (Cited on page 25.)

Kojima, Y., Fujisawa, K., & Motogi, K. 2017, Proceedings of the International Astronomical Union, 13, 336â337 (Cited on page 84.)

König, C., Urquhart, J. S., Csengeri, T., et al. 2017, A&A, 599, A139 (Cited on page 38.)

Kroupa, P. 2001, MNRAS, 322, 231 (Cited on pages 2, 54 and 90.)

Kruijssen, J. M. D., Longmore, S. N., Elmegreen, B. G., et al. 2014, MNRAS, 440, 3370 (Cited on page 20.)

Krumholz, M. R. & Bonnell, I. A. 2007, arXiv e-prints, arXiv:0712.0828 (Cited on page 4.)

Krumholz, M. R., Klein, R. I., McKee, C. F., Offner, S. S. R., & Cunningham, A. J. 2009, Science, 323, 754 (Cited on page 4.)

Krumholz, M. R. & Kruijssen, J. M. D. 2015, MNRAS, 453, 739 (Cited on page 20.)

Krumholz, M. R., Kruijssen, J. M. D., & Crocker, R. M. 2017, MNRAS, 466, 1213 (Cited on page 20.)

Kurtz, S., Churchwell, E., & Wood, D. O. S. 1994, ApJS, 91, 659 (Cited on page 7.)

Lada, C. J. 1999, The Origin of Stars and Planetary Systems, 540 (Cited on pages 3 and 4.)

Lada, C. J., Lombardi, M., & Alves, J. F. 2010, ApJ, 724, 687 (Cited on pages 20 and 21.)

Larson, R. B. 2003, Reports on Progress in Physics, 66, 1651 (Cited on pages 2 and 3.)

Leurini, S., Menten, K. M., & Walmsley, C. M. 2016, A&A, 592, A31 (Cited on page 57.)

Lis, D. C. & Goldsmith, P. F. 1990, ApJ, 356, 195 (Cited on page 20.)

Lis, D. C., Serabyn, E., Zylka, R., & Li, Y. 2001, ApJ, 550, 761 (Cited on page 20.)

Longmore, S. N., Bally, J., Testi, L., et al. 2013, MNRAS, 429, 987 (Cited on pages 20 and 21.)

Longmore, S. N., Rathborne, J., Bastian, N., et al. 2012, ApJ, 746, 117 (Cited on page 20.)

Lu, X., Zhang, Q., Kauffmann, J., et al. 2019, ApJ, 872, 171 (Cited on page 20.)

MacLeod, G. C. & Gaylard, M. J. 1992, MNRAS, 256, 519 (Cited on page 17.)

MacLeod, G. C., Gaylard, M. J., & Nicolson, G. D. 1992, MNRAS, 254, 1P (Cited on pages 17, 57 and 64.)

McClure-Griffiths, N. M., Dickey, J. M., Gaensler, B. M., et al. 2005, ApJS, 158, 178 (Cited on page 38.)

McKee, C. F. & Ostriker, E. C. 2007, ARA&A, 45, 565 (Cited on page 3.)

McKee, C. F. & Tan, J. C. 2003, ApJ, 585, 850 (Cited on page 4.)

Medina, S. N. X., Urquhart, J. S., Dzib, S. A., et al. 2019, A&A, 627, A175 (Cited on pages 41, 42, 46 and 65.)

Menten, K. M. 1991a, in Astronomical Society of the Pacific Conference Series, Vol. 16, Atoms, Ions and Molecules: New Results in Spectral Line Astrophysics, ed. A. D. Haschick & P. T. P. Ho, 119–136 (Cited on pages 17 and 57.)

Menten, K. M. 1991b, ApJ, 380, L75 (Cited on pages 8, 15, 57, 64 and 96.)

Menten, K. M. 1993, in Astrophysical Masers, ed. A. W. Clegg & G. E. Nedoluha (Berlin, Heidelberg: Springer Berlin Heidelberg), 199–202 (Cited on pages 57 and 64.)

Menten, K. M., Reid, M. J., Pratap, P., Moran, J. M., & Wilson, T. L. 1992, ApJ, 401, L39 (Cited on page 60.)

Mezger, P. G. & Henderson, A. P. 1967, ApJ, 147, 471 (Cited on page 7.)

Minier, V., Burton, M. G., Wong, T., Purcell, C., & Hill, T. 2003, in IAU Symposium, Vol. 221, IAU Symposium (Cited on pages 8, 57 and 64.)

Molinari, S., Swinyard, B., Bally, J., et al. 2010, A&A, 518, L100 (Cited on page 38.)

Moore, T. J. T., Plume, R., Thompson, M. A., et al. 2015, MNRAS, 453, 4264 (Cited on page 38.)

Morris, M. & Serabyn, E. 1996, ARA&A, 34, 645 (Cited on pages 20 and 51.)

Motte, F., Bontemps, S., & Louvet, F. 2018, ARA&A, 56, 41 (Cited on pages 2, 5, 6 and 16.)

Murray, N. & Chang, P. 2012, ApJ, 746, 75 (Cited on page 4.)

Nandakumar, G., Schultheis, M., Feldmeier-Krause, A., et al. 2018, A&A, 609, A109 (Cited on pages 51, 52, 53, 54, 89, 90 and 96.)

Neugebauer, G., Habing, H. J., van Duinen, R., et al. 1984, ApJ, 278, L1 (Cited on page 17.)

Nguyen, H., Rugel, M. R., Menten, K. M., et al. 2021, A&A, 651, A88 (Cited on pages 20, 53, 54 and 261.)

Nguyen, H., Urquhart, J., Brunthaler, A., et al. 2022, A&A, accepted, 1 (Cited on pages 18, 50, 59, 60, 64, 65, 66, 67, 68, 70, 77, 94 and 261.)

Olech, M., Szymczak, M., Wolak, P., Sarniak, R., & Bartkiewicz, A. 2019, MNRAS, 486, 1236 (Cited on pages 64 and 84.)

Ortiz-León, G. N., Menten, K. M., Brunthaler, A., et al. 2021, A&A, 651, A87 (Cited on pages 18, 57, 60, 61, 64, 68, 72 and 96.)

Pandian, J. D., Goldsmith, P. F., & Deshpande, A. A. 2007, ApJ, 656, 255 (Cited on pages 18, 19, 57, 58 and 64.)

Pandian, J. D., Leurini, S., Menten, K. M., Belloche, A., & Goldsmith, P. F. 2008, A&A, 489, 1175 (Cited on page 96.)

Pandian, J. D., Menten, K. M., & Goldsmith, P. F. 2009, ApJ, 706, 1609 (Cited on page 61.)

Parfenov, S. Y. & Sobolev, A. M. 2014, MNRAS, 444, 620 (Cited on page 64.)

Perley, R. A. & Butler, B. J. 2013a, ApJS, 204, 19 (Cited on page 47.)

Perley, R. A. & Butler, B. J. 2013b, ApJS, 206, 16 (Cited on page 47.)

Perley, R. A., Chandler, C. J., Butler, B. J., & Wrobel, J. M. 2011, ApJ, 739, L1 (Cited on pages 40 and 58.)

Pestalozzi, M. R., Minier, V., & Booth, R. S. 2005, A&A, 432, 737 (Cited on pages 17, 18, 57 and 64.)

Purcell, C. R., Hoare, M. G., Cotton, W. D., et al. 2013, ApJS, 205, 1 (Cited on page 38.)

Reber, G. 1944, ApJ, 100, 279 (Cited on page 25.)

Reid, M. J., Menten, K. M., Brunthaler, A., et al. 2019, ApJ, 885, 131 (Cited on pages 59, 60, 70, 72 and 91.)

Reid, M. J. & Moran, J. M. 1988, in Galactic and Extragalactic Radio Astronomy, ed. K. I. Kellermann & G. L. Verschuur, 255–294 (Cited on page 17.)

Rickert, M., Yusef-Zadeh, F., & Ott, J. 2019, MNRAS, 482, 5349 (Cited on pages 18, 19, 57 and 64.)

Robitaille, T. P., Meade, M. R., Babler, B. L., et al. 2008, The Astronomical Journal, 136, 2413 (Cited on page 38.)

Roman-Duval, J., Jackson, J. M., Heyer, M., et al. 2009, ApJ, 699, 1153 (Cited on page 70.)

Salpeter, E. E. 1955, ApJ, 121, 161 (Cited on page 2.)

Sanna, A., Menten, K. M., Carrasco-González, C., et al. 2015, ApJ, 804, L2 (Cited on page 64.)

Schmiedeke, A., Schilke, P., Möller, T., et al. 2016, A&A, 588, A143 (Cited on page 20.)

Schneider, F. R. N., Izzard, R. G., de Mink, S. E., et al. 2014, ApJ, 780, 117 (Cited on page 20.)

Schuller, F., Menten, K. M., Contreras, Y., et al. 2009a, A&A, 504, 415 (Cited on pages 22 and 70.)

Schuller, F., Menten, K. M., Contreras, Y., et al. 2009b, A&A, 504, 415 (Cited on page 38.)

Schuller, F., Urquhart, J. S., Csengeri, T., et al. 2021, MNRAS, 500, 3064 (Cited on pages 59 and 91.)

Schutte, A. J., van der Walt, D. J., Gaylard, M. J., & MacLeod, G. C. 1993, MNRAS, 261, 783 (Cited on page 17.)

Shu, F. H., Adams, F. C., & Lizano, S. 1987, ARA&A, 25, 23 (Cited on pages 3 and 4.)

Slysh, V. I., Val'tts, I. E., Kalenskii, S. V., et al. 1999, A&AS, 134, 115 (Cited on page 18.)

Slysh, V. I., Voronkov, M. A., Migenes, V., et al. 2001, MNRAS, 320, 217 (Cited on page 76.)

Smith, R. J., Longmore, S., & Bonnell, I. 2009, Monthly Notices of the Royal Astronomical Society, 400, 1775 (Cited on page 5.)

Sobolev, A. M., Ostrovskii, A. B., Kirsanova, M. S., et al. 2006, arXiv e-prints, astro (Cited on page 15.)

Spitzer, L. 1978, Physical processes in the interstellar medium (Cited on page 3.)

Stil, J. M., Taylor, A. R., Dickey, J. M., et al. 2006, AJ, 132, 1158 (Cited on page 38.)

Strömgren, B. 1939, ApJ, 89, 526 (Cited on page 7.)

Sugiyama, K., Nagase, K., Yonekura, Y., et al. 2017, PASJ, 69, 59 (Cited on page 82.)

Surcis, G., Vlemmings, W. H. T., van Langevelde, H. J., Hutawarakorn Kramer, B., & Bartkiewicz, A. 2019, A&A, 623, A130 (Cited on page 76.)

Szymczak, M., Hrynek, G., & Kus, A. J. 2000, A&AS, 143, 269 (Cited on page 18.)

Szymczak, M. & Kus, A. J. 2000, A&A, 360, 311 (Cited on page 18.)

Szymczak, M., Kus, A. J., Hrynek, G., Kěpa, A., & Pazderski, E. 2002, A&A, 392, 277 (Cited on page 19.)

Szymczak, M., Olech, M., Sarniak, R., Wolak, P., & Bartkiewicz, A. 2018, MNRAS, 474, 219 (Cited on page 64.)

Szymczak, M., Pillai, T., & Menten, K. M. 2005, A&A, 434, 613 (Cited on page 75.)

Szymczak, M., Wolak, P., & Bartkiewicz, A. 2015, MNRAS, 448, 2284 (Cited on page 82.)

Szymczak, M., Wolak, P., Bartkiewicz, A., & van Langevelde, H. J. 2011, A&A, 531, L3 (Cited on page 82.)

Taylor, A. R., Gibson, S. J., Peracaula, M., et al. 2003, AJ, 125, 3145 (Cited on page 38.)

Taylor, J. H. & Cordes, J. M. 1993, ApJ, 411, 674 (Cited on pages 59 and 91.)

Thomasson, P. 1986, QJRAS, 27, 413 (Cited on page 70.)

Thompson, A. R. 1999, in Astronomical Society of the Pacific Conference Series, Vol. 180, Synthesis Imaging in Radio Astronomy II, ed. G. B. Taylor, C. L. Carilli, & R. A. Perley, 11 (Cited on pages 25 and 34.)

Thompson, A. R., Moran, J. M., & Swenson, George W., J. 2017, Interferometry and Synthesis in Radio Astronomy, 3rd Edition (Cited on page 68.)

Thompson, M. A., Urquhart, J. S., Moore, T. J. T., & Morgan, L. K. 2012, MNRAS, 421, 408 (Cited on page 2.)

Tielens, A. G. G. M. 2005, The Physics and Chemistry of the Interstellar Medium (Cambridge Univ. Press) (Cited on page 9.)

Tielens, A. G. G. M. & Hagen, W. 1982, A&A, 114, 245 (Cited on page 9.)

Tigé, J., Motte, F., Russeil, D., et al. 2017, A&A, 602, A77 (Cited on pages 6 and 16.)

Urquhart, J. S., Busfield, A. L., Hoare, M. G., et al. 2007, A&A, 461, 11 (Cited on page 2.)

Urquhart, J. S., König, C., Giannetti, A., et al. 2018a, MNRAS, 473, 1059 (Cited on page 40.)

Urquhart, J. S., König, C., Giannetti, A., et al. 2018b, MNRAS, 473, 1059 (Cited on pages 69, 70, 72, 76 and 178.)

Urquhart, J. S., König, C., Giannetti, A., et al. 2018c, MNRAS, 473, 1059 (Cited on page 38.)

Urquhart, J. S., Moore, T. J. T., Menten, K. M., et al. 2015, MNRAS, 446, 3461 (Cited on pages 9 and 60.)

Urquhart, J. S., Moore, T. J. T., Schuller, F., et al. 2013a, MNRAS, 431, 1752 (Cited on pages 9 and 60.)

Urquhart, J. S., Thompson, M. A., Moore, T. J. T., et al. 2013b, MNRAS, 435, 400 (Cited on page 40.)

Urquhart, J. S., Wells, M. R. A., Pillai, T., et al. 2022, MNRAS, 510, 3389 (Cited on pages 69, 70, 72, 92 and 178.)

van der Walt, D. J. 2011, Bulletin de la Societe Royale des Sciences de Liege, 80, 260 (Cited on page 64.)

van der Walt, D. J., Gaylard, M. J., & MacLeod, G. C. 1995, A&AS, 110, 81 (Cited on page 18.)

van der Walt, D. J., Goedhart, S., & Gaylard, M. J. 2009, MNRAS, 398, 961 (Cited on pages 64 and 79.)

van der Walt, D. J., Maswanganye, J. P., Etoka, S., Goedhart, S., & van den Heever, S. P. 2016, A&A, 588, A47 (Cited on page 79.)

van der Walt, D. J., Retief, S. J. P., Gaylard, M. J., & MacLeod, G. C. 1996, MNRAS, 282, 1085 (Cited on pages 57 and 64.)

van Dishoeck, E. F. & Blake, G. A. 1998, ARA&A, 36, 317 (Cited on pages 9 and 16.)

van Dishoeck, E. F. & Hogerheijde, M. R. 1999, in NATO Advanced Study Institute (ASI) Series C, Vol. 540, The Origin of Stars and Planetary Systems, ed. C. J. Lada & N. D. Kylafis, 97 (Cited on page 9.)

Vázquez-Semadeni, E., Gómez, G. C., Jappsen, A.-K., Ballesteros-Paredes, J., & Klessen, R. S. 2009, The Astrophysical Journal, 707, 1023 (Cited on page 5.)

Voronkov, M. A., Caswell, J. L., Ellingsen, S. P., Green, J. A., & Breen, S. L. 2014, MNRAS, 439, 2584 (Cited on page 57.)

Voronkov, M. A., Caswell, J. L., Ellingsen, S. P., & Sobolev, A. M. 2010, MNRAS, 405, 2471 (Cited on page 57.)

Walsh, A. J., Breen, S. L., Britton, T., et al. 2011, MNRAS, 416, 1764 (Cited on page 38.)

Walsh, A. J., Burton, M. G., Hyland, A. R., & Robinson, G. 1998, MNRAS, 301, 640 (Cited on pages 57, 60, 64 and 77.)

Walsh, A. J., Hyland, A. R., Robinson, G., & Burton, M. G. 1997, MNRAS, 291, 261 (Cited on pages 18, 57 and 64.)

Walsh, A. J., Purcell, C. R., Longmore, S. N., et al. 2014, MNRAS, 442, 2240 (Cited on page 68.)

Wang, Y., Beuther, H., Rugel, M. R., et al. 2020, A&A, 634, A83 (Cited on page 38.)

Weaver, H., Williams, D. R. W., Dieter, N. H., & Lum, W. T. 1965, Nature, 208, 29 (Cited on page 8.)

Wilson, T. L., Rohlfs, K., & Huttemeister, S. 2012, Tools of Radio Astronomy, 5th edition (Cited on pages 26, 29 and 31.)

Wilson, T. L., Rohlfs, K., & Hüttemeister, S. 2013, Tools of Radio Astronomy (Cited on pages 25 and 37.)

Wolfire, M. G. & Cassinelli, J. P. 1987, ApJ, 319, 850 (Cited on page 4.)

Wood, D. O. S. & Churchwell, E. 1989, ApJ, 340, 265 (Cited on pages 7 and 17.)

Wright, E. L., Eisenhardt, P. R. M., Mainzer, A. K., et al. 2010, AJ, 140, 1868 (Cited on pages 18 and 38.)

Xu, Y., Li, J. J., Hachisuka, K., et al. 2008, A&A, 485, 729 (Cited on pages 8, 57 and 64.)

Yang, A., Urquhart, J., Brunthaler, A., et al. in prep, A&A, in prep, 1 (Cited on page 41.)

Yang, A. Y., Thompson, M. A., Tian, W. W., et al. 2019a, MNRAS, 482, 2681 (Cited on page 77.)

Yang, A. Y., Urquhart, J. S., Thompson, M. A., et al. 2021, A&A, 645, A110 (Cited on page 77.)

Yang, K., Chen, X., Shen, Z.-Q., et al. 2019b, ApJS, 241, 18 (Cited on pages 18, 57, 58 and 64.)

Yang, K., Chen, X., Shen, Z.-Q., et al. 2017, ApJ, 846, 160 (Cited on page 18.)

Yorke, H. W. & Sonnhalter, C. 2002, ApJ, 569, 846 (Cited on page 4.)

Zhang, B., Moscadelli, L., Sato, M., et al. 2014, ApJ, 781, 89 (Cited on page 75.)

Zinnecker, H. & Yorke, H. W. 2007, ARA&A, 45, 481 (Cited on page 2.)

Nomenclature

Frequently Used Acronyms

APEX	Atacama Pathfinder Experiment
ATLASGAL	APEX Telescope Large Area Survey of the Galaxy
CMB	Cosmic microwave background
CMZ	Central molecular zone
FIR	Far infrared
FWHM	Full width at half maximum
GC	Galactic centre
GLOSTAR	Global view on star formation in the Milky Way
GMC	Giant molecular cloud
IMF	Initial mass function
HC	Hyper-compact
HMC	Hot molecular core
HPBW	Half power beam width
ISM	Interstellar medium
(J)VLA	Karl G. Jansky Very Large Array
MDC	Massive dense core
MIR	mid-infrared
MMB	Methanol multi-beam
(M)YSO	(Massive) Young stellar object
NIR	Near infrared
PA	Position angle
PIM	Peak intensity map
PV	Position-velocity
S/N	Signal-to-noise ratio
SEC	Source Extraction Code
SFR	Star formation rate
UC	Ultra-compact
UV	ultraviolet
WISE	Wide-field Infrared Survey Explorer

Numerical Constants

π	$= 3.14156$
$1\,\mathrm{rad}$	$= 57.296\,\mathrm{degrees}$
e	$= 2.7183$

Physical Constants

Speed of light	$c = 2.9979 \times 10^{10}\,\mathrm{cm\,sec^{-1}}$
Planck's constant	$h = 6.626 \times 10^{-27}\,\mathrm{erg\,sec}$
Boltzmann's constant	$k_\mathrm{B} = 1.381 \times 10^{-16}\,\mathrm{erg\,deg^{-1}}$
Stefan–Boltzmann constant	$\sigma = 5.6704 \times 10^{-5}\,\mathrm{erg\,cm^{-2}\,s^{-1}\,K^{-4}}$
Electron mass	$m_\mathrm{e} = 9.110 \times 10^{-28}\,\mathrm{gr}$
Proton mass	$m_\mathrm{p} = 1.673 \times 10^{-24}\,\mathrm{gr}$
Mass of hydrogen atom	$m_\mathrm{H} = 1.673 \times 10^{-24}\,\mathrm{gr}$

Astronomical Constants

Astronomical unit ($1\,\mathrm{AU}$)	$= 1.496 \times 10^{13}\,\mathrm{cm}$
Parcec ($1\,\mathrm{pc}$)	$= 3.086 \times 10^{18}\,\mathrm{cm}$
Julian light year ($1\,\mathrm{ly}$)	$= 9.460730472 \times 10^{17}\,\mathrm{cm}$
Julian year ($1\,\mathrm{yr}$)	$= 3.15576 \times 10^{7}\,\mathrm{sec}$
Solar mass ($1\,\mathrm{M_\odot}$)	$= 1.989 \times 10^{27}\,\mathrm{gr}$
Solar luminosity ($1\,\mathrm{L_\odot}$)	$= 3.9 \times 10^{33}\,\mathrm{erg\,s^{-1}}$

List of Figures

List of Tables

Acknowledgements

This thesis is the written amalgamation of my impact (albeit minor) on the scientific progress of humanity. To get this far, I have had the opportunity of working with exemplary scientists and the luxury of meeting close friends. Now, at the end of this journey, I am left to reminisce on *their* impact on me.

In no specific order, I would like to first thank Dr. Quang Nguyen-Luong for starting me on this journey. If not for you, I would not have travelled to Germany to continue my studies.

A most profound thank you goes to Prof. Dr. Karl Menten who welcomed me into his group and trusted me with a project. Thank you for your understanding and for motivating me during the difficult times of this thesis. I also thank my thesis committee members Prof. Dr. Pavel Kroupa, Prof. Dr. Jochen Dingfelder, and Prof. Dr. Heiko Röglin for helping this thesis get across the finish line.

I spent my time at MPIfR working as part of the GLOSTAR collaboration and a big thank you goes out to all of its members. Thank you, Andreas Brunthaler for not only supervising me during my PhD but also during my Master's thesis. Now that I am finished, there will be more MCN space available! Thank you also to James Urquhart for asking the hard questions and giving very thorough comments on all my manuscripts. I attribute the quick submission of my publications in no small part to you. Thank you, Sergio Dzib for helping me along the way with all my CASA and calibration problems. You always seem to have the answer! Thanks also to Friedrich Wyrowski, Aiyuan Yang, Yan Gong, Gisela Ortiz-León, Jagadheep Pandian, and Sac Medina for their collaboration and help along the way. I'm sure the new members of GLOSTAR will be in great hands. A very grateful thanks goes to Michael Rugel. During your time at MPIfR, it is not an exaggeration to say that my thesis would not have come this far without your help. Your continued support and passion for science truly helped me to reach the end. Thank you also to Le Ngoc Tram for reading my manuscript. I would like to thank Dirk for his patience and for solving my IT issues. A warm thank you goes to Eva S., Barbara M., and Tuyet-Le T. for dealing with all the paperwork and making my time at MPIfR smooth.

Naturally, this thesis would not have come to fruition without the people I have the pleasure of calling friend. Gautam R., we've come a long way since that BCGS week in 2013. What started as you asking for Wi-Fi has turned into a lifelong friendship. Thanks for always convincing me to come along on your adventures even if we find ourselves in questionable circumstances. May our next trip fit somewhere between the excitement levels of Scotland and Nice. A Barcelona type trip now and then couldn't hurt either. Joseph K., I am deeply grateful for your advice which has guided me during some key moments in my life. The time we spent cooking (you), and eating (me) will never be forgotten. I appreciate everything you did in India to keep us alive! Laura V.G., thank you for the time we shared in Bonn together, without which, I would not have started this PhD journey.

A chalky thanks go to Jose G., Aya A., Tobi M., and Josi M., I looked forward to Sunday mornings for our bouldering sessions and for the much deserved beers right after. In particular Jose, mi padre, I know you appreciate the consequences of your inclusion. I look forward to 'seeing you soon', and surviving a few more trips with Gautam.

And to my fellow radio-lab monkeys Méllise B., Eric A., and Vishnu B., thanks for all the fun times we had developing the radio lab. To this day, I am still confused as to how we got some of those cables to work in the end.

Thank you to my fellow sub-mm students and post-docs, Manali J., Carsten K., Rosie C., Dario C., Veselina K., Parichay M., Michael M., Laure B., Ivalu B., Shampa B., and Laura B. for our conversations, always leaving me a little bit happier, and a little bit more motivated. Rohit D. and Sarwar K., you guys were a much-needed addition to the GLOSTAR group. I will remember fondly all the time we spent together at badminton, watching movies, or our discussions in general. Arshia J. and Dat H., I will forever cherish our sushi dates. Dat, thank you for putting up with me as your roommate, and for always making sure there is food for me to eat! Arshia, thanks for always wearing maroon on Wednesday, for always bringing me your news of the day, and for always checking in on me, even all the way from America.

To my officemates, past and present, Iason S., Yaoting Y., Richa S., Sac M., Ka Tat W., Nina B., and Fateme K., thanks for being a part of my journey in room 2.39, and always putting up with my random thoughts during the day. Especially Fateme and Nina, I know you both don't like getting sentimental, but I really feel like you have more than outgrown the title of 'officemate', and have been upgraded to 'Mitarbeiterin'. Thank you, Nina, for your questionable search history and thank you, Fateme, for always feeding me. And then we have Maitraiyee T., the honorary officemate who likes to pillage our office snacks. However, you do pay us back by being a very thoughtful and caring friend. I enjoyed the time we had as roommates and I really enjoyed your cooking, even your special 'cetmi' dish!

Thank you also to Tobias and Gül (strong), you both are so caring and thoughtful. Thanks for always checking up on me. I can't wait for our next road trip. Won-Ju! You always think of us and I am always so grateful for your advice, friendship, and also the supplies of Korean goodies you send my way. See you soon in Cologne!

To the badminton crew, Pritam P., Prajwal P., Jens E., and Maude C., I had a 'smashing' good time on and off the court and I am happy to call you my friends.

I also want to thank Benjamin S. for hosting the best parties Beuel has to offer, Rob M. and Yuki P. for partaking in Nintendo shenanigans and giving me delicious kimchi, Joey M. for introducing me to Sunday night NFL, Eleni G. for your uplifting and contagious laugh, Marilyn C. for always including me, Natasha P. for your 'unique' perspectives (and I promise one day I will have gossip worthy to share), Victoria Y. for never failing to brighten the room with your smile, Weiwei C. for always being my friend, and Benham J. for showing me the difference between 'pink' and 'red', or was it 'salmon'?

To my friends from Canada, Makaila H., Felicia M., and James C., a simple thank you is not enough to convey how much I appreciate your friendship and continued

support. I am sorry for all the missed milestones but the future is brighter and I can't wait to make more 'memories' with you guys. A special acknowledgement goes to Matt S., a true adventurer.

The Henning! I think everyone knows it was bromance at first sight. You are mi hermano sem mamma ól ekki and the fuego in mis pantalones. Thanks for all the codenames, legionnaires conquistadores, and OK beer.

There is truly nothing like the unconditional love and endless sacrifice of family. To that end, I want to thank my parents, Han and Nhung, and my siblings, San and Vithien for exactly this. Your support has kept me going all these years and I know it will continue to be the pillar that will help me go forward. I cannot thank you enough. To Ông Ngoại, Bà Ngoại, and Bà Nội, I wish I could have shared this with you, I wish I could have shared more time with you.

Now at the end of this rather lengthy document, I dedicate my appreciation to Franziska Leupold. These past years have shown me how fortunate I am to have met you. While I did not know you at the start of my PhD, suffice it to say that you, by far, have impacted me the most by the end of this journey. No matter which moment I look back on, you were supporting me during the hard times, and celebrating with me during the good times. Thank you for everything, thank you for being with me, and thank you for being you.